Perovskite materials for direct ionising radiation detection

Javier Mayén Guillén

▶ **To cite this version:**

Javier Mayén Guillén. Perovskite materials for direct ionising radiation detection. Chemical engineering. Université Grenoble Alpes [2020-..], 2023. English. NNT : 2023GRALI064 . tel-04352287

HAL Id: tel-04352287
https://theses.hal.science/tel-04352287

Submitted on 19 Dec 2023

HAL is a multi-disciplinary open access archive for the deposit and dissemination of scientific research documents, whether they are published or not. The documents may come from teaching and research institutions in France or abroad, or from public or private research centers.

L'archive ouverte pluridisciplinaire **HAL**, est destinée au dépôt et à la diffusion de documents scientifiques de niveau recherche, publiés ou non, émanant des établissements d'enseignement et de recherche français ou étrangers, des laboratoires publics ou privés.

THÈSE

Pour obtenir le grade de

DOCTEUR DE L'UNIVERSITÉ GRENOBLE ALPES

École doctorale : I-MEP2 - Ingénierie - Matériaux, Mécanique, Environnement, Energétique, Procédés, Production
Spécialité : 2MGE - Matériaux, Mécanique, Génie civil, Electrochimie
Unité de recherche : CEA Grenoble / LITEN

Matériaux pérovskites pour la détection directe de rayonnements ionisants

Perovskite materials for direct ionising radiation detection

Présentée par :

Javier Alejandro MAYEN GUILLEN

Direction de thèse :

Julien ZACCARO Chargé de recherche, Université Grenoble Alpes	Directeur de thèse
Jean-Marie VERILHAC CEA	Co-encadrant de thèse
Alain IBANEZ DIRECTEUR DE RECHERCHE, CNRS	Co-encadrant de thèse
Eric GROS D'AILLON CEA	Co-encadrant de thèse

Rapporteurs :

Valérie DUPRAY
MAITRESSE DE CONFERENCES HDR, Université de Rouen Normandie
Yvan BONNASSIEUX
PROFESSEUR, Ecole Polytechnique

Thèse soutenue publiquement le **26 septembre 2023**, devant le jury composé de :

Julien ZACCARO CHARGE DE RECHERCHE HDR, CNRS délégation Alpes	Directeur de thèse
Valérie DUPRAY MAITRESSE DE CONFERENCES HDR, Université de Rouen Normandie	Rapporteure
Yvan BONNASSIEUX PROFESSEUR, Ecole Polytechnique	Rapporteur
Elisabeth DJURADO PROFESSEURE DES UNIVERSITES, Grenoble INP	Présidente
Lionel HIRSCH DIRECTEUR DE RECHERCHE, CNRS délégation Aquitaine	Examinateur

Invités :

Eric GROS D'AILLON
DIRECTEUR DE RECHERCHE, CEA Grenoble
Alain IBANEZ
DIRECTEUR DE RECHERCHE, Institut Néel - Université Grenoble Alpes

Acknowledgements

One of the most significant chapters of my life has come to an end. I am filled with immense gratitude and satisfaction as I conclude this years-long journey of my PhD thesis, which materialises itself into this relatively simple manuscript. Naturally, an outsider or anyone who has not been through this process could say that most of the work has been done by me. However, like anything done in science, this thesis is the result of collaborative work within the "perovskite team" based here in Grenoble, involving the CEA Grenoble and the Institut Néel, as well as our partners across Europe. The completion of this work would not have been possible without the invaluable support, encouragement, and guidance from numerous individuals who played pivotal roles throughout this scientific, professional, and personal challenge that the PhD thesis represents.

First and foremost, I would like to express my deepest gratitude to Valérie Dupray, Yvan Bonnassieux, Elisabeth Djurado, and Lionel Hirsch for graciously accepting to be the referees and part of the thesis jury. Your willingness to contribute your expertise and valuable insights to evaluate my work is truly appreciated. Thank you for your time and consideration.

Secondly, I am profoundly grateful to my academic advisors and mentors. Your expertise, insightful feedback and constructive (sometimes challenging) criticism have been instrumental in shaping this research. I extend my thanks to Julien Zaccaro for his out-of-the-box mindset, critical thinking and resourceful nature during these years. His abundance of ideas has been invaluable to my work. I am also deeply appreciative of Jean-Marie Verilhac for his presence, support, dynamism and time management, which without it, I would have not accomplished half of the things I achieved. Additionally, I would like to express my gratitude for organising the team-building events. A special acknowledgment goes to Eric Gros d'Aillon for his pragmatic view on things, vast technical knowledge, and cultural insights, all of which have enriched this thesis work. I am also grateful for his straightforward and honest approach, which always comes from a place of goodwill. To both of you, Jean-Marie and Eric, I extend my thanks for being the core members of our group. Furthermore, I want to express my thanks to Alain Ibanez for consistently providing fresh insights and solutions to the scientific and technical challenges encountered along the way. I want to thank all of you for your availability and willingness to listen to me throughout this journey.

Thirdly, I would like to express my gratitude to the other members of the perovskite team. A special mention goes to my colleagues and post-doc friends, Ferdinand Lédée and Thibault Lemercier. Without Ferdi, I could not have accomplished my first first-author paper, and his ability to explain optoelectronics in a simple way has been invaluable. Thank you for your meticulousness and care in our works. To Tibaldito, I could not have asked for a "funnier" and more organised lab mate, always showing me support. I thank both of you for sharing

Acknowledgements

science, conferences, festivals, concerts and beers throughout this journey. I would also like to extend my thanks to Smaïl Amari and Oriane Baussens for being the pioneers and laying the foundation for the research work we have performed. Your contributions have set the stage for my thesis work. Furthermore, I want to thank Marian Chapran and Stéphanie Lombard for their support, willingness to help, and the fruitful discussions. Lastly, my appreciation goes to Louis Grenet and Yvan Faucheux for their contributions and involvement in our team's efforts.

I would like to thank also our collaborators. I am grateful to Marisé García-Batle, Agustin O. Alvarez, and Germà Garcia-Belmonte, along with their group at the INAM, Universitat Jaume I, in Castelló, Spain. I am equally thankful to Giovanni Armaroli and Beatrice Fraboni's group at the Università di Bologna, Italy. Giovanni, it has been a pleasure working alongside you and being your wingman during your stay with us in Grenoble. Furthermore, I want to express my gratitude to Stephanie H. Bennett and Paul J. Sellin's group at the University of Surrey, Guilford, UK. Lastly, I give thanks to Eduard Belas and his group at Univerzita Karlova in Prague, Czech Republic.

I am grateful to the members of the *Comité de Suivi Individuel*, Didier Chaussende and Stéphanie Pouget, for their invaluable and constructive feedback during our yearly meetings.

I am also immensely grateful for the hospitality and support I received during these last couple of years while being hosted within the LCO, DOPT, and OPTIMA lab facilities at CEA LITEN, CEA LETI, and Institut Néel, respectively, along with all the associated personnel. I want to express special thanks to Audrey Martinent and Lara Jabbour, as heads of the LCO lab, for their support in handling logistics and facilitating bureaucratic processes. I would like to extend my thanks to all the scientists and engineers who contributed to this thesis work by generously giving me their time and sharing their expertise in various characterisation techniques. Specifically, I am grateful to Sébastien Paris for his assistance with FESEM-EDX, Anass Benayad for his expertise in XPS, Mathieu Salaun for his guidance with TGA-MS, Corinne Félix for her insights into UV-Vis spectroscopy, David Jegouso for his help with FTIR, Sónia de Sousa Nobre for her support in PL, Sylvie Motellier for her assistance with ICP-MS, and Pierre Bouvier for his guidance in Raman spectroscopy. Moreover, I want to express my gratitude to Lina Kadura for always being ready for a good quality conversation, to Fabrice Emieux, Julia De Girolamo, Simon Charlot, Géraldine Lorin, Christelle Anglade, Krunoslav Romanjek, Helga Szambolics and Isabelle Rougeau.

I am also deeply grateful to my younger colleagues, interns, master students, fellow PhD students and researchers who have been with me throughout these years. The stimulating discussions covering a broad range of topics (very diverse indeed), the exchange of ideas, and clashes during coffee breaks, bar and restaurants assemblies, hikes (especially during the pandemic era), and engaging in escape games have made this academic journey all the more enjoyable and fulfilling. I would like to express my thanks to the following individuals. From CEA: Lucile Termeau, Romain Bellanger, Emma Pochon, Lucie Borget, Antoine Fondanèche, Fatine Gabriel, Alice Gontier, Loïc Paillardet, Jakob Ihrenberger, Mehrsa Rafie, Nathalie

Ronayette, Joseph Faudou, Simon Toinet, Louis Dubrulle, Manon Laurent and Benjamin Zanetti. From the Institut Néel: Kylia Marcus, Mackrine Nahra (alias *la Copine*), Maxime Gaignard (alias *le Voleur de Tasses*), Nathan Bassot, Redouane Boudjehem, Baptiste Vellet-Simond, Cathy Vang and Andrea Montero.

A special honorary mention and description are presented below for the following exceptional individuals. Auriane Despax, thank you for your joyful radiation and colourful clothing that always brought positivity to our interactions. Your willingness to listen to my complaints and your beautiful singing voice made our time together all the more enjoyable. Florian d'Ambra, you have been the oldest ally and a support throughout this chapter of my life. From the simplest practical banal matters to guiding me as a role model in life, your presence has been invaluable. Bruno Goes and Samyak Pratyush Prasad, thank you for being my fat-ass friends and gym bros, especially in this last year. Brunelio, despite the messiness at home, your caring nature as a roommate has provided me with much-needed comfort and support, especially during the intense writing phase of our manuscripts. To *Los Tres Mosqueteros*, Thibault Fresneau and Valentin Lafarge, I could not have asked for better co-workers sharing the same open-space. Your presence has made the work environment lively and enjoyable. Tibaldito (bis), thank you for the countless geek, pop culture and scientific exchanges. Your combination of goodness, artistic and scientific skills, and patience is a rare and admirable trait. Valento (alias… there are too many names to mention here), you have become my best friend during this chapter of my life. You have been a pillar in my daily, professional, and personal life, and your belief in my abilities has been a constant source of motivation during moments of self-doubt. You have made me a better person, and I am grateful for your existence, Valou. Additionally, thank you for introducing another brilliant character, Julien Hurtaud, into my life, and thank you for the wonderful times we have spent together.

To my friends and adopting family in Grenoble, I want to express my heartfelt gratitude to *La Latinada*, a wonderful group of individuals who have made my time in Grenoble truly special. Thank you to the following characters: Dayana and David Pino, Enrique Pulido, Armando García, Giovani Britton, Carolina and Diana Fernández, Andrea Zarrate, Louis Genty, Mohamed Salaheldin, Rosa Álvarez, Ana Bonilla, Catherine Garcés, Daniela Ramalho, David Ovalle, Denis Flores and Sergio Correa. Thank you Dayis and Quique, for being at the language exchange meeting before the arrival of COVID, opening the door to many adventures and laughs, especially the *perreo* nights. Thank you all for making me feel welcome and loved in this place.

I want to express my appreciation to all my friends who supported me from afar throughout this journey. Thank you for understanding and respecting the countless hours I spent immersed in "my little world" working on my PhD, and for providing the much-needed moments of respite and laughter. I would like to mention a few individuals who have been there for me throughout this time. From the Guatemalan gang: Fatima and Yamila Dary (and their husbands), María Cristina Jerez (and her family), Javier Putzeys, Javier Chinchilla and Camilo

Acknowledgements

Rivera. From my old Airbus group: Hugo Beria (for kidnapping me from time to time from Grenoble), Simone Tonnicchia, Vittorio Vercillo, Axel Gon Medaille and Alex Laroche. Thank you for the lasting friendships, encouragement and positive thoughts you have shared with me. I would also like to say a special thank you to Cynthia Rosón and her family for their support while I embarked on this PhD journey. Your love and encouragement have been a source of comfort and strength, especially during the challenges brought about by the pandemic and in the initial years of this adventure.

To my beloved family, sisters, *papá*, and *mamá*, I am filled with immense gratitude that words can hardly do justice to, but I will attempt to express it nonetheless. Your unwavering love, support, and countless sacrifices have been the solid foundation upon which I built my academic pursuits. Your belief in me, especially you, *madrecita*, who has always been my ultimate best friend in life, even during times when I doubted myself, has been a powerful driving force that has led me to this significant milestone. I am eternally thankful for your presence in my life. Throughout this journey, you have been my pillars of strength, offering encouragement and understanding, even during the most challenging moments. Your unwavering faith in my abilities and your constant reassurance have given me the courage to overcome obstacles and to keep moving forward. This achievement would not have been possible without you, never.

This thesis represents the culmination of years of relentless hard work, dedication, and the occasional back and neck pain, all intertwined with fruitful interactions. Each person mentioned here has played a role in shaping me both professionally and personally. I am humbled and deeply honoured to have been surrounded by such an exceptional support network, not only throughout this academic journey but also in all aspects of life.

With deepest gratitude and love,

Grenoble, July 28, 2023
Javier A. Mayén Guillén

Agradecimientos

Uno de los capítulos más importantes de mi vida ha llegado a su fin. Me siento lleno de inmensa gratitud y satisfacción al concluir este largo viaje de mi tesis doctoral, que se materializa en este manuscrito relativamente sencillo. Naturalmente, alguien ajeno o que no haya pasado por este proceso podría decir que la mayor parte del trabajo lo he realizado yo. Sin embargo, como ocurre en cualquier trabajo científico, esta tesis es el resultado del trabajo en colaboración dentro del "equipo de perovskitas" aquí en Grenoble, que involucra al CEA Grenoble y al Institut Néel, así como a nuestros colaboradores en toda Europa. La culminación de este trabajo no hubiera sido posible sin el invalorable apoyo, aliento y orientación de numerosas personas que desempeñaron roles fundamentales a lo largo de este desafío científico, profesional y personal que representa la tesis doctoral.

En primer lugar, me gustaría expresar mi más profunda gratitud a Valérie Dupray, Yvan Bonnassieux, Elisabeth Djurado y Lionel Hirsch por aceptar amablemente ser los evaluadores y formar parte del jurado de tesis. Su disposición para contribuir con su experiencia y valiosas ideas para evaluar mi trabajo es verdaderamente apreciada. Gracias por su tiempo y consideración.

En segundo lugar, estoy profundamente agradecido con mis asesores académicos y mentores. Su experiencia, comentarios perspicaces y críticas constructivas (a veces desafiantes) han sido fundamentales en la configuración de esta investigación. Extiendo mi agradecimiento a Julien Zaccaro por su mentalidad innovadora, pensamiento crítico y naturaleza ingeniosa durante estos años. Su abundancia de ideas ha sido invaluable para mi trabajo. También agradezco profundamente a Jean-Marie Verilhac por su presencia, apoyo, dinamismo y gestión del tiempo, sin los cuales no habría logrado la mitad de las cosas que he alcanzado. Además, quiero expresar mi gratitud por organizar los eventos del equipo. Un reconocimiento especial va a Eric Gros d'Aillon por su enfoque pragmático, vasto conocimiento técnico y perspectivas culturales, todos los cuales han enriquecido este trabajo de tesis. También estoy agradecido por su enfoque directo y honesto, que siempre proviene de un lugar de buena voluntad. A ambos, Jean-Marie y Eric, les extiendo mi agradecimiento por ser miembros fundamentales de nuestro grupo. Además, quiero expresar mi agradecimiento a Alain Ibanez por brindar constantemente ideas frescas y soluciones a los desafíos científicos y técnicos encontrados en el camino. Agradezco a todos ustedes por su disponibilidad y disposición para escucharme a lo largo de este viaje.

En tercer lugar, me gustaría expresar mi gratitud a los demás miembros del equipo de perovskitas. Una mención especial va a mis colegas y amigos post-doctorales, Ferdinand Lédée y Thibault Lemercier. Sin Ferdi, no habría podido completar mi primer artículo como primer autor, y su habilidad para explicar la optoelectrónica de manera sencilla ha sido inestimable.

Agradecimientos

Gracias por su minuciosidad y cuidado en nuestros trabajos. A Tibaldito, no podría haber pedido un compañero de laboratorio "más divertido" y organizado, siempre mostrándome apoyo. Les agradezco a ambos por compartir ciencia, conferencias, festivales, conciertos y cervezas a lo largo de este viaje. También quiero extender mi agradecimiento a Smaïl Amari y Oriane Baussens por ser los pioneros y sentar las bases para el trabajo de investigación que hemos realizado. Sus contribuciones han preparado el escenario para mi trabajo de tesis. Además, quiero agradecer a Marian Chapran y Stéphanie Lombard por su apoyo, disposición para ayudar y las fructíferas discusiones. Por último, mi agradecimiento va a Louis Grenet e Ivan Faucheux por sus contribuciones e implicación en los esfuerzos de nuestro equipo.

También quiero agradecer a nuestros colaboradores. Estoy agradecido con Marisé García-Batle, Agustin O. Alvarez y Germà Garcia-Belmonte, junto con su grupo en el INAM, Universitat Jaume I, en Castelló, España. Igualmente agradezco al grupo de Giovanni Armaroli y Beatrice Fraboni en la Università di Bologna, Italia. Giovanni, ha sido un placer trabajar junto a ti y ser tu compañero durante tu estancia con nosotros en Grenoble. Además, quiero expresar mi gratitud al grupo de Stephanie H. Bennett y Paul J. Sellin en la University of Surrey, Guilford, Reino Unido. Por último, doy gracias a Eduard Belas y su grupo en Univerzita Karlova en Praga, República Checa.

Estoy agradecido a los miembros del *Comité de Suivi Individuel*, Didier Chaussende y Stéphanie Pouget, por sus valiosas y constructivas retroalimentaciones durante nuestras reuniones anuales.

También estoy inmensamente agradecido por la hospitalidad y el apoyo que recibí durante estos últimos años mientras estuve alojado en las instalaciones de los laboratorios LCO, DOPT y OPTIMA en CEA LITEN, CEA LETI e Institut Néel, respectivamente, junto con todo el personal asociado. Quiero expresar un agradecimiento especial a Audrey Martinent y Lara Jabbour, como jefas del laboratorio LCO, por su apoyo en el manejo de la logística y la facilitación de los procesos burocráticos. Me gustaría extender mi agradecimiento a todos los científicos e ingenieros que contribuyeron a este trabajo de tesis al generosamente brindarme su tiempo y compartir su experiencia en diversas técnicas de caracterización. Específicamente, estoy agradecido a Sébastien Paris por su ayuda con FESEM-EDX, a Anass Benayad por su experiencia en XPS, a Mathieu Salaun por su orientación en TGA-MS, a Corinne Félix por sus conocimientos en espectroscopia UV-Vis, a David Jegouso por su ayuda con FTIR, a Sónia de Sousa Nobre por su apoyo en PL, a Sylvie Motellier por su asistencia con ICP-MS y a Pierre Bouvier por su orientación en espectroscopia Raman. Además, quiero expresar mi gratitud a Lina Kadura por estar siempre lista para una buena conversación de calidad, a Fabrice Emieux, Julia De Girolamo, Simon Charlot, Géraldine Lorin, Christelle Anglade, Krunoslav Romanjek, Helga Szambolics e Isabelle Rougeau.

También agradezco profundamente a mis jóvenes colegas, pasantes, estudiantes de maestría, compañeros de doctorado e investigadores que me han acompañado a lo largo de estos años. Las estimulantes discusiones sobre una amplia variedad de temas (muy diversos, de

hecho), el intercambio de ideas y los choques durante los descansos para el café, las reuniones en bares y restaurantes, las caminatas (especialmente durante la era de la pandemia) y la participación en juegos de escape han hecho que este viaje académico sea aún más agradable y satisfactorio. Me gustaría expresar mi agradecimiento a las siguientes personas. Del CEA: Lucile Termeau, Romain Bellanger, Emma Pochon, Lucie Borget, Antoine Fondanèche, Fatine Gabriel, Alice Gontier, Loïc Paillardet, Jakob Ihrenberger, Mehrsa Rafie, Nathalie Ronayette, Joseph Faudou, Simon Toinet, Louis Dubrulle, Manon Laurent y Benjamin Zanetti. Del Institut Néel: Kylia Marcus, Mackrine Nahra (alias *la Copine*), Maxime Gaignard (alias *le Voleur de Tasses*), Nathan Bassot, Redouane Boudjehem, Baptiste Vellet-Simond, Cathy Vang y Andrea Montero.

Se presenta una mención honorífica especial y una descripción a continuación para las siguientes personas excepcionales. Auriane Despax, gracias por tu radiante alegría y ropa colorida que siempre trajo positividad a nuestras interacciones. Tu disposición para escuchar mis quejas y tu hermosa voz al cantar hicieron que nuestro tiempo juntos fuera aún más agradable. Florian d'Ambra, has sido el aliado más antiguo y un apoyo durante todo este capítulo de mi vida. Desde los asuntos prácticos más simples hasta guiarme como modelo de vida, tu presencia ha sido invaluable. Bruno Goes y Samyak Pratyush Prasad, gracias por ser mis amigos *fat-ass* y compañeros de gimnasio, especialmente en este último año. Brunelio, a pesar del desorden en casa, tu naturaleza afectuosa como compañero de piso me ha brindado un confort y apoyo muy necesarios, especialmente durante la intensa fase de redacción de nuestros manuscritos. A *Los Tres Mosqueteros*, Thibault Fresneau y Valentin Lafarge, no podría haber pedido mejores compañeros de trabajo compartiendo el mismo *open-space*. Su presencia ha hecho que el ambiente de trabajo sea animado y agradable. Tibaldito (*bis*), gracias por los innumerables intercambios sobre cultura *geek*, pop y científica. Tu combinación de bondad, habilidades artísticas y científicas, y paciencia es una característica rara y admirable. Valento (alias... hay demasiados nombres para mencionar aquí), te has convertido en mi mejor amigo durante este capítulo de mi vida. Has sido un pilar en mi vida diaria, profesional y personal, y tu creencia en mis habilidades ha sido una fuente constante de motivación durante momentos de duda. Me has hecho una mejor persona, y estoy agradecido por tu existencia, Valou. Además, gracias por presentarme a otro personaje brillante, Julien Hurtaud, en mi vida, y gracias por los maravillosos momentos que hemos pasado juntos.

A mis amigos y familia adoptiva en Grenoble, quiero expresar mi sincera gratitud a *La Latinada*, un grupo maravilloso de personas que han hecho mi tiempo en Grenoble realmente especial. Gracias a los siguientes personajes: Dayana y David Pino, Enrique Pulido, Armando García, Giovani Britton, Carolina y Diana Fernández, Andrea Zarrate, Louis Genty, Mohamed Salaheldin, Rosa Álvarez, Ana Bonilla, Catherine Garcés, Daniela Ramalho, David Ovalle, Denis Flores y Sergio Correa. Gracias Dayis y Quique, por estar en la reunión de intercambio de idiomas antes de la llegada del COVID, abriendo la puerta a muchas aventuras y risas,

Agradecimientos

especialmente a las noches de perreo. Gracias a todos por hacerme sentir bienvenido y amado en este lugar.

Quiero expresar mi aprecio a todos mis amigos que me apoyaron desde lejos a lo largo de este viaje. Gracias por entender y respetar las innumerables horas que pasé inmerso en "mi pequeño mundo" trabajando en mi tesis doctoral, y por proporcionarme los momentos de respiro y risas tan necesarios. Me gustaría mencionar a algunas personas que estuvieron ahí para mí durante este tiempo. Del grupo de guatemaltecos: Fátima y Yamila Dary (y sus esposos), María Cristina Jerez (y su familia), Javier Putzeys, Javier Chinchilla y Camilo Rivera. De mi antiguo grupo de Airbus: Hugo Beria (por secuestrarme de vez en cuando de Grenoble), Simone Tonnicchia, Vittorio Vercillo, Axel Gon Medaille y Alex Laroche. Gracias por las amistades duraderas, el estímulo y los pensamientos positivos que compartieron conmigo. También quiero dar un agradecimiento especial a Cynthia Rosón y su familia por su apoyo mientras emprendía este viaje de doctorado. Su amor y aliento han sido una fuente de consuelo y fuerza, especialmente durante los desafíos que trajo la pandemia y en los primeros años de esta aventura.

A mi querida familia, hermanas, papá y mamá, estoy lleno de inmensa gratitud que las palabras apenas pueden hacer justicia, pero intentaré expresarlo de todos modos. Su inquebrantable amor, apoyo y los innumerables sacrificios han sido la sólida base sobre la cual construí mis estudios académicos. Su creencia en mí, especialmente tú, madrecita, que siempre has sido mi mejor amiga en la vida, incluso en momentos en que dudaba de mí mismo, ha sido una poderosa fuerza motriz que me ha llevado a este logro significativo. Estoy eternamente agradecido por tu presencia en mi vida. A lo largo de este viaje, ustedes han sido mis pilares de fuerza, ofreciendo aliento y comprensión, incluso durante los momentos más difíciles. Su fe inquebrantable en mis habilidades y su constante apoyo me han dado el valor para superar obstáculos y seguir adelante. Este logro no hubiera sido posible sin ustedes, nunca.

Esta tesis representa la culminación de años de trabajo arduo e incansable, dedicación y el ocasional dolor de espalda y cuello, todo entrelazado con interacciones fructíferas. Cada persona mencionada aquí ha desempeñado un papel en formarme tanto profesional como personalmente. Me siento honrado y profundamente agradecido de haber estado rodeado de una red de apoyo excepcional, no solo a lo largo de este viaje académico, sino también en todos los aspectos de la vida.

Con profunda gratitud y profundo amor,

Grenoble, Julio 28, 2023
Javier A. Mayén Guillén

Table of contents

Abstract

The development of new materials with higher sensitivity to high-energy ionising radiations, such as X- and γ-rays, and a reduced cost production than nowadays commercial detectors, is motor in the high-energy detection research. In medical imaging, the sensing of the ionising radiation can be done indirectly or directly. The latter uses a semiconductor layer that directly converts the incoming photons into electron-hole pairs which become collected charge carriers thanks to the presence of an electric field.

In this context, hybrid metal halide perovskites have been extensively studied during the last decade for the detection of energetic photons. Within the lead halide perovskites, methylammonium lead tribromide ($MAPbBr_3$) has been chosen for this thesis work as sensing material for medical grade X-ray detection. Efficient direct detection of energetic photons requires, from the employed semiconductor layer, a thickness and linear attenuation coefficient large enough to efficiently absorb most of the incoming radiation, large and balanced charge carrier mobility-lifetime product for efficient charge collection, high resistivity and low charge trap density to avoid charge trapping and decrease signal noise. Indeed, $MAPbBr_3$ show good X-ray absorption and a simple crystal growth from solution, therefore, well suited for medical imaging. Within our team, $MAPbBr_3$ single crystals (SCs) growth via modified inverse temperature crystallisation has been optimised in dimethylformamide. Evaluating this material in the form of SC devices is the most favourable way to directly access its intrinsic properties. The evaluation under X-ray irradiation exhibited a very good sensitivity, but a large dark current density (~ μA cm^{-2}), being about 3 orders of magnitude above the specifications required for radiation detectors.

The present thesis has been structured around three research axes to improve the overall optoelectronic performance of $MAPbBr_3$ SC devices in relevant medical imaging conditions. The first axis experiments with modifying the growth solution in order to alter the bulk chemical composition of $MAPbBr_3$ by adding chloride. $MAPb(Br_{0.85}Cl_{0.15})_3$ was identified as the composition showing the most improved charge carrier transport, with the highest sensitivity (3 μC mGy_{air}^{-1} cm^{-2} at 50 V mm^{-1}), and the lowest dark current density (43 nA mm^{-2} at 50 V mm^{-1}). The second axis highlighted the importance of the growth atmosphere and the induced doping that atmospheric water can have on the surface of the SC devices. SCs grown and tested in atmospheric conditions and those in fully inert atmosphere, respectively, were the ones with better performances, judged by a more intrinsic doping and improved electron transport. The last axis works as an introduction to post-treatments, healing point defects via methylammonium chloride vapours. This work proves how incorporated chloride levelled the Pb/halide stoichiometry and reorganized the defect structure, leading to better charge carrier transport and collection.

Abstract

This thesis work gives substantial insights regarding the synthesis in solution of hybrid perovskites, such as $MAPbBr_3$, and the influence that external stimuli have on them. It emphasises the potential of these materials as direct convertors for medical X-ray imaging devices, as well as the challenges that still need to be overcome.

Résumé

Le développement de nouveaux matériaux alliant une sensibilité accrue aux rayonnements ionisants de haute énergie, tels que les rayons X et γ, avec une production à moindre coût par rapport aux détecteurs commerciaux actuels, est un moteur dans la recherche sur la détection des hautes énergies. En imagerie médicale, la détection du signal de rayonnement ionisant peut être réalisée de manière indirecte ou directe. La seconde méthode utilise une couche semi-conductrice qui convertit directement les photons incidents en paires électron-trou, lesquelles deviennent des porteurs de charge collectés grâce à l'application d'un champ électrique.

Dans ce contexte, les pérovskites hybrides à base d'halogénures métalliques ont été largement étudiées au cours de la dernière décennie pour la détection des photons de haute énergie. Parmi les pérovskites à base de plomb, le tribromure de plomb de méthylammonium ($MAPbBr_3$) a été choisi pour ce travail de thèse comme matériau pour la détection des rayons X de qualité médicale. Pour une détection directe efficace des photons énergétiques, le semi-conducteur utilisé doit avoir une épaisseur et un coefficient d'atténuation linéaire suffisamment grands pour absorber efficacement la majorité du rayonnement incident, un produit de mobilité-temps de vie de porteurs de charge important et équilibré pour une collecte de charge efficace, une résistivité élevée, et une faible densité de pièges de charges pour éviter leur piégeage et réduire le bruit du signal. $MAPbBr_3$ présente effectivement une bonne absorption des rayons X et une croissance en solution simple, ce qui le rend bien adapté pour l'imagerie médicale. Au sein de notre équipe, la croissance de monocristaux de $MAPbBr_3$ par *modified inverse temperature crystallisation* a été optimisée dans du diméthylformamide. L'évaluation de ce matériau sous forme de dispositifs monocristallins est la manière la plus favorable pour accéder directement à ses propriétés intrinsèques. L'évaluation sous irradiation X a montré une très bonne sensibilité, mais une densité de courant d'obscurité élevée (~ $\mu A\ cm^{-2}$), près de 3 ordres de grandeur au-dessus des spécifications requises pour les détecteurs de rayonnement.

Cette thèse est structurée autour de trois axes de recherche visant à améliorer les performances optoélectroniques globales des dispositifs de $MAPbBr_3$ dans des conditions d'imagerie médicale pertinentes. Le premier axe porte sur des expériences visant à modifier la solution de croissance afin de modifier la composition chimique globale de $MAPbBr_3$ en ajoutant du chlorure. Il a été découvert que la composition $MAPb(Br_{0.85}Cl_{0.15})_3$ présentait la meilleure amélioration du transport des porteurs de charge, avec la sensibilité la plus élevée (3 $\mu C\ mGy_{air}^{-1}\ cm^{-2}$ à 50 $V\ mm^{-1}$), et la plus faible densité de courant d'obscurité (43 $nA\ mm^{-2}$ à 50 $V\ mm^{-1}$). Le deuxième axe a mis en évidence l'importance de l'atmosphère de croissance et du dopage induit par l'eau atmosphérique sur la surface des dispositifs. Les monocristaux grandis et testés dans des conditions atmosphériques et ceux dans une atmosphère

Résumé

entièrement inerte, ont montré de meilleures performances, à en juger par un dopage plus intrinsèque et un meilleur transport des électrons. Le dernier axe constitue une introduction au post-traitements, en réparant des défauts ponctuels à l'aide de vapeurs de chlorure de méthylammonium. Ce travail démontre comment le chlorure incorporé peut équilibrer la stœchiométrie Pb/halogénure et réorganiser la structure des défauts, conduisant à un meilleur transport et une meilleure collecte des porteurs de charge.

Ce travail de thèse apporte des informations substantielles sur la synthèse en solution des pérovskites hybrides, tels que $MAPbBr_3$, et l'influence des stimuli externes sur ces matériaux. Il met en évidence le potentiel de ces matériaux en tant que convertisseurs directs pour les imageurs médicaux de rayons X, ainsi que les défis qui restent à surmonter.

Abbreviations

A	Organic or inorganic cation
a.u.	Arbitrary unit
AC	Ambient condition
AMA	Active matrix array
ASIC	Application-specific integrated circuit
Asym.	Asymmetric
ATR	Attenuated total reflection
avg	Average
B	Metal cation
CCD	Charged-coupled device
CCE	Charge collection efficiency
CEA	*Commissariat à l'énergie atomique et aux énergies alternatives*
CMOS	Complementary metal-oxide-semiconductor
CNRS	*Centre national de la recherche scientifique*
CT	Computed tomography
CZT	Cadmium zinc telluride ($Cd_{1-x}Zn_xTe$)
DAQ	Data acquisition
DCM	Dichloromethane
DFT	Density functional theory
DMA	Dimethylamine
DMF	N,N-dimethylformamide
DMSO	Dimethylsulfoxide
DUT	Device under test
EDA	Ethylenediamine
EDX	Energy dispersive X-ray analysis
ETH	Electron transport layer
EtOAc	Ethyl acetate
FA^+/FA	Formamidinium/formamidine
FESEM	Field emission scanning electron microscopy
FPXI	Flat panel X-ray imager
FTIR	Fourier transform infrared spectroscopy
FWHM	Full width at half maximum
GB	Glovebox
GBL	γ-Butyrolactone
GDMS	Glow discharge mass spectrometry
HTL	Hole transport layer
IC	Inert condition
ICP-MS	Inductively coupled plasma mass spectrometry
IEC	International electrotechnical commission
IPA	Isopropanol or isopropyl alcohol

Abbreviations & symbols

ITC	Inverse temperature crystallisation
LETI	*Laboratoire d'électronique et de technologie de l'information*
LHP	Lead halide perovskite
LITEN	*Laboratoire d'innovation pour les technologies des énergies nouvelles et les nanomatériaux*
M	mol L^{-1}
MA^+/MA	Methylammonium/methylamine
MCT	Mercury-cadmium-telluride
MHP	Metal halide perovskite
MITC	Modified inverse temperature crystallisation
NIR	Near-infrared
NIST	National institute of standards and technology
OA^+/OA	Octylammonium/octylamine
OD	Optical density
PbAc	Lead acetate
PC	Polycrystalline or polycrystal
PCE	Power conversion efficiency
PEA^+/PEA	Phenethylammonium/phenethylamine
PICTS	Photoinduced current transient spectroscopy
PL	Photoluminescence
PMT	Photomultiplier tube
ppm	Parts-per-million
PTFE	Polytetrafluoroethylene
PV	Photovoltaic
RH	Relative humidity
SC	Single crystal
SCLC	Space charge limited current
SDD	Silicon drift detector
SNR	Signal-to-noise ratio
STL	Solution temperature lowering
Sym.	Symmetric
TFT	Thin-film transistor
TGA-MS	Thermogravimetric analysis coupled with mass spectrometry
ToF	Time of flight
UHV	Ultra-high vacuum
UV	Ultraviolet
Vis	Visible
VL	Vegard's law
wt.	Weight
wt.%	Percentage by weight
X	Halide or superoxide
XPS	X-ray photoelectron spectroscopy
XRD	X-ray powder diffraction

Symbols

$[A]$	Concentration of compound A
$[X]_{tot}$	Total amount of halide anions in solution
$\%Cl_{cryst}$	Crystal Cl content
$\%Cl_{sol}$	Solution Cl content
ΔA	Change in physical quantity A
ΔG	Gibbs free energy change
ΔG^*	Critical Gibbs free energy change
$\Delta_r G^0$	Standard Gibbs free energy of reaction
$\Delta_r H^0$	Standard enthalpy of reaction
$\Delta_r S^0$	Standard entropy of reaction
$\Delta\mu$	Chemical potential change
$\Delta\mu^*$	Critical chemical potential change
A	Quantum efficiency or absorbance
A and B	Constants
a_A	Lattice parameter of compound A
atom A (%)	Atomic percentage attributed by EDX quantification of element A
b	Burgers vector
C	Concentration
c	Speed of light
C^0	Standard concentration
C_0	Concentration of Cl^- anions at $x = 0$
D	Diffusion coefficient
D_X	X-ray dose
E	Incident X-ray photon or absorbed radiation energy
e	Elementary charge
E^*	X-ray deposited energy
E_a	Activation energy
E_g	Bandgap
E_{ph}	Photon energy
F	Electric field
h	Planck constant
I	Collectable or measured photocurrent
I_0	Total generated photocurrent
J	Current density
j_0	Steady nucleation rate
J_{dark}	Dark current density
k	Cl content partition coefficient
K^0	Equilibrium constant
k_B	Boltzmann constant
L	Photoconductor layer or sample thickness

Abbreviations & symbols

$L(t)$	Characteristic lineal dimension
L_0	Initial characteristic length of seed crystal
m	Mass
M	Molecular mass
m/z	Mass-to-charge ratio
m_0	Seed crystal mass
n	Number of solute molecules
N	Number of photons or generated charge carriers
N_0	Density of adsorption sites
p	Pressure
pK_a	Acid dissociation constant
Q	Collectable or measured charge
Q_0	Total generated charge
r	Particle radius
R	Gas constant
r^*	Critical radius
R_B	Bragg factor
R_{exp}	Expected weighted profile factor
R_F	Crystallographic factor
R_g	Growth rate
r_i	Ionic radius of ion i
R_p	Profile factor
R_{wp}	Weighted profile factor
S	Sensitivity
s	Solute solubility
S_d	Electrode surface area
S_{max}	Maximal theoretical sensitivity
S_p	Particle surface area
s_r	Surface recombination velocity
T	Temperature
t	Time
T_0	Initial temperature
T_{eq}	Equilibrium temperature
t_G	Tolerance factor
$T_{level\ i}$	Temperature at level i
T_r	Transmittance
t_t	Transit time
V	Applied bias or voltage
v	Photon frequency
$v(A)$ or $\delta(A)$	Vibrational modes of group A
V_A	Volume of compound A
V_C	Crystal volume
V_S	Solution volume

W	Ionisation energy
W_0	Intrinsic energy of electron-hole pair generation at "infinite field"
x	Distance from the entrance electrode/surface or depth
x_0	Electron-hole pair creation position
Y	Deviance
Z	Atomic number
α	Linear attenuation or absorption coefficient
α_2	Crystal growth kinetic parameter (mass deposition rate)
α_{en}	Energy absorption coefficient at energy of interest
β	Supersaturation
β^*	Critical supersaturation
β_v	Growth morphology constant
γ	Crystal/solution interfacial energy
Γ	Non-equilibrium Zeldovich factor
δ	X-ray attenuation depth
ε	MACl ratio in solution
ζ	Electron transition nature parameter
η_{CC}	Charge collection or induction efficiency
θ	Bragg angle
κ	Crystal growth kinetic parameter
λ	Wavelength
Λ	Exchange layer thickness
μ_e	Electron mobility
μ_h	Hole mobility
μ_i	Chemical potential of phase i
μ_{oh}	Octahedral factor
ρ	Resistivity
ρ_d	Density
σ_{cs}	Photon cross section
σ_{drift}	Conductivity drift
σ_r	Relative supersaturation
τ_e	Electron lifetime
τ_h	Hole lifetime
χ^2	Global reduced coefficient
Ω	Solute molecule volume
ω^*	Solute molecules diffusion from solution to critical particle frequency

Introduction

The strong penetrating capability of high-energy ionising radiation (X- and γ-rays) is attractive for non-destructive probing of condensed matter. In medical imaging, the information carried by the ionising radiation signal that has interacted with the human body can be sensed indirectly or directly. The former employs a scintillator, converting high-energy photons into ultraviolet (UV)-visible light (e.g. CsI(Tl), NaI(Tl)) and in turn photodiodes convert that light into electric signal. The latter is more straightforward as it uses a semiconductor layer (e.g. α-Se, HgI_2, $Cd_{1-x}Zn_xTe$ (CZT)) to directly converts the incoming photons into electron-hole pairs that become collected charge carriers thanks to the presence of an electric field.

Direct conversion offers significant advantages, including enhanced sensitivity to X-rays and improved spatial resolution. Consequently, patients are exposed to lower levels of X-rays, leading to improved diagnosis of various pathologies. Conversely, the current technologies mentioned earlier face challenges due to either a low absorption coefficient (a-Se) or high costs and limited compatibility with large surfaces (CZT). As a result, there is a pressing requirement for a photo-conversion material that can integrate all these properties, with the halide perovskite family emerging as a promising candidate for the next generation of semiconductors.

Direct detectors for high-energy photons require semiconducting materials with a thickness and linear attenuation coefficient large enough to efficiently absorb most of the incoming radiation, large and balanced charge carrier mobility (μ) - lifetime (τ) product ($\mu\tau$ product) for efficient charge collection, high resistivity and low charge trap density to avoid charge trapping and decrease signal noise.[1,2]

During the last decade, halide-based perovskite materials have generated strong and growing attention for being promising candidates for optoelectronic applications, and in particular for high-energy radiation detection. Indeed, hybrid (organic-inorganic) halide perovskite materials show good X-ray absorption, thanks to the presence of heavy elements such as lead,[3–5] a defect tolerant nature,[3,6,7] sufficient $\mu\tau$ product,[8] and simple crystal growth from solution.[9,10] Therefore, heavy metal halide perovskites are well suited for direct X-ray detection applications like medical imaging.[11] Additionally, these materials, in the form of single crystals (SC), exhibit no grain boundaries and possess very low trap densities.[2,3,6,7,12] From a fundamental point of view, working with SCs is the most favourable way to directly access their intrinsic bulk properties, which is critical to identify the best compounds for practical applications.

Methylammonium lead tribromide ($MAPbBr_3$, with $MA^+ = CH_3NH_3^+$) is among the most studied hybrid halide perovskites for high-energy radiation detection,[3,4,13] being more stable than its iodide-based counterpart, methylammonium lead triiodide ($MAPbI_3$).[14] It also

has a simpler phase diagram with no secondary phases of close compositions, and no phase transition close to room temperature. Within our team, during my predecessor's PhD thesis work, Dr. Smaïl Amari, $MAPbBr_3$ SCs growth via modified inverse temperature crystallisation (MITC) has been optimised in dimethylformamide (DMF) for direct X-ray radiation detection.[15,16] Their optoelectronic properties have been evaluated under X-ray illumination during the PhD thesis work of Dr. Oriane Baussens, with standardised characterisation and charge carrier transport analysis.[11,17] While the growth optimisation allowed reaching a very good sensitivity, they always presented a large dark current density (~ $\mu A\ cm^{-2}$), being several orders of magnitude above the specifications required for radiation detectors.[18] This crucial figure of merit for detectors corresponds to the leakage current of the device in the dark, and must be minimised by a combination of increased bulk resistivity and electrode engineering.[19,20]

In this context, the present thesis has been structured around three research axes to improve the overall optoelectronic performance of $MAPbBr_3$ SC device under X-ray radiation in relevant medical imaging conditions, and in general, to better understand the associated crystal growth chemistry and underlying physics as a semiconductor.

Chapter 1 of this work presents a bibliographic recompilation of all-important notions and requirements to understand, not only $MAPbBr_3$ positioning inside metal halide perovskites (MHPs), but also compared to state-of-the-art commercial detectors. First, generalities on high-energy detection, followed by the principles of X-ray medical imaging and associated materials are presented. A review on MHP materials follows, specifically on hybrid lead halide perovskites (LHPs) for the desired application. Both advantages and disadvantages of this family of materials are exposed. Chapter 2 describes in detail the theory and experimental procedures performed by our team to characterise $MAPbBr_3$ SC devices, establishing key optoelectronic figures of merit. It regroups the common materials and methods employed in the three research axes developed afterwards. These three studies were formulated querying in which stage of the material fabrication process we could intervene to attain the desired detection characteristics: before, during and after SC growth. Chapter 3 describes the first approach, the "before", to boost the material performance. The precursor solution was modified in order to alter the bulk chemical composition of $MAPbBr_3$ by employing anion engineering within the halide elements. In order to do so, bromine was partially substituted with chlorine during crystal growth leading to compounds of general formula $MAPb(Br_{1-x}Cl_x)_3$. The second approach, the "during", is exposed in Chapter 4. MITC crystal growths took place in different atmospheres to evaluate the impact of the environment chemical composition in the SC chemistry and X-ray response. Two crystal growth conditions were then tested during this study, one being in a standard laboratory and the other dry-inert glovebox atmospheres. The testing atmosphere is also assessed by performing a full inert synthesis-characterisation circuit, with samples having never seen atmospheric conditions. Chapter 5 addresses the third and last approach, the "after", to fight against the intrinsic nature of our base material. The study works as an introduction to post-treatments, highlighting the influence of temperature and chemical healing of defects.

The manuscript covers a large spectrum of characterisations and topics. The understanding of perovskites remains elusive for several aspects presented in both this work and the literature, due to the complexity of these enigmatic family of materials. Nevertheless, this thesis accents the potential that hybrid LHPs have as high-energy ionising radiations detectors and give substantial insights regarding its fabrication in solution and the potential they have for X-ray medical imaging.

References

(1) Johns, P. M.; Baciak, J. E.; Nino, J. C. Enhanced Gamma Ray Sensitivity in Bismuth Triiodide Sensors through Volumetric Defect Control. *Appl. Phys. Lett.* **2016**, *109* (9), 092105. https://doi.org/10.1063/1.4962293.

(2) Wei, H.; DeSantis, D.; Wei, W.; Deng, Y.; Guo, D.; Savenije, T. J.; Cao, L.; Huang, J. Dopant Compensation in Alloyed CH3NH3PbBr3−xClx Perovskite Single Crystals for Gamma-Ray Spectroscopy. *Nature Mater* **2017**, *16* (8), 826–833. https://doi.org/10.1038/nmat4927.

(3) Wei, H.; Fang, Y.; Mulligan, P.; Chuirazzi, W.; Fang, H.-H.; Wang, C.; Ecker, B. R.; Gao, Y.; Loi, M. A.; Cao, L.; Huang, J. Sensitive X-Ray Detectors Made of Methylammonium Lead Tribromide Perovskite Single Crystals. *Nature Photon* **2016**, *10* (5), 333–339. https://doi.org/10.1038/nphoton.2016.41.

(4) Tisdale, J. T.; Yoho, M.; Tsai, H.; Shrestha, S.; Fernando, K.; Baldwin, J. K.; Tretiak, S.; Vo, D.; Nie, W. Methylammonium Lead Tribromide Single Crystal Detectors towards Robust Gamma-Ray Photon Sensing. *Adv. Optical Mater.* **2020**, 2000233. https://doi.org/10.1002/adom.202000233.

(5) Liu, Y.; Zhang, Y.; Zhu, X.; Feng, J.; Spanopoulos, I.; Ke, W.; He, Y.; Ren, X.; Yang, Z.; Xiao, F.; Zhao, K.; Kanatzidis, M.; Liu, S. (Frank). Triple-Cation and Mixed-Halide Perovskite Single Crystal for High-Performance X-ray Imaging. *Adv. Mater.* **2021**, *33* (8), 2006010. https://doi.org/10.1002/adma.202006010.

(6) Dong, Q.; Fang, Y.; Shao, Y.; Mulligan, P.; Qiu, J.; Cao, L.; Huang, J. Electron-Hole Diffusion Lengths > 175 Mm in Solution-Grown $CH_3NH_3PbI_3$ Single Crystals. *Science* **2015**, *347* (6225), 967–970. https://doi.org/10.1126/science.aaa5760.

(7) Yin, W.-J.; Shi, T.; Yan, Y. Unusual Defect Physics in $CH_3NH_3PbI_3$ Perovskite Solar Cell Absorber. *Appl. Phys. Lett.* **2014**, *104* (6), 063903. https://doi.org/10.1063/1.4864778.

(8) Basiricò, L.; Ciavatti, A.; Fraboni, B. Solution-Grown Organic and Perovskite X-Ray Detectors: A New Paradigm for the Direct Detection of Ionizing Radiation. *Adv. Mater. Technol.* **2021**, *6* (1), 2000475. https://doi.org/10.1002/admt.202000475.

(9) Saidaminov, M. I.; Abdelhady, A. L.; Murali, B.; Alarousu, E.; Burlakov, V. M.; Peng, W.; Dursun, I.; Wang, L.; He, Y.; Maculan, G.; Goriely, A.; Wu, T.; Mohammed, O. F.; Bakr, O. M. High-Quality Bulk Hybrid Perovskite Single Crystals within Minutes by Inverse Temperature Crystallization. *Nat Commun* **2015**, *6* (1), 7586. https://doi.org/10.1038/ncomms8586.

(10) Saidaminov, M. I.; Abdelhady, A. L.; Maculan, G.; Bakr, O. M. Retrograde Solubility of Formamidinium and Methylammonium Lead Halide Perovskites Enabling Rapid Single Crystal Growth. *Chem. Commun.* **2015**, *51* (100), 17658–17661. https://doi.org/10.1039/C5CC06916E.

(11) Baussens, O.; Maturana, L.; Amari, S.; Zaccaro, J.; Verilhac, J.-M.; Hirsch, L.; Gros-Daillon, E. An Insight into the Charge Carriers Transport Properties and Electric Field Distribution of $CH_3NH_3PbBr_3$ Thick Single Crystals. *Appl. Phys. Lett.* **2020**, *117* (4), 041904. https://doi.org/10.1063/5.0011713.

(12) Arya, S.; Mahajan, P.; Gupta, R.; Srivastava, R.; Tailor, N. kumar; Satapathi, S.; Sumathi, R. R.; Datt, R.; Gupta, V. A Comprehensive Review on Synthesis and Applications of Single Crystal Perovskite Halides. *Progress in Solid State Chemistry* **2020**, 100286. https://doi.org/10.1016/j.progsolidstchem.2020.100286.

(13) Feng, A.; Xie, S.; Fu, X.; Chen, Z.; Zhu, W. Inch-Sized Thin Metal Halide Perovskite Single-Crystal Wafers for Sensitive X-Ray Detection. *Front. Chem.* **2022**, *9*, 823868. https://doi.org/10.3389/fchem.2021.823868.

(14) Juarez-Perez, E. J.; Hawash, Z.; Raga, S. R.; Ono, L. K.; Qi, Y. Thermal Degradation of $CH_3NH_3PbI_3$ Perovskite into NH_3 and CH_3I Gases Observed by Coupled Thermogravimetry–Mass Spectrometry Analysis. *Energy Environ. Sci.* **2016**, *9* (11), 3406–3410. https://doi.org/10.1039/C6EE02016J.

(15) Amari, S.; Verilhac, J.-M.; Gros D'Aillon, E.; Ibanez, A.; Zaccaro, J. Optimization of the Growth Conditions for High Quality $CH_3NH_3PbBr_3$ Hybrid Perovskite Single Crystals. *Crystal Growth & Design* **2020**, *20* (3), 1665–1672. https://doi.org/10.1021/acs.cgd.9b01429.

(16) Amari, S. Étude des matériaux pérovskites pour la détection directe des rayonnements ionisants. Ph.D. diss., Université Grenoble Alpes, Grenoble, France, 2020.

(17) Baussens, O. Nouveau matériau pérovskite pour la radiographie médicale. Ph.D. diss., Université de Bordeaux, 2021.

(18) Kasap, S. O.; Rowlands, J. A. Direct-Conversion Flat-Panel X-Ray Image Detectors. *IEE Proceedings - Circuits, Devices and Systems* **2002**, *149* (2), 85–96. https://doi.org/10.1049/ip-cds:20020350.

(19) Datta, A.; Zhong, Z.; Motakef, S. A New Generation of Direct X-Ray Detectors for Medical and Synchrotron Imaging Applications. *Sci Rep* **2020**, *10* (1), 20097. https://doi.org/10.1038/s41598-020-76647-5.

(20) He, Y.; Matei, L.; Jung, H. J.; McCall, K. M.; Chen, M.; Stoumpos, C. C.; Liu, Z.; Peters, J. A.; Chung, D. Y.; Wessels, B. W.; Wasielewski, M. R.; Dravid, V. P.; Burger, A.; Kanatzidis, M. G. High Spectral Resolution of Gamma-Rays at Room Temperature by Perovskite CsPbBr3 Single Crystals. *Nat Commun* **2018**, *9* (1), 1609. https://doi.org/10.1038/s41467-018-04073-3.

Chapter 1 – Generalities on high-energy radiation detection, medical X-ray imaging and metal halide perovskites

Table of contents

Chapter 1

Chapter 1

Generalities on high-energy radiation detection, medical X-ray imaging and metal halide perovskites

Introduction

To analyse matter, high-energy radiation with strong penetrating power is required to interact with the constituent atoms while traversing it. This radiation coming through called ionising radiation can be in form of photons or particles and has primordial information after that interaction. To detect the resulting radiation, detectors must be conceived based on the wave or particle physical properties. One of the most popular application having a huge societal impact is medical radiography, which is the focus point of this thesis work. Among the wide range of ionising radiations, X-rays are used for such purpose. Their potential harmful effects on patient had always pushed scientific research and industry to create detectors every time more sensible with improved image resolution. Within this context, hybrid lead halide perovskite materials have seen the light as new family of materials satisfying the needs of more performant X-ray detectors.

The following chapter is divided in two main parts. The first part presents an overview on the detection of high-energy radiation, specifically on X-rays and the materials employed for such purpose. A focus on the world of X-ray imaging and the underlying physical mechanisms takes place. It features the requirements and current state of X-ray radiation detection systems. The second section introduces the nowadays-popular metal halide perovskite materials, which includes hybrid lead halide perovskites. A review is made on this family of materials highlighting, firstly, the potential role they have as a semiconducting detector material meeting the needs the X-ray imaging applications, and secondly, the diverse forms perovskites can take, including polycrystal films and single crystals. Special attention is given to the synthesis of the latter. The chapter depicts all along the obstacles and challenges ahead hindering their performance and the efforts that have been made, and still need to be done, to mitigate their effects.

Chapter 1

1 High-energy radiation detection and X-ray imaging

1.1 Ionising radiations usage and detection

Since the discovery of X-rays in 1895,[1] will and effort have been focused on developing efficient large-area X-ray detectors for applications ranging from crystallography,[2] medicine,[3] to space exploration.[4] In the last decades, the medical field has seen a rise in the use of tests involving high doses of radiation, such as computed tomography (CT) imaging, bringing attention on radiation safety. To give some numbers, the number of CT scans performed in the United States rose from 3 million in 1980 to over 80 million in 2010. As for the dose involved, a one-time chest CT scan can have a dose equivalent to 2 years accumulation of natural background dose. Over 3.6 billion diagnostic X-ray examinations are performed every year in the world allowing resolving between 70 % and 80 % of diagnostic problems.[5] While the risk of cancer is relatively low for both patients and clinicians in well-equipped facilities, specific subsets of patients may be at greater risk from radiation exposure because of repetitive exposure and potential DNA damage.[6–8] From an imaging system point of view, to put things simply for low dose techniques, if higher doses are needed, it is mainly because the detector exhibits a low sensitivity which devolves from the properties of the sensing material used.

All medical applications employing X-rays imaging, being general radiography or other niche applications such as CT or mammography, would benefit from the development of more sensitive detection materials with lower manufacturing expenses. For instance, mammography has substantially increased globally.[8]

Beyond X-rays, an ionising radiation is defined as a radiation that is expected to produce an ionisation event, as opposed to a non-ionising radiation (e.g., visible light, infrared). It can be in the form of either electromagnetic waves (e.g., X- and γ-rays) or particles (e.g., α- and β-particles). **Figure 1-1-1-A** illustrates the positioning of ionising radiations in the electromagnetic spectrum.[9] X- and γ-rays can range from kilo- to mega electronvolts (0.1–1000 keV and 0.1–10 MeV, respectively) and are used in various photonics applications, such as medical imaging, industrial inspection, astronomy, nuclear energy industry, high-energy physics and radioisotope identification in homeland security.[6,10,11] **Figure 1-1-1-B** shows high-energy radiation spectrum and associated applications in different spectral regions. High-energy radiation detectors are classified into two primary types depending on the detection principle: indirect and direct detectors. On the one hand, indirect detection is a two-step process. First a scintillating material absorbs the high-energy photons and converts them to ultraviolet (UV) or visible light. These lower energy photons are subsequently detected and converted into electric signal by standard photodiodes arrays or photomultipliers.[11] On the other hand, direct detection is a single step process. A photoconductive material absorbs the high-energy radiation and the photogenerated charge carriers in it are collected using external

circuitry, which if pixelated allows generating a digital image. **Figure 1-1-2** illustrates the basic principles of both detection methods.

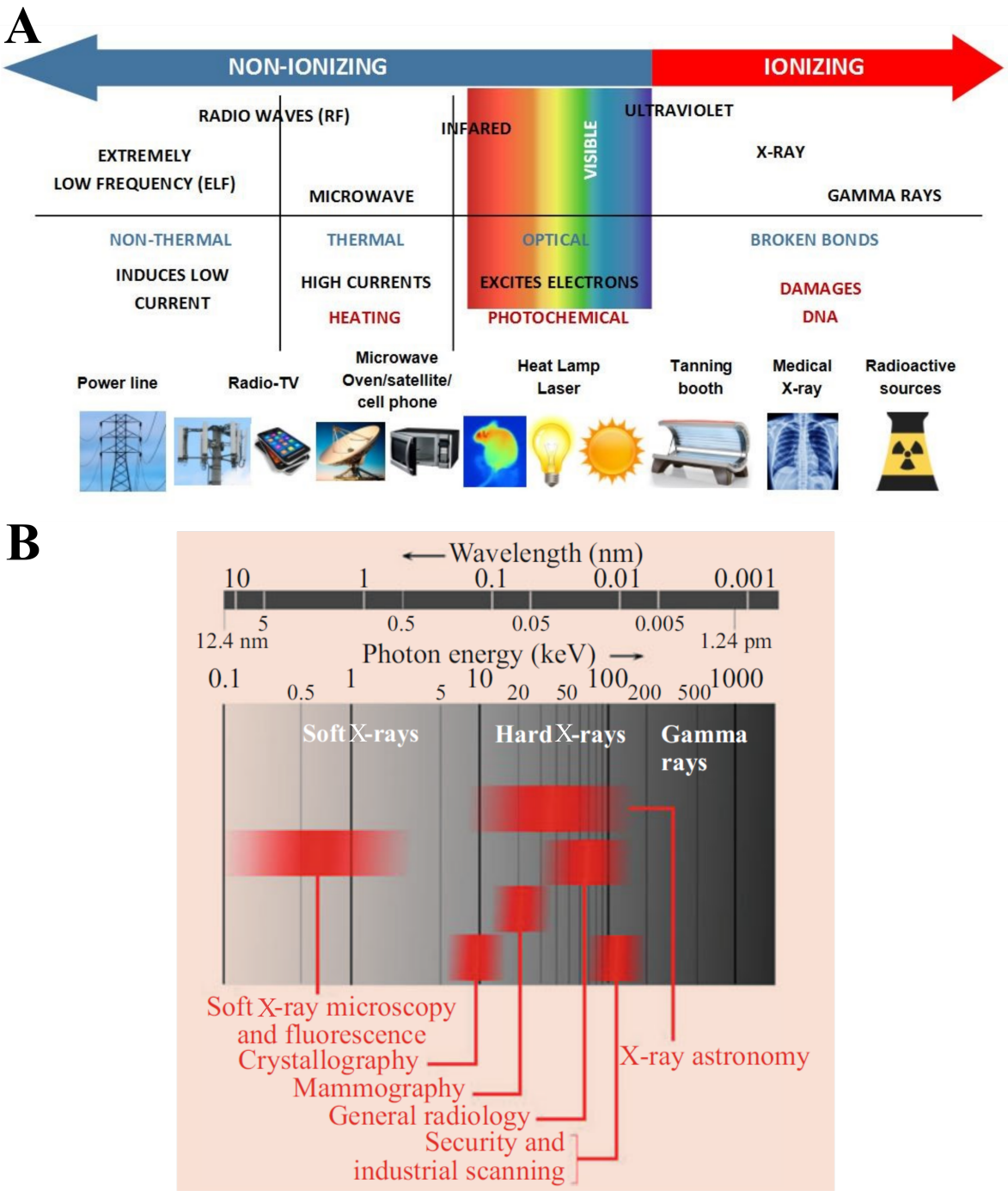

Figure 1-1-1 Ionising radiations. (A) Different types of electromagnetic radiation and associated applications. Two families of radiations can be distinguished: non-ionising and ionising. The latter includes high-energy photons: X- and γ-rays.[12] **(B)** The electromagnetic spectrum between soft X-rays and γ-rays, and their respective wavelengths and photon energies. Applications over various spectral regions are indicated.[13]

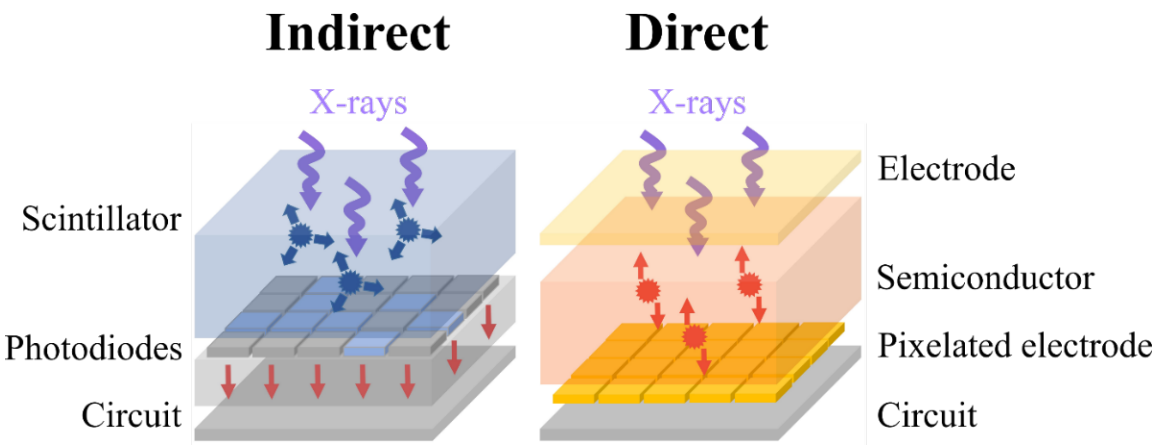

Figure 1-1-2. Schematic representation of both types of X-ray detection: indirect and direct.

A brief summary of the advantageous characteristics associated to both types of X-ray detection is depicted below in **Table 1-1-1**.

Table 1-1-1. Advantageous characteristics associated with indirect and direct X-ray detector technologies.[11]

Direct detectors	Indirect detectors
• Simpler to manufacture	• High operational stability
• No operational device thresholds	• No external bias required
• Higher spatial resolution	• Lower manufacturing cost
• Simpler device operation	• High temporal resolution

The basic principle of operation of an X-ray detector is described through the Shockley-Ramo theorem and the ionisation energy (i.e., electron and hole pair creation energy) that is introduced and used in formulating the responsivity of the detector.[13] We will now discuss the two types of detection and relevant figures of merit.

1.2 Indirect X-ray detection

As introduced before, indirect detection is a two-step process. The first one corresponds to the interaction between high-energy photons and the scintillating material: energy is lost by the high-energy photon and gained by an electron. It can lead to three main physical processes: **(i)** photoelectric absorption, **(ii)** Compton scattering, and **(iii)** electron and hole pair formation for energies above 1.022 MeV.[14] In the case of photoelectric effect, the incoming energy is fully absorbed by a bound electron, commonly a core electron located in the K- or L-shells, ejected into vacuum, thus ionising the host atom.[15] In contrast, the Compton scattering happens at higher energies and is attributed to inelastic interactions between a weakly bound electron and the high-energy photon. Only a fraction of the incoming photon is absorbed (a photon of lower energy is scattered) and the scattering electron is excited to a higher energy state. All processes are characterised by different absorption coefficients that are ultimately determined by the atomic number *Z* of the scintillating material and the photon energy.

The overall process leads to the generation of excitons of lower energy than the incoming photons (loosely bound hole–electron pair) that are transported to defect states, or activators (typically, thallium (Tl) or cerium (Ce)), within the scintillating material where they ultimately recombine and generate visible photons. The emitted light can then be detected using different types of photodetectors such as silicon (Si) photodiodes, thin-film phototransistors (photo-TFTs), photomultiplier tubes (PMTs), complementary metal–oxide–semiconductor (CMOS) photodetectors, silicon avalanche photodiodes, or charge-coupled devices (CCDs) coupled with the scintillating element.[11]

One of the main strengths of indirect scintillator detectors is that they are of low production cost and more stable than direct high-energy radiation detectors.[14,16] The most important figures of merit for scintillators include the light yield, light decay time, and environmental stability. The light yield describes the number of photons that are generated during the ionisation process per unit energy. The recombination centres in the scintillator could induce radiative but also nonradiative recombination (non-emissive and hence a loss in terms of process) due to the presence of defects and/or impurities. The growth and use of single crystals (SCs) as scintillating medium can suppress the concentration of these defects (trap states) and improve the luminescence yield of the system while helping to accelerate the photoluminescent processes.[11]

Even when using SC scintillators, the ultimate spatial resolution achievable by indirect imagers remains limited. Indeed, at the scintillation step, visible photons are emitted within a given solid angle, so each high-energy photon absorption event has a certain spread in the detectable light (Lambertian reflectance). Because of that, the spatial resolution achievable by indirect detection is generally close to the thickness of material used. In the case of standard scintillators, oxides, such as gadolinium oxysulfide (Gd_2O_2S),[17,18] can achieve good sensitivity

with very thick layers (several hundreds of micrometres), but at the expense of spatial resolution.

For medical imaging, commercial indirect detection is dominated by materials such as micro-columnar thallium-activated caesium iodide (CsI(Tl)) for medical radiography (~ 180 µm pixel pitch),[19,20] or thallium-activated sodium iodide (NaI(Tl)) for scintigraphy (~ 4 mm pixel pitch).[21,22]

1.3 Direct X-ray detection

The operating principle of direct high-energy radiation detectors is based on the direct conversion of the incoming X-ray photons into charge carriers by the sensing material, which is typically a semiconductor. As for the indirect detection, the interaction between the soft X-ray photons and the sensing material relies on photoelectric absorption, while the detection of hard X-ray photons is based on Compton scattering. Absorption of high-energy photons results in the generation of electron-hole pairs. As an example, for medical radiography 50 keV photons, 10 000 electrons are generated within a semiconductor with a bandgap of 1.5 eV, compared to 1 000 electrons measured in CsI. The resulting charge carriers are collected thanks to the presence of an external electric polarization field and a specific device electrode engineering.[6,23] The operation and efficiency of such detectors and the corresponding definitions and figures of merit that characterise them are listed in the following subparts.

1.3.1 X-ray absorption and linear attenuation coefficient

To begin with, the greater the interaction between the incoming radiation and the semiconducting material, the better the performance of the detector. In the case of X-ray medical imaging, almost all the incident X-ray radiation (> 90 %[24]) should be absorbed within the photoconductor to avoid unnecessary patient exposure. The linear attenuation coefficient α of this material characterises its ability to efficiently absorb high-energy photons.[11,25] Expressed differently, the X-ray attenuation depth δ, the reciprocal of α, must be substantially less than the photoconductor layer thickness L. The fraction of incident photons in the beam that are absorbed by the photoconductor depends on α of the used material and its thickness L; and is given by **Equation (1-1)**:[25]

$$A = 1 - e^{-\alpha L} = 1 - e^{-\frac{L}{\delta}} \quad (1\text{-}1)$$

Where A is the quantum efficiency, the X-ray attenuated or absorbed fraction, α is the linear attenuation coefficient (cm^{-1}), δ is the attenuation depth (cm) and L is the photoconductor thickness (cm), as mentioned above. From this equation, one can determine the attenuation depth δ, which corresponds to where the beam has been attenuated by 63%,[25] while an attenuation of more than 90 % can be achieved for a photoconductor thickness at least three times larger than δ: $L = \frac{3}{\alpha} = 3\delta$. Materials with high linear attenuation coefficients are thus of

interest. The coefficient α is a function of the photon energy E_{ph}, the atomic numbers Z and mass fraction of the constituting atoms, and the resulting density ρ_d of the material. If the sensing material is not a SC, the density also depends on structural properties and morphology, the effective density is then lowered. Thus, high density materials with high atomic numbers Z are favoured.[11,26]

1.3.2 Ionisation energy

Another key concept of the direct detection is how the absorbed high-energy photons are efficiently converted into charge carriers. This corresponds to the electron-hole pair creation (or ionisation) energy W, which is defined as the energy required to create a single free electron and hole pair, calculated by dividing the total adsorbed energy by the total number of extracted electrons.[11,25] This energy has to be relatively low to promote the photogeneration of a maximal number of charge carriers. Given the above definition, the free or collectable charge generated Q in the sensing material from an incident and absorbed radiation can be calculated from W and is defined by **Equation (1-2)**:

$$Q = e\frac{E}{W} \tag{1-2}$$

Where Q is the collectable charge created in the material (C), e is the elementary charge ($1.60217663 \times 10^{-19}$ C), E is the absorbed radiation energy (eV), and W is the ionisation energy (eV). For many crystalline semiconductors it is well-known that W can be estimated using the so-called Klein equation, which is made explicit in **Equation (1-3)**:[27,28]

$$W = \frac{14}{5}E_g + 0.5 \tag{1-3}$$

Where E_g is the material bandgap (eV). This rule suggests that semiconductors with a narrow bandgap should be preferred for low W. Unfortunately, narrow bandgap semiconductors suffer from higher concentrations of carriers at thermal equilibrium. Such concentrations lead to high residual conductivity in the absence of high-energy radiation (high dark current) which is detrimental for the application (see below).[25] Thus, ideally the sensing semiconductor should realize a compromise between a sufficiently narrow bandgap for efficient photogeneration of charges and a sufficiently wide one to limit the dark current and associated noise.[24] In this compromise, the minimisation of the ionisation energy W can be achieved by other means than tuning the bandgap. While it is a function of the bandgap of the absorbing material, it has been shown in the case of some materials like a-Se that W decreases sharply with the applied electric field. This behaviour can be described by **Equations (1-4)**[25] and **(1-5)**:[29]

$$W = W^0 + \frac{B}{F} \tag{1-4}$$

$$W = 2.2\,E_g + E_{ph} \tag{1-5}$$

Where W^0 is the intrinsic energy of electron-hole pair generation at "infinite field", B is a constant that weakly depends on the X-ray photon energy, F is the applied electric field, and

E_{ph} is the photon energy. Assessing the ideal W is a multi-parameter problem, which will depend on the nature of the employed material and an appropriate model describing what is happening in the inside.

1.3.3 Dark current, noise and electrode engineering

The dark current of the photoconductor is the current measured while being under a bias voltage in absence of detectable radiation. In imaging, it corresponds to an offset, which is suppressed by subtracting the image measure in the dark to the image under X-ray illumination. If this offset is too high, the residual noise on the resulting images can degrade the signal-to-noise ratio (SNR), raising the minimal signal and limiting the maximal exposure time. It should therefore be negligibly small. There have been several attempts to estimate what would constitute a negligible dark current density J_{dark} but it is generally accepted that it should preferably not exceed 10 pA mm^{-2}, depending on the clinical application.[25,30] The dark current, in most photoconductive semiconductors, is normally attributed to one of two factors: the rate of injection of carriers from the contacts into the photoconductor and the rate of thermal generation of carriers.[25] On the one hand, a small dark current requires the contacts to the photoconductor to be non-injecting, meaning that there is a proper alignment of the energy levels of the semiconductor and each specific electrode for extraction of electrons and holes, this is called electrode engineering. On the other hand, the rate of thermal generation of carriers from various defects or states in the bandgap should be negligibly small (i.e., dark conductivity tending to zero). Small dark conductivity generally requires a wide bandgap semiconductor, which conflicts with the condition of smaller ionisation energy, as exposed above. A compromise has to be found.

1.3.4 Mobility-lifetime product, charge collection efficiency and sensitivity

After charge carrier generation, the applied field F drifts the electrons and holes in opposite directions towards their respective collection electrodes. During this charge transport, due to recombination or trapping, carriers are partially lost. The drift mobility of the carrier is characterised by μ and its mean lifetime τ, which is directly affected by recombination or deep trapping. The electron and hole mobility–lifetime products ($\mu\tau$) expressed in cm^2 V^{-1} are key parameters and highlight the quality of a semiconductor X-ray detector. The larger the $\mu\tau$ product is, the higher the charge collection efficiency (CCE, labelled here η_{CC}) of the detector and its performance. Each charge carrier, electron and hole, possess its own $\mu\tau$ product, denoted $\mu_e\tau_e$ and $\mu_h\tau_h$, respectively. The mean distance drifted by the carrier, before it is trapped or disappears by recombination, is another important notion and it is symbolised by $\mu\tau F$. This distance is called the *schubweg* (travel or stroke length). Since most of the charges must be collected, for both electrons and holes, we need to ensure that the electron and hole *schubwegs*

are both much longer than the thickness of the photoconductive layer, that is, $\mu\tau F >> L$. The drift $\mu\tau$ product is normally called the range of the carrier, that is, its *schubweg* per unit field.[11,25]

The CCE is self-explanatory; it corresponds then to how good the original charge created within the material is extracted. This figure of merit does not have a unique explicit formula. However, it is particularly informative as it takes into consideration many aspects of the device: the nature of the sensing material, device configuration, charge injection on the electrodes, to name a few influencing parameters. It is a function of the attenuation depth δ, the *schubweg* for both charge carriers, as well as device dimensions. If the photoconductor layer is made thicker to capture more of the radiation (towards increasing X-ray attenuated fraction A), the $\mu\tau F >> L$ condition would eventually be lost, and CCE would start limiting the sensitivity,[25] which is described below.

The overall conversion efficiency of the incident radiation to collected charge relies on the three distinct processes discussed above. First is the X-ray attenuation in the photoconductor, determined by A, and the absorption of the radiation energy, determined by $(\frac{\alpha_{en}}{\alpha})$ E_{ph}, per attenuated photon in which α_{en} is the energy absorption coefficient at the energy of interest. The second process is the conversion of absorbed radiation to electron-hole pairs, which is determined by ionisation energy W. The third process is the drift and eventual collection of the photogenerated charge carriers, the efficiency of which is determined by CCE. It is useful to define the X-ray sensitivity S of a photoconductor as the charge collected per unit of incident radiation per unit of area, made explicit in **Equation (1-6)**:[25]

$$S = \frac{5.45 \times 10^{13}\, e}{\left(\frac{\alpha_{en}}{\rho_d}\right)_{air}} A \frac{\frac{\alpha_{en}}{\alpha} E_{ph}}{W} \eta_{CC} \tag{1-6}$$

Where S is the device sensitivity (C m^{-2} R^{-1}) (R = Roentgens) in SI units. The first term gives the incident photon fluence per Roentgen unit, the second is the attenuated fraction of the incident photons A, the third is the number of electron-hole pairs created per absorbed radiation energy, and the fourth is the fraction of those charges that are actually collected η_{CC}. The quantity $\left(\frac{\alpha_{en}}{\rho_d}\right)_{air}$ is the energy absorption coefficient per unit density for air. All terms in **Equation (1-6)** depend on the photon energy and, for most semiconductors, only the last term η_{CC}, depends on the applied field.

A high detection sensitivity is needed for X-rays detectors to generate high-quality images with good contrast at the lowest possible X-ray dose. The sensitivity can be improved by using two different approaches: **(i)** increasing the $\mu\tau$ product within the sensing material; and **(ii)** increasing the applied bias. The latter however is often limited by a simultaneous rise of noise/dark current.[11] Sensing materials that combine a high $\mu\tau$ product and have a low trap density exhibit two key features for achieving efficient direct X-ray detection.

The $\mu\tau$ product for a given sensing material can be estimated by using the standard or modified Hecht equation which are defined by **Equations (1-7)**[31] and **(1-8)**[32–34], respectively.

The Hecht model considers a device with a planar geometry having two parallel electrodes that cover the whole detector area:

$$Q = \frac{Q_0 \mu \tau V}{L^2}\left[1 - e^{-\frac{L^2}{\mu \tau V}}\right] \quad (1\text{-}7)$$

$$Q = \frac{Q_0 \mu \tau V}{L^2}\,\frac{1 - e^{-\frac{L^2}{\mu \tau V}}}{1 + \frac{L s_r}{V \mu}} \quad (1\text{-}8)$$

Where, like in **Equation (1-2)**, Q is the measured charge (C) (or photocurrent I(A)), Q_0 is the total charge (C) (or photocurrent I_0(A)) generated by the interaction, μ is the mobility (cm² V^{-1} s^{-1}), τ is the charge carrier lifetime (s), V is the applied bias (V) (where $V = F\,L$), L is the device thickness (cm), and s_r is the surface recombination velocity (cm s^{-1}). Both previous equations consider a single charge carrier, but for most semiconductors, both electrons and holes contribute to the measured charge Q, with different $\mu\tau$ product. Both contributions are taken into account by **Equation (1-9)**:

$$Q = \frac{Q_0 V}{L^2}\left[\mu_e \tau_e \left[1 - e^{-\frac{L x_o}{\mu_e \tau_e V}}\right] + \mu_h \tau_h \left[1 - e^{-\frac{L(L - x_o)}{\mu_h \tau_h V}}\right]\right] \quad (1\text{-}9)$$

Where μ_e and μ_h are the mobilities of electrons and hole, respectively (cm² V^{-1} s^{-1}), τ_e and τ_h are the lifetimes of electrons and hole, respectively (s), and x_o is the position where the electron-hole pair is created, where the X-ray absorption takes place inside the semiconductor (cm). The Hecht equation was developed to analytically characterise the charge collection process in semiconductor radiation detectors under uniform field, and permanent carrier trapping conditions.[31] The modified Hecht or Hecht-Many equation considers additionally the surface recombination s_r, developed originally for thin film photodetectors,[34] which requires the prior determination of the charge carrier mobility μ via characterisation techniques such as space charge limited current (SCLC) or time of flight (ToF).

1.3.5 Additional figures of merit

Other important concepts allowing assessing the performance of direct X-ray detectors, which are naturally linked to the ones previously introduced, are presented below:[6,11,24]

- The signal-to-noise ratio (SNR) defines the strength of the electrical-optical signal upon excitation to that of unwanted signal (noise such as the dark current or the readout circuit noise).
- The resistivity ρ of the sensing material needs to be sufficiently high. Thus, the applied bias V, used to collect the photogenerated charge carriers, does not cause an important flow of charges when the semiconductor is not irradiated (dark current), therefore favouring the SNR.

- The spatial resolution of the detector determines the image resolution and hence its sharpness. It is defined as the number of discernible line pairs per millimetre (lp mm^{-1}).
- The response time, which is defined as the time taken for the detector to respond to external stimuli (i.e., pulse of X-ray photons). Fast response helps to minimise the exposure duration time and/or enable higher frame rate during imaging, and is important for live medical imaging applications (e.g., cardiac surgery).
- Structural uniformity, which is determined, primarily, by the processing versatility of the active material employed.
- The operational stability, which relates to the detector ability to maintain a specific level of performance during operation (while being irradiated and over time).

Currently, few semiconductors (e.g., a-Se in mammography) present a combination of properties making them suitable for direct X-ray detection for medical imaging. Because they operate in a direct detection configuration, they present a rather good spatial resolution (3 lp mm^{-1} [35]) but the attained sensitivity remains limited for the most demanding applications, and the cost and technical difficulties associated with the realisation of flat panels of large area (40 cm × 40 cm) is too high to benefit the general population through standard medical radiography.

1.4 Flat panel X-ray imagers

Among the different applications for X-ray detection, medical X-ray imaging is one of the main applications, as well as, one of the most extensive modern applications of semiconductor detectors.

Flat panel X-ray imagers (FPXIs) are extensively used in imaging. In direct conversion FPXIs, the absorbed X-ray photons are directly converted to charges in the photoconductor and are collected by a matrix of pixelated electrodes. The image is defined by the charge distribution on the pixels. For pixel matrices, these FPXIs use either a TFT active matrix array (AMA) on a glass substrate, or for smaller areas, CMOS, CCD, or application-specific integrated circuit (ASIC) silicon chips as the sensor to read the image.[13]

The TFT-AMA and CMOS are currently the most popular for large size panel detectors. Several photoconductive semiconductors are used with these readout technologies: Si,[16] amorphous selenium (a-Se),[36] lead oxide (PbO),[37] lead iodide (PbI_2),[38] mercury (II) iodide (HgI_2),[39] and cadmium zinc telluride ($Cd_{1-x}Zn_xTe$) (CZT)[40] or thallium (I) bromide (TlBr).[41]

Figure 1-1-3 shows a simplified functional classification of X-ray detectors, which involves the dose measurement, X-ray energy spectrum, and X-ray imaging in the form of arrays. The latter class of imaging detectors is probably the most important application that has experienced unmatched growth in the last two decades.[13] For that, semiconductors are among

the most important class of detectors used for X-ray detection. This is where a new promising family of semiconducting materials make its entrance: metal halide perovskites.

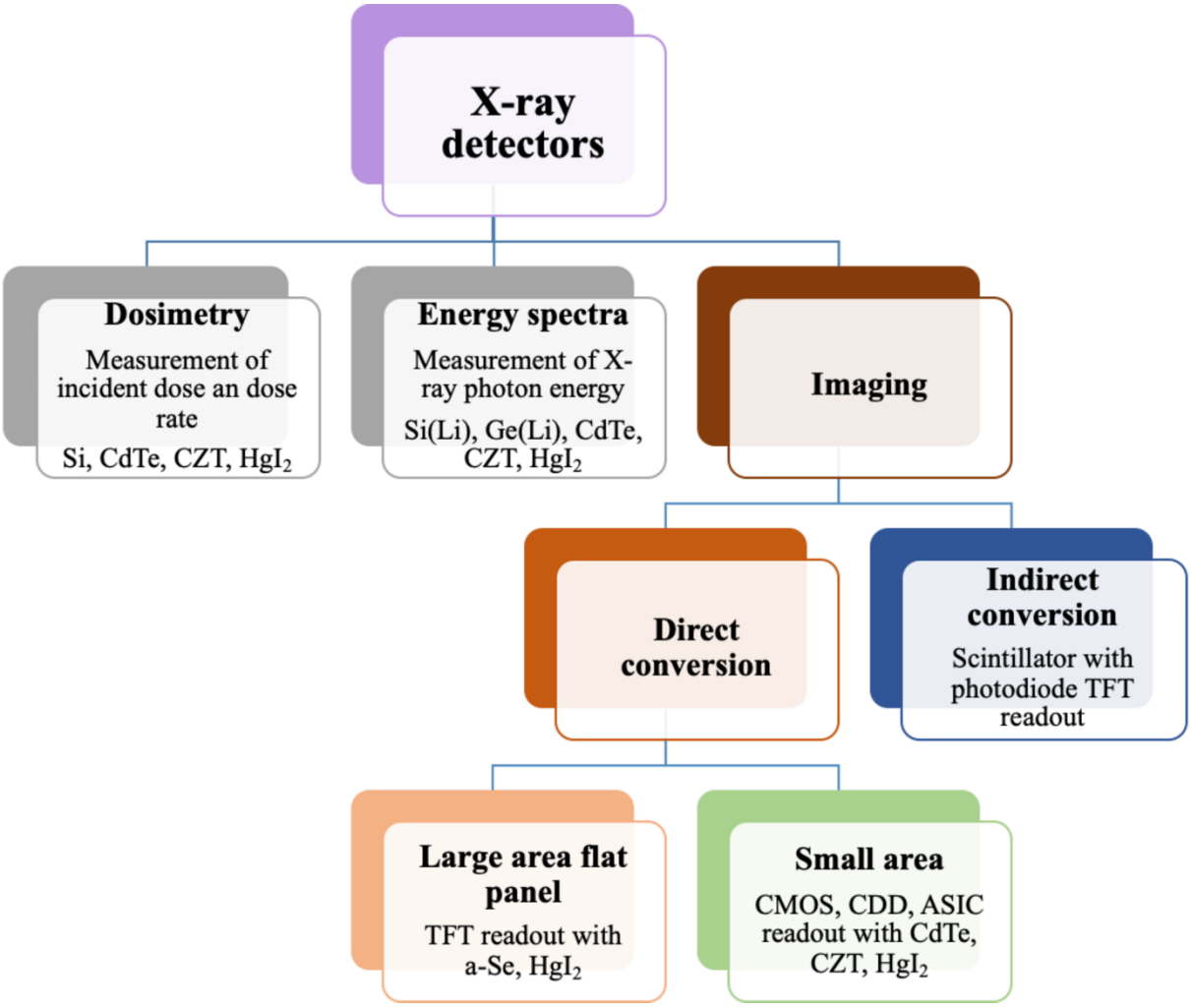

Figure 1-1-3. A simplified classification of X-ray detectors. The orange highlighted branch is the emphasis in this work. Figure inspired from reference.[13]

2 Metal halide perovskite materials

2.1 An overview on perovskites: history, structures and chemistry

Perovskites encompass a very large family of materials. The first material identified with a perovskite structure was the calcium titanium oxide mineral ($CaTiO_3$), discovered by Gustav Rose in 1839, and named after the Russian mineralogist Lev Perovski.[42,43] On the one hand, perovskite oxides have seen a blossoming during the 20th century. The ferroelectric properties of the deformed perovskite $BaTiO_3$ were discovered in the 1940s, becoming the first successful ferroelectric perovskite material.[44–46] Since that, perovskite oxides have found their way in many applications such as ferroelectrics ($PbZr_{1-x}Ti_xO_3$),[47] superconductors ($YBa_2Cu_3O_7$ - 1987 Nobel Prize),[48] multiferroics and nonlinear optics ($BiFeO_3$, $LiNbO_3$),[49] magnetoresistance ($Sr_{1-x}La_xMnO_3$),[50] among many others. On the other hand, halide perovskites have seen a tardier rise in interest. Even though these materials haven been known since the 19th century,[51] their properties, structural[52,53] and optoelectronical[54,55], have only been gradually discovered in the following 20th and 21st centuries.

Whether ideally cubic or distorted, a perovskite general formula would be $A^{+(3n-y)}B^{+y}(X^{-n})_3$ with $n \geq 1$ and $3n-1 \geq y \geq 1$,[24] but the shorter ABX_3 is commonly used. In this formula, the cation B forms a network of $[BX_6]^{y-6n}$ octahedra with the X anions. Each BX_6 octahedron is linked to neighbouring ones via its corners in all three directions, generating infinite 3D $[BX_3]^{y-3n}$ networks, as depicted in **Figure 1-2-1-A**.

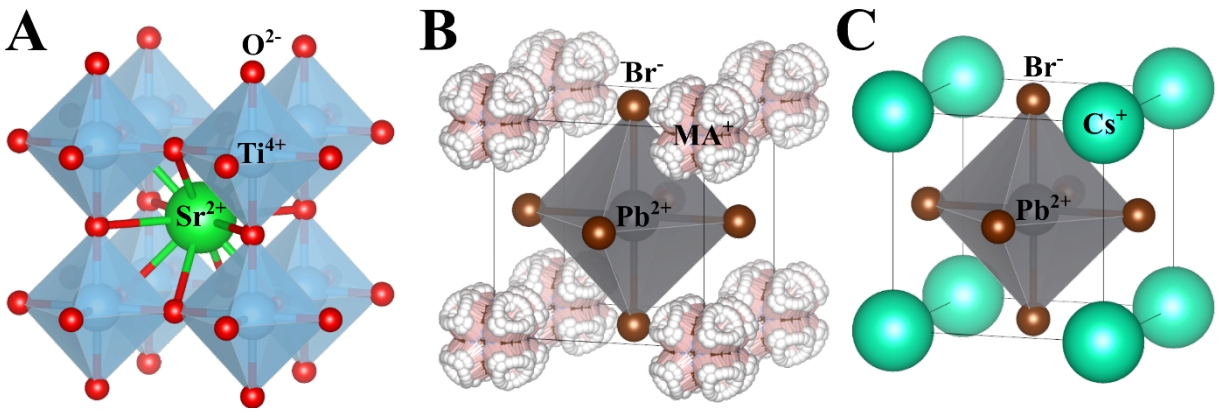

Figure 1-2-1. Perovskite structure examples. The figures above illustrate the unit cell of several perovskite structures: **(A)** $SrTiO_3$,[56] **(B)** $MAPbBr_3$[57] and **(C)** $CsPbBr_3$.[58] $SrTiO_3$ is the reference perovskite structure with cubic phase and part of $Pm\bar{3}m$ space group, at room temperature and atmospheric pressure. $MAPbBr_3$ and $CsPbBr_3$ are examples of hybrid and inorganic halide perovskites, respectively, with the same cubic phase and space group as $SrTiO_3$. **(A)** focus on the inorganic framework made by the $[BX_6]^{y-6n}$ octahedra surrounding the cation, while **(B)** and **(C)** highlight the different type of cations that can be employed in halide perovskites. **(B)** depicts all possible orientations of the organic cation MA^+ can have. Atomic radii were used for these illustrations.

This configuration is therefore sometimes called 3D perovskite. It leaves the A cation of the general formula situated at the centre of the cell, within a cuboctahedral coordination geometry formed by the 12 neighbouring X anions: AX_{12}. **Figure 1-2-1-A** illustrates such reference cubic perovskite structure with strontium titanate ($SrTiO_3$) unit cell ($Pm\bar{3}m$ space group) as well as alternative representations of cubic perovskites, **Figure 1-2-1-B** and **Figure 1-2-1-C**, locating the A cation at the cells corner and a BX_6 octahedron at the centre.

From a structural point of view, the formation of a perovskite with corner-sharing octahedra requires the formation of both BX_6 octahedron and AX_{12} cuboctahedron. For ions fulfilling the neutrality of the ABX_3 formula, this turns into two factors used to predict the stability of the perovskite structure from the corresponding ionic radii. First, the octahedral factor μ_{oh} is defined by **Equation (1-10)** and provides a measure of the BX_6 octahedral stability in the material:[59]

$$\mu_{oh} = \frac{r_B}{r_X} \tag{1-10}$$

Where r_i is the ionic radius of ion *i* (Å). The octahedral rule states that this factor should be in the range of $0.44 \leq \mu_{oh} \leq 0.9$. The BX_6 octahedron is the basic unit of the perovskite structure. If the octahedral factor μ_{oh} is too small the octahedron would be heavily distorted or could simply even not be formed precluding the existence of a perovskite phase.[59] Secondly, the tolerance factor t_G, introduced by Goldschmidt in 1926, is an assertion of the ability of the BX_6 octahedra to encapsulate the A cation, that is to say the formation of the AX_{12} cuboctahedra. The formula is given in **Equation (1-11)**:[60]

$$t_G = \frac{r_A + r_X}{\sqrt{2}(r_B + r_X)} \tag{1-11}$$

Where again r_i is the ionic radius of ion *i* (Å). For a perfect cubic perovskite lattice, t_G is close to 1. Empirically, many perovskites synthesised to date form in the range $0.81 \leq t_G \leq 1.0$. Hexagonal structures are typically formed when $t_G > 1$, and non-perovskite structures are formed when $t_G \leq 0.8$.[61] Having the tolerance t_G and octahedral μ_{oh} factors in the right ranges is generally indicative of favourable conditions for ABX_3 perovskite formation.

While perovskite oxides are the best known, a wide range of halide perovskite materials have been synthesised with a wide variety of ions, both organic and inorganic cations have also been developed and exploited for a vast range of applications.[62–65]

Metal halide perovskites (MHPs) have recently attracted a lot of attention. Halide-based perovskites with formula ABX_3 can also present 3D structures but unlike their oxide counterparts, they are much rarer as they can only be formed with specific combinations of elements. This is because the halide (X^-) anions (X = Cl, Br, I) impose two major differences in comparison to the superoxide (O^{2-}) anion. Firstly, they bear a smaller negative charge, which may only be compensated by a combination of A and B cations in lower oxidation states, leading to general formulas $A^I B^{II}(X^{-I})_3$ or $A^I_2 B^I B^{III}(X^{-I})_6$. Secondly, they have much larger

ionic radii, which precludes small metal ions from forming octahedral coordination geometry ($\mu_{oh} < 0.44$).[61]

Because of these restrictions, B^{II} candidate metal cations can only be selected from a limited set of elements, including: the alkaline earths (group 2) such as Sr or Ba;[66] the bivalent rare earths (lanthanide series) such as Eu,[67,68] Tm[69] or Yb,[69]; the heavier group 14 elements such as Ge,[70] Sn,[54,71] or the original Pb;[51–53] group 12 element Hg;[72] or group 11 Au, forming bi-cationic $A_2B_2X_6$ structures, called double perovskites.[73,74] Remarkably, there are no transition metals that can adopt the perovskite structure with halide anions, with few notable exceptions with Mn.[75] The above considerations do not apply for X = F^- because of its small size, it can stabilise the perovskite structure for virtually all the bivalent metal ions.[61]

A consequence of the limited choice in B^{II} satisfying the octahedral rule is that the number of A^I element satisfying the Goldschmidt rule is also limited to cations in a narrow window for each selected metal B^{II}. It may be a large inorganic or small organic cation leading to full inorganic or hybrid MHP, respectively. For the largest B^{II} metals, such as Pb^{2+}, only three A^+ cations known to date are able to stabilize the perovskite structure: caesium Cs^+, methylammonium ($CH_3NH_3^+$, MA^+) and formamidinium ($CH(NH_2)_2^+$, FA^+). Whereas, in agreement with the Goldschmidt rule, Cs^+ is the only elemental cation large enough to sustain the perovskite structure, for organic cations, it appears that it is not only the size that is important but also the distribution of the net positive charge. Thus, MA^+ and FA^+ are able to stabilise the perovskite structure, but cations with similar size abiding by the Goldschmidt rule, such as $HONH_3^+$,[61] $CH_3CH_2NH_3^+$,[76] or $(CH_3)_2NH_2^+$,[77] are not.

For a given MHP, the A^+ organic cation can be viewed as a structuring agent, in a similar fashion to the amines used in the formation of zeolites. When the cation is too small, the preferred structure is NH_4CdCl_3-type, which can be described as double chains of edge-sharing octahedra $[BX_5]^{3-}$. When the cation is too large, the preferred structure is $CsNiBr_3$-type, which consists of single-chains of face-sharing octahedra. If the size is even more increased, it can give rise to perovskite-like structures with a lower dimensionality (2D, 1D, 0D).[78–81] That way, "perovskites" can exist in a layered form (2D perovskite), with single plans of $[BX_6]$ octahedra separated by intercalated layers of spacer material (usually long amines such as butylamine, phenethylamine, among others) or in a mixed 2D/3D form where 3D-like layers, a couple of corner-sharing octahedra thick, are separated by intercalated layers (Ruddlesden-Popper phase).[82,83]

2.2 The resurgence of metal halide perovskites in optoelectronics

The pioneering work by Miyasaka et al. in 2009 laid the foundation for perovskite-based photovoltaic (PV) research and kicked off a scientific revolution on solar energy materials for third generation PV (excitonic solar cells) technologies.[11,84] They made the first attempt to use halide-based perovskites, methylammonium lead tribromide ($MAPbBr_3$) (see unit cell structure

in **Figure 1-2-1-B**) and methylammonium lead triiodide ($MAPbI_3$) as sensitizers in dye-sensitised solar cells with a power conversion efficiency (PCE) of ≈ 3.8 %. Since then, MHP materials have attracted enormous attention primarily due to their excellent properties. These favourable properties include simple and flexible chemistry,[85,86] bipolar charge conductivity,[87] long diffusion carrier lengths,[88] direct and tuneable bandgap,[61] high absorption coefficients,[89] high quantum yield,[90] and unmatched processing versatility.

From the early days, the research effort on MHP-based PVs has not been focused solely on improving the PCE but also the stability of the cell: replacement of liquid electrolyte with solid-state hole conductor.[91,92] This effort has, for now, culminated in the demonstration of MHP PVs with a certified PCE in excess of 26.1 % for single-junction cells and 33.7 % for MHP/Si tandem cells (monolithic),[93] as seen in reference[94]. Increasing the efficiency from 3.8 % to 26.1 % in over a decade is a remarkable achievement if one considers that analogous progress in traditional technologies, such as Si and GaAs solar cells, took 20 to 40 years to materialise. The tremendous progress is reflected in the fact that the reported PCEs for polycrystalline (PC) MHPs PVs are inferior only to devices based on SC semiconductors such as Si and GaAs.[11,94] Currently, the stability issue remains an open challenge as the main concern regarding MHPs for PV applications is their apparently inherent chemical and structural instability under ambient conditions.[95]

The same favourable properties for PV are now propelling MHPs at the forefront of research and development for other optoelectronics applications,[11,64] including lasers,[96,97] light-emitting diodes,[98,99] photodetectors,[100] sensors,[101] and particle detectors,[102] to name a few examples. For sensing applications, MHPs have demonstrated the ability to convert different environmental stimuli such as particles or photons into optical or electrical signals.

2.3 Metal halide perovskites for high-energy detection

The high-energy detection field also tries to benefit from the above-mentioned attractive properties of MHP materials. The associated research and development efforts have been intensified in recent years. The majority of the ongoing efforts are pointed towards improving the sensitivity and spatial resolution of the detection elements with the additional benefit of improved manufacturability.[103] Thus, the discovery and development of MHPs as a new class of materials that combine key functionalities required, with inexpensive manufacturing have become a hot research area.[6,11,55,61,64]

2.3.1 Outstanding response to high-energy ionising radiation

As indicated in part **1.3** and more specifically for direct X-ray detection, some key functionalities are required from the sensing material: high X-ray absorption, high charge carrier generation efficiency and high $\mu\tau$ product for better charge collection. The first can be determined directly from the crystal structure of the compound, the last two are harder to assess

and generally need precise characterisation. In that sense MHPs present a very good opportunity as their study for PV application provide good indications of their charge carrier generation and transport properties. Regarding the X-ray absorption, MHP based on heavy metals inherently fulfil this requirement with a high density (≈ 4 g cm^{-3}) due to their high compacity (e.g., 0.615 for caesium lead tribromide ($CsPbBr_3$)) and atoms with large atomic number Z (e.g., Cs (Z = 55), Pb (Z = 82), Sn (Z = 50), In (Z = 53), and Br (Z = 35)). The combined high density and high atomic numbers lead to large attenuation coefficients/short penetration depths, and so a total absorption of hard X-rays (50-100 keV) within hundreds of micrometres typically. Optoelectronically, their characterisation for PV showed sufficient $\mu\tau$ products (≈ 10^{-4} – 10^{-2} cm^2 V^{-1}),[32,104–106] low charge trap density (10^8 – 10^{13} cm^{-3}),[107–109] a defect tolerant nature,[32,88,110] short detection times (~ ns),[111–113] and a relatively high bulk resistivity (≈ 10^7 – 10^{10} Ω cm).[81,107,114,115] From a technical point of view, they can be synthesised in solution under mild or ambient conditions offering desired processing versatility at lower cost, when compared to established material technologies (e.g., cadmium telluride (CdTe) or CZT under controlled atmosphere in high temperature Bridgman-Stockbarger furnaces[116]).

Unsurprisingly, perovskite materials studied for PV application have also been prominently considered for high-energy radiation direct detection, with hybrid organic-inorganic compositions such as the prototypical $MAPbX_3$ (X = Br, I), having attracted most of the attention to date,[117,118] as well as, the inorganic $CsPbBr_3$.[105,119] **Figure 1-2-2** shows the attenuation coefficient α of MHPs of various compositions commonly studied along those of commercial materials (a-Se, CdTe and TlBr). As can be seen, the MHPs present attenuation coefficients similar to those of commercially deployed materials, meaning that they can achieve the required stopping power for X- and γ-rays within reasonable layer thickness, in the range of several hundred-micrometre layers. Moreover, some MHPs (e.g., $MAPbBr_3$, $MAPbI_3$) offer particularly wide absorption range that spans from the visible to hard X-rays part of the electromagnetic spectrum making then an excellent choice for several applications (e.g., mammography ~ 20 keV region, general radiography ~ 70-100 keV region).[11]

The seminal work on direct solid-state X-ray detection by a MHP was carried out by Stoumpos et al. in 2013 on $CsPbBr_3$.[33] Since then, the field of high-energy radiation detectors based on MHPs has flourished, with a certain number of technological and scientific hurdles to overcome and remaining open questions, in particular for the specific application of medical radiology.[11]

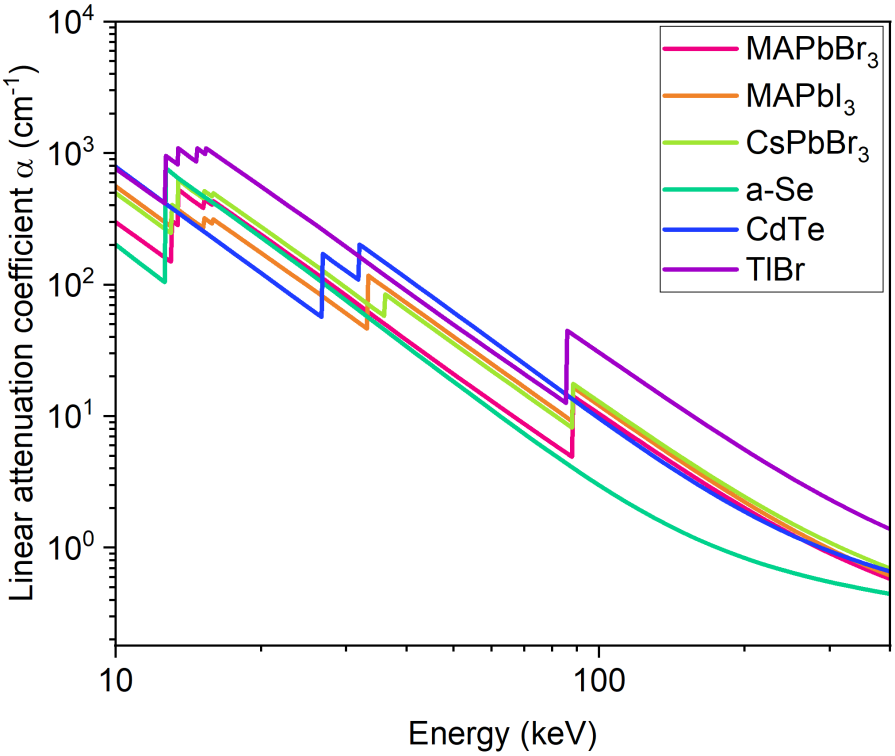

Figure 1-2-2. Linear attenuation coefficient α of several perovskite compositions ($MAPbBr_3$, $MAPbI_3$, and $CsPbBr_3$) compared to classic high-energy radiation detection semiconductors (a-Se, CdTe and TlBr) as a function of photon energy. The plots are based on simulations performed via NIST (National institute of standards and technology) database.[120]

2.3.2 Halide perovskites: new materials for medical X-ray detection and imaging

To date, all commercial X-ray detection systems, based either on direct or indirect detection systems, suffer from one or the other of the following shortcomings.[11] Low sensitivity, low X-ray absorption cross-section (e.g., a-Se for photon energies > 30 keV used for general radiography), material instabilities (e.g., PbI_2 and HgI_2), high charge trap density (e.g., CZT), limited spatial resolution (e.g., CsI(Tl)), high processing temperature during material crystallisation processes (e.g., Si, CZT) or high manufacturing cost (e.g., CdTe, CZT). Therefore, there is room for improvement for these detection systems at the sensing material level and that is where new materials like MHPs can provide a decisive edge. MHP-based prototype detectors have been developed for X-ray detection, showing the potential they have for such application.[32,121,122]

Among the above mentioned MHP having attracted the most scrutiny for direct X-ray detection, our group has selected the methylammonium lead tribromide ($MAPbBr_3$) as the model MHP material. This composition does not give the highest X-ray absorption (see **Figure 1-2-2**), close to 2-mm thickness layer is sufficient to absorb over 80 % of incident 20-70 keV X-rays,[24] but it presents an interesting compromise. Unlike $MAPbI_3$, which absorbs X-ray better, $MAPbBr_3$ has no phase transition in the device storage and photodetection

operating temperature range -20 °C – + 80°C.[123] It is also more chemically and thermally stable than its iodide-based counterpart.[124] $MAPbBr_3$ crystals will not suffer important volume variations leading to defect formation, and eventually, to fractures or peeling off the readout electric circuit. Also, the material can also be elaborated via low temperature synthesis in solution (< 100 °C),[24,125] and is relatively easy to obtain in the pure perovskite phase without parasitic ones, unlike $CsPbBr_3$.[126,127] Additionally, $MAPbBr_3$ features most of the favourable optoelectronic characteristics for high-energy detection already mentioned, making this semiconductor an interesting candidate for large-surface imaging application.

The upcoming part lists important aspects regarding synthesis of hybrid MHPs.

2.4 Synthesis of hybrid halide perovskites

The fact that MHPs can be synthesised in solution under mild conditions offers great flexibility in both synthesis route and chemical compositions. In recent years, there has been a great diversification of the types of MHPs in all sizes and forms: perovskite quantum dots (0D),[128] perovskite nanowires (1D),[129] perovskite nanosheets/nanoplatelets (2D),[130] and 3D textured perovskite assemblies (i.e., cuboid-like,[131] inverse opal-like,[132] coral-like,[133] or maze-like[134] morphologies, etc.) highlighting their potential in a wide range of optoelectronic applications. Ultimately, all these varieties rely on the two main forms of the perovskite: polycrystalline (PC) films and single crystals (SCs). For the former, a fine balance between perovskite nucleation and growth is critical to the film microstructure (uniformity and surface coverage), which essentially determines the performance of optoelectronic device.[135–137] The perovskite film format has been intensively researched and, as mentioned in part **2.2**, has already produced high-efficiency solar cells. The study of MHP in the form of SCs is more recent, as it requires a perfect control of nucleation to favour only growth.

Generally, the hybrid halide perovskites that are of interest to us here are characterised by relatively low incongruent melting temperatures but can advantageously be crystallised in solution by several methods.[86]

2.4.1 Polycrystal films

Perovskite films can be prepared by chemical and physical deposition techniques, mainly including one-step solution processing, two-step sequential deposition, vapour deposition and vapour assisted solution processing.[138,139] The experimental conditions of the deposition allow controlling the film quality. One-step solution processing is the simplest deposition method. As shown **Figure 1-2-3-A**, this method is implemented by spreading (here spin coating) a precursor solution or ink onto a substrate to form a homogeneous liquid film, which is dried and later annealed. In this modality, the precursor solution consists of perovskite precursors PbX_2 and MAX (X = Cl, Br, I) dissolved in a polar aprotic solvent such as γ-butyrolactone (GBL), N,N-dimethylformamide (DMF) or dimethylsulfoxide

(DMSO).[91,92,140,141] In the shown example, $MAPbI_3$ is synthesised by spin-coating a solution of PbI_2:MAI in GBL. This method can allow large-area full-printing manufacturing if a technique other that spin coating is used such as spray, blade or slot-die coatings.[142–144]

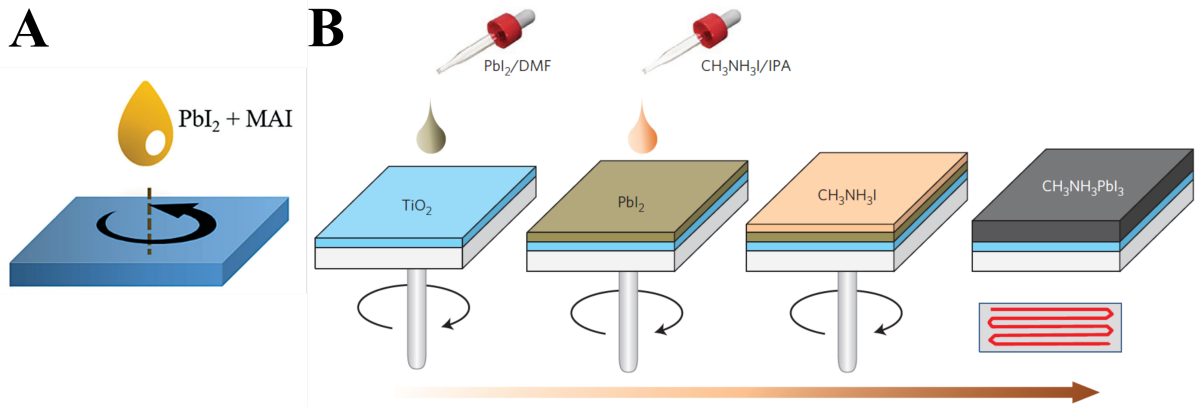

Figure 1-2-3. MHP PC film fabrication methods examples. (A) One-step solution-processing method. Reproduced from reference.[85] **(B)** Two-step spin-coating procedure. Reproduced from reference.[145] Both examples are for $MAPbI_3$ synthesis (IPA = isopropanol).

The two-step deposition method was further developed to gain a better control of the perovskite film morphology. In this method, only one precursor solution (PbX_2) is firstly spin-coated onto the substrate, followed by dipping or spin-coating a MAX-containing solution, as depicted in **Figure 1-2-3-B**, and annealing to form the perovskite film.[140,145,146] Vapour deposition method has also demonstrated to be an effective way to deposit uniform and dense perovskite but relatively thin films (~ hundreds of nanometres).[147]

Additionally, other techniques were developed like chemical vapour deposition by simultaneous sublimation of the precursors,[148] or by combining solution and vacuum deposition processes, like for low-temperature vapour-assisted solution process.[149]

The study of hybrid MHP PC films has mostly been driven by PV applications where very thin films (~ µm) with very large surface area (~ m^2) are needed. With such extreme aspect ratio, control over morphology and microstructure of the crystallised films is primordial. To that end, the use of additives,[150] both thermal[151] and solvent[152] annealing, as well as atmospheric effects[153] and solvent engineering[154] are being investigated to improve the film performances. Such processes are poorly appropriated to reach the high thicknesses (> 100 µm) required for X-ray detection.

2.4.2 Single crystals

The second main forms in which perovskite compounds have been studied are SCs. SCs have continuous, ideally undistorted, crystal lattices. There are no grain boundaries within the material, which results in fewer defects than PC counterparts. Because they are usually synthesised under milder conditions than PC films, SCs generally present improved optical and electrical properties, given their lower charge trap density, longer charge carrier diffusion length, and higher stability.[88,155] Therefore, like for any other semiconducting material, a good understanding and fine control of SC growth of perovskites can further reduce the density of structural defects and boost their optoelectronic performance.[85] For example, it was projected that perovskite SCs hold huge potential to further boost the PCE up to 25% in solar cells.[156] More fundamentally, bulk crystals are extremely valuable objects to assess and benchmark the intrinsic fundamental photophysical properties of a given material. They allow comparing different chemical composition and crystallographic packing without additional effects from grain boundaries in PC thin films or dimensionality in 2D nanoplates, 1D nanowires or 0D quantum dots. That is why in this work a special care has been given to the synthesis of bulk mm-sized SCs, to be able to grow them reproductively with comparable structural quality in order to study the correlation between their structures and optoelectronic characteristics. Moreover, the typical dimensions of the crystals (> 500 µm) match well the thicknesses required for high-energy radiation detection.

2.4.2.1 Growth of bulk single crystals

Almost all standard crystal growth methods have been used successfully for the growth of bulk MHP SCs. These include antisolvents vapour-assisted[155] and cooling-induced crystallisations,[157] seeded solution,[88,125,158] solvothermal,[159] hydrothermal,[160] or melt growths.[33,161] **Figure 1-2-4** shows schematic diagrams of some of these typical growth methods. **Figure 1-2-4-A** depicts an example of antisolvent vapour-assisted crystallisation method for production of both $MAPbI_3$ and $MAPbBr_3$ SCs using GBL and DMF as solvents, respectively, and CH_2Cl_2 (DCM) as diffusing antisolvent. **Figure 1-2-4-B**, in turn, illustrates a type of seeded solution-growth employing lead acetate (PbAc) and hydroiodic acid (HI) for $MAPbI_3$. **Figure 1-2-4-C** shows a typical melt growth for $CsPbBr_3$, the Bridgman-Stockbarger method, which consists in heating up PC material above its melting point and slowly cooling it from one end of its container, where a seed crystal is located.

As mentioned before, only inorganic MHPs are melting congruently. As a results melt growth methods are not suited for hybrid MHPs but only for inorganic MHPs such as $CsPbBr_3$.[86,162] Solution growth methods, on the contrary, can be applied to both inorganic and hybrid MHPs such as $MAPbX_3$ (X = Br, I). Indeed, their key requirement is to dispose of a suitable solvent. In the case of MHPs and more specifically lead halide perovskites (LHPs), the least soluble constituent is the lead halide salt PbX_2. Its counterpart, be it inorganic, such as

CsX, or organic, MAX, being more soluble, any solvent able to dissolve significant amounts of PbX_2 is a potential solvent for the crystallisation of LHP SCs in solution. $MAPbX_3$ (X = Br, I) can be grown in solution using solution temperature lowering (STL) which is part of the cooling-induced crystallisation techniques. This classic technique benefits from the direct solubility of $MAPbX_3$ in HX acid solution, which decreases with decreasing solution temperature.[163–165] The crystallisation can then be triggered and controlled by modifying specific growth conditions such as temperature, pressure, amount or nature of the solvent as we will see below.

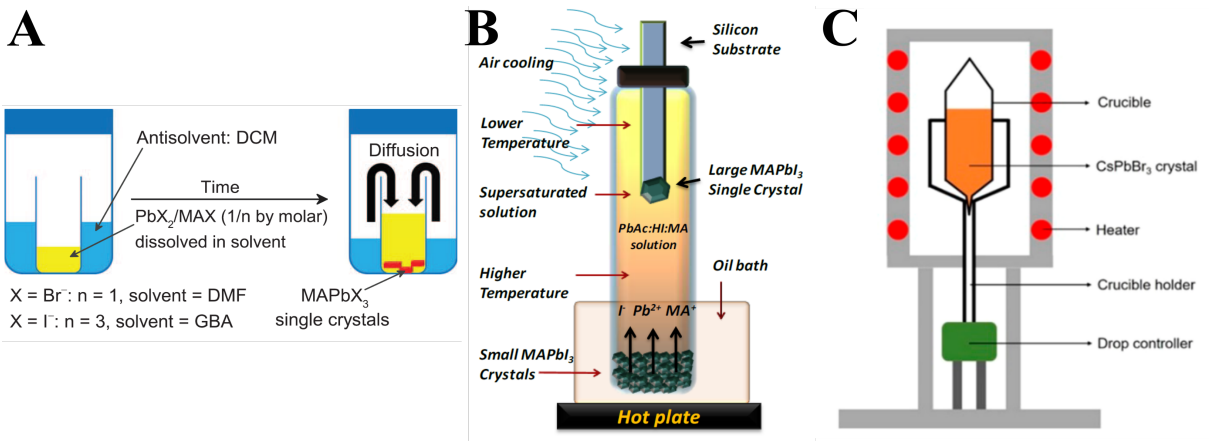

Figure 1-2-4. MHP SCs growth methods examples. (A) Antisolvent vapour-assisted crystallisation method for both $MAPbI_3$ and $MAPbBr_3$. Reproduced from reference.[155] **(B)** Top-seeded solution-growth method for $MAPbI_3$. Reproduced from reference.[88] **(C)** Vertical Bridgman furnace for $CsPbBr_3$. Reproduced from reference.[166]

2.4.2.2 Thermodynamics and kinetics of hybrid lead halide perovskites crystallisation in solution

2.4.2.2.1 Thermodynamic equilibrium in solution, supersaturation and metastable zone

Crystallisation is the process of producing a crystal, an ordered solid phase, from a disordered liquid or gas phase. The crystallisation process can be divided in two steps: nucleation and crystal growth. The predominant step depends on the experimental conditions and dictates the number of crystals and the resulting average size. To control the crystal size is fundamental for any crystallisation process.

Nucleation from solution consists in the formation of a stable solid phase from dissolved building blocks, the solute. Thus, it corresponds to the appearance of a solid phase in a liquid with the creation of an interface. As such, nucleation involves two opposing effects: an energy gain associated with building blocks going from a dissolved to a crystallised state and the energetic cost of forming the interface between the solution and the crystallised particle or cluster. Thermodynamically, the energy gain derives from the change in chemical potential of

the solute $\Delta\mu$ associated with the dissolved-to-crystallised transition. This gain is proportional to the number n of building blocks or solute molecules involved. The interfacial energy cost on the other hand is determined by the crystal/solution interfacial energy γ and the particle surface area S_p. Therefore, the Gibbs free energy change associated with the formation of that particle of surface area S_p and containing n solute molecules can be expressed as in **Equation (1-12)**:

$$\Delta G = -n\,\Delta\mu + S_p\,\gamma \tag{1-12}$$

Here the eventual anisotropy of the particle is overlooked and the same interfacial energy is considered for all facets. In this expression, the number of solute molecules n in the particle increases like the third power of the particle dimension. The particle surface area S_p also increases with the particle size but like the square of the particle size. If one considers, like in the classical nucleation theory, that the particle is spherical, the Gibbs free energy change associated with the formation of a particle of radius r can then be expressed by **Equation (1-13)**:

$$\Delta G = -\frac{4\pi\, r^3}{3\Omega}\Delta\mu + 4\pi\, r^2\,\gamma \tag{1-13}$$

Where Ω is the volume of a solute molecule. From this expression, one can see that for particles of smallest radius r, the r^2 term in the interfacial cost is dominant, leading to a positive ΔG: the smallest particles are thermodynamically unstable. For particles with r large enough, the r^3 term dominates and ΔG is negative: the particle is stable. The nucleation event corresponds to the moment when a particle no longer tends to re-dissolve but to grow. There is a specific threshold value r^*, the critical radius, where an increase in r no longer leads to an increase in ΔG but to a decrease (smaller or more negative). In other words, the critical radius is defined by $\left.\frac{\partial \Delta G}{\partial r}\right|_{r^*} = 0$. From the above expression of ΔG, one gets the Gibbs-Thomson-Freundlich **Equation (1-14)**:

$$r^* = \frac{2\Omega\,\gamma}{\Delta\mu} \tag{1-14}$$

The variation of Gibbs free energy at that nucleation threshold ΔG^* is maximum and positive; its value is the activation energy of nucleation, made explicit in **Equation (1-15)**:

$$\Delta G^* = \frac{16\pi\,\Omega^2\,\gamma^3}{3\Delta\mu} = \frac{4\pi\, r^{*2}\gamma}{3} \tag{1-15}$$

The steady nucleation rate j_0 is the number of particle per unit of time and solution volume crossing that r^* threshold (nucleation events s^{-1} cm^{-3}). It can then be expressed from the nucleation activation energy as in **Equation (1-16)**:[167,168]

$$j_0 = \omega^* \Gamma N_0 e^{-\frac{\Delta G^*}{k_B T}} \tag{1-16}$$

Where ω^* is the frequency at which the solute molecules diffuse from solution to the critical particle (s^{-1}), Γ is the non-equilibrium Zeldovich factor (which gives the probability that a nucleus at the top of the barrier will go on to form the new phase, rather than dissolve), N_0 is

the density of adsorption sites (≈ 1 × 10^{15} cm^{-2}) on a crystalline particle surface, k_B is the Boltzmann constant (1.380649 × 10^{-23} m^2 kg s^{-2} K^{-1}) and T is the temperature (K). The pre-exponential term $\omega^* \Gamma N_0$ in the equation is a very weak function of $\Delta\mu$ compared with the exponential term $e^{-\frac{\Delta G^*}{k_B T}}$, which varies very strongly.[169] As a result, the nucleation rate is practically zero for low $\Delta\mu$ and increases greatly beyond a threshold value $\Delta\mu^*$. It is only past that threshold that spontaneous nucleation may be observed within reasonable time and volume of solution.

What is apparent from the above expressions is that the crystallisation is driven by the change in chemical potential $\Delta\mu$ of the solute going from dissolved to crystallised state. The underlying idea is that the solute in the dissolved state was at a higher chemical potential, was out of equilibrium, and that it returned to a lower energy state, to equilibrium through the crystallisation process. These considerations lead to defining the two most important parameters of crystallisation in solution: the deviation from equilibrium or supersaturation, which is based on $\Delta\mu$ and the equilibrium in the dissolved state or solubility limit.

The solubility limit of a chemical species, the solute, is the maximal quantity that can be dissolved in a given solvent under given conditions (pressure, temperature, etc.). Beyond that limit, any solute introduced in solution would be in excess, and cannot be dissolved and will remain in a solid form. So, at the solubility limit, an equilibrium is achieved between crystallised and dissolved solute. The thermodynamic of this equilibrium can be defined by **Equation (1-17)**:

$$K^0(T) = \frac{C^0}{s} = e^{-\frac{\Delta_r G^0}{RT}} \tag{1-17}$$

Where K^0 is the equilibrium constant of the dissolution, $C^0$is the standard concentration (1 mol L^{-1}), s is the solute solubility limit, $\Delta_r G^0$is the associated Gibbs free energy of reaction (J mol^{-1}) and R is the gas constant (8.314463 J K^{-1} mol^{-1}). In this expression several simplifications have been made. First, the amount of solute corresponding to the solubility limit should be described by its activity, which is assimilated here to its concentration. The activities of the solid phase and solvent are approximated to 1 and the surface tensions are neglected.[24] The solubility limit *s* can subsequently be expressed as shown in **Equation (1-18)**:

$$s = C^0 e^{-\frac{\Delta_r G^0}{RT}} = C^0 e^{\frac{\Delta_r S^0}{R}} e^{\frac{-\Delta_r H^0}{RT}} \tag{1-18}$$

Where $\Delta_r S^0$and $\Delta_r H^0$ are the entropy and enthalpy of reaction, respectively. When considering both terms independents from the temperature, **Equation (1-18)** becomes the Van't Hoff equation. For most solute-solvent cases, the dissolution is endothermic ($\Delta_r H^0 > 0$) as strong solute-solute bounds are broken and replaced by weaker solute-solvent ones. In these cases, as per **Equation (1-18)**, the solubility limit *s* will increase with increasing temperature: this is called direct solubility. In some cases, especially when the solute is susceptible to combine with the solvent to form a defined compound, a solvate, the dissolution of the solute can be

exothermic ($\Delta_r H^0 < 0$) as the total enthalpy of the reaction now combines that of solute dissolution and solvate formation. In those few cases, the solubility limit will decrease with increasing temperature corresponding to a retrograde or inverse solubility, as shown in **Figure 1-2-5**.

The driving force of crystallisation is the change in chemical potential $\Delta\mu$ associated with the solute going from solvated to crystallised state. As mentioned above, the crystallised state is at equilibrium with the solute at the solubility limit, so they have same chemical potential: $\mu_l - \mu_s = 0$, where μ_l and μ_s are the chemical potentials of the dissolved (liquid) and crystallised (solid) phases, respectively. Hence, $\Delta\mu$ can be derived solely from the current chemical potential of the solute in the solution compared to that at the solubility limit *s* in the same conditions (pressure, temperature, etc.) as shown in **Equation (1-19)**:

$$\Delta\mu = \mu_l - \mu_s = k_B T \ln\left(\frac{C}{s}\right) \tag{1-19}$$

Here again, the quantities involved are not, as required, the solute activities (actual and at the solubility limit) are not used but the actual concentration C and the solubility limit s. A practical, adimensional, quantity is generally used to define the deviation from equilibrium, the supersaturation $\beta = \frac{C}{s}$. It is related to $\Delta\mu$ through the relation: $\Delta\mu = k_B T \ln(\beta)$. Alternatively, the relative supersaturation σ_r is also often used, it is defined as in **Equation (1-20)**:

$$\sigma_r = \frac{C - s}{s} = \beta - 1 \tag{1-20}$$

For the crystal growth step, the driving force remains the change in chemical potential, the supersaturation. In **Figure 1-2-5**, this corresponds to how far above the solubility limit (at the same temperature) the solution has been brought. The higher the supersaturation, the higher the growth rate will be. However, if SCs are to be grown, spontaneous nucleation can become a competing and more efficient crystallisation route at too high supersaturation. As discussed above the nucleation rate j_o remains negligible up to a limit $\Delta\mu^*$. So, if one manages to maintain a solution below the corresponding critical supersaturation β^*, this supersaturated solution will crystallise not by spontaneous nucleation but by crystal growth alone. This range of supersaturation is called the metastable zone as shown in **Figure 1-2-5**.[24,125,169] Beyond the metastable zone, the solution is in the labile zone, where crystallisation occurs through both growth and nucleation, the later becoming more prevalent as the supersaturation is increased. Hence, to ensure a steady high-quality growth of SCs, it is crucial to control the solution concentration, and to maintain it in the metastable zone.

The growth of SCs involves many phenomena on multiple scale in both space and time. The growth rate is influenced at a microscopic scale by events such as the deposition rate of the solute molecule onto the crystal surface or the diffusion of these molecules towards an incorporation site, but also on a macroscopic scale by the diffusion rate of the solute in the solution (mass transport) or the crystallisation heat extraction, to name a few.

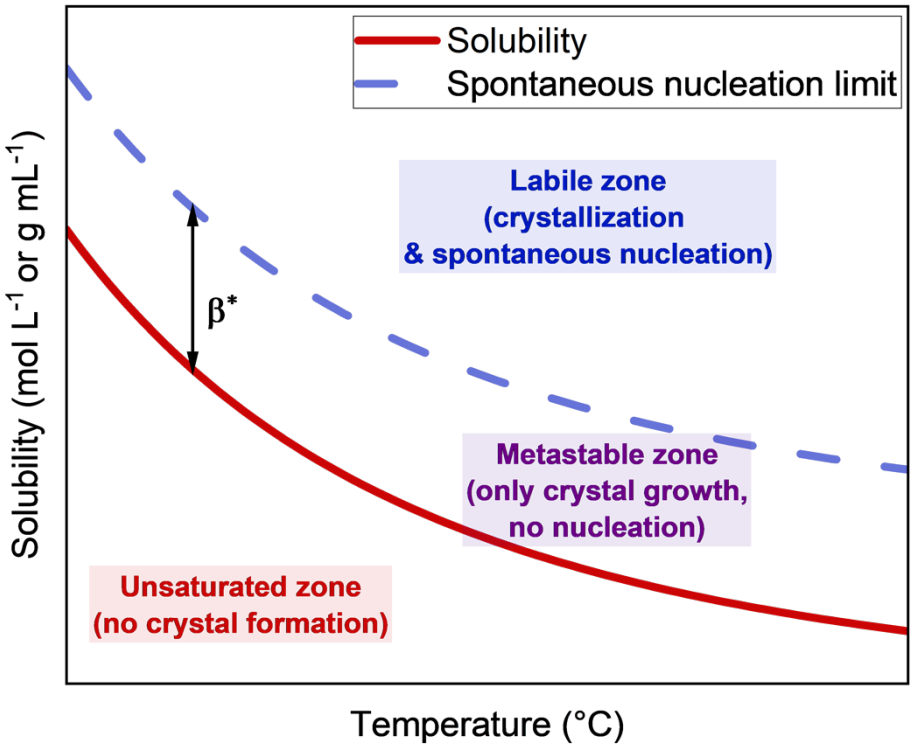

Figure 1-2-5. Retrograde solubility and supersaturation of a chemical species in a solution as a function of temperature. Three zones are highlighted: the unsaturated, metastable and labile zones. Within the metastable zone, there is just enough energy for crystal build-up but not for creation of new solute particles or clusters. The term β^* symbolises here the energy ΔG^* to overcome the spontaneous nucleation limit. Inspired from references.[24,169]

Even though, the complexity of crystal growth is not further developed, put simply, high quality crystal growth is favoured by lower temperatures, stationary growth conditions, good stabilisation of the crystal/solution growth interface and high chemical purity.

One can notice that the different physical quantities above were introduced considering a simple dissolution. In practice, as was alluded to when retrograde solubilities were mentioned, the thermodynamic equilibrium can involve more reactions than the simple dissolution of a solute in a solvent. This happens to be the case with most of the hybrid LHPs and among them, the ones involved in this work. Therefore, although the chemistry of the system is discussed in several instances along this work, a few insights are introduced at this point.

2.4.2.2.2 Hybrid lead halide perovskites solution equilibrium

The first challenge in the synthesis of hybrid LHPs, between which $MAPbX_3$ and $FAPbX_3$, is often to identify a solvent that can efficiently dissolve both organic and inorganic parts. For LHPs, the lead halide precursor (PbX_2) is the most challenging to dissolve. For that reason, the synthesis for LHPs in any form (quantum dots, thin films or SCs) is conducted in highly coordinating polar aprotic solvents such as DMF, DMSO, GBL or mixtures of them.

The coordinating ability of the solvent helps to dissolve the Pb^{2+} ions through the formation of Pb-solvent molecule complexes. Unsurprisingly, many lead-halide solvate phases have been identified as "intermediate" compounds in the synthesis of LHPs.[170,171] The existence of these solvates has a profound impact on the thermodynamic behaviour of the precursor solution and so on the crystallisation of LHPs. For one thing, the reference compound in solution is no longer the dissolved form of the perovskite but a solvate. As indicated above, in that case the enthalpy of formation/destabilisation of that complex is included into the enthalpy of the overall dissolution process and, for most LHPs in the solvents mentioned above, it leads to retrograde solubilities: see **Figure 1-2-6-A** for the case of $MAPbBr_3$ in DMF. These complexation and de-complexation reactions are temperature-dependent and different phases may be predominant in different temperature range. This dynamic then dictates the shape of the solubility curve which can change dramatically between different temperature intervals as is exemplified in **Figure 1-2-6-B** by the solubility curve of $MAPbI_3$ in GBL,[24] which presents both types of solubilities. It is worth nothing that the solvent molecules are large compared to halide anions, and so do not allow the construction of the octahedra frame that cages the organic cation; they may not easily substitute the halide in the perovskite structure.

Nayak et al. identified another feature of these solutions, which is the breaking up or dissolution of lead-containing colloids provoked by a temperature increase or changes in acidity of the solution and the solvent strength. They suggested that the colloid dissolution would increase the concentration of free ions in the solution, leading to supersaturation and the onset of crystallisation with increasing temperature.[172] These free ions are the primary phase serving as building blocks for the crystal construction. As discussed above, the presence of colloids is not necessary to explain the retrograde solubility. Both representations are not mutually exclusive and share a common consideration: a secondary phase is present in solution. Even if the perovskite compound that we are interested in is the most stable compound (the one with the lowest solubility with increasing temperature), the existence of the other compound has major impact on the crystallisation process. This less stable phase may be present in solution in the form of colloidal particles, as the formation of intermediate compounds with higher solubility is often first kinetically favoured over that of the most stable form (Ostwald's rule).

Within our group, solution chemistry studies have been performed to identify the potential origin of such "colloids" for $MAPbBr_3$, which results are summarised in Chapter 2.

As we have seen, the LHP crystallisation is not trivial and the solvent selection has far-reaching implications. Any procedure aiming at growing large SCs of high quality should take into consideration the existence of these complexes.

2.4.2.3 Lead halide perovskite solution growth and inverse temperature crystallisation

There are several ways to induce the crystallisation of perovskites from precursor solution. It may be by solvent evaporation resulting in a solute concentration increase beyond the solubility limit (spin coating of LHP films for PV, see **Figure 1-2-3-A**) or by lowering the solubility limit below the actual solute concentration by gradual addition of a non-solvent (antisolvent vapour-assisted crystallisation, see **Figure 1-2-4-A**).

An alternative, more suited to large volumes of solution, hence to the production of large crystals, is to use the dependence of the solubility limit on temperature. In that case, a solution of known solute concentration is set at the temperature allowing being at the solubility limit. Then, the temperature is varied to bring the solution to the supersaturated region. As the crystallisation consumes part of the solute in solution, the temperature is steadily adjusted to try to match the concentration decrease by a diminution of the solubility limit and maintain the system in the metastable zone. Because hybrid LHPs present retrograde solubilities, the crystallisation will be triggered and maintained by an increase in temperature, leading to what is called inverse temperature crystallisation (ITC). In 2015, Bakr et al. developed this crystal growth approach with DMF and GBL for the growth of $MAPbBr_3$ and $MAPbI_3$ SCs, respectively, with size and shape controllability.[126] The growth is carried out in the most simple manner by preparing highly concentrated solution (usually 1 M), corresponding to a solubility limit around 50-60 °C, and bringing it straight to 80°C, creating a very significant relative supersaturation σ_r (~ 40 %). After nucleation (often a single event in a 10 mL vial), a rapid growth of the nucleated crystal takes place under the very high supersaturation. A schematic of the procedure is shown in **Figure 1-2-6-C.** For each run, such process leads to a unique (or two, at most) SC of several millimetres in size in a matter of a few hours. There are several aspects of those growths that deserve to be discussed. The first is concerning the first step that is the nucleation of a unique crystal. It is extremely unusual to have such low nucleation rate especially considering the very high relative supersaturation employed and the high temperature of the solution. This suggests either exceptionally large metastable zone width or exceptionally slow nucleation kinetics. Another point is the high growth rates observed. In usual solution growth technique such as STL, the applied supersaturation is limited to 2-5 % and the growth rate achieved is of ~ 1 – 3 mm day^{-1} (~ 0.04 – 0.13 mm h^{-1}). Growth rates R_g generally have the following dependency on the relative supersaturation σ_r: $R_g \propto \sigma_r^2$. Therefore, considering the high relative supersaturation involved here (~ 40 %) growth rates two orders of magnitude higher (~ 5 mm h^{-1} – 1 cm h^{-1}) could be expected which is far from what is observed

($\leq$ 1 mm h^{-1}), yet still higher than conventional solution growth rates. However, this ease of SC growth contributed greatly to the appeal of this family of materials with the possibility to get mm-sized SCs to study with nothing but a hotplate and a couple of hours. If larger crystals are desired, because the temperature range can hardly be further increased, the volume of solution could be increased but then the nucleation of a single seed becomes less probable.

Figure 1-2-6-D depicts a variant to the ITC designed to solve that issue: a unique seed crystal is first created in a small volume of solution, and then transferred to an unspoiled new solution for further crystal growth. This transfer can be performed several times to fabricate cm-sized SCs.[158] All variation of the ITC synthesis technique are labelled in the literature as modified inverse temperature crystallisations (MITCs). In this context, our group has elaborated synthesis protocols for $MAPbBr_3$ material leading to SCs of standardised controlled quality, which are described in Chapter 2.

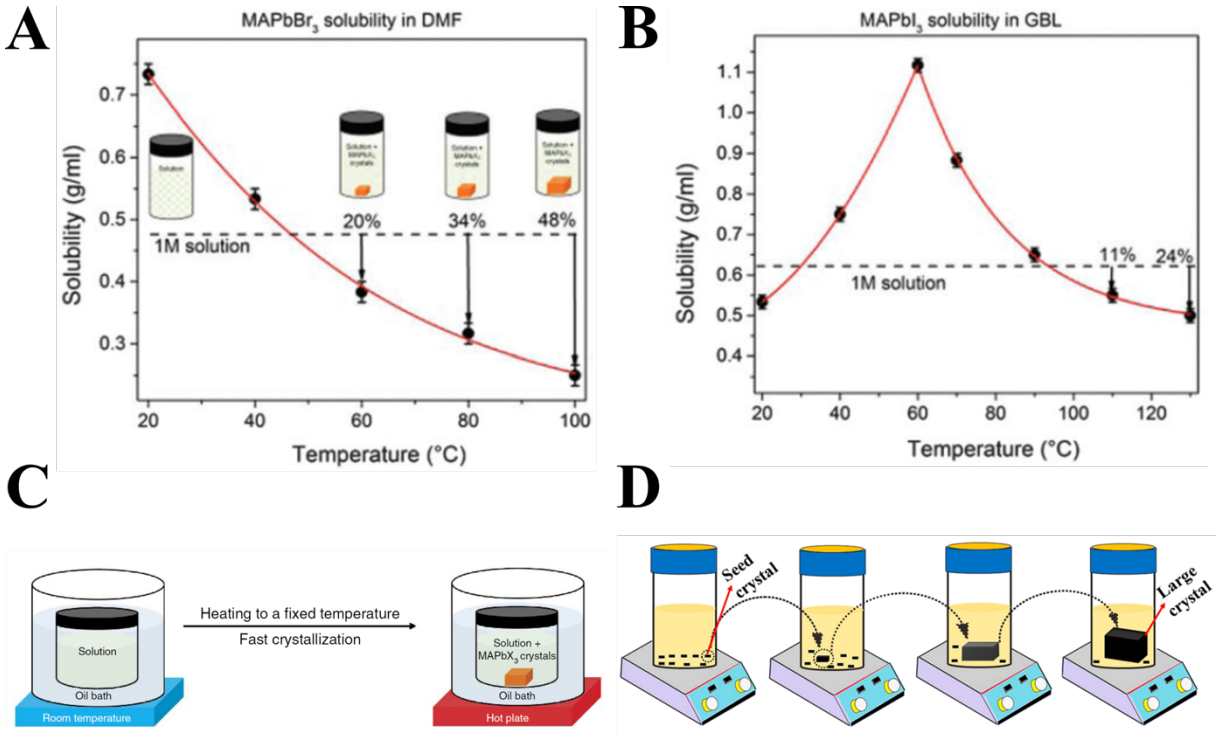

Figure 1-2-6. ITC and MITC methods examples. Solubility curves of **(A)** $MAPbI_3$ and **(B)** $MAPbBr_3$ in GBL and DMF, respectively. Reproduced from reference.[173] **(C)** ITC apparatus in which the crystallisation vial is immersed within a heating bath. Reproduced from reference.[126] **(D)** Large-size crystal growth using seed crystals by MITC method. Reproduced from reference.[64]

Whatever the ITC variant used, growth is almost systematically under very high supersaturation, which is known to favour several types of structural defects: incorporation of impurities, formation of liquid inclusions, among others. But despite their fast growth rates, both $MAPbBr_3$ and $MAPbI_3$ SCs exhibited charge transport characteristics comparable to those grown by slower conventional techniques like antisolvent vapour-assisted crystallisation.[126] Via

ITC, sizable $MAPbCl_3$ SCs were later synthesised through judicious selection of DMSO−DMF co-solution[174] and the successful growth of $FAPbX_3$ SCs took place.[173]

To recapitulate the solvents used to synthesise $MAPbX_3$ SCs via STL and ITC/MITC, and the associated type of solubility, **Table 1-2-1** is given below.

Table 1-2-1. Summary table of solvents used for $MAPbX_3$ SC synthesis.

Material	Crystal growth solvent	Type of solubility
$MAPbI_3$	GBL[126], HI/H_2O[163]	Retrograde, direct
$MAPbBr_3$	DMF[126], HBr/H_2O[165]	Retrograde, direct
$MAPbCl_3$	DMSO/DMF[174]	Retrograde

2.4.3 Defect formation and ion migration in halide perovskites

There can be a very wide variety of defects in a crystal, from extended defects, visible to the naked eye (e.g., PC, fractures, major heterogeneity or impurity incorporation), to atom size structural defects (point defects). Any of these may have a significant impact on the relevant properties of halide perovskites: charge carrier density, optical and charge transport properties. For each structure, deeper insights into which defects in the crystals may be associated with trap states are of major importance for the optimisation of the optoelectronic properties for the targeted application. This knowledge usually marks the difference between materials that are said to be “mature” and those still in an exploratory phase. The first step in this process is to identify what type of defects are actually present in the studied crystal. In this part, a short review on defects for halide perovskite crystals is described, mainly focussing on defect formation during crystal growth, point defects and related ion migration.

2.4.3.1 Crystalline defects

An ideal crystal structure is a perfectly ordered organisation of atoms, ions or molecules. As such, it represents a configuration of particularly low entropy. Therefore, for temperatures above 0 K, the system lowers its energy by introducing some degree of disorder, some deviation from the ideal periodicity. These deviations can take the form of spatial disorder or chemical substitution (entropy of mixing). These arrangements are driven by the energy cost associated with the formation of bounds that are distorted or of different nature (ionicity) and the gain in entropy. The latter being all the more important with increasing temperature, a higher density or more pronounced deviation from perfection can be tolerated at higher temperature. That is why it is generally advisable to synthesise crystals at the lowest possible temperature. Thus, having a certain level of defects is unavoidable but the synthesis stage can control what type

and in what density they are present. A brief description is made by defect family, in order of increasing dimensionality.

Firstly, there are 0D defects, also known as point defects. They correspond to a deviation from the ideal structure by just one atom or ion that can have the wrong charge or be at the wrong position (e.g., missing, substituted, interstitial). To unequivocally identify each type of defect, the Kröger–Vink notation is usually used to describe electric charge and lattice position of the point. It is primarily used for ionic crystals and is particularly useful for describing various defect reactions.[175] This notation is popular among halide perovskite literature, and goes as follow in **Equation (1-21)**:

$$M_S^C \tag{1-21}$$

M represents the involved species: it can be an element (e.g., O, Si, Br, Pb), a vacancy (V), an electron (e) or an electron hole (h). S corresponds to the lattice site (element) that M occupies or i if it is an interstitial position. C indicates the charge deviation of that defect from that of the site occupied (charge on the current site minus the charge on the original site). A null charge is denoted by x, a single net positive charge by $\bullet$ and a single net negative charge by $'$. The doubling of the last two then represents net double positive and negative charges, respectively. It has to be noted that the systematic indication of C is not common in the halide perovskite literature given that determining the defects in these materials is still an active research topic.

Among 0D defects, a first subgroup is the intrinsic point defects where only elements pertaining to the ideal structure are involved. They include vacancies (V_A^C), interstitials (A_i^C) and antisites (B_A^C), corresponding respectively to a missing A species, an A species located between sites, and a B species located at the site of another, here A, with respect to the perfect crystal lattice (ABX_3). On the other hand, defects involving chemical species not originally belonging to the crystal are labelled extrinsic point defects or impurities. They include also interstitials (Z_i^C) and substitutions (Z_A^C), where Z is the foreign species. **Figure 1-2-7-A** depicts some examples of point defects in a crystal lattice.

Even though entropy dictates that some level of point defects will be present in the structure, as experimentalist, one has to find the growth conditions keeping all these defects as low as possible and the composition as close as possible to the stoichiometric perfect crystal structure. Indeed, both intrinsic and extrinsic point defects can strongly affect the optoelectronic properties. The ability of the structure to accommodate different species can also be used in an advantageous way. In the last few years, using the possibility to make substitutions on all three sites of the ABX_3 perovskite structure, compositional engineering for PVs led to more complex "mixed" perovskites. In the formula, A and X sites are occupied by mixed cations and anions,[118] such as in $FA_xMA_{1-x}PbX_3$[176] or $(FA/MA)PbI_xBr_{3-x}$,[177] to provide an optimal optical bandgap in solar cells. Additionally, the incorporation of inorganic cations such as Cs and Rb improves the thermal, moisture, and photoelectric stabilities of mixed perovskites and favours the stability of perovskite phases,[178,179] especially true for double- and triple-cation $FA_xMA_yCs_{1-x-y}PbX_3$

alloys.[180,181] In these cases, a gain in entropy is achieved (entropy of mixing) without compromising the integrity of the perovskite structure.

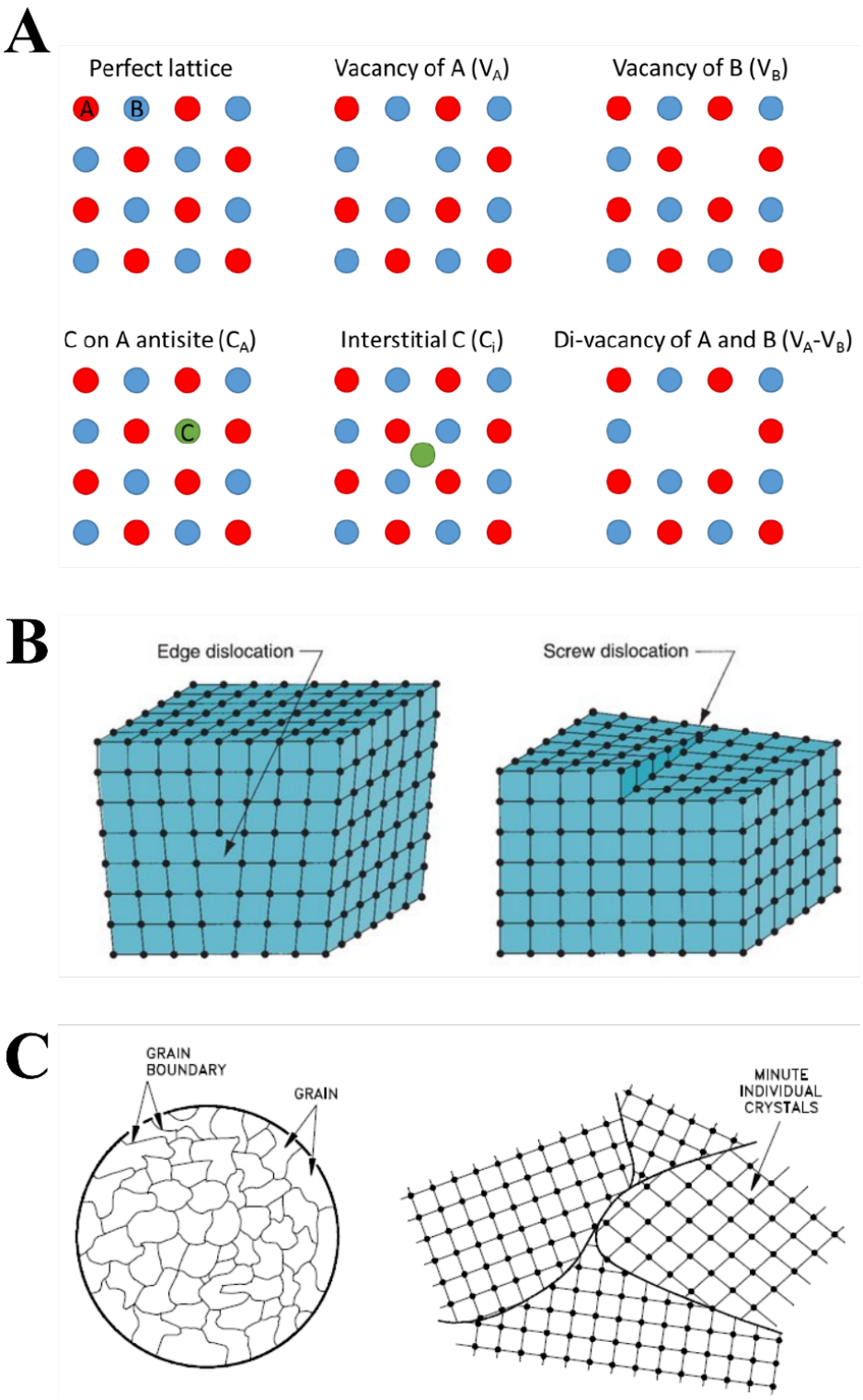

Figure 1-2-7. Defects in crystals. Schematic of different types of defects. **(A)** Intrinsic point defects in a NaCl type lattice composed of ions of A and B. The element C (green) is an extrinsic impurity. Reproduced from reference.[182] **(B)** Two types of line defects: (left) edge and (right) screw dislocations. Reproduced from reference.[183] **(C)** Grain and associated boundary: (left) at microscopic and (right) atomic levels. Reproduced from reference.[184]

1D defects are called dislocations, which can be described as a shift in the continuity of the crystal atomic arrangement in one direction (Burgers vector $\vec{b}$) and along a line (dislocation direction). $\vec{b}$ represents the direction and amplitude of the deformation caused by the dislocation. If it is parallel to the direction line, the dislocation is called “screw dislocation”, if it is perpendicular, it is an “edge dislocation” as illustrated in **Figure 1-2-7-B**. Dislocations of mixed nature, dislocations where the direction line is a closed loop may exist. These defects can be produced during or after crystal growth. During crystal growth, brutal changes in temperature or supersaturation can lead to the formation of liquid inclusions or incorporation of impurities. Dislocations are very efficient ways for the structure to release some of the elastic strain resulting from these major disruptions of the lattice. Additionally, important temperature gradients or mechanical strains can also favour their post-growth apparition. Dislocations can modify electronic band structures. For known semiconductors like CdTe, resistivity and carrier lifetime are weakened with increasing dislocation density.[185–188]

As 2D defects, one can find stacking faults and grain boundaries. The first is an alteration of an otherwise perfect stacking sequence of atomic plans (ABCABCABABCABC). It is often associated with a loop edge dislocation forming the edge of the fault. The grain boundary on the other hand is the interface between two single-crystalline domains of same or different crystal structure as depicted in **Figure 1-2-7-C**. It can correspond to growth sector boundary, crystal twinning or simply independent grain agglomeration. Even though, these are defects are 2D, they induce 3D disorientations in the global periodicity. Because of that, they cannot only alter the optoelectronic properties like dislocations, but also cause a loss of anisotropy. For example, charge carrier mobility can be maximised for certain crystal orientations only. This maximization is lost in a PC where all orientation are present.[166,189,190]

Finally, 3D defects are regrouped under the term inclusion (different phases from the crystal structure). They have several origins, all of which are, at least to a certain degree, within the control of the experimentalist. The inclusions can be solid, liquid or gaseous. The first might originate from synthesising the crystal in experimental conditions where two or more phases coexist. The phase diagram of the species is useful to set the right conditions (e.g., composition, temperature). In the case of solution growth, selecting a solvent that does not combine with the solute is most favourable. Liquid and gaseous inclusions can happen in case of instabilities at the growth front because of poor homogenisation of the concentration and/or temperature at the crystal-fluid interface. Crystals grown at high temperature, far from equilibrium and with a high concentration of impurity are more susceptible to contain them. Naturally, these inclusions also modify the mechanical, electronic and optical properties of the material.

2.4.3.2 Ion migration in hybrid lead halide perovskites

As mentioned above, LHPs and in general MHPs have shown many outstanding optoelectronic properties in spite of the remarkably limited care given to their elaboration. This earned them the reputation that still holds today, of being "defect resilient" materials. If the properties are indeed very promising, some features present real challenges for commercial applications, the main problem being ion migration.[191] Due to its inherent ionic nature and soft structure, the LHP crystal structure can be destabilised under the influence of environment (e.g., oxygen, temperature, humidity) or extrinsic stimuli (e.g. electric field, illumination). $MAPbX_3$ and $FAPbX_3$ perovskites have often been considered unstable, the first due to the volatile and moisture-sensitive nature of MA^+ [178,192] and the second because of poor thermodynamic stability of FA^+[180,193]. Unbound constituent ions can diffuse within and out of the perovskite photoactive layer, inducing many adverse phenomena, including current intensity-voltage hysteresis or phase segregation. Furthermore, migrating ions with highly reactive power, such as I^- and MA^+, may initiate a chain reaction throughout the whole device, which gives rise to the irreversible device decomposition and induces the migration of other ionic species. Thus, the ion migration will directly change the local stoichiometry and degrade the photophysical properties of the device. It has been a pillar in halide perovskite research since 2015, for both its characterisation and ultimately its limitation or suppression.

Understanding the dynamics behind the moving ions is fundamental. Some general considerations can be made: smaller ions deform less the lattice during migration and are thus more likely to migrate in response to external stimuli. However, ionic radius alone does not allow to directly differentiate the migrating ions,[194,195] one has to rely on a more complete description of the phenomena which is better quantified by the migration activation energy E_a.

Ion migration, whether it is of anions or cations, can be divided in intrinsic and extrinsic, like for point defects. For intrinsic migration, among the different ions forming the LHP structure, it has been established that the activation energy of Pb^{2+} is much higher than that of other ions, implying that there should be no significant lead migration.[196,197] There has been direct evidence derived from element distribution measurements confirming that Pb^{2+} would only migrate when the hybrid LHP material was completely decomposed.[194] Regarding intrinsic migration of anions (I^-, Br^- and Cl^-), halogen ions have been found to have a high mobility to diffuse out of the perovskite[196] and high reactivity with other device components,[198] leading to irreversible degradation. For a device based on mixed-halide perovskites ($AB(X_{1-x}X'_x)_3$), the light can induce a anion migration resulting in a halide phase segregation detrimental to the performance.[199,200] Concerning the cations (MA^+, FA^+ and Cs^+), MA^+ also is capable of diffusing,[196] and its mobility seems to be significantly boosted under various stimuli (e.g., light, electric field).[178,192,201,202] MA^+ can even initiate a degradation reaction when exposed to oxygen and environmental humidity, causing the release of volatile gas.[178,192,201] Even though FA^+ is larger than MA^+, it was found to also migrate and diffuse out of the sensing material in operating

devices.[203] However, and surprisingly, there is still lacking evidence of a correlation between FA^+ migration and performance deterioration. Compositional inhomogeneity induced by cation migration may occur likewise in mixed-cation perovskites.[204,205] When Cs^+ is added to improve stability; its separation has been observed but only for high dopant amounts.[180,206,207]

Apart from the intrinsic composition ions, other extrinsic species have been found to participate in migration processes. They can be impurities or dopant introduced in the reaction system (e.g., Li^+), or originate from device material degradation (e.g., protons H^+ from the perovskite, charge transport layers, or electrode). Li^+ is introduced as a dopant in perovskite films to improve the performance of both hole and electron transport layer (HTL and ETL, respectively).[208,209] But, migrating Li^+ reacts with the perovskite layer and forms Li-containing compounds, having a detrimental effect on performance.[210] The role of H^+ migration within hybrid LHP materials, despite theoretical findings, remains elusive. The only possible endogenous source of protons in $MAPbX_3$ is the deprotonation of the MA^+ cation.[211] However, since deprotonated MA is a very strong base ($pK_a = 10.66$), free H^+ are unlikely to be abundant and were found to play a negligible role.[212] External source of protons may exist. Numerous studies have established that water permeated the majority of the sample and performed a critical role in permitting protons to be produced and migrate. One study concluded that water can dissociate into H^+ at the $MAPbX_3$ surface and promote the deprotonation of MA.[213,214]

Finally, photoelectric devices are commonly formed by employing Ag, Au, and Al as electrodes. Depending on their redox potential, metal ions may form at the expense of Pb^{2+} leading to possible migrating metallic cations Ag^+ [215], Au^+ [216,217], and Al^{3+} [218] and the formation of various types of defects. As examples, when formed, AgI induces deep-level defects in an interface layer between the perovskite and electrode and deteriorates the performance of the devices.[215,219,220] The reaction of iodine with Au to form gold-iodide is not as easy thanks to a higher redox potential but it can occur in presence of visible or ultraviolet light. AuI also induces deep levels in the gap of the perovskite layer trapping both electrons and holes.[221] Finally, AlI_3 interferes with the carrier extraction of the perovskite layer.[218] Thus, the selection for optoelectronic devices of an electrode with good properties is not enough, it is fundamental that it also has good chemical compatibility at the interface with the perovskite.

Figure 1-2-8 summarises all the moving chemical species detailed in this part contributing to parasitic ion migration in an optoelectronic device and shows where they may affect the device performance.

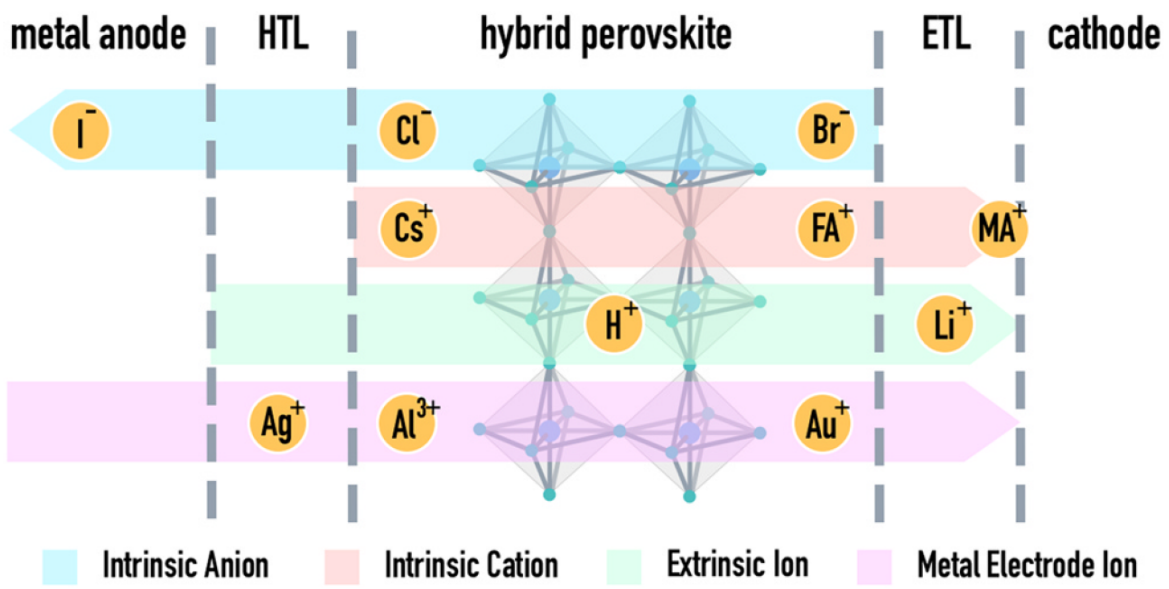

Figure 1-2-8. Diffusion range and tendency of migrating ions in perovskites optoelectronic devices. Reproduced from reference.[222]

Conclusion

As we have seen, the synthesis of materials with high performance for direct X-ray detection covers a very broad range of aspects. The easiness from a technical point of view pushes direct detection as a better alternative than the indirect one, with less critical steps. Direct detection relies on the selection of an appropriate semiconducting material with high stopping power of X-rays and high conversion efficiency of the energetic photons into electric charges. LHPs present an attractive compromise with its relatively easy elaboration in solution, allowing growing cm-sized SCs in a couple of hours via ITC method, and optoelectronic properties, including competing mobility-lifetime products, attenuation coefficients and a defect resilient nature, when compared with commercialised technologies.

The solvents used for organic-inorganic hybrid LHPs present a very convoluted chemistry, given origin to an intermediary phase after precursors dissolution but a very broad metastable zone, ideal for crystal growth. ITC and MTIC methods, by rising the temperature, provoke an important supersaturation in solution, thus inducing rapid crystal growth. The synthesis of a crystal comes with a specific set of defects defined by the experimental conditions. Identifying and limiting the defect structures is at the core of perovskite materials research. Point defect along with parasitic ion migration ceil the optoelectronic properties of MHPs and specially, hybrid LHPs.

Within our group, among the vast family of MHP and LHP materials, $MAPbBr_3$ was selected to fulfil the task of semiconducting material for direct X-ray detection. Based on the thesis results of my predecessors, Smaïl Amari[24] and Oriane Baussens,[223] and respective works, $MAPbBr_3$ still lacks the requirements for this application at the moment, including relatively low resistivity, high dark current density, as well as electrical stability over time while applying an electric field. Thus, the main goal of this work is to investigate ways to improve the behaviour of $MAPbBr_3$ under X-ray illumination. Three axes of study were approached to attain this objective and better understand the sensing material. The first consists in elaborating mixed halide perovskite compositions, resulting in entropy gain without disrupting the integrity of the SC structure. This anion engineering within the halide elements plays with the solution chemistry before crystal growth. The second exposes the impact of the environmental chemistry, by synthesising SCs in different atmospheres and evaluating the presence of extrinsic species during synthesis and characterisation. The third works as an aperture to understand the influence of annealing and chemical healing treatments on the stoichiometry of the perovskite under controlled atmosphere.

References

(1) Röntgen, W. C. On a New Kind of Rays. *Science* **1896**, *3* (59), 227–231. https://doi.org/10.1126/science.3.59.227.

(2) Tegze, M.; Faigel, G. X-Ray Holography with Atomic Resolution. *Nature* **1996**, *380* (6569), 49–51. https://doi.org/10.1038/380049a0.

(3) Gill, H. S.; Elshahat, B.; Kokil, A.; Li, L.; Mosurkal, R.; Zygmanski, P.; Sajo, E.; Kumar, J. Flexible Perovskite Based X-Ray Detectors for Dose Monitoring in Medical Imaging Applications. *Physics in Medicine* **2018**, *5*, 20–23. https://doi.org/10.1016/j.phmed.2018.04.001.

(4) Rieder, R.; Economou, T.; Wänke, H.; Turkevich, A.; Crisp, J.; Brückner, J.; Dreibus, G.; McSween, H. Y. The Chemical Composition of Martian Soil and Rocks Returned by the Mobile Alpha Proton X-Ray Spectrometer: Preliminary Results from the X-Ray Mode. *Science* **1997**, *278* (5344), 1771–1774. https://doi.org/10.1126/science.278.5344.1771.

(5) Mitchell, C.; https://www.facebook.com/pahowho. *PAHO/WHO | World Radiography Day: Two-Thirds of the World's Population has no Access to Diagnostic Imaging*. Pan American Health Organization / World Health Organization. https://www3.paho.org/hq/index.php?option=com_content&view=article&id=7410:2012-dia-radiografia-dos-tercios-poblacion-mundial-no-tiene-acceso-diagnostico-imagen&Itemid=0&lang=en#gsc.tab=0 (accessed 2023-02-20).

(6) Wei, H.; Huang, J. Halide Lead Perovskites for Ionizing Radiation Detection. *Nat Commun* **2019**, *10* (1), 1066. https://doi.org/10.1038/s41467-019-08981-w.

(7) Lin, E. C. Radiation Risk From Medical Imaging. *Mayo Clinic Proceedings* **2010**, *85* (12), 1142–1146. https://doi.org/10.4065/mcp.2010.0260.

(8) Mahesh, M.; Ansari, A. J.; Mettler, F. A. Patient Exposure from Radiologic and Nuclear Medicine Procedures in the United States and Worldwide: 2009–2018. *Radiology* **2022**, 221263. https://doi.org/10.1148/radiol.221263.

(9) Jones, J. A.; Casey, R. C.; Karouia, F. 14.10 - Ionizing Radiation as a Carcinogen*. In *Comprehensive Toxicology (Second Edition)*; McQueen, C. A., Ed.; Elsevier: Oxford, 2010; pp 181–228. https://doi.org/10.1016/B978-0-08-046884-6.01411-1.

(10) Heiss, W.; Brabec, C. Perovskites Target X-Ray Detection. *Nature Photon* **2016**, *10* (5), 288–289. https://doi.org/10.1038/nphoton.2016.54.

(11) Kakavelakis, G.; Gedda, M.; Panagiotopoulos, A.; Kymakis, E.; Anthopoulos, T. D.; Petridis, K. Metal Halide Perovskites for High-Energy Radiation Detection. *Adv. Sci.* **2020**, *7* (22), 2002098. https://doi.org/10.1002/advs.202002098.

(12) *Non-Ionizing Radiation Safety | EHS*. https://www.ehs.washington.edu/radiation/non-ionizing-radiation-safety (accessed 2023-01-27).

(13) *Springer Handbook of Semiconductor Devices*; Rudan, M., Brunetti, R., Reggiani, S.,

Eds.; Springer Handbooks; Springer International Publishing: Cham, 2023. https://doi.org/10.1007/978-3-030-79827-7.

(14) Martz, H. E.; Logan, C. M.; Schneberk, D. J.; Shull, P. J. *X-Ray Imaging: Fundamentals, Industrial Techniques and Applications*; CRC Press: Boca Raton, 2016. https://doi.org/10.1201/9781315375199.

(15) Wheaton, B. R. Photoelectric Effect. In *Compendium of Quantum Physics*; Greenberger, D., Hentschel, K., Weinert, F., Eds.; Springer: Berlin, Heidelberg, 2009; pp 472–475. https://doi.org/10.1007/978-3-540-70626-7_143.

(16) Guerra, M.; Manso, M.; Longelin, S.; Pessanha, S.; Carvalho, M. L. Performance of Three Different Si X-Ray Detectors for Portable XRF Spectrometers in Cultural Heritage Applications. *J. Inst.* **2012**, *7* (10), C10004. https://doi.org/10.1088/1748-0221/7/10/C10004.

(17) Nakamura, R. Improvements in the X-Ray Characteristics of Gd2O2S:Pr Ceramic Scintillators. *Journal of the American Ceramic Society* **1999**, *82* (9), 2407–2410. https://doi.org/10.1111/j.1151-2916.1999.tb02097.x.

(18) Chen, K.; Ren, J.; Zhao, C.; Liao, F.; Yuan, D.; Lei, L.; Zhao, Y. High-Sensitivity Fiber-Optic X-Ray Detectors Employing Gadolinium Oxysulfide Composites. *Opt. Express, OE* **2021**, *29* (14), 22578–22592. https://doi.org/10.1364/OE.431770.

(19) Nagarkar, V. V.; Gupta, T. K.; Miller, S. R.; Klugerman, Y.; Squillante, M. R.; Entine, G. Structured CsI(Tl) Scintillators for X-Ray Imaging Applications. *IEEE Transactions on Nuclear Science* **1998**, *45* (3), 492–496. https://doi.org/10.1109/23.682433.

(20) Starkenburg, D. J.; Johns, P. M.; Baciak, J. E.; Nino, J. C.; Xue, J. Thin Film Organic Photodetectors for Indirect X-Ray Detection Demonstrating Low Dose Rate Sensitivity at Low Voltage Operation. *Journal of Applied Physics* **2017**, *122* (22), 225502. https://doi.org/10.1063/1.4999759.

(21) West, H. I.; Meyerhof, W. E.; Hofstadter, R. Detection of X-Rays by Means of NaI(Tl) Scintillation Counters. *Phys. Rev.* **1951**, *81* (1), 141–142. https://doi.org/10.1103/PhysRev.81.141.

(22) Maeng, S.; Lee, S. H.; Park, S. J.; Choi, W. C. Detection Efficiency Evaluation for Low Energy of a NaI(Tl) Scintillation Detector. *Radiation Physics and Chemistry* **2022**, *199*, 110325. https://doi.org/10.1016/j.radphyschem.2022.110325.

(23) Büchele, P.; Richter, M.; Tedde, S. F.; Matt, G. J.; Ankah, G. N.; Fischer, R.; Biele, M.; Metzger, W.; Lilliu, S.; Bikondoa, O.; Macdonald, J. E.; Brabec, C. J.; Kraus, T.; Lemmer, U.; Schmidt, O. X-Ray Imaging with Scintillator-Sensitized Hybrid Organic Photodetectors. *Nature Photon* **2015**, *9* (12), 843–848. https://doi.org/10.1038/nphoton.2015.216.

(24) Amari, S. Étude des matériaux pérovskites pour la détection directe des rayonnements ionisants. Ph.D. diss., Université Grenoble Alpes, Grenoble, France, 2020.

(25) Kasap, S.; Frey, J. B.; Belev, G.; Tousignant, O.; Mani, H.; Greenspan, J.; Laperriere, L.; Bubon, O.; Reznik, A.; DeCrescenzo, G.; Karim, K. S.; Rowlands, J. A. Amorphous and Polycrystalline Photoconductors for Direct Conversion Flat Panel X-Ray Image Sensors.

Sensors **2011**, *11* (5), 5112–5157. https://doi.org/10.3390/s110505112.

(26) Evans, R. D. *The Atomic Nucleus*; Tata McGraw-Hill, 1982.

(27) Klein, C. A. Bandgap Dependence and Related Features of Radiation Ionization Energies in Semiconductors. *Journal of Applied Physics* **1968**, *39* (4), 2029–2038. https://doi.org/10.1063/1.1656484.

(28) Alig, R. C.; Bloom, S. Electron-Hole-Pair Creation Energies in Semiconductors. *Phys. Rev. Lett.* **1975**, *35* (22), 1522–1525. https://doi.org/10.1103/PhysRevLett.35.1522.

(29) Que, W.; Rowlands, J. A. X-Ray Imaging Using Amorphous Selenium: Inherent Spatial Resolution. *Medical Physics* **1995**, *22* (4), 365–374. https://doi.org/10.1118/1.597471.

(30) Kasap, S. O.; Rowlands, J. A. Direct-Conversion Flat-Panel X-Ray Image Detectors. *IEE Proceedings - Circuits, Devices and Systems* **2002**, *149* (2), 85–96. https://doi.org/10.1049/ip-cds:20020350.

(31) Hecht, K. Zum Mechanismus des lichtelektrischen Primärstromes in isolierenden Kristallen. *Z. Physik* **1932**, *77* (3–4), 235–245. https://doi.org/10.1007/BF01338917.

(32) Wei, H.; Fang, Y.; Mulligan, P.; Chuirazzi, W.; Fang, H.-H.; Wang, C.; Ecker, B. R.; Gao, Y.; Loi, M. A.; Cao, L.; Huang, J. Sensitive X-Ray Detectors Made of Methylammonium Lead Tribromide Perovskite Single Crystals. *Nature Photon* **2016**, *10* (5), 333–339. https://doi.org/10.1038/nphoton.2016.41.

(33) Stoumpos, C. C.; Malliakas, C. D.; Peters, J. A.; Liu, Z.; Sebastian, M.; Im, J.; Chasapis, T. C.; Wibowo, A. C.; Chung, D. Y.; Freeman, A. J.; Wessels, B. W.; Kanatzidis, M. G. Crystal Growth of the Perovskite Semiconductor CsPbBr3 : A New Material for High-Energy Radiation Detection. *Crystal Growth & Design* **2013**, *13* (7), 2722–2727. https://doi.org/10.1021/cg400645t.

(34) Many, A. High-Field Effects in Photoconducting Cadmium Sulphide. *Journal of Physics and Chemistry of Solids* **1965**, *26* (3), 575–578. https://doi.org/10.1016/0022-3697(65)90133-2.

(35) Huda, W.; Abrahams, R. B. X-Ray-Based Medical Imaging and Resolution. *American Journal of Roentgenology* **2015**, *204* (4), W393–W397. https://doi.org/10.2214/AJR.14.13126.

(36) Kasap, S. O. X-Ray Sensitivity of Photoconductors: Application to Stabilized a-Se. *J. Phys. D: Appl. Phys.* **2000**, *33* (21), 2853. https://doi.org/10.1088/0022-3727/33/21/326.

(37) Simon, M.; Ford, R. A.; Franklin, A. R.; Grabowski, S. P.; Menser, B.; Much, G.; Nascetti, A.; Overdick, M.; Powell, M. J.; Wiechert, D. U. PbO as Direct Conversion X-Ray Detector Material. In *Medical Imaging 2004: Physics of Medical Imaging*; SPIE, 2004; Vol. 5368, pp 188–199. https://doi.org/10.1117/12.533010.

(38) Street, R. A.; Ready, S. E.; Lemmi, F.; Shah, K. S.; Bennett, P.; Dmitriyev, Y. Electronic Transport in Polycrystalline Pbl2 Films. *Journal of Applied Physics* **1999**, *86* (5), 2660–2667. https://doi.org/10.1063/1.371107.

(39) Zentai, G.; Schieber, M.; Partain, L.; Pavlyuchkova, R.; Proano, C. Large Area Mercuric Iodide and Lead Iodide X-Ray Detectors for Medical and Non-Destructive Industrial Imaging.

Journal of Crystal Growth **2005**, *275* (1), e1327–e1331. https://doi.org/10.1016/j.jcrysgro.2004.11.105.

(40) Szeles, C. CdZnTe and CdTe Materials for X-Ray and Gamma Ray Radiation Detector Applications. *physica status solidi (b)* **2004**, *241* (3), 783–790. https://doi.org/10.1002/pssb.200304296.

(41) Hitomi, K.; Muroi, O.; Shoji, T.; Hiratate, Y.; Ishibashi, H.; Ishii, M. Thallium Bromide Photodetectors for Scintillation Detection. *Nuclear Instruments and Methods in Physics Research Section A: Accelerators, Spectrometers, Detectors and Associated Equipment* **2000**, *448* (3), 571–575. https://doi.org/10.1016/S0168-9002(00)00290-4.

(42) Rose, G. *De novis quibusdam fossilibus quae in montibus uraliis inveniuntur*; typis A.G. Schadii: Berolini, 1839.

(43) Kay, H. F.; Bailey, P. C. Structure and Properties of CaTiO3. *Acta Crystallographica* **1957**, *10* (3), 219–226. https://doi.org/10.1107/S0365110X57000675.

(44) Megaw, H. D. G. Solids. Crystal Structure of Barium Titanium Oxide and Other Double Oxides of the Perovskite Type. *Transactions of the Faraday Society* **1946**, *42* (0), A224–A231. https://doi.org/10.1039/TF946420A224.

(45) Megaw, H. D. Crystal Structure of Barium Titanium Oxide at Different Temperatures. *Experientia* **1946**, *2* (5), 183–184. https://doi.org/10.1007/BF02156449.

(46) Megaw, H. D. Temperature Changes in the Crystal Structure of Barium Titanium Oxide. *Proceedings of the Royal Society of London. Series A, Mathematical and Physical Sciences* **1947**, *189* (1017), 261–283.

(47) Ok, K. M.; Chi, E. O.; Halasyamani, P. S. Bulk Characterization Methods for Non-Centrosymmetric Materials: Second-Harmonic Generation, Piezoelectricity, Pyroelectricity, and Ferroelectricity. *Chem. Soc. Rev.* **2006**, *35* (8), 710–717. https://doi.org/10.1039/B511119F.

(48) Bednorz, J. G.; Müller, K. A. Possible HighTc Superconductivity in the Ba−La−Cu−O System. *Z. Physik B - Condensed Matter* **1986**, *64* (2), 189–193. https://doi.org/10.1007/BF01303701.

(49) Ito, T.; Ushiyama, T.; Yanagisawa, Y.; Kumai, R.; Tomioka, Y. Growth of Highly Insulating Bulk Single Crystals of Multiferroic BiFeO3 and Their Inherent Internal Strains in the Domain-Switching Process. *Crystal Growth & Design* **2011**, *11* (11), 5139–5143. https://doi.org/10.1021/cg201068m.

(50) Raveau, B. The Crucial Role of Mixed Valence in the Magnetoresistance Properties of Manganites and Cobaltites. *Philosophical Transactions of the Royal Society A: Mathematical, Physical and Engineering Sciences* **2007**, *366* (1862), 83–92. https://doi.org/10.1098/rsta.2007.2141.

(51) Wells, H. L. Über Die Cäsium- Und Kalium-Bleihalogenide. *Zeitschrift für anorganische Chemie* **1893**, *3* (1), 195–210. https://doi.org/10.1002/zaac.18930030124.

(52) Møller, Chr. Kn. Crystal Structure and Photoconductivity of Cæsium Plumbohalides.

Nature **1958**, *182*, 1436. https://doi.org/10.1038/1821436a0.

(53) Weber, D. $CH_3NH_3PbX_3$, ein Pb(II)-System mit kubischer Perowskitstruktur / $CH_3NH_3PbX_3$, a Pb(II)-System with Cubic Perovskite Structure. *Zeitschrift für Naturforschung B* **1978**, *33* (12), 1443–1445. https://doi.org/10.1515/znb-1978-1214.

(54) Mitzi, D. B.; Liang, K. Synthesis, Resistivity, and Thermal Properties of the Cubic Perovskite NH2CH=NH2SnI3and Related Systems. *Journal of Solid State Chemistry* **1997**, *134* (2), 376–381. https://doi.org/10.1006/jssc.1997.7593.

(55) Stoumpos, C. C.; Malliakas, C. D.; Kanatzidis, M. G. Semiconducting Tin and Lead Iodide Perovskites with Organic Cations: Phase Transitions, High Mobilities, and Near-Infrared Photoluminescent Properties. *Inorg. Chem.* **2013**, *52* (15), 9019–9038. https://doi.org/10.1021/ic401215x.

(56) Al-Shakarchi, E. K.; Mahmood, N. B. Three Techniques Used to Produce BaTiO₃ Fine Powder. *JMP* **2011**, *02* (11), 1420–1428. https://doi.org/10.4236/jmp.2011.211175.

(57) Elbaz, G. A.; Straus, D. B.; Semonin, O. E.; Hull, T. D.; Paley, D. W.; Kim, P.; Owen, J. S.; Kagan, C. R.; Roy, X. Unbalanced Hole and Electron Diffusion in Lead Bromide Perovskites. *Nano Lett.* **2017**, *17* (3), 1727–1732. https://doi.org/10.1021/acs.nanolett.6b05022.

(58) Rodová, M.; Brožek, J.; Knížek, K.; Nitsch, K. Phase Transitions in Ternary Caesium Lead Bromide. *Journal of Thermal Analysis and Calorimetry* **2003**, *71* (2), 667–673. https://doi.org/10.1023/A:1022836800820.

(59) Li, C.; Lu, X.; Ding, W.; Feng, L.; Gao, Y.; Guo, Z. Formability of ABX3 (X = F, Cl, Br, I) Halide Perovskites. *Acta Crystallogr B* **2008**, *64* (Pt 6), 702–707. https://doi.org/10.1107/S0108768108032734.

(60) Goldschmidt, V. M. Die Gesetze der Krystallochemie. *Naturwissenschaften* **1926**, *14* (21), 477–485. https://doi.org/10.1007/BF01507527.

(61) Stoumpos, C. C.; Kanatzidis, M. G. The Renaissance of Halide Perovskites and Their Evolution as Emerging Semiconductors. *Acc. Chem. Res.* **2015**, *48* (10), 2791–2802. https://doi.org/10.1021/acs.accounts.5b00229.

(62) Zhang, W.; Eperon, G. E.; Snaith, H. J. Metal Halide Perovskites for Energy Applications. *Nat Energy* **2016**, *1* (6), 1–8. https://doi.org/10.1038/nenergy.2016.48.

(63) Chouhan, L.; Ghimire, S.; Subrahmanyam, C.; Miyasaka, T.; Biju, V. Synthesis, Optoelectronic Properties and Applications of Halide Perovskites. *Chem. Soc. Rev.* **2020**, *49* (10), 2869–2885. https://doi.org/10.1039/C9CS00848A.

(64) Babu, R.; Giribabu, L.; Singh, S. P. Recent Advances in Halide-Based Perovskite Crystals and Their Optoelectronic Applications. *Crystal Growth & Design* **2018**, *18* (4), 2645–2664. https://doi.org/10.1021/acs.cgd.7b01767.

(65) Arya, S.; Mahajan, P.; Gupta, R.; Srivastava, R.; Tailor, N. kumar; Satapathi, S.; Sumathi, R. R.; Datt, R.; Gupta, V. A Comprehensive Review on Synthesis and Applications of Single Crystal Perovskite Halides. *Progress in Solid State Chemistry* **2020**, 100286.

https://doi.org/10.1016/j.progsolidstchem.2020.100286.

(66) Shirwadkar, U.; van Loef, E. V. D.; Hawrami, R.; Mukhopadhyay, S.; Glodo, J.; Shah, K. S. New Promising Scintillators for Gamma-Ray Spectroscopy: Cs(Ba,Sr)(Br,I)3. In *2011 IEEE Nuclear Science Symposium Conference Record*; 2011; pp 1583–1585. https://doi.org/10.1109/NSSMIC.2011.6154636.

(67) Ehrenberg, H.; Fuess, H.; Hesse, S.; Zimmermann, J.; von Seggern, H.; Knapp, M. Structures of CsEuBr3 and Its Degradation Product Cs2EuBr5.10H2O. *Acta Crystallogr B* **2007**, *63* (Pt 2), 201–204. https://doi.org/10.1107/S0108768106049032.

(68) Hesse, S.; Zimmermann, J.; von Seggern, H.; Ehrenberg, H.; Fuess, H.; Fasel, C.; Riedel, R. CsEuBr3: Crystal Structure and Its Role in the Photostimulation of CsBr:Eu2+. *Journal of Applied Physics* **2006**, *100* (8), 083506. https://doi.org/10.1063/1.2358328.

(69) Schilling, G.; Kunert, C.; Schleid, T.; Meyer, G. Metallothermische Reduktion der Tribromide und -iodide von Thulium und Ytterbium mit Alkalimetallen. *Zeitschrift für anorganische und allgemeine Chemie* **1992**, *618* (12), 7–12. https://doi.org/10.1002/zaac.19926180102.

(70) Thiele, G.; Rotter, H. W.; Schmidt, K. D. Die Kristallstrukturen und Phasentransformationen von RbGeBr3. *Zeitschrift für anorganische und allgemeine Chemie* **1988**, *559* (1), 7–16. https://doi.org/10.1002/zaac.19885590101.

(71) Yamada, K.; Funabiki, S.; Horimoto, H.; Matsui, T.; Okuda, T.; Ichiba, S. Structural Phase Transitions of the Polymorphs of CsSnI3 by Means of Rietveld Analysis of the X-Ray Diffraction. *Chem. Lett.* **1991**, *20* (5), 801–804. https://doi.org/10.1246/cl.1991.801.

(72) Lv, S.; Wu, Q.; Meng, X.; Kang, L.; Zhong, C.; Lin, Z.; Hu, Z.; Chen, X.; Qin, J. A Promising New Nonlinear Optical Crystal with High Laser Damage Threshold for Application in the IR Region: Synthesis, Crystal Structure and Properties of Noncentrosymmetric CsHgBr3. *J. Mater. Chem. C* **2014**, *2* (33), 6796–6801. https://doi.org/10.1039/C4TC00565A.

(73) Strähle, J.; Gelinek, J.; Kölmel, M.; Nemecek, A.-M. Die Kristallstruktur Der Salze K2Au2I6 Und Cs2AgxAuI1-XAuIIIBr6. Ein Beitrag Zur Kristallchemie Der Alkalihexahalogenoaurate(I,III) / Crystal Structure of the Salts K2Au2I6 and Cs2AgxAuI1-XAuIIIBr6. A Contribution to the Crystal Chemistry of the Alkali Hexahalogeno Aurates(I,III). *Zeitschrift für Naturforschung B* **1979**, *34* (8), 1047–1052. https://doi.org/10.1515/znb-1979-0801.

(74) Kojima, N.; Hasegawa, M.; Kitagawa, H.; Kikegawa, T.; Shimomura, O. P-T Phase Diagram and Gold Valence State of the Perovskite-Type Mixed-Valence Compounds Cs2Au2X6 (X = Cl, Br, and I) under High Pressures. *J. Am. Chem. Soc.* **1994**, *116* (25), 11368–11374. https://doi.org/10.1021/ja00104a016.

(75) Horowitz, A.; Amit, M.; Makovsky, J.; Dor, L. B.; Kalman, Z. H. Structure Types and Phase Transformations in KMnCl 3 and TlMnCl 3. *Journal of Solid State Chemistry France* **1982**, *43*, 107–125. https://doi.org/10.1016/0022-4596(82)90220-1.

(76) Im, J.-H.; Chung, J.; Kim, S.-J.; Park, N.-G. Synthesis, Structure, and Photovoltaic

Property of a Nanocrystalline 2H Perovskite-Type Novel Sensitizer (CH3CH2NH3)PbI3. *Nanoscale Res Lett* **2012**, *7* (1), 353. https://doi.org/10.1186/1556-276X-7-353.

(77) Crystal Structure of Dimethylammonium Triiodostannate(II), (CH3)2NH2SnI3. *Zeitschrift für Kristallographie - Crystalline Materials* **1996**, *211* (1), 48–48. https://doi.org/10.1524/zkri.1996.211.1.48.

(78) Wang, S.; Mitzi, D. B.; Feild, C. A.; Guloy, A. Synthesis and Characterization of [NH2C(I):NH2]3MI5 (M = Sn, Pb): Stereochemical Activity in Divalent Tin and Lead Halides Containing Single .Ltbbrac.110.Rtbbrac. Perovskite Sheets. *J. Am. Chem. Soc.* **1995**, *117* (19), 5297–5302. https://doi.org/10.1021/ja00124a012.

(79) Cao, D. H.; Stoumpos, C. C.; Farha, O. K.; Hupp, J. T.; Kanatzidis, M. G. 2D Homologous Perovskites as Light-Absorbing Materials for Solar Cell Applications. *J. Am. Chem. Soc.* **2015**, *137* (24), 7843–7850. https://doi.org/10.1021/jacs.5b03796.

(80) Hoffman, J. M.; Che, X.; Sidhik, S.; Li, X.; Hadar, I.; Blancon, J.-C.; Yamaguchi, H.; Kepenekian, M.; Katan, C.; Even, J.; Stoumpos, C. C.; Mohite, A. D.; Kanatzidis, M. G. From 2D to 1D Electronic Dimensionality in Halide Perovskites with Stepped and Flat Layers Using Propylammonium as a Spacer. *J. Am. Chem. Soc.* **2019**, *141* (27), 10661–10676. https://doi.org/10.1021/jacs.9b02846.

(81) Liu, Y.; Xu, Z.; Yang, Z.; Zhang, Y.; Cui, J.; He, Y.; Ye, H.; Zhao, K.; Sun, H.; Lu, R.; Liu, M.; Kanatzidis, M. G.; Liu, S. (Frank). Inch-Size 0D-Structured Lead-Free Perovskite Single Crystals for Highly Sensitive Stable X-Ray Imaging. *Matter* **2020**, S2590238520301880. https://doi.org/10.1016/j.matt.2020.04.017.

(82) Leung, T. L.; Ahmad, I.; Syed, A. A.; Ng, A. M. C.; Popović, J.; Djurišić, A. B. Stability of 2D and Quasi-2D Perovskite Materials and Devices. *Commun Mater* **2022**, *3* (1), 1–10. https://doi.org/10.1038/s43246-022-00285-9.

(83) Gao, X.; Zhang, X.; Yin, W.; Wang, H.; Hu, Y.; Zhang, Q.; Shi, Z.; Colvin, V. L.; Yu, W. W.; Zhang, Y. Ruddlesden–Popper Perovskites: Synthesis and Optical Properties for Optoelectronic Applications. *Advanced Science* **2019**, *6* (22), 1900941. https://doi.org/10.1002/advs.201900941.

(84) Kojima, A.; Teshima, K.; Shirai, Y.; Miyasaka, T. Organometal Halide Perovskites as Visible-Light Sensitizers for Photovoltaic Cells. *J. Am. Chem. Soc.* **2009**, *131* (17), 6050–6051. https://doi.org/10.1021/ja809598r.

(85) Chen, Y.; He, M.; Peng, J.; Sun, Y.; Liang, Z. Structure and Growth Control of Organic–Inorganic Halide Perovskites for Optoelectronics: From Polycrystalline Films to Single Crystals. *Advanced Science* **2016**, *3* (4), 1500392. https://doi.org/10.1002/advs.201500392.

(86) Xu, J.; Ma, J.; Gu, Y.; Li, Y.; Li, Y.; Shen, H.; Zhang, Z.; Ma, Y. Progress of Metal Halide Perovskite Crystals From a Crystal Growth Point of View. *Cryst. Res. Technol.* **2023**, *58* (1), 2200128. https://doi.org/10.1002/crat.202200128.

(87) Giorgi, G.; Fujisawa, J.-I.; Segawa, H.; Yamashita, K. Small Photocarrier Effective Masses Featuring Ambipolar Transport in Methylammonium Lead Iodide Perovskite: A

Density Functional Analysis. *J. Phys. Chem. Lett.* **2013**, *4* (24), 4213–4216. https://doi.org/10.1021/jz4023865.

(88) Dong, Q.; Fang, Y.; Shao, Y.; Mulligan, P.; Qiu, J.; Cao, L.; Huang, J. Electron-Hole Diffusion Lengths > 175 Mm in Solution-Grown $CH_3NH_3PbI_3$ Single Crystals. *Science* **2015**, *347* (6225), 967–970. https://doi.org/10.1126/science.aaa5760.

(89) De Wolf, S.; Holovsky, J.; Moon, S.-J.; Löper, P.; Niesen, B.; Ledinsky, M.; Haug, F.-J.; Yum, J.-H.; Ballif, C. Organometallic Halide Perovskites: Sharp Optical Absorption Edge and Its Relation to Photovoltaic Performance. *J. Phys. Chem. Lett.* **2014**, *5* (6), 1035–1039. https://doi.org/10.1021/jz500279b.

(90) Poli, I.; Kim, G.-W.; Wong, E. L.; Treglia, A.; Folpini, G.; Petrozza, A. High External Photoluminescence Quantum Yield in Tin Halide Perovskite Thin Films. *ACS Energy Lett.* **2021**, *6* (2), 609–611. https://doi.org/10.1021/acsenergylett.0c02612.

(91) Lee, M. M.; Teuscher, J.; Miyasaka, T.; Murakami, T. N.; Snaith, H. J. Efficient Hybrid Solar Cells Based on Meso-Superstructured Organometal Halide Perovskites. *Science* **2012**, *338* (6107), 643–647. https://doi.org/10.1126/science.1228604.

(92) Kim, H.-S.; Lee, C.-R.; Im, J.-H.; Lee, K.-B.; Moehl, T.; Marchioro, A.; Moon, S.-J.; Humphry-Baker, R.; Yum, J.-H.; Moser, J. E.; Grätzel, M.; Park, N.-G. Lead Iodide Perovskite Sensitized All-Solid-State Submicron Thin Film Mesoscopic Solar Cell with Efficiency Exceeding 9%. *Sci Rep* **2012**, *2* (1), 591. https://doi.org/10.1038/srep00591.

(93) *Interactive Best Research-Cell Efficiency Chart*. https://www.nrel.gov/pv/interactive-cell-efficiency.html (accessed 2023-07-19).

(94) *Best Research-Cell Efficiency Chart*. https://www.nrel.gov/pv/cell-efficiency.html (accessed 2023-07-19).

(95) Wang, R.; Mujahid, M.; Duan, Y.; Wang, Z.-K.; Xue, J.; Yang, Y. A Review of Perovskites Solar Cell Stability. *Advanced Functional Materials* **2019**, *29* (47), 1808843. https://doi.org/10.1002/adfm.201808843.

(96) Stylianakis, M. M.; Maksudov, T.; Panagiotopoulos, A.; Kakavelakis, G.; Petridis, K. Inorganic and Hybrid Perovskite Based Laser Devices: A Review. *Materials* **2019**, *12* (6), 859. https://doi.org/10.3390/ma12060859.

(97) Zhang, Q.; Shang, Q.; Su, R.; Do, T. T. H.; Xiong, Q. Halide Perovskite Semiconductor Lasers: Materials, Cavity Design, and Low Threshold. *Nano Lett.* **2021**, *21* (5), 1903–1914. https://doi.org/10.1021/acs.nanolett.0c03593.

(98) Van Le, Q.; Jang, H. W.; Kim, S. Y. Recent Advances toward High-Efficiency Halide Perovskite Light-Emitting Diodes: Review and Perspective. *Small Methods* **2018**, *2* (10), 1700419. https://doi.org/10.1002/smtd.201700419.

(99) Ji, K.; Anaya, M.; Abfalterer, A.; Stranks, S. D. Halide Perovskite Light-Emitting Diode Technologies. *Advanced Optical Materials* **2021**, *9* (18), 2002128. https://doi.org/10.1002/adom.202002128.

(100) Miao, J.; Zhang, F. Recent Progress on Highly Sensitive Perovskite Photodetectors. *J.*

Mater. Chem. C **2019**, *7* (7), 1741–1791. https://doi.org/10.1039/C8TC06089D.
(101) Shellaiah, M.; Sun, K. W. Review on Sensing Applications of Perovskite Nanomaterials. *Chemosensors* **2020**, *8* (3), 55. https://doi.org/10.3390/chemosensors8030055.
(102) Liu, F.; Wu, R.; Zeng, Y.; Wei, J.; Li, H.; Manna, L.; Mohite, A. D. Halide Perovskites and Perovskite Related Materials for Particle Radiation Detection. *Nanoscale* **2022**, *14* (18), 6743–6760. https://doi.org/10.1039/D2NR01292H.
(103) *Next-Generation Semiconductors Pervoskites for Detecting Nuclear Radiation from X- and Gamma-ray Sources – HDIAC*. https://hdiac.org/articles/next-generation-semiconductors-pervoskites-for-detectin-nuclear-radiation-from-x-and-y-ray-sources/ (accessed 2023-02-17).
(104) Kim, Y. C.; Kim, K. H.; Son, D.-Y.; Jeong, D.-N.; Seo, J.-Y.; Choi, Y. S.; Han, I. T.; Lee, S. Y.; Park, N.-G. Printable Organometallic Perovskite Enables Large-Area, Low-Dose X-Ray Imaging. *Nature* **2017**, *550* (7674), 87–91. https://doi.org/10.1038/nature24032.
(105) Zhang, H.; Wang, F.; Lu, Y.; Sun, Q.; Xu, Y.; Zhang, B.-B.; Jie, W.; Kanatzidis, M. G. High-Sensitivity X-Ray Detectors Based on Solution-Grown Caesium Lead Bromide Single Crystals. *J. Mater. Chem. C* **2020**, *8* (4), 1248–1256. https://doi.org/10.1039/C9TC05490A.
(106) Zheng, X.; Zhao, W.; Wang, P.; Tan, H.; Saidaminov, M. I.; Tie, S.; Chen, L.; Peng, Y.; Long, J.; Zhang, W.-H. Ultrasensitive and Stable X-Ray Detection Using Zero-Dimensional Lead-Free Perovskites. *Journal of Energy Chemistry* **2020**, *49*, 299–306. https://doi.org/10.1016/j.jechem.2020.02.049.
(107) Wei, H.; DeSantis, D.; Wei, W.; Deng, Y.; Guo, D.; Savenije, T. J.; Cao, L.; Huang, J. Dopant Compensation in Alloyed CH3NH3PbBr3−xClx Perovskite Single Crystals for Gamma-Ray Spectroscopy. *Nature Mater* **2017**, *16* (8), 826–833. https://doi.org/10.1038/nmat4927.
(108) Li, L.; Liu, X.; Zhang, H.; Zhang, B.; Jie, W.; Sellin, P. J.; Hu, C.; Zeng, G.; Xu, Y. Enhanced X-Ray Sensitivity of MAPbBr3 Detector by Tailoring the Interface-States Density. *ACS Appl. Mater. Interfaces* **2019**, *11* (7), 7522–7528. https://doi.org/10.1021/acsami.8b18598.
(109) Ni, Z.; Bao, C.; Liu, Y.; Jiang, Q.; Wu, W.-Q.; Chen, S.; Dai, X.; Chen, B.; Hartweg, B.; Yu, Z.; Holman, Z.; Huang, J. Resolving Spatial and Energetic Distributions of Trap States in Metal Halide Perovskite Solar Cells. *Science* **2020**, *367* (6484), 1352–1358. https://doi.org/10.1126/science.aba0893.
(110) Yin, W.-J.; Shi, T.; Yan, Y. Unusual Defect Physics in $CH_3NH_3PbI_3$ Perovskite Solar Cell Absorber. *Appl. Phys. Lett.* **2014**, *104* (6), 063903. https://doi.org/10.1063/1.4864778.
(111) Heo, J. H.; Shin, D. H.; Park, J. K.; Kim, D. H.; Lee, S. J.; Im, S. H. High-Performance Next-Generation Perovskite Nanocrystal Scintillator for Nondestructive X-Ray Imaging. *Advanced Materials* **2018**, *30* (40), 1801743. https://doi.org/10.1002/adma.201801743.
(112) Chen, Q.; Wu, J.; Ou, X.; Huang, B.; Almutlaq, J.; Zhumekenov, A. A.; Guan, X.; Han, S.; Liang, L.; Yi, Z.; Li, J.; Xie, X.; Wang, Y.; Li, Y.; Fan, D.; Teh, D. B. L.; All, A. H.; Mohammed, O. F.; Bakr, O. M.; Wu, T.; Bettinelli, M.; Yang, H.; Huang, W.; Liu, X. All-Inorganic Perovskite Nanocrystal Scintillators. *Nature* **2018**, *561* (7721), 88–93.

https://doi.org/10.1038/s41586-018-0451-1.
(113) Mykhaylyk, V. B.; Kraus, H.; Saliba, M. Bright and Fast Scintillation of Organolead Perovskite MAPbBr3 at Low Temperatures. *Mater. Horiz.* **2019**, *6* (8), 1740–1747. https://doi.org/10.1039/C9MH00281B.
(114) Xia, M.; Yuan, J.; Niu, G.; Du, X.; Yin, L.; Pan, W.; Luo, J.; Li, Z.; Zhao, H.; Xue, K.; Miao, X.; Tang, J. Unveiling the Structural Descriptor of A $_3$ B $_2$ X $_9$ Perovskite Derivatives toward X-Ray Detectors with Low Detection Limit and High Stability. *Adv. Funct. Mater.* **2020**, 1910648. https://doi.org/10.1002/adfm.201910648.
(115) Rybin, N.; Ghosh, D.; Tisdale, J.; Shrestha, S.; Yoho, M.; Vo, D.; Even, J.; Katan, C.; Nie, W.; Neukirch, A. J.; Tretiak, S. Effects of Chlorine Mixing on Optoelectronics, Ion Migration, and Gamma-Ray Detection in Bromide Perovskites. *Chem. Mater.* **2020**, *32* (5), 1854–1863. https://doi.org/10.1021/acs.chemmater.9b04244.
(116) Shen, J.; Aidun, D. K.; Regel, L.; Wilcox, W. R. Characterization of Precipitates in CdTe and Cd1−xZnxTe Grown by Vertical Bridgman-Stockbarger Technique. *Journal of Crystal Growth* **1993**, *132* (1), 250–260. https://doi.org/10.1016/0022-0248(93)90269-3.
(117) Wehrenfennig, C.; Eperon, G. E.; Johnston, M. B.; Snaith, H. J.; Herz, L. M. High Charge Carrier Mobilities and Lifetimes in Organolead Trihalide Perovskites. *Advanced Materials* **2014**, *26* (10), 1584–1589. https://doi.org/10.1002/adma.201305172.
(118) Ono, L. K.; Juarez-Perez, E. J.; Qi, Y. Progress on Perovskite Materials and Solar Cells with Mixed Cations and Halide Anions. *ACS Appl. Mater. Interfaces* **2017**, *9* (36), 30197–30246. https://doi.org/10.1021/acsami.7b06001.
(119) He, Y.; Matei, L.; Jung, H. J.; McCall, K. M.; Chen, M.; Stoumpos, C. C.; Liu, Z.; Peters, J. A.; Chung, D. Y.; Wessels, B. W.; Wasielewski, M. R.; Dravid, V. P.; Burger, A.; Kanatzidis, M. G. High Spectral Resolution of Gamma-Rays at Room Temperature by Perovskite CsPbBr3 Single Crystals. *Nat Commun* **2018**, *9* (1), 1609. https://doi.org/10.1038/s41467-018-04073-3.
(120) *NIST X-Ray Form Factor, Atten. Scatt. Tables Form Page*. https://physics.nist.gov/PhysRefData/FFast/html/form.html (accessed 2023-02-20).
(121) Liu, J.; Shabbir, B.; Wang, C.; Wan, T.; Ou, Q.; Yu, P.; Tadich, A.; Jiao, X.; Chu, D.; Qi, D.; Li, D.; Kan, R.; Huang, Y.; Dong, Y.; Jasieniak, J.; Zhang, Y.; Bao, Q. Flexible, Printable Soft-X-Ray Detectors Based on All-Inorganic Perovskite Quantum Dots. *Advanced Materials* **2019**, *31* (30), 1901644. https://doi.org/10.1002/adma.201901644.
(122) Ciavatti, A.; Sorrentino, R.; Basiricò, L.; Passarella, B.; Caironi, M.; Petrozza, A.; Fraboni, B. High-Sensitivity Flexible X-Ray Detectors Based on Printed Perovskite Inks. *Advanced Functional Materials* **2021**, *31* (11), 2009072. https://doi.org/10.1002/adfm.202009072.
(123) Onoda-Yamamuro, N.; Matsuo, T.; Suga, H. Calorimetric and IR Spectroscopic Studies of Phase Transitions in Methylammonium Trihalogenoplumbates (II)†. *Journal of Physics and Chemistry of Solids* **1990**, *51* (12), 1383–1395. https://doi.org/10.1016/0022-3697(90)90021-7.

(124) Juarez-Perez, E. J.; Hawash, Z.; Raga, S. R.; Ono, L. K.; Qi, Y. Thermal Degradation of $CH_3NH_3PbI_3$ Perovskite into NH_3 and CH_3I Gases Observed by Coupled Thermogravimetry–Mass Spectrometry Analysis. *Energy Environ. Sci.* **2016**, *9* (11), 3406–3410. https://doi.org/10.1039/C6EE02016J.

(125) Amari, S.; Verilhac, J.-M.; Gros D'Aillon, E.; Ibanez, A.; Zaccaro, J. Optimization of the Growth Conditions for High Quality $CH_3NH_3PbBr_3$ Hybrid Perovskite Single Crystals. *Crystal Growth & Design* **2020**, *20* (3), 1665–1672. https://doi.org/10.1021/acs.cgd.9b01429.

(126) Saidaminov, M. I.; Abdelhady, A. L.; Murali, B.; Alarousu, E.; Burlakov, V. M.; Peng, W.; Dursun, I.; Wang, L.; He, Y.; Maculan, G.; Goriely, A.; Wu, T.; Mohammed, O. F.; Bakr, O. M. High-Quality Bulk Hybrid Perovskite Single Crystals within Minutes by Inverse Temperature Crystallization. *Nat Commun* **2015**, *6* (1), 7586. https://doi.org/10.1038/ncomms8586.

(127) Rakita, Y.; Kedem, N.; Gupta, S.; Sadhanala, A.; Kalchenko, V.; Böhm, M. L.; Kulbak, M.; Friend, R. H.; Cahen, D.; Hodes, G. Low-Temperature Solution-Grown CsPbBr3 Single Crystals and Their Characterization. *Crystal Growth & Design* **2016**, *16* (10), 5717–5725. https://doi.org/10.1021/acs.cgd.6b00764.

(128) Schmidt, L. C.; Pertegás, A.; González-Carrero, S.; Malinkiewicz, O.; Agouram, S.; Mínguez Espallargas, G.; Bolink, H. J.; Galian, R. E.; Pérez-Prieto, J. Nontemplate Synthesis of CH3NH3PbBr3 Perovskite Nanoparticles. *J. Am. Chem. Soc.* **2014**, *136* (3), 850–853. https://doi.org/10.1021/ja4109209.

(129) Im, J.-H.; Luo, J.; Franckevičius, M.; Pellet, N.; Gao, P.; Moehl, T.; Zakeeruddin, S. M.; Nazeeruddin, M. K.; Grätzel, M.; Park, N.-G. Nanowire Perovskite Solar Cell. *Nano Lett.* **2015**, *15* (3), 2120–2126. https://doi.org/10.1021/acs.nanolett.5b00046.

(130) Song, J.; Xu, L.; Li, J.; Xue, J.; Dong, Y.; Li, X.; Zeng, H. Monolayer and Few-Layer All-Inorganic Perovskites as a New Family of Two-Dimensional Semiconductors for Printable Optoelectronic Devices. *Advanced Materials* **2016**, *28* (24), 4861–4869. https://doi.org/10.1002/adma.201600225.

(131) Xiao, Z.; Bi, C.; Shao, Y.; Dong, Q.; Wang, Q.; Yuan, Y.; Wang, C.; Gao, Y.; Huang, J. Efficient, High Yield Perovskite Photovoltaic Devices Grown by Interdiffusion of Solution-Processed Precursor Stacking Layers. *Energy Environ. Sci.* **2014**, *7* (8), 2619–2623. https://doi.org/10.1039/C4EE01138D.

(132) Chen, K.; Tüysüz, H. Morphology-Controlled Synthesis of Organometal Halide Perovskite Inverse Opals. *Angewandte Chemie International Edition* **2015**, *54* (46), 13806–13810. https://doi.org/10.1002/anie.201506367.

(133) Lu, Y.-A.; Chang, T.-H.; Wu, S.-H.; Liu, C.-C.; Lai, K.-W.; Chang, Y.-C.; Chang, Y.-C.; Lu, H.-C.; Chu, C.-W.; Ho, K.-C. Coral-like Perovskite Nanostructures for Enhanced Light-Harvesting and Accelerated Charge Extraction in Perovskite Solar Cells. *Nano Energy* **2019**, *58*, 138–146. https://doi.org/10.1016/j.nanoen.2019.01.014.

(134) Liao, J.-F.; Wu, W.-Q.; Jiang, Y.; Kuang, D.-B.; Wang, L. Maze-Like Halide Perovskite

Films for Efficient Electron Transport Layer-Free Perovskite Solar Cells. *Solar RRL* **2019**, *3* (3), 1800268. https://doi.org/10.1002/solr.201800268.

(135) Zhao, Y.; Zhu, K. Solution Chemistry Engineering toward High-Efficiency Perovskite Solar Cells. *J. Phys. Chem. Lett.* **2014**, *5* (23), 4175–4186. https://doi.org/10.1021/jz501983v.

(136) Eperon, G. E.; Burlakov, V. M.; Docampo, P.; Goriely, A.; Snaith, H. J. Morphological Control for High Performance, Solution-Processed Planar Heterojunction Perovskite Solar Cells. *Advanced Functional Materials* **2014**, *24* (1), 151–157. https://doi.org/10.1002/adfm.201302090.

(137) Zhang, C.; Kuang, D.-B.; Wu, W.-Q. A Review of Diverse Halide Perovskite Morphologies for Efficient Optoelectronic Applications. *Small Methods* **2020**, *4* (2), 1900662. https://doi.org/10.1002/smtd.201900662.

(138) Stranks, S. D.; Nayak, P. K.; Zhang, W.; Stergiopoulos, T.; Snaith, H. J. Formation of Thin Films of Organic–Inorganic Perovskites for High-Efficiency Solar Cells. *Angewandte Chemie International Edition* **2015**, *54* (11), 3240–3248. https://doi.org/10.1002/anie.201410214.

(139) Song, T.-B.; Chen, Q.; Zhou, H.; Jiang, C.; Wang, H.-H.; Yang, Y. (Michael); Liu, Y.; You, J.; Yang, Y. Perovskite Solar Cells: Film Formation and Properties. *J. Mater. Chem. A* **2015**, *3* (17), 9032–9050. https://doi.org/10.1039/C4TA05246C.

(140) Zhou, H.; Chen, Q.; Li, G.; Luo, S.; Song, T.; Duan, H.-S.; Hong, Z.; You, J.; Liu, Y.; Yang, Y. Interface Engineering of Highly Efficient Perovskite Solar Cells. *Science* **2014**, *345* (6196), 542–546. https://doi.org/10.1126/science.1254050.

(141) Wojciechowski, K.; Saliba, M.; Leijtens, T.; Abate, A.; Snaith, H. J. Sub-150 °C Processed Meso-Superstructured Perovskite Solar Cells with Enhanced Efficiency. *Energy Environ. Sci.* **2014**, *7* (3), 1142–1147. https://doi.org/10.1039/C3EE43707H.

(142) Gamliel, S.; Dymshits, A.; Aharon, S.; Terkieltaub, E.; Etgar, L. Micrometer Sized Perovskite Crystals in Planar Hole Conductor Free Solar Cells. *J. Phys. Chem. C* **2015**, *119* (34), 19722–19728. https://doi.org/10.1021/acs.jpcc.5b07554.

(143) Deng, Y.; Peng, E.; Shao, Y.; Xiao, Z.; Dong, Q.; Huang, J. Scalable Fabrication of Efficient Organolead Trihalide Perovskite Solar Cells with Doctor-Bladed Active Layers. *Energy Environ. Sci.* **2015**, *8* (5), 1544–1550. https://doi.org/10.1039/C4EE03907F.

(144) Hwang, K.; Jung, Y.-S.; Heo, Y.-J.; Scholes, F. H.; Watkins, S. E.; Subbiah, J.; Jones, D. J.; Kim, D.-Y.; Vak, D. Toward Large Scale Roll-to-Roll Production of Fully Printed Perovskite Solar Cells. *Advanced Materials* **2015**, *27* (7), 1241–1247. https://doi.org/10.1002/adma.201404598.

(145) Im, J.-H.; Jang, I.-H.; Pellet, N.; Grätzel, M.; Park, N.-G. Growth of CH3NH3PbI3 Cuboids with Controlled Size for High-Efficiency Perovskite Solar Cells. *Nature Nanotech* **2014**, *9* (11), 927–932. https://doi.org/10.1038/nnano.2014.181.

(146) Burschka, J.; Pellet, N.; Moon, S.-J.; Humphry-Baker, R.; Gao, P.; Nazeeruddin, M. K.; Grätzel, M. Sequential Deposition as a Route to High-Performance Perovskite-Sensitized Solar

Cells. *Nature* **2013**, *499* (7458), 316–319. https://doi.org/10.1038/nature12340.

(147) Liu, M.; Johnston, M. B.; Snaith, H. J. Efficient Planar Heterojunction Perovskite Solar Cells by Vapour Deposition. *Nature* **2013**, *501* (7467), 395–398. https://doi.org/10.1038/nature12509.

(148) Tavakoli, M. M.; Gu, L.; Gao, Y.; Reckmeier, C.; He, J.; Rogach, A. L.; Yao, Y.; Fan, Z. Fabrication of Efficient Planar Perovskite Solar Cells Using a One-Step Chemical Vapor Deposition Method. *Sci Rep* **2015**, *5* (1), 14083. https://doi.org/10.1038/srep14083.

(149) Chen, Q.; Zhou, H.; Hong, Z.; Luo, S.; Duan, H.-S.; Wang, H.-H.; Liu, Y.; Li, G.; Yang, Y. Planar Heterojunction Perovskite Solar Cells via Vapor-Assisted Solution Process. *J. Am. Chem. Soc.* **2014**, *136* (2), 622–625. https://doi.org/10.1021/ja411509g.

(150) Zhao, Y.; Zhu, K. CH3NH3Cl-Assisted One-Step Solution Growth of CH3NH3PbI3: Structure, Charge-Carrier Dynamics, and Photovoltaic Properties of Perovskite Solar Cells. *J. Phys. Chem. C* **2014**, *118* (18), 9412–9418. https://doi.org/10.1021/jp502696w.

(151) Dualeh, A.; Tétreault, N.; Moehl, T.; Gao, P.; Nazeeruddin, M. K.; Grätzel, M. Effect of Annealing Temperature on Film Morphology of Organic–Inorganic Hybrid Pervoskite Solid-State Solar Cells. *Advanced Functional Materials* **2014**, *24* (21), 3250–3258. https://doi.org/10.1002/adfm.201304022.

(152) Yu, H.; Liu, X.; Xia, Y.; Dong, Q.; Zhang, K.; Wang, Z.; Zhou, Y.; Song, B.; Li, Y. Room-Temperature Mixed-Solvent-Vapor Annealing for High Performance Perovskite Solar Cells. *J. Mater. Chem. A* **2015**, *4* (1), 321–326. https://doi.org/10.1039/C5TA08565A.

(153) You, J.; Yang, Y. (Michael); Hong, Z.; Song, T.-B.; Meng, L.; Liu, Y.; Jiang, C.; Zhou, H.; Chang, W.-H.; Li, G.; Yang, Y. Moisture Assisted Perovskite Film Growth for High Performance Solar Cells. *Appl. Phys. Lett.* **2014**, *105* (18), 183902. https://doi.org/10.1063/1.4901510.

(154) Rong, Y.; Tang, Z.; Zhao, Y.; Zhong, X.; Venkatesan, S.; Graham, H.; Patton, M.; Jing, Y.; Guloy, A. M.; Yao, Y. Solvent Engineering towards Controlled Grain Growth in Perovskite Planar Heterojunction Solar Cells. *Nanoscale* **2015**, *7* (24), 10595–10599. https://doi.org/10.1039/C5NR02866C.

(155) Shi, D.; Adinolfi, V.; Comin, R.; Yuan, M.; Alarousu, E.; Buin, A.; Chen, Y.; Hoogland, S.; Rothenberger, A.; Katsiev, K.; Losovyj, Y.; Zhang, X.; Dowben, P. A.; Mohammed, O. F.; Sargent, E. H.; Bakr, O. M. Low Trap-State Density and Long Carrier Diffusion in Organolead Trihalide Perovskite Single Crystals. *Science* **2015**, *347* (6221), 519–522. https://doi.org/10.1126/science.aaa2725.

(156) Huang, J.; Shao, Y.; Dong, Q. Organometal Trihalide Perovskite Single Crystals: A Next Wave of Materials for 25% Efficiency Photovoltaics and Applications Beyond? *J. Phys. Chem. Lett.* **2015**, *6* (16), 3218–3227. https://doi.org/10.1021/acs.jpclett.5b01419.

(157) Fang, Y.; Dong, Q.; Shao, Y.; Yuan, Y.; Huang, J. Highly Narrowband Perovskite Single-Crystal Photodetectors Enabled by Surface-Charge Recombination. *Nature Photon* **2015**, *9* (10), 679–686. https://doi.org/10.1038/nphoton.2015.156.

(158) Liu, Y.; Yang, Z.; Cui, D.; Ren, X.; Sun, J.; Liu, X.; Zhang, J.; Wei, Q.; Fan, H.; Yu, F.; Zhang, X.; Zhao, C.; Liu, S. (Frank). Two-Inch-Sized Perovskite CH3NH3PbX3 (X = Cl, Br, I) Crystals: Growth and Characterization. *Advanced Materials* **2015**, *27* (35), 5176–5183. https://doi.org/10.1002/adma.201502597.

(159) Zhang, T.; Yang, M.; Benson, E. E.; Li, Z.; van de Lagemaat, J.; Luther, J. M.; Yan, Y.; Zhu, K.; Zhao, Y. A Facile Solvothermal Growth of Single Crystal Mixed Halide Perovskite $CH_3NH_3Pb(Br_{1-x}Cl_x)_3$. *Chem. Commun.* **2015**, *51* (37), 7820–7823. https://doi.org/10.1039/C5CC01835H.

(160) Shao, D.; Zhu, W.; Xin, G.; Lian, J.; Sawyer, S. Inorganic Vacancy-Ordered Perovskite Cs2SnCl6:Bi/GaN Heterojunction Photodiode for Narrowband, Visible-Blind UV Detection. *Appl. Phys. Lett.* **2019**, *115* (12), 121106. https://doi.org/10.1063/1.5123226.

(161) Chung, I.; Lee, B.; He, J.; Chang, R. P. H.; Kanatzidis, M. G. All-Solid-State Dye-Sensitized Solar Cells with High Efficiency. *Nature* **2012**, *485* (7399), 486–489. https://doi.org/10.1038/nature11067.

(162) Dang, Y.; Ju, D.; Wang, L.; Tao, X. Recent Progress in the Synthesis of Hybrid Halide Perovskite Single Crystals. *CrystEngComm* **2016**, *18* (24), 4476–4484. https://doi.org/10.1039/C6CE00655H.

(163) Poglitsch, A.; Weber, D. Dynamic Disorder in Methylammoniumtrihalogenoplumbates (II) Observed by Millimeter-wave Spectroscopy. *J. Chem. Phys.* **1987**, *87* (11), 6373–6378. https://doi.org/10.1063/1.453467.

(164) Lian, Z.; Yan, Q.; Lv, Q.; Wang, Y.; Liu, L.; Zhang, L.; Pan, S.; Li, Q.; Wang, L.; Sun, J.-L. High-Performance Planar-Type Photodetector on (100) Facet of MAPbI3 Single Crystal. *Sci Rep* **2015**, *5* (1), 16563. https://doi.org/10.1038/srep16563.

(165) Su, J.; Sang, L.; Wang, D.; Lu, D.; Wang, W.; Wen, Y. Solution Growth and Morphology of CH3NH3PbBr3 Single Crystals in Different Solvents. *Crystal Research and Technology* **2016**, *51* (11), 650–655. https://doi.org/10.1002/crat.201600193.

(166) Zhang, P.; Zhang, G.; Liu, L.; Ju, D.; Zhang, L.; Cheng, K.; Tao, X. Anisotropic Optoelectronic Properties of Melt-Grown Bulk CsPbBr3 Single Crystal. *J. Phys. Chem. Lett.* **2018**, *9* (17), 5040–5046. https://doi.org/10.1021/acs.jpclett.8b01945.

(167) *Handbook of Crystal Growth: Fundamentals*, 2nd ed.; Nishinaga, T., Ed.; Elsevier: Boston, 2015; Vol. 1. https://doi.org/10.1016/B978-0-444-56369-9.12001-5.

(168) Pound, G. M.; Simnad, M. T.; Yang, L. Heterogeneous Nucleation of Crystals from Vapor. *J. Chem. Phys.* **1954**, *22* (7), 1215–1219. https://doi.org/10.1063/1.1740336.

(169) Liu, Y.; Zhang, Y.; Yang, Z.; Feng, J.; Xu, Z.; Li, Q.; Hu, M.; Ye, H.; Zhang, X.; Liu, M.; Zhao, K.; Liu, S. Low-Temperature-Gradient Crystallization for Multi-Inch High-Quality Perovskite Single Crystals for Record Performance Photodetectors. *Materials Today* **2019**, *22*, 67–75. https://doi.org/10.1016/j.mattod.2018.04.002.

(170) Ferri, D.; Salvatore, F.; Vasca, E. Complex Formation Between Lead(II) and Bromide Ions. *Journal of Coordination Chemistry* **1989**, *20* (1), 11–20.

https://doi.org/10.1080/00958978909408843.
(171) Hamill, J. C.; Schwartz, J.; Loo, Y.-L. Influence of Solvent Coordination on Hybrid Organic–Inorganic Perovskite Formation. *ACS Energy Lett.* **2018**, *3* (1), 92–97. https://doi.org/10.1021/acsenergylett.7b01057.
(172) Nayak, P. K.; Moore, D. T.; Wenger, B.; Nayak, S.; Haghighirad, A. A.; Fineberg, A.; Noel, N. K.; Reid, O. G.; Rumbles, G.; Kukura, P.; Vincent, K. A.; Snaith, H. J. Mechanism for Rapid Growth of Organic–Inorganic Halide Perovskite Crystals. *Nat Commun* **2016**, *7* (1), 13303. https://doi.org/10.1038/ncomms13303.
(173) Saidaminov, M. I.; Abdelhady, A. L.; Maculan, G.; Bakr, O. M. Retrograde Solubility of Formamidinium and Methylammonium Lead Halide Perovskites Enabling Rapid Single Crystal Growth. *Chem. Commun.* **2015**, *51* (100), 17658–17661. https://doi.org/10.1039/C5CC06916E.
(174) Maculan, G.; Sheikh, A. D.; Abdelhady, A. L.; Saidaminov, M. I.; Haque, M. A.; Murali, B.; Alarousu, E.; Mohammed, O. F.; Wu, T.; Bakr, O. M. $CH_3NH_3PbCl_3$ Single Crystals: Inverse Temperature Crystallization and Visible-Blind UV-Photodetector. *J. Phys. Chem. Lett.* **2015**, *6* (19), 3781–3786. https://doi.org/10.1021/acs.jpclett.5b01666.
(175) Kröger, F. A.; Vink, H. J. Relations between the Concentrations of Imperfections in Crystalline Solids. In *Solid State Physics*; Seitz, F., Turnbull, D., Eds.; Academic Press, 1956; Vol. 3, pp 307–435. https://doi.org/10.1016/S0081-1947(08)60135-6.
(176) Li, G.; Zhang, T.; Guo, N.; Xu, F.; Qian, X.; Zhao, Y. Ion-Exchange-Induced 2D–3D Conversion of HMA1−xFAxPbI3Cl Perovskite into a High-Quality MA1−xFAxPbI3 Perovskite. *Angewandte Chemie International Edition* **2016**, *55* (43), 13460–13464. https://doi.org/10.1002/anie.201606801.
(177) Reyna, Y.; Salado, M.; Kazim, S.; Pérez-Tomas, A.; Ahmad, S.; Lira-Cantu, M. Performance and Stability of Mixed FAPbI3(0.85)MAPbBr3(0.15) Halide Perovskite Solar Cells under Outdoor Conditions and the Effect of Low Light Irradiation. *Nano Energy* **2016**, *30*, 570–579. https://doi.org/10.1016/j.nanoen.2016.10.053.
(178) Lin, D.; Shi, T.; Xie, H.; Wan, F.; Ren, X.; Liu, K.; Zhao, Y.; Ke, L.; Lin, Y.; Gao, Y.; Xu, X.; Xie, W.; Liu, P.; Yuan, Y. Ion Migration Accelerated Reaction between Oxygen and Metal Halide Perovskites in Light and Its Suppression by Cesium Incorporation. *Advanced Energy Materials* **2021**, *11* (8), 2002552. https://doi.org/10.1002/aenm.202002552.
(179) Matsui, T.; Yokoyama, T.; Negami, T.; Sekiguchi, T.; Saliba, M.; Grätzel, M.; Segawa, H. Effect of Rubidium for Thermal Stability of Triple-Cation Perovskite Solar Cells. *Chem. Lett.* **2018**, *47* (6), 814–816. https://doi.org/10.1246/cl.180211.
(180) Zhang, S.; Wu, S.; Chen, R.; Chen, W.; Huang, Y.; Zhu, H.; Yang, Z.; Chen, W. Controlling Orientation Diversity of Mixed Ion Perovskites: Reduced Crystal Microstrain and Improved Structural Stability. *J. Phys. Chem. Lett.* **2019**, *10* (11), 2898–2903. https://doi.org/10.1021/acs.jpclett.9b01180.
(181) Roose, B. Ion Migration Drives Self-Passivation in Perovskite Solar Cells and Is

Enhanced by Light Soaking. *RSC Adv.* **2021**, *11* (20), 12095–12101. https://doi.org/10.1039/D1RA01166A.

(182) Eeles, A. Performance Characterisation of Photovoltaic Devices: Managing the Effects of High Capacitance and Metastability. Ph.D. diss., Loughborough University, 2016.

(183) Molla, R. S. *A Study on Manufacturing of Deformed Bar (G 60-400W) at Elite Iron and Steel Industries*; 2018. https://doi.org/10.13140/RG.2.2.24320.33289.

(184) *Grain Structure and Boundary*. Mypdh.engineer. https://mypdh.engineer/lessons/grain-structure-and-boundary-2/ (accessed 2023-03-05).

(185) Figielski, T. Dislocations as Electrically Active Centres in Semiconductors—Half a Century from the Discovery. *J. Phys.: Condens. Matter* **2002**, *14* (48), 12665. https://doi.org/10.1088/0953-8984/14/48/301.

(186) List, R. S. Electrical Effects of Dislocations and Other Crystallographic Defects in Hg0.78Cd0.22Te n-on-p Photodiodes. *J. Electron. Mater.* **1993**, *22* (8), 1017–1025. https://doi.org/10.1007/BF02817519.

(187) Mahajan, S. Defects in Semiconductors and Their Effects on Devices. *Acta Materialia* **2000**, *48* (1), 137–149. https://doi.org/10.1016/S1359-6454(99)00292-X.

(188) Kurtz, A. D.; Kulin, S. A.; Averbach, B. L. Effect of Dislocations on the Minority Carrier Lifetime in Semiconductors. *Phys. Rev.* **1956**, *101* (4), 1285–1291. https://doi.org/10.1103/PhysRev.101.1285.

(189) Zou, Y.; Yuan, S.; Buyruk, A.; Eichhorn, J.; Yin, S.; Reus, M. A.; Xiao, T.; Pratap, S.; Liang, S.; Weindl, C. L.; Chen, W.; Mu, C.; Sharp, I. D.; Ameri, T.; Schwartzkopf, M.; Roth, S. V.; Müller-Buschbaum, P. The Influence of CsBr on Crystal Orientation and Optoelectronic Properties of $MAPbI_3$ -Based Solar Cells. *ACS Appl. Mater. Interfaces* **2022**, *14* (2), 2958–2967. https://doi.org/10.1021/acsami.1c22184.

(190) Zhang, L.; Liu, Y.; Ye, X.; Han, Q.; Ge, C.; Cui, S.; Guo, Q.; Zheng, X.; Zhai, Z.; Tao, X. Exploring Anisotropy on Oriented Wafers of $MAPbBr_3$ Crystals Grown by Controlled Antisolvent Diffusion. *Crystal Growth & Design* **2018**, *18* (11), 6652–6660. https://doi.org/10.1021/acs.cgd.8b00896.

(191) Zhang, T.; Hu, C.; Yang, S. Ion Migration: A "Double-Edged Sword" for Halide-Perovskite-Based Electronic Devices. *Small Methods* **2020**, *4* (5), 1900552. https://doi.org/10.1002/smtd.201900552.

(192) Bryant, D.; Aristidou, N.; Pont, S.; Sanchez-Molina, I.; Chotchunangatchaval, T.; Wheeler, S.; Durrant, J. R.; Haque, S. A. Light and Oxygen Induced Degradation Limits the Operational Stability of Methylammonium Lead Triiodide Perovskite Solar Cells. *Energy Environ. Sci.* **2016**, *9* (5), 1655–1660. https://doi.org/10.1039/C6EE00409A.

(193) Slimi, B.; Mollar, M.; Assaker, I. B.; Kriaa, I.; Chtourou, R.; Marí, B. Perovskite FA1-XMAxPbI3 for Solar Cells: Films Formation and Properties. *Energy Procedia* **2016**, *102*, 87–95. https://doi.org/10.1016/j.egypro.2016.11.322.

(194) Yuan, Y.; Wang, Q.; Shao, Y.; Lu, H.; Li, T.; Gruverman, A.; Huang, J. Electric-Field-

Driven Reversible Conversion Between Methylammonium Lead Triiodide Perovskites and Lead Iodide at Elevated Temperatures. *Advanced Energy Materials* **2016**, *6* (2), 1501803. https://doi.org/10.1002/aenm.201501803.

(195) Xiao, Z.; Yuan, Y.; Shao, Y.; Wang, Q.; Dong, Q.; Bi, C.; Sharma, P.; Gruverman, A.; Huang, J. Giant Switchable Photovoltaic Effect in Organometal Trihalide Perovskite Devices. *Nature Mater* **2015**, *14* (2), 193–198. https://doi.org/10.1038/nmat4150.

(196) Eames, C.; Frost, J. M.; Barnes, P. R. F.; O'Regan, B. C.; Walsh, A.; Islam, M. S. Ionic Transport in Hybrid Lead Iodide Perovskite Solar Cells. *Nature Communications* **2015**, *6*. https://doi.org/10.1038/ncomms8497.

(197) Yuan, Y.; Huang, J. Ion Migration in Organometal Trihalide Perovskite and Its Impact on Photovoltaic Efficiency and Stability. *Acc. Chem. Res.* **2016**, *49* (2), 286–293. https://doi.org/10.1021/acs.accounts.5b00420.

(198) Besleaga, C.; Abramiuc, L. E.; Stancu, V.; Tomulescu, A. G.; Sima, M.; Trinca, L.; Plugaru, N.; Pintilie, L.; Nemnes, G. A.; Iliescu, M.; Svavarsson, H. G.; Manolescu, A.; Pintilie, I. Iodine Migration and Degradation of Perovskite Solar Cells Enhanced by Metallic Electrodes. *J. Phys. Chem. Lett.* **2016**, *7* (24), 5168–5175. https://doi.org/10.1021/acs.jpclett.6b02375.

(199) Brennan, M. C.; Ruth, A.; Kamat, P. V.; Kuno, M. Photoinduced Anion Segregation in Mixed Halide Perovskites. *Trends in Chemistry* **2020**, *2* (4), 282–301. https://doi.org/10.1016/j.trechm.2020.01.010.

(200) Brennan, M. C.; Draguta, S.; Kamat, P. V.; Kuno, M. Light-Induced Anion Phase Segregation in Mixed Halide Perovskites. *ACS Energy Lett.* **2018**, *3* (1), 204–213. https://doi.org/10.1021/acsenergylett.7b01151.

(201) Leijtens, T.; Hoke, E. T.; Grancini, G.; Slotcavage, D. J.; Eperon, G. E.; Ball, J. M.; De Bastiani, M.; Bowring, A. R.; Martino, N.; Wojciechowski, K.; McGehee, M. D.; Snaith, H. J.; Petrozza, A. Mapping Electric Field-Induced Switchable Poling and Structural Degradation in Hybrid Lead Halide Perovskite Thin Films. *Advanced Energy Materials* **2015**, *5* (20), 1500962. https://doi.org/10.1002/aenm.201500962.

(202) Yamilova, O. R.; Danilov, A. V.; Mangrulkar, M.; Fedotov, Y. S.; Luchkin, S. Yu.; Babenko, S. D.; Bredikhin, S. I.; Aldoshin, S. M.; Stevenson, K. J.; Troshin, P. A. Reduction of Methylammonium Cations as a Major Electrochemical Degradation Pathway in MAPbI3 Perovskite Solar Cells. *J. Phys. Chem. Lett.* **2020**, *11* (1), 221–228. https://doi.org/10.1021/acs.jpclett.9b03161.

(203) Christians, J. A.; Schulz, P.; Tinkham, J. S.; Schloemer, T. H.; Harvey, S. P.; Tremolet de Villers, B. J.; Sellinger, A.; Berry, J. J.; Luther, J. M. Tailored Interfaces of Unencapsulated Perovskite Solar Cells for >1,000 Hour Operational Stability. *Nat Energy* **2018**, *3* (1), 68–74. https://doi.org/10.1038/s41560-017-0067-y.

(204) Guo, X.; Ngai, K.; Qin, M.; Lu, X.; Xu, J.; Long, M. The Compatibility of Methylammonium and Formamidinium in Mixed Cation Perovskite: The Optoelectronic and Stability Properties. *Nanotechnology* **2020**, *32* (7), 075406. https://doi.org/10.1088/1361-

6528/abc50c.

(205) Chatterjee, R.; Pavlovetc, I. M.; Aleshire, K.; Hartland, G. V.; Kuno, M. Subdiffraction Infrared Imaging of Mixed Cation Perovskites: Probing Local Cation Heterogeneities. *ACS Energy Lett.* **2018**, *3* (2), 469–475. https://doi.org/10.1021/acsenergylett.7b01306.

(206) Tennyson, E. M.; Roose, B.; Garrett, J. L.; Gong, C.; Munday, J. N.; Abate, A.; Leite, M. S. Cesium-Incorporated Triple Cation Perovskites Deliver Fully Reversible and Stable Nanoscale Voltage Response. *ACS Nano* **2019**, *13* (2), 1538–1546. https://doi.org/10.1021/acsnano.8b07295.

(207) Kubicki, D. J.; Prochowicz, D.; Hofstetter, A.; Zakeeruddin, S. M.; Grätzel, M.; Emsley, L. Phase Segregation in Cs-, Rb- and K-Doped Mixed-Cation (MA)x(FA)1–XPbI3 Hybrid Perovskites from Solid-State NMR. *J. Am. Chem. Soc.* **2017**, *139* (40), 14173–14180. https://doi.org/10.1021/jacs.7b07223.

(208) Li, Z.; Xiao, C.; Yang, Y.; Harvey, S. P.; Kim, D. H.; Christians, J. A.; Yang, M.; Schulz, P.; Nanayakkara, S. U.; Jiang, C.-S.; Luther, J. M.; Berry, J. J.; Beard, M. C.; Al-Jassim, M. M.; Zhu, K. Extrinsic Ion Migration in Perovskite Solar Cells. *Energy Environ. Sci.* **2017**, *10* (5), 1234–1242. https://doi.org/10.1039/C7EE00358G.

(209) Ding, C.; Huang, R.; Ahläng, C.; Lin, J.; Zhang, L.; Zhang, D.; Luo, Q.; Li, F.; Österbacka, R.; Ma, C.-Q. Synergetic Effects of Electrochemical Oxidation of Spiro-OMeTAD and Li+ Ion Migration for Improving the Performance of n–i–p Type Perovskite Solar Cells. *J. Mater. Chem. A* **2021**, *9* (12), 7575–7585. https://doi.org/10.1039/D0TA12458C.

(210) Dawson, J. A.; Naylor, A. J.; Eames, C.; Roberts, M.; Zhang, W.; Snaith, H. J.; Bruce, P. G.; Islam, M. S. Mechanisms of Lithium Intercalation and Conversion Processes in Organic–Inorganic Halide Perovskites. *ACS Energy Lett.* **2017**, *2* (8), 1818–1824. https://doi.org/10.1021/acsenergylett.7b00437.

(211) Cardenas-Daw, C.; Simon, T.; Stolarczyk, J. K.; Feldmann, J. Migration of Constituent Protons in Hybrid Organic–Inorganic Perovskite Triggers Intrinsic Doping. *J. Am. Chem. Soc.* **2017**, *139* (46), 16462–16465. https://doi.org/10.1021/jacs.7b09319.

(212) Frost, J. M.; Walsh, A. What Is Moving in Hybrid Halide Perovskite Solar Cells? *Acc. Chem. Res.* **2016**, *49* (3), 528–535. https://doi.org/10.1021/acs.accounts.5b00431.

(213) Sadhu, S.; Buffeteau, T.; Sandrez, S.; Hirsch, L.; Bassani, D. M. Observing the Migration of Hydrogen Species in Hybrid Perovskite Materials through D/H Isotope Exchange. *J. Am. Chem. Soc.* **2020**, *142* (23), 10431–10437. https://doi.org/10.1021/jacs.0c02597.

(214) Ceratti, D. R.; Zohar, A.; Kozlov, R.; Dong, H.; Uraltsev, G.; Girshevitz, O.; Pinkas, I.; Avram, L.; Hodes, G.; Cahen, D. Eppur Si Muove: Proton Diffusion in Halide Perovskite Single Crystals. *Adv. Mater.* **2020**, *32* (46), 2002467. https://doi.org/10.1002/adma.202002467.

(215) Zhang, T.; Meng, X.; Bai, Y.; Xiao, S.; Hu, C.; Yang, Y.; Chen, H.; Yang, S. Profiling the Organic Cation-Dependent Degradation of Organolead Halide Perovskite Solar Cells. *J. Mater. Chem. A* **2017**, *5* (3), 1103–1111. https://doi.org/10.1039/C6TA09687E.

(216) Kerner, R. A.; Zhao, L.; Harvey, S. P.; Berry, J. J.; Schwartz, J.; Rand, B. P. Low

Threshold Voltages Electrochemically Drive Gold Migration in Halide Perovskite Devices. *ACS Energy Lett.* **2020**, *5* (11), 3352–3356. https://doi.org/10.1021/acsenergylett.0c01805.

(217) Domanski, K.; Correa-Baena, J.-P.; Mine, N.; Nazeeruddin, M. K.; Abate, A.; Saliba, M.; Tress, W.; Hagfeldt, A.; Grätzel, M. Not All That Glitters Is Gold: Metal-Migration-Induced Degradation in Perovskite Solar Cells. *ACS Nano* **2016**, *10* (6), 6306–6314. https://doi.org/10.1021/acsnano.6b02613.

(218) Ding, H.; Li, B.; Zareen, S.; Li, G.; Tu, Y.; Zhang, D.; Cao, X.; Xu, Q.; Yang, S.; Tait, S. L.; Zhu, J. In Situ Investigations of Al/Perovskite Interfacial Structures. *ACS Appl. Mater. Interfaces* **2020**, *12* (25), 28861–28868. https://doi.org/10.1021/acsami.0c06458.

(219) Kato, Y.; Ono, L. K.; Lee, M. V.; Wang, S.; Raga, S. R.; Qi, Y. Silver Iodide Formation in Methyl Ammonium Lead Iodide Perovskite Solar Cells with Silver Top Electrodes. *Advanced Materials Interfaces* **2015**, *2* (13), 1500195. https://doi.org/10.1002/admi.201500195.

(220) Liang, J.-J.; Li, M.; Zhu, J.-Y.; Zong, H.; Zhang, Y.; Jain, S. M.; Wang, Z.-K. Detrimental Effect of Silver Doping in Spiro-MeOTAD on the Device Performance of Perovskite Solar Cells. *Organic Electronics* **2019**, *69*, 343–347. https://doi.org/10.1016/j.orgel.2019.03.036.

(221) Lu, Y.; Ge, Y.; Sui, M. Different Degradation Mechanism of CH3NH3PbI3 Based Perovskite Solar Cells under Ultraviolet and Visible Light Illumination. *Acta Chimica Sinica* **2021**, *79* (3), 344. https://doi.org/10.6023/A20100476.

(222) Yan, X.; Fan, W.; Cheng, F.; Sun, H.; Xu, C.; Wang, L.; Kang, Z.; Zhang, Y. Ion Migration in Hybrid Perovskites: Classification, Identification, and Manipulation. *Nano Today* **2022**, *44*, 101503. https://doi.org/10.1016/j.nantod.2022.101503.

(223) Baussens, O. Nouveau matériau pérovskite pour la radiographie médicale. Ph.D. diss., Université de Bordeaux, 2021.

Chapter 2 – Materials and methods

Table of contents

Chapter 2

Chapter 2

Materials and methods

Introduction

The following chapter describes all the technical aspects of the synthesis and characterisation of methylammonium lead tribromide ($MAPbBr_3$) perovskite single crystals (SCs) and devices based on them. Crystal growth via inverse temperature crystallisation (ITC) and modified versions (MITCs) methods are detailed as well as the device optoelectronic characterisation.

As indicated in the previous chapter, defects in the crystal structure can and often play a major role in the semiconductor optoelectronic properties. The type and number of defects formed can be influenced by the crystal growth conditions. These conditions encompass a broad spectrum of elements influencing the crystal growth, such as the nature of the chemical compounds involved, their purity, the environment (e.g., temperature, humidity) as well as the eventual perturbations. As we are interested in revealing the impact of specific modifications in the crystal structure, it is of paramount importance to avoid as much as possible variations of other parameters. To that end, it is crucial to synthesise SCs of similar quality and characterise them with a standardised protocol. In the past years, our group has developed during Amari's and Baussens' thesis works, on the one hand, a crystal growth process leading to SCs of reproducible quality,[1] and on the other hand, a standardised optoelectronic characterisation protocol.[2] Both are detailed hereafter.

Chapter 2

1 Growth of single crystals of reproducible quality

The gradual understanding of $MAPbBr_3$ growth in solution has led to a strict MITC method allowing synthesising mm-sized SCs of reproducible quality. The sample reproducibility is of the highest order of importance for the evaluation of a given optoelectronic property or to see the impact of a parameter change during the life cycle of a SC sample.

1.1 Growth solution and chemical system

As seen in Chapter 1, to grow hybrid $MAPbX_3$ (X = I, Br, Cl) requires specific synthesis conditions given the complex chemistry behind. The solvent used has to be able to dissolve both organic and inorganic parts: so far, just a few solvents known are able to do this task successfully. In the case of $MAPbBr_3$, N,N-dimethylformamide (DMF) is the polar aprotic solvent accomplishing this. A $MAPbBr_3$ solution is prepared by dissolving in DMF, halogenated precursors lead (II) bromide ($PbBr_2$) and methylammonium bromide (MABr). Due to the low solubility of $PbBr_2$, high purity of this precursor is required (5N) to avoid an insoluble fraction, thus altering the stoichiometry of the crystal and creating defects.

The materials used for the synthesis of $MAPbBr_3$ SCs were: DMF (Sigma Aldrich, anhydrous, 99.8 % and Acros Organics, 99,8%, Extra Dry over Molecular Sieve, AcroSeal® (zeolites)), $PbBr_2$ (Sigma Aldrich, 99.999 % trace metals basis; Alfa Aesar, Puratronic®, 99,998% (metals basis); and ultra-dry, 99,999% (metals basis)), MABr (GreatCell Solar, ≥ 99 %). The materials used for the preparation of the growth solution were used as received. Different products are given for DMF and $PbBr_2$, which use depend on the different studies described in the upcoming chapters.

A typical growth solution is a stoichiometric mixture of precursors $PbBr_2$:MABr 1:1 in DMF at 1 mol L^{-1} (1 M). A 1:1 ratio is targeted for the growth of a stoichiometric SC. Concentrations lower than 1 M may require higher solution volumes or temperatures to produce SCs of same dimension than that at 1 M, which complicate laboratory synthesis. Concentrations higher than 1 M can lead to the apparition of a white solid phase at low temperature (~ 25 °C) corresponding to lead-solvent (Pb-DMF) solvates, encapsulating then Pb^{2+} available to build the inorganic octahedra perovskite network. Thus, a 1 M concentration represents a good compromise, allowing a practical and homogeneous precursor solution at room temperature.

Within a 20 mL borosilicate glass flask, $PbBr_2$ is firstly introduced, then MABr and lastly DMF. The precursor solution preparation takes place in a glovebox (Ar atmosphere, H_2O and O_2 contents below 10 ppm) at CEA LITEN, to avoid any interaction with the environment (e.g. humidity, dust particles), such impact is precisely the subject of the study presented in Chapter 4. DMF is known to be hygroscopic.[3] Both precursor powders and solvent were mixed with a magnetic stirrer overnight at room temperature for full dissolution of the precursors and stabilisation of all chemical species present. A 1 M solution has an equilibrium temperature of

T_{eq} = 58.3 °C, far above room temperature. The next day, the solution is filtered using a borosilicate glass or polyethylene syringe and polytetrafluoroethylene (PTFE) filter with a pore size of 0.2 µm with the objective of eliminating any non-miscible parasitic solids. At room temperature, the growth solution obtained is well below the solubility limit and while being in an Ar atmosphere, it can be stored without any risk of spontaneous crystallisation or degradation. It is usually used for crystal growth within 24 h.

1.2 Single crystal growth

In previous work, it has been shown that one of the main sources of variability in crystal quality originates from the seed the crystal grows from, especially if the seed results from spontaneous nucleation.[1,4] Therefore, all the crystal growths conducted here are seeded growths, high quality seeds being selected among the ones produced by spontaneous nucleation.

1.2.1 Seed preparation and preliminary steps

The formation of seed crystals is simply based on bringing the growth solution beyond the metastable zone, as shown in Chapter 1, to trigger the formation of nuclei within the solution. By starting from a temperature below the equilibrium temperature of the perovskite, namely T_{eq} = 58.3°C (for 1 M $PbBr_2$:MABr 1:1 solution, see retrograde solubility curve (s-T) in **Figure 2-1-1**), and setting an abrupt change of temperature, usually ≥ 81.5 °C, spontaneous nucleation is naturally induced. To produce seed crystals, the growth run has to be interrupted so little crystals (~ 1-2 mm long) can be extracted from the solution. To facilitate spontaneous nucleation, we ensured that the meniscus of the solution is well embedded in the heating system used. Indeed, the solvent evaporation, being increased by the meniscus curvature, leads to a local increase in solute concentration and a favoured point of nucleation.

A monocrystalline seed crystal has to be selected with specific characteristics to produce high quality SCs. The seed crystal has to be ideally ~ 1 mm long, with regular edges and plane surfaces, indicative that it is not made up of several agglomerated crystals but effectively a SC. Seed crystals were then further selected through observation between crossed polarisers according to their level internal stress. Examples of selected and rejected seed crystals can be observed in **Figure 2-1-2-A** and **Figure 2-1-2-B**, respectively.

Because the equilibrium temperature of the growth solution is about 58.3 °C, the next challenge is to engage the seed in the growth solution at a temperature significantly higher than the room temperature, but just below equilibrium to effectively start the growth run. Two methods have been used. The first consists in simply dropping the seed crystal inside the precursor solution while being heated at this temperature below equilibrium. The seed rests at the bottom of the vial hopefully in the centre before the growth starts, as shown in the schematics depicted in **Figure 2-1-2-C** and **Figure 2-1-2-E**. While being simple, this method

presents several shortcomings. First, it risks projecting solution on the inner walls of the vials that can later lead to parasitic nucleation.

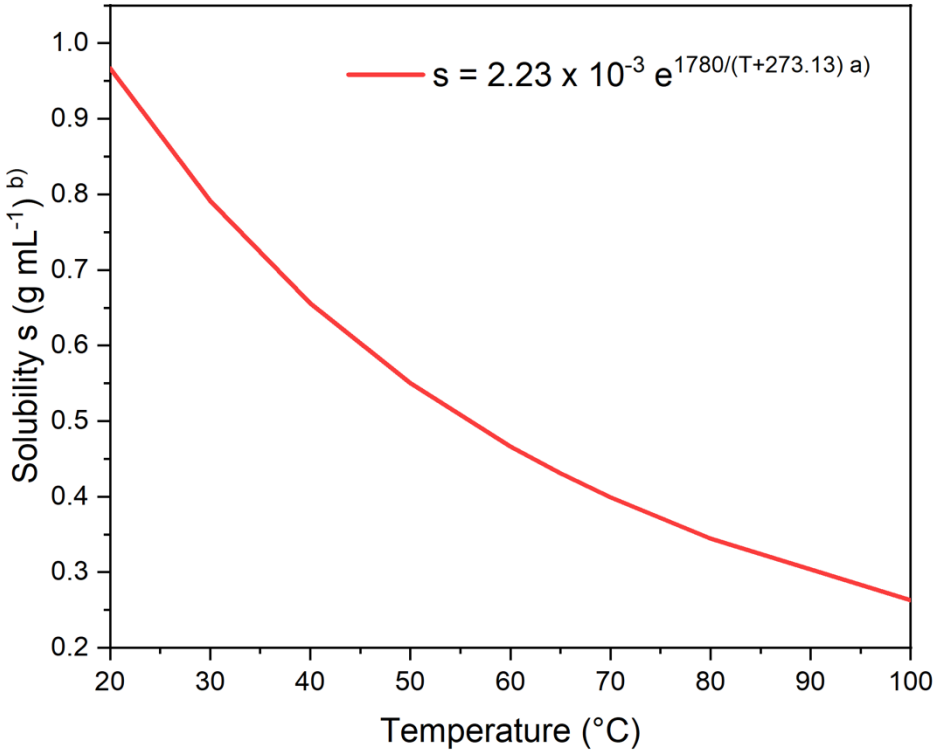

Figure 2-1-1. Retrograde solubility of $MAPbBr_3$ in DMF. [a] The $MAPbBr_3$ Van't Hoff fitting equation is extracted from Amari's work.[4] [b] Grams of perovskite per millilitre of solvent at 20 °C (density considered constant).

Second, the bottom of the vial being not perfectly flat, the growing crystal will accommodate this bottom shape rendering a significant portion of the volume unusable. The other method consists in gluing the seed crystal on a flat surface at the bottom of the vial and then adding the growth solution in. In that case, the seed crystal is mounted on a piece of Si wafer with silicone glue (Elkem Silicones CAF 4). The ensemble is then glued to the bottom of the vial, mostly in order to avoid dead space bellow the wafer where solution would be trapped and parasitic nucleation would take place. In addition, sufficient exposed area to the solution must be secured to allow large SC growth with a proper positioning of the silicone glue at the bottom of the seed crystal. **Figure 2-1-2-D** and **Figure 2-1-2-F** illustrate how the SC is fixed to the bottom of the vial on a Si wafer. Both the seed crystal secured at the bottom of an empty vial and the growth solution are thermalized at the temperature below equilibrium, then the solution is added to the vial containing the seed and the growth run is started. The starting temperature is selected so the solution handled is undersaturated, ensuring that it will not trigger any nucleation. It has also to take into consideration any uncertainty on the actual solution equilibrium temperature.

Because of the strong dependency on temperature of the $MAPbBr_3$ solubility in DMF (high curve slope), any uncertainty on the solution concentration, on the weighted precursors can shift significantly the equilibrium temperature (about 1 °C for an error of a couple of milligrams). To accommodate for this uncertainty the initial temperature is chosen 2.3 °C below the equilibrium: 56°C for the targeted 58.3°C. This is followed by two temperature steps, called the regrowth protocol: one to stop the seed partial dissolution ($T_{level\ 1}$ = 58.8 °C) and the other one to ensure the reconstruction of seed ($T_{level\ 2}$ = 62.6 °C) under moderate relative supersaturation (σ_r < 7 %).

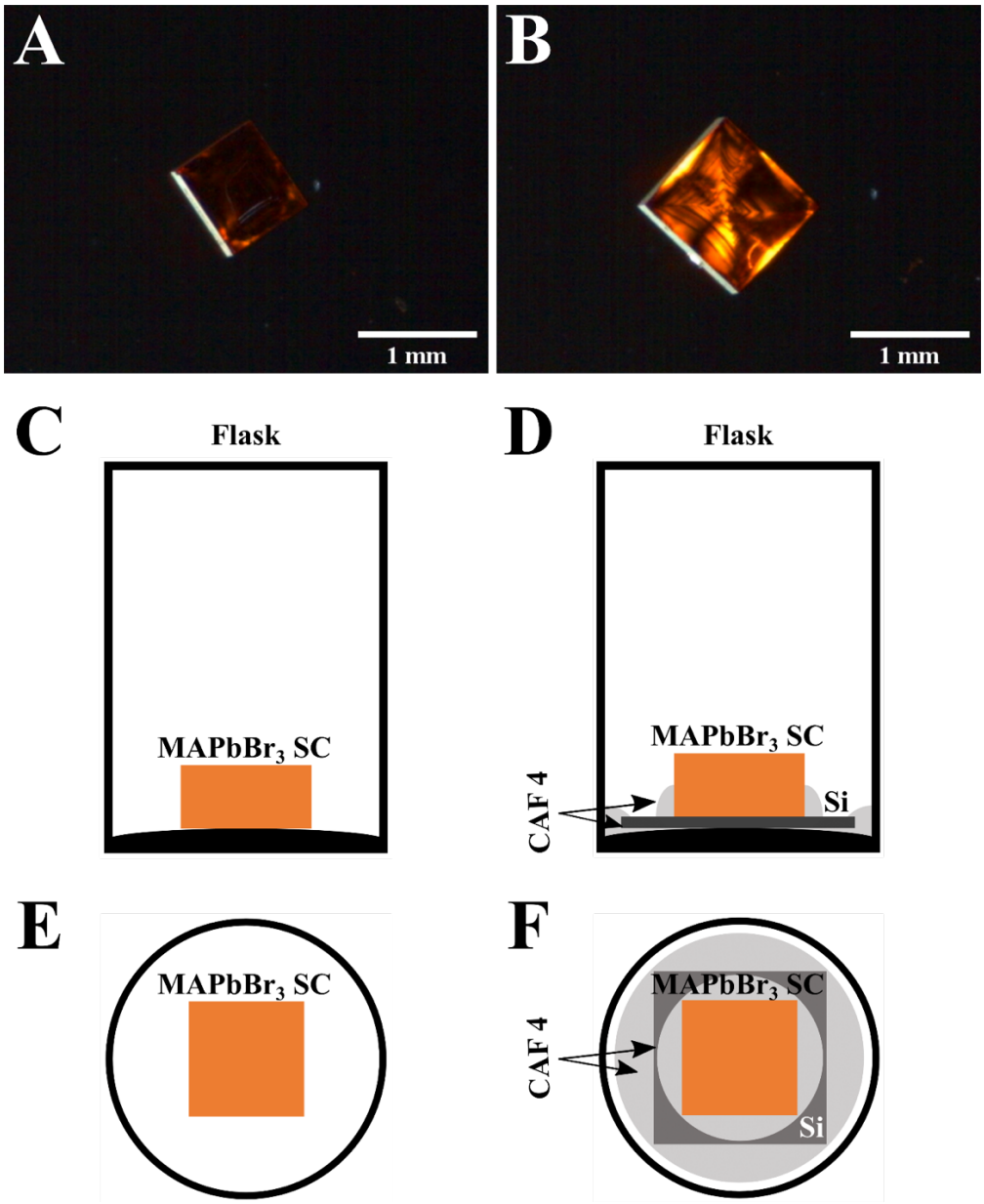

Figure 2-1-2. Seed crystal selection and preparation. (A) Seed crystal with low dislocation density, preferable for seeded crystal growth, observed between crossed polarizers. **(B)** Mechanically stressed seed crystal with many dislocations. Schematic representations of seeded crystal growth preparation with non-glued seed crystal **(C)** side and **(E)** top views, and glued seed crystal **(D)** side and **(F)** top views. The schematics are not in scale.

1.2.2 Crystal growth

1.2.2.1 Setup

With a seed crystal in the growth solution under moderate supersaturation, as indicated in Chapter 1, the crystallisation is controlled through the modification of the precursor solution temperature. Because the solubility is retrograde, this corresponds to a temperature increase. The advancement of the growth relies then on a setup with a programmable heating device. As it is highly beneficial to dispose of several samples for each growth condition considered, a setup allowing the simultaneous growth of up to six crystals has been developed at Institut Néel, CNRS, as depicted in **Figure 2-1-3-A**. It consists of a Peltier temperature regulator equipped with a six-vials slots heating Al plate, in charge naturally of the seed containing-vials heating. The bench is coupled with a double jacket for the precursor solution thermalisation, thermally regulated with water by a Thermo Haake refrigerated-heating circulator (ThermoFisher Scientific), equipped with a PT100 probe. Thermal conductive paste is used in the slots for good plate-vials heat transfer.

In order to improve the control of the growth conditions, a calibration of the actual temperature in the vials as a function of the system setpoint was performed. A first study evaluated the vertical temperature gradient in 3.5 mL of DMF contained in a vial (representing 7 mm of solution height), then a second one establishing the correlation between the temperature setpoint and that at the flask bottom for the different slots. All details concerning the correction needed to achieve the right temperature at the flask bottom can be found in **Appendix – Chapter 2**.

The growth solution is naturally convected, given the fact that forced mechanical stirring would induce spontaneous nucleation in the solution (higher surface exposed to the solution, higher chances for nuclei to appear). Small growth solution volumes favour then the homogenisation of the solution and reduce the gradient temperature. The solution volume in each vial is then fixed to 3.5 mL, ensuring additionally that the solution meniscus is aligned with the plate upper level to be slightly colder than the bulk of the solution and avoid nucleation.

A starting growth run, just after solution addition on the seed crystals is shown in **Figure 2-1-3-B**.

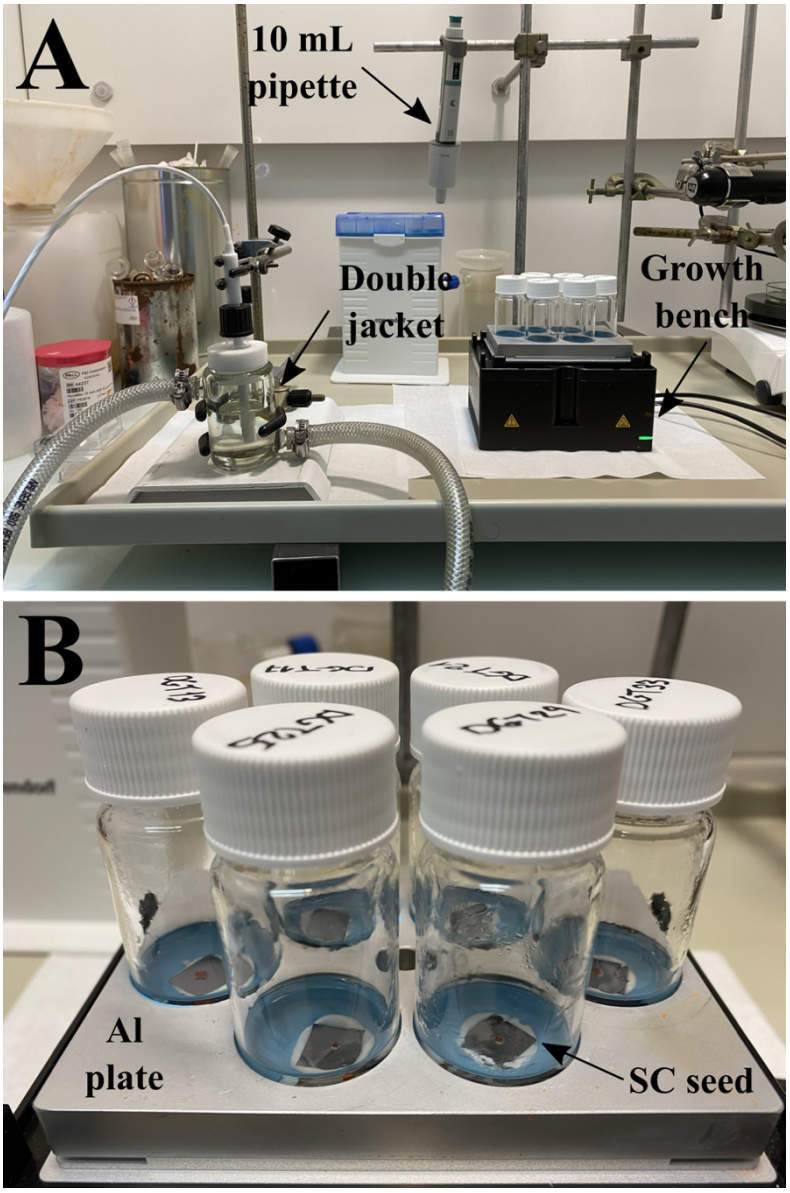

Figure 2-1-3. Six-single crystals simultaneous production setup. (A) Simultaneous production Al plate (right) with double jacket containing the precursor solution (left). **(B)** Ongoing crystal growth inside six flasks with 3.5 mL of precursor solution on crystal growth bench.

1.2.2.2 Temperature increase management and supersaturation evolution

In addition to using good seed crystals, another key element to achieve reproducibly high crystal quality is by avoiding harsh variations in the growth conditions. Thus, it is highly beneficial to try to maintain a constant supersaturation during growth.[5,6] This is hardly done during growths varying abruptly the temperature. For example, the ITC presented before as being a simple and easy method to produce hybrid lead halide perovskite (LHP) SCs,[7] corresponds to a single temperature step going from a point below equilibrium to a point in the spontaneous nucleation zone (labile zone) (≥ 81.5 °C). It is translated into a violent jump in supersaturation: going from 7 % to up to 42 % in 30 min (see red plot in **Figure 2-1-5**), and

later gradually decreasing as the temperature is maintained. Our group has demonstrated that, even with good quality seed crystals this temperature profile leads, in a significant portion of growth runs, to PCs or SCs of reduced quality.

Usually, strategies to grow crystals of good quality are based on linear temperature profiles. They are in most cases successful, very easy to set, practical and allow less violent supersaturation variations than the ITC, but in the case of $MAPbBr_3$ in DMF the limits of that approach is reached rapidly. Indeed, like for most hybrid LHPs in polar aprotic solvents, the solubility of $MAPbBr_3$ in DMF in highly nonlinear. It presents a very pronounced curvature with a slope decreasing significantly as a function of temperature as previously seen in **Figure 2-1-1**. Therefore, as the growth proceeds, a slower temperature increase is necessary to create less violent supersaturation changes. A linear temperature profile can hardly maintain a constant supersaturation, as depicted by the blue plot in **Figure 2-1-5**: firstly, a less violent supersaturation increase than that of ITC is induced by the profile, going from 7 % to up to 34 % for a 4 h-temperature profile. As the crystal grows, the number of sites to incorporate solute molecules also increases. Accordingly, the crystal ability to consume solute from the solution increases during the growth. Both phenomena lead to the same consequence: when a linear ramp is employed for a wide temperature range, once the maximum is attained, the supersaturation finishes by decreasing with advancing growth (in the example, after 4 h). Linear ramps can lead to long growth times as well as strong variations in supersaturation, reducing potentially the crystalline quality.

With the objective of maintaining constant the supersaturation, to stabilise the crystal growth mechanism and so to produce homogeneous SCs with low defect content, within our group, a nonlinear temperature profile was defined. This profile aims to compensate at any given time the crystal consumption of solute by a temperature variation adapted to the actual s-T curve. It corresponds to a mass balance between the desaturation-saturation of the growth solution. This balance depends on several parameters. On the one hand, the desaturation varies according to the growth mechanism involved, the crystal size, and supersaturation; on the other hand, the saturation, the creation of supersaturation, relies on the solubility, the actual temperature and the solution volume. By considering several types of crystal growth mechanisms: rough growth, bi-dimensional germination, and spiral growth, a unified solution was defined allowing having the temperature as a function of time. The specific case of $MAPbBr_3$ in DMF is described below.

Let first consider the desaturation side of the mass balance: the solute consumption. The observation of the microtopography of $MAPbBr_3$ SC faces showed characteristic growth hillocks indicating that the growth mechanism involved is a step flow with screw dislocations emerging from the faces serving as step sources, which is called spiral growth. The unitary steps exiting from the dislocation at the surface tend to bend and, as they advance, roll up in a spiral-shape around the dislocation to form growth hillocks that ultimately cover the whole face. During this type of growth, the incorporation of crystallising entities takes place at kinks in the

unitary growth step. If one considers the step roughness to be constant over the temperature range of the growth run, then the number of incorporation sites is proportional to the step length. Using the Archimedean spiral as model, one can see that the arc length of the steps circling the dislocation is proportional to the spiral outer diameter, which corresponds to the width of the face it was formed on. In other words, in a spiral growth, the ability of a crystal to desaturate the solution is proportional to the faces width. If one assumes (as is often the case) that under constant supersaturation the crystal will grow homothetically, thus at any given time all its faces widths are proportional to a chosen characteristic lineal dimension *L(t)* (e.g., crystal width, height).

As a result, the solute mass deposition rate ($\frac{dm}{dt}$, solute lost to the growth) can be seen as being proportional to *L(t)*:

$$\frac{dm}{dt} = \kappa\, L(t) \tag{2-1}$$

Where κ is the parameter taking into account not only the proportionality of the number of incorporation sites to $L(t)$ but also the incorporation rate at those sites, dependent in turn on the supersaturation or mass transport. Because we considered the crystals to grow in a homothetic way, the volume of the growing crystal V_c can be defined at any time from the chosen characteristic lineal dimension *L(t)*:

$$V_c = \beta_v\, L(t)^3 \tag{2-2}$$

Where β_v is a constant taking into account the growth morphology of the crystal. From this volume and the crystal density ρ_d (g cm^{-3}), **Equation (2-1)** can then be written as a differential equation on *L(t)*:

$$\frac{dm}{dt} = \rho_d\, \beta_v \frac{dL(t)^3}{dt} \Rightarrow \rho_d\, \beta_v \frac{dL(t)^3}{dt} = \kappa\, L(t) \tag{2-3}$$

$$Hence\ \frac{dL(t)^2}{dt} = \alpha_2 = \frac{2}{3}\frac{\kappa}{\rho_d\, \beta_v} \tag{2-4}$$

Where α_2 (mm^2 h^{-1}) is the parameter representing the growth kinetics (mass deposition rate) depending on the crystal morphology, supersaturation, and mass transport. After integration of **Equation (2-4)**:

$$L(t) = ({L_0}^2 + \alpha_2\, t)^{\frac{1}{2}} \tag{2-5}$$

Where L_0 is the initial characteristic length of the seed crystal (mm). Finally, from this expression, the mass of the growing crystal, corresponding to the first term of our mass balance, can be expressed as follows:

$$m(t) = \rho_d\, \beta_v\, ({L_0}^2 + \alpha_2\, t)^{\frac{3}{2}} \tag{2-6}$$

Figure 2-1-4 shows the evolution of the characteristic lineal dimension for different α_2 parameters.

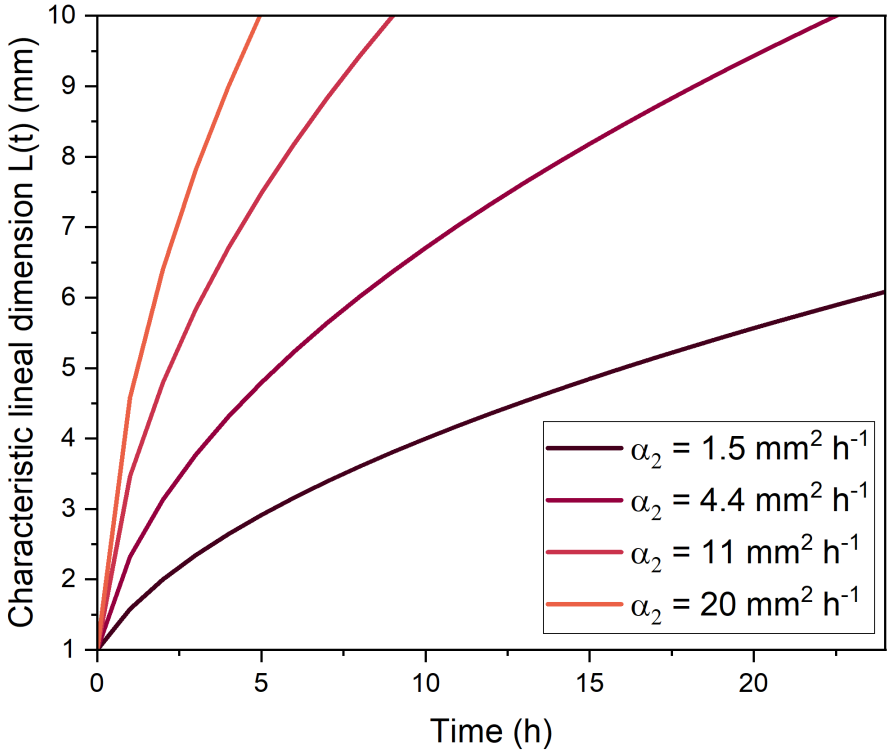

Figure 2-1-4. Evolution of characteristic lineal dimension *L(t)* for different kinetic parameters α_2 = 1.5, 4.4, 11 and 20 mm^2 h^{-1} for L_0 = 1 mm.

One can see that, under our assumption of stationary incorporation of growth units, *L(t)* increases rapidly at the initial stage of the growth but then fades significantly. That is why the popular strategy to modify the temperature ramp during the growth to maintain a constant extension of the crystal (constant growth rate, linear *L(t)*) is not optimal either, as it means that to maintain the elongation, the incorporation rate at the kinks has to increase with increased number of sites.

If we now consider the other side of the mass balance: the supersaturation generation, in other words, the mass made available by the temperature variation, one of the key points to take into account is the non-linearity of the solubility limit as a function of temperature. As discussed in Chapter 1, it usually follows a Van't Hoff type **Equation (2-7)**:

$$s(T) = A\, e^{\frac{B}{T}} \tag{2-7}$$

Where A (g mL^{-1}) and B (K) are terms linked to entropy and enthalpy of precursors dissolution and complex reactions, and T is the temperature (K). The overall mass of solute m_{solute} made available for the growth at any given time is then directly linked to the solubility limit and the actual temperature T via **Equation (2-8)**:

$$m_{solute}(t) = A\, V_s (e^{\frac{B}{T_0}} - e^{\frac{B}{T(t)}}) \tag{2-8}$$

Where V_s is the solution volume (mL) and T_0 is the temperature at the beginning of the crystal growth (°C) setting the initial supersaturation to be maintained throughout the growth ($T_0 \neq T_{eq}$). Thus, the mass balance equilibrium is achieved and maintained at every moment of

the crystal growth if the crystallised mass $m(t) - m_0$ is equal to the mass made available for growth by the temperature variation, where $m_0 = \rho\ \beta_v\ {L_0}^3$ is the mass of the seed crystal (g). By combining **Equations (2-6)** and **(2-8)**, on can extract a nonlinear expression of the temperature as a function of time for spiral growth:

$$\rho_d\ \beta_v\ ({L_0}^2 + \alpha_2\ t)^{\frac{3}{2}} - \ m_0 = \ A\ V_s(e^{\frac{B}{T_0}} - e^{\frac{B}{T(t)}})$$

$$\Leftrightarrow T(t) = \frac{B}{\ln\left[\frac{\rho_d\ \beta_v}{A\ V_s}\ ({L_0}^3 - ({L_0}^2 + \alpha_2\ t)^{\frac{3}{2}}) + e^{\frac{B}{T_0}}\right]} \qquad (2\text{-}9)$$

Equation (2-9) is thus called an adaptive temperature profile. As indicated before, it takes into consideration the solubility non-linearity (A, B), the growing crystal morphology (β_v), the initial conditions: seed dimension L_0, temperature T_0 and volume of the growth solution V_s. If several seeds are used, L_0 is the average characteristic dimension and V_s is the total solution volume divided by the number of seeds. With this equation, one can easily predetermine an adapted nonlinear temperature profile if the solution volume, the starting temperature or the number of seeds changes from one growth run to the next.

The only adjustable parameter left for optimisation is the kinetic parameter α_2. Because it includes many aspects of the growth, it has to be defined for each solute-solvent system and for each targeted supersaturation to maintain constant. To validate the ability of these temperature profiles to maintain a constant supersaturation, growth runs were conducted with timed image acquisition to measure $L(t)$ and so $m(t)$, to follow experimentally the mass balance. **Figure 2-1-5** presents the estimated relative supersaturations from the mass balance. As can be seen, the temperature step of the ITC (red plot) as well as the 4 h-linear temperature profile (blue plot), correspond to important variations of supersaturation. Therefore, even if these temperature profiles lead to SCs, they are not favourable for the synthesis of materials of optimal homogeneity and quality. With adaptive temperature profiles on the contrary, limited supersaturation variation may be achieved (green plots).

Even if this type of ramp softens the supersaturation changes, thus the defect formation, in the specific case of $MAPbBr_3$ in DMF a compromise had to be found. Indeed, the kinetic parameter α_2 maintaining the initial supersaturation of 7 % would lead to a growth run of several days to reach the final temperature of 81.5 °C. Yet, in our system, if the metastable zone width is larger than 40 % in the first hours, it seems to reduce over time and spontaneous nucleation occurs within 10-12 h even at much lower supersaturation. Therefore, a compromise was identified with a kinetic parameter α_2 of 11 $mm^2\ h^{-1}$ leading to growth runs shorter than 12 h but corresponding to a mass balance equilibrium at 15 % supersaturation. In that case either the starting supersaturation was set at 7 % (T_0 = 62.6 °C, α_2 = 4.4 $mm^2\ h^{-1}$) and the system slowly drifted towards15% (dark green curve in **Figure 2-1-5**) or set at 15% (T_0 = 67.2°C, α_2 = 11 $mm^2\ h^{-1}$) and the adaptive temperature profile kept it constant (light green curve in **Figure 2-1-5**). The standard crystal growth procedure considers T_0 = 62.6 °C as the starting

temperature of the profile and 81.5 °C as the ending temperature. **Table 2-1-1** recaps in detail all parameters necessary to employ adaptive temperature **Equation (2-9)**.

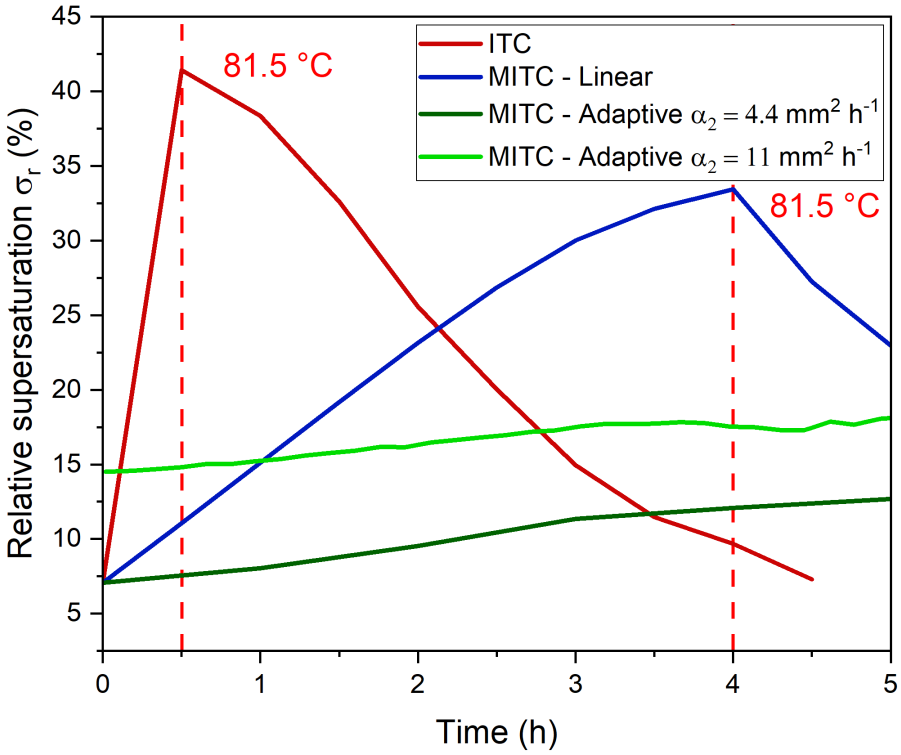

Figure 2-1-5. Relative supersaturation evolution as function of time for a 4 h-crystal growth for three types of temperature profiles. Red plot: ITC protocol with a setpoint of 81.5 °C. Blue plot: Linear temperature ramp (+ 5.6 °C h^{-1}). Green plots: Adaptive temperature ramps for $\alpha_2 = 4.4$ mm^2 h^{-1} and 11 mm^2 h^{-1}.

Precursor solution and seed preparations, as well as crystal growth, were performed by myself with the assistance of Julien Zaccaro and Thibault Lemercier, with the collaboration of Giovanni Armaroli in Chapter 4.

Table 2-1-1. Summary of all parameters involved in a spiral crystal growth with adaptive temperature ramp for $MAPbBr_3$ in DMF.

Parameter	Value for $MAPbBr_3$ in DMF
A	2.23×10^{-3} g mL^{-1} [a]
B	1780 K [a]
ρ_d	3.82 g cm^{-3} [b]
β_v	½ [c]
L_0	~ 1 mm
T_0	62.6 °C [d]
V_s	3.5 mL [e]
α_2	Adjustable (in mm^2 h^{-1})

[a] A and B term values were determined during Amari's thesis work.[1]
[b] The density ρ_d of $MAPbBr_3$.
[c] The seed crystal volume is considered half a cube: $V_c = \frac{1}{2}\ cube\ volume = \frac{1}{2}\ L^3$ with $\beta_v = ½$.
[d] Last temperature of the regrowth protocol.
[e] Volume of growth solution per vial.

1.2.2.3 Specificities of $MAPbBr_3$ growth in DMF

Some peculiarities of the crystal growth of $MAPbBr_3$ in DMF have already been mentioned: a retrograde solubility, a surprisingly wide metastable zone width (in the first hours at least) leading to a low nucleation rate and a high growth rate at supersaturations of up to 40 %, when most standard growths in solution are conducted under 2-3 % supersaturations. All these features can be traced back to the formation of a complex between the lead and solvent molecules. Speciation calculi based on the equilibrium constants of the $Pb{\bullet}DMF_6^{+2}$ complex as well as bromoplumbates species $[PbBr_n]^{2-n}$ showed that in our chemical system (1M $MABr:PbBr_2$ stoichiometric solution in DMF), the lead-solvent complex is the dominant lead species in solution (50 %) while the perovskite building block $PbBr_3^-$ only accounts for 33 %.[1] Incidentally, while tracking the $MAPbBr_3$ growth kinetics for the development of the adaptive temperature ramps, we have observed a marked reduction of the growth kinetics at the end of the growth runs in spite of still having significant relative supersaturation (7-10 % calculated from mass balance). It appears that the growth rate drops when the crystallisation yield reaches 33% (33 % of the lead species in excess in solution are consumed by the growth). This limitation of the crystallisation yield could be explained by the presence of lead-solvent complex in solution. As long as the crystallisation yield is below 33%, the growth proceeds from the $PbBr_3^-$

species in solution and the growth kinetics are determined by mass transport, surface diffusion, incorporation kinetics, to name a few. Growth beyond the 33 % crystallisation yield would then require the destabilisation of the $Pb{\bullet}DMF_6^{+2}$ complex which needs additional energy, and has slower kinetics, becoming the limiting factor for the growth. Growing very large crystals, beyond the 33% yield, then requires extremely long times to accommodate this slower kinetics, which then run into the limitation of spontaneous nucleation. This change in crystallisation regime is not taken into consideration in our model of adaptive temperature ramps. It is thus primordial to apply this method in a low crystallisation yield region where the α_2 values are dependent on supersaturation and not on complex destabilisation.

2 Device fabrication

The grown crystals present a very favourable cubic morphology with widths and heights of a few millimetres. They can readily be made into optoelectronic devices by polishing the top and bottom surfaces (by removing the seed, creating a flat surface), and then depositing metal electrodes.

2.1 Standard polishing procedure

The polishing step is very important on perovskites and on materials in general, because it creates the active surface, which is then in direct contact with the metallic electrode. The protocol, previously established by Marian Chapran, was executed at CEA LETI, and it is detailed below.

The SC to be polished is mounted on a movable piston, depicted in **Figure 2-2-1-A** and **Figure 2-2-1-B**, maintained perpendicular to the polishing plan by the polishing tool body, shown in **Figure 2-2-1-C**. The crystal is fixed to the piston by the same silicone glue (Elkem Silicones CAF 4) used for the crystal growth. A glass slab is intercalated between the crystal and the piston to avoid any redox reaction between the Pb^{2+} of the crystal and the aluminium piston. The first side of the crystal to be polished is the seed side. The top natural growth face is fixed to the piston and will serve as a crystallographic orientation reference. The other crystal face is first lapped on a series of disks with silicon carbon abrasive of decreasing grain size, down to a few micrometres: P400, P1200, P2400 and P4000. If the amount of material to be removed is limited some of the coarser grains may be skipped. During that lapping process, a fluid is added to help clear the material removed from the crystal. In our case isopropyl alcohol (IPA) was selected as it is a very mild perovskite solvent and so contributes to the removal of material and leads to smoother surfaces. The polishing procedure is then both chemical[8] and mechanical: the surface is totally reconstructed. After that lapping stage, a flat surface has been formed, its roughness is then reduced by the polishing stage. The two polishing steps are conducted with free diamond abrasive in anhydrous pastes (1 and ¼ μm) on different support disks (RAM and NT, respectively) to obtain an optical-grade surface. All disks and pastes were purchased from PRESI.[9] Because of the relatively low hardness of the hybrid perovskites, all lapping and polishing steps are conducted with limited pressure and last only between 20 to 60 seconds each. At the end of each step the SC surface is clean thoroughly with ethyl acetate (EtOAc). **Table 2-2-1** reports the disks and lubricants (solvents or pastes) used in the various steps. The crystal is then carefully removed from the support. The process is repeated for the other side (non-seeded side). After polishing both sides, the crystal is put in a toluene bath overnight to wash away any impurity from the process, as illustrated in **Figure 2-2-1-D**, and then cleaned one last time with toluene.

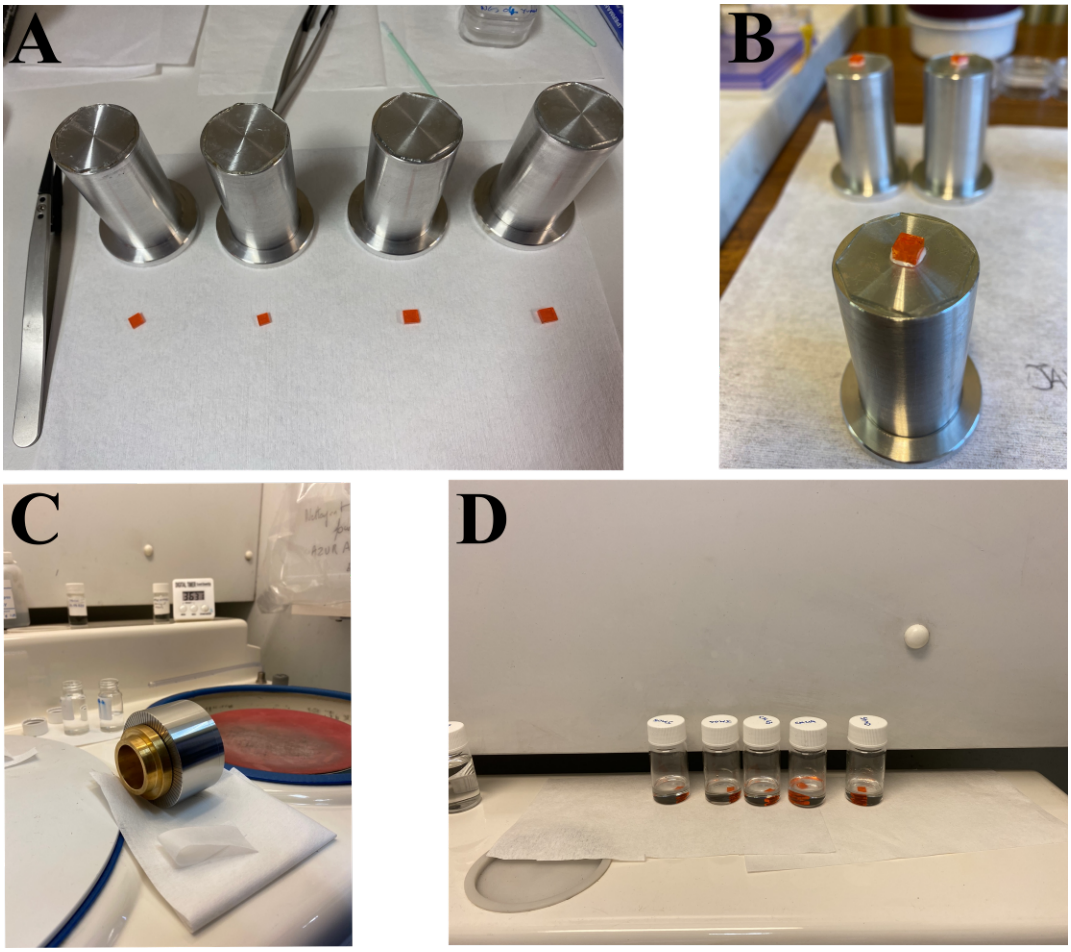

Figure 2-2-1. Polishing procedure of SCs. (A) Al pistons with glued glass on top beside hybrid SCs waiting for gluing procedure. **(B)** SC glued on piston with Elkem Silicones CAF 4. **(C)** Two-part metallic handle used for lapping and polishing. **(D)** Polished SCs left overnight in toluene for cleaning.

Table 2-2-1. Polishing procedure employed.

Step	Polishing disk	Solvent/paste
Lapping	P400/P1200/P2400/P4000	IPA
Polishing	RAM	1 µm anhydrous diamond paste
Polishing	NT	¼ µm anhydrous diamond paste

2.2 Metal electrode deposition

Chromium metal (Cr, Sigma Aldrich, powder, 99.5%, −100 mesh) was selected as the metal electrode because of its compatible work function, neutral chemical reactivity towards the hybrid LHP and more stable electric signal when compared to typical Au,[10] which reacts chemically with halide perovskites, as seen in Chapter 1. The electrode deposition was done by evaporation of Cr in a Braun evaporator via Joule heating inside a glovebox under Ar atmosphere. The Cr is placed over a crucible at the bottom of the machine, and the SCs at the top, over a W nacelle, cased within a chuck, as seen in **Figure 2-2-2-A**. A metallic Ni or alloy mask is used to define the geometry of the electrode on the perovskite, maximising the coverage of the surface. A 2×10^{-6} bars vacuum and a 0.8 Å s^{-1} deposition rate were used during the procedure. The temperature of the chuck, and thus of the samples temperature does not exceed 100 °C. Thicknesses of 100 and 30 nm were deposited on each side, respectively, leading to devices with a Cr (30 nm)/perovskite SC/Cr (100 nm) configuration. The thinner Cr layer was used to act as a semi-transparent electrode. This configuration provides the electrical contact for bias application and charge collection while being transparent to the excitation laser used in the Time of Flight (ToF) experiments. A sample device example is shown in **Figure 2-2-2-B**. The procedure was exclusively executed by Marian Chapran or Stéphanie Lombard at CEA LITEN.

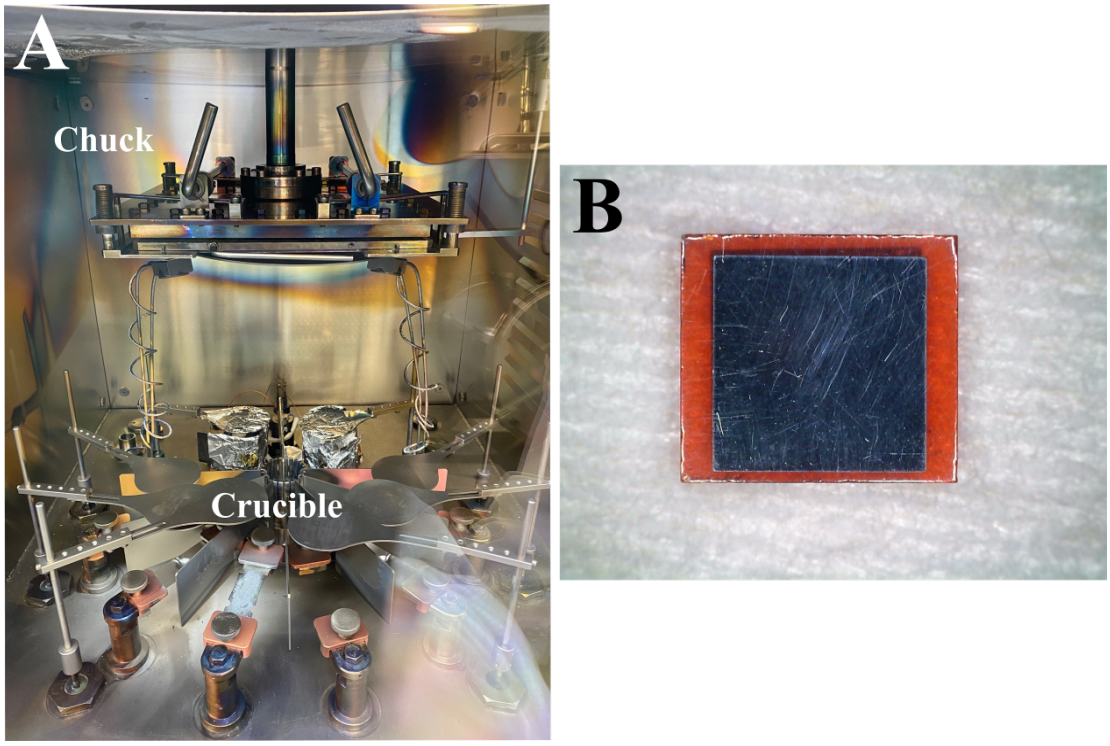

Figure 2-2-2. Cr electrode deposition. (A) Evaporator inside: the Cr crucible and the sample chuck are located at the bottom and top of the machine, respectively. **(B)** Perovskite SC device with Cr electrodes deposited on each side.

3 Optoelectronic characterisation

The optoelectronic characterisation represents a key aspect, indicating if our $MAPbBr_3$ material fulfils the requirements needed for direct X-ray detection. As presented in detail in Chapter 1, the sensing material has to present electric stability (no hysteresis, low dark current while being under bias) and environmental resilience (no photochemical reactivity with the surrounding environment, e.g., humidity, oxygen, radiation). The semiconductor has to present as well high resistivity and relatively high sensitivity towards X-ray illumination. The standardised protocol for medical grade X-rays detection allow assessing resistivity, dark current, current stability over time, sensitivity and charge carrier transport properties.

3.1 Test box

The standard procedure employs a brass box for current density-voltage (J-V), current density-time (J-t) and sensitivity-voltage (S-V) measurements. The SC device is sandwiched between conductive silicone layers on the inside, as depicted in **Figure 2-3-1-A**. The silicon layers are doped with Cu and Ag, to assure better electrical conductivity and a softer interface with the internal contacts given the delicate mechanical handling of the SC. The boxes work as Faraday cages to avoid interactions with any external electromagnetic field. The box side facing the X-ray source possess a hole with a lead collimator, allowing the irradiation of a small and controlled area of the SC electrode. The test box is connected to the ground and keeps also the SC device in the dark. **Figure 2-3-1-B** depicts an example of SC inside brass box being tested under X-ray illumination.

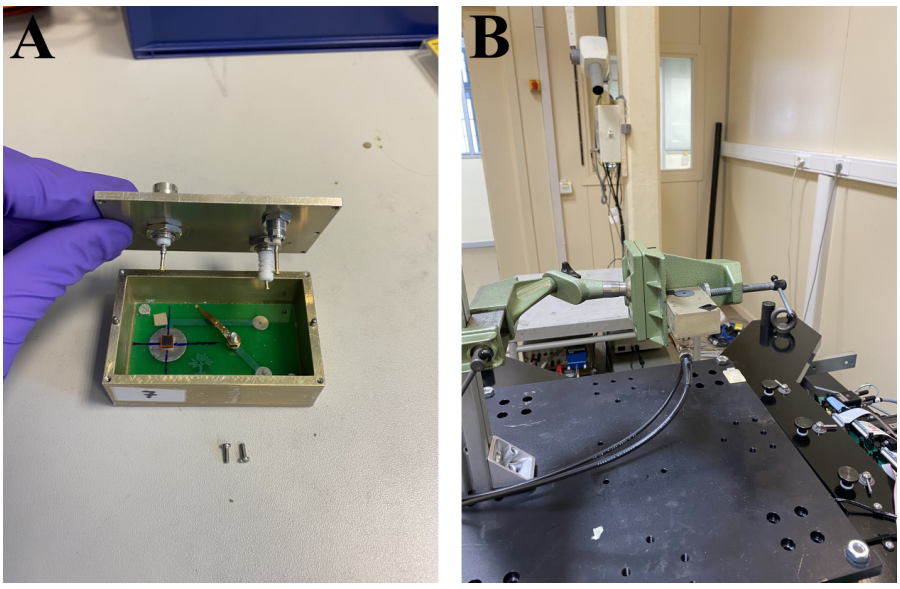

Figure 2-3-1. Optoelectronic standard test box. (A) Interior of brass box with SC device in the inside, sandwiched between silicone layers. **(B)** SC device being tested inside brass box under X-ray illumination.

3.2 Sensitivity tests

3.2.1 X-ray source

X-rays are generated via a sealed tube with a W anode and operated at a 70 kV accelerating voltage, which is typical for chest radiography. The emitted X-ray photons are internally filtrated by a 0.8 mm-thick Be and 2.5 mm-thick Al plates. To evaluate the radiation received by the SC device after X-ray absorption by a "human body", a 21 mm-thick Al layer is additionally added to simulate the average human body density. A total of 23.5 mm Al filtration takes then place. This filtered X-ray source corresponds to a standardised radiation quality labelled RQA5. The resulting spectrum of the X-ray beam, presented in **Figure 2-3-2**, is rather broad (35-67 keV), with an average photon energy around 53 keV. Experimental sensitivity *S* values were measured by irradiating with this source, the devices with 10 X-ray pulses of 100 ms at 4 Hz, corresponding to a 24 μGy_{air} dose per pulse. The test box is located 1 m below the source. The incident X-ray dose was calibrated using a UNIDOS dosimeter (PTW), shown in **Figure 2-3-3**. The X-ray tube setups are summarised in **Table 2-3-1**. The experimental settings follow the characteristic medical radiography setups described in IEC (International electrotechnical commission) 62220 International Standard.[11]

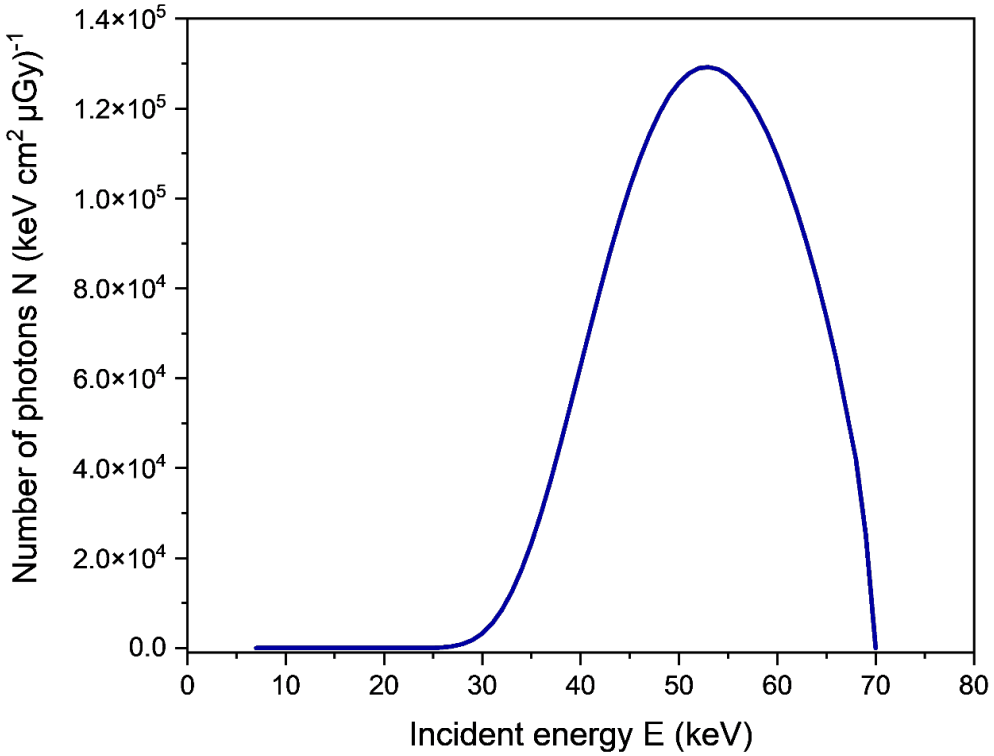

Figure 2-3-2. Photons distribution *N*, at 1 m, as a function of their energy *E* coming from medical grade RQA5 quality X-ray source. *N* is based on a simulation from references.[12,13] Average photon energy is around 53 keV.

Figure 2-3-3. PTW UNIDOS dosimeter used to calibrate the X-ray dose delivered by the tube in atmospheric conditions.

Table 2-3-1. X-ray tube setups.

Tube voltage	70 kV
X-ray mean energy	53 keV
Tube current	100 mA
Filtration	0.8 mm Be, 23.5 mm Al
Work distance	1 m
Pulse width	100 ms
Pulse frequency	4 Hz

3.2.2 Mobility-lifetime product, Hecht equation and sensitivity measurements

As stated in Chapter 1, one of the key figures of merit for direct conversion is the mobility-lifetime ($\mu\tau$) product of the charge carriers. While being under X-ray radiation, a measured charge or photocurrent Q is generated within the sensing material, corresponding to extracted electron-hole pairs created in the SC bulk. Theoretically, the generated charge Q may be related to the $\mu\tau$ product via the Hecht equation[14] or its modified version.[15–17] The Hecht equation considering the contribution of both electrons and holes to the photocurrent is defined in **Equation (2-10)**:

$$Q(V) = Q_0 \left\{ \frac{\mu_e \tau_e V}{L^2} \left[1 - e^{-\frac{Lx}{\mu_e \tau_e V}} \right] + \frac{\mu_h \tau_h V}{L^2} \left[1 - e^{-\frac{L(L-x)}{\mu_h \tau_h V}} \right] \right\} \quad (2\text{-}10)$$

Where Q is the measured charge (C), Q_0 is the total charge (C) generated by the interaction (or integrated photocurrent for both), μ_e and μ_h are the mobilities of electrons and hole, respectively (cm² V^{-1} s^{-1}), τ_e and τ_h are the lifetimes of electrons and hole, respectively (s), x the distance from the entrance electrode and the X-ray interaction position within the crystal (called here depth) (cm), V is the applied bias (V), and L is the device thickness (cm).

This equation derives from the Ramo theorem and only describes the current induced on the electrodes by the motion of photogenerated charges inside the semiconductor in the presence of charge recombination via trapping sites.[18] A few hypotheses, some mentioned in Chapter 1, are assumed by the Hecht equation: **(i)** the device has a planar geometry (the electrodes face each other and their dimensions largely exceed the thickness of the detector); **(ii)** each charge carrier is defined by one mobility value that is constant with the electric field, the charge carrier can only be trapped once (no detrapping); and **(iii)** the electric field F is uniform throughout the detector and is equal to V/L.

As a first step to determine the charge Q, the energy deposition by incident X-rays as a function of the depth is calculated following **Equation (2-11)**:

$$E^*(x) = \sum_E N(E) \cdot E \cdot A(x, E) \quad (2\text{-}11)$$

Where E^* is the deposited energy (keV), x is the interaction depth (cm), E is the energy of the incident X-ray photon (keV), N is the number of photons at each energy E from the incident RQA5 quality spectrum (photon distribution shown in **Figure 2-3-2**), A is the absorbed fraction which is a function of the depth x and incident photon energy E. The latter is computed as for Beer-Lambert's law in **Equation (2-12)**:

$$A(x, E) = T_r(x, E) - T_r(x + dx, E) = e^{-\sigma_{cs}(E) \cdot \rho_d \cdot x} - e^{-\sigma_{cs}(E) \cdot \rho_d \cdot (x + dx)} \quad (2\text{-}12)$$

Where T_r is the transmitted fraction, σ_{cs} is the photon cross section as function of energy (cm^2 g^{-1}), and ρ_d is the material density (g cm^{-3}). At the given energy and for $MAPbBr_3$, the photoelectric cross-section dominates over Rayleigh and Compton scattering, which can be neglected. For illustrative purposes, the deposited energy E^* was simulated for a 2 mm-thick $MAPbBr_3$ SC, plotted in **Figure 2-3-4**, to show that the entire crystal volume contributes to the generation of charge carriers with a given distribution of the photogenerated electron-hole pairs. A simplified schematic is shown in **Figure 2-3-5**.

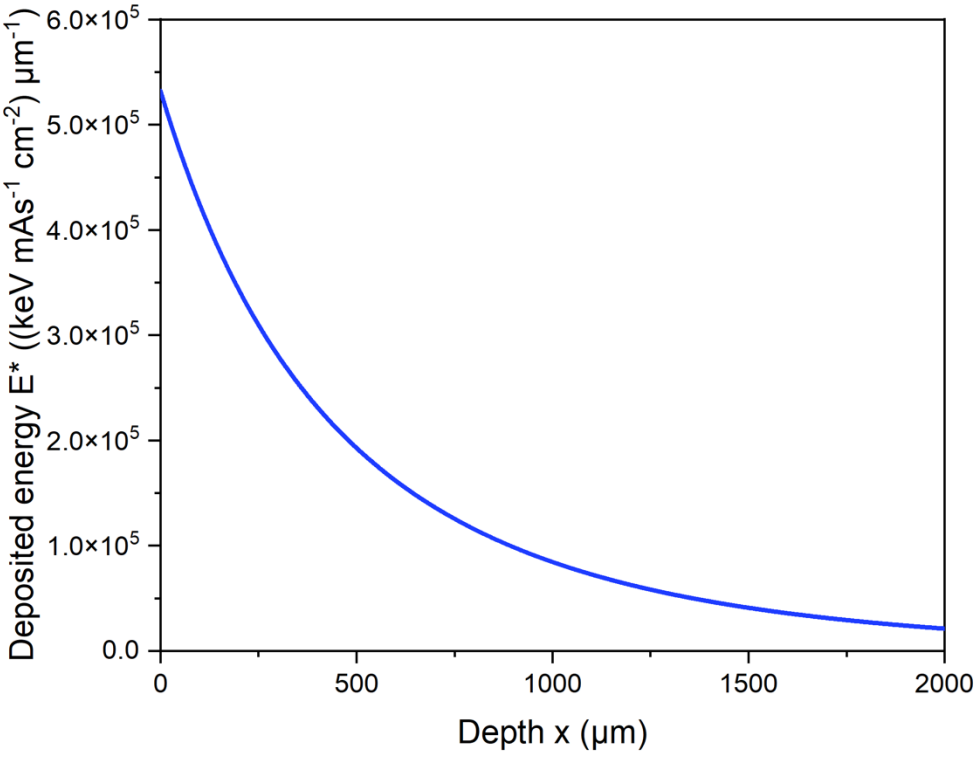

Figure 2-3-4. Simulated deposited energy E^* on a 2 mm-thick $MAPbBr_3$ SC, with a 1 µm step. The absorbed energy decreases with increasing depth x. Nevertheless, electron-hole pairs are generated in the entire volume.

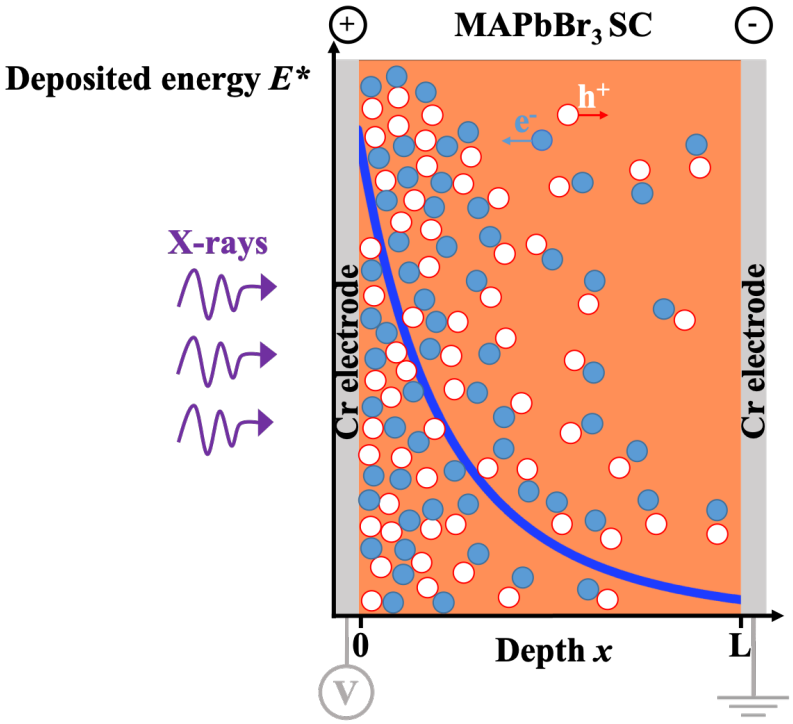

Figure 2-3-5. Schematic representation of photogenerated charge carriers in $MAPbBr_3$ SC device with Cr electrodes while being under X-ray illumination at the anode and under bias. The deposited energy E^* is plotted as a function of the X-ray interaction position in the crystal bulk (blue line).

As a second step, in order to estimate both charge carrier $\mu\tau$ products, the charge collection efficiency (CCE or η_{CC}) as function of the depth x was calculated using the two-charge carrier Hecht equation (**Equation (2-10)**). The CCE is defined in **Equation (2-13)**:[19]

$$\eta_{CC}(x,V) = \frac{\mu_e \tau_e V}{L^2}\left[1 - e^{-\frac{Lx}{\mu_e \tau_e V}}\right] + \frac{\mu_h \tau_h V}{L^2}\left[1 - e^{-\frac{L(L-x)}{\mu_h \tau_h V}}\right] \quad (2\text{-}13)$$

Where η_{CC} is the charge induction efficiency. In **Figure 2-3-5**, electrons and holes flow in the negative and positive x direction, with $\mu_e \tau_e V/L$ and $\mu_h \tau_h V/L$ being the mean free path, respectively, while X-rays enter the device by the anode.

Finally, the measured charge Q as a function of the externally applied bias can be written as in **Equation (2-14)**:

$$Q(V) = \sum_x e\frac{E^*(x)}{W}\,\eta_{CC}(x,V) = \sum_x Q_0(x)\,\eta_{CC}(x,V) \quad (2\text{-}14)$$

Where e is the elementary charge (C), W is the electron-hole pair creation energy that was calculated using Klein's rule $W = \frac{14}{5}E_g + 0.5$ with E_g the band gap energy (eV) (see Chapter 1).[20] The theoretical total charge created in whole SC volume is then defined by $Q_0 = e\frac{E^*(x)}{W}$, and the maximal theoretical sensitivity value S_{max} of a device can be calculated by dividing Q_0 by the electrode surface area S_d (cm^2) and the received dose D_X (Gy_{air}), yielding the sensitivity expressed in μC mGy_{air}^{-1} cm^{-2} as explicitly shown in **Equation (2-15)**:

$$S_{max} = \frac{Q_0}{S_d\, D_X} \quad (2\text{-}15)$$

Experimentally, the measured charge Q is determined by integrating the measured photocurrent over the X-ray pulse duration. In order to reduce experimental errors, each photocurrent measurement was repeated and the measured charge Q averaged over 10 pulses and as for S_{max}, divided by the samples electrode surface area S_d and received dose D_X to obtain experimental S value (**Equation (2-16)**):

$$S(V) = \frac{Q(V)}{S_d\, D_X} \quad (2\text{-}16)$$

By sweeping the externally applied bias, one can obtain the measured charge Q as function of bias, or in other words, the S-V curve of the detector. S_{max} values can be used for normalisation of the resulting S values for comparison between device samples.

As shown later in Chapter 3, the experimental data can be fitted with **Equation (2-14)** by adjusting only two fitting parameters, namely mobility-lifetime product of electrons $\mu_e\tau_e$ and that corresponding to holes $\mu_h\tau_h$. The Q_0 value is fixed instead of leaving it as a free parameter as commonly done in the literature. We believe that this prevents misinterpretation of S-V data. The simulation is called a two-charge carriers Hecht fit. It is critical that the hypothesis $F = V/L$ is verified in order to fit correctly the data.

It has been pointed out that an externally applied bias displaces mobile ions towards the electrode interfaces in LHPs. This leads to ion accumulation at the vicinity of the electrodes

distorting then of the electric field in the device.[21–23] Thus, given the influence that bias background has on the sensing material, because of this parasitic ion migration in the crystal, a rigorous protocol was established to allow reproducibility and comparability between the different samples. That said positive biases are first measured then negative ones. 0 V-sensitivity is measured before starting and finishing each loop. In both domains, *S* values are determined for several increasing voltages (in absolute values) first forward, and then a few selected voltages are targeted again in reserve, before going back to 0 V. A biasing protocol example is given below (in V): 0, 5 , 10, 20, 40, 60, 80, 100, 60, 20, 5, 0, -5, -10, -20, -40, -60, -80, -100, -60, -20, -5, 0. The biasing is symmetrical. Depending on the sample thickness, the voltage was adapted permitting to yield an internal 50 V mm^{-1} electric field. All the sensitivity values provided in this work were then evaluated at an electric field of 50 V mm^{-1}.

For most samples, they were tested right after Cr electrodes evaporation. When comparative studies were considered, to make sure that the semiconductors are exposed to the same radiation dose, so with similar potential device damage under X-rays,[24] SC devices were tested right after the other or in parallel (up to 2 devices in separated test boxes).

Figure 2-3-6 illustrates the medical grade X-ray testing platform used for determination of *S* values through this work. A Keithley 487 is used as power source and Keithley 428 is used as current amplifier. A data acquisition (DAQ) USB board NI-6221 (National Instruments) is employed to trigger the X-ray shot and digitise the output of the current amplifier. An oscilloscope is also used to check the different signals including their synchronisation. Sensitivity tests were performed by Marian Chapran, Eric Gros d'Aillon, Ferdinand Lédée or myself at CEA LETI.

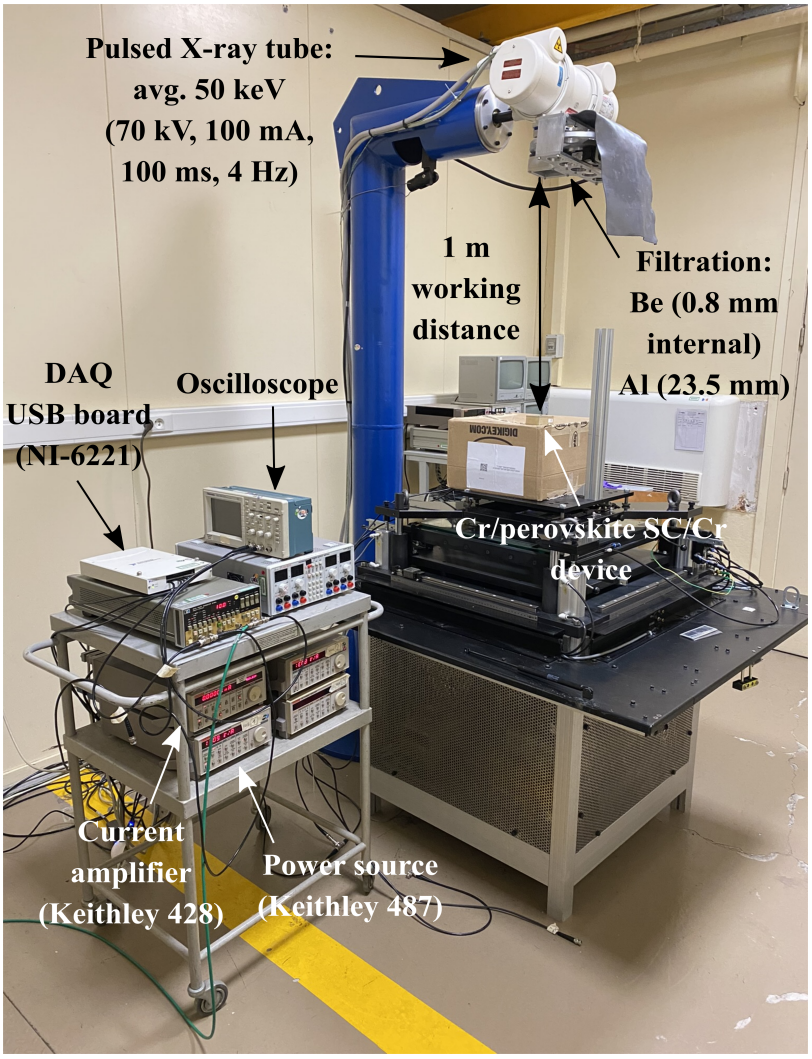

Figure 2-3-6. Photo and description of medical settings used for X-ray irradiation and determination of the sensitivity *S* of samples.

3.3 Current density – time

J-t measurements are recorded while performing S-V data (see part **3.2**) and allow determining the dark current density as function of the voltage J_{dark}-V (nA mm^{-2}). An acquisition rate of 1 point s^{-1} is used. Following the evolution of the current density with time can provide valuable information on the conductivity drift σ_{drift}, as detailed in Chapter 3, or to detect signal changes provoked by external stimulus as achieved in Chapter 4.

3.4 Current density – voltage and resistivity

The J-V characteristics are generated at the same time as J-t measurements, thus during sensitivity tests (see part **3.2**). While proceeding with the sensitivity determination protocol, voltage values are systematically normalised to the sample thickness. The bias thus resulting electric field *F* is swept forward and backward from 0 to +50 V mm^{-1} then from 0 to -50 V mm^{-1}, respectively, yielding a sweeping step of ~ 7 V mm^{-1} in average. For each voltage

step, a stabilisation of 30 s takes place, with a voltage ramp of 1 V s^{-1} between each bias value. The J-t as a function of bias is then converted into current density-electric field (J-F) characteristics by considering the current value after a fixed delay of 10 s in general. Hysteresis and resistivity of the device can be assessed during this procedure. Resistivity values were estimated from the linearization of the J-F curves according to the Ohm's law (**Equation (2-17)**):

$$\rho = \frac{F}{J} \tag{2-17}$$

Where ρ is the resistivity (Ω mm), F is the applied electric field (V mm^{-1}), and J is the current density (A mm^{-2}). Resistivity ρ values are determined by linear fitting of the data.

It is worth pointing out that J_{dark} in J_{dark}-V curves (part **3.3**) is different from the J in J-F used for resistivity determination: even though both are recorded during J-t data acquisition in the dark. The first one is measured before recording the photocurrent induced by the X-rays (~ 30-50 s after setting the voltage), and the second one is chosen with a certain delay after the voltage is established (usually ~ 5-15 s) where the least hysteresis in the J-F curve was found.

3.5 Laser time of flight

Laser ToF measurements allow determining transit times t_t and thus charge carrier mobilities μ. The formers are defined as the time needed for the charge carrier to fully cruise the SC thickness. For that, a pulsed N_2 laser was employed using a 337 nm wavelength and an 800 ps impulsion time. The energy of the photon has to be higher than the bandgap E_g of the semiconductor (E_g = 2.21 eV for $MAPbBr_3$), but sufficiently low to generate electro-hole pairs within a small volume close to the electrode (> 2.4 eV, < 520 nm). In other words, the ultraviolet photons are fully absorbed within a few nanometres. The laser beam is attenuated by an optical filter with a transmission coefficient of 0.16 before irradiating the semi-transparent 30 nm-thick Cr electrode of the Cr/perovskite SC/Cr testing device, placed within a test box. The semi-transparent electrode has a transmission coefficient between 0.01 and 0.004.[2] The device being polarised, the charges drift towards their respective collection electrodes. Charge carriers from the irradiated electrode are collected almost instantly. The other charge carriers transit through the entire thickness of the device before being collected. A schematic representation of the experiment is shown in **Figure 2-3-7**. The transit movement creates a photocurrent I until the charge carriers are collected. It is possible to determine the transit time t_t by measuring the duration of this photocurrent. The generated photocurrent can be described by **Equations (2-18)** and **(2-19)**:

$$I = \frac{e\,N}{t_t} = e\,N\,\frac{\mu\,F}{L} \tag{2-18}$$

$$with\ t_t = \frac{L}{\mu\,F} \tag{2-19}$$

Where e is the elementary charge (C), N is the number of generated charge carriers, either for holes or electrons, t_t is the transit time (s), μ is the charge carrier mobility (cm² V^{-1} s^{-1}), F is the applied electric field (V cm^{-1}), and L is the device thickness (cm). If a SC device is without traps and with a homogeneous internal electric field, the charge carrier effective mobility can be calculated using **Equation (2-20)**, where V is the voltage (V):[2]

$$\mu = \frac{L^2}{V\, t_t} \tag{2-20}$$

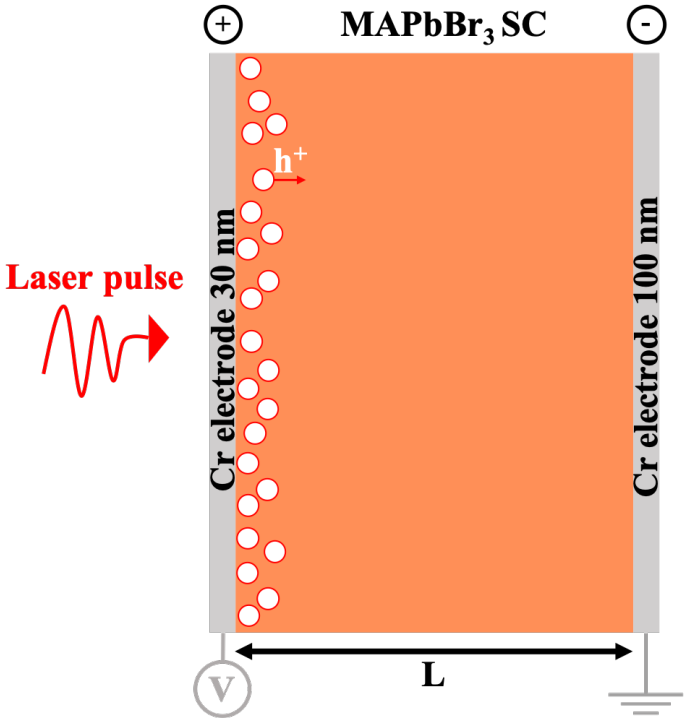

Figure 2-3-7. Schematic representation of ToF measurements. In the figure, just holes are represented for determination of hole mobility μ_h. The 30 nm-thick Cr electrode is targeted by the laser.

Figure 2-3-8-A depicts an example of the laser-induced photocurrent as a function of time for a SC device. The figure shows different charge carrier transits, called waveforms, for different voltages. The inflection points, which represent the arrival of charge carriers at the collecting electrode, are plotted in red for each waveform. To facilitate the t_t value determination, **Equations (2-18)** and **(2-19)** can be divided and multiplied, respectively, by the voltage, yielding the V-independent relations in **Equations (2-21)** and **(2-22)**:

$$\frac{I}{V} = \frac{e\, N\, \mu}{L^2} \tag{2-21}$$

$$t_t\, V = \frac{L^2}{\mu} \tag{2-22}$$

By plotting $\frac{I}{V}$ as a function of $t \times V$, the example presented in **Figure 2-3-8-A** becomes **Figure 2-3-8-B**, leaving the transit time maxima as a constant, which is determined graphically.

Thus, with **Equation (2-20)**, one can determine the charge carrier mobilities. Determining both electron and hole mobilities allows unravelling more information about transport properties within the material (e.g., symmetry and velocity of the charge transport). The experimental setup used for this is illustrated in **Figure 2-3-9**. ToF measurements were executed by Eric Gros d'Aillon and Ferdinand Lédée at CEA LETI.

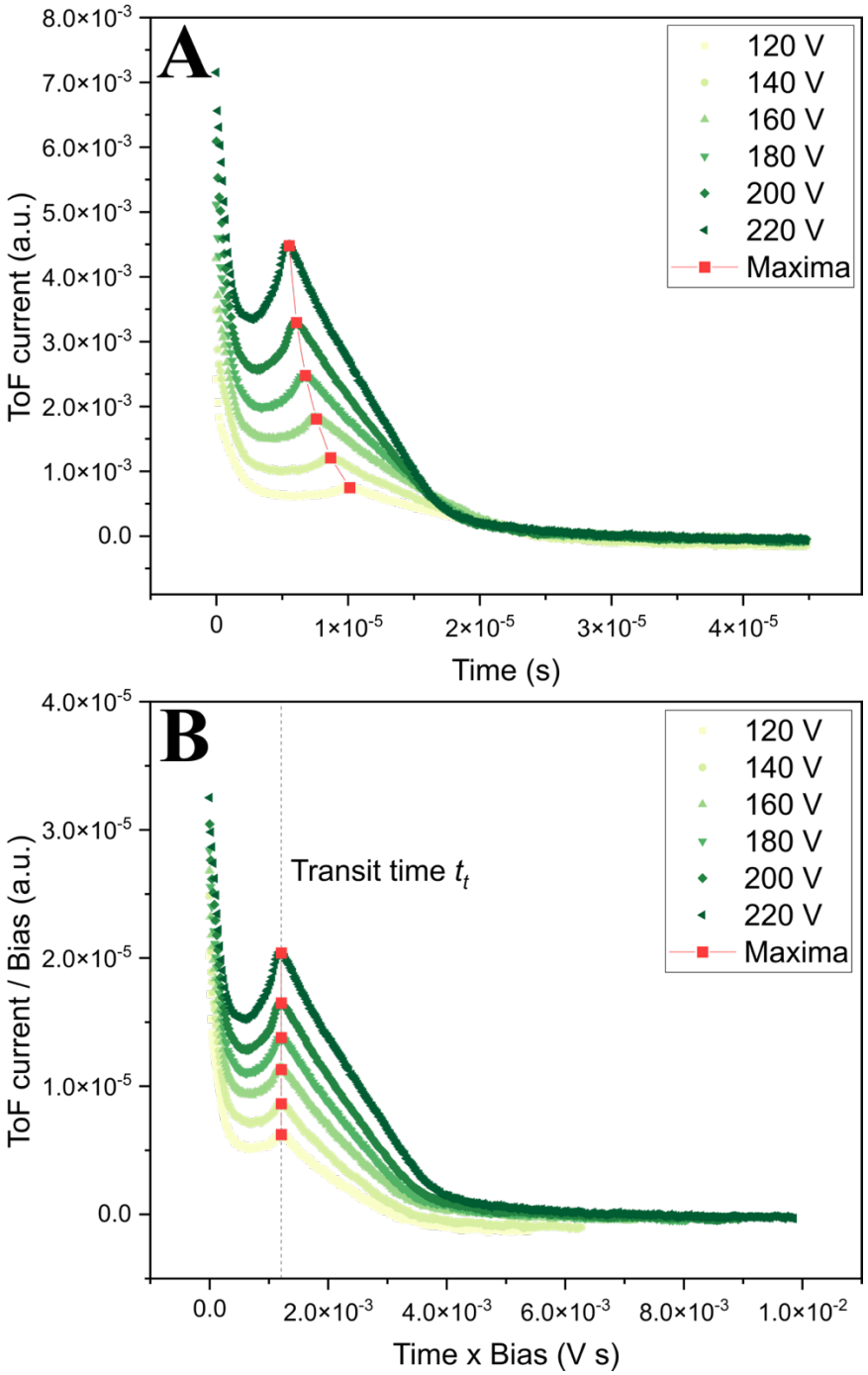

Figure 2-3-8. Determination of charge carrier transit time t_t. (A) Laser ToF current of holes as a function of time for different voltages. To determine the transit time t_t of the charge carrier, the *x*- and *y*-axes are divided and multiplied by the bias, respectively, yielding plot **(B)**, independent of the voltage. A graphic determination takes then place.

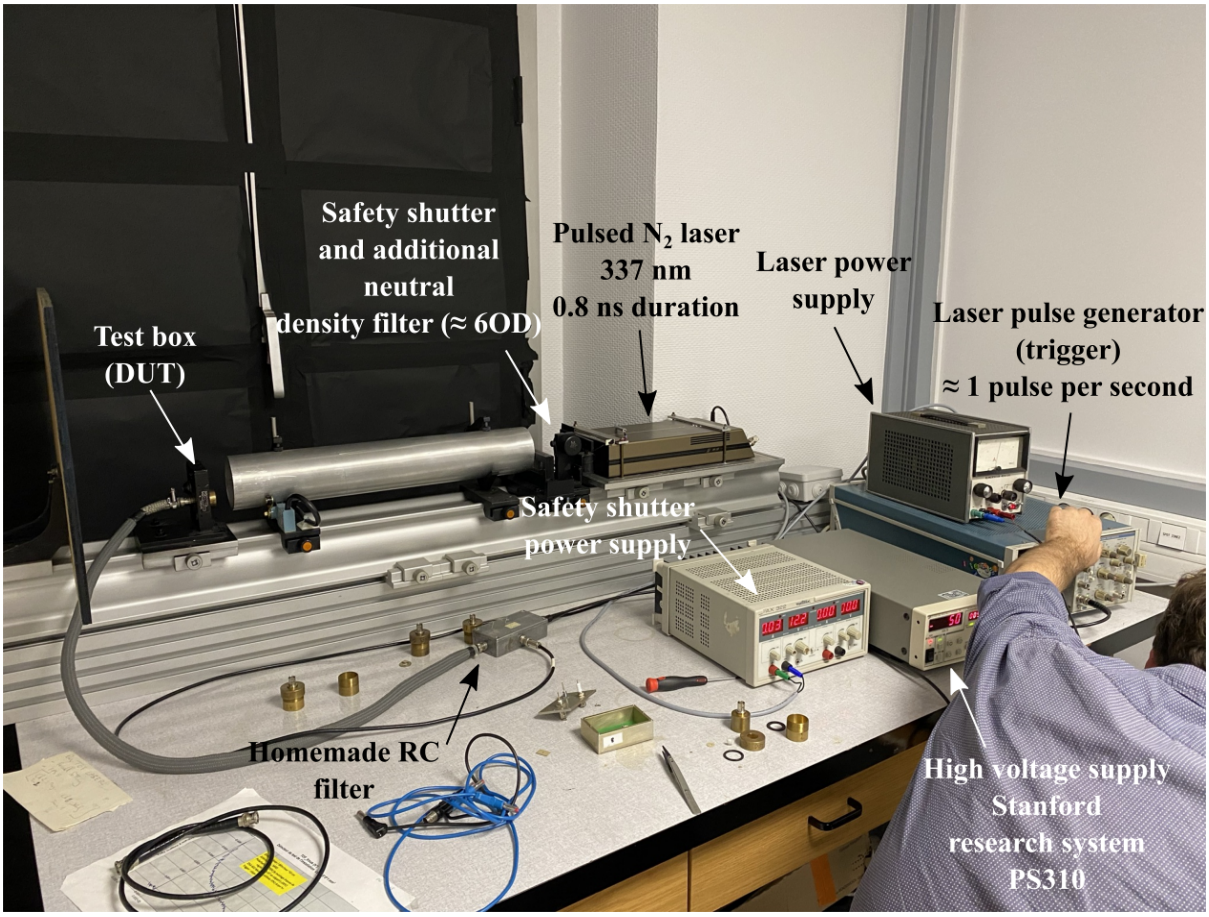

Figure 2-3-9. Detailed laser ToF setup used for determination of charge carrier mobility μ of SC devices. Additionally, a Tektronix TDS 744A oscilloscope was used for current readout (not shown in the photo). DUT = device under test, OD = optical density.

Conclusion

This chapter describes the batch production route of $MAPbBr_3$ SCs of high reproducible quality via adaptive temperature profiles, taking into consideration the supersaturation evolution of the growth solution, through a seeded crystal growth process. Special attention is given to the growth solution in terms of purity of the precursors and preparation, which takes place within a glovebox to avoid interaction with the immediate environment. The reduced supersaturation changes of our MITC method, when compared to original ITC and linear profiles, results in SCs with low defect content: low strained character and dislocation density.[1,4] The SCs are systematically transformed into optoelectronic devices, after lapping and polishing their faces and depositing metallic electrodes, leading to $Cr/MAPbBr_3/Cr$ detectors.

The standardised characterisation of the SC devices via J-V and J-t allow determining the hysteresis and resistivity ρ, and the dark current density J_{dark}, conductivity σ_{drift} and the stability of the electric signal over time, respectively. The sensitivity S of the devices are also established with the possibility to estimate the mobility-lifetime $\mu\tau$ product via a two-charge carriers Hecht modelling. Additionally, via laser ToF measurements, the mobility μ of the charge carriers can be estimated.

All elements necessary for the understating of the following chapters have been laid out. Chapters 3 to 5 are focused on the results and associated discussions of the three study axes employed to improve the X-ray response of $MAPbBr_3$ and understand the underlying chemistry and physics.

References

(1) Amari, S. Étude des matériaux pérovskites pour la détection directe des rayonnements ionisants. Ph.D. diss., Université Grenoble Alpes, Grenoble, France, 2020.

(2) Baussens, O. Nouveau matériau pérovskite pour la radiographie médicale. Ph.D. diss., Université de Bordeaux, 2021.

(3) Hui, Y.; Webster, R. D. Absorption of Water into Organic Solvents Used for Electrochemistry under Conventional Operating Conditions. *Anal. Chem.* **2011**, *83* (3), 976–981. https://doi.org/10.1021/ac102734a.

(4) Amari, S.; Verilhac, J.-M.; Gros D'Aillon, E.; Ibanez, A.; Zaccaro, J. Optimization of the Growth Conditions for High Quality $CH_3NH_3PbBr_3$ Hybrid Perovskite Single Crystals. *Crystal Growth & Design* **2020**, *20* (3), 1665–1672. https://doi.org/10.1021/acs.cgd.9b01429.

(5) Scheel, H. J.; Elwell, D. Stable Growth Rates and Temperature Programming in Flux Growth. *Journal of Crystal Growth* **1972**, *12* (2), 153–161. https://doi.org/10.1016/0022-0248(72)90045-0.

(6) Jones, W. F.; Wiencek, J. M.; Darcy, P. A. Improvements in Lysozyme Crystal Quality via Temperature-Controlled Growth at Low Ionic Strength. *Journal of Crystal Growth* **2001**, *232* (1), 221–228. https://doi.org/10.1016/S0022-0248(01)01064-8.

(7) Saidaminov, M. I.; Abdelhady, A. L.; Murali, B.; Alarousu, E.; Burlakov, V. M.; Peng, W.; Dursun, I.; Wang, L.; He, Y.; Maculan, G.; Goriely, A.; Wu, T.; Mohammed, O. F.; Bakr, O. M. High-Quality Bulk Hybrid Perovskite Single Crystals within Minutes by Inverse Temperature Crystallization. *Nat Commun* **2015**, *6* (1), 7586. https://doi.org/10.1038/ncomms8586.

(8) Tan, S.; Huang, T.; Yavuz, I.; Wang, R.; Weber, M. H.; Zhao, Y.; Abdelsamie, M.; Liao, M. E.; Wang, H.-C.; Huynh, K.; Wei, K.-H.; Xue, J.; Babbe, F.; Goorsky, M. S.; Lee, J.-W.; Sutter-Fella, C. M.; Yang, Y. Surface Reconstruction of Halide Perovskites During Post-Treatment. *J. Am. Chem. Soc.* **2021**, *143* (18), 6781–6786. https://doi.org/10.1021/jacs.1c00757.

(9) *Catalogues*. Presi. https://www.presi.com/catalogues/ (accessed 2023-02-10).

(10) Pospisil, J.; Guerrero, A.; Zmeskal, O.; Weiter, M.; Gallardo, J. J.; Navas, J.; Garcia-Belmonte, G. Reversible Formation of Gold Halides in Single-Crystal Hybrid-Perovskite/Au Interface upon Biasing and Effect on Electronic Carrier Injection. *Advanced Functional Materials* **2019**, *29* (32), 1900881. https://doi.org/10.1002/adfm.201900881.

(11) INTERNATIONAL STANDARD IEC 62220-1 : Medical Electrical Equipment – Characteristics of Digital X-Ray Imaging Devices. International Electrotechnical Commission June 2007.

(12) Poludniowski, G. G.; Evans, P. M. Calculation of X-Ray Spectra Emerging from an x-Ray Tube. Part I. Electron Penetration Characteristics in x-Ray Targets. *Med Phys* **2007**, *34* (6),

2164–2174. https://doi.org/10.1118/1.2734725.

(13) Poludniowski, G. G. Calculation of X-Ray Spectra Emerging from an x-Ray Tube. Part II. X-Ray Production and Filtration in x-Ray Targets. *Medical Physics* **2007**, *34* (6Part1), 2175–2186. https://doi.org/10.1118/1.2734726.

(14) Hecht, K. Zum Mechanismus des lichtelektrischen Primärstromes in isolierenden Kristallen. *Z. Physik* **1932**, *77* (3–4), 235–245. https://doi.org/10.1007/BF01338917.

(15) Many, A. High-Field Effects in Photoconducting Cadmium Sulphide. *Journal of Physics and Chemistry of Solids* **1965**, *26* (3), 575–578. https://doi.org/10.1016/0022-3697(65)90133-2.

(16) Stoumpos, C. C.; Malliakas, C. D.; Peters, J. A.; Liu, Z.; Sebastian, M.; Im, J.; Chasapis, T. C.; Wibowo, A. C.; Chung, D. Y.; Freeman, A. J.; Wessels, B. W.; Kanatzidis, M. G. Crystal Growth of the Perovskite Semiconductor $CsPbBr_3$: A New Material for High-Energy Radiation Detection. *Crystal Growth & Design* **2013**, *13* (7), 2722–2727. https://doi.org/10.1021/cg400645t.

(17) Wei, H.; Fang, Y.; Mulligan, P.; Chuirazzi, W.; Fang, H.-H.; Wang, C.; Ecker, B. R.; Gao, Y.; Loi, M. A.; Cao, L.; Huang, J. Sensitive X-Ray Detectors Made of Methylammonium Lead Tribromide Perovskite Single Crystals. *Nature Photon* **2016**, *10* (5), 333–339. https://doi.org/10.1038/nphoton.2016.41.

(18) Ramo, S. Currents Induced by Electron Motion. *Proc. IRE* **1939**, *27* (9), 584–585. https://doi.org/10.1109/JRPROC.1939.228757.

(19) Bertolini, G.; Coche, A. *Semiconductor Detectors*; Wiley, 1968.

(20) Klein, C. A. Bandgap Dependence and Related Features of Radiation Ionization Energies in Semiconductors. *Journal of Applied Physics* **1968**, *39* (4), 2029–2038. https://doi.org/10.1063/1.1656484.

(21) Baussens, O.; Maturana, L.; Amari, S.; Zaccaro, J.; Verilhac, J.-M.; Hirsch, L.; Gros-Daillon, E. An Insight into the Charge Carriers Transport Properties and Electric Field Distribution of $CH_3NH_3PbBr_3$ Thick Single Crystals. *Appl. Phys. Lett.* **2020**, *117* (4), 041904. https://doi.org/10.1063/5.0011713.

(22) Musiienko, A.; Ceratti, D. R.; Pipek, J.; Brynza, M.; Elhadidy, H.; Belas, E.; Betušiak, M.; Delport, G.; Praus, P. Defects in Hybrid Perovskites: The Secret of Efficient Charge Transport. *Adv. Funct. Mater.* **2021**, *31* (48), 2104467. https://doi.org/10.1002/adfm.202104467.

(23) Jia, S.; Xiao, Y.; Hu, M.; He, X.; Bu, N.; Li, N.; Liu, Y.; Zhang, Y.; Cui, J.; Ren, X.; Zhao, K.; Liu, M.; Wang, S.; Yuan, N.; Ding, J.; Yang, Z.; Liu, S. Ion-Accumulation-Induced Charge Tunneling for High Gain Factor in P–I–N-Structured Perovskite $CH_3NH_3PbI_3$ X-Ray Detector. *Adv. Mater. Technol.* **2021**, 2100908. https://doi.org/10.1002/admt.202100908.

(24) Armaroli, G.; Ferlauto, L.; Lédée, F.; Lini, M.; Ciavatti, A.; Kovtun, A.; Borgatti, F.; Calabrese, G.; Milita, S.; Fraboni, B.; Cavalcoli, D. X-Ray-Induced Modification of the Photophysical Properties of $MAPbBr_3$ Single Crystals. *ACS Appl. Mater. Interfaces* **2021**,

acsami.1c16072. https://doi.org/10.1021/acsami.1c16072.

Chapter 3 – Mixed halide compositions: Anion engineering in $MAPb(Br_{1-x}Cl_x)_3$ solid solution

Table of contents

Chapter 3

Chapter 3

Mixed halide compositions: Anion engineering in $MAPb(Br_{1-x}Cl_x)_3$ solid solution

Introduction

As previously described, during Amari's[1] and Baussens'[2] PhD works, the synthesis of $MAPbBr_3$ SCs growth via MITC has been optimised in DMF for direct X-ray radiation detection.[3,4] While the growth optimisation allowed reaching a very good sensitivity under X-ray illumination, they always presented a large dark current density J_{dark} (~ μA cm^{-2}), several orders of magnitude above the specifications required for radiation detectors.[5] This crucial figure of merit for detectors corresponds to the leakage current of the device in the dark, and must be minimised by a combination of increased bulk resistivity ρ and electrode engineering.[6,7]

In this context, to reduce the dark current and improve device stability, it has been recently proposed to modify the bulk chemical composition of $MAPbBr_3$ by partially substituting bromine with chlorine leading to compounds of general formula $MAPb(Br_{1-x}Cl_x)_3$.[8] According to several studies, this anion engineering would lead to higher bulk resistivity ρ, increased charge carrier mobility μ and lifetime τ, and lower hysteresis compared to base material.[8–12] However, the origin of those improvements remains unclear. On the one hand, Rybin et al.[8] and Wang et al.[12] attributed the improvements to the suppression of Br^- anions migration, induced by lattice contraction and a decrease in halide vacancy (V_X). On the other hand, Wei et al.[9] proposed a dopant compensation mechanism as the source of electronic neutrality and subsequent increased resistivity. A possible explanation of this discrepancy may be that these different studies were based on crystals made by different methods. Indeed, $MAPbBr_3$ can present different crystal quality depending on the growth method employed, as it has been observed in PVs.[13] As for the above-mentioned studies, the difference in growth procedure may translate into different defect structures; hence a different impact of the halide substitution, either mostly electronic, structural or a mixture of both. Furthermore, we noticed that these studies draw different conclusions regarding the performance dependency on the Cl-composition and no consensus on the optimal Cl content has been established to date.

If defects are key in understanding Cl addition effect, then specific attention should be given to crystal growth to ensure that the defect structures are comparable between crystals. For instance, the studies cited above relay on spontaneous nucleation as the initial stage of crystal synthesis. While this can lead to high quality crystals, we have observed that it yields generally crystals with a large diversity of defect content (dislocation density, strains) and properties.[4] Also, in many of these studies, mixed halide crystals are grown in DMF/DMSO (dimethyl sulfoxide) mixtures of varying proportions.[10,12] While it makes sense to compensate the lower solubility of chloride species in DMF by introducing an increasing proportion of DMSO with increasing Cl content, it could have an adverse effect on the grown crystals properties as it has been claimed that DMSO favours the formation of defects (MA^+ vacancies V_{MA}) in $MAPbBr_3$ when it is used in large proportions (> 3 %).[14]

It is to avoid this kind of pitfalls that the specific procedure introduced in the previous chapter was developed, to insure the formation of SCs of controlled quality. The growths of $MAPb(Br_{1-x}Cl_x)_3$ SCs took place in DMF, from seeds and under conditions similar to the ones described in Chapter 2, leading to crystals with low and reproducible defect content.[4] In that sense, if an optimal Cl content was identified, it could not be argued that it resulted from an adverse effect of DMSO or the employed crystal growth technique, but solely from the presence of Cl in the structure. Growth solutions with different solution Cl contents were selected in the range where optimal properties have been previously identified. It was reported that Cl contents above 19 % induce detrimental defects in the structure.[15] For each content, compositional, optical and electrical characterisations of the resulting SCs were systematically undertaken to evaluate the crystals properties. Energy dispersive X-ray analysis (EDX) via field emission scanning electron microscopy (FESEM), and X-ray powder diffraction (XRD) allowed to determine the Cl content inside the crystal lattice ($\%Cl_{cryst}$) and the cell parameter a. The optical band gap E_g, via ultraviolet-visible (UV-Vis) spectroscopy, and steady-state photoluminescence (PL) as a function of Cl content were determined. After crystal polishing and Cr electrodes deposition, the optoelectronic performance of each composition was evaluated via current density-voltage (J-V) sweeps, current density-time (J-t) and laser time of flight (ToF) measurements. The response under X-ray radiation (sensitivity-voltage (S-V) measurements) was assessed in relevant medical imaging conditions, as detailed in Chapter 2 (pulsed X-rays at 4 Hz, 100 ms pulse duration, 24 μGy_{air} per pulse RQA5 quality beam corresponding to an angiography exam). S-V data were subsequently modelled using two-charge carriers Hecht equation for evaluation of mobility-lifetime $\mu\tau$ product.

Moreover, while the performance of $MAPb(Br_{1-x}Cl_x)_3$ SCs has largely been assessed for γ-ray detection,[8,9,16,17] its performance as X-ray detector, and specially for radiography applications has been seldom reported.[9,18] To contribute to the understanding of the impact of Cl incorporation in $MAPbBr_3$, we present here a study on the properties of mixed halide $MAPb(Br_{1-x}Cl_x)_3$ SCs, grown by adaptive temperature ramps and supported by significant device sampling per composition. The crystal growth method and characterisation conditions

lead to the existence of an optimum in Cl content. The study is part of an article published in early 2023.[19] This chapter replicates and further expands some aspects of this publication.

Chapter 3

1 Precursor solution preparation and crystal growth

Cl-containing SCs were grown via the method described in Chapter 2. The crystal growth was performed in DMF (Sigma Aldrich, anhydrous, 99.8 %) for $MAPbBr_3$ and mixed halide compositions. Because Cl-containing precursors are sparingly soluble in DMF,[20] and to avoid introducing DMSO for the mixed compositions, we chose to introduce chloride via the most soluble precursor: methylammonium chloride (MACl, GreatCell Solar, ≥ 99 %), partially replacing methylammonium bromide (MABr, GreatCell Solar, ≥ 99 %) in the preparation of the precursor solutions. A stoichiometric ratio 1:1 was kept between lead (II) bromide ($PbBr_2$, Sigma Aldrich, 99.999 % trace metals basis) and MAX (X = Br, Cl). **Equation (3-1)** defines the total halide *X* content in solution, while **Equations (3-2)** and **(3-3)** defines the solution Cl content and the ratio ε, respectively:

$$[X]_{tot} = [PbBr_2] + (1-\varepsilon)\,[MABr] + \varepsilon\,[MACl]$$
$$[X]_{tot} = 2\,[X] + (1-\varepsilon)\,[X] + \varepsilon\,[X] \quad (3\text{-}1)$$

$$\%Cl_{sol} = \frac{\varepsilon\,[X]}{2\,[X] + (1-\varepsilon)\,[X] + \varepsilon\,[X]} = \frac{\varepsilon}{3} \quad (3\text{-}2)$$

$$With\ \varepsilon = \frac{[MACl]}{[MABr] + [MACl]} = \frac{[MACl]}{[PbBr_2]} \quad (3\text{-}3)$$

Where $[X]_{tot}$ is the total amount of halide anions in solution (mol L^{-1}), $[A]$ is the concentration of compound A (mol L^{-1}), $\%Cl_{sol}$ is the Cl content in solution, and ε is the proportion of MACl introduced with respect to $PbBr_2$.

The selected Cl contents in solution were $\%Cl_{sol}$ = 0, 1, 2, 5, 10 and 100, where $\%Cl_{sol}$ = 0 and 100 are the full bromide and chloride compositions $MAPbBr_3$ and $MAPbCl_3$, respectively. For $MAPbBr_3$ and all mixed halide compositions, the precursors were dissolved in DMF to obtain 1 M solutions. For $MAPbCl_3$, a 2 M solution was prepared by dissolving the precursors lead (II) chloride ($PbCl_2$, Sigma Aldrich, 99.999 % trace metals basis) and MACl in a DMF/DMSO (Sigma Aldrich, anhydrous, ≥ 99.9 %) mixture (3:7 in volume).[20]

Because of its inherently stochastic nature, spontaneous nucleation may give rise to crystals of varying quality with extended defects such as grains boundaries, strains or dislocations, which make the comparison between crystals of a given composition less straightforward and may induce different actions of Cl^- anions in the structure. To ensure comparability, the crystals of all compositions were grown from seeds of similar quality. Firstly, for each selected $\%Cl_{sol}$, a high-quality seed of matching composition was obtained by spontaneous nucleation; secondly, a seed-assisted crystal growth run in a solution of same Cl content was performed to obtain SCs of reproducible quality and bigger dimensions for this study. Different adaptive temperature ramps were employed to accommodate the changes in solubility associated with the different concentrations of Cl-species introduced. The lower solubility of Cl-species also impact the growth conditions as it leads to a global lower solubility

and slightly lower solubility-temperature ratios for mixed halide perovskites with increasing Cl content. The solubility curves of $MAPbBr_3$ and $\%Cl_{sol}$ = 10 ($MAPb(Br_{0.85}Cl_{0.15})_3$ in DMF can be found in **Appendix – Chapter 3**. On the one hand, an average increase of 5.5°C h^{-1} for $MAPbBr_3$ ($\%Cl_{sol}$ = 0) and $\%Cl_{sol}$ = 1, and on the other hand, an average increase of 1°C h^{-1} for $\%Cl_{sol}$ = 2, 5 and 10 were used. Even though $MAPbCl_3$ ($\%Cl_{sol}$ = 100) was grown in a completely different solvent (DMF:DMSO), its temperature ramp was also accordingly adjusted to 1.6°C h^{-1} as average increase. One can notice that the temperature ramp used for $MAPbBr_3$ and $\%Cl_{sol}$ = 1 was reduced by a factor of about 5 for $\%Cl_{sol}$ = 2, 5, 10. This reduction of the temperature ramp (1/5) was more important than that of the solubility-temperature ratio (1/2) to ensure that the solution stays in the reduced metastable zone and avoid significant spontaneous nucleation in Cl-rich solutions. It is because nucleation would become predominant in growth conditions used for $MAPbBr_3$ that we limited our study to rather low Cl contents, in order to grow mm-sized crystals of different Cl contents but under similar growth conditions. Additionally, it has been observed that Cl concentration above %Cl = 19 ($MAPb(Br_{0.81}Cl_{0.19})_3$) may induce detrimental defects (e.g., µm-scale voids on the crystal surface,[15] MA and halide vacancies, V_{MA}[21] and V_{Br},[9,21], respectively). At the end of the growth process, SCs of different crystal Cl content ($\%Cl_{cryst}$) were obtained.

The SCs were polished and Cr electrodes were deposited on each side. Ultimately, a total of 51 crystals of 4 mm × 4 mm × 2 mm on average were grown during this work to provide sufficient statistical weight to the characterisations. **Table 3-1-1** summarises the crystal growth parameters employed and **Figure 3-1-1** shows the resulting devices with their respective thicknesses in inset.

Table 3-1-1. Crystal growth parameters for the anion engineering study. The study is based on six series of SC growth. Each series contains a specimen of the six compositions.

Material [a)]	Targeted $\%Cl_{sol}$ [%]	α_2 [mm^2 h^{-1}]	Growth temperature range [°C]	Duration [h]	Average increase [°C h^{-1}]
$MAPbBr_3$	0.00	9.09	65.5-85.5	3 h 39	5.5
$MAPb(Br_{0.98}Cl_{0.02})_3$	1.00	9.09	65.5-85.5	3 h 39	5.5
$MAPb(Br_{0.97}Cl_{0.03})_3$	2.00	1.65	65.5-85.5	20 h 07	1
$MAPb(Br_{0.92}Cl_{0.08})_3$	5.00	1.65	65.5-85.5	20 h 07	1
$MAPb(Br_{0.85}Cl_{0.15})_3$	10.00	1.65	65.5-85.5	20 h 07	1
$MAPbCl_3$	100.00	3.10	40.1-73.3	20 h 07	1.6

[a)] The *x* values given in the above chemical formulae is given by $\%Cl_{cryst}$, determined using Vegard's law (VL) and the XRD data, which are described later on.

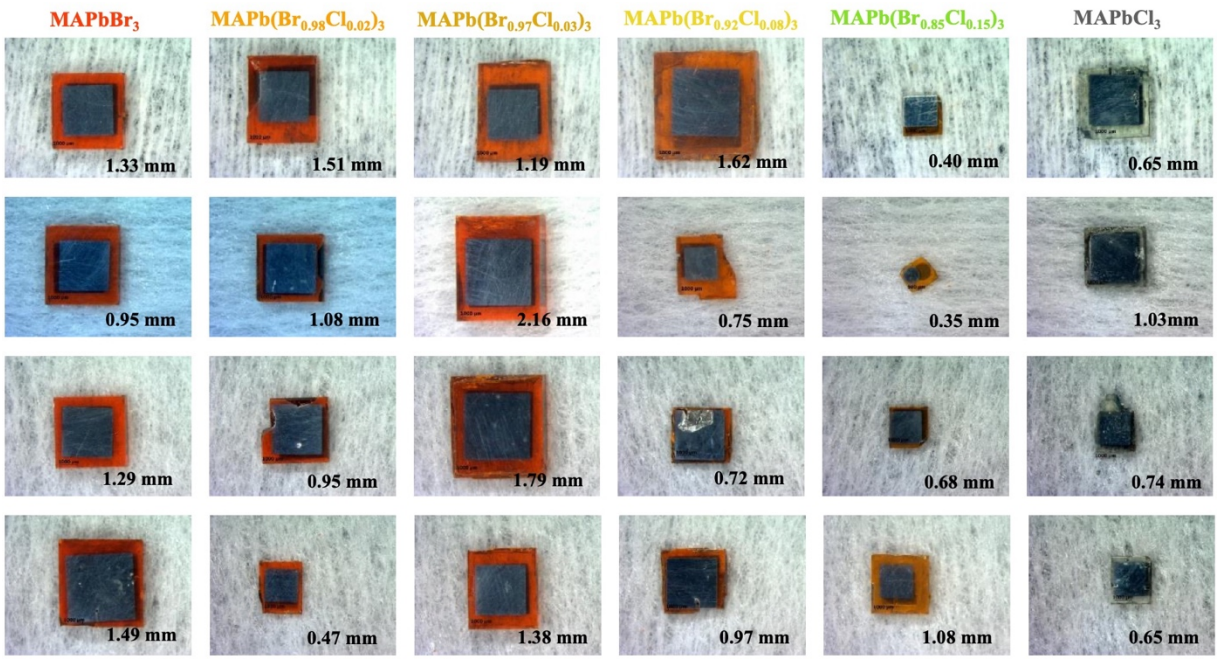

Figure 3-1-1. Diversity of $MAPb(Br_{1-x}Cl_x)_3$ SC devices produced for optoelectronic characterisation: J-V sweeps for hysteresis and resistivity ρ measurements, J-t measurements for conductivity drift σ_{drift} determination, sensitivity tests under X-ray illumination and laser ToF measurements for hole mobility μ_h determination. SC device thickness is given in inset at the bottom right of every picture.

2 Chemical and structural characterisations

In general, through various physical-chemical phenomena such as differences in speciation, complexation and diffusion, the amount of substituent incorporated in the crystal (denoted here $\%Cl_{cryst}$) differs from that introduced in the initial growth solution ($\%Cl_{sol}$). For that reason, our first task was to determine the amount of Cl in the crystals for each solution composition. The Cl content of the crystals was determined using two independent techniques, EDX and XRD. EDX measurements also allowed establishing the Pb/halide (Pb/X) ratio to evaluate the impact of the addition of Cl on the SC stoichiometry. Inductively coupled plasma mass spectrometry (ICP-MS) was also realised on $MAPbBr_3$, for further chemical characterisation of the SC bulk. Samples and holders for EDX and XRD characterisations are shown in **Figure 3-2-1-A** and **Figure 3-2-1-B**, respectively.

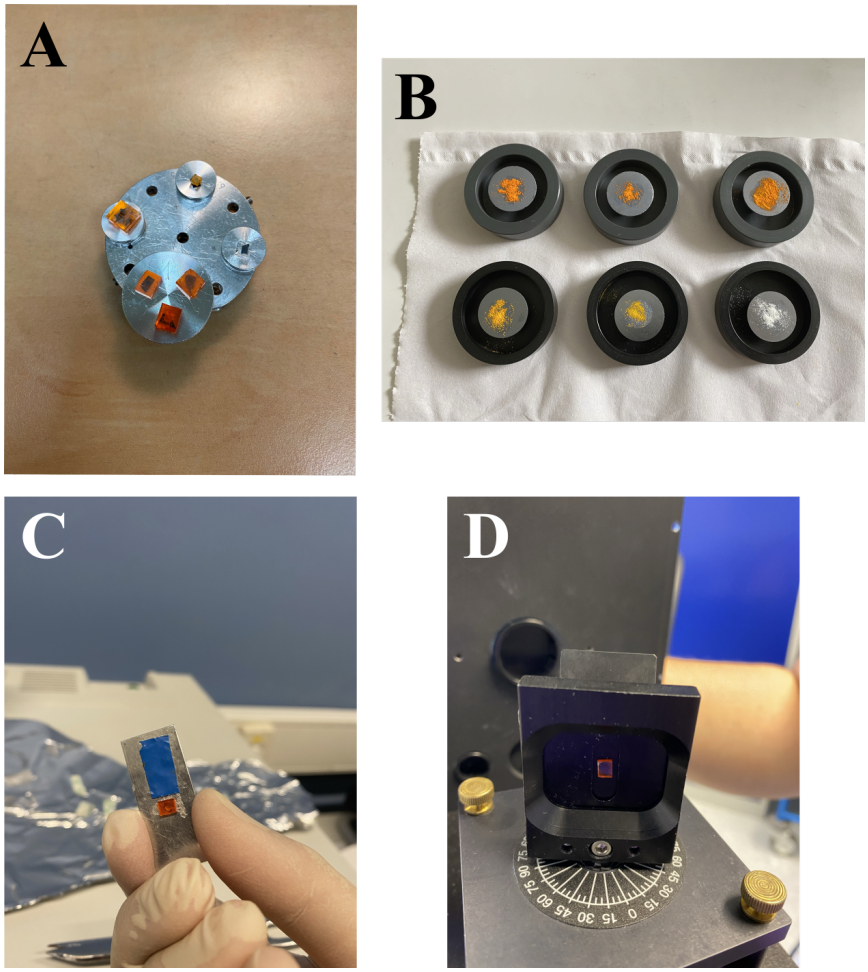

Figure 3-2-1. Material characterisation examples. (A) Series of $MAPb(Br_{1-x}Cl_x)_3$ SCs on metallic support glued with carbon tape for FESEM-EDX analysis and determination of $\%Cl_{cryst\text{-}EDX}$ and Pb/X ratios. **(B)** Series of ground $MAPb(Br_{1-x}Cl_x)_3$ SCs for determination of lattice parameter *a* and $\%Cl_{cryst\text{-}XRD}$ content. **(C)** SC on UV-Vis support glued with tape: the same crystal surface is exposed to the beam for each measurement through the small aperture. **(D)** SC on PL support stuck with grease.

Chapter 3

2.1 Substitution of Br with Cl and determination of crystal Cl content

2.1.1 FESEM-EDX analysis

A field-emission scanning electron microscope (FESEM) Ultra+ (ZEISS) associated with a SDD (silicon drift detector, Bruker) for EDX working in high vacuum mode with a 10 kV voltage and an aperture of 30 µm was used. It allowed determining both Cl content $\%Cl_{cryst\text{-}EDX}$ and Pb/X ratio on flat natural faces of several SCs grown from each solution composition. For all measurements, the acquisition was fixed at 100 000 counts (~ 2 min integration time) with a working distance of 8 mm. The electron beam penetration depth is inferior to 900 nm and the pear-shaped interaction volume was estimated at ~ 1 μm^3 for $MAPbBr_3$. For data analysis, Esprit (Bruker) software with P/B-ZAF mode for elemental quantification was used. As the lightest element (H, C and N) belonging to the organic molecules cannot be measured, the elements taken into account for quantification were Cl, Br and Pb. The recorded spectra were normalised to the Br L_α peak of $MAPbBr_3$. $\%Cl_{cryst\text{-}EDX}$ and Pb/X ratio values were then determined using Cl K_α (2.621 keV), Br L_α (1.48 keV) and Pb M_α (2.345 keV) emission lines, and **Equations (3-4)** and **(3-5)**:

$$\%Cl_{cryst-EDX} = \frac{atom\ Cl\ (\%)}{atom\ Cl\ (\%)\ +\ atom\ Br\ (\%)} \tag{3-4}$$

$$\frac{Pb}{X} = \frac{atom\ Pb\ (\%)}{atom\ Cl\ (\%)\ +atom\ Br\ (\%)} \tag{3-5}$$

Where $atom\ A$ (%) is the atomic percentage attributed by EDX quantification of element A, and X is the total amount of halide (%).

It should be noted that, after correcting the spectra background with the Esprit software, the personalised P/B-ZAF quantification method gives a percentage of Cl automatically: the searched elements (Cl, Br and Pb) are set by default to be quantified (user decision). Because of the existence of a small peak of lead, Pb M_γ (2.65 keV, not used for quantification in this technique), near the quantification peak of chlorine, Cl K_α (2.621 keV), during deconvolution, Pb M_γ and Cl K_α peaks partially overlap, even though the former is far less intense. As a result, the software tends to always find a small percentage of Cl. Background noise and Pb M_γ contribute then to it, even in the case of $MAPbBr_3$ (about 0.2 ± 0.1 %). This small percentage is thus included in the uncertainty of the Cl content determination, which is especially important for low Cl content crystals. The EDX instrument was not calibrated with reference chemical species for chlorine, bromine and lead, but samples were compared relatively to $MAPbBr_3$ and $MAPbCl_3$, full bromide and chloride crystals, respectively. The error percentage associated with this quantification is ± 1 %. The FESEM-EDX analysis was conducted with the guidance of Sébastien Paris at Institut Néel.

For most measurements performed in this study, surfaces of around 10^4 µm^2 were used, and between 3 to 4 measurements were made on each SC sample. **Figure 3-2-2-A** shows an example of measurements sequence and **Figure 3-2-2-B** illustrates the surface taken into account in the measurements. To assess the $MAPb(Br_{1-x}Cl_x)_3$ crystals composition, at least 14 measurements were executed on five series, each containing one element of each composition studied.

A profile study was also performed for SCs grown from growth solution compositions $\%Cl_{sol} = 2$ (**Figure 3-2-2-C**) and 5 (**Figure 3-2-2-D**) to determine the composition evolution throughout their growth. Given that the electron beam has a penetration depth below 1 µm, to evaluate the Cl distribution in the crystal bulk, SCs of both compositions were cleaved. This gave access to the history of the Cl incorporation from seed (bottom) to the latest stage of crystal growth (top).

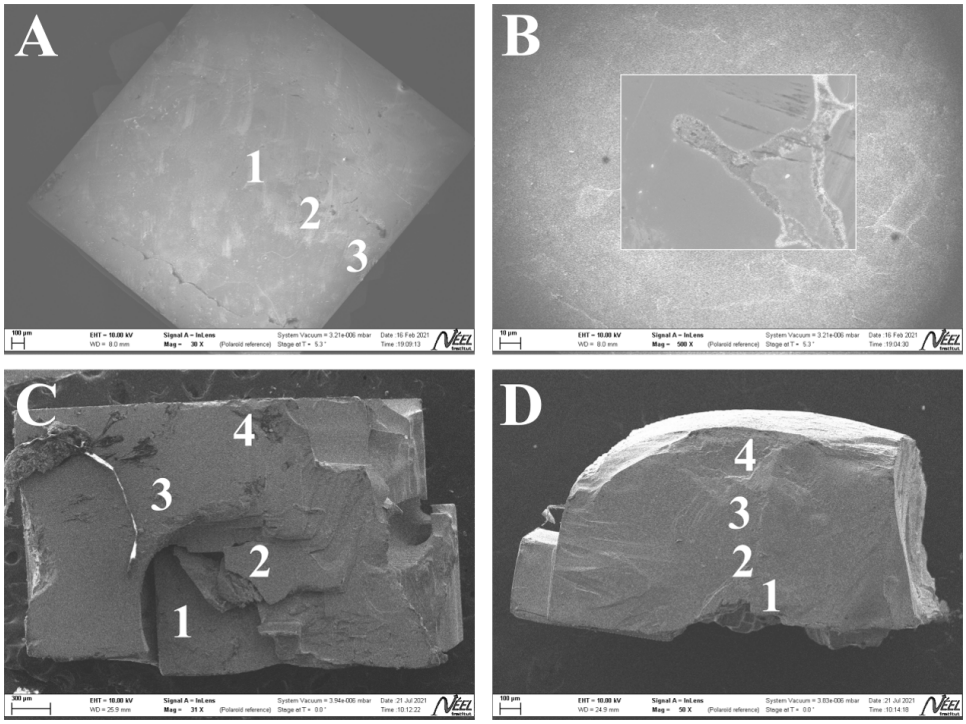

Figure 3-2-2. SEM-EDX measurements. (A) Sequence example of superficial EDX measurements, from centre to exterior, for determination of inorganic elements Cl, Br and Pb. **(B)** Window measurement example with a surface close to 10^4 µm^2. EDX profile study on **(C)** $MAPb(Br_{0.97}Cl_{0.03})_3$ ($\%Cl_{sol} = 2$) and **(D)** $MAPb(Br_{0.92}Cl_{0.08})_3$ ($\%Cl_{sol} = 5$), from bottom (seed side) to top.

EDX spectra examples are overlaid in **Figure 3-2-3** showing only a narrow energy range centred on the Cl K_α emission line. Full range EDX spectra can be found in **Figure A 3-2-1**. The most striking feature is the expected progressive rise of Cl^- anions in the crystal (from red to light green lines) with increasing $\%Cl_{sol}$. Plotting the Cl concentrations in the crystal derived from these EDX measurements ($\%Cl_{cryst\text{-}EDX}$) against the ones in solution $\%Cl_{sol}$ (green plot in **Figure 3-2-4-A** and **Figure 3-2-4-B**) shows an efficient incorporation of Cl^- anions in the

crystal structure with a partition coefficient k higher than unity ($\%Cl_{cryst} > \%Cl_{sol}$) (see **Table 3-2-1** for overall values).

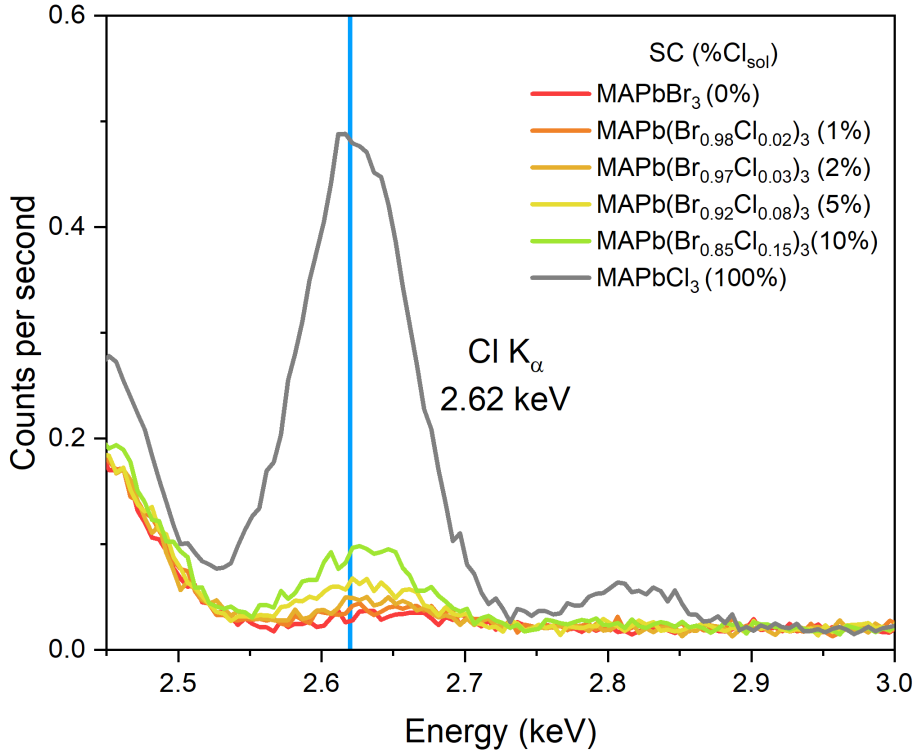

Figure 3-2-3. EDX spectra overlaid centred on Cl K_α (2.621 keV) emission line to show progressive and preferential substitution of Br^- with Cl^- anions. From bottom to top: $MAPbBr_3$, $MAPb(Br_{0.98}Cl_{0.02})_3$, $MAPb(Br_{0.97}Cl_{0.03})_3$, $MAPb(Br_{0.92}Cl_{0.08})_3$, $MAPb(Br_{0.85}Cl_{0.15})_3$ and $MAPbCl_3$.

A possible explanation of the partition coefficient being above unity ($k > 1$) could derive from the lower solubility of Cl-species as evidenced by the lower solubility of $MAPbCl_3$ precursors in DMF when compared to that of $MAPbBr_3$.[20] One can then assume that chloroplumbate complexes present in the growth solution would precipitate faster and contribute more to the structure build-up than bromoplumbate ones. As a consequence, during crystal growth, Cl-enriched perovskite is initially deposited and the solution becomes progressively poorer in Cl. This drift in Cl content in solution can result in significant compositional heterogeneity between the inner/early growth and the outer/late growth parts of large SCs. To quantify such heterogeneity in our crystals, the profile study by EDX was performed for $\%Cl_{sol}$ = 2 and 5, to try and see any evolution of Cl content in the crystal thickness. For $\%Cl_{sol}$ = 2, due to the level of uncertainty of EDX measurements and surface microtopography heterogeneity of the crystal (**Figure 3-2-2-C** and **Figure 3-2-5-A**), no clear trend was observed (relatively constant Cl content). For $\%Cl_{sol}$ = 5, on the contrary, a decreasing Cl content can be observed, going from 8.2 ± 0.6 % close to the seed (bottom) of the crystal to 6.5 ± 0.6 % for later growth (top) (**Figure 3-2-2-D** and **Figure 3-2-5-A**). Because the late growth of the crystal occurs in the solution most depleted in Cl from the initial ratio $\%Cl_{sol}$, the

Cl content values of the crystals estimated by EDX probably underestimate the average Cl content of the whole bulk crystal. That is why, to obtain an estimate more representative of the average Cl content, we relayed on XRD.

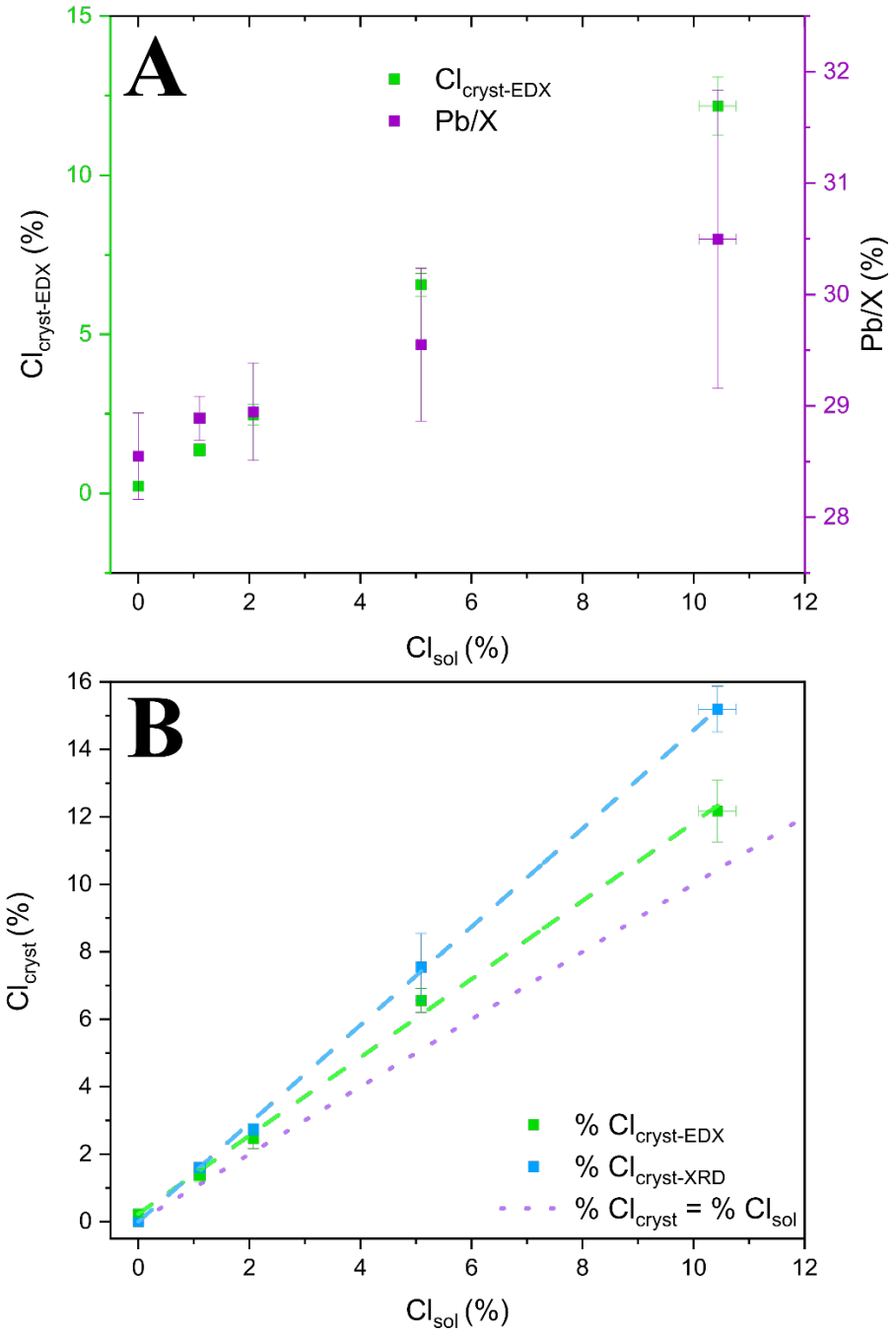

Figure 3-2-4. Substitution of Br^- by Cl^- anions. **(A)** Correlation between solution Cl content $\%Cl_{sol}$ and both crystal Cl content $\%Cl_{cryst-EDX}$ (green squares) and Pb/halide ratio (Pb/X) (purple squares) determined by EDX, respectively. Reference $MAPbBr_3$ and mixed halide compositions are plotted. **(B)** Correlation between solution Cl content, $\%Cl_{sol}$, and both crystal Cl contents $\%Cl_{cryst-EDX}$ and $\%Cl_{cryst-XRD}$ determined by EDX (green squares and dot line) and Vegard's law (VL) from XRD data (blue squares and dot line), respectively. Ideal partition coefficient equal to unity ($k = 1$) is displayed with purple dots ($\%Cl_{cryst} = \%Cl_{sol}$).

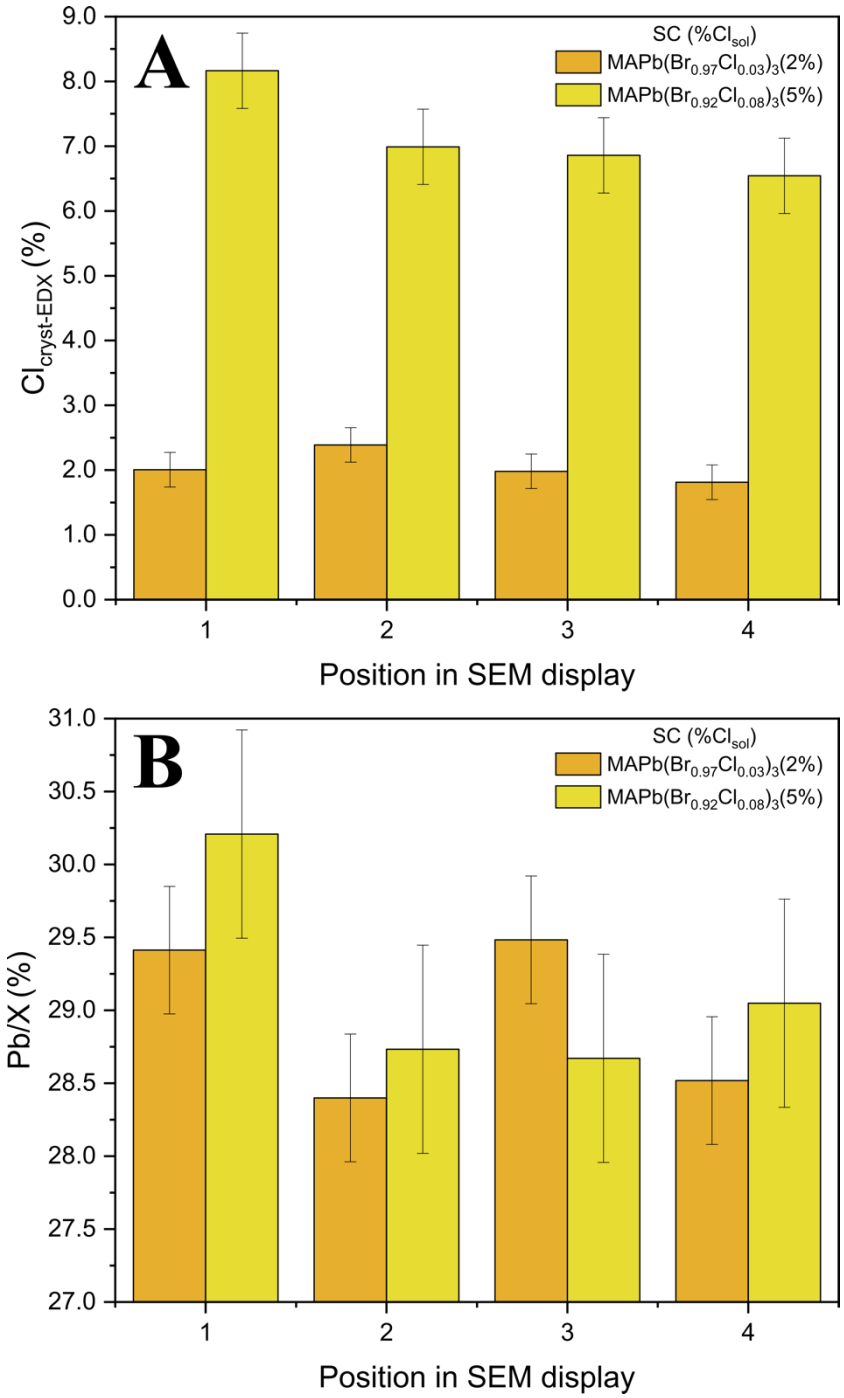

Figure 3-2-5. EDX profile study. (A) Cl content %Cl$_{cryst-EDX}$ and **(B)** Pb/halide (Pb/X) ratio determined for profile study for MAPbBr$_{0.97}$Cl$_{0.03}$ (%Cl$_{sol}$ = 2) and MAPbBr$_{0.92}$Cl$_{0.08}$ (%Cl$_{sol}$ = 5) SCs.

2.1.2 XRD analysis, Le Bail refinement and Vegard's law

Indeed, another way to estimate the average Cl content of the crystals is through its impact on the unit cell parameter *a*. XRD data were recorded on ground crystals so that whole volume of the crystals contributes to the measurement (see **Figure 3-2-1-B)**. For XRD, a D8 Endeavor diffractometer (Bruker) equipped with a Johanssonn monochromator working in Bragg-Brentano θ-2θ geometry was used (X-ray source Cu K$_\alpha$ λ = 1.5406 Å). An acquisition

time of 2.5 s was set using a 0.01 ° step, 2θ values ranging from 5 ° to 90 °. Le Bail refinements using FullProf software (Toolbar FullProf Suite Version July 2017[22]) were performed for lattice parameters *a* determination on the resulting diffractograms, with the guidance of Julien Zaccaro.

If one considers that a full solid solution exists for the $MAPb(Br_{1-x}Cl_x)_3$ system, the cell parameter *a* will follow Vegard's law (VL) with varying Cl content. The latter could thus be determined via XRD and is defined via **Equation (3-6)** derived from VL:

$$\%Cl_{cryst-XRD} = \frac{a_{MAPb(Br_{1-x}Cl_x)_3} - a_{MAPbBr_3}}{a_{MAPbCl_3} - a_{MAPbBr_3}} \quad (3\text{-}6)$$

Where $\%Cl_{cryst-XRD}$ is the molar fraction of $MAPbCl_3$ in the solid solution and the Cl content associated with XRD, $a_{MAPb(Br_{1-x}Cl_x)_3}$ is the lattice parameter of the solid solution (Å), and a_{MAPbBr_3} and a_{MAPbCl_3} are the lattice parameters of pure constituents $MAPbBr_3$ and $MAPbCl_3$ (Å), respectively.

The XRD patterns obtained for all compositions were very similar without any extra peak. This indicates that all studied compositions appear isomorphous with the existence of a continuous solid solution between $MAPbBr_3$ and $MAPbCl_3$. It is worth saying that this is valid in the $\%Cl_{cryst}$ range considered in this work. Therefore, the unit cell parameter *a* is expected to follow VL as a function of the Cl content. Indeed, the patterns show small peak shifts towardshigher angles with increasing Cl content, which is associated with a contraction of the unit cell: see **Figure 3-2-6-A** for XRD diffractograms of all compositions and **Figure 3-2-6-B** for a zoom on (100) peak shift as example. This contraction is related to the substitution of Br^- by Cl^- anions of smaller ionic radius (r_{Cl^-} (1.81 Å) < r_{Br^-} (1.92 Å)) and consequently shorter length of Pb−Cl than Pb−Br bonds.[8] By performing Le Bail refinements of diffractograms from crystals grown in each mixed halide solution composition as well as pure $MAPbBr_3$ and $MAPbCl_3$, lattice parameters *a* were precisely determined (see **Table 3-3-1**). The background was first corrected, then different parameters were adjusted one by one to reduce the global reduced χ^2 coefficient, which defines how close the fitting is to the experimental diffractogram. Such parameters were adjusted in the following order and included: the zero offset, the lattice parameter *a* itself, the full width at half maximum (FWHM), peak shape, FWHM and peak asymmetry related functions. Reliability factors for points with Bragg contributions are shown in **Table A 3-3-1**.

By applying **Equation (3-6)** and using the cell parameters of the pure phases determined by the refinement, the average Cl content of the crystals of intermediate compositions ($\%Cl_{cryst-XRD}$) were calculated. In **Figure 3-2-4-B**, the resulting values are plotted as a function of $\%Cl_{sol}$ (blue line); confirming that the Cl partition coefficient *k* is higher than unity. These values are also higher than those obtained by EDX ($\%Cl_{cryst-EDX}$). That is most certainly because XRD gives an estimation that is based on the whole volume of the crystals. Therefore, they involve all growth stages, unlike EDX performed on the natural faces of the different SCs, only interacting with the latest growth stage where the Cl content is the lowest. In addition,

the $\%Cl_{cryst\text{-}XRD}$ values obtained are more reproducible with lower uncertainty: so, they were considered to be more representative and are the ones used in the rest of this manuscript to define our crystal Cl content. $\%Cl_{cryst\text{-}XRD}$ being shortened to $\%Cl_{cryst}$ (see **Table 3-2-1** for overall values). The resulting material compositions are then: $MAPbBr_3$, $MAPb(Br_{0.98}Cl_{0.02})_3$, $MAPb(Br_{0.97}Cl_{0.03})_3$, $MAPb(Br_{0.92}Cl_{0.08})_3$, $MAPb(Br_{0.85}Cl_{0.15})_3$ and $MAPbCl_3$, corresponding to $\%Cl_{sol}$ = 0, 1, 2, 5, 10 and 100 %, respectively.

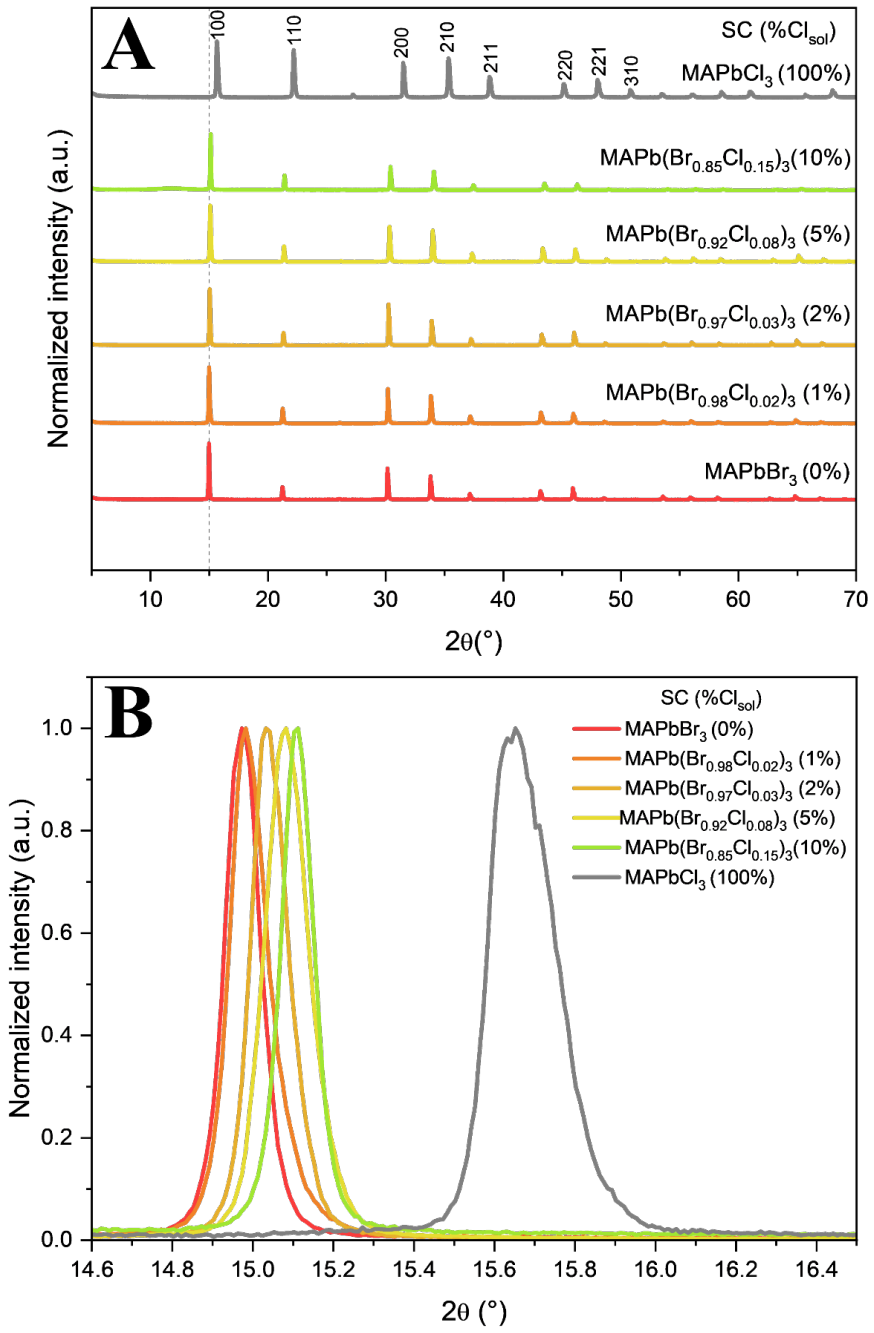

Figure 3-2-6 XRD data. (A) Powder XRD diffractograms overlaid with principal crystallographic planes, illustrating overall peak shifts to higher angles with increasing Cl content. Cubic phase and space group $Pm\bar{3}m$ were maintained for all synthesised SCs. **(B)** Zoom on (100) peak shift, resulting from the lattice contraction induced by the substitution of Br^- with Cl^- anions.

2.2 Crystals Pb/halide stoichiometry

Because the FESEM-EDX measurements quantify all the heavy elements present in the structure, besides the Cl content and its homogeneity in the crystals, they can also shed some light on the lead-halogen (Pb-X) stoichiometry, which is correlated with the point defects present. By using the EDX measurements presented above, we estimated local values of the Pb/X ratio for the different synthesised crystals and also within the same SCs (see **Table 3-2-1** for overall values). Between crystals of different composition, it appears that Pb/X ratio gets closer to ABX_3 stoichiometry (33.3%) with increasing Cl incorporation (**Figure 3-2-4-A**): raising from 28.5 ± 0.4 % for $MAPbBr_3$ to 30.5 ± 1.3 % for $MAPb(Br_{0.85}Cl_{0.15})_3$, while $MAPbCl_3$ has a Pb/X ratio of 34.3 ± 0.9 %. Now regarding the Pb/X ratio of the profile study, within the $MAPb(Br_{0.92}Cl_{0.08})_3$ SC, the same tendency was observed. That is to say a Pb/X value closer to the stoichiometry was observed for the early stages of the crystal growth (richer in Cl at the seed side, position 1 in **Figure 3-2-5-B**), decreasing for the later growth (poorer in Cl, positions 2 to 4 of the same figure). This highlights that the compositional heterogeneity is not a simple Br-Cl substitution, but also changes in the stoichiometry of the structure, moving away from a "Pb poor" situation with Cl incorporation. This shift of the Pb-X stoichiometry, accompanying the Cl incorporation may be attributed to a decrease in lead vacancies V_{Pb}, or conversely an increase in interstitial halide X_i or halide antisite X_{Pb}. As already indicated, our EDX measurements were limited to a depth inferior to 900 nm, so ICP-MS analyses, involving the whole SC, were additionally done with $MAPbBr_3$ for bulk stoichiometry analysis (see **Table A 3-4-1**) to complement the Pb/X ratio trends. The analyses were performed by Sylvie Motellier at CEA Grenoble.

For these ICP-MS analyses, $MAPbBr_3$ SCs were partially dissolved in ultra-pure water in a mass/volume ratio of 1/200. After 24 h, a 65 % nitric acid (HNO_3) aqueous solution was added for complete dissolution of the crystals, in a volume ratio $V_{nitirc\ acid}/V_{original\ solution}$ of 1/100. The samples were overall diluted by a 2×10^4 factor before analysis. An ICP-MS 7900x spectrometer (Agilent Technologies) was used for the quantification of elemental inorganic content of ^{79}Br and ^{207}Pb. A radio frequency power of 1550 W, an Ar plasma and nebulizer gas flow rates of 15 and 1.15 L min^{-1}, respectively, and an integration time/mass of 0.1 s were employed. The error percentage associated with this quantification is ± 5 %. The results showed that, for a whole SC, the Pb/X ratio corresponds to a 32.9 ± 1.7 % stoichiometry for pure bromide samples (close to 33.3% theoretical value), when localised EDX measurement showed a ratio of 28.5 ± 0.4 %, meaning that there could be local deviations from stoichiometry of the Pb/X ratio. These results are correlated with optoelectronic properties further on.

Table 3-2-1. Summary of $MAPb(Br_{1-x}Cl_x)_3$ SC production and associated Cl content in growth solution, and Cl content and Pb/X ratio inside the crystal structure. [a)]

Material [b)]	Targeted $\%Cl_{sol}$ [%]	Experimental $\%Cl_{sol}$ [c)] [%]	$\%Cl_{cryst}$ via EDX [%]	$\%Cl_{cryst}$ via VL-XRD [%]	Pb/X ratio via EDX [%]
$MAPbBr_3$	0.00	0.00 [d)]	0.23 ± 0.10	0.00 [e)]	28.55 ± 0.39
$MAPb(Br_{0.98}Cl_{0.02})_3$	1.00	1.11 ± 0.10	1.37 ± 0.19	1.60 ± 0.11	28.89 ± 0.20
$MAPb(Br_{0.97}Cl_{0.03})_3$	2.00	2.07 ± 0.03	2.47 ± 0.31	2.73 ± 0.18	28.95 ± 0.44
$MAPb(Br_{0.92}Cl_{0.08})_3$	5.00	5.09 ± 0.06	6.56± 0.36	7.55 ± 1.00	29.55 ± 0.69
$MAPb(Br_{0.85}Cl_{0.15})_3$	10.00	10.43 ± 0.34	12.17 ± 0.91	15.19 ± 0.68	30.50 ± 1.34
$MAPbCl_3$	100.00	100.00	99.63 ± 0.14	100.00 [e)]	34.27 ± 0.90

[a)] All values presented in columns 3 to 6 are averages of all weights and measurements done on the synthesised SCs.
[b)] The *x* values given in the above chemical formulae is given by $\%Cl_{cryst}$, determined using Vegard's law (VL) and the XRD data.
[c)] $\%Cl_{sol}$ values are here determined by the amount of MACl matter (average value is used here).
[d)] No MACl added.
[e)] Theoretical values.

3 Optoelectronic characterisation

The incorporation of Cl in the structure not only induces a contraction of the unit cell but also seems to affect the point defects present, which may have a significant impact on the optoelectronic properties of the device. The most obvious one is a visible change of the crystal colour with increasing Cl content as seen in **Figure 3-3-1-A**, which is a clear indication of change in optical band gap.

Once the $\%Cl_{cryst}$ content was determined, PL and UV-Vis spectroscopies were employed to detect optical changes caused by the incorporation of Cl in the structure, especially on the band gap E_g. Samples and holders for UV-Vis and PL characterisations are shown in **Figure 3-2-1-C** and **Figure 3-2-1-D**, respectively.

To get a better view of which electronic modifications the Cl presence brings, a few specificities were performed during the standardised optoelectronic characterisation described in Chapter 2. During J-t recordings, conductivity drifts σ_{drift} were analysed to assess the stability in the dark, and sensitivity values were normalised to the X-ray absorbed fraction of the SC device to better estimate the impact of Cl incorporation, while getting rid of the differences of dimension of the devices.

3.1 Optical band gap: UV-Vis and PL spectroscopies

The optical band gaps E_g were determined via UV-Vis spectroscopy (see **Table 3-3-1**). For transmittance data, a Lambda 900 UV-Vis-NIR (Ultraviolet – Visible – Near-infrared) spectrometer (PerkinElmer) was used with a wavelength range of 400-600 nm, a 0.1 nm step and equipped with a Tungsten lamp. The measurements were performed with the help of Corinne Félix at Institut Néel. Tauc plots were charted using **Equation (3-7)** with the help of **Equations (3-8)** to **(3-10)**, to extract the respective optical band gaps E_g of the SCs. In the Tauc plot, E_g was determined at the intersection between the *x*-axis and a linear fitting of the linear part in the onset region.

$$(\alpha h\nu)^{\frac{1}{\zeta}} = B(h\nu - E_g) \tag{3-7}$$

$$h\nu = \frac{hc}{\lambda e} \tag{3-8}$$

$$\alpha = \frac{ln(10)\ A}{L} \tag{3-9}$$

$$A = -\log T_r \tag{3-10}$$

With α is the absorption coefficient (m^{-1}), h is the Planck constant (6.62607×10^{-34} m^2 kg s^{-1}), ν is the photon frequency (Hz), E_g is the optical band gap energy (eV), B is a constant, ζ is a factor depending on the nature of the electron transition and equal to 1/2 or 2 for the direct and indirect transition band gaps, respectively (here ζ = 1/2),[23] c is the speed of light

(299 792 458 m s^{-1}), λ is the wavelength (m), A is the absorbance, T_r is the transmittance, L is the sample thickness (m), and e is the elementary charge (C).

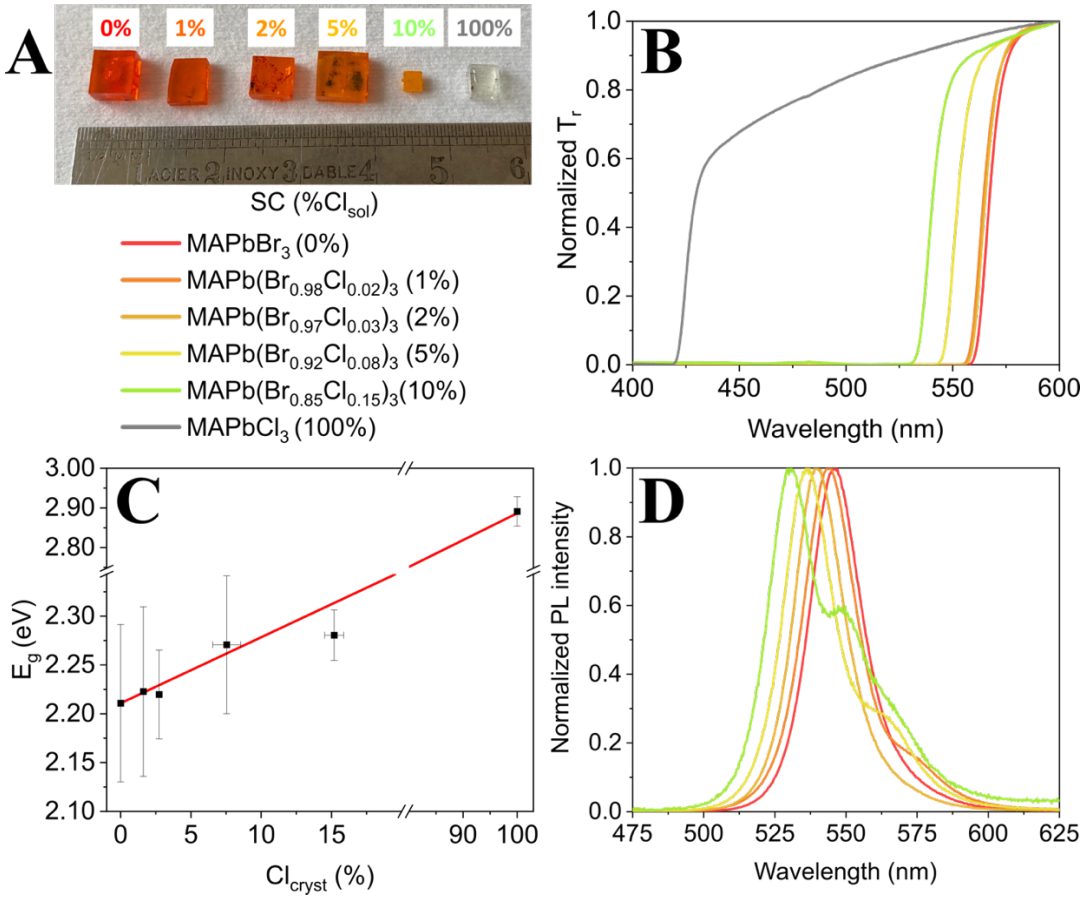

Figure 3-3-1. Optical properties of MAPb($Br_{1-x}Cl_x$)$_3$ SCs. (A) Resulting SCs (from left to right): $MAPbBr_3$, $MAPb(Br_{0.98}Cl_{0.02})_3$, $MAPb(Br_{0.97}Cl_{0.03})_3$, $MAPb(Br_{0.92}Cl_{0.08})_3$, $MAPb(Br_{0.85}Cl_{0.15})_3$ and $MAPbCl_3$ (targeted $\%Cl_{sol}$ written in colour above each SC). **(B)** Normalised transmittance spectra overlaid showing gradual absorption transition blue shift with increasing Cl content, synonym of increasing optical band gap E_g. **(C)** Optical band gap E_g as a function of crystal Cl content $\%Cl_{cryst}$. **(D)** Steady-state PL spectra overlaid showing gradual blue shift of associated PL maxima with increasing Cl content.

The recorded transmission T_r, plotted in **Figure 3-3-1-B**, shows a gradual blue shift in absorption onset. The band gap values extracted from the corresponding Tauc plots, shown in **Figure 3-3-2**, are plotted as a function of $\%Cl_{cryst}$ in **Figure 3-3-1-C**. This shows a linear increase of E_g with rising Cl content for the considered range.

The PL spectra were recorded at room temperature with a double grating excitation and emission spectrometers Fluorolog-3 model FL3-22 (Horiba Jobin Yvon-Spex) coupled to a R928 photomultiplier (Hamamatsu). The excitation wavelength was 350 nm coming from a Xe arc lamp (450 W). The measurements were conducted with the assistance of Marian Chapran at CEA LITEN. The PL spectra, in **Figure 3-3-1-D**, displays also a gradual blue shift of excitation PL maxima, corroborating the E_g increase. It worth pointing out that the shoulder or

double peak phenomenon observed for some of the SCs has been previously associated with a combination of PL generated on the top surface (major peak) and filtered PL leaking out from the top surface and edges of the crystal after self-absorption and multiple reflection (secondary peak/shoulder).[24] The main PL emission peak of $MAPbBr_3$ SCs is caused by the radiative recombination of excitons at room temperature for the cubic structure.[25] A priori, the same mechanism takes place for mixed halide $MAPb(Br_{1-x}Cl_x)_3$ SCs.

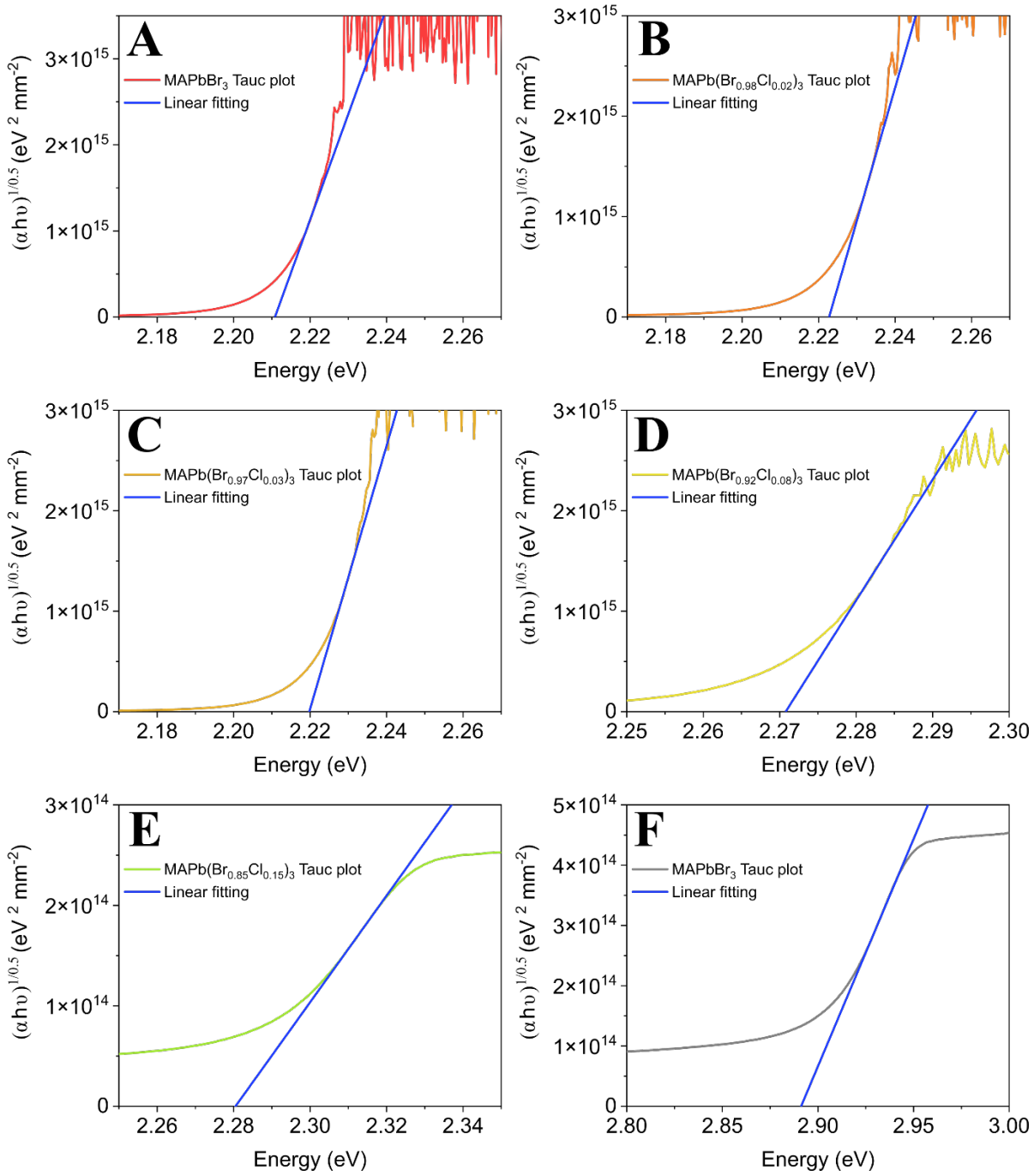

Figure 3-3-2. Tauc plots for $MAPb(Br_{1-x}Cl_x)_3$ SCs giving optical band gaps of: **(A)** E_g = 2.21 ± 0.08 eV for $MAPbBr_3$, **(B)** E_g = 2.22 ± 0.09 eV for $MAPb(Br_{0.98}Cl_{0.02})_3$, **(C)** E_g = 2.21 ± 0.05 eV for $MAPb(Br_{0.97}Cl_{0.03})_3$, **(D)** E_g = 2.27 ± 0.07 eV for $MAPb(Br_{0.92}Cl_{0.08})_3$, **(E)** E_g = 2.28 ± 0.03 eV for $MAPb(Br_{0.85}Cl_{0.15})_3$ and **(F)** E_g = 2.89 ± 0.04 eV for $MAPbCl_3$.

Table 3-3-1. Summary of $MAPb(Br_{1-x}Cl_x)_3$ SC production and associated optical band gap E_g, lattice parameter a, X-ray photon cross section σ_{cs}, molecular mass M, density ρ_d and attenuation length δ.

Material [a]	E_g [b] [eV]	a [c] [Å]	σ_{cs} [d] [$cm^2\ g^{-1}$]	M [e] [$g\ mol^{-1}$]	ρ_d [$g\ cm^{-3}$]	δ [mm]
$MAPbBr_3$	2.21 ± 0.08	5.928 ± 0.003	5.248	478.9	3.817	0.499
$MAPb(Br_{0.98}Cl_{0.02})_3$	2.22 ± 0.09	5.924 ± 0.003	5.243	477.6	3.814	0.500
$MAPb(Br_{0.97}Cl_{0.03})_3$	2.21 ± 0.05	5.921 ± 0.003	5.239	476.2	3.809	0.501
$MAPb(Br_{0.92}Cl_{0.08})_3$	2.27 ± 0.07	5.909 ± 0.005	5.225	472.2	3.796	0.504
$MAPb(Br_{0.85}Cl_{0.15})_3$	2.28 ± 0.03	5.890 ± 0.001	5.201	465.5	3.783	0.508
$MAPbCl_3$	2.89 ± 0.04	5.683 ± 0.001	4.626	345.4	3.139	0.689

[a] The x values given in the above chemical formulae is given by $\%Cl_{cryst}$, determined using Vegard's law (VL) and the XRD data.
[b] Optical bang gap E_g extracted via Tauc plot.
[c] Lattice parameter a extracted via Le Bail refinement on XRD diffractogram.
[d] X-ray photon cross section σ_{cs} obtained from NIST database at 50 keV.
[e] Molecular masses were calculated using targeted $\%Cl_{sol}$ values.

3.2 $MAPb(Br_{1-x}Cl_x)_3$ SC devices characterisation

Among the 51 crystals grown in this work, around one half was dedicated to physicochemical characterisations. The other half, 24 crystals (four series), photographed in **Figure 3-1-1**, were used to make $Cr/MAPb(Br_{1-x}Cl_x)_3/Cr$ optoelectronic devices. The results discussed below are extracted from the measurements performed on four different series, containing each an exemplary of every composition. From 2 to 4 SCs per composition were evaluated, depending on the characterisation technique (J-V, J-t, sensitivity and ToF measurements). The employed protocol is described in Chapter 2.

3.2.1 Current density stability and conductivity drifts

The first characterisation of a semiconducting material is generally the determination its J-V curves. By doing so, the stability of the internal electric field and the ohmic behaviour of the $Cr/MAPb(Br_{1-x}Cl_x)_3/Cr$ devices can be assessed. As voltage values were systematically normalised to the sample thickness, J-V and thus current density-electric field (J-E) characteristics were measured in the dark for electric fields ranging from -50 to 50 V mm^{-1}, using a 1 V s^{-1} scan rate. Each device was measured 5 times consecutively.

Globally, J-V sweeps of all devices do not exhibit any significant hysteresis whatever the composition, with or without chloride: see **Figure 3-3-4-A** for J-V sweeps example on a

single series and **Figure A 3-5-1** to **Figure A 3-5-4** for all evaluated series. Such hysteresis feature is commonly attributed to mechanisms induced by ion migration under non-equilibrium conditions.[26] Previous studies reported a hysteresis decrease for $MAPb(Br_{1-x}Cl_x)_3$ compositions compared to the pure bromide one.[8,12] They favoured a structural approach to this ion migration, by considering that the unit cell contraction and distortions induced by the presence of Cl inside the crystal lattice would reduce Br^- anions migration and consequently stabilise the current density under large electric field.[8] In our case, the reference $MAPbBr_3$ samples are already free from hysteresis and so do not benefit from such positive effect related to Cl addition.

Resistivity values were extracted from the J-V sweeps in the ohmic region reaching an average value of $\rho_{avg} = 1.1 \times 10^8$ Ω cm for $MAPbBr_3$, the crystals with mixed halide composition being in the same order of magnitude with the exception of $MAPbCl_3$, which is significantly less resistive ($\rho_{avg} = 2.9 \times 10^7$ Ω cm) as showed in **Figure 3-3-3**. In the present work, we found that the addition of small amounts of chloride during crystal growth does not improve the resistivity as oppositely demonstrated by Wei et al.[9] for $MAPb(Br_{0.98}Cl_{0.02})_3$ SC and Rybin et al.[8] for $MAPb(Br_{0.95}Cl_{0.05})_3$ reaching resistivities of 3.60×10^9 Ω cm and $1.522 \pm 0.156 \times 10^9$ Ω cm, respectively. In both studies, the increase of resistivity with optimal chloride compositions is 5 times above their reference $MAPbBr_3$ samples. A dopant compensation mechanistic approach has been proposed to explain the benefits of adding Cl in $MAPbBr_3$ by considering that it is intrinsically a p-type semiconductor due to lead vacancies V_{Pb} and that $MAPbCl_3$ is intrinsically a n-type semiconductor due to halide vacancies V_X.[9]

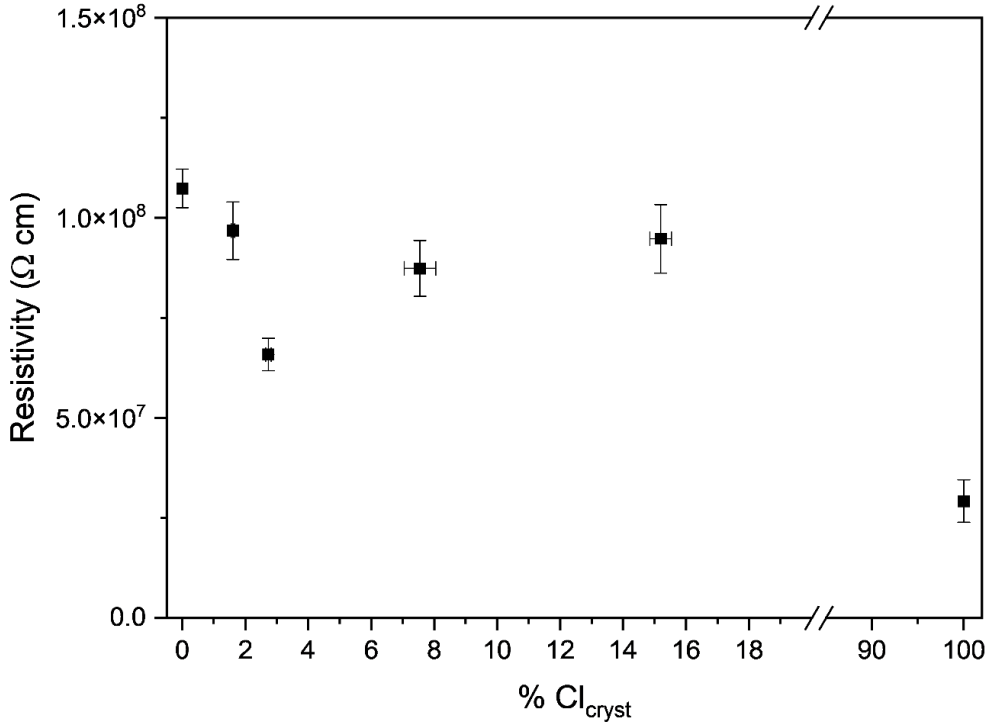

Figure 3-3-3. $MAPb(Br_{1-x}Cl_x)_3$ SC devices resulting average resistivity ρ_{avg} as a function of crystal Cl content $\%Cl_{cryst}$.

It is important at this point to define the term "doping" which is broadly used in halide perovskites literature to describe the introduction of any kind of impurity into the crystal lattice to control growth, stability and/or tune optoelectronic properties.[27,28] We refer to electrical doping when an impurity or defect generates free carriers or shifts the Fermi level,[29] which is the case in the work of Wei et al.[9] This doping relies on the formation of intrinsic (vacancies, interstitials or site substitutions) and/or extrinsic (impurities) defects. In the case of $MAPbBr_3$, Shi et al. showed a predominantly unipolar self-doping character, with a tuning range from degenerately p-doped under Br-rich and Pb-poor condition to intrinsic or slightly n-doped in Br-poor and Pb-rich condition.[30] According to EDX data (**Figure 3-2-4-A**), in our case, we are dealing with a "thermal equilibrium grown" Br-rich and Pb-poor $MAPbBr_3$ SC, with a Pb/Br ratio of 28.5 ± 0.4 % (which would point to V_{Pb} as predominant, thus p-doped) and a Cl-poor and Pb-rich $MAPbCl_3$ SC, with a Pb/Cl ratio of 34.3 ± 0.9 % (V_X predominant, thus n-doped). Stoichiometry is progressively reached with increasing Cl content, being the closest to it with a Pb/X value of 30.5 ± 1.3 % for $MAPb(Br_{0.85}Cl_{0.15})_3$ (similar population proportion then for both V_{Pb} and V_X).

One would then expect a dopant compensation in our SCs, but the above-mentioned improvements were not seen in this study for both hysteresis and resistivity, even though our SCs are in the considered optimal range %Cl ≈ 2 - 17 ($MAPb(Br_{0.98}Cl_{0.02})_3$ - $MAPb(Br_{0.83}Cl_{0.17})_3$).[8,9,12] The difference in behaviour with respect to the literature could be partially explained by the initial type of doping of $MAPbBr_3$ and associated defect structures. Experimental conditions leading to an n-type $MAPbBr_3$ reference would explain why addition of Cl do not have a significant impact on the resistivity. In that case, the n-type self-compensation brought by Cl would be inefficient. By taking into consideration just intrinsic defect doping, we could consider to control the initial doping by tuning the precursors ratio PbX_2/AX in $APbX_3$, A being any cation forming the 3D structure. Despite a few experimental examples managing a transition from p-type to n-type for $MAPbI_3$ and $FAPbI_3$ (FA^+ = formamidinium),[31,32] just one transition from p-type to n-type with increasing $PbBr_2$/MABr ratio has been observed in $MAPbBr_3$ SC.[33] Even if the type of doping can be reversed, intrinsic carrier densities of $\sim 10^7$ cm^{-3} (determined via Hall effect)[33] for both p-type (Pb-poor) and n-type (Pb-rich) suggest a limited doping range achievable through precursors ratio variations.[29] Regarding now just extrinsic defect doping, the inclusion of impurities in $MAPbBr_3$ have also been studied with the particular objective to alter the unipolar p-type character described earlier.[30] Nevertheless, none of the impurities considered could achieve n-type doping, owing to heavy compensation from intrinsic defects, such as V_{Pb} and V_{Br}.[29,34] Based on these arguments and the lead deficient Pb/Br ratio measured by EDX, our $MAPbBr_3$ references could be effectively considered as a p-doped material, where no benefits in terms of resistivity and electrical stability were obtained from adding Cl. We noticed that all attempts to measure the n- or p-type polarity of our $MAPbBr_3$ devices by hot probe method failed due to lack of reproducibility and stability of the results, most probably due to interference of parasitic

ion migration during the measurements. It is worth noting that the way Cl^- anions interacts with the host crystal lattice is unknown. Considering that we are dealing with a solid solution, according to the XRD data, one considers that Cl substitutes Br in the octahedron. However, potentially other positions could be occupied by Cl^- anions, such as interstitials Cl_i, creating new defects as well as inducing other defects with other chemical species and/or band structure modifications. We have to take into consideration that adding Cl in solution impacts several aspects such as the chemistry involved during crystal growth: there is a decrease in solubility and an increase in the diversity of lead complexes involved by the addition of MACl. Incorporating Cl in the $MAPbBr_3$ structure would improve the resistivity and hysteresis like for previous works for a given set of defects thanks to the interactions of Cl with these, causing the reported changes in electrical properties.

An important point should be made to partially explain the diversity of optoelectronic properties found in the literature for $MAPbBr_3$, $MAPb(Br_{1-x}Cl_x)_3$ and $MAPbCl_3$, which can also be extended to all type of perovskites. The properties of most if not any material depends intrinsically on the crystal growth and associated methods. In the literature, different synthesis techniques with different experimental settings are being employed sometimes to produce crystals that are then subsequently compared for a single characteristic or property. In the case of SCs, even for the ITC method, sample-to-sample variability in crystal quality and performance is well known for $MAPbBr_3$, which can exceed an order of magnitude for a given optoelectronic property very easily.[29] Indeed, the crystal quality depends significantly on various experimental parameters such as thermodynamic equilibrium, impurity rate, supersaturation regime applied to the solution through rate and nature of the employed temperature ramp. As shown in Chapter 2, optimisation of SC growth has been one of our main targets to attain device sampling reproducibility.[1,4] When comparing SCs grown by abrupt ITC method (heating up precursors solution till passing supersaturation limit temperature), linear temperature and adaptive temperature ramps (MITC methods) taking into consideration solution supersaturation evolution throughout crystal growth, one can reduce the variability in crystalline quality and optoelectronic properties for the latter. Nevertheless, even crystals within an optimised crystal growth production batch can present elements pathologically bad or with above average performance despite having reduced this variability. We are then potentially discussing about apparent maxima/minima with non-optimised SCs that could be benefiting from Cl addition. This being said, small amounts of chloride could potentially have a positive impact on resistivity or sensitivity for SCs with certain type of defects where a dopant compensation mechanism could take place.

One possible positive impact associated with the improved stoichiometry accompanying the Cl incorporation is an improved stability over time of the device (lower ionic conductivity). Following the evolution of the current density with time can then provide valuable information on the conductivity drift. For J-t measurements, the samples were constantly biased at

50 V mm^{-1} and both dark current density and conductivity drift values were measured. The conductivity drift is defined by **Equation (3-11)**:

$$\sigma_{drift} = \frac{1}{F}\frac{\Delta J}{\Delta t} \quad (3\text{-}11)$$

Where σ_{drift} is the conductivity drift (S mm^{-1} s^{-1}), ΔJ is the difference in dark current density after 10 min under bias (nA mm^{-2}), Δt is the time difference (here 10 min); and F is the applied electric field (here 50 V mm^{-1}). During the J-t measurements in the dark, the SC devices showed stable signal over time, as shown in **Figure 3-3-4-B**. For the evaluation time of 10 min, $MAPbBr_3$ showed a conductivity drift σ_{drift} of 7.9 × 10^{-5} S m^{-1} s^{-1}, which gradually decreased with increasing Cl content, reaching a minimal value of 2.9 × 10^{-5} S m^{-1} s^{-1} for $MAPb(Br_{0.85}Cl_{0.15})_3$. Both values correspond to drifts of 4.7 % and 3.8 % of initial dark current under 50 V mm^{-1}, respectively. This improvement may be linked to improved stoichiometry (Pb/X ratio) of $MAPb(Br_{0.85}Cl_{0.15})_3$ when compared to $MAPbBr_3$, as shown in the previous part. It has to be noted that all compositions drifts were lower than what was previously reported in the literature (see **Table 3-3-2** for all compositions σ_{drift} values).[9]

Table 3-3-2. Summary of $MAPb(Br_{1-x}Cl_x)_3$ SC production and associated J-t analyses including average dark current density J_{mean}, difference in dark current density after 10 min under bias ΔJ, conductivity drift σ_{drift} and associated percentage of initial dark current drift after 10 min at 50 V mm^{-1} *%drift*.

Material[a)]	J_{mean}[b)] [nA mm^{-2}]	ΔJ[c)] [nA mm^{-2}]	σ_{drift} [S m^{-1} s^{-1}]	*%drift* [%]
$MAPbBr_3$	46.71	2.19	7.95 × 10^{-5}	4.70
$MAPb(Br_{0.98}Cl_{0.02})_3$	52.81	1.34	4.59 × 10^{-5}	2.53
$MAPb(Br_{0.97}Cl_{0.03})_3$	79.87	1.17	4.53 × 10^{-5}	1.47
$MAPb(Br_{0.92}Cl_{0.08})_3$	58.18	1.37	4.42 × 10^{-5}	2.35
$MAPb(Br_{0.85}Cl_{0.15})_3$	22.41	0.86	2.92 × 10^{-5}	3.84
$MAPbCl_3$	109.51	4.00	8.95 × 10^{-5}	3.66

a) The *x* values given in the above chemical formulae is given by $\%Cl_{cryst}$, determined using Vegard's law (VL) and the XRD data.
b) J_{mean} values were established after stabilisation of the signal till the end of the measurement.
c) The selected start and end times to define ΔJ were averaged over 20 s.

While the benefit of Cl incorporation on the resistivity remained elusive, it could still boost the device performance for direct X-ray detection through indirect ways. Therefore, we determined the sensitivity *S* for the X-ray detection devices of all Cl contents.

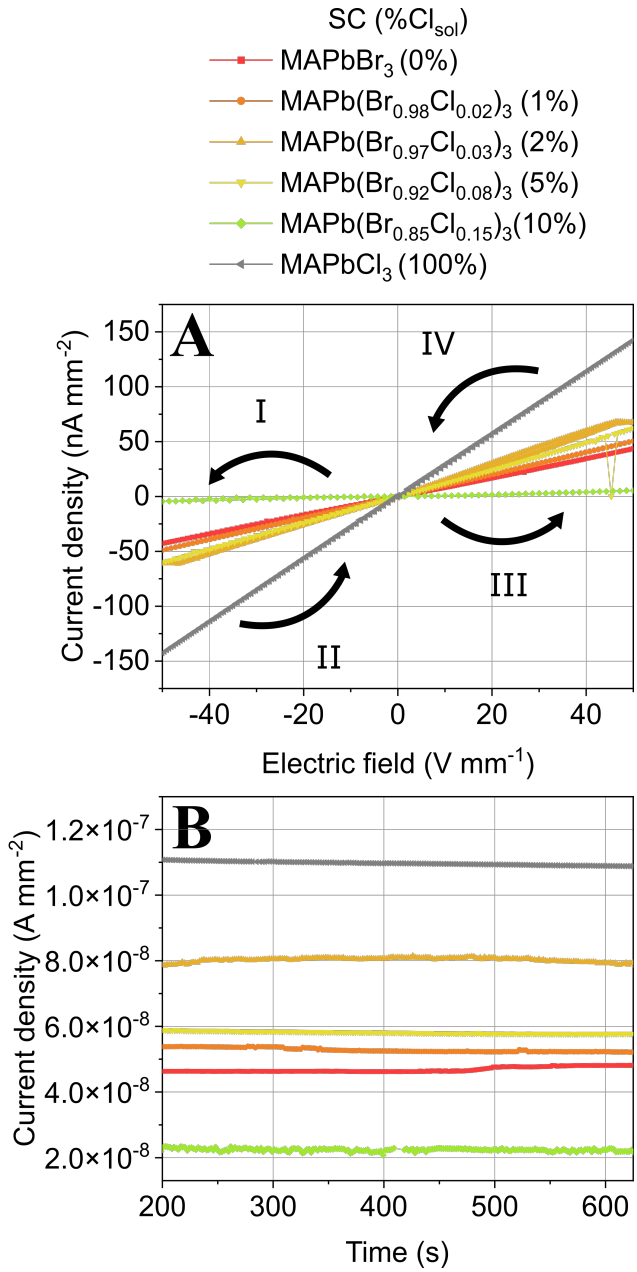

Figure 3-3-4. Electric stability of MAPb(Br$_{1-x}$Cl$_x$)$_3$ SC devices. (A) Example of J-V sweeps performed for a series of SC devices forward from 0 to -50 V mm^{-1} (step I), then from -50 to 50 V mm^{-1} (step II then III), and back to 0 V mm^{-1} (step IV). **(B)** Dark current stability of SC devices under electrical field of 50 V mm^{-1}.

3.2.2 Sensitivity

We measured photocurrent pulses under X-ray illumination to acquire the sensitivity values for the different MAPb(Br$_{1-x}$Cl$_x$)$_3$ compositions: see **Figure 3-3-5** for average sensitivity S_{avg} values and **Figure A 3-6-1** for an example of stable photocurrent generated under pulsed X-ray irradiation for the MAPb(Br$_{0.85}$Cl$_{0.15}$)$_3$ SC device. Comparable S_{avg} values were extracted by using the specific and reproducible biasing protocol, described in Chapter 2. An evident difference is seen once again between MAPbBr$_3$ and MAPbCl$_3$. The former shows an average sensitivity value of S_{avg} = 0.88 µC mGy$_{air}^{-1}$ cm^{-2} and the latter an average value of

S_{avg} = 0.40 µC mGy_{air}^{-1} cm^{-2}, both evaluated at 50 V mm^{-1}. For intermediate compositions $MAPb(Br_{1-x}Cl_x)_3$, an optimal performance was found for $MAPb(Br_{0.85}Cl_{0.15})_3$ reaching a sensitivity value of S_{avg} = 1.87 µC mGy_{air}^{-1} cm^{-2} in average and a maximal one of $S \approx 3$ µC mGy_{air}^{-1} cm^{-2} at 50 V mm^{-1}. This value is higher than the sensitivity of CsI(Tl) - or a-Se-based flat panels (0.5 and 0.3 µC mGy_{air}^{-1} cm^{-2} at RQA5 spectral quality, respectively). It worth noting, that a comparison between this $MAPb(Br_{0.85}Cl_{0.15})_3$ SC and CsI(Tl) or a-Se PCs is not fair, given the different nature of the tested material and how different the way to determine the sensitivity in a semiconductor can be. Nevertheless, $MAPb(Br_{0.85}Cl_{0.15})_3$ appears as the most promising composition in this study, doubling $MAPbBr_3$ sensitivity and coupling with the Pb/X ratio closest to stoichiometry. Such improvement in sensitivity may be related to a change in the charge collection efficiency symbolised by the $\mu\tau$ product.[35] This eventuality is discussed further down.

To get a better insight in the Cl effect on the optoelectronic properties, we measured the charge carrier mobility as a function of Cl content by using laser ToF technique.

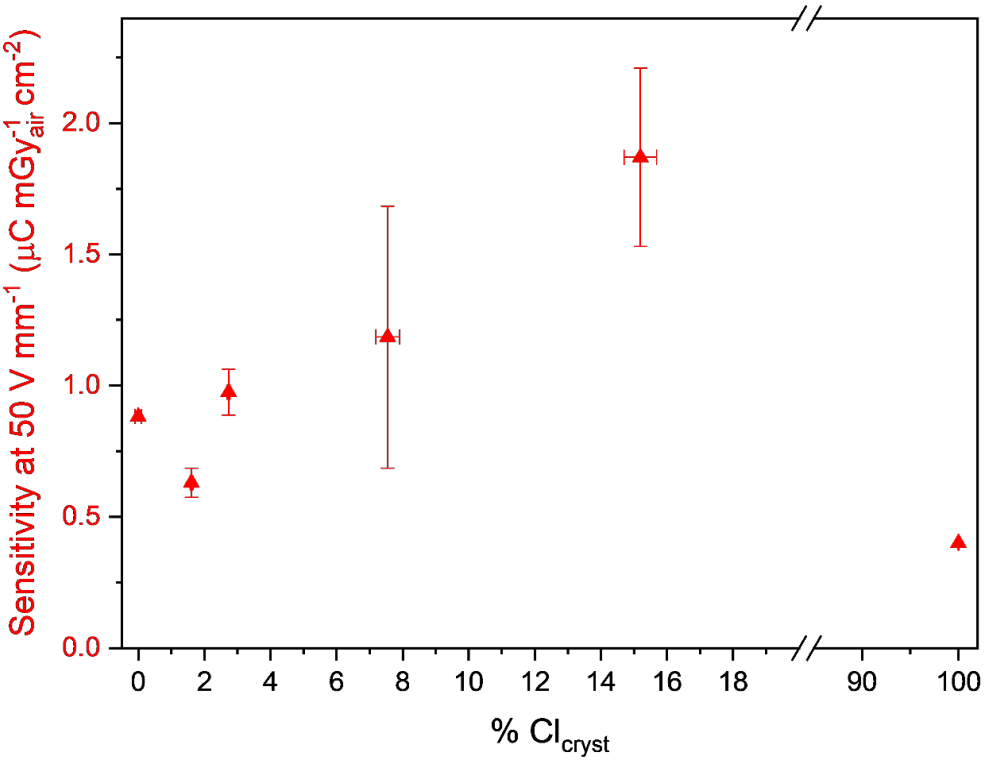

Figure 3-3-5. $MAPb(Br_{1-x}Cl_x)_3$ SC devices resulting average sensitivity S_{avg} as a function of crystal Cl content $\%Cl_{cryst}$.

3.2.3 Charge carrier mobility

In contrast to resistivity and sensitivity, a decrease in hole mobility μ_h was observed when Cl content increases: see **Figure 3-3-6** for average hole values $\mu_{h\text{-}avg}$ and **Figure 3-3-7** for examples of transit times recorded during ToF measurements per composition. It is worth pointing out that no electron mobility μ_e could be satisfactorily drawn from the measurements.

The reason for that has already been explained by our group in a previous work on $MAPbBr_3$ SC devices: the mobility-lifetime product of electrons ($\mu_e\tau_e$) is not large enough to allow electrons to fully transit their path.[2,3] Even though the average hole mobility $\mu_{h\text{-}avg}$ decreases from 15.8 to 9.2 $cm^2\ V^{-1}\ s^{-1}$ for $MAPbBr_3$ and $MAPb(Br_{0.85}Cl_{0.15})_3$, respectively, sensitivity doubles, meaning an enhancement of the $\mu_h\tau_h$ product, and therefore a potential increase in hole lifetime τ_h.

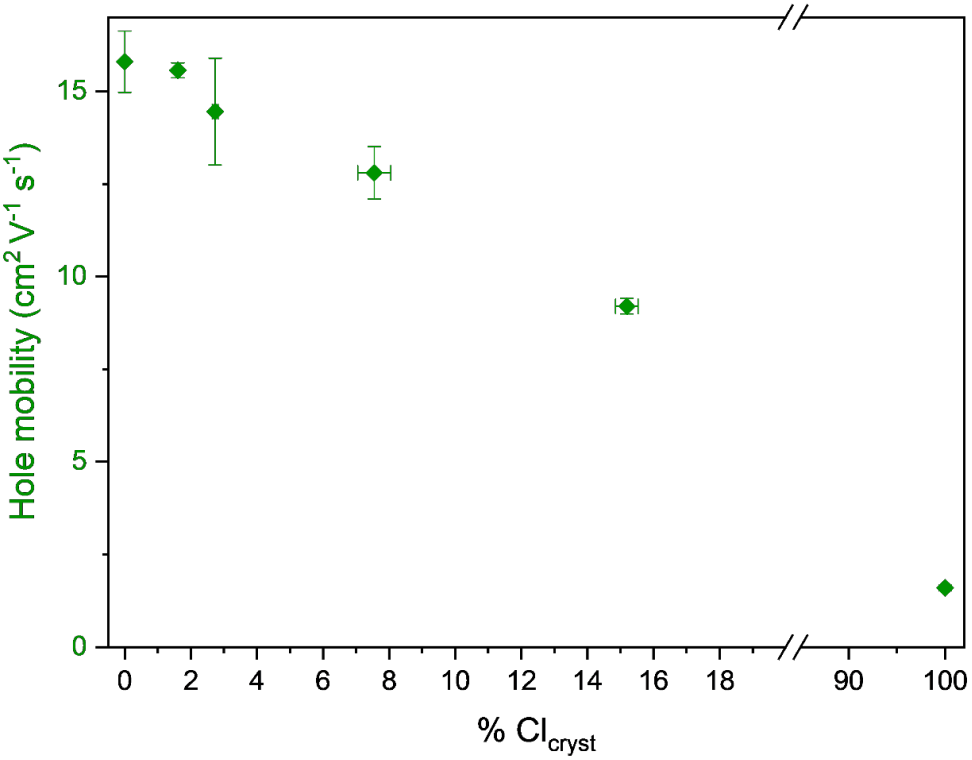

Figure 3-3-6. $MAPb(Br_{1-x}Cl_x)_3$ SC devices resulting average hole mobility $\mu_{h\text{-}avg}$ as a function of crystal Cl content $\%Cl_{cryst}$.

To explain such longer lifetime of charge carriers in $MAPb(Br_{1-x}Cl_x)_3$ materials, a few mechanisms highlighting band and defect structural alterations have been proposed. Firstly, Li et al.[15] reported, by using time-resolved photoluminescence spectroscopy with two-photon femtosecond laser excitation experiments, that incorporation of Cl inside SCs to a maximum of %Cl = 19 ($MAPb(Br_{0.81}Cl_{0.19})_3$) would create longer lifetime. Higher concentrations of Cl in the SC bulk would lead to measurable defect formation within the crystal, which would act as trapping sites effectively reducing the PL lifetime. A Rashba effect (momentum-dependent splitting of spin bands) in the bulk was theorised to be at the origin of this longer lifetime.[15] Secondly, another hypothesis presented by Tyler Mix et al.,[36] via transient reflectivity spectroscopy and nonadiabatic molecular dynamics simulations, explained that the addition of Cl increases the observed rate of hot carrier cooling and the calculated electron−phonon coupling constants. This induces a smaller ambipolar mobility,[36] which would be consistent with our hole mobility evolution. Incorporation of Cl^- anions would effectively induce more

structural fluctuations in $MAPb(Br_{1-x}Cl_x)_3$ than in $MAPbBr_3$ samples, additionally causing excess energy to dissipate faster and subsequently stabilising charge carriers.

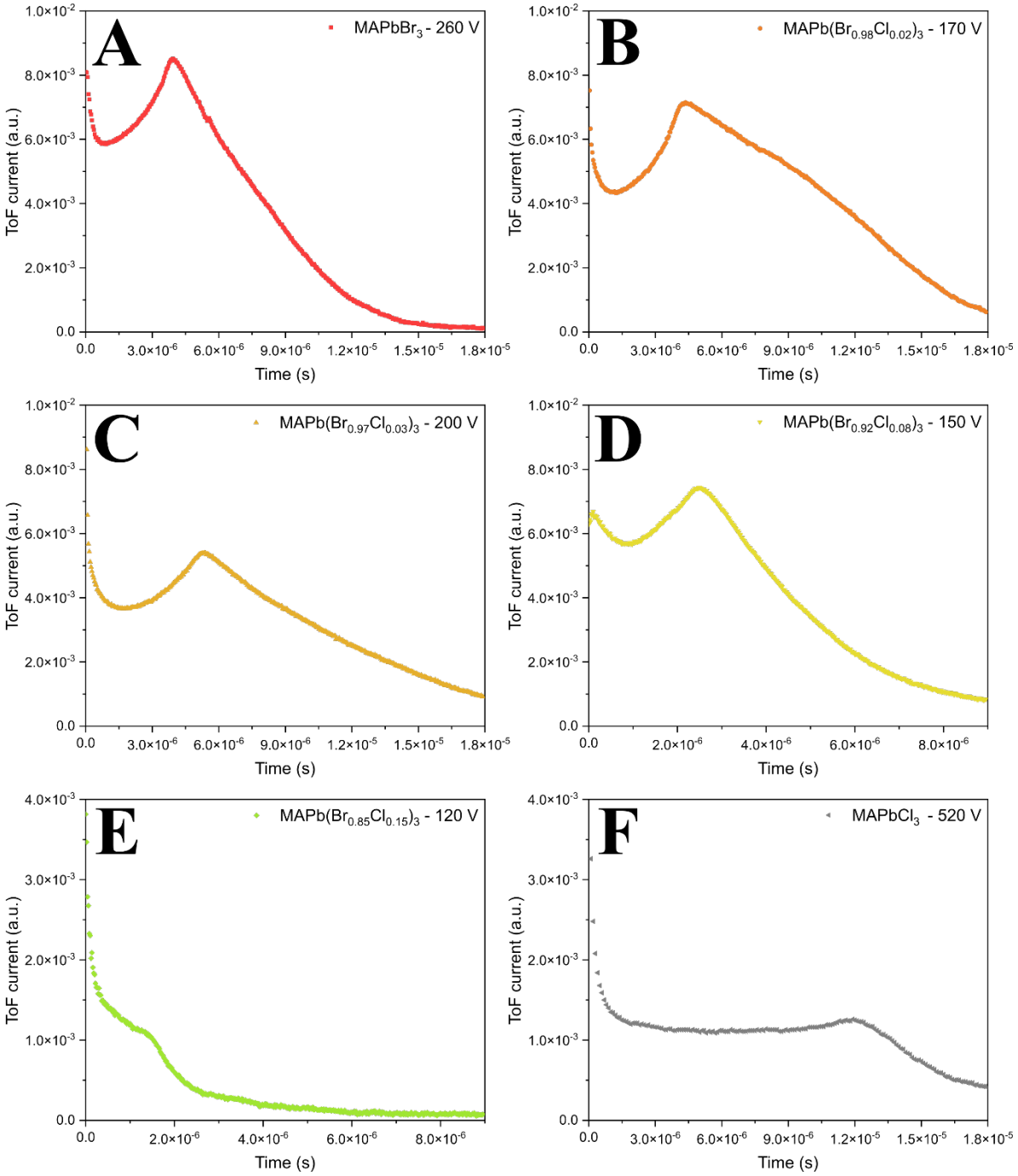

Figure 3-3-7. Laser ToF measurements on $MAPb(Br_{1-x}Cl_x)_3$ SC devices: **(A)** at 260 V for $MAPbBr_3$, **(B)** at 170 V for $MAPb(Br_{0.98}Cl_{0.02})_3$, **(C)** at 200 V for $MAPb(Br_{0.97}Cl_{0.03})_3$, **(D)** at 150 V for $MAPb(Br_{0.92}Cl_{0.08})_3$, **(E)** at 120 V for $MAPb(Br_{0.85}Cl_{0.15})_3$ and **(F)** at 520 V for $MAPbCl_3$.

Even if two-photon-excited photoluminescence, reflectivity and laser ToF measurements rely on different phenomena, the underlying physics should be the same and

lifetime is expected to increase with increasing Cl content up to a certain limit, perhaps thanks to mechanisms such as the Rashba effect and/or faster hot carrier cooling. During ToF experiments, the electron transit time was not high enough to exceed the electron lifetime; hence, no improvement nor degradation of it with varying Cl content could be evaluated. Despite this and not having measured μ_e, the same logic as for holes could be applied to electrons: a gradual increase of lifetime τ_e could be considered while incorporating chlorine in the $MAPbBr_3$ structure, thus leading to an improvement of the electron diffusion length.

3.2.4 Two-charge carriers Hecht modelling

To back up the hypothesis of longer lifetime for both charge carriers, modelling has been performed on S-V data to extract mobility-lifetime of the SC devices. Mobility-lifetime product $\mu\tau$ estimation using Hecht equation[37] or the so-called modified Hecht equation[38–40] is a powerful tool to assess the quality of an X-ray sensitive semiconductor. As seen in Chapter 2, it relies essentially on the measurement of the photocurrent – or time integral of the photocurrent – flowing in the material under X-ray illumination as a function of the externally applied bias. These equations must be handled with great care, as they are based on several assumptions that shall be verified beforehand. Both equations derivate from the Ramo theorem, hence, they rule out any contribution that may originates from other effects that might alter the $\mu\tau$ product values extracted from the Hecht fits, such as photoconductive gain.[41] Among the hypotheses made explicit in Chapter 2, it is critical that the electric field F is uniform throughout the detector and equal to V/L ($F = V/L$) in order to fit correctly the data using Hecht equation. Yet, a growing number of reports tend to point out that an externally applied bias displaces mobile ions towardsthe electrodes interfaces, and lead to distortion of the electric field in the device.[42–44] Ion accumulation at the vicinity of the electrode may occur more intensely during steady-state measurements involving continuous biasing procedures,[45] which is typically the case of X-ray induced photocurrent measurements. Such effects attributed to ion migration have been reported for several perovskite materials, $MAPbBr_3$,[42,46] $CsPbBr_3$[47] and $MAPbI_3$,[48] and thus seem to be a typical feature of perovskite optoelectronics. This must be taken into account when one carries out estimation of $\mu\tau$ products, as a non-uniform electric field in the device may alter the quality of the Hecht fits and lead to wrong conclusions.[49]

That being said, we performed a complete analysis of the integrated currents generated under X-ray pulses. The data was fit, by Eric Gros d'Aillon and Ferdinand Lédée, using the two-carriers Hecht equation (**Equation (3-12)**) to extract both electron and holes $\mu\tau$ products:[50]

$$\eta_{cc}(x,V) = \frac{\mu_e \tau_e V}{L^2}\left[1 - e^{-\frac{xL}{\mu_e \tau_e V}}\right] + \frac{\mu_h \tau_h V}{L^2}\left[1 - e^{-\frac{L(L-x)}{\mu_h \tau_h V}}\right] \quad (3\text{-}12)$$

Where η_{cc} is the charge induction efficiency, μ_e and μ_h are the mobilities of electrons and holes ($cm^2\ V^{-1}\ s^{-1}$), respectively, $\tau_e$and τ_h are the lifetimes of electrons and holes (s), respectively, L is the device thickness (cm), x is the X-ray interaction position in the crystal (cm), and V is the

applied bias (V). Unlike the one-carrier Hecht equation, the two-carriers counterpart considers the contributions of both electrons and holes to the photocurrent, and thus requires to take into account the distribution of photogenerated charges that decays exponentially within the depth of the material, as seen in Chapter 2. Both, this distribution and the electron-hole pair creation energy W were adapted for each crystal composition. This leads to a more accurate evaluation of $\mu\tau$ products for high X-ray energies, as well as discrimination of electron and holes mobility-lifetime products. It should be noted that we considered a uniform electric field in our model. The relevancy of this assumption depending on the sample composition will be discussed later on. A deeper work is underway considering a non-uniform electric field as well as several types of trapping centres, which will be published in a future paper.

The model depicted above was used to fit the experimental sensitivities under X-rays for each perovskite sample. All the S-V curves and the best corresponding fits are plotted in **Figure 3-3-8**, S values are normalised to the maximal theoretical values S_{max}, defined in the previous chapter.

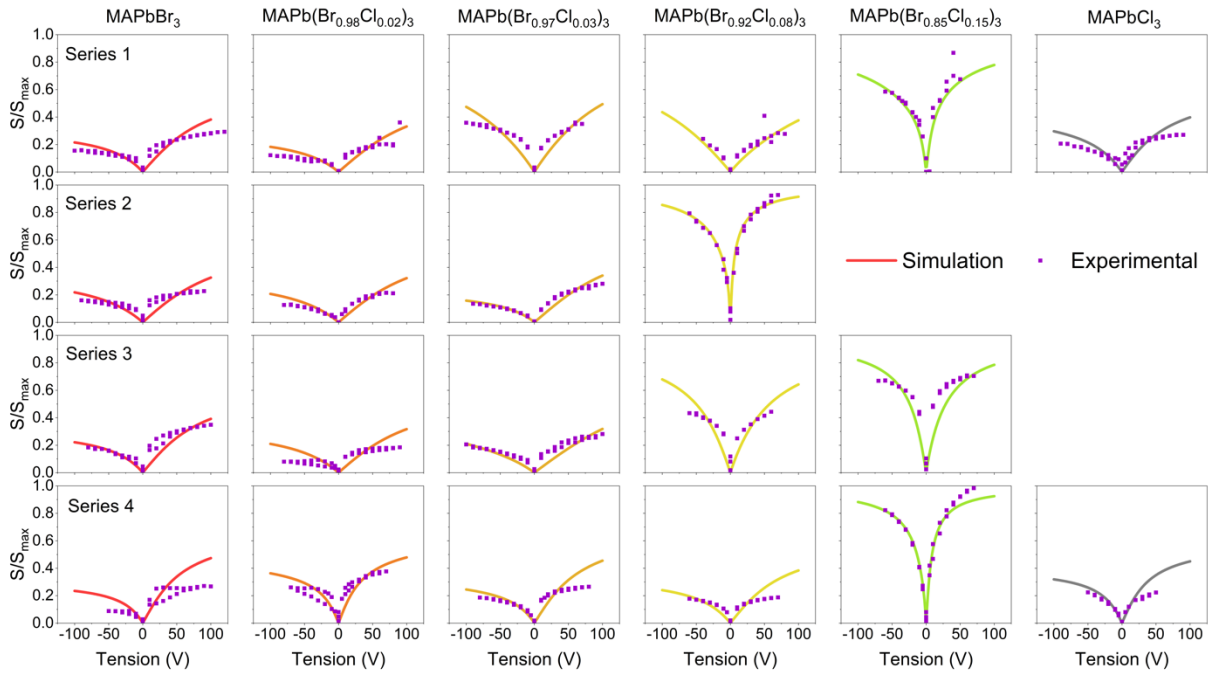

Figure 3-3-8. All four series experimental sensitivity-voltage (S-V) curves (purple plots) and associated fittings (colour plots) using the two-charge carriers Hecht equation allowing extracting both holes and electrons mobility-lifetime products, $\mu_h\tau_h$ and $\mu_e\tau_e$, respectively. S values are normalised to the maximal theoretical sensitivity value S_{max}.

On the one hand, it can be seen that for most of the samples, the experimental data fit poorly to the model. More precisely, for all $MAPbBr_3$, $MAPb(Br_{0.98}Cl_{0.02})_3$, $MAPb(Br_{0.97}Cl_{0.03})_3$ samples and almost all $MAPb(Br_{0.92}Cl_{0.08})_3$ samples, the S-V curves reach a plateau with increasing voltage with a lower value than that of the model prediction. This essentially means that even with bias values extending to infinity the charge induction efficiency will never reach

unity – which is not in accordance with **Equation (3-12)**. **Figure 3-3-9-A** depicts an example of generated photocurrent in $MAPbBr_3$ SC device under X-ray irradiation at three different voltages and **Figure 3-3-9-C** shows its associated experimental data and Hecht modelling. An explanation lies in the relevancy of the starting hypothesis: $F = V/L$, which is implicitly or explicitly admitted in the vast majority of publications involving perovskite ionising radiation detectors.[9,38,39,51–54] Yet a non-constant electric field in the device will greatly change the outcome of the Hecht fits, as it has been showed in previous works on linear decreasing electric fields.[42,49] In addition, Liu et al. showed that ion accumulation at the vicinity of the electrodes leads to significant decrease of the electric field in the volume of the detector as the net charges induce by the mobile ions screen the externally applied electric field.[44] This effect creates in the middle of the detector a "dead zone" for the photogenerated charges, severely impeding the charge induction efficiency.

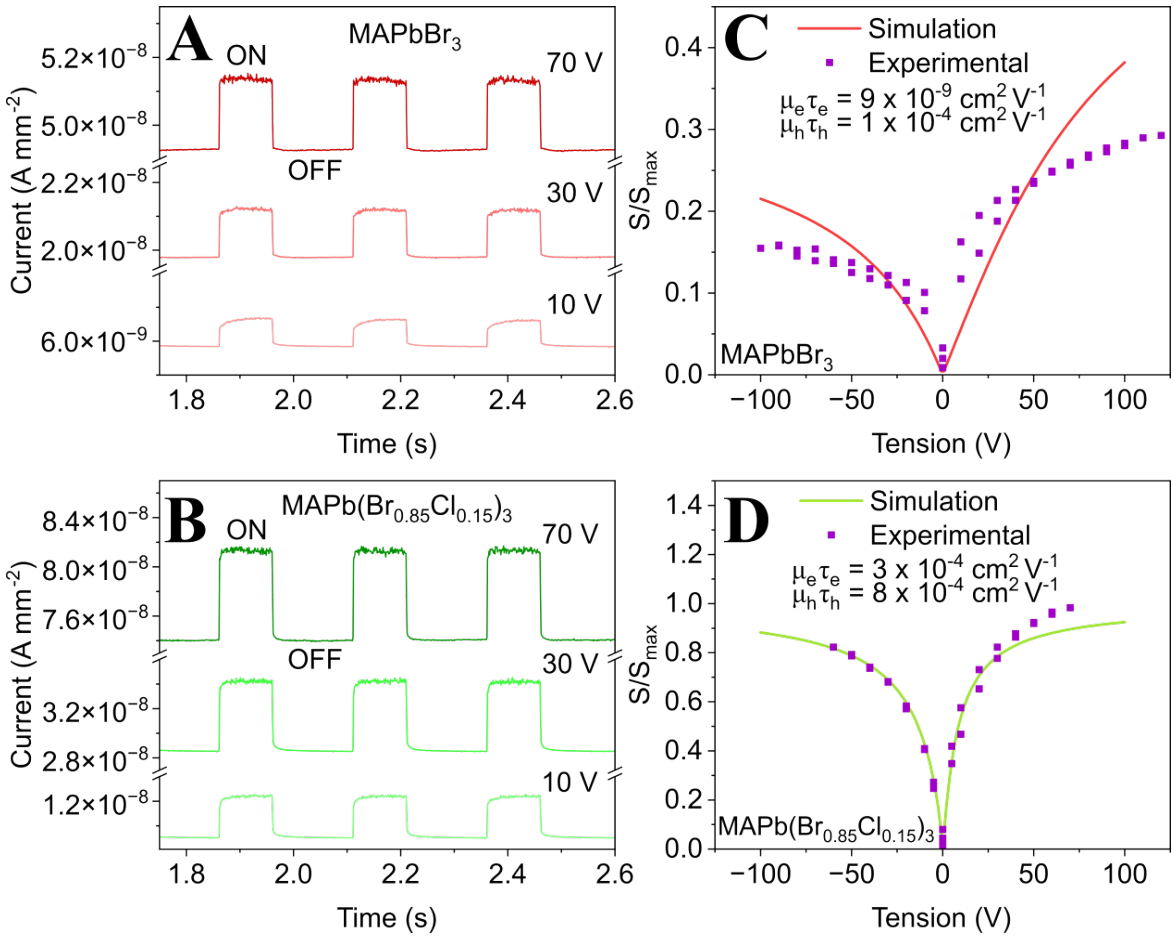

Figure 3-3-9. Two-charge carriers Hecht modelling. Photocurrent generated under pulsed X-ray irradiation during 100 ms at 4 Hz on **(A)** $MAPbBr_3$ and **(B)** $MAPb(Br_{0.85}Cl_{0.15})_3$ SC devices for sensitivity measurements at 10, 30 and 70 V. **(C)** Series 1 $MAPbBr_3$ SC device S-V simulation (red plot) and experimental (purple plot) curves and **(D)** series 4 $MAPb(Br_{0.85}Cl_{0.15})_3$ SC device S-V simulation (green plot) and experimental (purple plot) curves. The simulated S-V curve results from the Hecht fit for two-charge carriers. Associated $\mu\tau$ products are displayed in inset.

On the other hand, the model fits correctly for at least one $MAPb(Br_{0.92}Cl_{0.08})_3$ and two $MAPb(Br_{0.85}Cl_{0.15})_3$ crystals, which implies that there is uniformity of the electric field in all the volume of the detector for these samples. **Figure 3-3-9-B** depicts an example of generated photocurrent in $MAPb(Br_{0.85}Cl_{0.15})_3$ SC device under X-ray irradiation at three different voltages and **Figure 3-3-9-D** shows its associated experimental data and Hecht modelling. We believe this improvement of the fit stems from the increase of the Pb/X ratio, which gets closer to the ABX_3 stoichiometry with increasing Cl content (**Figure 3-2-4-A**). Being closer to stoichiometry translates into a reduction of the density of defects (e.g. halide vacancies V_X) that in halide perovskites are mobile and contribute to ion mobility upon application of an external electric field.[26,48,55] Also, at a local level, while Br^- anions would screen each other (low binding energy with Pb) resulting in ion migration, Cl^- anions would reduce this screening in the inorganic octahedra, probably due to difference in binding between Pb-Cl and Pb-Br.[12] The lower defect density in $MAPb(Br_{0.92}Cl_{0.08})_3$ and $MAPb(Br_{0.85}Cl_{0.15})_3$ crystals would prevent the build-up of the ionic space charges near the electrodes, and maintain the uniformity of the electric field in the device. These results are in good accordance with the observed decrease in conductivity drift with increasing Cl content (**Table 3-3-2**). Conductivity drift is widely attributed to the movement of mobile ions, and it was reported that lower density of defects associated with mobile ions reduces dark current drift.[56,57] More specifically for series 4 $MAPb(Br_{0.85}Cl_{0.15})_3$ SC device, the two-carriers Hecht model fits the experimental data well and yields very high $\mu\tau$ product value of $\mu_h\tau_h = 8 \times 10^{-4}$ cm² V^{-1} for holes and $\mu_e\tau_e = 3 \times 10^{-4}$ cm² V^{-1} for electrons, respectively. By using laser ToF-determined hole mobility μ_h, hole lifetimes for $MAPbBr_3$ and $MAPb(Br_{0.85}Cl_{0.15})_3$ are estimated at $\tau_h = 7$ µs and $\tau_h = 75$ µs, respectively, confirming our initial hypothesis to some extent. These values are in accordance with the hole ToF measurements themselves. **Figure 3-3-10** shows the ToF hole current waveforms for $MAPbBr_3$ and $MAPb(Br_{0.85}Cl_{0.15})$ devices at different biases.

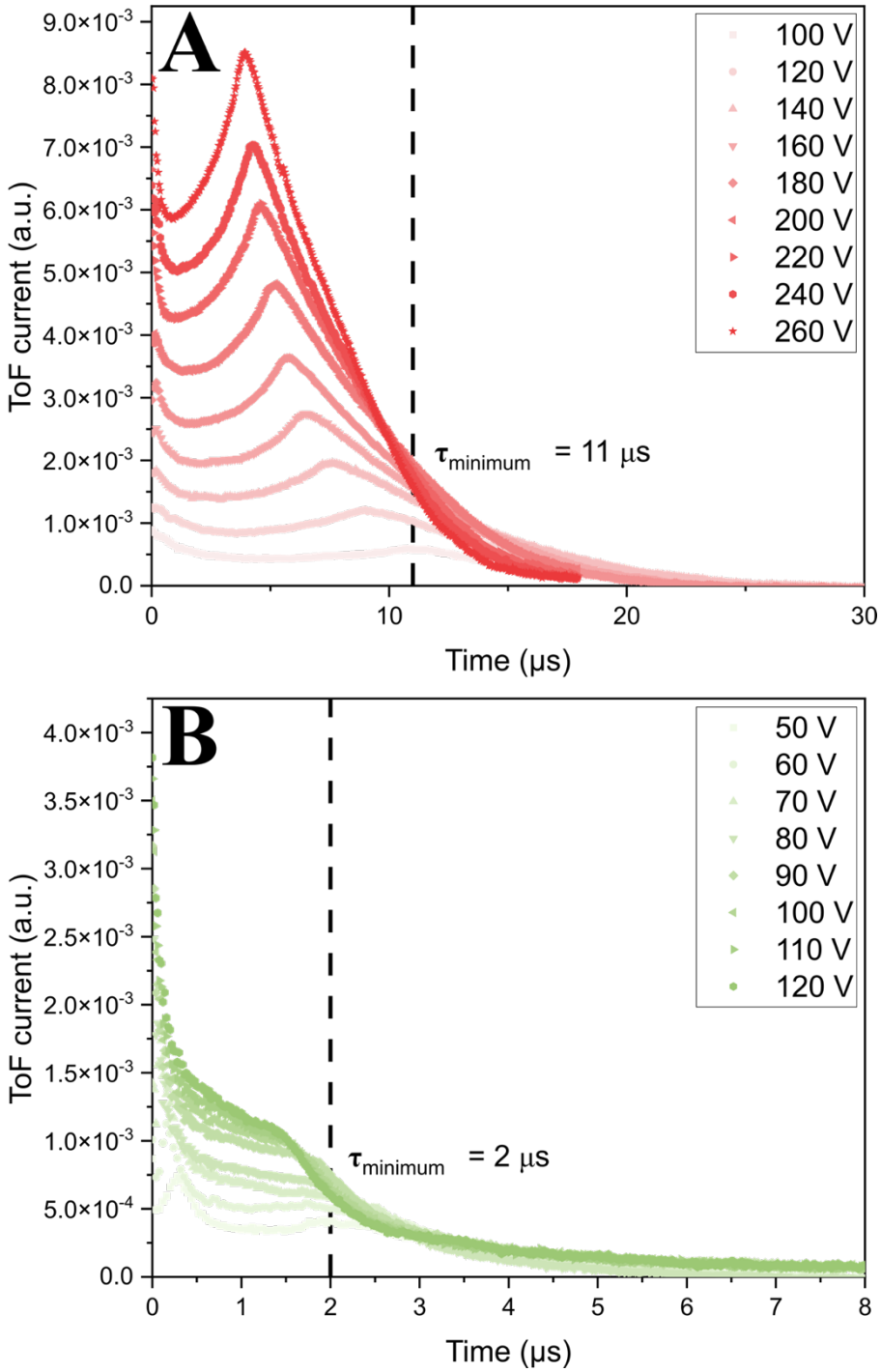

Figure 3-3-10. Hole ToF waveforms at different biases for **(A)** $MAPbBr_3$ and **(B)** $MAPb(Br_{0.85}Cl_{0.15})_3$ SC devices.

For $MAPb(Br_{0.85}Cl_{0.15})$, a clear inflection of the waveform can be observed at a moderate voltage of 50 V, indicating a transit time for holes of t_t = 2 μs (see Chapter 2). It implies that the lifetime of holes cannot be lower than 2 μs in the drift-diffusion regime. These lifetimes in the microsecond range agree with results from previous works.[42,58] All $\mu\tau$ product values for both electrons and holes extracted from two-charge carriers Hecht model are displayed in **Table A 3-6-1**. These values are significantly better than that of a-Se, comparable to that of the

highest quality TlBr and close to that of state of the art materials for high-energy radiation detection, CdTe and CZT (see **Table 3-3-3**).[59–62] However, these results suggest that further development in the base material quality and/or synthesis is needed to attain state-of-the-art performances (e.g. precursors purification, doping, post-treatments).

Table 3-3-3. $MAPbBr_3$, $MAPb(Br_{0.85}Cl_{0.15})_3$ and some known ionising radiation detectors mobility μ, lifetime τ and $\mu\tau$ product values for electrons and holes

Material	Electron mobility μ_e [$cm^2\ V^{-1}\ s^{-1}$]	Hole mobility μ_h [$cm^2\ V^{-1}\ s^{-1}$]	Electron lifetime τ_e [s]	Hole lifetime τ_h [s]	$\mu_e\tau_e$ product [$cm^2\ V^{-1}$]	$\mu_h\tau_h$ product [$cm^2\ V^{-1}$]
a-Se [a]	0.005	0.14	10^{-6}	10^{-6}	5×10^{-9}	1.4×10^{-7}
TlBr [a]	6	-	2.5×10^{-6}	-	1.6×10^{-5}	1.5×10^{-6}
CdTe [a]	1100	100	3×10^{-6}	2×10^{-6}	3.3×10^{-3}	2×10^{-4}
CZT [a]	1350	120	10^{-6}	5×10^{-8}	1×10^{-3}	6×10^{-6}
$MAPbBr_3$ [b]	-	15 [c]	-	7×10^{-6} [d]	9×10^{-7}	1×10^{-4}
$MAPb(Br_{0.85}Cl_{0.15})_3$ [b]	-	11 [c]	-	7.5×10^{-5} [d]	2.5×10^{-4}	8×10^{-4}

[a] Extracted from reference.[59]
[b] This work: series 3 $MAPbBr_3$ and series 4 $MAPb(Br_{0.85}Cl_{0.15})_3$ were chosen here for the comparative table because of their relatively good Hecht fitting for two-charge carriers.
[c] Hole mobilities μ_h determined via laser ToF measurements.
[d] Hole lifetime τ_h estimated from the two-charge carriers Hecht fitting $\mu_h\tau_h$ product and measured laser ToF hole mobility μ_h.

3.2.5 Sensitivity coupled with X-ray absorbed fraction and dark current density

As said earlier and seen in **Figure 3-1-1**, the size disparity of the SC devices results in different deposited Cr electrodes surface, illuminated surfaces and thus different X-ray absorbed fraction. For each SC device the experimental sensitivity *S* was normalised to the absorbed X-ray fraction (*% absorbed X-ray*). This absorbed X-ray absorbed fraction *A* was calculated for every sample following the Beer-Lambert's law (**Equation (3-13)**):

$$A = 1 - e^{-\sigma_{cs}\rho_d L} = 1 - e^{-\frac{L}{\delta}} \quad (3\text{-}13)$$

Where σ_{cs} is the X-ray photon cross section ($cm^2\ g^{-1}$), ρ_d is the material density ($g\ cm^{-3}$), L is the device thickness (cm), and δ is the attenuation depth (cm). For the sake of simplicity, cross section σ_{cs} values were obtained from the NIST database for each Cl content at the mean energy of 50 keV, considering only photoelectric interaction,[63] and ρ_d values were derived, for each composition, from the molecular mass and the cell parameter *a* determined via XRD. The

attenuation depth values are by default determined, showing a slight increase with increasing Cl content (see **Table 3-3-1**).

Additionally, and as complement to the discussion, dark current density $J_{dark\text{-}avg}$ values were also extracted, as seen in **Figure 3-3-11**, and remained relatively unchanged with increasing Cl content for mixed halide compositions when compared to the base material $MAPbBr_3$.

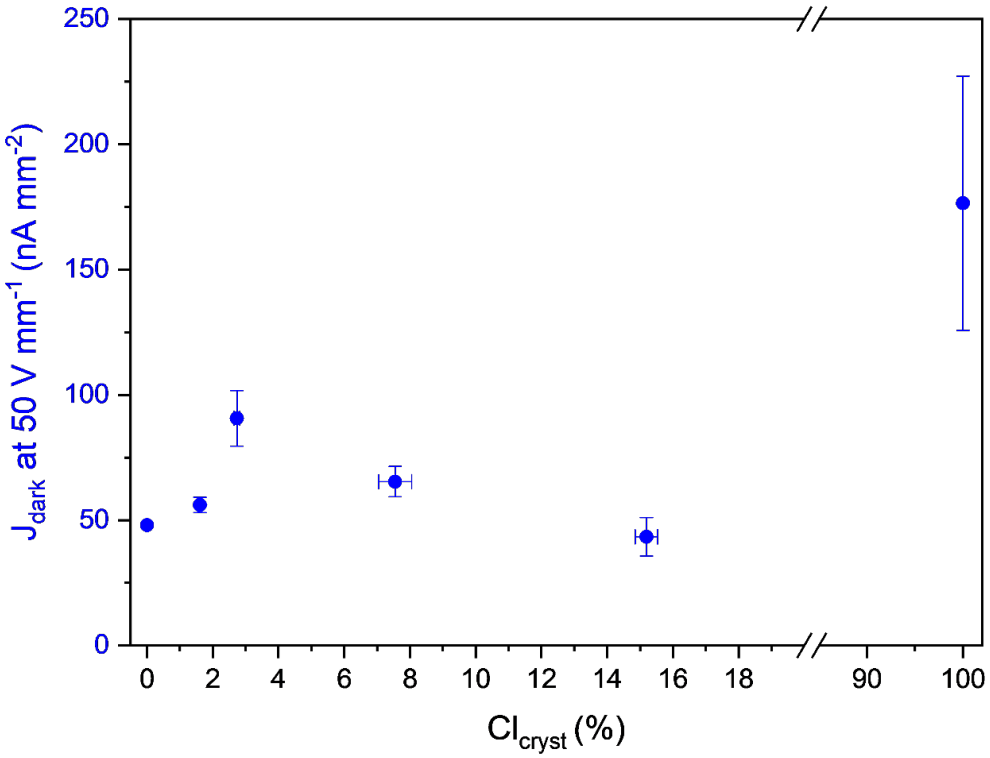

Figure 3-3-11. $MAPb(Br_{1-x}Cl_x)_3$ SC devices resulting average dark current density $J_{dark\text{-}avg}$ as a function of crystal Cl content $\%Cl_{cryst}$.

Nevertheless, when plotting the normalised *S/% absorbed X-ray* values as a function of J_{dark} values per SC device sample, as illustrated in **Figure 3-3-12**, one can see the benefits of doping $MAPbBr_3$ with $\%Cl_{cryst} = 15$ ($MAPb(Br_{0.85}Cl_{0.15})_3$). Thus, $MAPb(Br_{0.85}Cl_{0.15})_3$ stands out as the most interesting composition for detection of medical-grade X-rays of this study by showing the highest S values ($S_{avg} = 1.87$ μC mGy_{air}^{-1} cm^{-2} at 50 V mm^{-1}) and the lowest J_{dark} values recorded ($J_{dark\text{-}avg} = 43.4$ nA mm^{-2} at 50 V mm^{-1}).

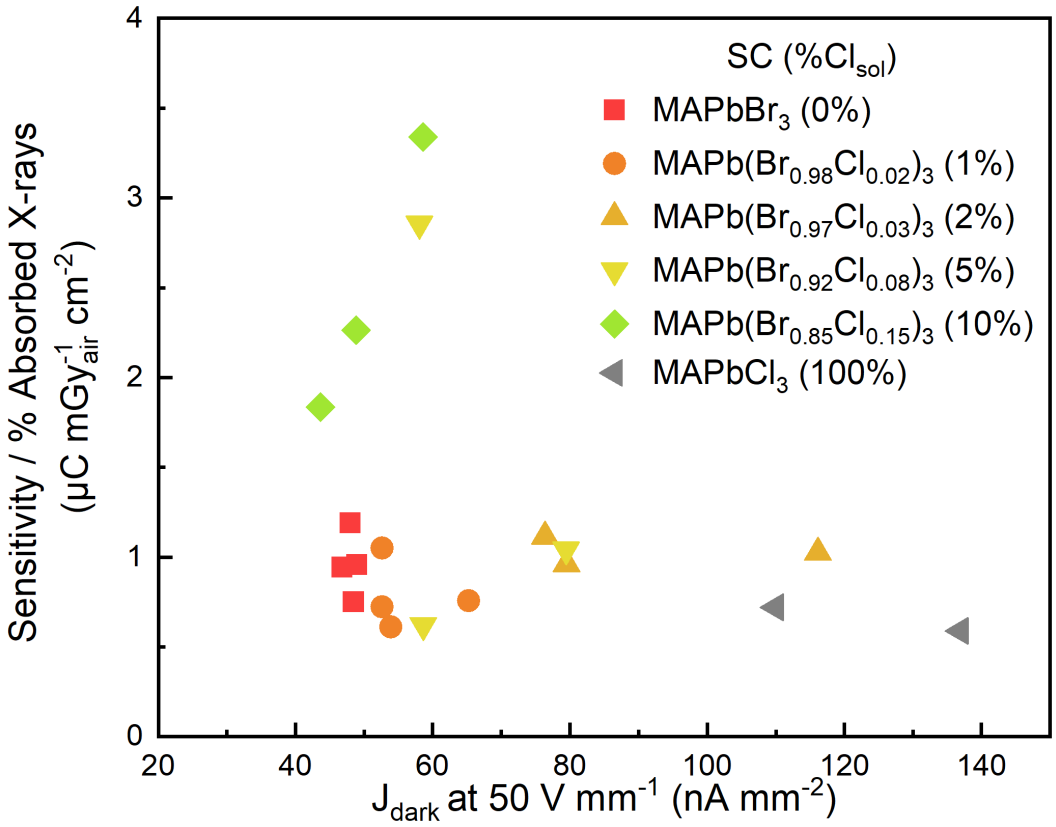

Figure 3-3-12. Sensitivity normalised to the percentage of absorbed X-rays as a function of dark current density J_{dark} at 50 V mm^{-1}.

Conclusion

This study presents evidence of the successful substitution of Br^- by Cl^- anions in $MAPbBr_3$ SCs, with a careful quantification of the crystal bulk Cl content. The results partially corroborate previous works on this material.[8–10] Optoelectronic evaluation, meticulously performed in X-ray medical radiography conditions and backed up by a systematic crystal batch production, reveals the high quality of synthesised $MAPb(Br_{1-x}Cl_x)_3$ SCs. They exhibit no hysteresis during current-voltage measurements and negligible conductivity drift. This linked to the optimised-growth nature of $MAPb(Br_{1-x}Cl_x)_3$ SCs produced by our synthesis method, which has allowed obtaining crystals with low defect content. We observe here an optimum in Cl content for $MAPb(Br_{0.85}Cl_{0.15})_3$, standing out as the most interesting composition, by showing the highest sensitivity ($S \approx 3$ µC mGy_{air}^{-1} cm^{-2} at 50 V mm^{-1}), the lowest dark current density ($J_{dark} \approx 43$ nA mm^{-2} at 50 V mm^{-1}) and the lowest conductivity drift ($\sigma_{drift} \approx 3 \times 10^{-5}$ S m^{-1} s^{-1} at 50 V mm^{-1}). An extensive analysis of the X-ray induced photocurrent by a two-charge carriers Hecht model indicates superior charge transport properties in the $MAPb(Br_{0.85}Cl_{0.15})_3$ SC for both carrier types. Notably, EDX data suggest that Cl incorporation in the crystal lattice increases the Pb/X (X = Br, Cl) ratio that approaches ABX_3 stoichiometry for the $MAPb(Br_{0.85}Cl_{0.15})_3$ composition. We propose that this improvement in stoichiometry corresponds to a reduction of point defects in the lead-halide framework, thus to a lower fraction of mobile ionic defects (V_X, X_i), resulting in an enhancement of the charge induction efficiency under X-rays irradiation. In addition, while laser ToF measurements indicate that hole mobility decreases with increasing Cl content, the two-charge carriers Hecht model suggests that Cl incorporation increases the hole lifetime reaching $\tau_h = 75$ µs for $MAPb(Br_{0.85}Cl_{0.15})_3$. These results confirm the generally good charge transport properties of $MAPb(Br_{1-x}Cl_x)_3$ perovskites. However, they highlight the need for further efforts to achieve state-of-the-art performance levels comparable to materials such as CdTe and CZT. In particular, even if the dark current density has been slightly reduced by the Cl incorporation, its level remains significantly higher by several orders of magnitude for the desired application. In this sense, other approaches must be investigated to solve this problem.

References

(1) Amari, S. Étude des matériaux pérovskites pour la détection directe des rayonnements ionisants. Ph.D. diss., Université Grenoble Alpes, Grenoble, France, 2020.

(2) Baussens, O. Nouveau matériau pérovskite pour la radiographie médicale. Ph.D. diss., Université de Bordeaux, 2021.

(3) Baussens, O.; Maturana, L.; Amari, S.; Zaccaro, J.; Verilhac, J.-M.; Hirsch, L.; Gros-Daillon, E. An Insight into the Charge Carriers Transport Properties and Electric Field Distribution of $CH_3NH_3PbBr_3$ Thick Single Crystals. *Appl. Phys. Lett.* **2020**, *117* (4), 041904. https://doi.org/10.1063/5.0011713.

(4) Amari, S.; Verilhac, J.-M.; Gros D'Aillon, E.; Ibanez, A.; Zaccaro, J. Optimization of the Growth Conditions for High Quality $CH_3NH_3PbBr_3$ Hybrid Perovskite Single Crystals. *Crystal Growth & Design* **2020**, *20* (3), 1665–1672. https://doi.org/10.1021/acs.cgd.9b01429.

(5) Kasap, S. O.; Rowlands, J. A. Direct-Conversion Flat-Panel X-Ray Image Detectors. *IEE Proceedings - Circuits, Devices and Systems* **2002**, *149* (2), 85–96. https://doi.org/10.1049/ip-cds:20020350.

(6) Datta, A.; Zhong, Z.; Motakef, S. A New Generation of Direct X-Ray Detectors for Medical and Synchrotron Imaging Applications. *Sci Rep* **2020**, *10* (1), 20097. https://doi.org/10.1038/s41598-020-76647-5.

(7) He, Y.; Matei, L.; Jung, H. J.; McCall, K. M.; Chen, M.; Stoumpos, C. C.; Liu, Z.; Peters, J. A.; Chung, D. Y.; Wessels, B. W.; Wasielewski, M. R.; Dravid, V. P.; Burger, A.; Kanatzidis, M. G. High Spectral Resolution of Gamma-Rays at Room Temperature by Perovskite CsPbBr3 Single Crystals. *Nat Commun* **2018**, *9* (1), 1609. https://doi.org/10.1038/s41467-018-04073-3.

(8) Rybin, N.; Ghosh, D.; Tisdale, J.; Shrestha, S.; Yoho, M.; Vo, D.; Even, J.; Katan, C.; Nie, W.; Neukirch, A. J.; Tretiak, S. Effects of Chlorine Mixing on Optoelectronics, Ion Migration, and Gamma-Ray Detection in Bromide Perovskites. *Chem. Mater.* **2020**, *32* (5), 1854–1863. https://doi.org/10.1021/acs.chemmater.9b04244.

(9) Wei, H.; DeSantis, D.; Wei, W.; Deng, Y.; Guo, D.; Savenije, T. J.; Cao, L.; Huang, J. Dopant Compensation in Alloyed CH3NH3PbBr3−xClx Perovskite Single Crystals for Gamma-Ray Spectroscopy. *Nature Mater* **2017**, *16* (8), 826–833. https://doi.org/10.1038/nmat4927.

(10) Qiu, L.; Wang, Z.; Luo, S.; Li, C.; Wang, L.; Ke, S.; Shu, L. Perovskite MAPb(Br1−Cl)3 Single Crystals: Solution Growth and Electrical Properties. *Journal of Crystal Growth* **2020**, *549*, 125869. https://doi.org/10.1016/j.jcrysgro.2020.125869.

(11) Mannodi-Kanakkithodi, A.; Park, J.-S.; Martinson, A. B. F.; Chan, M. K. Y. Defect Energetics in Pseudo-Cubic Mixed Halide Lead Perovskites from First-Principles. *J. Phys. Chem. C* **2020**, *124* (31), 16729–16738. https://doi.org/10.1021/acs.jpcc.0c02486.

(12) Wang, X.; Li, Y.; Xu, Y.; Pan, Y.; Wu, Y.; Li, G.; Huang, Q.; Zhang, Q.; Li, Q.; Zhang, X.; Chen, J.; Lei, W. Ion Migrations in Lead Halide Perovskite Single Crystals with Different Halide Components. *Phys. Status Solidi B* **2020**, 1900784. https://doi.org/10.1002/pssb.201900784.

(13) Jena, A. K.; Kulkarni, A.; Miyasaka, T. Halide Perovskite Photovoltaics: Background, Status, and Future Prospects. *Chem. Rev.* **2019**, *119* (5), 3036–3103. https://doi.org/10.1021/acs.chemrev.8b00539.

(14) Jiang, W.; Di, H.; Sun, H.; Zhao, C.; Liao, F.; Zhao, Y. Role of DMSO Concentration in the Crystallization Process of MAPbBr3 Perovskite Single Crystal Films. *Journal of Crystal Growth* **2020**, *550*, 125880. https://doi.org/10.1016/j.jcrysgro.2020.125880.

(15) Li, Z.; Kolodziej, C.; Zhang, T.; McCleese, C.; Kovalsky, A.; Zhao, Y.; Lambrecht, W. R. L.; Burda, C. Optoelectronic Dichotomy of Mixed Halide $CH_3NH_3Pb(Br_{1-x}Cl_x)_3$ Single Crystals: Surface versus Bulk Photoluminescence. *J. Am. Chem. Soc.* **2018**, *140* (37), 11811–11819. https://doi.org/10.1021/jacs.8b07560.

(16) Tisdale, J. T.; Yoho, M.; Tsai, H.; Shrestha, S.; Fernando, K.; Baldwin, J. K.; Tretiak, S.; Vo, D.; Nie, W. Methylammonium Lead Tribromide Single Crystal Detectors towards Robust Gamma-Ray Photon Sensing. *Adv. Optical Mater.* **2020**, 2000233. https://doi.org/10.1002/adom.202000233.

(17) Liu, F.; Yoho, M.; Tsai, H.; Fernando, K.; Tisdale, J.; Shrestha, S.; Baldwin, J. K.; Mohite, A. D.; Tretiak, S.; Vo, D. T.; Nie, W. The Working Principle of Hybrid Perovskite Gamma-Ray Photon Counter. *Materials Today* **2020**, S1369702120300730. https://doi.org/10.1016/j.mattod.2020.02.022.

(18) Jiang, S.; Wang, X.; Wu, Y.; Li, Y.; Zhang, Q.; Li, G.; Wu, Y.; Zhang, W.; Zhang, X.; Wang, B.; Chen, J.; Lei, W. Balance Lead in Solution-Processed CH3NH3PbBrxCl(3−x) Single Crystals for High Performance X-Ray Detection. *Materials Letters* **2019**, *236*, 26–29. https://doi.org/10.1016/j.matlet.2018.10.055.

(19) Mayén Guillén, J.; Lédée, F.; Baussens, O.; Chapran, M.; Lemercier, T.; Verilhac, J.-M.; Gros-Daillon, E.; Ibanez, A.; Zaccaro, J. MAPb(Br1–XClx)3 Hybrid Perovskite Materials for Direct X-Ray Detection. *ACS Appl. Electron. Mater.* **2023**. https://doi.org/10.1021/acsaelm.3c00114.

(20) Maculan, G.; Sheikh, A. D.; Abdelhady, A. L.; Saidaminov, M. I.; Haque, M. A.; Murali, B.; Alarousu, E.; Mohammed, O. F.; Wu, T.; Bakr, O. M. $CH_3NH_3PbCl_3$ Single Crystals: Inverse Temperature Crystallization and Visible-Blind UV-Photodetector. *J. Phys. Chem. Lett.* **2015**, *6* (19), 3781–3786. https://doi.org/10.1021/acs.jpclett.5b01666.

(21) Steirer, K. X.; Schulz, P.; Teeter, G.; Stevanovic, V.; Yang, M.; Zhu, K.; Berry, J. J. Defect Tolerance in Methylammonium Lead Triiodide Perovskite. *ACS Energy Lett.* **2016**, *1* (2), 360–366. https://doi.org/10.1021/acsenergylett.6b00196.

(22) Rodriguez-Carvajal, J. Recent Developments of the Program FULLPROF, in Commission on Powder Diffraction. *IUCr Newsl.* **2001**, *26*.

(23) Makuła, P.; Pacia, M.; Macyk, W. How To Correctly Determine the Band Gap Energy of Modified Semiconductor Photocatalysts Based on UV–Vis Spectra. *J. Phys. Chem. Lett.* **2018**, *9* (23), 6814–6817. https://doi.org/10.1021/acs.jpclett.8b02892.

(24) Fang, Y.; Wei, H.; Dong, Q.; Huang, J. Quantification of Re-Absorption and Re-Emission Processes to Determine Photon Recycling Efficiency in Perovskite Single Crystals. *Nat Commun* **2017**, *8* (1), 14417. https://doi.org/10.1038/ncomms14417.

(25) Diab, H.; Arnold, C.; Lédée, F.; Trippé-Allard, G.; Delport, G.; Vilar, C.; Bretenaker, F.; Barjon, J.; Lauret, J.-S.; Deleporte, E.; Garrot, D. Impact of Reabsorption on the Emission Spectra and Recombination Dynamics of Hybrid Perovskite Single Crystals. *J. Phys. Chem. Lett.* **2017**, *8* (13), 2977–2983. https://doi.org/10.1021/acs.jpclett.7b00998.

(26) García-Batlle, M.; Baussens, O.; Amari, S.; Zaccaro, J.; Gros-Daillon, E.; Verilhac, J.; Guerrero, A.; Garcia-Belmonte, G. Moving Ions Vary Electronic Conductivity in Lead Bromide Perovskite Single Crystals through Dynamic Doping. *Adv. Electron. Mater.* **2020**, *6* (10), 2000485. https://doi.org/10.1002/aelm.202000485.

(27) Zhang, X.; Li, L.; Sun, Z.; Luo, J. Rational Chemical Doping of Metal Halide Perovskites. *Chem. Soc. Rev.* **2019**, *48* (2), 517–539. https://doi.org/10.1039/C8CS00563J.

(28) Zhou, Y.; Chen, J.; Bakr, O. M.; Sun, H.-T. Metal-Doped Lead Halide Perovskites: Synthesis, Properties, and Optoelectronic Applications. *Chem. Mater.* **2018**, *30* (19), 6589–6613. https://doi.org/10.1021/acs.chemmater.8b02989.

(29) Euvrard, J.; Yan, Y.; Mitzi, D. B. Electrical Doping in Halide Perovskites. *Nat Rev Mater* **2021**, *6* (6), 531–549. https://doi.org/10.1038/s41578-021-00286-z.

(30) Shi, T.; Yin, W.-J.; Hong, F.; Zhu, K.; Yan, Y. Unipolar Self-Doping Behavior in Perovskite $CH_3NH_3PbBr_3$. *Appl. Phys. Lett.* **2015**, *106* (10), 103902. https://doi.org/10.1063/1.4914544.

(31) Wang, Q.; Shao, Y.; Xie, H.; Lyu, L.; Liu, X.; Gao, Y.; Huang, J. Qualifying Composition Dependent *p* and *n* Self-Doping in $CH_3NH_3PbI_3$. *Appl. Phys. Lett.* **2014**, *105* (16), 163508. https://doi.org/10.1063/1.4899051.

(32) Paul, G.; Chatterjee, S.; Bhunia, H.; Pal, A. J. Self-Doping in Hybrid Halide Perovskites via Precursor Stoichiometry: To Probe the Type of Conductivity through Scanning Tunneling Spectroscopy. *J. Phys. Chem. C* **2018**, *122* (35), 20194–20199. https://doi.org/10.1021/acs.jpcc.8b06968.

(33) Su, Z.; Chen, Y.; Li, X.; Wang, S.; Xiao, Y. The Modulation of Opto-Electronic Properties of CH3NH3PbBr3 Crystal. *J Mater Sci: Mater Electron* **2017**, *28* (15), 11053–11058. https://doi.org/10.1007/s10854-017-6889-3.

(34) McCluskey, M. D.; McCluskey, M. D.; Haller, E. E.; Haller, E. E. *Dopants and Defects in Semiconductors*, 2nd ed.; CRC Press: Boca Raton, 2018. https://doi.org/10.1201/b21986.

(35) Kasap, S.; Frey, J. B.; Belev, G.; Tousignant, O.; Mani, H.; Greenspan, J.; Laperriere, L.; Bubon, O.; Reznik, A.; DeCrescenzo, G.; Karim, K. S.; Rowlands, J. A. Amorphous and Polycrystalline Photoconductors for Direct Conversion Flat Panel X-Ray Image Sensors.

Sensors **2011**, *11* (5), 5112–5157. https://doi.org/10.3390/s110505112.

(36) Mix, L. T.; Ghosh, D.; Tisdale, J.; Lee, M.-C.; O'Neal, K. R.; Sirica, N.; Neukirch, A. J.; Nie, W.; Taylor, A. J.; Prasankumar, R. P.; Tretiak, S.; Yarotski, D. A. Hot Carrier Cooling and Recombination Dynamics of Chlorine-Doped Hybrid Perovskite Single Crystals. *J. Phys. Chem. Lett.* **2020**, *11* (19), 8430–8436. https://doi.org/10.1021/acs.jpclett.0c02243.

(37) Hecht, K. Zum Mechanismus des lichtelektrischen Primärstromes in isolierenden Kristallen. *Z. Physik* **1932**, *77* (3–4), 235–245. https://doi.org/10.1007/BF01338917.

(38) Wei, H.; Fang, Y.; Mulligan, P.; Chuirazzi, W.; Fang, H.-H.; Wang, C.; Ecker, B. R.; Gao, Y.; Loi, M. A.; Cao, L.; Huang, J. Sensitive X-Ray Detectors Made of Methylammonium Lead Tribromide Perovskite Single Crystals. *Nature Photon* **2016**, *10* (5), 333–339. https://doi.org/10.1038/nphoton.2016.41.

(39) Stoumpos, C. C.; Malliakas, C. D.; Peters, J. A.; Liu, Z.; Sebastian, M.; Im, J.; Chasapis, T. C.; Wibowo, A. C.; Chung, D. Y.; Freeman, A. J.; Wessels, B. W.; Kanatzidis, M. G. Crystal Growth of the Perovskite Semiconductor CsPbBr3 : A New Material for High-Energy Radiation Detection. *Crystal Growth & Design* **2013**, *13* (7), 2722–2727. https://doi.org/10.1021/cg400645t.

(40) Many, A. High-Field Effects in Photoconducting Cadmium Sulphide. *Journal of Physics and Chemistry of Solids* **1965**, *26* (3), 575–578. https://doi.org/10.1016/0022-3697(65)90133-2.

(41) Venugopalan, V.; Sorrentino, R.; Topolovsek, P.; Nava, D.; Neutzner, S.; Ferrari, G.; Petrozza, A.; Caironi, M. High-Detectivity Perovskite Light Detectors Printed in Air from Benign Solvents. *Chem* **2019**, *5* (4), 868–880. https://doi.org/10.1016/j.chempr.2019.01.007.

(42) Baussens, O.; Maturana, L.; Amari, S.; Zaccaro, J.; Verilhac, J.-M.; Hirsch, L.; Gros-Daillon, E. An Insight into the Charge Carriers Transport Properties and Electric Field Distribution of $CH_3NH_3PbBr_3$ Thick Single Crystals. *Appl. Phys. Lett.* **2020**, *117* (4), 041904. https://doi.org/10.1063/5.0011713.

(43) Musiienko, A.; Ceratti, D. R.; Pipek, J.; Brynza, M.; Elhadidy, H.; Belas, E.; Betušiak, M.; Delport, G.; Praus, P. Defects in Hybrid Perovskites: The Secret of Efficient Charge Transport. *Adv. Funct. Mater.* **2021**, *31* (48), 2104467. https://doi.org/10.1002/adfm.202104467.

(44) Jia, S.; Xiao, Y.; Hu, M.; He, X.; Bu, N.; Li, N.; Liu, Y.; Zhang, Y.; Cui, J.; Ren, X.; Zhao, K.; Liu, M.; Wang, S.; Yuan, N.; Ding, J.; Yang, Z.; Liu, S. Ion-Accumulation-Induced Charge Tunneling for High Gain Factor in P–I–N-Structured Perovskite $CH_3NH_3PbI_3$ X-Ray Detector. *Adv. Mater. Technol.* **2021**, 2100908. https://doi.org/10.1002/admt.202100908.

(45) Duijnstee, E. A.; Ball, J. M.; Le Corre, V. M.; Koster, L. J. A.; Snaith, H. J.; Lim, J. Toward Understanding Space-Charge Limited Current Measurements on Metal Halide Perovskites. *ACS Energy Lett.* **2020**, *5* (2), 376–384. https://doi.org/10.1021/acsenergylett.9b02720.

(46) García-Batlle, M.; Mayén Guillén, J.; Chapran, M.; Baussens, O.; Zaccaro, J.; Verilhac,

J.-M.; Gros-Daillon, E.; Guerrero, A.; Almora, O.; Garcia-Belmonte, G. Coupling between Ion Drift and Kinetics of Electronic Current Transients in $MAPbBr_3$ Single Crystals. *ACS Energy Lett.* **2022**, *7* (3), 946–951. https://doi.org/10.1021/acsenergylett.1c02578.

(47) Almora, O.; Matt, G. J.; These, A.; Kanak, A.; Levchuk, I.; Shrestha, S.; Osvet, A.; Brabec, C. J.; Garcia-Belmonte, G. Surface versus Bulk Currents and Ionic Space-Charge Effects in $CsPbBr_3$ Single Crystals. *J. Phys. Chem. Lett.* **2022**, *13* (17), 3824–3830. https://doi.org/10.1021/acs.jpclett.2c00804.

(48) García-Batlle, M.; Deumel, S.; Huerdler, J. E.; Tedde, S. F.; Guerrero, A.; Almora, O.; Garcia-Belmonte, G. Mobile Ion-Driven Modulation of Electronic Conductivity Explains Long-Timescale Electrical Response in Lead Iodide Perovskite Thick Pellets. *ACS Appl. Mater. Interfaces* **2021**, *13* (30), 35617–35624. https://doi.org/10.1021/acsami.1c06046.

(49) Zanichelli, M.; Santi, A.; Pavesi, M.; Zappettini, A. Charge Collection in Semi-Insulator Radiation Detectors in the Presence of a Linear Decreasing Electric Field. *J. Phys. D: Appl. Phys.* **2013**, *46* (36), 365103. https://doi.org/10.1088/0022-3727/46/36/365103.

(50) Bertolini, G.; Coche, A. *Semiconductor Detectors*, Eds. Interscience.; Wiley, 1968.

(51) Wei, W.; Zhang, Y.; Xu, Q.; Wei, H.; Fang, Y.; Wang, Q.; Deng, Y.; Li, T.; Gruverman, A.; Cao, L.; Huang, J. Monolithic Integration of Hybrid Perovskite Single Crystals with Heterogenous Substrate for Highly Sensitive X-Ray Imaging. *Nature Photon* **2017**, *11* (5), 315–321. https://doi.org/10.1038/nphoton.2017.43.

(52) Xia, M.; Song, Z.; Wu, H.; Du, X.; He, X.; Pang, J.; Luo, H.; Jin, L.; Li, G.; Niu, G.; Tang, J. Compact and Large-Area Perovskite Films Achieved via Soft-Pressing and Multi-Functional Polymerizable Binder for Flat-Panel X-Ray Imager. *Adv Funct Materials* **2022**, 2110729. https://doi.org/10.1002/adfm.202110729.

(53) Kim, Y. C.; Kim, K. H.; Son, D.-Y.; Jeong, D.-N.; Seo, J.-Y.; Choi, Y. S.; Han, I. T.; Lee, S. Y.; Park, N.-G. Printable Organometallic Perovskite Enables Large-Area, Low-Dose X-Ray Imaging. *Nature* **2017**, *550* (7674), 87–91. https://doi.org/10.1038/nature24032.

(54) Zhang, H.; Wang, F.; Lu, Y.; Sun, Q.; Xu, Y.; Zhang, B.-B.; Jie, W.; Kanatzidis, M. G. High-Sensitivity X-Ray Detectors Based on Solution-Grown Caesium Lead Bromide Single Crystals. *J. Mater. Chem. C* **2020**, *8* (4), 1248–1256. https://doi.org/10.1039/C9TC05490A.

(55) Musiienko, A.; Moravec, P.; Grill, R.; Praus, P.; Vasylchenko, I.; Pekarek, J.; Tisdale, J.; Ridzonova, K.; Belas, E.; Landová, L.; Hu, B.; Lukosi, E.; Ahmadi, M. Deep Levels, Charge Transport and Mixed Conductivity in Organometallic Halide Perovskites. *Energy Environ. Sci.* **2019**, *12* (4), 1413–1425. https://doi.org/10.1039/C9EE00311H.

(56) Feng, Y.; Pan, L.; Wei, H.; Liu, Y.; Ni, Z.; Zhao, J.; Rudd, P. N.; Cao, L. R.; Huang, J. Low Defects Density $CsPbBr_3$ Single Crystals Grown by an Additive Assisted Method for Gamma-Ray Detection. *J. Mater. Chem. C* **2020**, *8* (33), 11360–11368. https://doi.org/10.1039/D0TC02706E.

(57) Du, X.; Liu, Y.; Pan, W.; Pang, J.; Zhu, J.; Zhao, S.; Chen, C.; Yu, Y.; Xiao, Z.; Niu, G.; Tang, J. Chemical Potential Diagram Guided Rational Tuning of Electrical Properties: A

Case Study of $CsPbBr_3$ for X-ray Detection. *Advanced Materials* **2022**, 2110252. https://doi.org/10.1002/adma.202110252.

(58) Musiienko, A.; Pipek, J.; Praus, P.; Brynza, M.; Belas, E.; Dryzhakov, B.; Du, M.-H.; Ahmadi, M.; Grill, R. Deciphering the Effect of Traps on Electronic Charge Transport Properties of Methylammonium Lead Tribromide Perovskite. *Sci. Adv.* **2020**, *6* (37), eabb6393. https://doi.org/10.1126/sciadv.abb6393.

(59) Schlesinger, T. E.; James, R. B. *Semiconductors for Room Temperature Nuclear Detector Applications*, Academic Press.; Semiconductors and Semimetals; 1995; Vol. 43.

(60) Schlesinger, T. E.; Toney, J. E.; Yoon, H.; Lee, E. Y.; Brunett, B. A.; Franks, L.; James, R. B. Cadmium Zinc Telluride and Its Use as a Nuclear Radiation Detector Material. *Materials Science and Engineering: R: Reports* **2001**, *32* (4–5), 103–189. https://doi.org/10.1016/S0927-796X(01)00027-4.

(61) Kim, H.; Churilov, A.; Ciampi, G.; Cirignano, L.; Higgins, W.; Kim, S.; O'Dougherty, P.; Olschner, F.; Shah, K. Continued Development of Thallium Bromide and Related Compounds for Gamma-Ray Spectrometers. *Nuclear Instruments and Methods in Physics Research Section A: Accelerators, Spectrometers, Detectors and Associated Equipment* **2011**, *629* (1), 192–196. https://doi.org/10.1016/j.nima.2010.10.097.

(62) Li, Y.; Adeagbo, E.; Koughia, C.; Simonson, B.; Pettipas, R. D.; Mishchenko, A.; Arnab, S. M.; Laperrière, L.; Belev, G.; Stevens, A. L.; Kasap, S. O.; Kelly, T. L. Direct Conversion X-Ray Detectors with 70 PA Cm^{-2} Dark Currents Coated from an Alcohol-Based Perovskite Ink. *J. Mater. Chem. C* **2022**, *10* (4), 1228–1235. https://doi.org/10.1039/D1TC05338H.

(63) *NIST XCOM: Element/Compound/Mixture*. https://physics.nist.gov/PhysRefData/Xcom/html/xcom1.html (accessed 2022-07-18).

Chapter 4 – Influence of crystal growth environment and testing atmosphere

Table of contents

Chapter 4

Chapter 4

Influence of crystal growth environment and testing atmosphere

Introduction

The network of corner sharing lead-halide octahedra plays a central role in the mobility and collection of charge carriers in MHPs. That is why, in the previous chapter, we tried compositional engineering on the halide site. It confirmed that the chemical composition and stoichiometry of a hybrid LHP SC can influence significantly its optoelectronic properties. In that context, the chemical composition was intentionally altered, but other paths might alter the perovskite composition. A possible one is through chemical exchanges with the environment. It has been suggested that environmental H_2O, or N_2 and O_2 molecules induce an n- and p-doping on $MAPbBr_3$, respectively,[1] and that, in particular, water has a passivating effect till a certain exposure before degradation of the material.[2] Even though, SCs would never be exposed to a relative humidity (RH) higher than 50 % in a laboratory, inducing this degradation, studying the differences between growing crystals in uncontrolled standard laboratory and controlled glovebox atmospheres can bring insights on the interactions that the perovskite has with its surroundings. So, to estimate the impact of the environment and better understand the mechanisms involved, it was decided to synthesise SCs under two different atmospheres. The resulting crystals were later subjected to structural and optoelectronic characterisations to assess the influence of the environment at various stages of the synthesis-to-X-ray response evaluation process. These stages include: precursors and solvent storage and handling, crystal growth, device preparation, and optoelectronic characterisation. This gives us an opportunity to identify the eventual associated chemical species and their impact on the optoelectronic properties, especially on resistivity ρ, dark current density J_{dark} and sensitivity S under X-ray illumination.

This study of the influence of the environment is divided in two axes: one investigates its impact through the crystal synthesis, the second is centred on its impact during the device preparation and characterisation under X-ray irradiation.

Regarding the first axis, two extreme conditions were then set. The first one consists in using precursors exposed to air for extended time, preparing the precursor solution and growing the crystals in standard laboratory conditions, labelled the ambient condition (AC). For the

second one, ultra-dry precursors were instead used. Both solution preparation and SC growth take place in a dry and oxygen-free Ar atmosphere glovebox, labelled the inert condition (IC). The optoelectronic characterisation is then performed in standard ambient conditions. If different chemistries are involved during the synthesis, in these two different atmospheres, their impact should be noticed while performing structural characterisation of the SCs and establishing their X-ray response.

The second axis aims at estimating the impact that changes or possible degradation, caused by the interactions with the environment, might have on the optoelectronic properties, while being under bias and ionising radiation. Indeed, the potential degradation could have a major detrimental impact, obscuring the effect of the different chemical compositions we are trying to evidence in the first axis. Henceforth, the device preparation and characterisation were conducted in inert atmosphere as well, to achieve a fully inert synthesis-characterisation chain for the IC SCs. A comparison study between the AC and IC is elaborated: while the precursor solution preparation and crystal growth develop in the respective atmospheres for both conditions, as stated before, both families of SCs are instead prepared and tested in inert conditions. In order to do that, the optoelectronic characterisation takes place within special sealed test boxes. Thus, both standard and Ar testing atmospheres impact are then examined.

As for Chapter 3, the performances of the devices were assessed under standard X-ray medical conditions. SCs were obtained via seeded crystal growths in DMF, and using adaptive temperature ramps, leading to crystals with low and reproducible defect content.[3] For each growth condition, compositional, optical and electrical characterisations of the resulting SCs were systematically undertaken to evaluate the crystal ability to incorporate extrinsic species and properties. Material characterisation techniques, including Fourier transform infrared spectroscopy (FTIR), inductively coupled plasma mass spectroscopy (ICP-MS), glow discharge mass spectrometry (GDMS), thermogravimetric analysis coupled with mass spectrometry (TGA-MS) and X-ray photoelectron spectroscopy (XPS), were employed to check differences in chemical composition between both families of SCs. The device preparation and optoelectronic performance evaluation were conducted following the general procedures already introduced in Chapter 2. Only for the inert atmosphere testing (second axis), the crystals were conveyed under Ar to glovebox for polishing and electrode deposition. Both AC and IC SCs were then transferred, always in glovebox, into the specifically designed inert atmosphere sealed test boxes.

This chapter is divided into three sections: the first presents the chemical and structural characterisations of SCs grown from both AC and IC, the second describes the devices preparation and the optoelectronic characterisation protocols followed, and the last exposes the optoelectronic performances in both atmospheric and inert testing conditions.

This work contributes to the understanding of the impact of humidity and oxygen on the properties of $MAPbBr_3$ SCs. It was performed in collaboration with the Giovanni Armaroli

from the University of Bologna (Italy),[4] who performed photoinduced current transient spectroscopy (PICTS) analyses.

Chapter 4

1 Impact of the environment during crystal growth

1.1 Precursor solution preparation and crystal growth

As stated earlier in Chapter 2, the purity and water content of the precursors and solvent is primordial for the synthesis of high quality SCs. To evidence the impact of the environment, drastically different conditions were set. The “ambient condition” (AC) represents the scenario where the least care was taken, so the system was extensively exposed to the atmosphere of a standard chemistry laboratory. The "inert condition" (IC) represents the scenario where only trace amounts of H_2O and O_2 molecules were present inside Ar atmosphere gloveboxes during both growth solution preparation and crystal growth processes.

Accordingly, two sets of precursor materials were used. For the IC, DMF (Acros Organics, 99,8%, Extra Dry over Molecular Sieve, AcroSeal®), $PbBr_2$ (Alfa Aesar, ultra-dry, 99,999% (metals basis)) and MABr (GreatCell Solar, ≥ 99 %), respective unspoiled new containers were opened inside a glovebox (with H_2O and O_2 < 10 ppm) to maintain the lowest possible water content. The zeolites present in the Acros Organics DMF assures the anhydrous state of the solvent. This first ultra-dry glovebox, located at CEA Grenoble, was used for growth solution preparation and crystal storage. After precursor solution preparation, the vials are sealed with Parafilm before being transported to a second Ar atmosphere glovebox located at Institut Néel. For the AC, the same products were used, but they were first exposed to air for a period ranging from 36 h to several weeks. Both precursor solution preparation and crystal growth were executed in contact with the laboratory atmosphere.

Let us consider the example of the water intake of DMF, it was demonstrated that when pre-dried DMF is exposed to 50 % humidity in standard atmospheric conditions at 22 °C, in a matter of 2 h 20, the H_2O concentration went from 730 to 23 150 ppm, which means an intake rate of 90 ppm min^{-1}.[5] Thus, organic solvents, such as DMF, represent then vectors allowing the incorporation of environmental species into the solution system. It is worth noting that the percentages given above for $PbBr_2$ refers to the purity of the metal and not the halogens.

SCs were grown by our MITC methods: stoichiometric ($PbBr_2$:MABr 1:1 ratio) 1 M solutions in DMF were prepared. The ITC method was employed to obtain seeds by spontaneous nucleation in standard atmospheric conditions. SCs for both conditions were then obtained by seed-assisted growths with adaptive temperature ramps, lasting between 4 to 20 h, with different kinetic parameters α_2. Because collecting, mounting seeds and transferring the growth solution was extremely unpractical in a glovebox, for both conditions, the seeds were just dropped into the growth solution, once the thermalisation was complete, as described in Chapter 2. Since the whole process was carried out either under a fume hood (AC) or in the dedicated glovebox (IC), the precursor solution preparation and crystal growth were conducted with the atmosphere trapped in the vial above the solution corresponding to their respective

conditions. As mentioned earlier, two main parameters were considered in this study: O_2 and H_2O (humidity) contents. **Table 4-1-1** summarises the environmental conditions and the potential intake of oxygen and water before (precursor solution preparation) and during crystal growth. **Figure 4-1-1** shows the setup used for IC growths inside the Ar-glovebox, which was utilised for growth at Institut Néel. For both conditions, after crystal growth, the SCs are subsequently dried and put in membrane boxes. All SC samples are transferred to the storage glovebox via a sealed tube to avoid exposure to air.

Table 4-1-1. Precursor solution preparation and crystal growth vial experimental settings for both AC and IC. Regarding the quantity of H_2O and O_2, for the AC, the specified values are estimations; for the IC, the specified values were measured.

	Environmental parameter		Products	
Condition	H_2O	O_2	DMF H_2O content [a]	Precursors
Standard lab **Ambient**	~ 10^4 ppm (~ 50% RH) [b]	2.10^5 ppm (atmospheric)	~ 10^4 ppm	Bare ultra-dry $PbBr_2$ and MABr
Ar atmosphere glovebox used for growth **Inert**	100-900 ppm	1700 - 2700 ppm	< 7 ppm With septum and zeolites	

[a] The DMF water intake was estimated according to reference.[5]
[b] RH = relative humidity

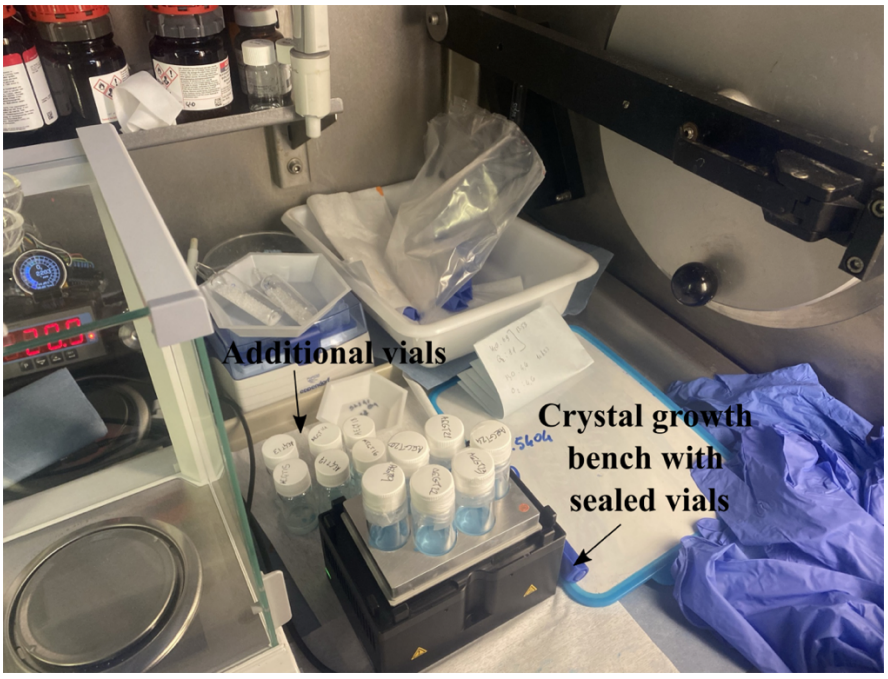

Figure 4-1-1. Ongoing inert condition (IC) crystal growth for several parafilm-sealed vials on growth bench within crystal growth Ar-glovebox.

At this stage, a first important observation was made regarding the crystallisation of the solutions prepared under these two different conditions. Statistically speaking, the solution prepared under AC showed very little spontaneous nucleation, to such an extent that expecting to grow SCs from spontaneous nucleation would have been unsuccessful. This is a first indication of an impact of the environment on the chemistry of the system. In the case of $MAPbI_3$, Zuo et al. demonstrated that H_2O molecules in perovskite precursors not only influence the aggregation of iodoplumbate complexes but also the coordination environment of Pb^{2+} cation in precursor solutions. According to their results, H_2O molecules not only coordinate with Pb^{2+} ions via Pb-O, but also promote organic solvents, such as DMF and DMSO, to coordinate with Pb^{2+} ions. This coordination leads to Pb-O linkages making and Pb-I breaking. Both behaviours of water molecules can retard the formation of high-order iodoplumbate $[PbI_n]^{2-n}$ complexes,[6] thus impacting the kinetics of nucleation and growth of LHPs. These reactions can help the fabrication of high-quality SCs and films by tailoring the growth process. Extrapolating this reasoning to $MAPbBr_3$ would allow explaining the difficulty to grow SCs via spontaneous nucleation, even though the metastable zone of an anhydrous solution of perovskite in DMF would have been overpassed. In other terms, environmental water imposes an additional barrier for nucleation and crystal growth.

As seen above, the presence of foreign species in the growth solution can have a significant impact on the build-up of the crystal, thus on the optoelectronic properties of the final crystal. Indeed, even if in small amounts, a fraction of these impurities can be incorporated in the crystal structure, all the more easily if the supersaturation is high. They can then lead to the formation of point defects detrimental to the photogeneration and collection of charge carriers. Therefore, our first concern was to try to evidence any potential incorporation of environmental species in the SCs.

1.2 Chemical and structural characterisations

Extrinsic species such as H_2O, O_2 or CO_2 are made of light elements and therefore, they are particularly hard to detect in small amounts (~ ppm). Yet, they can impact the chemical composition of the crystal in several ways. They may form complexes in solution (like the lead-water mentioned above),[6] be directly incorporated in the crystal structure (e.g., substitution of Br^- with OH^- ions),[7] or lead to heterovalent bi-substitution,[8] which corresponds to the joint incorporation of two species with different valence than the ions they replace, but maintaining electroneutrality in the structure. Even if H- and/or O-containing species remain undetected, the first two ways would impact the Pb/Br stoichiometry, which is more readily measurable. The case of heterovalent bi-substitution could be more elusive, unless it involves a heavy ion as co-substituent.

Several characterisation techniques were employed to see any differences in growing SCs in chemically uncontrolled and controlled conditions. Some techniques give the elemental

compositions of the different SCs (ICP-MS, GDMS), while others give information about the chemical species present in both crystal surface and bulk (FTIR, XPS). TGA-MS gives insights on the thermodynamic stability and degradation of $MAPbBr_3$.

1.2.1 Elemental analysis: stoichiometry and detection of impurities

Elemental analysis allowed detecting two things: firstly, the Pb/Br ratio of the perovskite material, done by ICP-MS, and secondly, the potential presence of extrinsic dopers, done by GDMS. ICP-MS and GDMS analyses are complementary techniques. The latter allows an easy isotopic dilution analysis, while the former allows a multi-element screening with high sensitivity.[9] ICP-MS and GDMS analyses were performed by Sylvie Motellier at CEA Grenoble and Eurofins EAG Laboratories in Toulouse, respectively.

ICP-MS employed one SC per growth condition. Identically as in Chapter 3, they were partially dissolved in ultra-pure water in a mass/volume ratio of 1/200. After 24 h, a 65 % nitric acid (HNO_3) aqueous solution is added for complete dissolution of the crystals, in a volume ratio $V_{nitirc\ acid}/V_{original\ solution}$ of 1/100. The samples were overall diluted by a 2×10^4 factor before analysis. An ICP-MS 7900x spectrometer (Agilent Technologies) was used for the quantification of elemental inorganic content of ^{79}Br and ^{207}Pb. A radio frequency power of 1550 W, an Ar plasma and nebulizer gas flow rates of 15 and 1.15 L min^{-1}, respectively, and an integration time/mass of 0.1 s were employed.

The results showed a Pb/Br ratio of 33.1 ± 0.8 % and 32.7 ± 0.4 % for SCs obtained from the AC and IC, respectively, as shown in **Table 4-1-2**. According to these bulk compositions, the Pb-X stoichiometry is already close to the theoretical 33.3 %, showing no difference between both crystal growth conditions.

Table 4-1-2. Pb and Br concentrations determined via ICP-MS in a H_2O/HNO_3 mixture and associated Pb/X ratio for $MAPbBr_3$ SCs grown in ambient (AC) and inert (IC) growth conditions. [a)]

Sample	^{207}Pb [µg/kg]	^{79}Br [µg/kg]	Resulting Pb/Br ratio via ICP-MS [%]
AC SC	103.4 ± 1	120.45 ± 0.8	33.1 ± 0.8
IC SC	138.1 ± 0.7	163.0 ± 0.4	32.7 ± 0.4

[a)] The Pb and Br concentrations presented here are given per kg of $MAPbBr_3$ SC. Only the most common isotope was considered for quantification.

Even if the perovskite structure construction is mediated by water introduced via hydrated precursors, as mentioned earlier in the discussion, the crystal growth leads to the same structure. Indeed, full dissolution of the precursors in solution took place for both conditions, especially for $PbBr_2$. The purity of $PbBr_2$ is primordial for this to happen, given that low-purity

products may contain lead oxides or hydroxyl groups as contaminants, provoking the presence an insoluble fraction of solid when preparing the growth solution in DMF, as we have previously observed. ICP-MS results corroborate then that the full dissolution of the precursors, or solution stoichiometry, leads also to crystal stoichiometry, even with potential environmental species involved.

In order to assess these species, GDMS with two SCs per growth condition was performed. They were first smashed, then a small piece of crystal was put at the end of an ultrapure Ta binder, previously analysed. An Astrum (Nu Instruments) high resolution glow discharge mass spectrometer (GDMS) was employed using a Pin cell, alumina as insulator, an Ar discharge gas, and a glow discharge of 1 kV and 2 mA. A Faraday cup detector was used with an ion counting of 160 ms, ion currents of ~ 1×10^{-11} A (Pb), and a resolution of ~ 3500. A standard relative sensitivity factor was used. Each content is at least measured between 3 to 5 times, averages are used in the results. The error percentage associated with this quantification is ± 20 %.

Table 4-1-3 recompiles the results from the main impurities detected: Cl being the principal one followed by Na and Al elements. Cl and Al contents seem slightly higher for the AC SCs when compared to IC ones. No significant difference is observed for the rest of quantified elements. For all scanned and quantified chemical elements, see **Table A 4-1-1** to **Table A 4-1-4**.

Table 4-1-3. GDMS analytical results on $MAPbBr_3$ SCs grown from both ambient (AC) and inert (IC) conditions. Two samples per conditions were used.

Element	AC SC #1 [ppm wt.]	AC SC #2 [ppm wt.]	IC SC #1 [ppm wt.]	IC SC #2 [ppm wt.]
Na	0.43	0.37	< 0.1	0.52
Al	0.43	0.43	0.09	0.09
Si	0.10	0.16	0.11	0.11
P	0.19	1.0	0.08	0.74
S	< 0.05	0.06	< 0.05	0.10
Cl	52	27	10	3.5
K	0.13	1.7	< 0.1	2.7

The higher amount of impurities for the AC can be potentially explained by the longer exposure to the local environment, when compared to the IC, hence more exposed to cross-contaminations such as dust or chemical vapours coming for the laboratory fume hood. We remind that the same raw materials references (precursors, solvent) were used for the AC and IC. This extended exposition yielded a less pure growth solution, with environmental species favouring the incorporation of impurities such as Cl and Al. Nevertheless, the air exposure and

associated environmental impurities does not seem to affect the overall stoichiometry as seen above. A closer look is undertaken, in the upcoming part, with respect to bulk and surface differences, and local stoichiometries in the SCs.

1.2.2 Extrinsic chemical species: H_2O and O_2

In the search of extrinsic species potentially differentiating both growth conditions, a focus was made on detecting water or the hydroxyl function (-OH). Several studies have showed how water is able to infiltrate in the perovskite structure, especially in polycrystalline thin films. Indeed, once the thin film, fabricated in dry and controlled conditions, is exposed to higher humidity, water can penetrate the inter-granular space of the polycrystal (PC).[10] Raman and FTIR spectroscopies bring to light the presence of characteristic vibrational modes of the perovskite structure and that associated to the presence of water. Firstly, Raman analyses were performed on our samples in order to study both conditions. Two different spectrometers were employed, with the help of Pierre Bouvier at the Institut Néel. The vibrational modes of the octahedra network are observable with this technique at low wavenumbers: lattice and MA-inorganic cage vibrations. Perturbations in the Pb coordination sphere could be then distinguished in theory. Given that these modes are situated near the Rayleigh ray of the source (among others), it was difficult to differentiate peaks associated with the source and that of the SC samples, and obtain clear measurements. It was then decided to switch to FTIR spectroscopy, which gives similar information regarding the organic part of the hybrid perovskite. As water makes its path through the material, a distinctive peak around 3500 cm^{-1} in the infrared absorption spectra appears.

Müller et al. showed by FTIR that water infiltrates the $MAPbI_3$ structure in a timescale of seconds, and that the process is reversible upon exposing the film to a dry atmosphere (e.g., N_2 or O_2).[7] Similarly, Zhu et al. evidenced the decomposition of $MAPbI_3$ into its monohydrated form $MAPbI_3 \cdot H_2O$, the source of it being the affinity that MA has with H_2O molecules.[11] Even though this affinity exists, the formation of this monohydrated form is hard and depends on the exposition time, vapour pressure, relative humidity, presence of light, to name a few, but especially on the porosity of the material (e.g., size of the grains, flatness of the surface, cracks). Porous structures would favour the trapping and adsorption of water. Similar studies were carried out also on $MAPbBr_3$[12] and mixed halide compositions $MAPbI_{3-x}Br_x$.[13]

With the help of David Jegouso at Institut Néel, we performed FTIR using a Vertex 70V spectrometer (Bruker) in attenuated total reflection (ATR) mode under primary vacuum (< 1 hPa) on previously ground SCs. A Globar source, a KBr separator and a MCT (Mercury-Cadmium-Telluride) detector with liquid nitrogen were used for the spectral response. 1 min measurements were performed with a resolution of 4 cm^{-1}. It was decided to grind the SCs of both conditions: firstly, to obtain contributions from the bulk of the crystals and see if the

atmosphere humidity got incorporated in the structure and not just on the surface, especially for the AC. Secondly, to avoid the total saturation of the detector from the high reflectivity of bare SC surfaces, as seen during preliminary trials.

The spectral results are shown **Figure 4-1-2**, centred around 3200 cm^{-1}, where potential water related vibrational modes should be observed. The full ATR-FTIR spectra can be found in **Figure A 4-2-1**. The associated peak assignation, detailed in **Table 4-1-4**, was mainly based on the work of Glaser et al.[14] and almost perfectly matched the experimental spectrum, with most of the main visible peaks identified (indexes 1 to 6). For comparison, the spectra were normalised to the symmetrical NH_3 stretch vibrational mode peak (~ 3200 cm^{-1}) as the methylammonium is not expected to be impacted by environmental species incorporation.

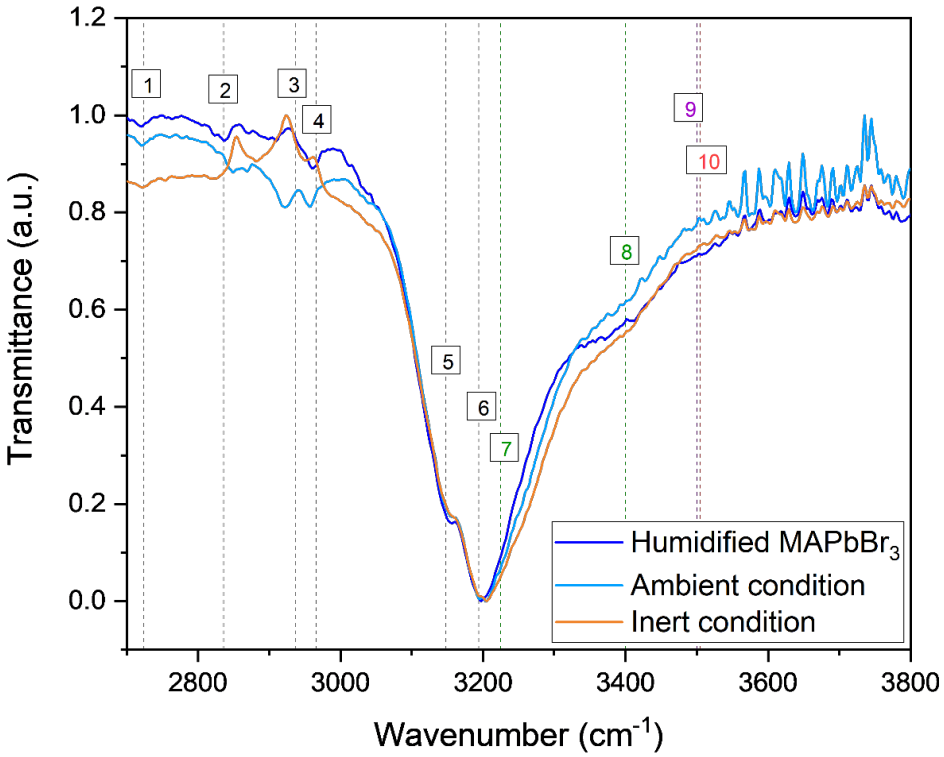

Figure 4-1-2. ATR-FTIR transmittance data normalised to the symmetrical NH_3 stretch vibrational mode peak (~ 3200 cm^{-1}) between 2700 and 3800 cm^{-1} for evaluation of potential vibrational modes related to water presence in ground SCs grown from both growth conditions and humidified $MAPbBr_3$. For index description refer to **Table 4-1-4**.

When comparing in **Figure 4-1-2** the AC (light blue plot) and IC (orange plot) SCs, no relevant difference is observed. The broad peak corresponds to a contribution of several vibrational modes: including two MA modes (indexes 5 and 6) in $MAPbBr_3$, and potentially modes associated to the presence of water. These modes were identified from Gan's work on mixed halide $MAPb(I_{1-x}Br_x)_3$ film:[13] index 7 corresponds to intercalated H_2O molecules (3225 cm^{-1}), and index 8 corresponds to υ(OH) modes of C-OH group (3400 cm^{-1}). An additional peak was also described by them at 1350 cm^{-1} corresponding to C-OH in-plane bend, but was not present in our spectra as seen in **Figure A 4-2-1**. Given that we are dealing with

ground SCs, the presence of intercalated water would make sense, even though the grain size of $MAPb(I_{1-x}Br_x)_3$ film is huge compared to ours. So, comparing a PC to a SC makes the evaluation harder and less appropriate. Also, it was found that the degradation rate under moisture scales linearly with grain size, showing that grain boundaries offer preferential sites for water molecules adsorption.[15] That said, PCs are more affected by water than SCs. Additionally, it has been well established that $MAPbI_3$ is more reactive towards moisture than $MAPbBr_3$, which composes the main matrix of the mixed halide perovskite discussed here. While index 7 is less evident, the weak and broad peak around 3400 cm^{-1} pointed out by index 8 seems more accentuated than that at index 7. This peak, identical for both conditions, seems to indicate that hydroxyl groups, coming from environment species, could have infiltrated the SC structure in a similar manner, whether they were adsorbed on the powder surface or incorporated in the structure as it happened for $MAPbI_{3-x}Br_x$ film.[13]

To clarify the interpretation of these peaks and on whether water was adsorbed on the grains during FTIR test or infiltrated in the structure during synthesis, an additional SC was ground and exposed to close to 100 % RH at 70°C for a couple of hours within a close space by evaporating distilled water as depicted in **Figure 4-1-3**.

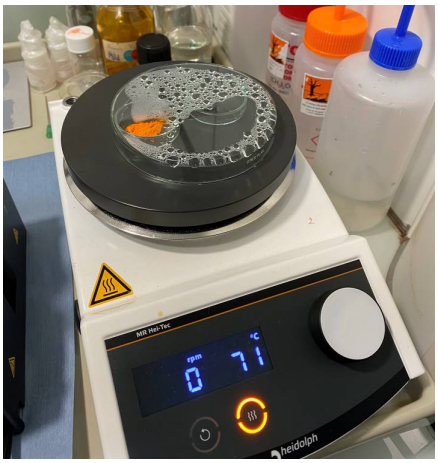

Figure 4-1-3. Humidified $MAPbBr_3$ SC powder for evaluation of water incorporation during ATR-FTIR analysis.

The resulting spectrum is plotted in dark blue in **Figure 4-1-2**. Index 7 peak did not change and index 8 broad peak at 3400 cm^{-1}, seems slightly stronger. This peak would correspond to C-OH groups, as said earlier, which is surprising as it does not correspond to any species of the crystal or the environment. If DMF molecules remained adsorbed on the crystal surface, this would mean that a protonation would be required, which is very unlikely (pK_a= -0.3). The presence of C-OH resulting from a reaction involving the crystal and environment would also be speculative at best, like for the primary amine from the structure with environmental CO_2 forming methylcarbamic acid (CH_3-NH-COOH).[16] This absorption band at 3400 cm^{-1} is also visible in some FTIR spectra of PbOHBr, but not always, and a sharp band at about 3500 cm^{-1} would also be expected.[17,18] In **Figure 4-1-2**, indexes 9 and 10 were

placed respectively where the O-H signature was found by Müller et al. in $MAPbI_3$ PC[7] and the hydroxyl vibrational mode for PbOHBr.[18] No peak was observed in those ranges.

The deconvolution of the observed peaks, especially the ones indexed 5 to 8 was also performed but resulted problematic due to the noisy baseline of the three spectra, and yielded, for, a given index-vibrational mode, peaks of similar areas.

Even though the identification of this peak is uncertain, the fact that it showed no significant difference between the AC and IC, and that reinforced post-growth exposure to water lead to a barely amplified bump at 3400 cm^{-1}, suggest that this ambiguity could be associated with an environmental impact on the perovskite surface. It worth repeating that, after synthesis, all SCs were stored in the same glovebox, potentially exposed the same chemical entities (e.g., solvent vapours). In spite of very different synthesis environments, there is no clear sign of environmental species (e.g., H_2O, O_2) or one of their by-products (e.g., hydroxyl group) being incorporated in the structure during crystal growth. A possible explanation of the resilience of $MAPbBr_3$ synthesis in solution against environmental species should lay in the chemistry of system. Among the several entry ways of these species (e.g., water uptake by hygroscopic DMF or MABr), the most serious one to consider would be the environmental degradation of $PbBr_2$ precursor into stable lead oxide or hydroxide compounds (e.g., PbOHBr) prior to the synthesis. But even in that case, the interaction of water with $MAPbI_3$, highlighted by Zuo et al and discussed earlier in this chapter,[6] introduces an important mechanism: their work claims that in solution, water coordinated to Pb^{2+} promotes the formation of lead-solvent complexes (e.g., with DMF or DMSO). If these highly coordinating solvent used for hybrid LHP synthesis[19] are able to displace not only water but all the environmental species coordinated to lead, then it would explain the resilience of $MAPbBr_3$ synthesis towards these species. Upon dissolution of the precursors, lead becomes fully coordinated with solvent molecules, whatever the original species coordinating it or present in solution. These molecules can later be replaced with halide ions upon the crystallisation of the perovskite. The most stable phase, under the right thermodynamic conditions is then grown, depending on $MAPbBr_3$ concentration and temperature. This considered, one would be surprised to find no impact of those impurities in the grown crystals, especially if they are produced by degraded precursors, as they would at least induce a deviation from stoichiometry. It is important to remember at this point that SC growth presents a significant difference from that of thin film prepared for PV applications. In the latter, the solution or ink is fully evaporated: so, all species contained are crystallised. In SC growth, because the solubility remains quite high at the final temperature of the process, only a fraction of the dissolved precursors crystallises in the form of perovskite (the crystal growth yield is not total, see Chapter 2). In our experimental conditions, more than half of the dissolved ions remain in solution (the crystallisation yield of $MAPbBr_3$ is below 33%, see Chapter 2). It can then constitute a buffer large enough to accommodate deviations from stoichiometry, avoiding a major impact on the SC composition, and making it more chemically resilient than thin films made by evaporation.

Table 4-1-4. Assignment of the different peaks measured in ATR-FTIR based on the literature. Below are the wavenumbers of vibrational modes, corresponding to those identified in various studies for similar materials or potentially present chemical species.

Index	Wavenumber [cm^{-1}]	Peak assignment	Material studied
1	2724	Sym. NH_3^+ bend υ_3 + CH_3-NH_3^+ rock υ_{11}	$MAPbBr_3$ SC/PC [a) 14]
2	2836	Asym. NH_3^+ bend υ_9 + υ_{11}	$MAPbBr_3$ SC/PC [14]
3	2937	Sym. CH_3 stretch υ_2	$MAPbBr_3$ SC/PC [14]
4	2966	Asym. CH_3 stretch υ_8	$MAPbBr_3$ SC/PC [14]
5	3148	Sym. NH_3 stretch υ_1	$MAPbBr_3$ SC/PC [14]
6	3194	Asym. NH_3 stretch υ_7	$MAPbBr_3$ SC/PC [14]
7	3225	Intercalated H_2O	$MAPb(I_{1-x}Br_x)_3$ PC [a) 13]
8	3400	υ(OH) modes of C-OH	$MAPb(I_{1-x}Br_x)_3$ PC [13]
9	~ 3500	O-H signature	$MAPbI_3$ PC [a) 7]
10	3505	υ(OH)	PbOHBr [b) 18]

a) PC = polycrystal (thin film).
b) PbOHBr is synthesised in a aqueous solution containing KBr and lead (II) acetate.

With the doubt of whether the FTIR observations correspond to the bulk or surface of the hybrid structure, a special attention was given to the characterisation of IC and AC crystals surface. To try to elucidate the question of the absorption peak at 3400 cm^{-1} and evidence the possible presence of foreign species, XPS analysis was performed by Anass Benayad at CEA Grenoble. A total of four SCs were used: for each condition, one crystal was devoted to surface analysis and another one was cleaved inside an Ar atmosphere glovebox (same glovebox as for IC SC synthesis and storage, described in **Table 4-1-1**) for the analysis of the bulk of crystals. The sample holder was mounted with the four samples in the same glovebox as depicted in **Figure 3-2-1-A**. A PHI Quantes instrument (ULVAC-PHI) using a monochromatic beam (X-ray source Al K_α = 1486.6 eV) of 30-50 μm in diameter and 12 W of power was employed. For the crystal surface analysis, a single measurement took place, and for bulk analysis, the beam was focused on 4 to 5 points of the cleaved surfaces. As illustrated in **Figure 3-2-1-B**, a distinction was made between “bottom” and “top”, corresponding to the last stage of growth

and seed sides, respectively. High-resolution core level analyses were performed using a pass energy of 69 eV, which corresponds to an energy resolution of 0.6 eV. All XPS measurements were carried out under ultra-high vacuum (UHV) conditions (7.10^{-8} Pa). Each core level peak was recorded within one to three scans with a scan rate of 0.1 eV s^{-1}. The binding energy calibration was performed using self-contained perovskite metallic lead (Pb^0) Pb $4f_{7/2}$ (136.9 eV) (Fermi level alignment to 0 eV). The core level binding energies were recorded within an error of ± 0.1 eV. Curve fitting and background subtraction were accomplished using MultiPak (ULVAC-PHI) software for quantitative analysis.

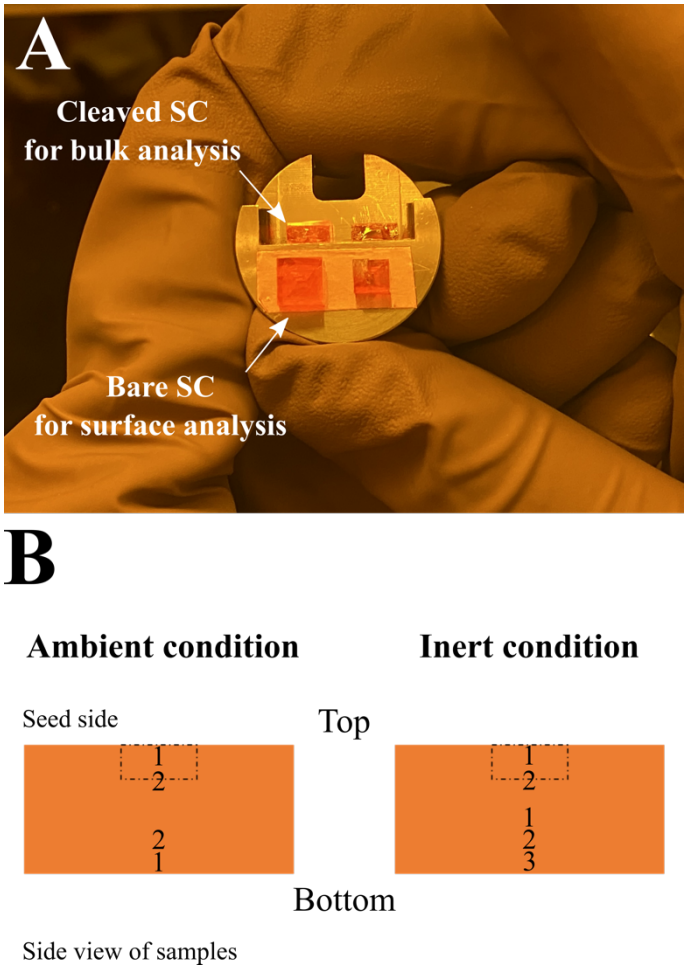

Figure 4-1-4. XPS analysis. (A) AC and IC SCs for surface and bulk analyses via XPS: two samples per atmospheric condition are used for the study. Bare (bottom) and cleaved (top) SCs allow analysis of the surface and bulk chemistry, respectively. **(B)** Schematic representation of cleaved SCs of both growth conditions for bulk analysis: the study is divided in "top" and "bottom" regions, each with 2 and 2-3 measurements on the cleaved surface, respectively.

A first qualitative scan was performed to identify all elements present in surface and bulk samples. In **Figure 4-1-5**, we can see the different orbital peaks measured on the crystal surface for both conditions. Besides little variations in terms of intensity, both spectra are almost identical with no peak corresponding to other elements than those belonging to the perovskite,

with the exception of oxygen. High resolution spectra were subsequently recorded for the following orbitals: C 1s, N 1s, O 1s, Br 3p, Br 3d and Pb 4f. All spectra can be found in **Figure A 4-3-1** and **Figure A 4-3-2**.

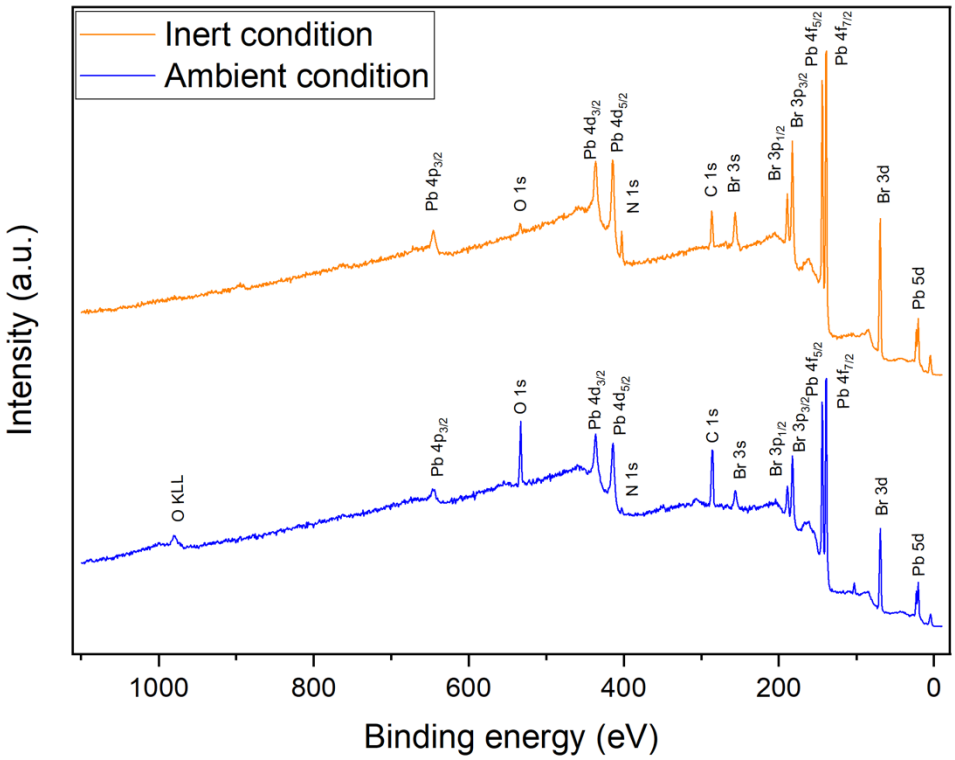

Figure 4-1-5. XPS overview scan on bare surface of both AC and IC SCs. This type of scan is performed to qualitatively identify the main elements orbitals.

The study focuses on O and C, and Pb elements, given that they are the elements allowing the detection of extrinsic species (e.g., H_2O, O_2, CO_2, -OH), and modifications in the inorganic framework, respectively. The cases of O, C and Pb are depicted in **Figure 4-1-6**. All spectra for a growth condition are grouped in a single chart: both surface and bulk analyses for comparative reasons.

Regarding O 1s, **Figure 4-1-6-A1** and **Figure 4-1-6-B1**, bring to light the relatively low content of O in most spectra (most signals are drowned in the noise), with the exception of the surface spectrum for the AC SC. This proves the adsorption of O-containing species on the surface, but not in the bulk of the material. We can thus not only discard the idea of incorporation of environmental species but also of solvent (DMF, $HCO\text{-}N(CH_3)_2$). This is a very significant result as it establishes without ambiguity that, inert environment is not mandatory for the synthesis of high purity $MAPbBr_3$ crystals, as environmental species present in solution are not incorporated the structure. Finally, the presence of O on the surface of the AC crystal can readily be attributed to its exposure to ambient air as it was retrieved from the growth vial in standard atmospheric conditions. The observable peaks had a binding energy

comprised between 532.3 and 532.8 eV, matching Kirmani et al. results, where they attributed this peak to hydroxy O-H.[20]

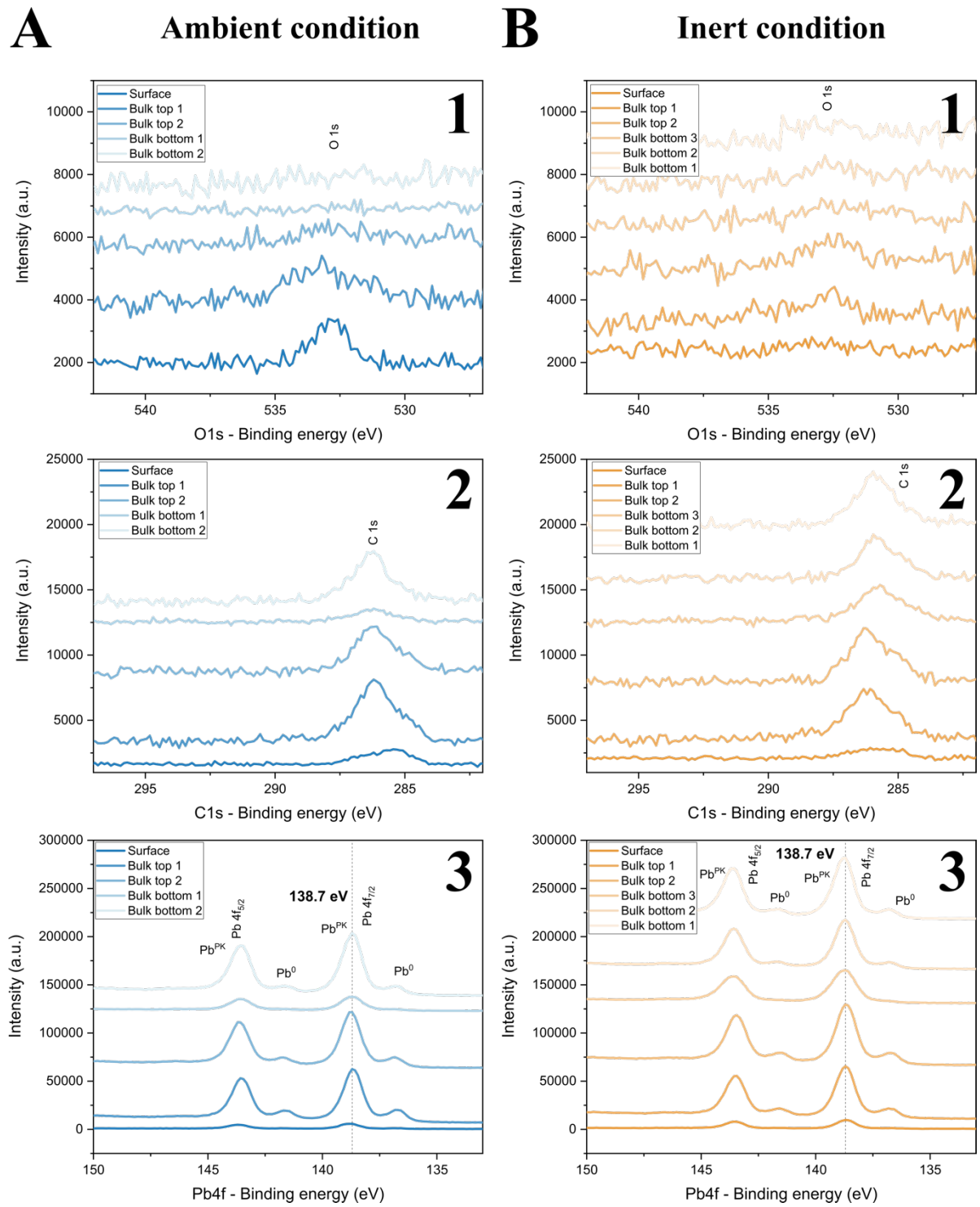

Figure 4-1-6. XPS high resolution spectra of O, C and Pb. (A) AC and **(B)** IC SCs O 1s **(1)**, C 1s **(2)** and Pb 4f **(3)** XPS spectra for both surface and bulk analysis. O 1s and C 1s peaks are situated between 532.3 – 532.8 eV, and 285.4 – 286.3 eV, respectively. The lead associated to the perovskite structure Pb^{PK} and metallic lead Pb^{0} are found at 138.7 and 136.8 eV, respectively. For legend understanding, see **Figure 4-1-4-B**.

With respect to C 1s, the peaks were situated between 285.4 and 286.3 eV in **Figure 4-1-6-A2** and **Figure 4-1-6-B2**. A lower binding energy shift is observed for surface measurements, when compared to that of the bulk. Kirmani et al. identified three types of peaks corresponding to: amorphous carbon (~ 285 eV), carbon belonging to MA (~ 286.2 eV), and carbon belonging to oxygen functionalities (~ 287 eV).[20] In our results, we believe that carbon-based species may have been deposited on the surface of the crystals, leading to the C 1s peak shift to around 285.4 eV for both surface measurements, as seen specially in **Figure 4-1-6-A2**. The MA-associated carbon was perceived more importantly in the bulk between 285.7 and 286.6 eV. It is worth pointing out that bulk measurements presented a slight tail at lower binding energies, potentially meaning the presence of amorphous carbon as well. Both ranges matched again Kirmani's work. The last peak enumerated by them was not seen here: C-O bond could be potentially hidden within the MA-associated peak, given the overlap in binding energies of C-N and C-OH bonds.

Regarding Pb, the analysis proved to be more complicated. **Figure 4-1-6-A3** and **Figure 4-1-6-B3**, highlight the diversity of Pb variants in the structures. In most cases, a major peak is systematically accompanied by a smaller peak on the right, both $4f_{7/2}$, with associated doublet peaks $4f_{5/2}$. A single satellite peak was also observed on the left of $4f_{5/2}$, but it is not visible here given its relatively low intensity: see **Figure A 4-3-3-A** for a better look at all three peaks of lead. The major doublet was assigned to the lead of the perovskite structure Pb^{PK}, and the small doublet to metallic lead Pb^0. The presence of Pb^0 was put to use as an internal calibration at 136.9 eV, allowing to define Pb^{PK} biding energy at 138.7 eV. The systematic presence of Pb^0 can be attributed to an experimental artefact. Previous research teams, including, Armaroli et al., showed how $MAPbBr_3$ is degraded when exposed to X-rays, especially focused in small areas, as in XPS measurements, resulting in the apparition of metallic lead Pb^0, bromide vacancies V_{Br} and the volatilisation of MABr and Br_2 in UHV.[1,21] In our case also, for both crystal growth conditions, the Pb^0 content appears to be dependent on the duration spent under the probe beam during each measurement (approximately 15 minutes per measurement). This implies that cleaved surfaces received more irradiation compared to bare surfaces, considering the number of measurements conducted. This explains the more pronounced Pb^0 peaks observed.

Quantitative analysis was performed by deconvoluting the high-resolution spectra of all mentioned elements. A pseudo-Voight profile is used to fit the spectra systematically: a convolution of a Cauchy-Lorentz (20 %) and a Gaussian (80 %) distributions is selected. Several functions were used to fit Pb 4f and Br 3d: examples of deconvolution are depicted in **Figure A 4-3-3-A** and **Figure A 4-3-3-B**, respectively. A Shirley baseline was also used.

The quantitative results, given in molar percentages, are plotted in **Figure 4-1-7**. Once again, a single chart summarises the whole surface and bulk analyses. By observing **Figure 4-1-7-A1** and **Figure 4-1-7-B1**, several things can be pointed out.

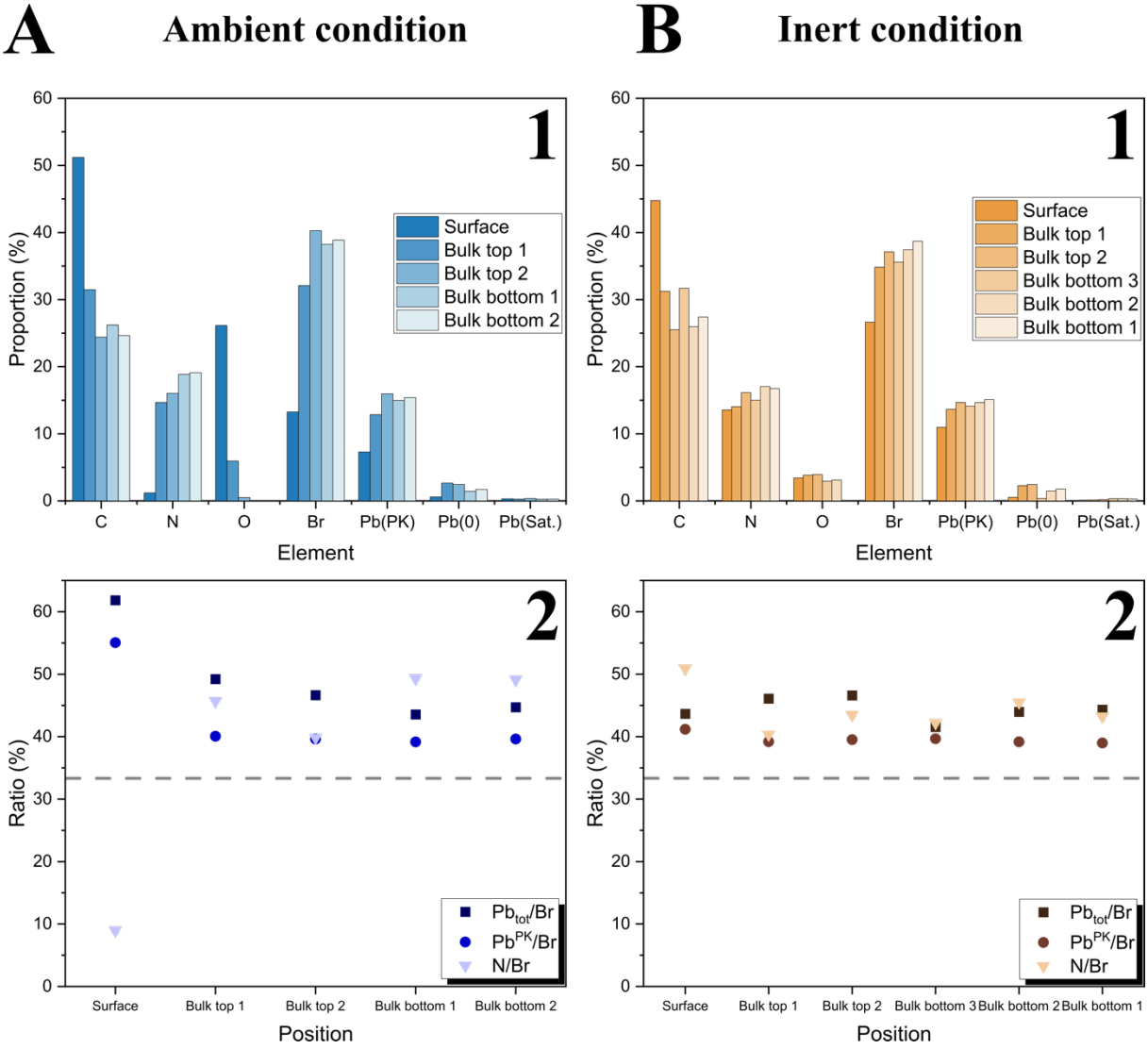

Figure 4-1-7. XPS quantitative results after deconvolution of peaks. (A) AC and **(B)** IC SCs quantitative results. The chemical elements quantified are: C, N, O, Br and Pb. Lead quantification is divided by three based on the different Pb-peaks observed: perovskite lead Pb^{PK}, metallic lead Pb^{0}, and an unattributed peak named Pb satellite. **(1)** histograms illustrate the relative proportion of each element for both surface and bulk studies. **(2)** plots depict different ratio: Pb_{tot}/Br, Pb^{PK}/Br, and N/Br. The grey dash line points out theoretical 33.33 % Pb/Br and N/Br ratios of the structure. For legend understanding, see **Figure 4-1-4-B**.

Firstly, the evident higher O content is numerically confirmed for the AC SC surface, when compared to the other condition and bulk measurements. Likewise, the higher Pb^{0} content of bulk measurements, when compared to surface ones, is corroborated. Secondly, one can observe that even if the O 1s signals of the surface and bulk analyses, seen in both **Figure 4-1-6-A1** and **Figure 4-1-6-B1**, are mixed with the background noise, the atomic quantification yields non-negligible contents of oxygen (< 4 %) (**Figure 4-1-7-A1** and **Figure 4-1-7-B1**). This is caused by a deconvolution artefact assigning a small percentage of oxygen. Thirdly, an excessive amount of carbon (all forms) can be also noticed in the surface when compared to the bulk, which it would be coherent with the 3400 cm^{-1} bumps in the FTIR

spectra and the higher O content for the AC, corresponding to C-OH group presence, even though no C 1s peak was found. The more abundant presence of C and O on the surface when compared to that of the bulk (cleaved surfaces) has also been confirmed by Kirmani et al.[20] All three FTIR spectra being similar would mean that we are dealing with a surface effect of the material. Also, in the XPS data, nitrogen is particularly low for the AC SC surface. We could hypothesise that a potential reaction of the amine yielding the alcohol function could take place.

The FTIR and XPS data of both growth conditions are very similar. The results point out at the presence of carbonaceous species with hydroxyl groups for both conditions, more importantly for the AC. The AC also presents a loss of nitrogen and bromine when compared to the IC, potentially linked to the departure of volatile precursor MABr.

To give further meaning to these results, the following ratios were established to see trends within the SCs, differences between surface/bulk and growth conditions: Pb_{tot}/Br, Pb^{PK}/Br and N/Br, as shown in **Figure 4-1-7-A2** and **Figure 4-1-7-B2**. These ratios were selected to see modifications in the stoichiometry similarly as was performed for $MAPb(Br_{1-x}Cl_x)_3$ SCs via EDX in Chapter 3. The first two are related and give indications about the inorganic stoichiometry: while Pb_{tot}/Br ratio considers lead in all its forms, the Pb^{PK}/Br ratio considers just the lead contributing to the perovskite structure. The third ratio give indications about the organic stoichiometry. Both stoichiometries are theoretically at 33.33 %. Both Pb_{tot}/Br and Pb^{PK}/Br follow the same trend, Pb_{tot}/Br being above Pb^{PK}/Br systematically for both conditions, given that the first ratio considers the other forms of lead potentially coordinating differently, including Pb^0. The ratio is then overestimated. Globally, the ratios seem to be shifted to Pb-rich and N-rich (> 33.33%, the grey dash line in the figure marks the stoichiometric value), with Pb/Br values higher than the ones seen in Chapter 3, for Pb_{tot}/Br and Pb^{PK}/Br. This, however, may not be directly taken as compositions in the crystal structure as the results can be biased by the loss of Br from the tested surface via volatilisation, under UHV, of MABr or Br_2, as previously mentioned. That considered, the AC SC surface presents additionally the deficit in nitrogen discussed earlier, also seen in **Figure 4-1-7-B2**.

These observations do not point out at any radically different chemical composition between ambient and inert growth conditions, especially in the bulk. Nevertheless, XPS measurements give some insights concerning the presence of carbonaceous and oxygenated species on the surface, especially for the AC SC, which would correspond to the presence of C-OH groups, as seen in the FTIR spectra. This contamination is present for both conditions and even more accentuated for the AC, which makes sense considering the time spent exposed to the atmosphere. The adsorption of C- and O-containing species is also correlated to a loss of the amine function and/or precursor MABr, which is more important on the crystal surface for ambient-grown SCs.

1.2.3 Thermal stability and degradation of $MAPbBr_3$

Another way to expose incorporated species could be through decomposition differences or degradation products proper to a growth condition. So TGA-MS was conducted, under the guidance of Mathieu Salaun at Institut Néel. The thermal stability of the perovskite and the by-products were analysed under inert atmosphere. The thermogravimetric analysis was conducted in a TAG 16 (Steram) equipment coupled with a HAL 201 RC (Hiden Analytical) mass spectrometer. The furnace was purged with a flow of Ar gas and a primary vacuum (< 1 mbar) was used. The samples, ground SCs, were put in a Pt crucible inside a symmetrical analyser and left for 1 h at 30 °C for temperature stabilisation, prior to the measurement. A temperature range of 30-700 °C and a ramp of 2 K min^{-1} were applied. The TGA baseline drift precision was ± 1µg. Regarding the MS, the mass-to-charge ratios (m/z), presented in **Table 4-1-5**, were followed in time, with the objective of identifying as many chemical specimens/fragments as possible during the degradation process of the perovskite. Their selection was based on previous works[22,23] and the characteristic m/z ratios were selected from NIST database.[24] The logic behind this selection was to include all base materials needed for the synthesis of the $MAPbBr_3$ (precursors and solvent) and small organic molecules with high thermodynamic stability (stable degradation products).

Table 4-1-5. TGA-MS selected m/z ratios to follow degradation products of $MAPbBr_3$ SCs [a)]

m/z ratio studied	Assigned parent species [b)]	Potential other parent species [c)]
15	CH_3Br (bromomethane)	NH_3, MA, DMA
17	NH_3, H_2O	MA
18	H_2O	NH_3, MA
30	CH_3NH_2 (MA)	DMA, NO
42	$(CH_3)_2NH$ (dimethylamine – DMA)	-
44	DMA	CO_2
94	CH_3Br	-

[a)] The structure of the detected ion is not shown here, just the parent molecule.
[b)] The selected species have a relative intensity above 20 % according to NIST database.[24]
[c)] These other species present the m/z in question, but they are in the minority.[24]

To avoid overloading the software with too many m/z ratio values to follow, several preliminary tests were performed to discard potential species, which are presented in **Table 4-1-6**. Regarding the H_2O and O_2 contents, the focus entities in this chapter, the Ar tank used indicates contents lower than 3 and 2 ppm, respectively. After two purges of the sample chamber, water, oxygen and air partial pressure indicators were around 10^{-10}, 10^{-11} and 10^{-11} Torr, respectively.

Table 4-1-6. TGA-MS discarded m/z ratios during degradation products of $MAPbBr_3$ SCs [a)]

m/z ratio discarded	Discarded parent species [b)]	Commentary
32	O_2	Not detected
73	DMF	Not present
80	HBr (hydrobromic acid)	Not present
160	Br_2 (diatomic bromine)	Present [a)]

[a)] The structure of the main discarded ion is not shown here, just the parent molecule.
[b)] For Br_2, the molecule was previously detected as a degradation product during Amari's work, and not considered here.

Figure 4-1-8 combines both TGA and MS analysis results showing that the two growth conditions exhibit the same three mass losses. It should be noted that the AC, does not attain -100 % mass loss, due to a measurement/input error of the SC mass, an offset of ~ 3 % is present (mass evolution stops at ~ 97 %). The AC seems also to be shifted from the IC by close to ~ 5 °C. This is possibly explained by the higher mass used for the AC SC (28 mg), compared to the IC SC (22.5 mg).

The first mass loss corresponds to approximately ~ 21 %, which starts around 170 °C and finishes at around 330 °C, not only perfectly matches the detection of NH_3 and/or CH_3Br (m/z = 15 and 94, respectively) but also corresponds quite well to the $MABr/MAPbBr_3$ ratio (23.3 wt.%). The ratio m/z = 15 could represent both entities, but most likely it corresponds to CH_3Br, given the shape of m/z = 94. It is worth precising that the assignation of m/z ratios equal to 15, 17 or 18 is not straightforward, because they are characteristic degradation masses shared by ammonia, water, MA and dimethylamine (DMA) (see **Table 4-1-5**). This mass loss can then be attributed to the departure of MABr from the structure.

A small bump can be seen as soon as the first loss finishes, in the 330-360 °C temperature range. The bump was only observed for temperature ramps close to 2 K min^{-1}. It corresponds to a mass loss of 2 %, potentially linked to a tardive arrival of more NH_3/CH_3Br:

a small shoulder on the right of first m/z = 15 and 94 peaks can be observed, and the 2 wt.% would account for MABr remaining in the structure, and/or another unidentified species.

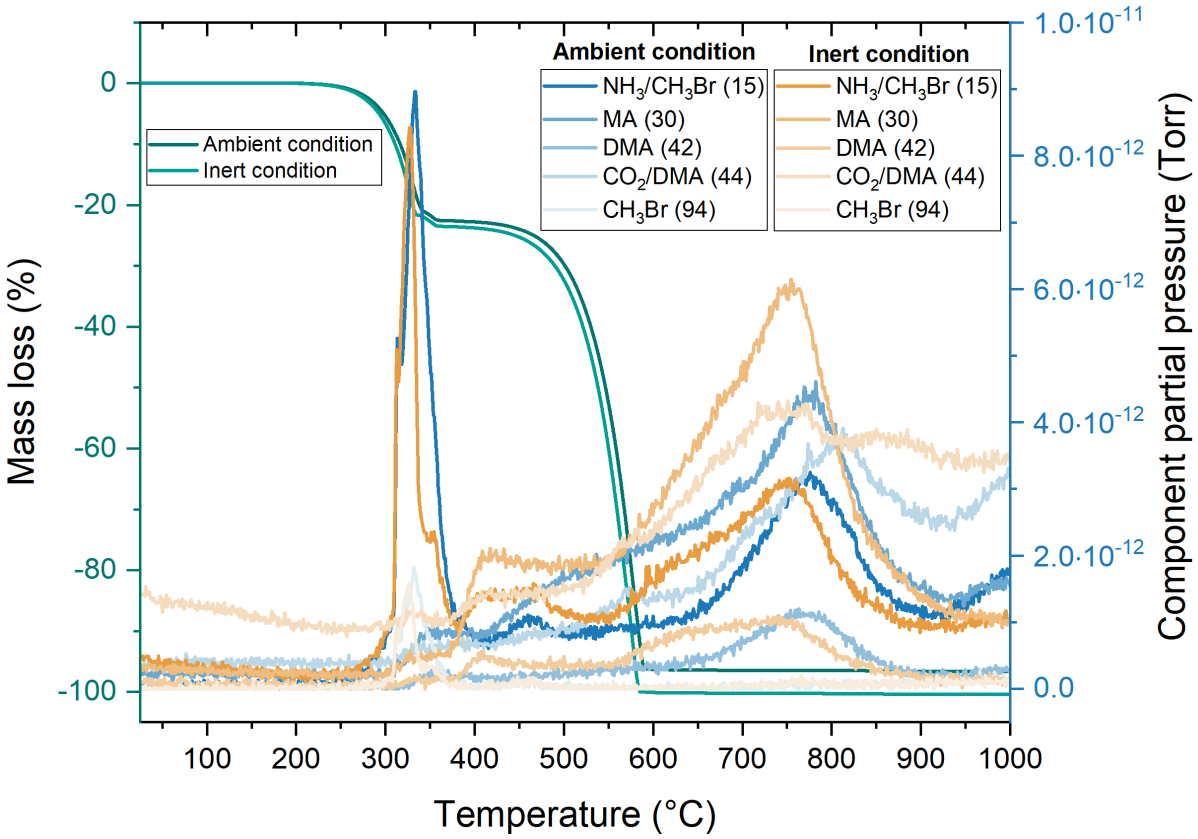

Figure 4-1-8. TGA-MS data showing principal mass losses and associated degradation products. Water is omitted here given its larger partial pressure, which value corresponds to the water content of the experimental carrier gas (Ar).

The last mass loss extends over a longer temperature range, between 460 and 570 °C, and corresponds to the evacuation all the remaining chemical species (100 wt.% loss). It represents the remaining ~ 77 %. Because of the limitation in m/z ratio the mass spectrometer can follow, lead species were not tracked, only lighter species derived from the organic part of the hybrid perovskite structure. For both conditions, as of 370 °C is reached, all followed light species partial pressures were rising and continuously detected: NH_3/CH_3Br, MA, DMA, and potentially CO_2 as well. One possible explanation is that the inorganic framework of the hybrid structure may retain in part the degradation products and releases them as it is lost up to 570 °C. Beyond that temperature, when the samples degradation is complete (100 % mass loss), these increasing component partial pressures probably correspond to the late arrival of the degradation products of the organic part, generated during the first mass loss. It corresponds to the degassing from the different parts of the experimental chamber and pipes connecting the heating chamber and mass spectrometer. Indeed, the partial pressures of light species reached their peaks after 700 °C, when the experiment system is at its hottest point, therefore, the most prone to degas any deposited organic species on the internal walls of the equipment. Our

findings regarding the sequential loss of organic and inorganic parts and the identified degradation products are partially corroborated by similar studies on $MAPbI_3$ and $MAPbBr_3$.[23,25]

Now regarding the possible presence of environmental species in the crystals of each conditions, some remarks can be made. Firstly, water, one possible major environmental species, was omitted in **Figure 4-1-8** because of its larger partial pressure. However, its value was the same for both conditions and corresponds to the water content of the experimental setup (Ar tank and pipes), and thus could not be related to $MAPbBr_3$ SCs content. All evaluated m/z ratios are depicted in **Figure A 4-4-1**. Secondly, neither the AC nor IC showed any evidence of the presence of the solvent, DMF, as was suggested by the absence of oxygen in the XPS analysis (bulk measurements). Lastly, the main m/z ratio associated to O_2 was not detected either. Also, the m/z = 44 corresponds most likely to DMA and not to CO_2, given the partial pressures evolution. This would mean that the O-containing species present in the XPS measurements (surface measurements), correlated with the bump around 3400 cm^{-1} in the FTIR spectra, are most likely adsorbed H_2O molecules, whose signal was lost in the carrier gas water content contribution. This adsorbed water corroborates the increased FTIR signal of humidified $MAPbBr_3$ powder and does not rely on questionable surface reaction for the formation of the C-OH function.

As an intermediate conclusion to this first section, several characterisation techniques have been employed in order to evidence the effect of the crystal growth environment on the chemical composition of the crystals, and by extension, the nature and concentration of the point defects. The measurements expose the high resilience of $MAPbBr_3$ chemical system against perturbations by species coming from the environment. We attributed this to the strong complexing power of the solvents used for the crystallisation of hybrid LHPs. Nevertheless, we have observed a specific behaviour of the samples surface, such as the presence of adsorbed water and variations in composition, as revealed by XPS measurements. This indicates that if the crystals are elaborated under very different atmospheres, they will present very similar bulk composition but different surface composition.

The main parameter, differentiating AC from IC SCs, is then their longer exposition to environmental humidity. The absorption and adsorption of water by the solvent and precursors, respectively, is translated by a far higher involvement of water in the growth solution, explaining the struggle of the spontaneous nucleation to happen in the AC vials, as seen earlier, as well as the lack of parasitic crystals while performing the growths. Water would act as a mediator in the growth solution. It is worth repeating, that this “humidity” does not go inside the bulk of the SCs, as shown in the XPS analysis, which means that from a structural point of view, the perovskite is resilient to the incorporation of water- or oxygen-related extrinsic defects. Nevertheless, surface water might affect the SC bulk via acid-base chemical equilibria, as evidenced by a work made by Ceratti et al., in which they showed that both H_2O and MA^+ species participate in these type of reactions, provoking proton H^+ diffusion inside $MAPbI_3$,

$MAPbBr_3$ and $FAPbBr_3$ SCs. They said that this H^+ diffusion and associated proton vacancies V_H would be the major contributor to ion migration in hybrid MHPs, which opposes the more popular theories based on I^- or Br^- anions migrations as the main phenomena.[26]

After growth, the environment can interact with the surface, eventually degrading (e.g., loss of MABr, apparition of metallic lead Pb^0, proton diffusion) or enhancing (e.g., passivation of defects by water) the optoelectronic behaviour of the crystal. Therefore, we pursued the study of the environment influence by evaluating its post-growth impact.

2 Impact of the environment after crystal growth: device fabrication and optoelectronic characterisation

The surface and bulk of a SC have different properties, given the fact that the surface is susceptible to solvent dissolution immediately after being synthesised in solution, and is exposed to any environmental change after growth. These differences in properties are correlated to differences in defect content, both macro- (e.g., cavities, dislocations) and atomic-level defects (e.g., stoichiometry changes, impurities). Accordingly, several studies have demonstrated that the surface can easily undergo degradation under moisture.[1,27]

According to Song et al., $MAPbI_3$ and $MAPbBr_3$ films are both affected by moisture after crystallisation following different stages. For the former, four different stages can be identified. Firstly, H_2O molecules form H-bonds with uncoordinated I atoms, provoking a surface passivation, thus inducing longer PL and greater photocurrent. Secondly, water molecules form a continuous network fully covering the surface, n-doping (free electrons into the bulk) and reducing the PL. Thirdly, water saturation causes the dissolution of the perovskite inorganic framework, creating a monohydrated layer and an isolating barrier between surface and bulk material. Lastly, if the hydration continues, the perovskite fully decomposes into PbI_2 and volatile organic fragments (e.g., HI, MA). In the case of $MAPbBr_3$, the same first two stages take place: first surface passivation by water (improving optoelectronic performance), then the continuous network of water causes the n-type doping, generating a photo-inactive material. For $MAPbBr_3$, the stronger ionicity of the Pb-Br bond makes an easier charge injection (higher electron density). The last two stages were not evidenced, proving the better structural stability against humidity of $MAPbBr_3$.[2]

As stated earlier, PCs are more sensitive than SCs to moisture penetration inside the material, because of their grain boundaries.[15] This implies that our SCs, constituted by a single grain, should be more resilient to moisture degradation than thin films. Yet, even a monolayer of degraded perovskite or adsorbed species may impact the charge collection at the interface with the electrode. So, we studied the impact of the post-growth environment on the measured properties during storage, device preparation and optoelectronic characterisation.

To do so, after synthesis, SCs from both ambient and inert conditions are divided into two groups. SCs in the first group are prepared and characterised under standard atmospheric conditions. SCs in the second group crystals pass through device preparation and characterisation in inert atmosphere. In practice, the first group leave the storage glovebox for the usual polishing procedure and are optoelectronically tested as described in Chapter 2. The second group follows a complete chain under Ar atmosphere: storage-device preparation-optoelectronic characterisation. They are polished inside the storage glovebox, following the same procedure used for the first group. As a further precaution against potential water intake during polishing, isopropyl alcohol (IPA, Sigma Aldrich, anhydrous, 99.5 %) and toluene

(Sigma Aldrich, anhydrous, 99.8 %) were newly opened and used inside the glovebox, as lubricant and cleaning solvents, respectively. The polishing setup is depicted in **Figure 4-2-1**.

Figure 4-2-1. Polishing setup for SCs in the storage Ar atmosphere glovebox.

To complete the device fabrication, standard Cr evaporation took place also inside the storage glovebox, as detailed in Chapter 2, leading to the Cr/$MAPbBr_3$ SC/Cr configuration devices for both conditions. Two different setups were used for optoelectronic characterisations. The first group, immerged in a post-growth ambient condition, was tested within the standard brass boxes (see Chapter 2 and **Figure 4-2-3**). A total of 14 SC devices were analysed in standard atmosphere: 8 AC and 6 IC SC devices. For the second group these devices were mounted within sealed test boxes with enough tightness to keep the atmosphere of the glovebox inside throughout the characterisations. Indeed, they maintain inside a small overpressure of the pressurised glovebox where they were sealed. The optoelectronic performance was assessed based on a total of 4 SC devices: 2 AC and 2 IC SC devices. As for the brass boxes, the SC device is sandwiched with silicone layers doped with Cu and Ag, in turn in contact with 1.1 mm-thick glass coated with Cu electrodes. An exemplary is shown in **Figure 4-2-2-A** and **Figure 4-2-2-B**. Sealed test boxes work also as Faraday cages, they are connected to the ground and keep the SC device in the dark. As opposed to the brass testing box, no Pb collimator is used on the top side of the sealed box facing the X-ray source. This difference is taken into account further on in the discussion.

In the previous part we have seen that the synthesis conditions have no significant impact on the chemistry, on the stoichiometry of the perovskite structure. Yet, optoelectronic properties can be strongly influenced by even very small amounts of point defects. So, comparisons within each group will allow for better assessment of the influence of the crystal growth conditions. Comparison between the two “post-growth exposure groups” will help bring

to light new insights on the influence of air in the preparation and characterisation of our devices. The IC SCs in the fully inert synthesis-characterisation circuit are of particular interest as these crystals never see atmospheric conditions. **Figure 4-2-3** illustrates the experimental protocols followed for both groups of crystals.

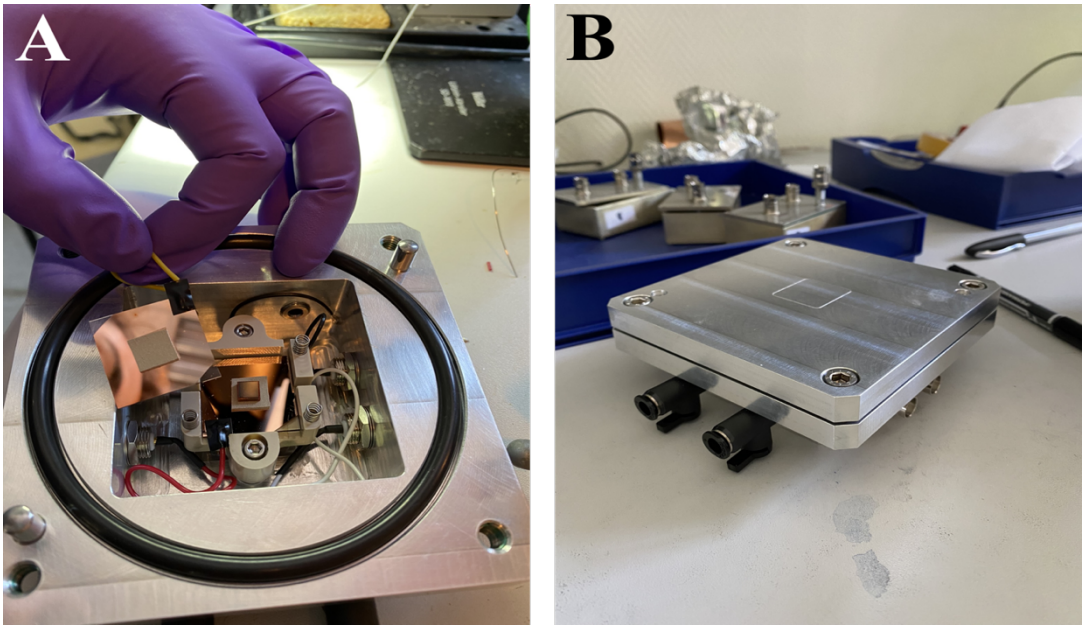

Figure 4-2-2. Inert atmosphere optoelectronic test box. (A) Interior of sealed aluminium test box with SC device in the inside, sandwiched between silicone layers **(B)** Exterior of sealed box for inert atmosphere tests.

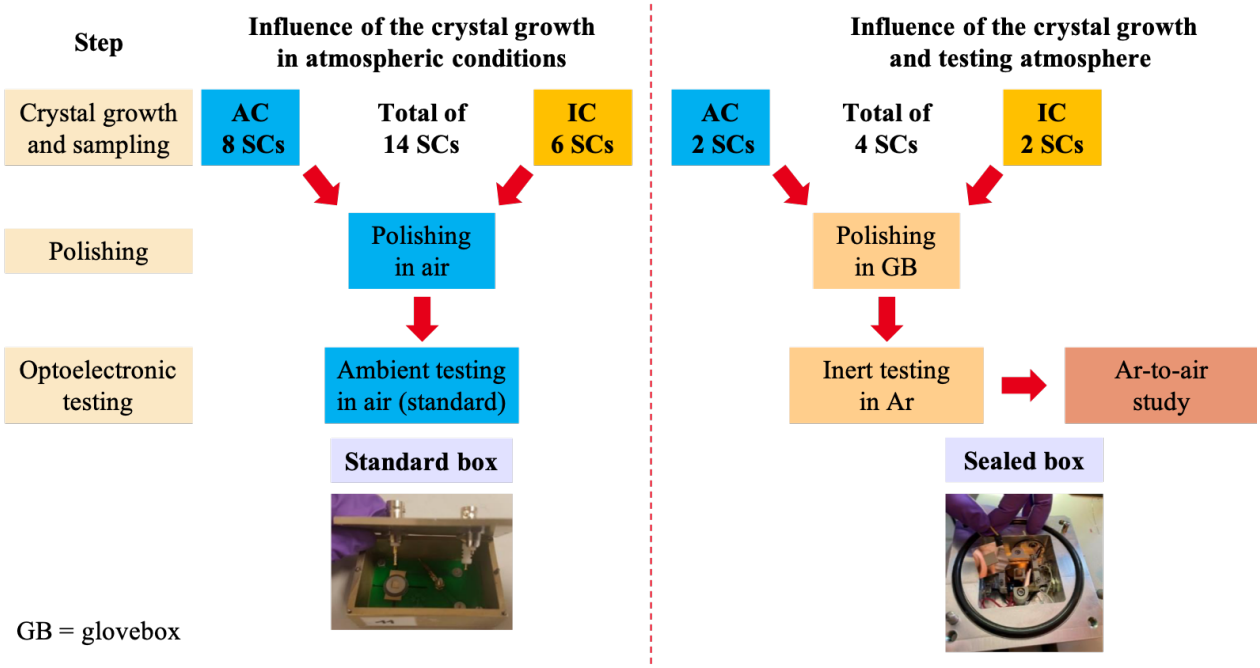

Figure 4-2-3. Optoelectronic characterisation protocols followed to establish the influence of the crystal growth and testing atmospheres.

Chapter 4

3 Optoelectronic performance: impact of the environment

As it was done in Chapter 3, the main parameters chosen for the evaluation of the optoelectronic performance of SC devices are: the dark current density J_{dark}, the sensitivity S, the resistivity ρ, and the charge carrier mobilities μ_e and μ_h. The experimental protocols for S-V, J-t and laser ToF measurements were those described in Chapter 2. As indicated above, to assess the impact of the growth condition through optoelectronic characterisations, comparisons were made between AC and IC SC devices. At first, because the analysis was easier and more devices could be considered, we characterised the selected devices under atmospheric conditions. Thereafter, the influence of the characterisation atmosphere is evaluated for the two couple of devices. To take into consideration the difference in thicknesses of the different SC devices, J_{dark} and S values are plotted as function of the electric field F rather than the biasing voltage, resulting in J_{dark}-F and S-F curves. The thicknesses of the samples, comprised between 1.35 and 2.41 mm, resulted in the absorption of 93 to 99 % of the incoming X-rays. For the first axis of study, the average thicknesses were 1.80 and 1.93 mm for the AC and IC, respectively, and for the second axis, they were 1.99 and 1.80 mm for the AC and IC, respectively, allowing a fair comparison between the growth conditions at a given electric field.

3.1 Influence of the crystal growth conditions on the optoelectronic performance under atmospheric conditions

For the 14 devices (8 AC and 6 IC SCs) prepared (just polishing) and tested under ambient conditions, resistivity ρ values, shown in **Figure 4-3-1**, were extracted from current density-electric field (J-F) data, in turn extracted from J-t recordings, as described in Chapter 2. One can observe that both families of crystals have similar resistivities, in the same order of magnitude, slightly higher for IC SCs, but with a larger variability.

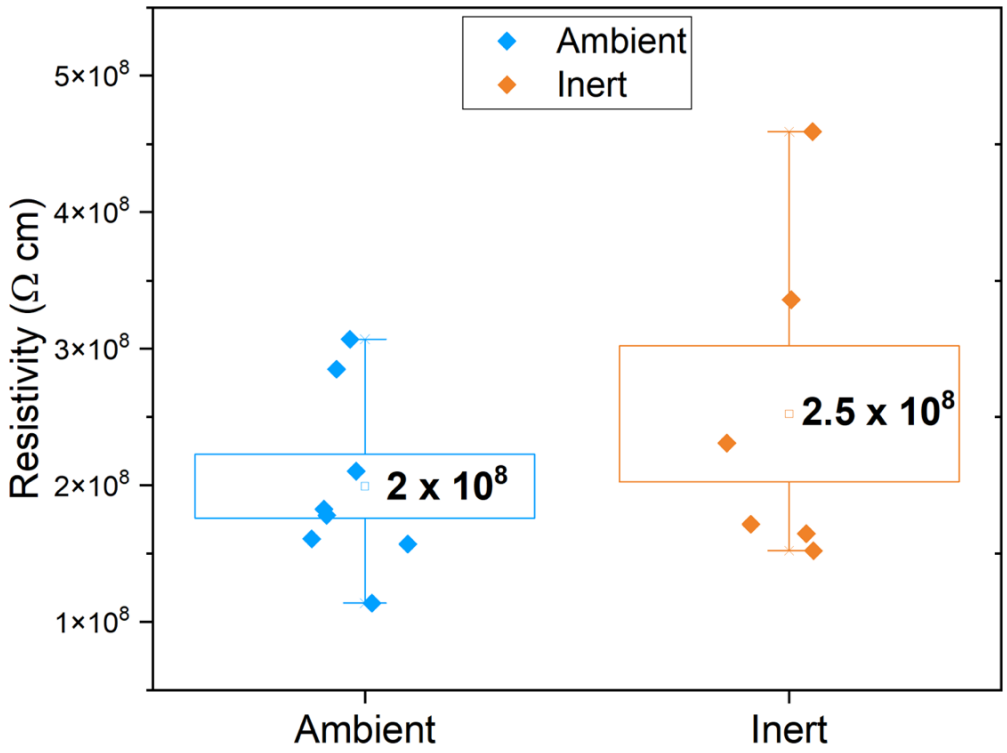

Figure 4-3-1. Statistical repartition of resistivity ρ values for all evaluated SCs. The plot above considers the 14 SC devices that were analysed in standard atmosphere: 8 AC and 6 IC SC devices.

$J_{dark.}$ and S values are depicted in **Figure 4-3-2-A** and **Figure 4-3-3-A**, respectively. Concerning the dark current density J_{dark}, the behaviour for both growth conditions is similar. They are in the same order of magnitude and its values increase linearly with increasing electric field. To highlight the negligible difference of dark current density between devices from both growth conditions, **Figure 4-3-2-B** presents the statistical repartition of J_{dark} values at 50 V mm^{-1}. This is similar to what was observed for the resistivity, given that both physical quantities are intimately linked by Ohm's law.

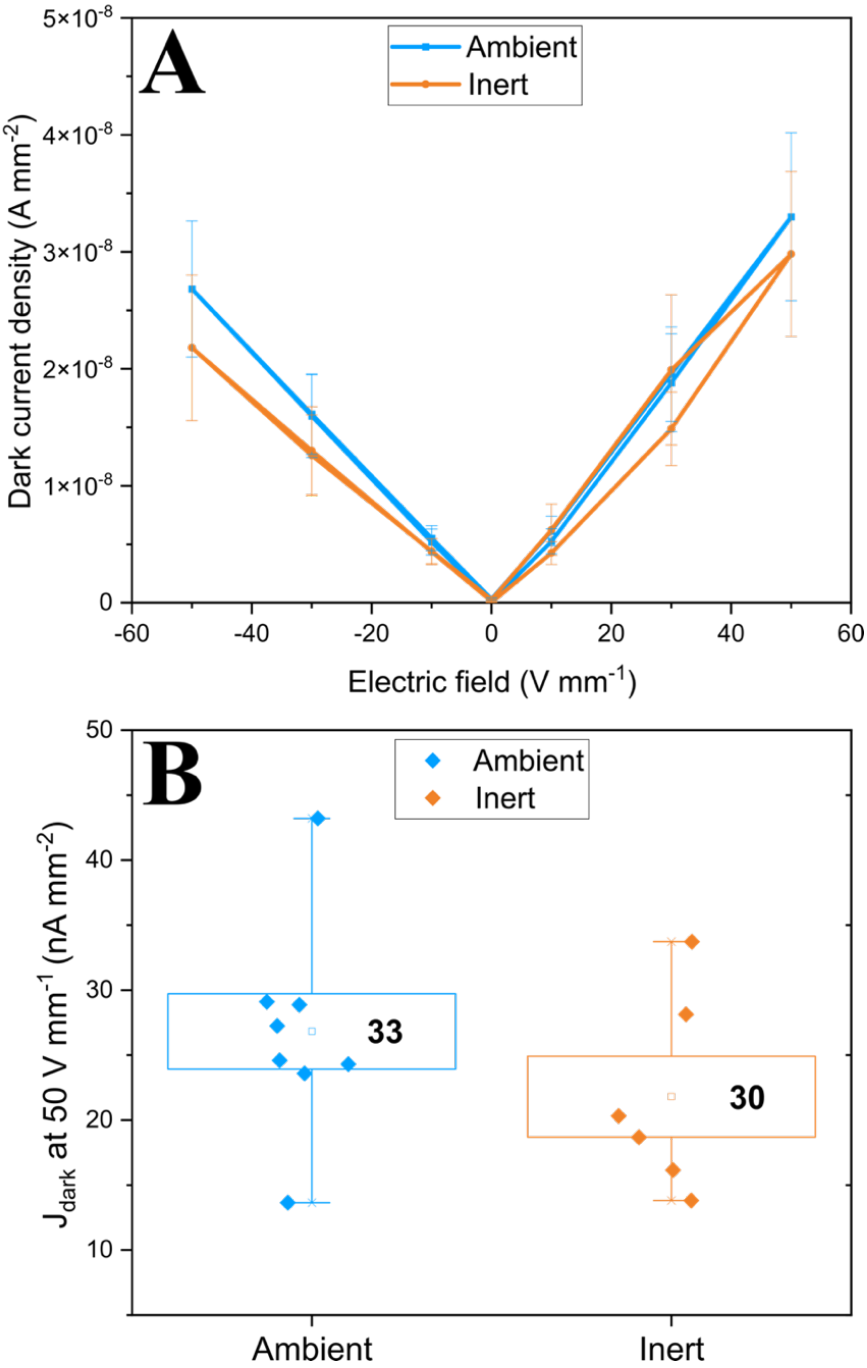

Figure 4-3-2. Dark current density comparison between AC and IC SC devices. (A) Dark current density as a function of the resulting electric field for both set of crystals in atmospheric conditions. **(B)** Statistical repartition of dark current density J_{dark} values for all evaluated SCs at 50 V mm^{-1}. The plots above consider the 14 SC devices that were analysed in standard atmosphere: 8 AC and 6 IC SC devices.

With respect to sensitivity, some differences can be seen in **Figure 4-3-3-A**. Firstly, for both positive and negative electric fields, the AC devices seem to have slightly higher *S* values when compared with IC devices, especially for high negative biases. **Figure 4-3-3-B** illustrates the statistical repartition of the *S* values measured for the different devices at 50 V mm^{-1}, showing the little upper hand of AC SCs.

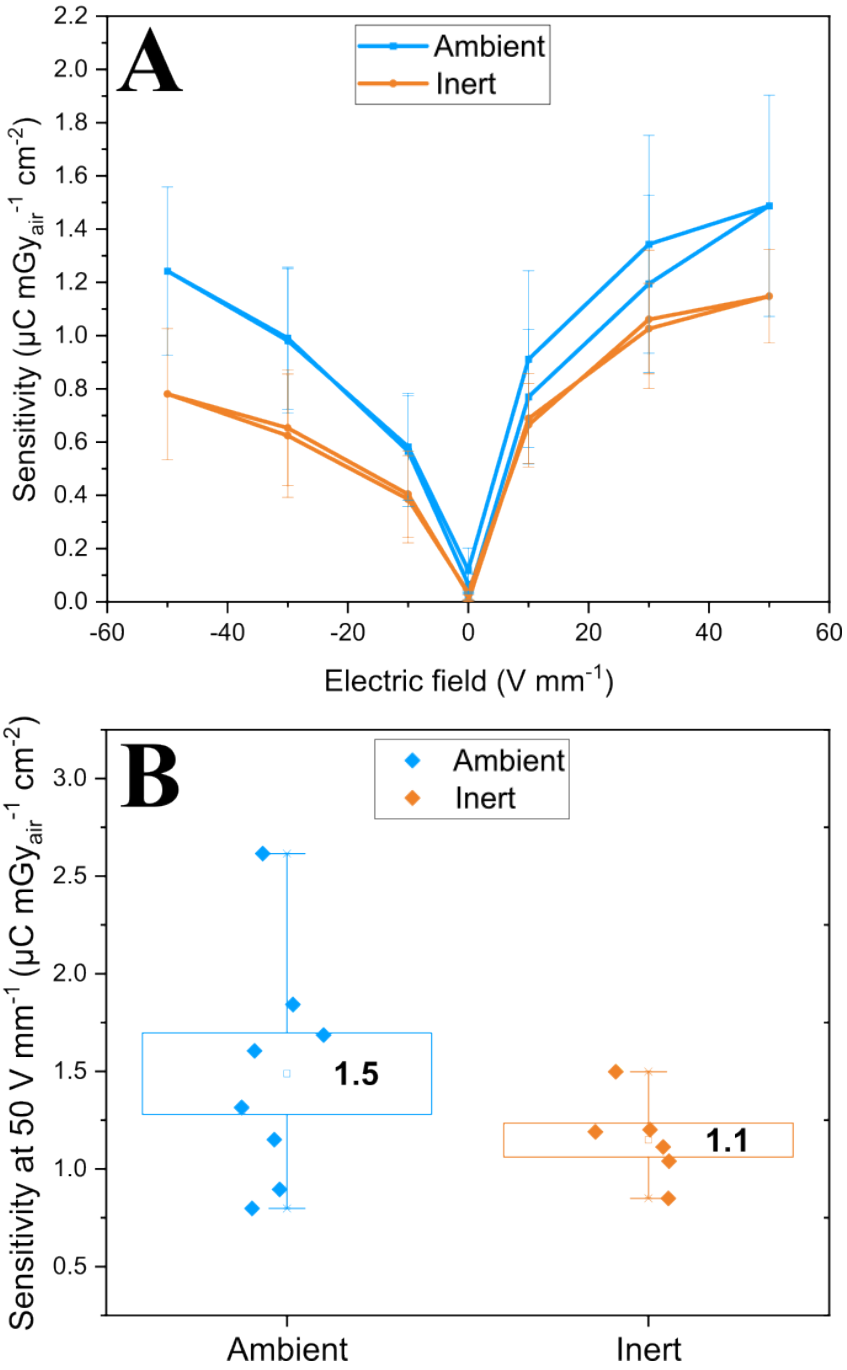

Figure 4-3-3. Sensitivity comparison between AC and IC SC devices. (A) Sensitivity as a function of the resulting electric field for both set of crystals in atmospheric conditions. **(B)** Statistical repartition of sensitivity *S* values for all evaluated SCs at 50 V mm^{-1}. The plots above consider the 14 SC devices that were analysed in standard atmosphere: 8 AC and 6 IC SC devices.

Besides a lower sensitivity for high electric fields for the IC, other differences between AC and IC devices are worth noting. On the one hand, when reversing the biasing from 50 V mm^{-1}, IC SC devices present lower hysteresis (**Figure 4-3-3-A**) and variability (lower standard deviation in **Figure 4-3-3-B**). On the other hand, the AC devices present more symmetrical S-V (or S-F) curves. In the ideal case, having a high sensitivity means having high

charge carrier collection, thus less charge carriers trapped by point defects. The symmetry degree of S-V curves is directly linked to the transport properties of electrons and holes in the semiconductor. In Chapter 3, we saw that performing Hecht fits on them allow estimating mobility-lifetime $\mu\tau$ products of both charge carriers. Even though, the Hecht equation do not properly fit $MAPbBr_3$ SC device response under X-ray illumination, because of parasitic ion migration,[28,29] laser ToF were performed as usual to estimate charge carrier mobilities.

Examples of resulting ToF measurements for a couple of AC SC devices are depicted in **Figure 4-3-4**. On the one hand, **Figure 4-3-4-A** (first device) and **Figure 4-3-4-B** (second device) show the waveform signals of holes transit: hole mobility μ_h is successfully determined for both SCs. On the other hand, **Figure 4-3-4-C** (first device) show the waveform signals of electron transit: electron mobility μ_e is determined just for one SC. Given that some devices did not present the pseudo-rectangular proper shape, low SNR, and/or enough inflexion in the corresponding waveforms as seen in **Figure 4-3-4-D** (second device), the transit time, hence mobility value of the charge carriers could not be determined. Thus, the sampling for mobility determination was lower than for J_{dark}-F or S-F data: 7 AC and 3 IC SCs for hole mobility, and 3 AC and 1 IC SCs for electron mobility, were studied. ToF measurements examples for IC SC devices are not shown here given the shape similarity of the waveforms with AC SCs.

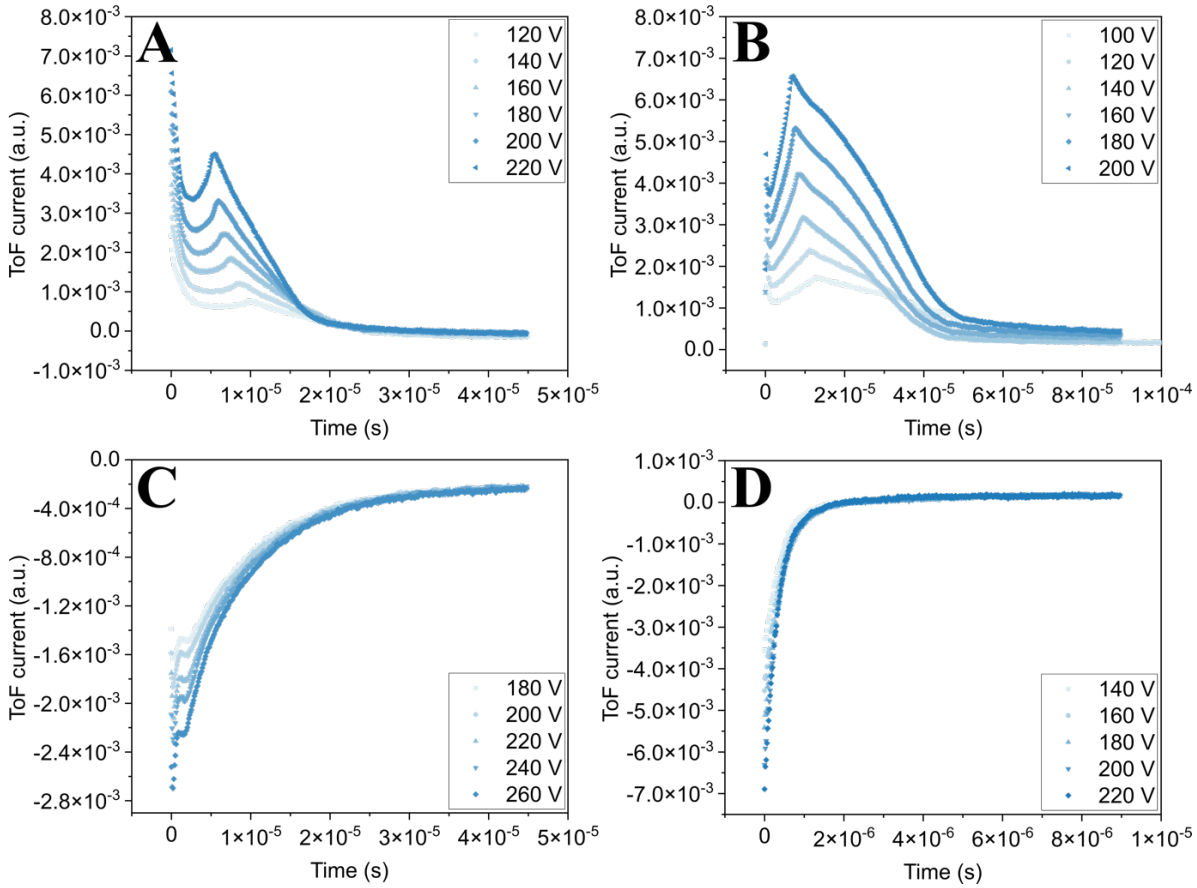

Figure 4-3-4. ToF measurements on two AC SC devices. Charge carrier transit waveforms at different voltages for determination of hole (**(A)** and **(B)**) and electron (**(C)** and **(D)**) mobilities.

The rapid decrease at the beginning is likely due to a sufficiently deep trap or a decreasing electric field, indicating a strong accumulation of charges near the laser input electrode. The subsequent increase is probably caused by a rising electric field, which also signifies an accumulation of charges near the opposite electrode. A "bathtub-shaped" field could create this shape.[30]

On the one hand, **Figure 4-3-5-A** presents the resulting hole mobilities μ_h for both type of devices. Both growth conditions present very similar values, coherent with our standard $MAPbBr_3$ SC device.[30] Therefore, hole mobility cannot be seen as the origin of the differences in sensitivity between AC and IC devices. On the other hand, and as major discovery in this chapter and thesis work, several AC SCs devices presented electron mobility μ_e, while it was measured only one time in IC SCs. The electron mobility almost doubles in average the hole mobility as exposed in **Figure 4-3-5-B**. Cr/$MAPbBr_3$/Cr devices produced via the standard procedure, described in Chapter 2, do not usually exhibit electron mobility, as pointed out during Chapter 3 discussion.

An enhanced contribution of the electrons to the sensitivity for the AC sample could explain the difference in symmetry of the S-F curves, when comparing positive and negative biases. The fact that we were able to determine hole mobility for most samples but electron mobility for only some devices, indicates a difference not only of mobility but more globally of the ability of electrons to migrate within the semiconductor to be collected. This ability is represented by the product $\mu\tau F$, also named the *schubweg* ("travel distance"). In the cases at hand, the fact that electrons were not always detectable contrary to holes, would indicate that the *schubwegs* of electrons $\mu_e\tau_e F$ is inferior to that of holes ($\mu_e\tau_e F < \mu_h\tau_h F$). Baussens hypothesised that the difficulty to measure electron mobility μ_e was caused by an electron lifetime τ_e inferior to that of hole τ_h, and especially lower than its transit time t_t. The former was estimated at ~ 1 µs and the latter at ~ 10 µs.[30] The dissymmetry in charge transport would explain why $MAPbBr_3$ does not attain the maximal sensitivity theoretical S_{max} value, in both bias domains, which is defined as the sensitivity when all the charge Q_0 generated by X-rays in the material is collected, as explained in Chapter 2.

If we now consider the difference of electron detectability between the AC- and IC-based devices, the measured mobility seems to be quite similar, in terms of proportions: 42.8 % and 33.3 %, respectively, among the samples presenting as well hole mobility. So, the difference in behaviour between AC and IC devices regarding electrons could come from differences in lifetime and/or in residual p-doping. Indeed, $MAPbBr_3$ is believed to have a p-doped character,[31] as stated in Chapter 3, which means that, if we assume that the doping concentration is sufficiently high to have electrons and hole with similar mobilities or at least in the same order of magnitude, the $\mu\tau$ product relies mainly in the lifetime. Counter-balancing the intrinsic doping of $MAPbBr_3$ would boost the charge transport of electrons, by rising potentially their lifetime τ_e thus their $\mu_e\tau_e$ product, making them detectable, potentially with an even higher mobility than that of holes.

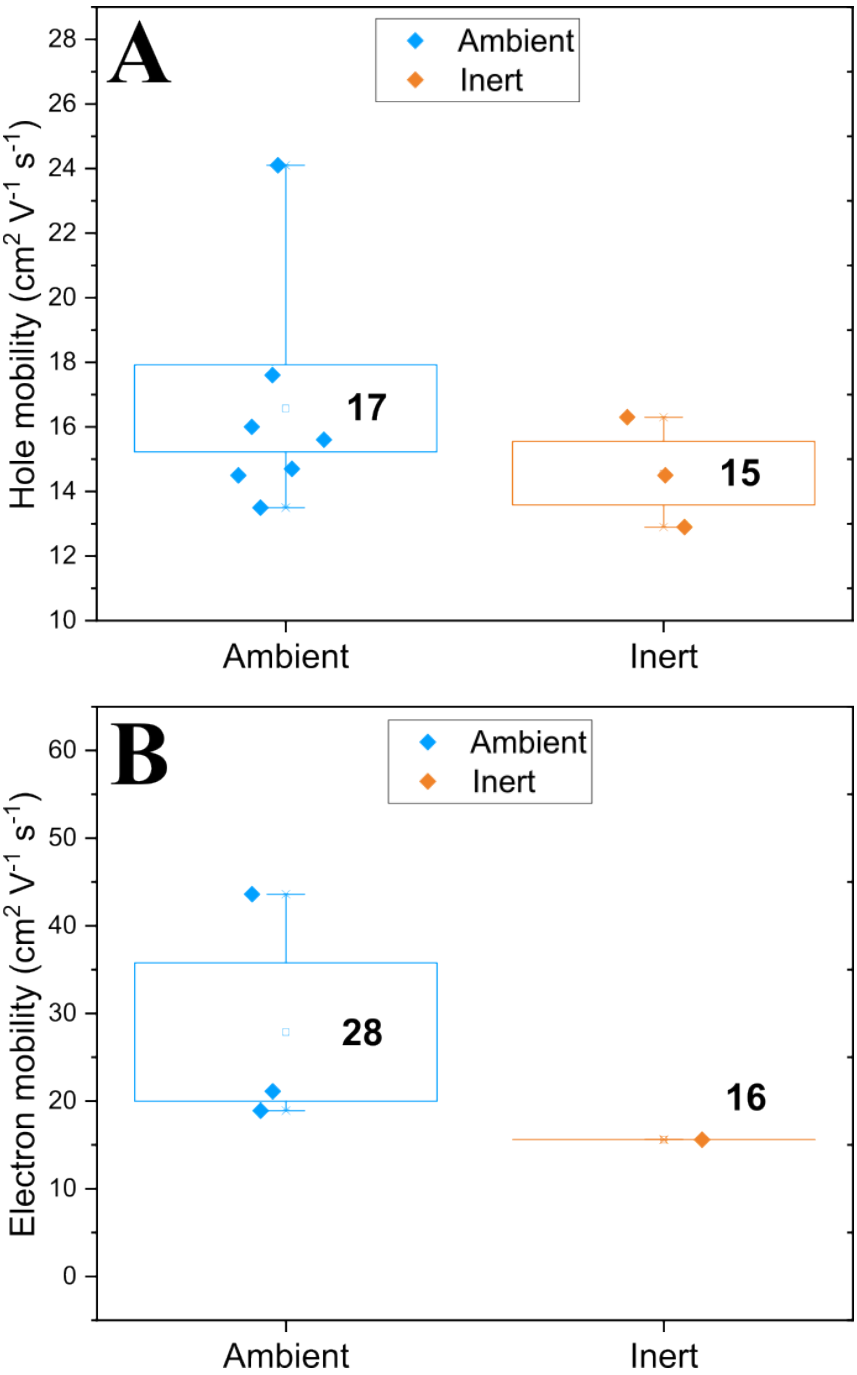

Figure 4-3-5. Hole and electron mobilities comparison between AC and IC SC devices. Statistical repartition of **(A)** electron and **(B)** hole mobilities values, μ_e and μ_h, respectively. The plots above consider: for hole mobility, 10 SC devices (7 AC and 3 IC SCs), and for electron mobility, just 4 SC devices (3 AC and 1 IC SCs). The devices were analysed in standard atmosphere.

Therefore, the higher degree of symmetry in the charge transport properties observed for the AC samples over IC ones, could be due to a counter-balance of the p-doping character. In the previous part **1.2**, we saw that the only difference between AC and IC samples was a higher number of environmental molecules that we identified as H_2O on the surface of AC samples. The presence of water would be coherent with the counter-balancing of their p-doping

as several research teams have proven the n-doping effect of H_2O molecules.[1,2] As proved by XPS analysis, we would be dealing with a surface effect. This then raises the question whether the compensation of the p-doping at the surface would be sufficient to impact the electron detectability, and hence the sensitivity measurements. Almora et al. demonstrated, via current transients and impedance spectroscopy, that surface and bulk differ in transport properties, and that surface currents greatly contribute to the total electrical current in MHP SCs.[32] Therefore, it is highly possible that the presence of water on the surface can have a significant impact on the optoelectrical performance of MHP devices, as we see here in the S-F curves and the charge carrier properties.

It worth pointing out that Wang et al. evidenced a surface p-doping for N_2 and O_2 molecules. While both species were not evidenced in the material characterisation, if the opposite was the case, they might just accentuate the p-doped character of $MAPbBr_3$ on the surface.[1] The same could be said about Al impurities detected for the AC crystals in the GDMS results: Al could be present as Al^{3+} ions.

The optoelectronic characterisation of AC and IC SC devices under standard atmospheric conditions lead to the hypothesis that water present in the surface for the AC devices is the principal reason responsible for the difference in behaviour observed in the sensitivity measurements. Water would induce then the symmetrisation of the S-F curves, thus an amelioration of the charge transport properties via induced longer lifetimes of electrons τ_e, thus improving the $\mu_e\tau_e$ product. The behaviour of holes would remain the same as for SC devices produced via the standard synthesis procedure, for both growth crystal growth conditions.

Water can intervene at several steps of the synthesis-optoelectronic characterisation process. Nevertheless, water does not seem to be adsorbed on the surface of IC devices during the characterisation in open air. This is why it was decided to test the total absence of air via the sealed boxes described in the previous part. The influence of the testing atmosphere while performing the optoelectronic characterisation and its impact under X-ray irradiation on both SC growth conditions are exanimated in the next part.

3.2 Influence of the crystal growth conditions and testing atmosphere on optoelectronic properties

3.2.1 Testing in Ar atmosphere

The influence of air exposure during testing, including under X-ray irradiation, was evaluated by performing the J-t measurements in the sealed test box described in part **2**. Each device is mounted in the sealed box in the storage Ar-glovebox as stated earlier.

The outcome in Ar atmosphere is represented in both **Figure 4-3-6-A** and **Figure 4-3-6-B**. For most electric fields considered, both growth conditions have similar J_{dark}

values, especially in the negative biases. At positive biases, the AC lose its symmetry with increasing electric field when compared to the IC and its negative branch. Its J_{dark} value doubles at 50 V mm^{-1} with respect to -50 V mm^{-1}.

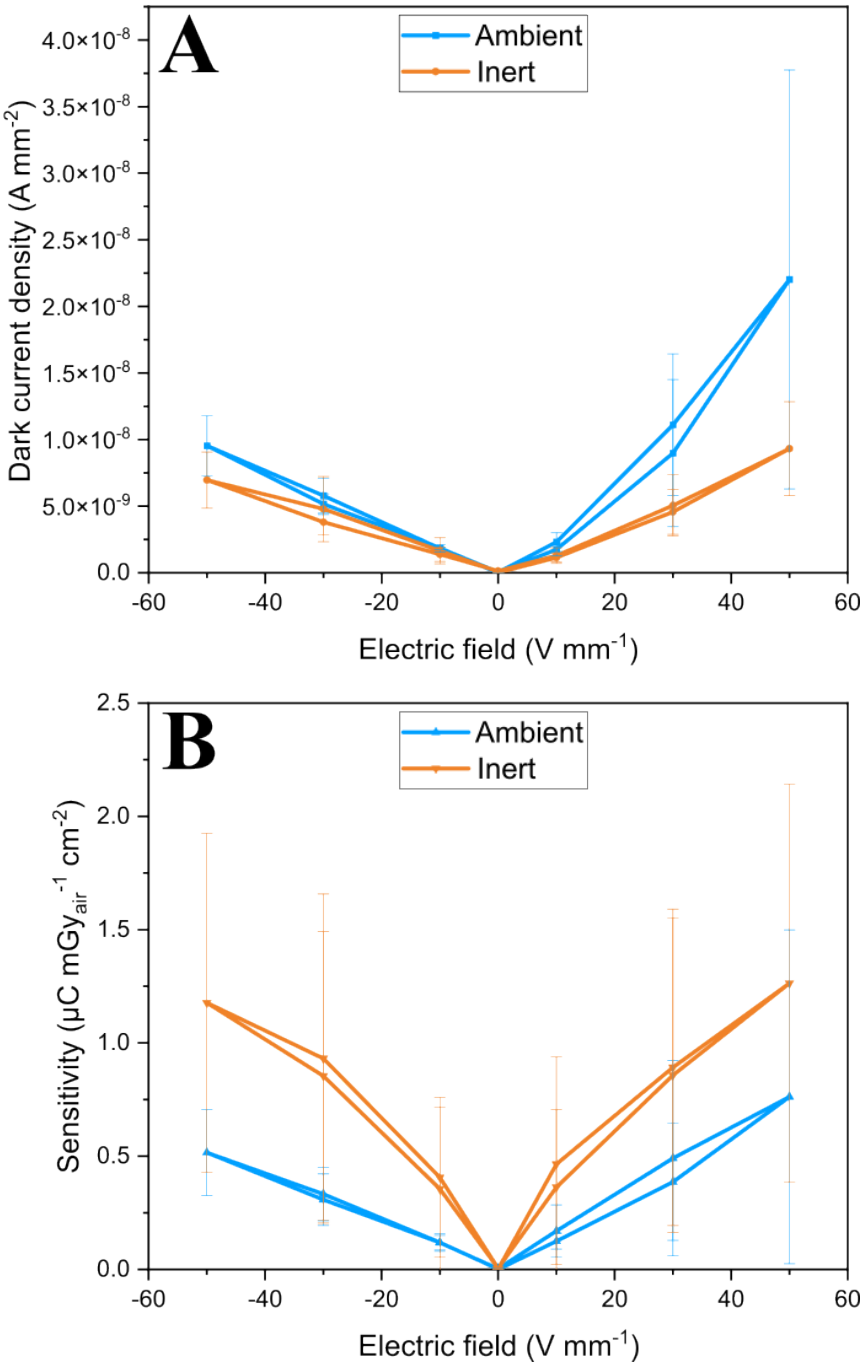

Figure 4-3-6. Optoelectronic performance in Ar atmosphere. (A) Dark current density and **(B)** corrected sensitivity as a function of the resulting electric field for both set of crystals in inert testing conditions. The plots above consider the 4 SC devices that were analysed in Ar atmosphere: 2 AC and 2 IC SC devices.

For the determination of the sensitivities, because no collimator was used with the sealed boxes, it was decided to take into consideration the whole surface of the SC device and not just

the surface of the electrode like in the previous characterisations. By not considering the whole surface, covered and not covered by the Cr electrode, the sensitivity *S* is overestimated and cannot be directly compared with previous values. This pitfall will be addressed later on, but these measurements still provide interesting input. A comparison of the results with the brass box protocol (just electrode surface considered) and the ones using this surface correction for the sealed box can be found in **Figure A 4-5-1**. **Figure 4-3-6-B** shows only then corrected *S* values obtained for both growth conditions, prepared and analysed under inert atmosphere.

Here, contrary to what was observed for device preparation and testing in atmospheric conditions, on average the IC SC devices have significantly higher *S* values than the AC ones. Overall, both growth conditions have a symmetrical response to X-rays. In the previous part, the higher symmetry and sensitivity of the AC were attributed to better charge carrier transport within the material: both electron and hole *schubwegs* were "equilibrated" thanks to the presence of water. Here, in Ar testing atmosphere, one can suppose the same thing: both AC and IC devices could have the same significative contributions of both electrons and holes. This suggests that we may be able to measure both mobilities. This enhanced contribution of electron was associated to water surface effect, allowing the compensation of the natural p-doped character of $MAPbBr_3$. Here, the improvement of the IC sensitivity takes place during the X-ray evaluation in inert atmosphere, which makes harder to attribute the same mechanism. Notwithstanding, it is possible. If we consider that surface passivation of the device makes water intervene in the process, then a test in atmospheric conditions with a certain moisture level and under X-rays can lead to a n-doping of the surface in anyway. The difference in behaviour of AC and IC devices could be explained if one considers that they do not have the same initial doping: AC devices would be p-doped and IC devices would have a state closer to the intrinsic one, defined by the precursors themselves. Consequently, the analysis in atmospheric conditions allows the n-doping of their surfaces, which has different consequences on both types of devices. AC devices, rather p-doped, are compensated and become more intrinsic on the surface, thus having their sensitivities improved. Instead, the IC devices, rather intrinsic, see their performance downgraded. In contrast, during inert atmosphere testing, the n-doping does not take place, which means that AC SC devices stayed p-doped on the surface and their response under X-rays is worse than that of IC devices, staying close to the intrinsic state.

To further test this hypothesis, it would be required to compare identical samples of each type of device, tested under different conditions (Ar and air) but with the same apparatus (sealed test box without collimator). That is why, during the course of testing under Ar atmosphere, sample were exposed to air, and their behaviour under both atmospheres and the transition between the two was studied (see **Figure 4-2-3**). As the number of samples per condition is relatively small, a statistical presentation would not have much meaning, that is why instead we present characterisations per SC device.

3.2.2 Ar-to-air tests: J_{dark}-V and S-V

The protocol followed for this study is as follows. The usual full biasing cycle (1st loop) is done in Ar atmosphere. The cycle allows reaching standard evaluation electric fields ranging from 0 to +50 V mm^{-1} (forward and reverse) and from 0 to -50 V mm^{-1} (forward and reverse). Then, for the transition from Ar to air atmosphere, the voltage is kept at -10 V (with the exception of one sample, kept at 10 V) for 1 to 2 min for current stabilisation. The box valve is subsequently opened to let ambient air inside. Given that the box is slightly over pressurised, the air entry must be relatively weak at first, with an inferior exposition to air than that in standard atmospheric conditions for a couple of seconds. J-t data is recorded for approximately 45 min while making sensitivity acquisitions repeatedly. At the end of this time period, another full biasing cycle is accomplished (2nd loop) in ambient air. An example of the procedure can be found in **Figure 4-3-7**. The procedure allows several things: **(i)** comparing the S-V data between Ar and air atmospheres without experimental discrepancies and **(ii)** analyse the Ar-to-air transition via its impacts on the J-t continuous monitoring.

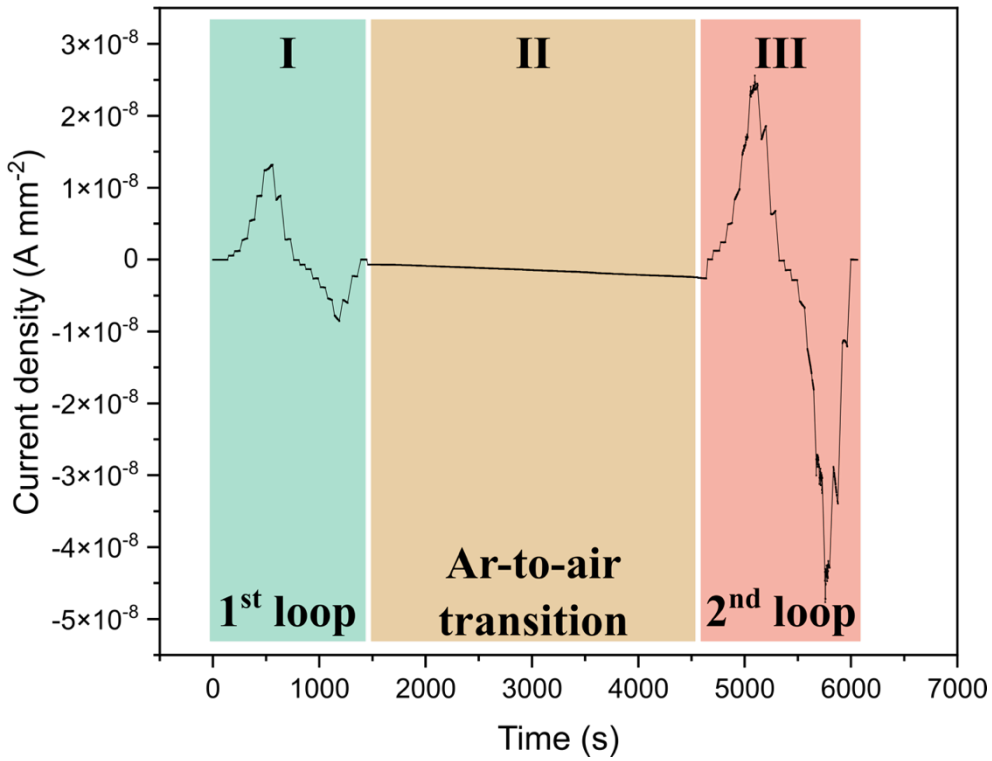

Figure 4-3-7. Current density as a function of time for AC SC **(1)**. Three different steps can be observed: S-V in Ar atmosphere (step I - 1st loop), Ar-to-air transition evaluation (step II), and S-V in air (step III - 2nd loop).

The dark current density and sensitivity in Ar and air atmospheres are presented in **Figure 4-3-8** and **Figure 4-3-9**, respectively. For both figures, each graph corresponds to a given device. AC and IC SC devices are in the left **(A)** and right **(B)** columns, respectively.

Each graph contains two plots: in green (*Ar*), the test performed in Ar atmosphere, and in red (*Air*) the test performed in air atmosphere.

With respect to dark current density (**Figure 4-3-8**), the exposure to air makes J_{dark} values higher and J-t signal noisier, which is translated into a loss of symmetry between negative and positive bias domains and more hysteresis, when compared to Ar-tests.

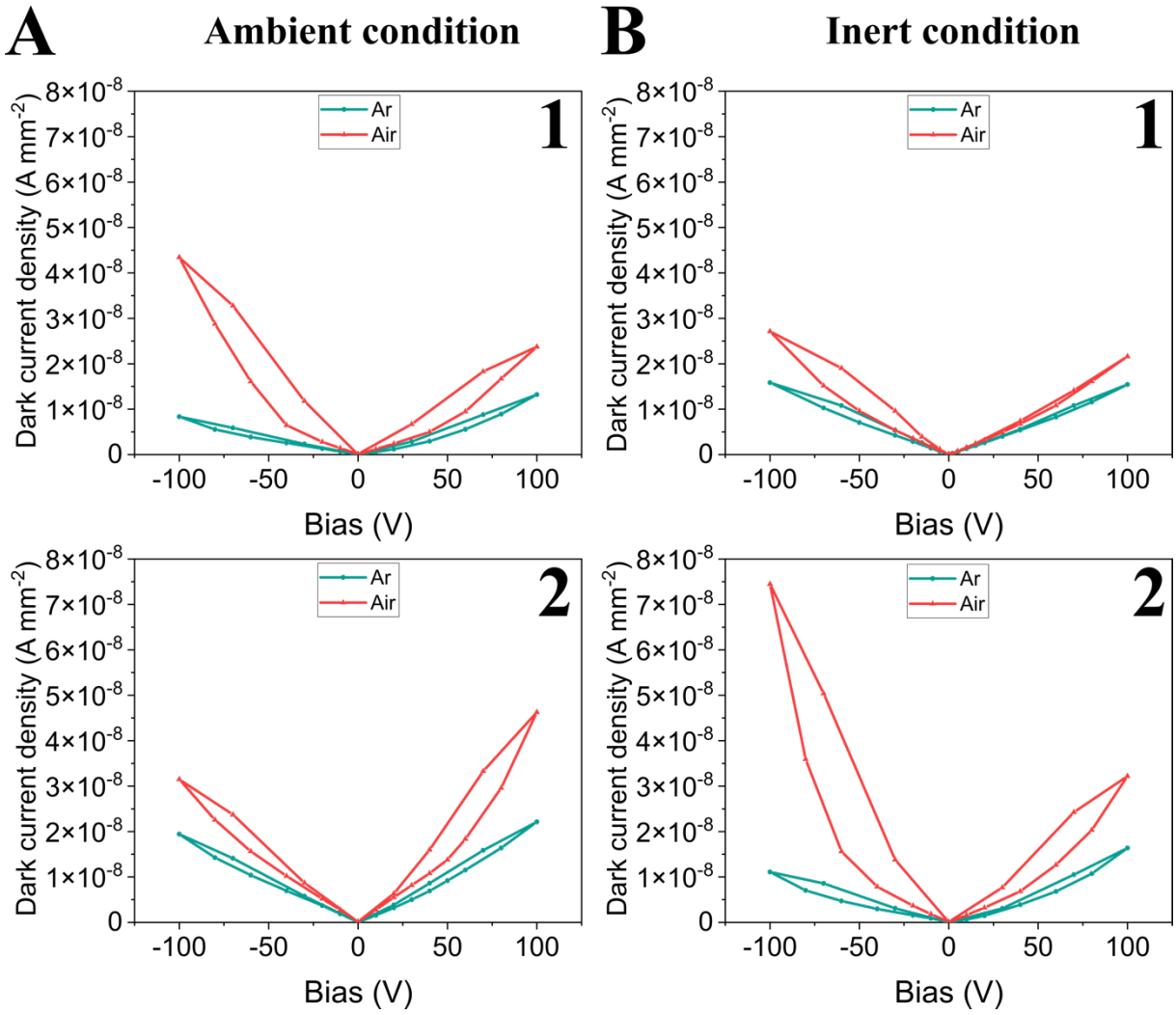

Figure 4-3-8. Dark current density comparison between AC and IC SC devices in Ar and air atmospheres. Dark current density as a function of bias for **(A)** the AC: SCs **(1)** and **(2)**, for **(B)** the IC: SCs **(1)** and **(2)**. Headers refer to synthesis conditions. J_{dark}-V measurements take place in Ar (green plots – 1st loop) and air (red plots – 2nd loop) atmospheres. After the 1st loop is completed, the sealed box is opened to air, to evaluate the impact of air on the device.

This change in dark current can be explained by our main hypothesis regarding the effect of the atmosphere chemical composition on the contact surface, especially with the presence of N_2, O_2 and H_2O, as seen earlier.[1] But, because the two measurements are done in sequence, one should also consider the possible influence of the biasing history of the sample: before being tested in air (2nd loop), the sample is tested in Ar (1st loop). The 1st loop can influence the charge distribution within the bulk and so modify the internal electric field perceived by the charge

carrier. As mentioned in Chapter 3, the ion migration (mainly Br^-) inside the structure is possible. Thus associated charged point defects (e.g., interstitials Br_i and vacancies V_{Br}) can accumulate at the vicinity of the electrodes, screening incoming charge carriers and deforming the internal electric field.[28–30] This effect is expected to takes place especially for long biasing protocols like for these tests.

As a result of this, the mixed electronic-ionic current density can potentially contribute to more noise in the signal and a current drift like the one seen in **Figure 4-3-7**. When comparing the J-t data 1st (step I) and 2nd (step III) loops: one can see that at every voltage increment performed, the current drift is more important in the 2nd loop than in the 1st loop, and even more with increasing biasing time. Migration-accumulation of charge species and defects at the metal-semiconductor interface could also lead to photoconductive gain, worsening the outcoming signal.[33] One could hypothesised that the resulting configuration of point defects could form a Schottky contact similar to the ones seen at the interface between a metal and an organic semiconductor. Band bending would occur and trapped charge carriers would provoke the injection (tunnelling process) of the reciprocal charge carriers from the Cr electrode into the material.[34]

Regarding the measured sensitivity (**Figure 4-3-9**), the transition from Ar to air seems to leads to mixed behaviours. For a first pair (AC SC **(2)** and IC SC **(1)**), the air exposure does not seem to influence radically the S-V data: symmetry and hysteresis are unchanged, even though the J_{dark} values raised for those samples (**Figure 4-3-8**). The second pair (AC SC **(1)** and IC SC **(2)**) was apparently more affected by the presence of air, especially at negative biases: symmetry is lost and the hysteresis is very important. These observations on the behaviour of the sensitivity could also be explained by the two hypotheses stated earlier regarding the dark current: surface doping, enhanced ion migration by the long biasing time and thus photoconductive gain.

The study of the dark current and sensitivity under different atmospheres has enabled us to get some insights into the behaviour of $MAPbBr_3$. The main features to be considered are: the ion migration contribution in the internal bulk dynamics under bias, and the surface chemical reactivity of the device. The latter seems to be correlated with the synthesis conditions as air atmosphere does not have the same effect on AC and IC devices. Whether it is the same for the ion migration remains unclear at this stage.

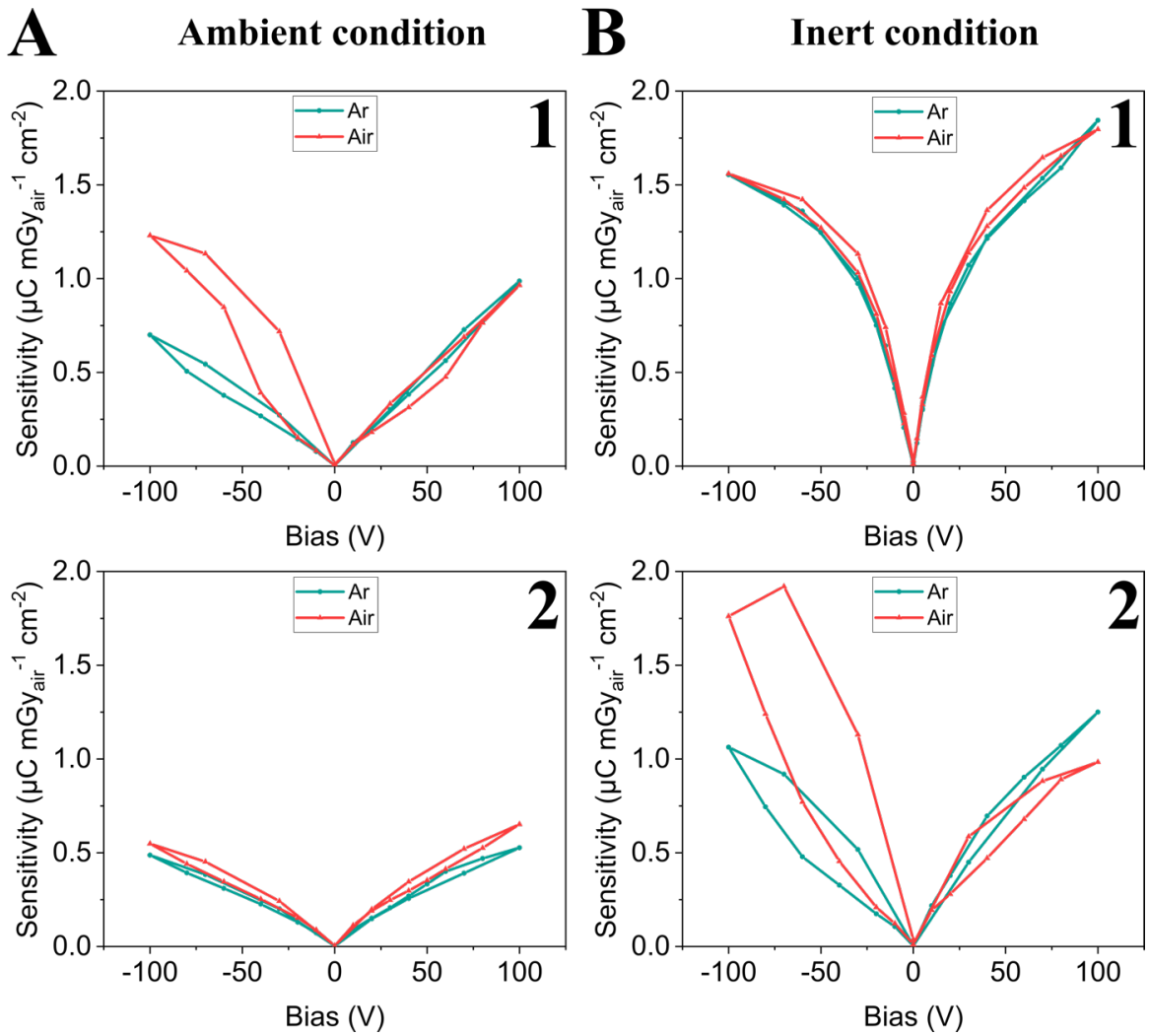

Figure 4-3-9. Sensitivity comparison between AC and IC SC devices in Ar and air atmospheres. Sensitivity as a function of bias for **(A)** the AC: SCs **(1)** and **(2)**, for **(B)** the IC: SCs **(1)** and **(2)**. Headers refer to synthesis conditions. S-V measurements take place in Ar (green plots – 1st loop) and air (red plots – 2nd loop) atmospheres. After the 1st loop is completed, the sealed box is opened to air, to evaluate the impact of air on the device.

3.2.3 Ar-to-air transition – Effect of air on J-t measurements

The characterisations presented above, on sequential exposition of the devices to argon then air, offers an original perspective to test the validity of one of our hypotheses: the air-surface reactivity. Considering that ion migration affects the results gathered over extended periods of time (long duration of the voltage swipes), if one looks at changes over short time periods then the impact of ion migration should be reduced. If in that short time period a dramatic change in environment takes place then the impact of air could be more readily observable. That is why we took a particular interest in the transient part of the protocol presented above (step II in **Figure 4-3-7**), when air was introduced in the chamber of the sealed test box under constant biasing. Looking closer into the step II in **Figure 4-3-10-A**, one can observe that the air introduction corresponds to an abrupt change of slope, as made explicit in

Figure 4-3-10-B. This event is quite subtle, about one order of magnitude less (~ 10^{-9} A mm^{-2}) when compared to the J_{dark} value at -10 V (~ 10^{-8} A mm^{-2}).

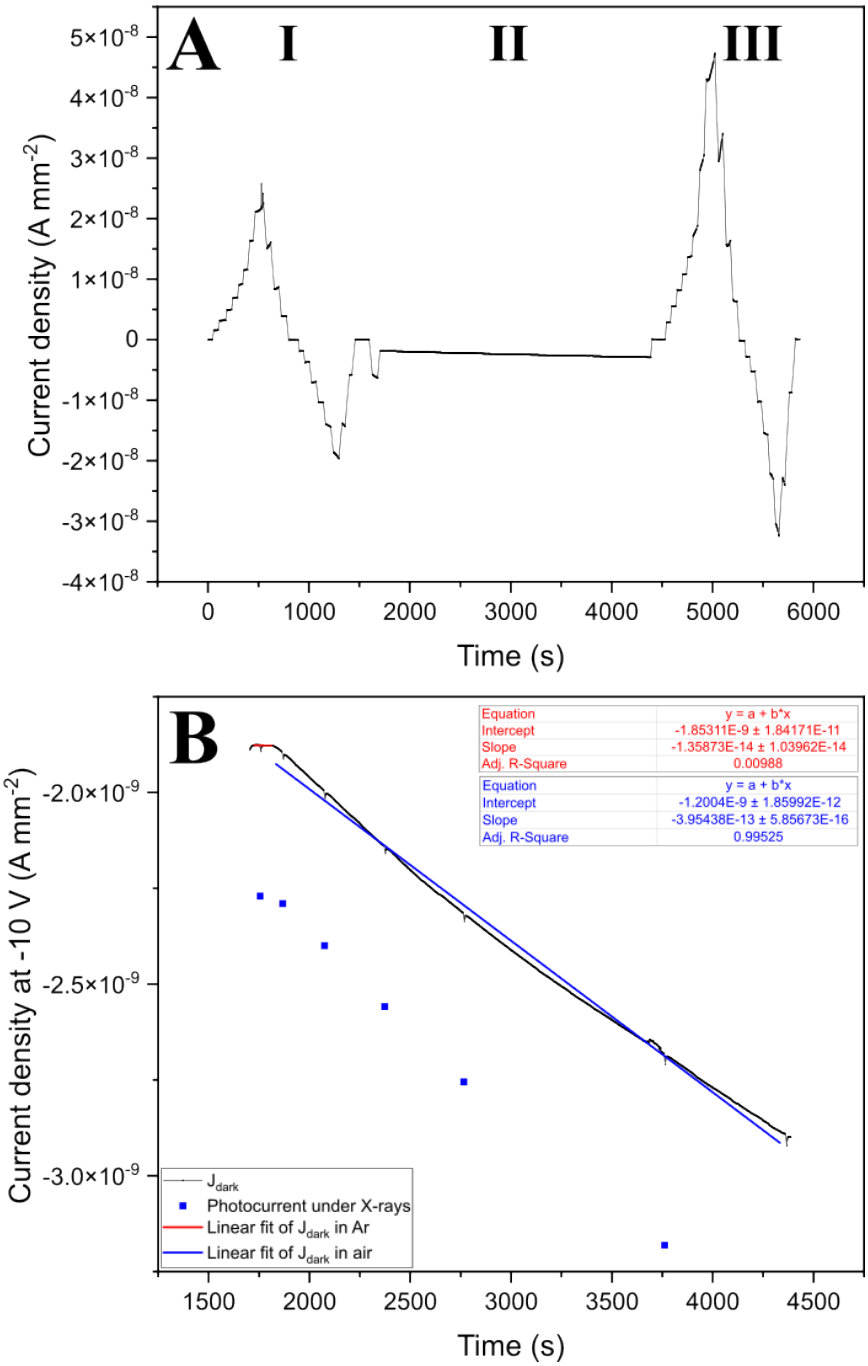

Figure 4-3-10. J-t data in inert and atmospheric testing conditions and Ar-to-air transition analysis for AC (2). (A) Current density as a function of time. The three different steps can be observed (steps I, II and III). It is worth pointing that before stabilising -10 V, a -30 V bias is set for a couple of minutes by error for this device. **(B)** Step II zoom illustrating the slope change of J-t when the valve is opened: a -10 V bias is used and X-rays were shot for sensitivity measurements (blue squares). Two linear fits are performed corresponding to the segments where the SC device is in Ar (red) and air (blue) atmospheres.

Before opening the valve, the J-t signal is drifting (part fitted in red in **Figure 4-3-10-B**, slope 10^{-14} (A.mm^{-2}) s^{-1}), this can reasonably be attributed to the ion migration discussed above. Once the valve is opened, the contact with air makes the current drift faster (part fitted in blue in **Figure 4-3-10-B**, slope 10^{-13} (A.mm^{-2}) s^{-1}) and stays monotonous till the step III is performed by the operator. The same analysis was performed for all four AC and IC SC devices: see annexe **Figure A 4-5-2** and **Figure A 4-5-3**.

The drift in dark current is also manifested in a continuous drift of the sensitivity data during this -10 V-constant biasing, as depicted in **Figure 4-3-11**. Hence, this change in behaviour of the dark current and the sensitivity, upon exposure to air do not disprove the influence of ion migration but support our hypothesis of a concomitant air/surface reaction.

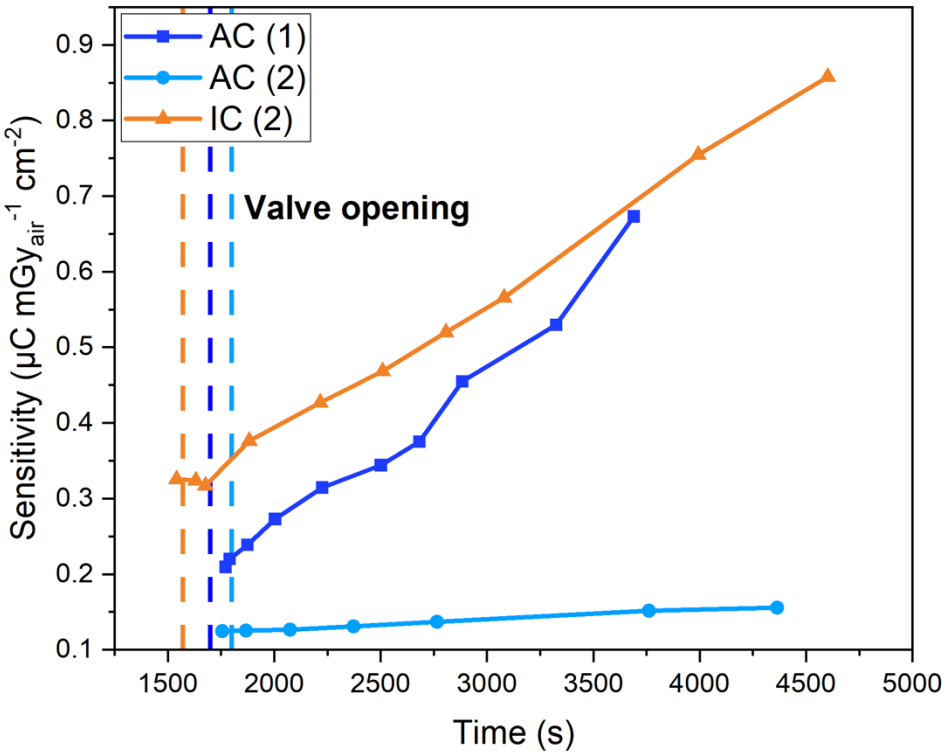

Figure 4-3-11. Sensitivity drift while being at -10 V for Ar-to-air transition analysis. The data shown here correspond to the sensitivity extracted from the pulsed irradiations seen in the J-t curve in **Figure 4-3-10-B** (blue squares). IC SC **(1)** is excluded from the plot (study performed at 10 V). The *S* values depicted here are not corrected.

3.2.4 Charge carrier mobility after air exposition

It is hard to dissociate the influence of several parameters (e.g., growth and testing atmospheres), given the dynamic nature of the defect architecture of $MAPbBr_3$ and hybrid MHPs in general, driven in the bulk mainly by ion migration. That said, the slight upper hand of the AC seen when the devices are tested in standard atmospheric conditions, does not seem to appear when the AC devices are polished in glovebox. It is more the opposite that is seen in the Ar-air comparison study, as seen in **Figure 4-3-6**: the IC performs better in terms of sensitivity. Even if the sampling for inert characterisation was smaller compared to the one performed for atmospheric conditions, we determined the mobility of both electrons and holes via laser ToF measurements for the four devices as well.

Like in the case of the previous study, some mobility values could not be extracted (e.g., noise, shape of waveforms). Nevertheless, electron mobility was found in 2 out 4 devices, the ones having a symmetric S-V response: both IC SCs. These measurements done on devices prepared in inert atmosphere confirms what was first observed for devices prepared and characterised under atmospheric conditions: a S-V symmetric response is correlated with an electron contribution. The results are summarised in **Table 4-3-1**. Because the determination of the mobility is tricky sometimes, the unusually high values (e.g. μ_h for AC SC **(2)** and μ_e for IC SC **(2)**) have to be regarded with caution and one may consider that both IC devices presented both charge carrier mobilities in the same order of magnitude usually measured for our SCs.

It is interesting to note that only the IC devices prepared under inert atmosphere showed measurable electron mobility, which is precisely what one would expect from the assumption used in part **3.2.1** (AC SC p-doped, IC SC more "intrinsic"). However, because these samples were exposed to air during the second biasing loop this cannot be taken as proof, unless one considers that the preparation in atmospheric conditions has more impact on electron mobility than the characterisation in atmospheric conditions.

Table 4-3-1. Electron and hole mobilities measured for Ar-air testing atmosphere comparison study via laser ToF.

Sample	Electron mobility μ_e [$cm^2\ V^{-1}\ s^{-1}$]	Hole mobility μ_h [$cm^2\ V^{-1}\ s^{-1}$]
AC **(1)**	-	-
AC **(2)**	-	51
IC **(1)**	22.1	16.5
IC **(2)**	62	23.6

Conclusion

This study not only presents the influence of growing $MAPbBr_3$ SCs in both ambient and inert atmospheres, but also the influence of the testing atmosphere. Growth solutions and crystal growth in DMF via adaptive temperature ramps took place in uncontrolled standard laboratory and controlled oxygen-less Ar atmosphere glovebox conditions, labelled the AC and IC, respectively.

This work evidences the impact of the environment at the synthesis stage. Some interesting differences between the AC and IC have been observed. Regarding the bulk of crystals, GDMS showed that some impurities are more present in the AC than in the IC. Some of these impurities (e.g., Na^+) could substitute ions of the structure (MA^+, Br^-) without doping it. Additionally, the more important presence of Al in AC crystals could lead to an enhanced p-doped character of the perovskite. XPS analysis showed a surprising resilience of the synthesis towards the incorporation of environmental species in the bulk structure. However, a specific behaviour of the crystals surface was found depending on the synthesis environment: the AC surface is more Br deficient and is N deficient (MABr deficiency at AC crystal surface) and present more exogenous O when compared to IC crystals. So, AC crystals are considered more p-doped and with a surface significantly different from that of IC crystals. FTIR analysis indicated that O-containing species are present on the AC surface, possibly corresponding to adsorbed H_2O molecules, inducing a n-doping of the material.

From an optoelectronic point of view, when testing the SC devices in atmospheric conditions, the AC seem to have the upper hand when confronted to the IC, by showing slightly higher sensitivity values, more symmetrical S-V data for both positive and negative bias domains, and more statistically measurable mobilities for both charge carriers, which has been a rare event within our group. This might be a result of the n-doping and passivating effect caused by superficial water cumulated in during the whole synthesis-characterisation process, leading to better charge transport properties in the SC device.

To quantify the effect of the atmosphere while establishing the optoelectronic performance of the devices, a fully inert synthesis-characterisation circuit was employed using newly-designed sealed boxes. Assessing the impact of the testing atmosphere presents some challenges as not only the atmosphere but also the biasing history of the device may influence the measurements. Tests in Ar and then in air atmospheres showed an impact of the environment of the device preparation and characterisation. Some properties seemed relatively unaffected (e.g., resistivity and dark current) but other showed a more dramatic impact. In particular, IC samples showed lower sensitivity than AC ones in ambient air preparation-analysis, but exhibited a higher sensitivity when prepared and analysed under inert atmosphere.

To explain this change, we hypothesised that the two types of samples had different doping states depending on the growth environment, which would be coherent with the chemical analysis presented above, and so the interaction of the preparation-analysis

atmosphere with their surface lead to overall different performances. AC crystals would initially show a stronger p-doping than IC crystals, that would be more intrinsic. Ambient atmosphere preparation and analysis would lead to surface interaction with environmental species having an n-doping effect (we suppose mainly water[11]). As a result, the AC would benefit from air preparation/characterisation as it would reduce its surface p-doping nature, but it would be detrimental to IC devices which were originally more intrinsic and thus becoming rather n-doped at the surface.

Because the optoelectronic characterisation setups for the two studies (testing in atmospheric and inert conditions) were too different (brass boxes compared to sealed boxes) and given the dispersion of values in each group of samples, no fine comparison was possible. Therefore, the use of the same samples and setup for both environments with a sequential Ar-to-air experiment confirmed that, with preparation and analysis under inert atmosphere, IC-based devices seemed to show higher sensitivity than AC based ones. However, the comparison of sensitivity in Ar and air was not straightforward as the effect of the atmosphere was blurred by the ion migration in the structure. As evidenced by the group of Garcia-Belmonte, devices that remain for an extended period of time under constant bias will see a drift in their properties (e.g., sensitivity, dark current).[28] To minimise the impact of this sample "aging" under bias, we observed the J-t data transient behaviour of the devices upon opening the test chamber to air. It confirmed that both AC and IC SC devices are affected by the exposure to air during the test by accelerating the J-t measurement drift, which is an element of our hypothesis. This suggests that the same effect occurs on both types of samples, but that they have different initial properties (AC more p-doped, IC more intrinsic). An indirect supporting element of that last point comes from the determination of the charge carrier mobility via laser ToF characterisation. For samples prepared (grown and polished) and analysed under atmospheric conditions, electron mobility could be detected almost exclusively in the AC samples while for samples prepared under inert atmosphere it could be determined only in IC devices. This could be viewed as an indication of a more intrinsic semiconductor for the latter, which is precisely what our hypothesis advances.

In addition to the effects of ion motion in the structure that causes the properties to drift and change over time under bias, the properties of a device appear to be also sensitive to the environment. At the synthesis stage, the presence of impurities (environmental or others) will affect the overall doping state of the semiconductor such Al for AC samples, but also the sensitivity of the surface to the environment: AC samples show surfaces with MABr deficiency, and H_2O molecules supposedly adsorbed. How the chemistry of the system makes the perovskite surface more sensitive has not been elucidated in spite of several chemical analyses, but it seems reasonable to assume that a correlation exists between impurities and the surface reactivity, promoted by halide/lead vacancies, among potentially other point defects. For the device preparation-analysis stage, the air or inert environments have an effect on the properties. This could be seen at the preparation stage: different ToF mobility results for samples prepared

in different atmospheres (detectability of electron mobility); and during the characterisation: change in behaviour observed during the Ar-to-air transition (accentuated J-t drift). The ToF measurements are coherent with our hypothesis. But, for Ar-to-air study measurements, the samples were exposed to air after preparation-analysis under inert atmosphere, before ToF measurement. At the end, the synthesis stage was the only element differentiating the two families of crystals. So, this confirmation should be taken with caution as is the corollary idea that the polishing environment is more critical than the analysis environment, at least for the first couple of biasing loops.

The presented work highlights the benefits of device preparation and potential encapsulation in inert gas atmospheres or crystal growth in atmospheric conditions with controlled humidity, as well as, as how susceptible is $MAPbBr_3$ towards its surroundings and an external stimulus. As we have seen, the surface plays a significant role in the optoelectronic response of the material. Depending on the synthesis conditions, the surface may exhibit significant deviation from stoichiometry. We believe that these observations could also explain the wide variability in performance reported in the literature for a given perovskite composition, and why it is so difficult to compare results with other groups. Considering this surface sensitivity, in the next chapter, a post-growth treatment was performed, exposing SCs to various atmospheres in an attempt to repair the surface from potential constituent losses or even to potentially compensate for vacancies in the bulk.

References

(1) Wang, C.; Ecker, B. R.; Wei, H.; Huang, J.; Gao, Y. Environmental Surface Stability of the MAPbBr $_3$ Single Crystal. *J. Phys. Chem. C* **2018**, *122* (6), 3513–3522. https://doi.org/10.1021/acs.jpcc.7b12740.

(2) Song, Z.; Shrestha, N.; Watthage, S. C.; Liyanage, G. K.; Almutawah, Z. S.; Ahangharnejhad, R. H.; Phillips, A. B.; Ellingson, R. J.; Heben, M. J. Impact of Moisture on Photoexcited Charge Carrier Dynamics in Methylammonium Lead Halide Perovskites. *J. Phys. Chem. Lett.* **2018**, *9* (21), 6312–6320. https://doi.org/10.1021/acs.jpclett.8b02595.

(3) Amari, S.; Verilhac, J.-M.; Gros D'Aillon, E.; Ibanez, A.; Zaccaro, J. Optimization of the Growth Conditions for High Quality CH $_3$ NH $_3$ PbBr $_3$ Hybrid Perovskite Single Crystals. *Crystal Growth & Design* **2020**, *20* (3), 1665–1672. https://doi.org/10.1021/acs.cgd.9b01429.

(4) Armaroli, G. Optoelectronic Investigation of Defects in Hybrid Metal Halide Perovskites. Ph.D. diss., Università di Bologna, Bologna, Italy, 2023.

(5) Hui, Y.; Webster, R. D. Absorption of Water into Organic Solvents Used for Electrochemistry under Conventional Operating Conditions. *Anal. Chem.* **2011**, *83* (3), 976–981. https://doi.org/10.1021/ac102734a.

(6) Zuo, S.; Niu, W.; Chu, S.; An, P.; Huang, H.; Zheng, L.; Zhao, L.; Zhang, J. Water-Regulated Lead Halide Perovskites Precursor Solution: Perovskite Structure Making and Breaking. *J. Phys. Chem. Lett.* **2023**, 4876–4885. https://doi.org/10.1021/acs.jpclett.3c00683.

(7) Müller, C.; Glaser, T.; Plogmeyer, M.; Sendner, M.; Döring, S.; Bakulin, A. A.; Brzuska, C.; Scheer, R.; Pshenichnikov, M. S.; Kowalsky, W.; Pucci, A.; Lovrinčić, R. Water Infiltration in Methylammonium Lead Iodide Perovskite: Fast and Inconspicuous. *Chem. Mater.* **2015**, *27* (22), 7835–7841. https://doi.org/10.1021/acs.chemmater.5b03883.

(8) Shen, L.; Chen, R.; Zhang, D.; Yilmazoglu, U. C.; Gu, K.; Sarmiento, J. S.; Zhu, T.; Zheng, L.; Zheng, J.; Wang, H.; Liu, C.; Gong, X. High-Performance Perovskite Photovoltaics by Heterovalent Substituted Mixed Perovskites. *Advanced Functional Materials* **2022**, *32* (47), 2207911. https://doi.org/10.1002/adfm.202207911.

(9) Aldave De Las Heras, L.; Bocci, F.; Betti, M.; Actis-Dato, L. O. Comparison between the Use of Direct Current Glow Discharge Mass Spectrometry and Inductively Coupled Plasma Quadrupole Mass Spectrometry for the Analysis of Trace Elements in Nuclear Samples. *Fresenius' Journal of Analytical Chemistry* **2000**, *368* (1), 95–102. https://doi.org/10.1007/s002160000529.

(10) Chen, B.; Wang, S.; Song, Y.; Li, C.; Hao, F. A Critical Review on the Moisture Stability of Halide Perovskite Films and Solar Cells. *Chemical Engineering Journal* **2022**, *430*, 132701. https://doi.org/10.1016/j.cej.2021.132701.

(11) Zhu, Z.; Hadjiev, V. G.; Rong, Y.; Guo, R.; Cao, B.; Tang, Z.; Qin, F.; Li, Y.; Wang, Y.; Hao, F.; Venkatesan, S.; Li, W.; Baldelli, S.; Guloy, A. M.; Fang, H.; Hu, Y.; Yao, Y.;

Wang, Z.; Bao, J. Interaction of Organic Cation with Water Molecule in Perovskite MAPbI3: From Dynamic Orientational Disorder to Hydrogen Bonding. *Chem. Mater.* **2016**, *28* (20), 7385–7393. https://doi.org/10.1021/acs.chemmater.6b02883.

(12) Li, G.; Zhang, W.; She, C.; Jia, S.; Liu, S.; Yue, F.; Jing, C.; Cheng, Y.; Chu, J. Stable Fluorescent NH3 Sensor Based on MAPbBr3 Encapsulated by Tetrabutylammonium Cations. *Journal of Alloys and Compounds* **2020**, *835*, 155386. https://doi.org/10.1016/j.jallcom.2020.155386.

(13) Gan, Z.; Yu, Z.; Meng, M.; Xia, W.; Zhang, X. Hydration of Mixed Halide Perovskites Investigated by Fourier Transform Infrared Spectroscopy. *APL Materials* **2019**, *7* (3), 031107. https://doi.org/10.1063/1.5087914.

(14) Glaser, T.; Müller, C.; Sendner, M.; Krekeler, C.; Semonin, O. E.; Hull, T. D.; Yaffe, O.; Owen, J. S.; Kowalsky, W.; Pucci, A.; Lovrinčić, R. Infrared Spectroscopic Study of Vibrational Modes in Methylammonium Lead Halide Perovskites. *J. Phys. Chem. Lett.* **2015**, *6* (15), 2913–2918. https://doi.org/10.1021/acs.jpclett.5b01309.

(15) Wang, Q.; Chen, B.; Liu, Y.; Deng, Y.; Bai, Y.; Dong, Q.; Huang, J. Scaling Behavior of Moisture-Induced Grain Degradation in Polycrystalline Hybrid Perovskite Thin Films. *Energy Environ. Sci.* **2017**, *10* (2), 516–522. https://doi.org/10.1039/C6EE02941H.

(16) Mannisto, J. K.; Pavlovic, L.; Tiainen, T.; Nieger, M.; Sahari, A.; Hopmann, K. H.; Repo, T. Mechanistic Insights into Carbamate Formation from CO_2 and Amines: The Role of Guanidine–CO_2 Adducts. *Catal. Sci. Technol.* **2021**, *11* (20), 6877–6886. https://doi.org/10.1039/D1CY01433A.

(17) Ioannidis, Th. A.; Kyriakis, N.; Zouboulis, A. I.; Akrivos, P. Lead and Bromide Precipitation from Aqueous Acidic Solutions. Potential Exploitation in Industrial Applications. *Desalination* **2007**, *211* (1–3), 272–285. https://doi.org/10.1016/j.desal.2006.03.598.

(18) Ramamurthy, P.; Secco, E. A.; Badri, M. Studies on Metal Hydroxy Compounds. X. Thermal Analyses, Decomposition Kinetics, and Infrared Spectra of Lead Halide (Cl, Br, I) Derivatives. *Can. J. Chem.* **1970**, *48* (16), 2617–2622. https://doi.org/10.1139/v70-438.

(19) Hamill, J. C.; Schwartz, J.; Loo, Y.-L. Influence of Solvent Coordination on Hybrid Organic–Inorganic Perovskite Formation. *ACS Energy Lett.* **2018**, *3* (1), 92–97. https://doi.org/10.1021/acsenergylett.7b01057.

(20) Kirmani, A. R.; Mansour, A. E.; Yang, C.; Munir, R.; El-Zohry, A. M.; Mohammed, O. F.; Amassian, A. Facile and Noninvasive Passivation, Doping and Chemical Tuning of Macroscopic Hybrid Perovskite Crystals. *PLoS ONE* **2020**, *15* (3), e0230540. https://doi.org/10.1371/journal.pone.0230540.

(21) Armaroli, G.; Ferlauto, L.; Lédée, F.; Lini, M.; Ciavatti, A.; Kovtun, A.; Borgatti, F.; Calabrese, G.; Milita, S.; Fraboni, B.; Cavalcoli, D. X-Ray-Induced Modification of the Photophysical Properties of $MAPbBr_3$ Single Crystals. *ACS Appl. Mater. Interfaces* **2021**, acsami.1c16072. https://doi.org/10.1021/acsami.1c16072.

(22) Amari, S. Étude des matériaux pérovskites pour la détection directe des rayonnements

ionisants. Ph.D. diss., Université Grenoble Alpes, Grenoble, France, 2020.

(23) Juarez-Perez, E. J.; Ono, L. K.; Maeda, M.; Jiang, Y.; Hawash, Z.; Qi, Y. Photodecomposition and Thermal Decomposition in Methylammonium Halide Lead Perovskites and Inferred Design Principles to Increase Photovoltaic Device Stability. *J. Mater. Chem. A* **2018**, *6* (20), 9604–9612. https://doi.org/10.1039/C8TA03501F.

(24) *WebBook de Chimie NIST*. https://doi.org/10.18434/T4D303.

(25) Juarez-Perez, E. J.; Ono, L. K.; Qi, Y. Thermal Degradation of Formamidinium Based Lead Halide Perovskites into *Sym* -Triazine and Hydrogen Cyanide Observed by Coupled Thermogravimetry-Mass Spectrometry Analysis. *J. Mater. Chem. A* **2019**, *7* (28), 16912–16919. https://doi.org/10.1039/C9TA06058H.

(26) Ceratti, D. R.; Zohar, A.; Kozlov, R.; Dong, H.; Uraltsev, G.; Girshevitz, O.; Pinkas, I.; Avram, L.; Hodes, G.; Cahen, D. Eppur Si Muove: Proton Diffusion in Halide Perovskite Single Crystals. *Adv. Mater.* **2020**, *32* (46), 2002467. https://doi.org/10.1002/adma.202002467.

(27) Mannino, G.; Deretzis, I.; Smecca, E.; Giannazzo, F.; Valastro, S.; Fisicaro, G.; La Magna, A.; Ceratti, D.; Alberti, A. CsPbBr3, MAPbBr3, and FAPbBr3 Bromide Perovskite Single Crystals: Interband Critical Points under Dry N2 and Optical Degradation under Humid Air. *J. Phys. Chem. C* **2021**, *125* (9), 4938–4945. https://doi.org/10.1021/acs.jpcc.0c10144.

(28) García-Batlle, M.; Mayén Guillén, J.; Chapran, M.; Baussens, O.; Zaccaro, J.; Verilhac, J.-M.; Gros-Daillon, E.; Guerrero, A.; Almora, O.; Garcia-Belmonte, G. Coupling between Ion Drift and Kinetics of Electronic Current Transients in $MAPbBr_3$ Single Crystals. *ACS Energy Lett.* **2022**, 946–951. https://doi.org/10.1021/acsenergylett.1c02578.

(29) García-Batlle, M.; Baussens, O.; Amari, S.; Zaccaro, J.; Gros-Daillon, E.; Verilhac, J.; Guerrero, A.; Garcia-Belmonte, G. Moving Ions Vary Electronic Conductivity in Lead Bromide Perovskite Single Crystals through Dynamic Doping. *Adv. Electron. Mater.* **2020**, *6* (10), 2000485. https://doi.org/10.1002/aelm.202000485.

(30) Baussens, O. Nouveau matériau pérovskite pour la radiographie médicale. Ph.D. diss., Université de Bordeaux, 2021.

(31) Shi, T.; Yin, W.-J.; Hong, F.; Zhu, K.; Yan, Y. Unipolar Self-Doping Behavior in Perovskite $CH_3NH_3PbBr_3$. *Appl. Phys. Lett.* **2015**, *106* (10), 103902. https://doi.org/10.1063/1.4914544.

(32) Almora, O.; Matt, G. J.; These, A.; Kanak, A.; Levchuk, I.; Shrestha, S.; Osvet, A.; Brabec, C. J.; Garcia-Belmonte, G. Surface versus Bulk Currents and Ionic Space-Charge Effects in $CsPbBr_3$ Single Crystals. *J. Phys. Chem. Lett.* **2022**, *13* (17), 3824–3830. https://doi.org/10.1021/acs.jpclett.2c00804.

(33) Dan, Y.; Zhao, X.; Chen, K.; Mesli, A. A Photoconductor Intrinsically Has No Gain. *ACS Photonics* **2018**, *5* (10), 4111–4116. https://doi.org/10.1021/acsphotonics.8b00805.

(34) Yang, M.; Chang, H.; Chen, J.; Zhu, X. Multiplier Effects of Photodetectors—Source of Gain. *Coatings* **2023**, *13* (6), 1088. https://doi.org/10.3390/coatings13061088.

Chapter 5 – Post-treatments: thermal annealing and chemical healing

Table of contents

Chapter 5

Chapter 5

Post-treatments: thermal annealing and chemical healing

Introduction

In the previous chapter we have seen that $MAPbBr_3$ is sensitive to its environment with the bulk and surface being affected in different ways at different stages: synthesis, device preparation, and optoelectronic characterisation. The presence of point defects in the bulk or surface will significantly affect the performance of the final device: in the bulk, vacancies or interstitial ions can increase the ion migration under bias, and in the surface, the interaction with the environment may lead to changes in the contribution of carriers in the charge transport, hence in the X-ray detection sensitivity. That is why, even with few clues on the nature of the defects present, researchers have tried to balance the deficiencies of hybrid LHPs, by chemically passivating the surface/bulk of crystals. Liquid chemical passivation of the surface has been achieved by Tan et al. in $FAPbI_3$, by using octylammonium bromide (OABr) anchorage, after surface reconstruction using IPA, which exposes defects working as bonding sites.[1] Once the long amine molecules are grafted, they isolate the crystal surface from further external interaction. The same logic was applied in $MAPbBr_3$, by Chen et al., with tert-amyl alcohol instead of IPA, and using phenethylammonium bromide (PEABr) and precursor MABr as passivating and healing amines, respectively. It resulted in enhanced properties such as resistivity, lowered dark current density and signal hysteresis, as well as, a better response under X-rays.[2] Similar approaches have also been done with ethylenediamine (EDA).[3]

Vapour chemical healing has also been performed on $MAPbBr_3$ SCs. In order to passivate bromide vacancies V_{Br} (MABr deficit), Kirmani et al. exposed SCs to dibromine Br_2 vapour. This induced an improvement in the stoichiometry for moderate exposures, but for longer exposures, the incorporation of Br^- anions induced a p-doping. The deficiency of Br^- anions would provoke a n-doping of the surface: Pb^{2+} cations would trap electrons, forming metallic Pb^0.[4] Pb^0 has been suggested to pin the Fermi level near the conduction band minimum resulting in this n-type character of perovskites.[5] Also, Pb^0 would act as exciton quencher. During treatment, incorporated bromide would accept electrons from Pb^0: the bromination reaction results in a rise in Br content, and the suppression of traps (Pb^0 content reduced).[6] If

the exposure to bromine vapour continues, Br^- anions would start to accumulate, creating bromine interstitials Br_i (p-doping). This would mean that applying treatments with Br-containing agents can module the surface doping of LHPs: by playing with the exposure time, one could target an n-type or p-type healing mechanism. Again, the same logic was used by Zhu et al. with MA vapour for solar cell improved performance.[7] Both molecules not only share chemical components (Br, MA) with $MAPbBr_3$ precursor products but they also work as reactants to passivate defects, enabling surface reconstruction[7] and diffusion of species within the bulk.[6] The $MAPbBr_3$ structure with its vacancies would act as a sponge being able to incorporate the same constituent species (Br^-, MA^+) and similar entities (e.g., I^- , Cl^-, H_2O) on the surface. These matter transports are moderated by the Gibbs free energy at the fluid/crystal interface, following Le Chatelier-Braun's principle.

The previous chapter dedicated to study the impact of the environment at the synthesis and characterisation stages, evidenced the specific importance of SCs surface, and the studies presented above showed that post-growth treatment in a specific atmosphere could indeed improve key features of the device. Therefore, we decided to study the impact of post-growth treatments to heal our $MAPbBr_3$ SCs by annealing them in a methylammonium halide (MAX) atmosphere. Indeed, the XPS results presented in Chapter 4 seem to indicate that, if there is a loss of ions at the surface, it is not only Br^- or MA^+ but both are depleted. So, unlike the studies by Kirmani et al.[6] and Zhu et al.[7], we annealed $MAPbBr_3$ crystals in a MACl atmosphere. MACl was chosen for two reasons: first, in Chapter 3, we have observed the easy incorporation of Cl^- anions in the $MAPb(Br_{x-1}Cl_x)_3$ solid solution (partition coefficient $k > 1$), and second, an EDX quantification will allow confirming the incorporation of Cl and its extent.

For this study, $MAPbBr_3$ SCs were grown and prepared following the standard procedures described in Chapter 2. A first group of samples was used to study the influence of the annealing alone on the optoelectronic performance, then a second group was used to evaluate the exposure to MACl, both from a structural and optoelectronic point of views. This work constitutes our first trial of a more general SC thermal annealing and chemical healing procedure via sublimation of MAX precursors (X = I, Br, Cl).

1 Influence of the temperature on optoelectronic properties

A Büchi furnace, depicted in **Figure 5-1-1**, enabling temperatures of up to 300 °C under controlled atmosphere, was used for the different treatments of the SC devices. For determination of the temperature influence on the optoelectronic properties, a total of 6 SC devices were used. Before any annealing procedure, the SC devices were evaluated under X-ray illumination to consider sample-to-sample variability. Then, 4 SCs were annealed and 2 SCs were used as reference, placed outside and next to the furnace. The reference crystals were used to consider any impact the iterative characterisation runs might have: repetitive biasing, or environmental interactions during analysis, as seen in the previous chapter. The remaining samples were annealed together in an inert Ar atmosphere at a pressure of 1.5 bars. The annealing process was conducted at four different temperatures sequentially: 100, 150, 200, and 250 °C, with a duration of 1 h 15 min at each temperature. Subsequently, they were evaluated for resistivity ρ and sensitivity S determination after each treatment. Temperature indicator stickers, "T-stickers" in **Figure 5-1-1**, were placed inside the furnace to ensure that the desired temperature was reached. The schematic in **Figure 5-1-2** summarises the annealing experimental setup. It is worth mentioning that the devices were annealed at the Institut Néel and tested at CEA LETI with the help of Thibault Lemercier and Eric Gros d'Aillon, respectively.

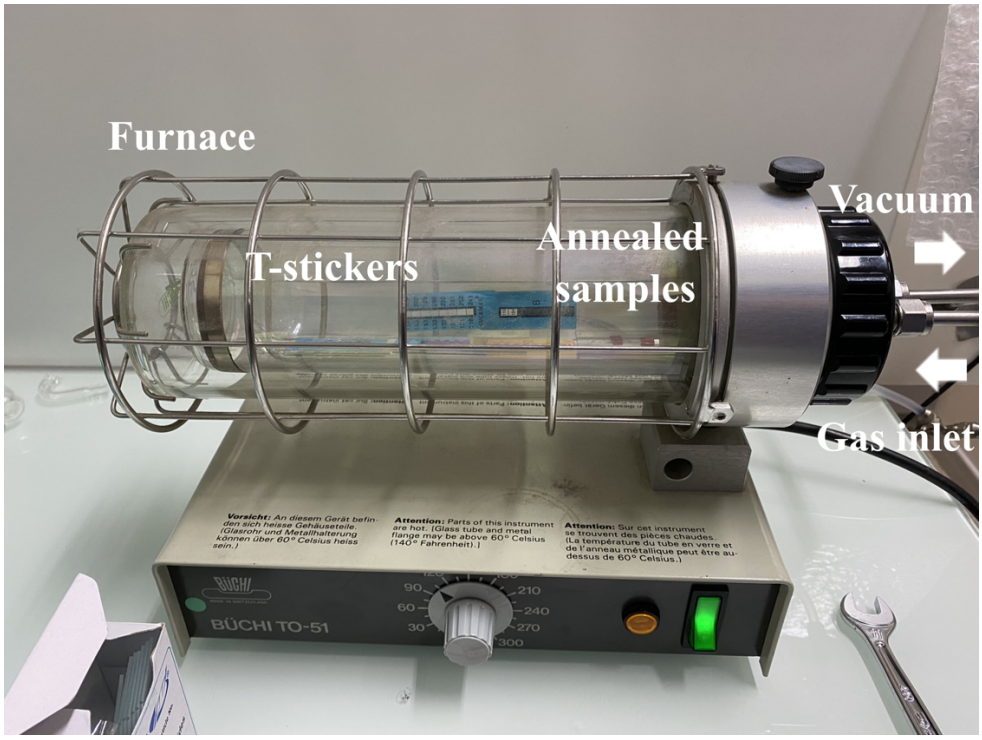

Figure 5-1-1. Büchi furnace with inert Ar atmosphere, T-stickers and SC devices in the inside for determination of the temperature influence on the optoelectronic performance.

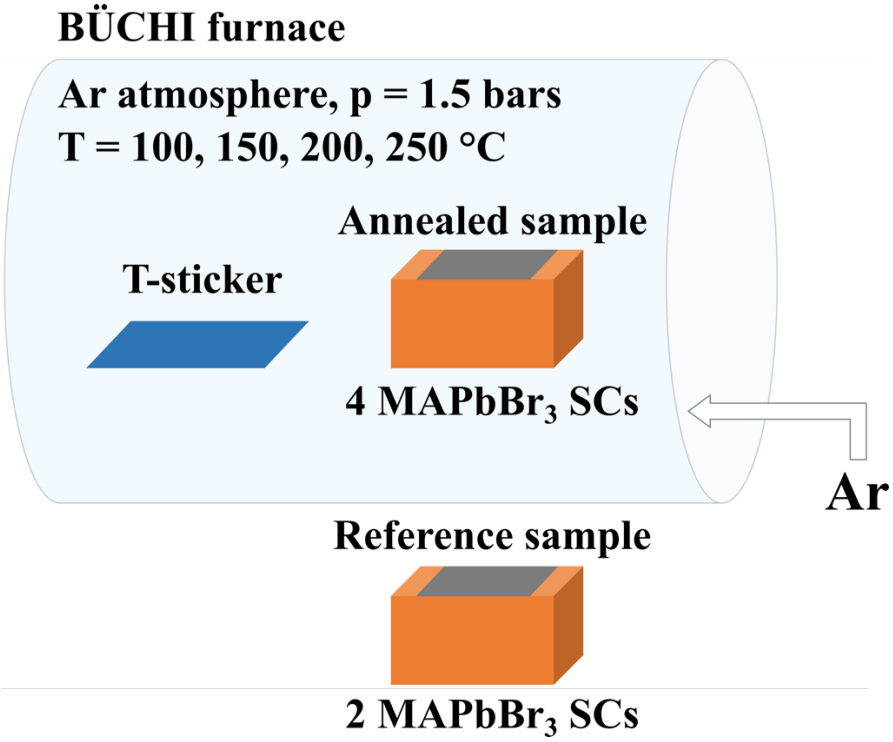

Figure 5-1-2. Schematic of the setup used to determine the influence of the temperature on the optoelectronic performance. Juts one annealed and one reference samples are shown in the schematic.

As it was indicated above, resistivity and sensitivity were determined for all devices after all annealing temperatures. But, as we have seen in Chapter 4, resistivity and dark current are not very much influenced by the environment. Nevertheless, the averaged resistivity values for both reference and annealed samples were extracted, normalised to the initial value (pre-annealing resistivity), and plotted in **Figure 5-1-3**. All samples resistivities evolution are shown in **Figure A 5-1-1**. It can be observed that for the two groups of SCs, the resistivity goes down, after reaching a maximum at 100 °C. Because both groups of devices behave the same, this is probably connected to the air exposition and not to the thermal annealing.

We considered that the impact of the temperature would be better evaluated using the sensitivity as an indicative parameter (S-T data) as it brings more insights in terms of charge transport, gain and response stability.

S-V data were collected for all six devices after all annealing steps. The results can be found in **Figure A 5-2-1** to **Figure A 5-2-6**. An example, visible in **Figure 5-1-4**, shows that the S-V data tend to be overcrowded for the type of analysis we are interested in here, and trends with temperature are difficult to notice. Nevertheless, one should point out that with increasing annealing temperature, the S-V plots did not show any increase in hysteresis or dissymmetry between positive and negative bias branches. So, to better evidence possible trends, the sensitivity data was preferred to be shown for three different electric fields as a function of the annealing temperatures, taking then into consideration the sample thickness.

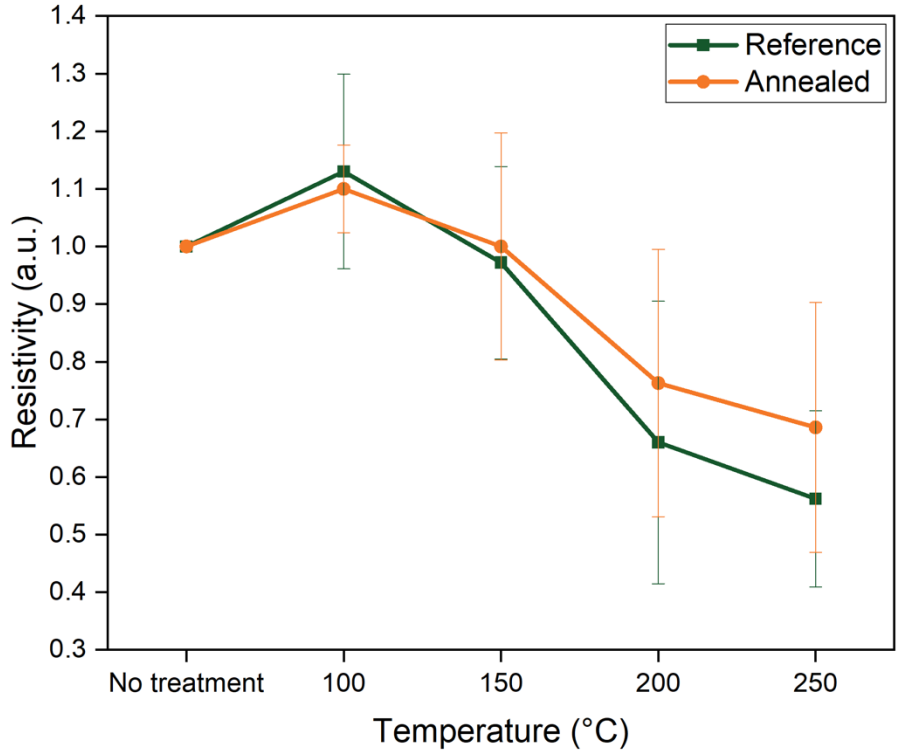

Figure 5-1-3. Averaged resistivity as a function of the annealing temperature. The data is normalised to the resistivity of the un-annealed device.

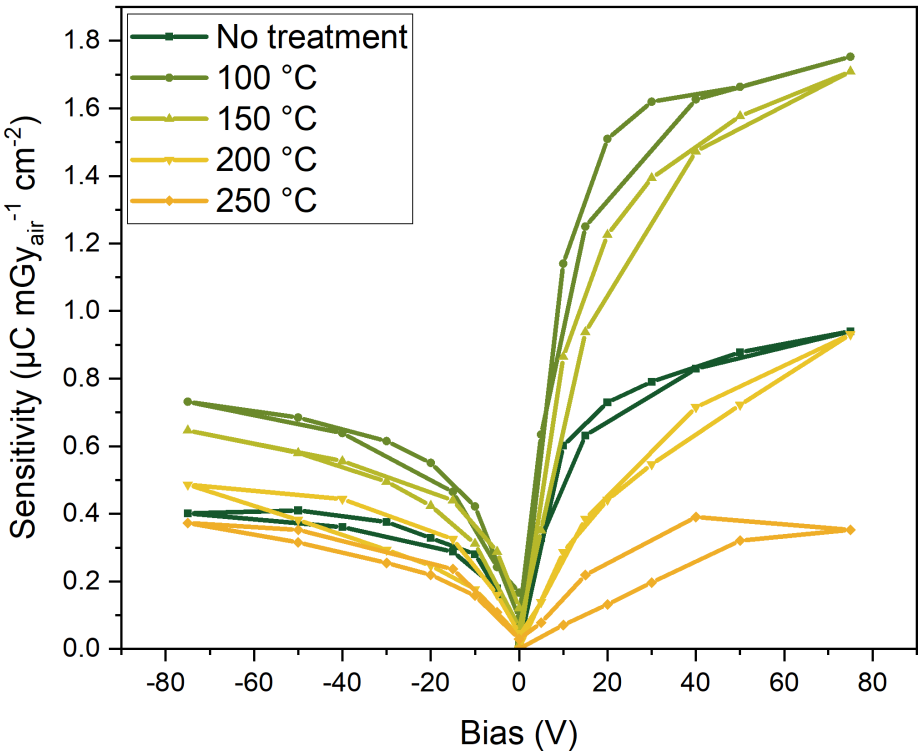

Figure 5-1-4. Annealed sample **(F)** S-V data evolution as a function of the annealing temperature.

The devices thicknesses were comprised between 1.43 and 2.17 mm, corresponding to X-ray absorptions comprised between 94 and 99 %, respectively. This means that sample thickness is not a crucial parameter in the comparison of S-V data among the different samples.

The evolution of sensitivity of the four devices with annealing temperatures (S-T) are summarised in **Figure 5-1-5**. The sensitivities are presented for the different biasing electric fields: two in the positive domain and one in the negative one. The point is to analyse differences of performance in both bias domains, and also in relatively low and high electric fields. For devices **(A)** to **(D)** the chosen electric fields were: 50, 10 and -40 V mm^{-1}, and for samples **(E)** and **(F)**, 30, 10, -30 V mm^{-1}. The extreme electric fields for the last two samples were chosen lower than that of the two other annealed and reference samples, in order to assess the symmetry of the response for a less extreme bias. The 10 V mm^{-1} electric field represents the common comparative point among the evaluated samples.

Reference samples **(A)** and **(B)** show the usual variance in X-ray response that $MAPbBr_3$ SCs systematically have. For both samples, the repetitive characterisation, after each annealing of the other group, leads to more variation of the sensitivity at positive biases than at the negative ones. Such evolution of the sensitivity can be linked to the parasitic ion migration and/or increasing air exposure, as discussed in the previous chapter. The increasing atmospheric exposition time, which includes the time of the annealing and optoelectronic test itself, might influence the crystal surface. In addition, repetitive biasing for the sequential analyses would exacerbate the ions migration in the device and its impact on the measured sensitivity. At a given electric field, sensitivity seems to gradually increase, potentially linked to a photoconductive gain mechanism as described in Chapter 4.

Regarding the annealed devices, they also show a certain variability and heterogeneity in the sensitivity evolution: sample behaviour varies importantly from one device to the other, and from one electric field to the other, in terms of *S* values. Most of the studied electric fields have the same trend within a single device. When comparing the samples with themselves, with the exception of sample **(E),** whose *S* values constantly decreased with increasing temperature, 3 out of 4 samples (devices **(C)**, **(D)** and **(F)** in **Figure 5-1-5**) present an increased sensitivity for an annealing at 100 or 150 °C at any given electric field. This is similar to the maximum seen for the resistivity. Such optimisation of the resistivity and sensitivity could be explained by a reorganization of the SC point defects/ions within the structure. Beyond that point, between 150 and 200 °C, the sensitivity starts to be hindered for all samples, which is probably a sign of the onset of the degradation of the perovskite. Indeed, this reduction of sensitivity cannot be attributed to the repetitive analysis of the devices since we have seen that with the reference samples, it would rather lead to a moderate increase in sensitivity. Additionally, when observing **Figure 5-1-4** and when comparing +/- 30 V mm^{-1} electric fields for samples **(E)** and **(F)** in **Figure 5-1-5**, one can see that the dissymmetry in the plots is conserved through the whole study. Also, we see that negative biases lead to lower *S* values when compared to positive biases. These observations indicate that potentially both electron and hole charge transports

remain unchanged. Also, 200 °C onwards, both positive and negative bias branches are "levelled" (*S* values decreased), meaning that both charge carrier transports are hindered by the perovskite degradation (see **Figure A 5-2-1** to **Figure A 5-2-6)**.

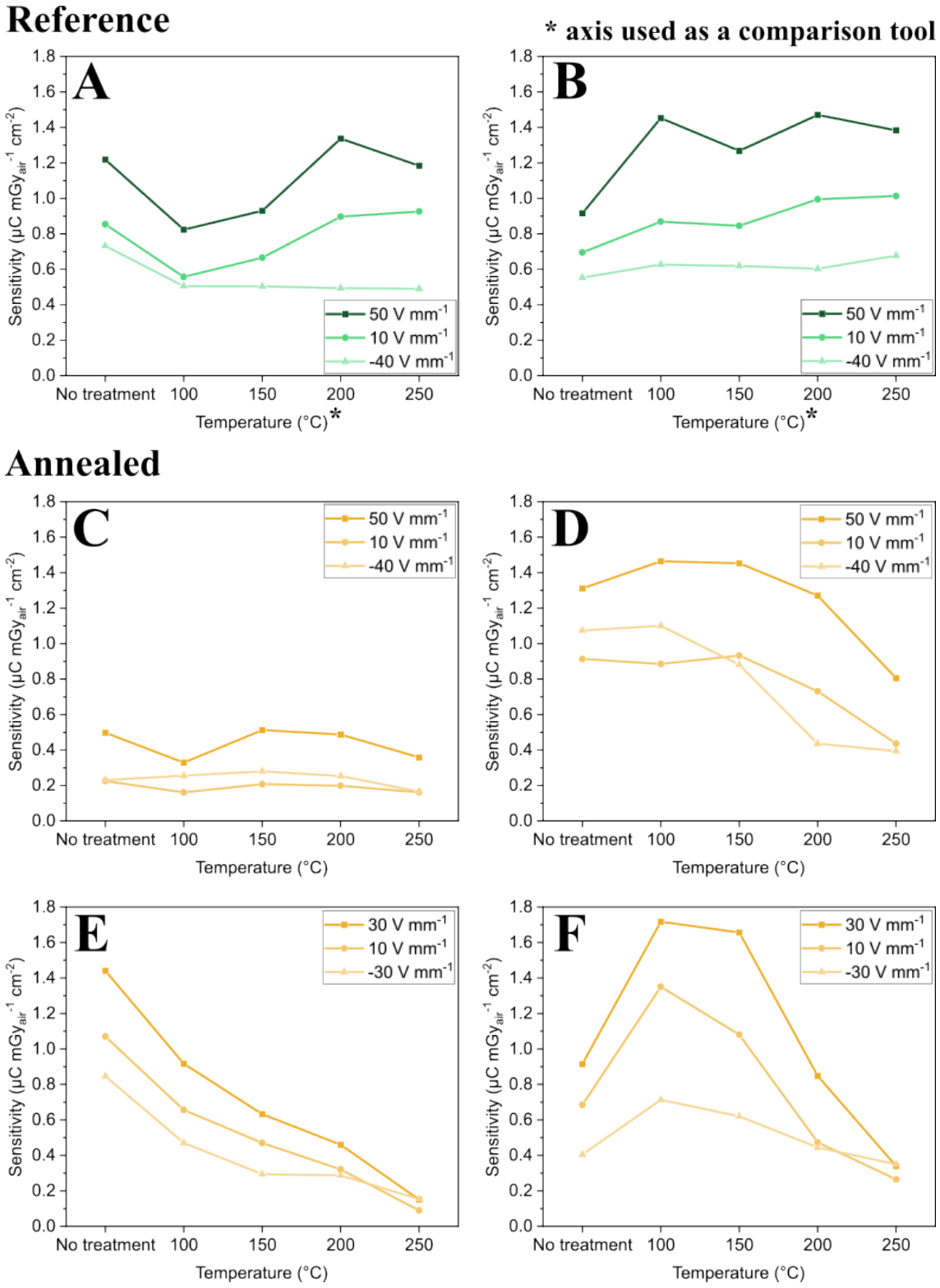

Figure 5-1-5. Sensitivity evolution as a function of the annealing temperature. Two reference SC devices **(A)** and **(B)**, along with four annealed samples **(C)** to **(F)**, were tested. Three different electric fields are plotted per sample.

Furthermore, **Figure 5-1-6** depicts the visual aspect of the two reference and two annealed SC devices at the end of the study. As can be seen in the photograph, the surfaces of the annealed samples show some deterioration. At the end of the 200 °C cycle, the devices present an opaque and milky surface (originally with an optical quality). Even though no XRD measurements were performed on the annealed samples, we know from TGA-MS data, shown in Chapter 4, that the perovskite degradation, from SCs grown in air and inert atmospheres, starts with the volatilisation of NH_3/CH_3Br with a detected onset at ~ 170 °C (with a temperature ramp of 2 K min^{-1}). Therefore, annealing at 200 °C for over an hour most probably leads, at least at the surface, to some loss of MABr. The perovskite structure is then lost and $PbBr_2$ would start to form.[8]

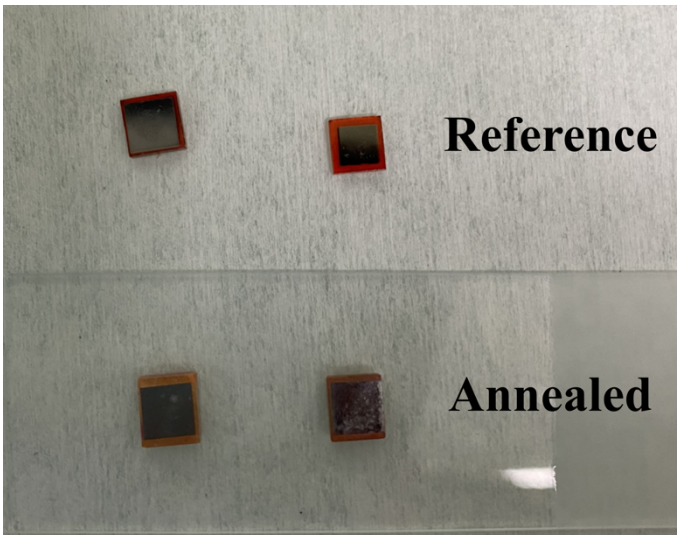

Figure 5-1-6. Reference and annealed SC devices after completion of all annealing cycles. One can observed the surface degradation of the annealed samples.

This first study shows that, in spite of sample-to-sample variation, the effect of repetitive analysis and annealing could be estimated. Most importantly, the sensitivity is not modified in major ways by repetitive analysis (reference samples), but annealing above 150°C leads to its diminution (annealed samples), most probably due to the onset of the structure decomposition. So, if one expects an improvement of $MAPbBr_3$ device performance through defect healing via exposure to MACl vapours, it should only be done at temperatures not exceeding 150 °C, yet above room temperature in order to potentially reorganise defects in the structure.

2 MACl vapour chemical healing

The same Büchi furnace was used for the MACl treatment of the second group of SC devices. Because the purpose is to have ions incorporated in the structure of the device, it raises the question whether the Cr electrodes block this incorporation. Thus, two types of samples were used in this study: bare SC (not polished, without Cr electrodes), and SC devices (with Cr electrodes). A first group was composed by 1 bare SC and 1 SC device. It was exclusively used to study the penetration and diffusion of sublimated species, here Cl^- anions, within the crystals. A second group, composed by two devices, was dedicated to study the impact of the treatment on optoelectronic properties (resistivity ρ, dark current J_{dark}, sensitivity S). In order to evaluate the reference properties of those samples before the MACl treatment, devices were prepared as usual: polishing, then Cr electrode deposition. Then, to discard the hypothesis that Cr electrodes could block the sublimated species from incorporating the structure, the Cr electrodes on both sides of one of the devices were completely removed by polishing the surface with ¼ µm anhydrous diamond paste on NT polishing disk (see Chapter 2). After the MACl treatment, electrodes were again deposited on that sample for optoelectronic characterisation.

An annealing temperature of 150 °C was chosen according to the results of the previous part. Based on vapour pressure data, MACl vapor pressure at 150°C is 3.07×10^{-4} bars.[9] Therefore, a residual pressure of 0.9 bars of air was set inside the furnace using a pump, as seen in **Figure 5-2-1-A**, to favour the sublimation of the MACl powder (GreatCell Solar, ≥ 99 %) (same product used in Chapter 3). MACl was put in a Petri dish, covered by a Teflon mesh upon which the different crystals to be treated were placed. This insured a close proximity (< 1 cm) without direct contact between the crystals and MACl. The chemical treatment lasted for 27 h 20 min overall. The schematic in **Figure 5-2-2** summarises the experimental setup.

A picture of all four samples after treatment, still on the mesh covering the petri dish, can be seen in **Figure 5-2-1-B**. Upon close inspection, the SCs appeared opaque and the surface seemed liquefied. The photograph in **Figure 5-2-3**, shows a SC device with this surface liquefaction, on all six faces of the cube, having permeated the protective paper used in the membrane box. The SC presents the characteristic light orange colour associated to the Cl incorporation in the $MAPbBr_3$ structure, as previously seen in Chapter 3.

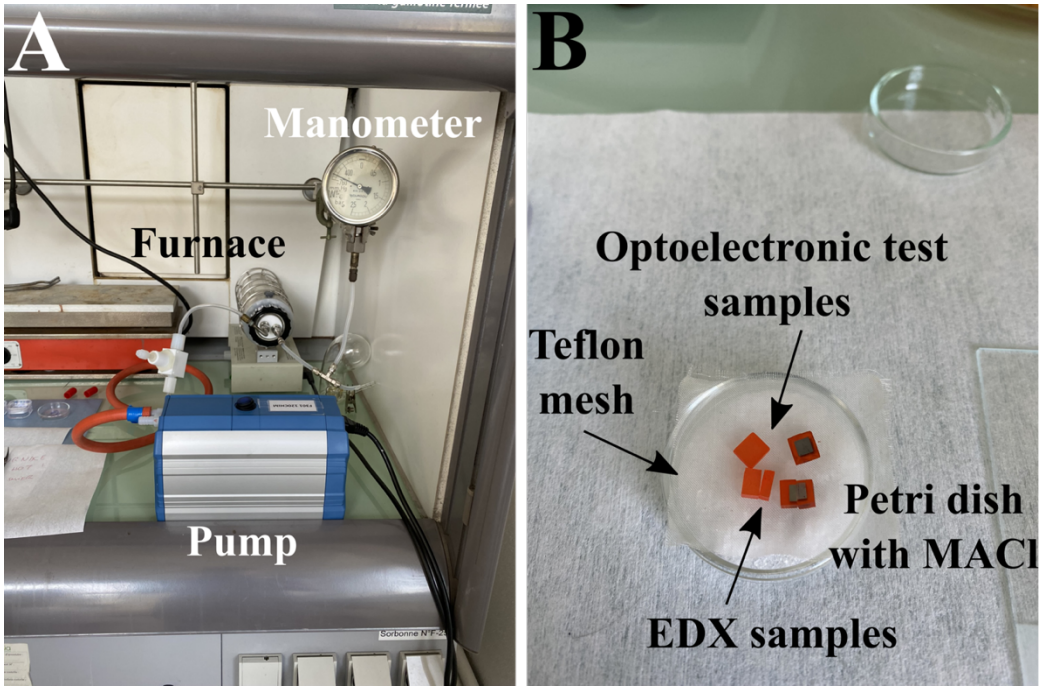

Figure 5-2-1. MACl vapour chemical treatment. (A) Setup used for MACl treatment where a vacuum pump and a manometer can be seen. **(B)** Four SCs after MACl treatment on top of a Teflon mesh covering in turn a Petri dish containing the MACl powder. EDX samples were cleaved for bulk analysis.

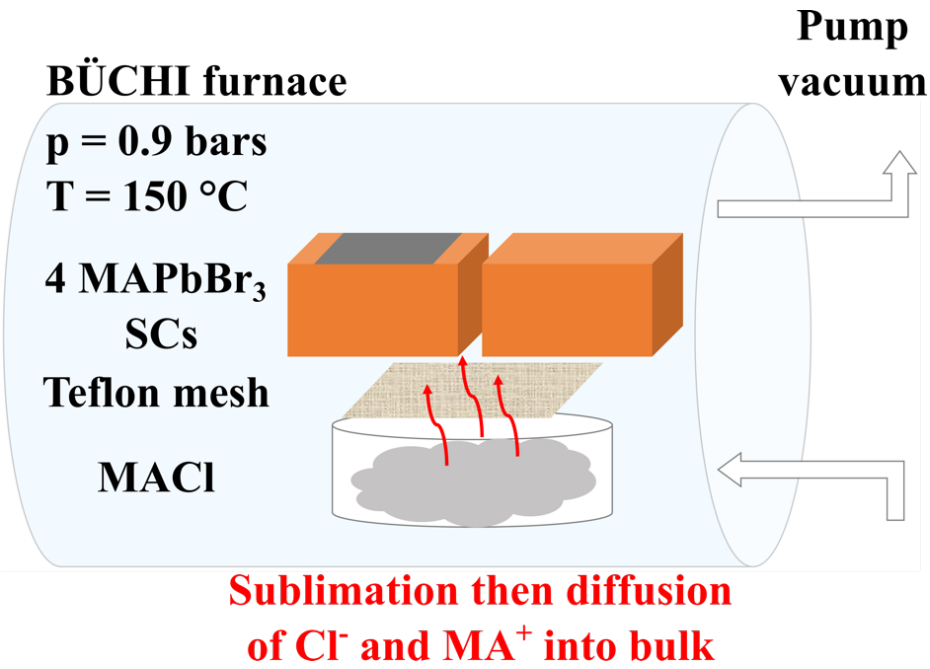

Figure 5-2-2. Schematic of the vapour chemical healing with MACl setup used to evaluate the impact of migrating species on optoelectronic performance. Just one treated sample with Cr electrodes and one without them are shown in the schematic.

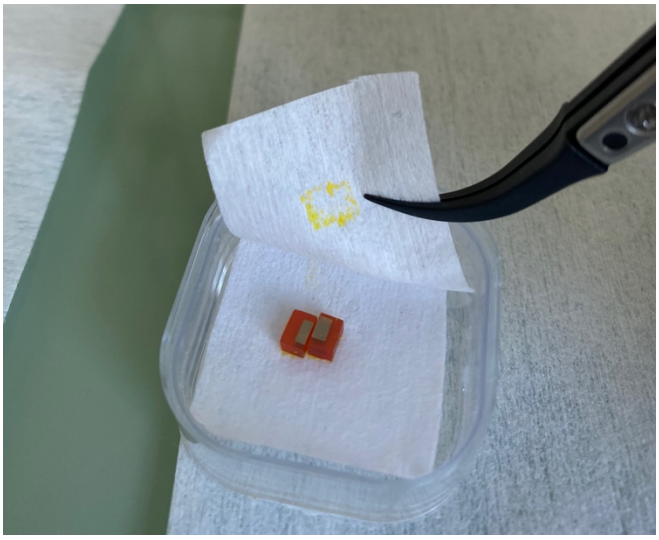

Figure 5-2-3. SC device used for EDX analysis after MACl treatment. The sample is cleaved for bulk measurements. It can be seen that the surface was liquefied by the treatment: a partial dissolution of the surface took place, giving a characteristic colour when chlorine is present in the $MAPbBr_3$ structure.

Zhou et al. evidenced a chemical reaction when exposing PC $MAPbI_3$ to MA gas, leading to the apparition of an intermediate liquid phase layer of chemical formula $MAPbI_3 \bullet xMA$. The subsequent degassing of MA, allows a morphological reorganisation of the film, thus the healing of the material in term of defects and improved performance in PVs.[10] The same mechanism could have taken place within our case study. The sublimation of MACl would lead to MACl gas molecules, as made explicit by **Equation (5-1)**, which would react with $MAPbBr_3$ on the crystal surface, as described by **Equation (5-2)**, thus inducing the observed liquefaction of the perovskite. Both reactions can be reversible:

$$MACl_{(s)} \leftrightharpoons MACl_{(g)} \tag{5-1}$$

$$MAPbBr_{3(s)} + x\ MACl_{(g)} \leftrightharpoons MAPbBr_3 \cdot x\ MACl_{(l)} \tag{5-2}$$

A more complicated chemical mechanism could be structured while considering also the potential dissociation of $MACl_{(g)}$ into $MA_{(g)}$ and $HCl_{(g)}$. Protonation and deprotonation reactions among the present entities could also take place. Nevertheless, whichever path is taken, when the system temperature goes back to ambient temperature, the reactions would lead to the formation of a solidified $MAPb(Br_{1-x}Cl_x)_3$ coating on top of the $MAPbBr_3$ SC, given the solid solution nature of hybrid $MAPbX_3$ perovskites.

Chapter 5

2.1 Cl diffusion inside the crystal: EDX analysis

To analyse the penetration of Cl within the bulk of the crystals, cleaved surfaces were prepared for the bare SC and SC with Cr electrodes. Three parts in the SCs were identified depending on their orientation with respect to the MACl powder: top, lateral and bottom regions. A schematic illustration of the MACl post-treatment can be found again in **Figure 5-2-4-A**, with the labelling used for the EDX measurements. There was no lateral analysis for the SC device.

The Cl content after MACl treatment is far less important than the ones estimated in Chapter 3 and it is expected to vary over much smaller distances. So, the experimental conditions for EDX quantification are more critical than those previously defined. As for UV[11] and X-rays[12] radiations, hybrid MHPs are susceptible to structural and chemical degradation when exposed to energetic particle such as electrons. In particular, as the area to be probed has to be smaller, local damage is more relevant with a risk of bias in the results, by volatilising Cl-containing species present on the surface. Surface degradation takes place when the electron beam is too focused on a relatively small surface. The surface to be analysed is then chosen to reach a compromise between potential surface degradation and enough signal of the searched element. Ultimately, far smaller surfaces were then considered when compared to those of Chapter 3 (~ 100 µm × 100 µm). For most measurements, 6 µm × 2 µm rectangular-shaped windows were used, called here segments. For such small areas, even keeping the electron beam canon as little time as possible on each segment to minimise surface damage, cracks and holes were produced while performing the measurements. Such damage can be seen near the edge of the crystal in **Figure 5-2-4-B** that shows an example of EDX measurement and the 1 µm × 1 µm grid adopted to define the measurement windows. A measurement sequence starts from the edge of the cleaved face and proceeds in the crystal bulk direction until the detection limit of the EDX technique is reached, where the Cl K_α signal starts mixing with background noise. The quantification technique employed here was built with the help of Sébastien Paris at Institut Néel.

An edge effect was noticed at the beginning of the measurement sequence. Lower signal was recorded probably linked to an uneven measurement surface at the very edge of the cleaved surface. Thus, lower crystal Cl content $\%Cl_{cryst}$ values were estimated for "surface" depth. This is corroborated by both **Figure 5-2-5-A** and **Figure 5-2-6-A** first segment measurements for both the bottom and lateral regions plots (at 2 µm depth), for both $\%Cl_{cryst}$ and Pb/X (X = Br + Cl) values. Keeping that in mind, this allowed measuring, for both samples, the penetration depth of Cl^- anions in the different regions (top, bottom, lateral faces). The same settings in the Esprit software as in Chapter 3 for the element quantification were used here, as well as the definition of crystal Cl content $\%Cl_{cryst}$ and Pb/X ratio (**Equations (3-4)** and **(3-5)**, respectively).

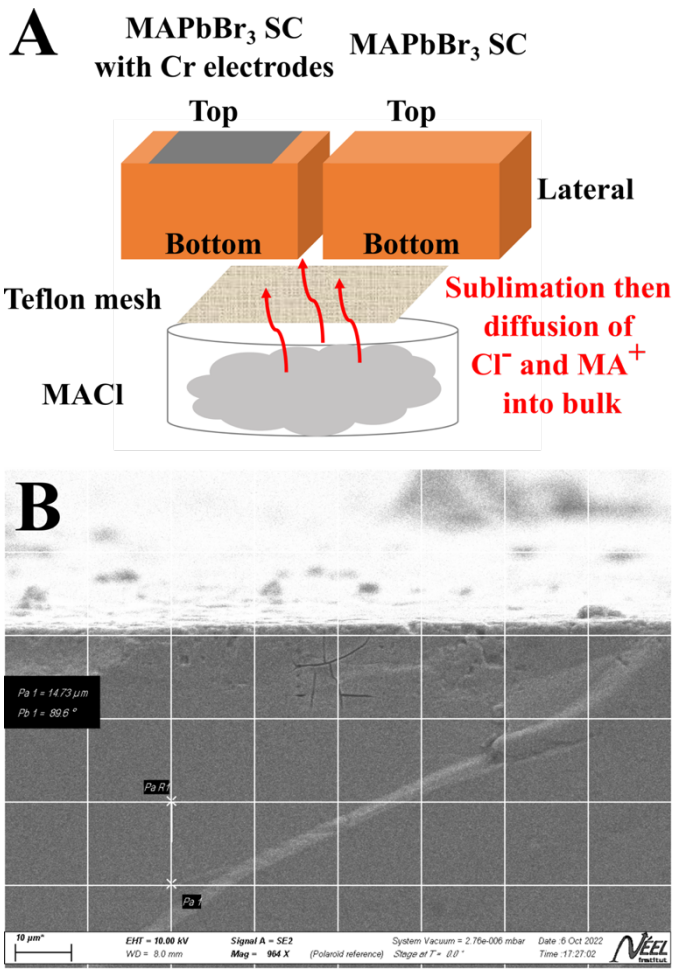

Figure 5-2-4. SEM-EDX measurements for MACl post-treatment study. (A) Schematic representation of MACl treatment on two types of SCs: with and without Cr electrodes. **(B)** EDX analysis performed on rectangle-shaped windows (segments). For the majority of measurements, a surface of 12 µm^2 (6 µm × 2 µm) was used, with a unit cell representing 1 µm^2 (1 µm × 1 µm, single square).

To illustrate the obtained measurements, the spectra for the bottom region are shown in **Figure 5-2-5**. **Figure 5-2-5-A** and **Figure 5-2-5-B**, focused on the Cl K_α emission peak, depict the gradual penetration of Cl inside the structure for the bare SC and SC device (with Cr electrode), respectively. Each figure is composed of a set of spectra, each recorded at a given depth (the "0" being defined as the surface). In the legend, a colour code indicates if the peak deconvolution led to a Cl content (green values) or not (red values). Thus, based on the EDX detection limit, a first estimation of the penetration depth can be defined. By comparing both graphs, it is clear that the presence of Cr at the interface hinders the penetration of the anions. It worth pointing out that, for the bare SC, two additional dimensions of segments were used to accelerate the analysis, the resulting spectra are shown in **Figure A 5-3-1**. The spectra for the other regions, top and lateral, can be found in **Figure A 5-3-2** and **Figure A 5-3-3**, respectively.

Table 5-2-1 summarises the Cl penetration depth estimated by this technique for all regions for both samples, allowing two conclusions to be drawn. Firstly, the bottom region,

directly facing the MACl powder, absorbs more anions. The impact of the face orientation goes, in decreasing order of incorporation, from the bottom region, followed by the lateral region, and in last position, the top region. Secondly, the presence of Cr atoms on the surface constitutes a barrier to Cl incorporation. If these two conclusions are not really surprising, these first estimations allow estimating the magnitude and relative importance of these experimental settings.

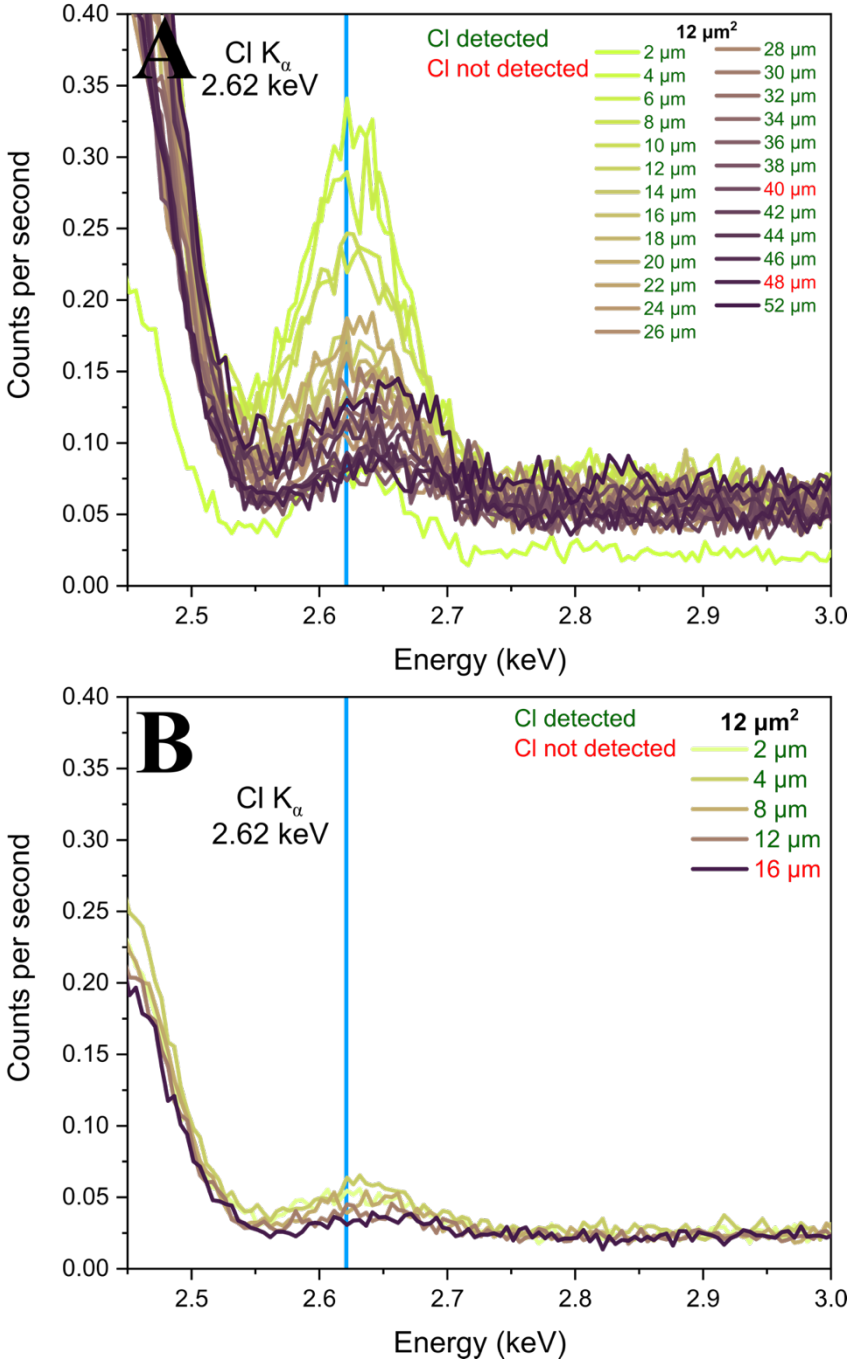

Figure 5-2-5 Bottom region EDX spectra. Spectra for **(A)** bare SC and **(B)** SC with Cr electrodes. The spectra are centred in the Cl K_α emission peak. In the legend, the header in black indicates the surface of the segment used for the measurements. Depth values come in two colours: green for when a Cl content was measured, and red for when it was not.

Table 5-2-1. Penetration depths estimated by EDX measurements on cleaved bare $MAPbBr_3$ SC and SC with Cr electrodes after 27 h 20 min of chemical post-treatment with MACl vapour.

Region	SC without Cr electrodes [μm]	SC with Cr electrodes [μm]
Top	12-14	12-14
Lateral	60-95	–
Bottom	110-125	10-16

The diffusion of the Cl in both samples and across all evaluated regions of the crystals is better appreciated in **Figure 5-2-6**, showing the evolution of the measured $\%Cl_{cryst}$ content as a function of the penetration depth, alongside with the evolution of the Pb/X ratio. When comparing both samples, the much higher penetration in the bare crystal **(A)** than in the one with Cr electrode **(B)** is highlighted again, especially one can notice that the graphs have different scales: up to 130 and 17.5 μm, respectively.

Disregarding the very first values which are impacted by the edge effect mentioned earlier, the Cl content decreases monotonously from the surface to deeper layers within the bulk, for both crystals. They look like a standard diffusion model, an exponential decrease of Cl species in the structure. Yet, because of the partial surface liquefaction and other considerations, their modelling was not obvious and will be presented at a later stage.

Another interesting feature presented in **Figure 5-2-6** is the Pb/X ratio analysis. It proved quite tricky to determine, leading to somewhat high variance of the calculated ratios. However, it can be seen that the richer in chlorine the region is, the closer to the stoichiometry the structure is. This benefit is observable for both types of samples. Such improvement of stoichiometry was already observed in Chapter 3. We saw then that upon crystallisation, the presence of Cl allows the perovskite structure getting closer to stoichiometry (Pb/X = 33.3 %): rising from 28.5 ± 0.4 % for $MAPbBr_3$ to 30.5 ± 1.3 % for $MAPb(Br_{0.85}Cl_{0.15})_3$ (for surface analysis). Here, the vapor treatment led in the first micrometres of the bare SC to even higher Cl contents than those observed in the $MAPb(Br_{0.85}Cl_{0.15})_3$ SCs. The highest values reached here were in the bottom region and were over $\%Cl_{cryst}$ = 15 and Pb/X = 30 %. This validates our choice of MACl as treating agent by confirming the easy incorporation of Cl^- anions in the structure, as corroborated by the results in Chapter 3. The post-growth incorporation of Cl is correlated to a compositional improvement: going from a halide-poor composition to a more stoichiometric composition, indicating that it is not a simple exchange of Br with Cl that takes place. It can either correspond to a healing of defects with Cl^- anions, filling bromide vacancies V_{Br}, thus resulting in Cl_{Br} substitutions, or to a creation of new defects with Cl^- anions taking interstitials or antisite positions: Cl_i, Cl_{Pb} or Cl_{MA}.

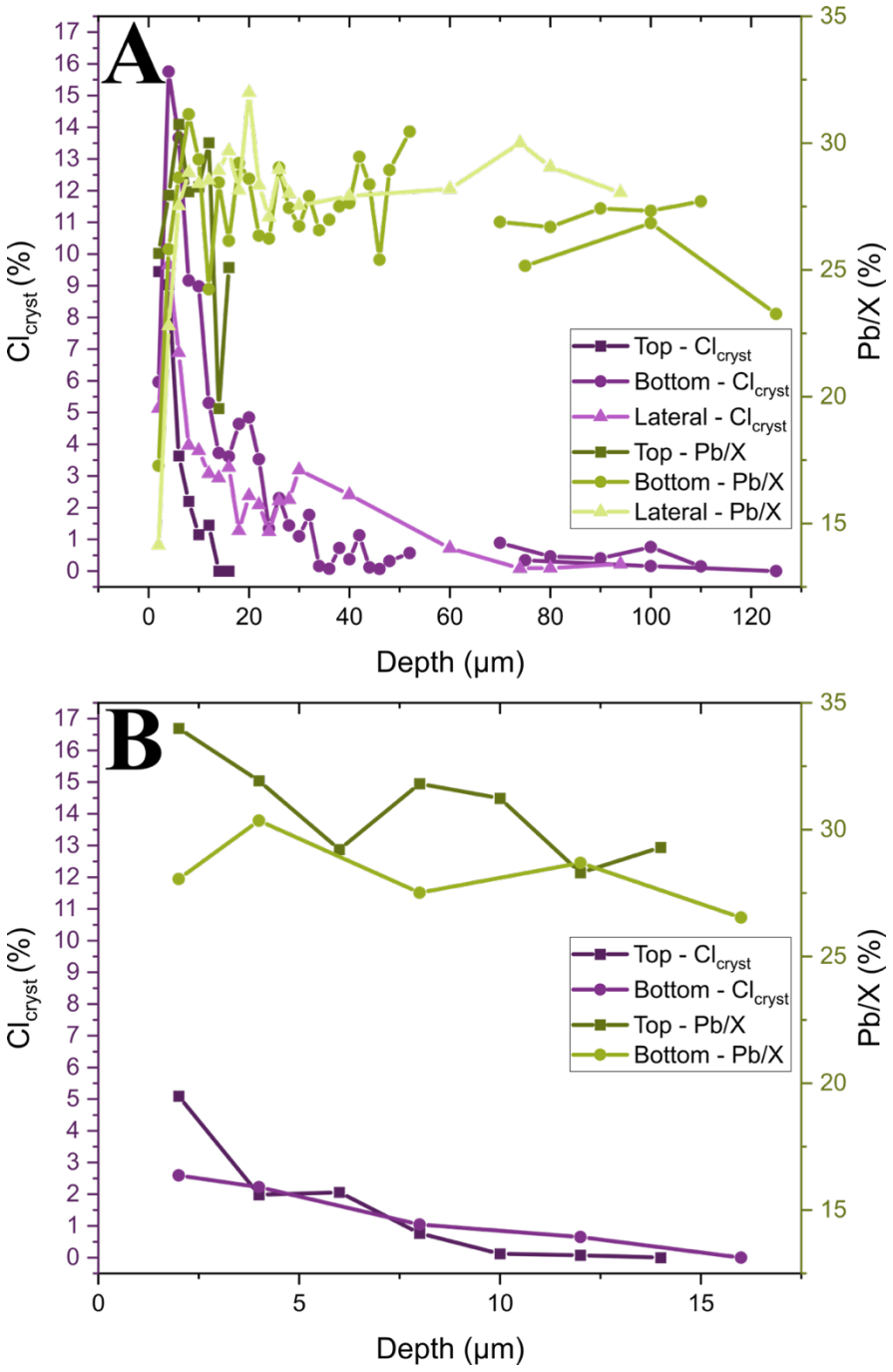

Figure 5-2-6. Quantification measurements for crystal Cl content %Cl$_{cryst}$ and Pb/X ratio. Evolution of both %Cl$_{cryst}$ and Pb/X values for **(A)** bare SC and **(B)** SC with Cr electrodes. Each figure includes the trends observed for the different studied regions: top, bottom and lateral (just for the bare SC).

Which point defects seem more likely to exist than the others have been a research topic for several years in MHPs. Via Density Functional Theory (DFT) simulations, Motti et al. calculated that, in halide-medium conditions for $MAPbBr_3$, the most stable defects are MA and bromide interstitials, MA_i and Br_i, respectively (slight p-doped character), but the ones representing deep trap levels were lead vacancies V_{Pb}, Br_i and lead interstitials Pb_i. V_{Br} defects also exist but in lower densities.[13] Whereas Mannodi-Kanakkithodi et al. defined in a study on

$MAPbX_3$ (X = I, Br, Cl) compositions the most stable defects in Pb-rich conditions. For $MAPbBr_3$, V_{Br}, MA vacancies V_{MA}, V_{Pb}, followed by antisite Pb_{MA}, are the defects with lowest formation energies. V_{Pb}, V_{Br} and Pb_{MA} represent the main internal bandgap defects. For $MAPbCl_3$, Pb_{MA}, V_{MA} and chlorine vacancies V_{Cl} are the ones with the lowest formation energies, with V_{Pb}, V_{Cl} and Pb_{MA} representing in turn the main internal bandgap defects. Self-interstitials were also shown to be stable, but with higher formation energies.[14] Based on this, one could say that after MACl treatment, Cl_{Pb} and Cl_{MA} defects seem unlikely to be formed (too high in energy), but rather Cl_{Br} substitutions and Cl_i interstitials.

The results above prove that post-growth exposure to vapour, in this case to perovskite precursor MACl, results in the incorporation of halide species inside the structure, at least for the first hundreds of micrometres (bottom region). This surface incorporation seems beneficial regarding the improvement of the structure stoichiometry. Because ions, and specifically halides, have shown the ability to move inside the structure, one is then tempted to use this procedure to improve not only the surface but the whole bulk. This would require to assess the treatment time required which is dictated by halide ions diffusion properties, hence to characterise the diffusion process of chloride in the structure. To that end, the EDX Cl content data presented in **Figure 5-2-6** were fitted by the complementary error function, solution to Fick's second law, made explicit in **Equation (5-3)**.[15] The following assumptions are made to apply this model: **(i)** the entire furnace is saturated with gaseous MACl, presumably also in its dissociated form with MA^+ and Cl^- ions; **(ii)** the diffusion is treated as a one-dimensional problem perpendicular to the crystal surface (along a *x*-axis), and **(iii)** the distribution of the diffusing species outside of the crystal and its incorporation at the first atomic layer are modelled by the quantity C_0, defined as the concentration of Cl^- anions at $x = 0$:

$$C(x) = C_0 \, erfc\left(\frac{x}{\Lambda}\right) \tag{5-3}$$

Where Λ is the exchange layer thickness.[15] This can in turn be used to determine the diffusion coefficient D using the following **Equation (5-4)**:

$$\Lambda = 2\sqrt{D\,t} \iff D = \frac{\Lambda^2}{4\,t} \tag{5-4}$$

Where D ($m^2\ s^{-1}$) is the diffusion coefficient of chloride and t is the time (s). This modelling for both SCs with and without Cr electrodes is shown in **Figure 5-2-7-A** and **Figure 5-2-7-B**, respectively, with associated fitting parameters in inset ($A = C_0$ and $B = \Lambda$). The extracted D coefficients are summarised in **Table 5-2-2**.

In the modelling presented above, it was considered that the different regions see the same initial Cl concentration at the surface C_0, but the D values, shown in **Table 5-2-2**, are very different for each region. This suggests that the different faces would have a different behaviour towards the MACl vapour exposure, with a reaction advancing more rapidly in a given region than the other, induced by the relative proximity to the MACl powder. However, this seems unlikely given that the faces are identical from crystallographic point of view. The results point

out the fact that the first assumption **(i)** is not respected: the furnace is not saturated in MACl vapour and that the local environment seen by each face is different. Thus, the concentration C_0 at each face is different: the vapour would be more concentrated at the bottom region than in the two others, the mass transport would then be more accelerated for the bottom region.

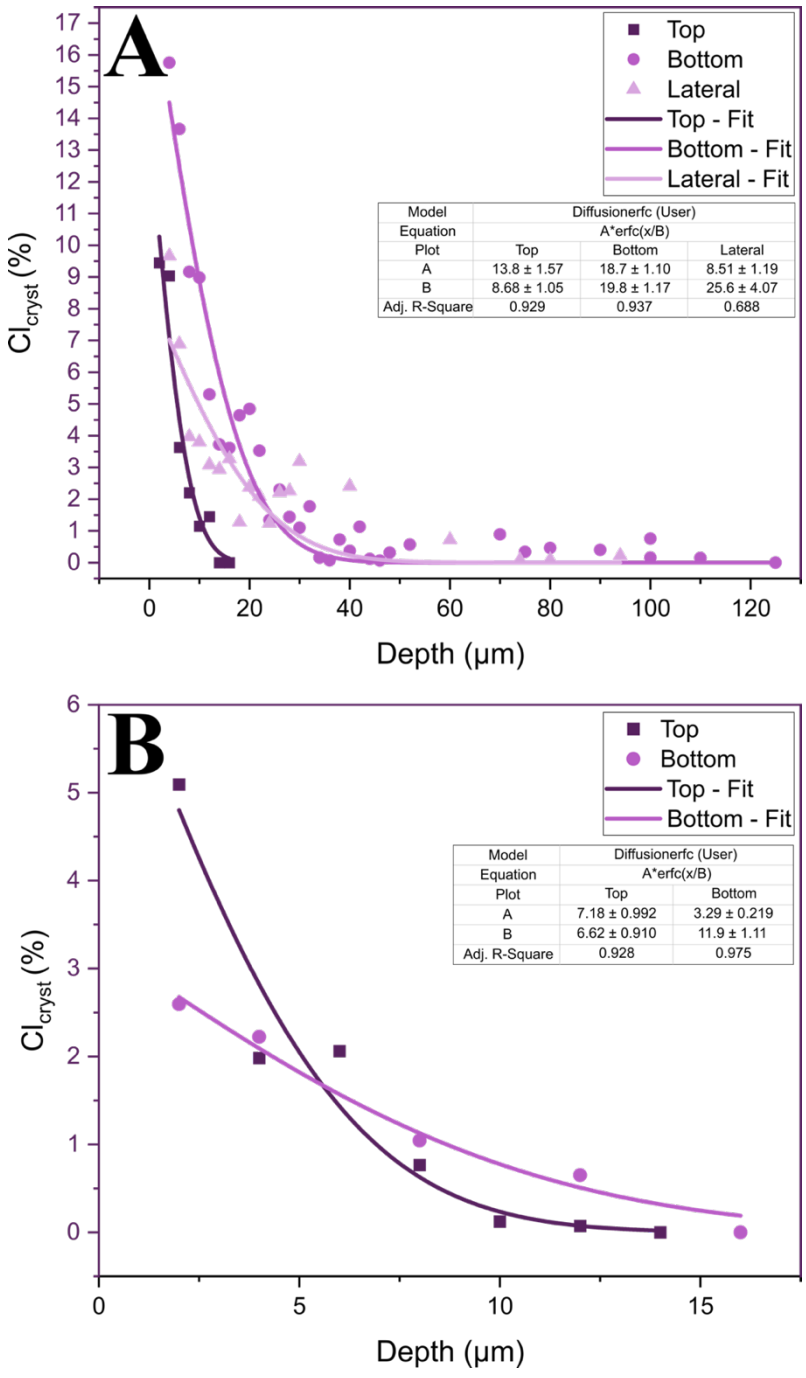

Figure 5-2-7. One-dimension diffusion analysis of Cl^- anions in the different studied regions. Modelling of EDX data via the complementary error function solution of Fick's second law for **(A)** bare SC and **(B)** SC with Cr electrodes. Each figure includes the fits performed for the different studied regions: top, bottom and lateral (just for the bare SC).

Table 5-2-2. Diffusion coefficients extracted via 1D-diffusion modelling of Cl^- anions for all the studied regions in both SC samples, with and without Cr electrodes.

Region	SC without Cr electrodes [$m^2\ s^{-1}$]	SC with Cr electrodes [$m^2\ s^{-1}$]
Top	1.9×10^{-4}	1.1×10^{-4}
Lateral	1.7×10^{-3}	–
Bottom	9.8×10^{-4}	3.6×10^{-4}

The ion diffusion depends on the temperature, diffusion direction and number of point defects, especially vacancies. Yet, for all three parameters, there is no reason to think that they substantially differ from one face to the other. With species propagating in the same medium, the diffusion coefficients should be similar, especially if one compares both polished faces of the SC device (top and bottom), which would have almost identical surface structure and point defects, in theory. Nevertheless, the results can still be used to compare relatively the different regions of both types of samples. *D* values are effectively higher for bottom regions than for the other regions within a single sample, and they are higher for bare SC than for the device for a given region: again, Cr represents a Cl diffusion barrier.

An important detail potentially biasing the results above is the fact that the liquefied layer on the SCs was partially wiped out by the membrane box protective paper as seen in **Figure 5-2-3**. This means that the penetration depths given in **Table 5-2-1** are under estimations because the initial surface is lost. The Cl diffusion would start form liquefied mixed halide perovskite $MAPb(Br_{1-x}Cl_x)_3$ and not from gaseous MACl.

All this considered, a few elements can be stated at this point. The healing treatment must be performed under a lower MACl vapour pressure, thus lower temperature, and for longer periods of time, to avoid excessively liquefying the crystal surface. Also, as stated before, it should be executed before Cr electrode deposition, given the decreased diffusivity induced by it. That said, more experiments are required to verify this.

In the experimental work presented in this chapter, the diffusion of the organic counterpart of the Cl^- anions, be it MA^+ cations or neutral MA, was not performed. Mostly because of the difficulty to measure changes in methylamine content. The role of amines has already been highlighted in the literature as species able to chemically bond with the perovskite surface, which allow building a protective layer on the surface (chemical anchorage).[3] That said, their role in vapour processes should also be considered.

Furthermore, even if the treatment presented above only modifies the crystal on a limited depth, because of the systematic ion migration in the structure, it may have an impact later on, upon the polarisation of the device. While being under bias, the ion migration would induce the motion of the newly entered defects/chemical species across the entire volume of the crystal. By producing a new configuration of defects in the perovskite bulk, MACl treatment might bring some benefits in the response under X-ray illumination.

2.2 Impact of MACl treatment on optoelectronic performance

The SC devices used for optoelectronic characterisation are depicted in **Figure 5-2-8**, after chemical post-treatment. Because the electrodes were removed on SC **(A)** before the MACl treatment, Cr electrodes were re-deposited on the liquefied then solidified layer after it for the optoelectronic characterisation. It exhibits no major visual changes when compared to the standard SC device, besides a slightly darker electrode colour. The SC **(B)** was treated with its Cr electrodes, as mentioned above. It is worth mentioning that these electrodes appeared degraded during the treatment: the Cr deposit was partially dissolved when the surface was liquefied.

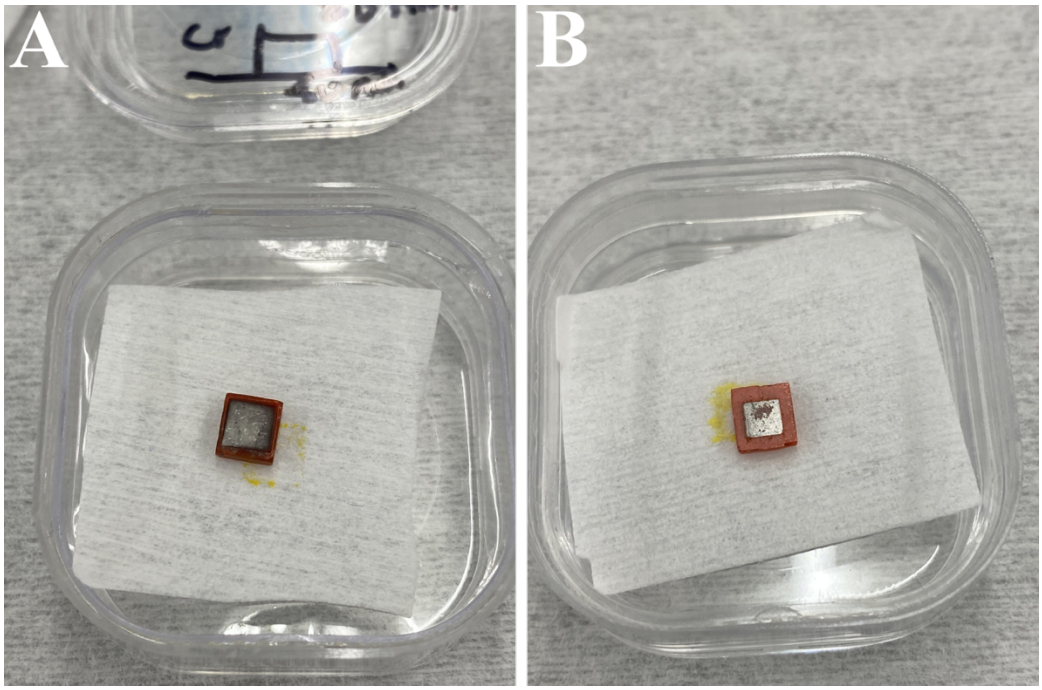

Figure 5-2-8. SC devices after MACl treatment. (A) SC device after MACl treatment and Cr electrode re-deposition. A slightly darkened electrode can be observed. **(B)** SC device after MACl treatment with Cr electrodes. The electrodes were degraded and deposition uniformity lost.

Both devices **(A)** and **(B)** were then analysed to determine resistivity ρ, dark current J_{dark} and sensitivity S. The devices thicknesses were 1.56 and 1.35 mm, respectively, corresponding to X-ray absorptions of 96 and 93 %, respectively. As in part **1**, S-V data was used for comparison. **Figure 5-2-9** presents the optoelectronic performances of both SC devices before (green plot) and after (blue plot) treatment. **Figure 5-2-9-A1** and **Figure 5-2-9-B1** depicts the J_{dark}-V data. On the one hand, for the SC **(A)**, the MACl treatment results in reduced hysteresis but most importantly in an important reduction of J_{dark}: reduced by up to two orders of magnitude for the negative biases (from ~ 10^{-6} to ~ 10^{-8} A mm^{-2}), and by one order of magnitude for the positive biases (from ~ 10^{-7} to ~ 10^{-8} A mm^{-2}). The resulting J_{dark}-V curve is then more

symmetrical for both positive and negative bias domains, leading to similar J_{dark} limit values of about 10 nA mm^{-2}. On the other hand, SC **(B)** sees its dark current and hysteresis increased, potentially due to the degradation of the contacts.

Regarding the sensitivity, **Figure 5-2-9-A2** and **Figure 5-2-9-B2** expose the measured values as a function of biasing voltage (S-V). For the SC device **(A)**, the performance is increased. It doubles in both bias domains, without degradation of the hysteresis. For device **(B)**, the overall sensitivity is not significantly modified but the hysteresis is noticeably increased. For this device, above 75 V, the sensitivity is markedly higher but then a photoconductive gain effect, as described in Chapter 4, coupled with the electrode degradation, could be at the origin of the higher *S* values.

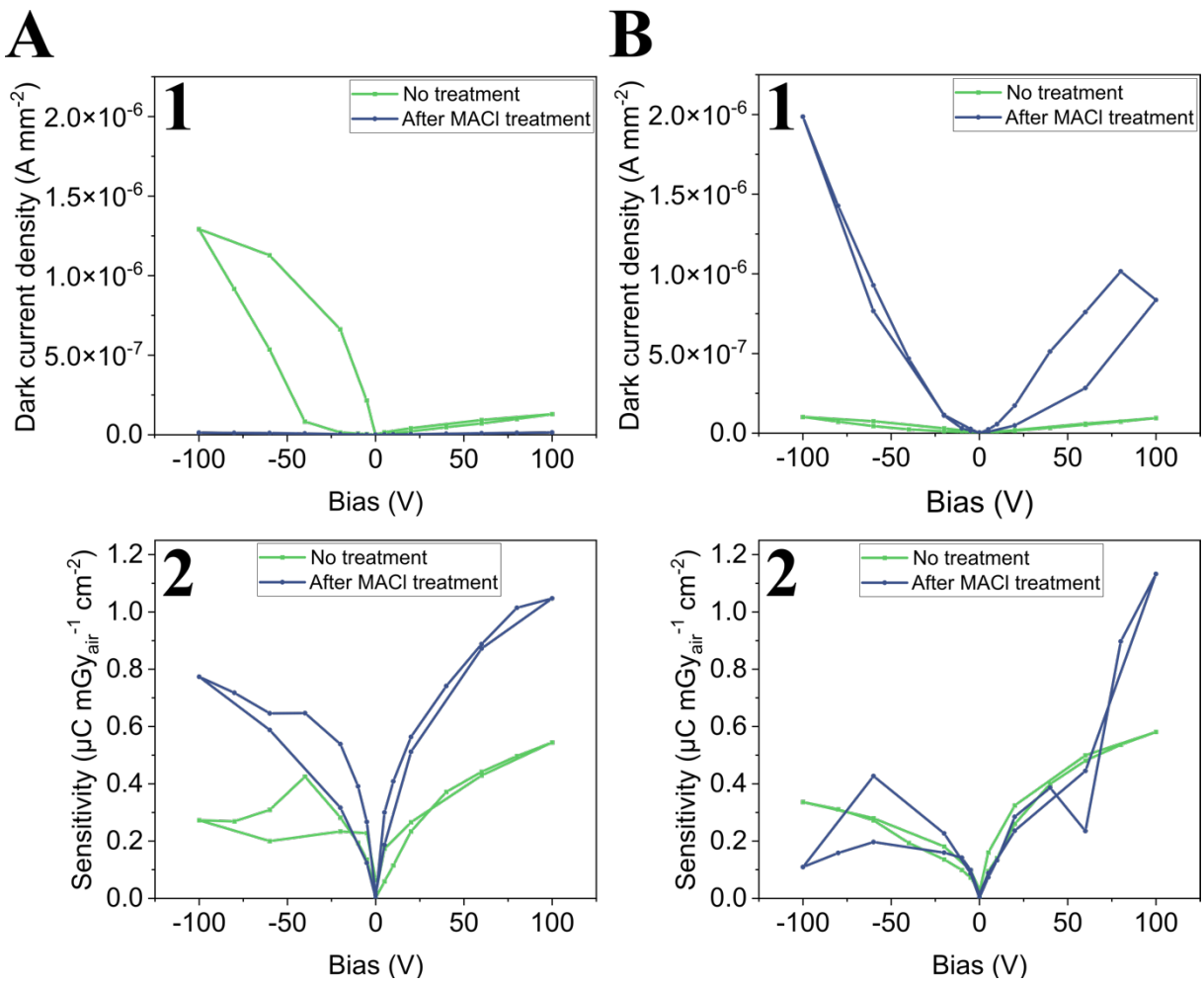

Figure 5-2-9. Optoelectronic performance of MACl treated SC devices. (1) J_{dark}-V and **(2)** S-V data for SC devices **(A)** and **(B)**. Each figure presents systematically the performance before (green plot) and after (blue plot) treatment.

The results exposed here are incomplete, should be reproduced and confirmed, but they give promising results for the post-treatment of $MAPbBr_3$. Indeed, precursors such as MACl and MABr, showed relative easiness to be volatilised within enclosed spaces, with tuneable pressure and temperature.[9,16] The optoelectronic characterisation findings are summarised in

Figure 5-2-10, illustrating key properties before and after treatment: resistivity, dark current density and sensitivity, both at 50 V mm^{-1}. When the treatment is performed on a bare crystal (without Cr electrodes), we see an improvement of all three figures, while, when the treatment is done with the electrodes, the performance is globally degraded.

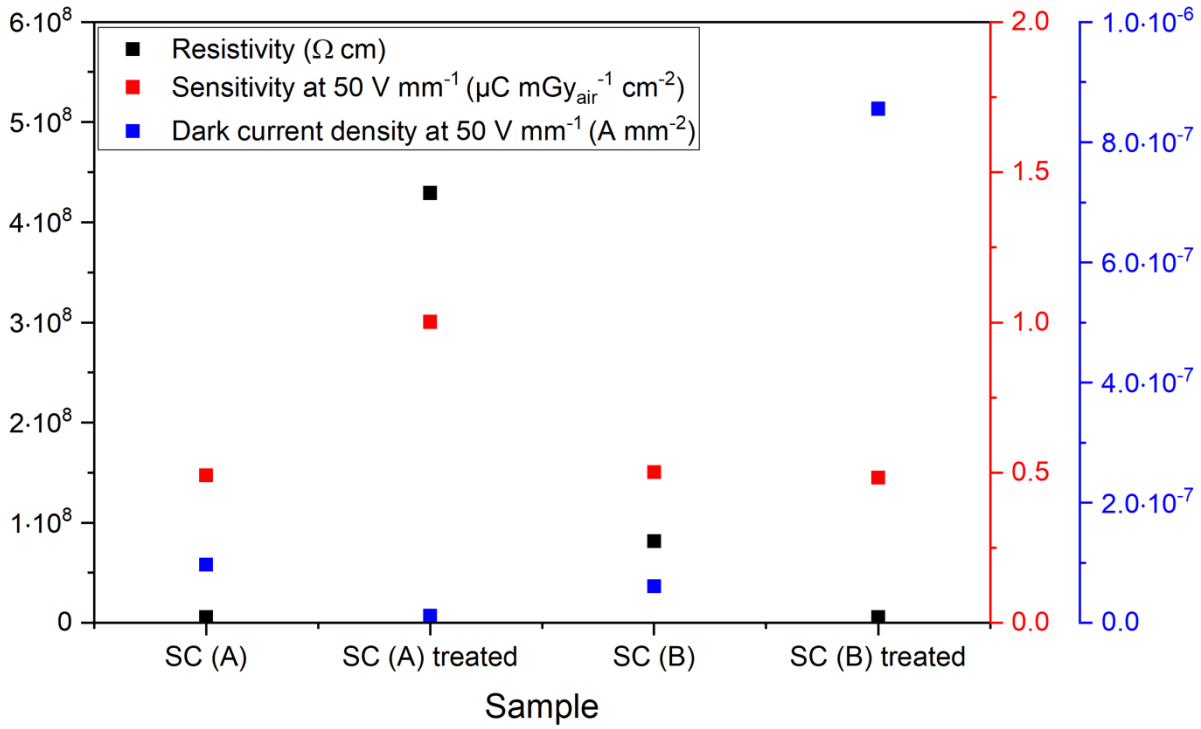

Figure 5-2-10. Optoelectronic key figures of merit before and after MACl treatment for both SC devices: resistivity ρ (black), sensitivity S (blue) and dark current density J_{dark} (red), both at 50 V mm^{-1}.

Conclusion

The study described here presents the impact of annealing at different temperatures and chemical treatment of $MAPbBr_3$ SC devices by MACl vapours.

Regarding annealing in an Ar atmosphere, the S-T and ρ-T data show that the devices preserved or improved their optoelectronic performances under X-ray illumination for annealing temperatures up to 150 °C. For higher temperatures, material degradation took place and so performance declined. Visually, the perovskite surface turned milky. Based on our TGA-MS study, we proposed the departure of small volatile molecules, degradation products of MABr, with conjoint formation of $PbBr_2$. This hindered key figures of merit like the sensitivity.

The second part exposes the attempt to improve the performance of $MAPbBr_3$ by a post-growth treatment with volatile MACl powder. The sublimation of MACl under reduced pressure and controlled temperature resulted in the successful vapour treatment of SCs. This process was accompanied with a partial liquefaction of the crystal surface. Even though part of the surface was lost to due liquefaction, penetration depths of the Cl^- anions were determined for distinct regions of the crystal via EDX. Depending on their positioning towards the source of MACl vapour, different penetration depths were estimated with a maximum of 125 and 16 µm for a bare SC and a SC with Cr electrodes on the surface, respectively. The difference in penetration between crystals with and without electrodes evidence that the Cr interferes with the incorporation of Cl, and that the vapour treatment deteriorates them. That is why electrodes should be deposited after the treatment, metal atoms layers represent a barrier for diffusing species such as chloride. High Cl content in the crystals was systematically associated with close to stoichiometry Pb/X ratios, confirming the trend seen previously in Chapter 3. This indicates that, close to the surface, point defects such as Br vacancies V_{Br} might have been healed by Cl incorporation (Cl_{Br} substitutions), but also that other point defects may have been created (e.g., Cl_i). The relaxation of these defects in the structure (e.g., migration, aggregation, association with other defects) may occur in a very substantial volume via the systematic ion migration, which would be exacerbated under biasing. As such, the successful surface incorporation of chlorine, could have significant impact on the properties. The optoelectronic performances were then tested under medical grade X-rays. Given the low number of samples tested, no conclusive answers were obtained, but the MACl treatment seems to improve key figures of merit such resistivity, sensitivity and dark current density.

Besides confirming those first results with more samples, a few elements should also be considered to further study this chemical vapour treatment process. Firstly, longer treatments, probably adjusting conjointly pressure and temperature, should be tested to see if post-growth incorporation of volatile constituents, such as MA^+ and Cl^- used here, can diffuse to the core of the crystal effectively improving the overall stoichiometry. This could also give insights into the relative importance of surface and volume defects in the device performance. Secondly,

after chemical treatment, to take advantage of the ion dynamics within the crystal, biasing cycles could be performed: going several times from positive to negative, and vice versa. This might help the relaxation of the new defect structures, leading to a composition closer to stoichiometry. This biasing process could potentially take place within the furnace while executing the healing procedure, like it is done for quartz crystals (by sweeping at 1 kV cm^{-1} at 500 °C). This would improve the stability in time of the device. It could also limit ion migration and accumulation of ions at the electrodes, thus homogenising the internal electric field and consequently improving the charge transport in the perovskite structure. Thirdly, experimenting with other similar precursors, such as MABr, MAI, FABr or CsBr, could help to better understand the mechanisms involved in the post-growth treatments. More generally, those studies would bring a better understanding on what defects are present in the structure, and which ones must be annihilated in order to enhance the high-energy radiation response.

References

(1) Tan, S.; Huang, T.; Yavuz, I.; Wang, R.; Weber, M. H.; Zhao, Y.; Abdelsamie, M.; Liao, M. E.; Wang, H.-C.; Huynh, K.; Wei, K.-H.; Xue, J.; Babbe, F.; Goorsky, M. S.; Lee, J.-W.; Sutter-Fella, C. M.; Yang, Y. Surface Reconstruction of Halide Perovskites During Post-Treatment. *J. Am. Chem. Soc.* **2021**, *143* (18), 6781–6786. https://doi.org/10.1021/jacs.1c00757.

(2) Chen, L.; Wang, H.; Zhang, W.; Li, F.; Wang, Z.; Wang, X.; Shao, Y.; Shao, J. Surface Passivation of $MAPbBr_3$ Perovskite Single Crystals to Suppress Ion Migration and Enhance Photoelectronic Performance. *ACS Appl. Mater. Interfaces* **2022**, acsami.1c21948. https://doi.org/10.1021/acsami.1c21948.

(3) Lee, S.; Park, J. H.; Lee, B. R.; Jung, E. D.; Yu, J. C.; Di Nuzzo, D.; Friend, R. H.; Song, M. H. Amine-Based Passivating Materials for Enhanced Optical Properties and Performance of Organic–Inorganic Perovskites in Light-Emitting Diodes. *J. Phys. Chem. Lett.* **2017**, *8* (8), 1784–1792. https://doi.org/10.1021/acs.jpclett.7b00372.

(4) Shkrob, I. A.; Marin, T. W. Charge Trapping in Photovoltaically Active Perovskites and Related Halogenoplumbate Compounds. *J. Phys. Chem. Lett.* **2014**, *5* (7), 1066–1071. https://doi.org/10.1021/jz5004022.

(5) Zu, F.-S.; Amsalem, P.; Salzmann, I.; Wang, R.-B.; Ralaiarisoa, M.; Kowarik, S.; Duhm, S.; Koch, N. Impact of White Light Illumination on the Electronic and Chemical Structures of Mixed Halide and Single Crystal Perovskites. *Advanced Optical Materials* **2017**, *5* (9), 1700139. https://doi.org/10.1002/adom.201700139.

(6) Kirmani, A. R.; Mansour, A. E.; Yang, C.; Munir, R.; El-Zohry, A. M.; Mohammed, O. F.; Amassian, A. Facile and Noninvasive Passivation, Doping and Chemical Tuning of Macroscopic Hybrid Perovskite Crystals. *PLoS ONE* **2020**, *15* (3), e0230540. https://doi.org/10.1371/journal.pone.0230540.

(7) Zhu, H.; Pan, L.; Eickemeyer, F. T.; Hope, M. A.; Ouellette, O.; Alanazi, A. Q. M.; Gao, J.; Baumeler, T. P.; Li, X.; Wang, S.; Zakeeruddin, S. M.; Liu, Y.; Emsley, L.; Grätzel, M. Efficient and Stable Large Bandgap $MAPbBr_3$ Perovskite Solar Cell Attaining an Open Circuit Voltage of 1.65 V. *ACS Energy Lett.* **2022**, 1112–1119. https://doi.org/10.1021/acsenergylett.1c02431.

(8) Juarez-Perez, E. J.; Ono, L. K.; Maeda, M.; Jiang, Y.; Hawash, Z.; Qi, Y. Photodecomposition and Thermal Decomposition in Methylammonium Halide Lead Perovskites and Inferred Design Principles to Increase Photovoltaic Device Stability. *J. Mater. Chem. A* **2018**, *6* (20), 9604–9612. https://doi.org/10.1039/C8TA03501F.

(9) Ivanov, I. L.; Bolyachkina, M. S.; Mazurin, M. O.; Tsvetkov, D. S.; Sereda, V. V.; Zuev, A. Yu. Vapor Pressure of Methylammonium Halides. Part I: Setup Verification and Vapor Pressure of Methylammonium Chloride. *Thermochimica Acta* **2017**, *658*, 24–30.

https://doi.org/10.1016/j.tca.2017.10.021.

(10) Zhou, Z.; Wang, Z.; Zhou, Y.; Pang, S.; Wang, D.; Xu, H.; Liu, Z.; Padture, N. P.; Cui, G. Methylamine-Gas-Induced Defect-Healing Behavior of CH3NH3PbI3 Thin Films for Perovskite Solar Cells. *Angewandte Chemie International Edition* **2015**, *54* (33), 9705–9709. https://doi.org/10.1002/anie.201504379.

(11) Lee, S.-W.; Kim, S.; Bae, S.; Cho, K.; Chung, T.; Mundt, L. E.; Lee, S.; Park, S.; Park, H.; Schubert, M. C.; Glunz, S. W.; Ko, Y.; Jun, Y.; Kang, Y.; Lee, H.-S.; Kim, D. UV Degradation and Recovery of Perovskite Solar Cells. *Sci Rep* **2016**, *6* (1), 38150. https://doi.org/10.1038/srep38150.

(12) Armaroli, G.; Ferlauto, L.; Lédée, F.; Lini, M.; Ciavatti, A.; Kovtun, A.; Borgatti, F.; Calabrese, G.; Milita, S.; Fraboni, B.; Cavalcoli, D. X-Ray-Induced Modification of the Photophysical Properties of $MAPbBr_3$ Single Crystals. *ACS Appl. Mater. Interfaces* **2021**, acsami.1c16072. https://doi.org/10.1021/acsami.1c16072.

(13) Motti, S. G.; Meggiolaro, D.; Martani, S.; Sorrentino, R.; Barker, A. J.; De Angelis, F.; Petrozza, A. Defect Activity in Lead Halide Perovskites. *Advanced Materials* **2019**, *31* (47), 1901183. https://doi.org/10.1002/adma.201901183.

(14) Mannodi-Kanakkithodi, A.; Park, J.-S.; Martinson, A. B. F.; Chan, M. K. Y. Defect Energetics in Pseudo-Cubic Mixed Halide Lead Perovskites from First-Principles. *J. Phys. Chem. C* **2020**, *124* (31), 16729–16738. https://doi.org/10.1021/acs.jpcc.0c02486.

(15) Piquard, J.; Zaccaro, J.; Pintault, B.; Maunier, C.; Ibanez, A. Origins of Optical Defects in Rapidly Grown DKDP Crystals. *CrystEngComm* **2019**, *21* (2), 372–378. https://doi.org/10.1039/C8CE01693C.

(16) Ivanov, I. L.; Mazurin, M. O.; Tsvetkov, D. S.; Malyshkin, D. A.; Sereda, V. V.; Zuev, A. Yu. Vapor Pressure of Methylammonium Halides. Part II: Vapor Pressure and Standard Entropy of Methylammonium Bromide. *Thermochimica Acta* **2019**, *674*, 58–62. https://doi.org/10.1016/j.tca.2019.02.008.

Conclusion and perspectives

For the past decade, hybrid MHPs have been regarded as bearing great potential for optoelectronic applications either as light harvesters/converters or light emitters. Bringing these materials to maturity, that is being able to take full advantage of this potential requires identifying the nature and origin of defects present in those semiconductors. As we have seen throughout this work, in the case of the benchmark material $MAPbBr_3$, it is very difficult to understand and subsequently change the nature of defects and intrinsic doping.[1] This is mainly due to the internal dynamics of the charges in this family of compounds, which includes unidentified point defects and parasitic ion migration. The evolution with time and under external influence (e.g., environment, biasing voltage, ionising radiation) of the underlying chemistry would be at the origin of the so-called defect tolerance and/or self-healing mechanisms which are attractive properties.[2] At the same time, these mechanisms blur the picture of the defect landscape, hindering the optimisation of these materials. Researchers are then confronted to a double-edged sword.

This ever-changing configuration is challenging not only for the experimental but also theoretical analysis as most models and DFT calculations in the literature consider "static" lattices without its dynamics. The community is faced with the challenge of identifying the pertinent defects in a system where lattice dynamics may be operative on a time scale that is comparable with that of electron processes, relevant for charge capture or recombination.[3] In the literature, while combining characterisation and modelling, it was speculated that the main internal bandgap defects impacting the charge carriers could be interstitials (Pb_i, Br_i) and vacancies (V_{Pb}, V_{Br}) with different charges,[4] and even Pb_{MA} substitution.[5]

The presence and number of interstitials, vacancies or substitutions are defined by the growth method of the PC or SC. These defects seem to be subsequently mobilised by the internal ion dynamics, defining its charge transport physics, thus determining how good the semiconductor for a given application is. Even though which particular defect should be avoided remains an open question, based on the literature, one should try to avoid the formation of deficiencies, deviations from the constituent stoichiometries (e.g., Pb/X, A/X), in the synthesis of $APbX_3$ hybrid perovskites. The stoichiometry should also be maintained at the surface of the perovskite; hence a special care should be taken regarding post-synthesis handling and treatment. By doing this, one could stabilise the structure overall, and improve the response under medical grade X-rays, as we have performed, to some extent, during this thesis work.

Our first approach, presented in Chapter 3, was to use the partial substitution of Br^- by Cl^- anions in $MAPbBr_3$ SCs, as a way to lower the density of point defects upon synthesis. From a thermodynamic perspective, such substitution introduces an increase of the entropy of mixing,

while avoiding the formation of halide vacancies V_X which are detrimental, at least, due to the promotion of ion migration. Also, Cl^- anions being smaller than Br^- anions, one would anticipate that this substitution would allow the accommodation of more distorted environments, thereby filling halide sites that would otherwise remain vacant. The optoelectronic evaluation of intermediate compositions of the $MAPb(Br_{1-x}Cl_x)_3$ solid solution revealed the high quality of the resulting SC devices: no hysteresis in J-V sweeps and negligible conductivity drift. An optimum in Cl content was identified for $MAPb(Br_{0.85}Cl_{0.15})_3$, showing the highest sensitivity ($S \approx 3$ µC mGy_{air}^{-1} cm^{-2} at 50 V mm^{-1}), the lowest dark current density ($J_{dark} \approx 43$ nA mm^{-2} at 50 V mm^{-1}) and the lowest conductivity drift ($\sigma_{drift} \approx 3 \times 10^{-5}$ S m^{-1} s^{-1} at 50 V mm^{-1}). We showed that the two-charge carriers Hecht model does not fit properly S-V data for $MAPbBr_3$, but that for the $MAPb(Br_{0.85}Cl_{0.15})_3$ composition, the modelling seems to better fit the charge transport in the material, indicative of its superiority. The Cl incorporation was correlated to a Pb/X ratio approaching the ABX_3 stoichiometry and to an increase in hole lifetime, going from 10 µs for $MAPbBr_3$ to 75 µs for $MAPb(Br_{0.85}Cl_{0.15})_3$. This improvement in stoichiometry was linked to a reduction of point defects, thus to a lower fraction of mobile ionic defects (e.g., V_X, X_i), resulting in the seen enhancement of the charge induction efficiency under X-rays irradiation.

The clear impact of deliberately modifying the chemical composition of the hybrid perovskite prompted us to explore other potential pathways for unintentional alterations in the chemical composition. In Chapter 4, we studied the impact and potential improvement that can occur due to the environment, in the broadest sense possible: environmental degradation of the precursors, environment of the crystal growth, and that of the device preparation and characterisation. SCs were successfully grown in uncontrolled standard laboratory and controlled inert Ar atmosphere glovebox conditions. SCs grown in ambient condition (AC), when compared to the SCs grown in inert atmosphere (IC), presented more impurities in the bulk, such as Cl^- and Al^{3+} ions, potentially enhancing the intrinsic p-doped character of $MAPbBr_3$.[6] We have demonstrated that the solution system of bromoplumbate complexes in DMF is very resilient to the incorporation of environmental species in the bulk structure such as water or oxygen, as suggested by previous works.[7–9] However, differences in the chemical composition between the surface and the bulk were noticed. AC crystals were deficient in MABr, and presented adsorbed water molecules on their surface, inducing a n-doping on the surface.[10] This n-doping proved beneficial for the X-ray response when compared to the IC SCs: they exhibit higher sensitivity and symmetrical S-V data. This was associated to an enhanced carrier transport for electrons which was translated into statistically measurable electron mobility μ_e for the associate devices. We considered this finding quite significant as it is generally impossible to satisfactorily measure μ_e values with $MAPbBr_3$ devices. A fully inert synthesis-characterisation circuit allow putting in evidence the impact of the testing atmosphere for both families of crystals, by first performing evaluations in Ar and then in air atmospheres. The outcome was reversed in Ar atmosphere, when compared to atmospheric conditions testing: IC SCs had higher sensitivity than AC SCs, also presenting systematically electron mobility.

We hypothesised that the two types of samples started with different doping states depending on the growth environment. Therefore, the interaction of the preparation-analysis atmosphere with their surface lead to overall different performances. For the testing in atmospheric conditions, AC crystals show a stronger p-doped character and IC crystals are more intrinsic. The former would benefit from the n-doping compensation from environmental water, as opposed to the latter, which would be downgraded by the n-doping. In the inert testing, the intrinsic IC crystals would likely perform better under X-rays, as they would not have undergone n-doping on their surface. Nevertheless, both families are affected by the exposure to air, as proven by the acceleration of the signal drifts during J-t measurements, but with different surface impacts defining the final performance of the device. All of this considered, how the chemistry of the system makes the perovskite surface more sensitive has not been clarified in the perovskite scientific community, but it seems coherent to assume that a correlation exists between impurities and the surface reactivity, promoted by V_{Pb} and/or V_{Br} point defects, among potentially others intervening with the local Pb/X stoichiometry.

The evidence we have observed regarding the impact of the post-growth environment on the surface chemistry of the SCs has led us to explore its potential beneficial applications. Chapter 5 presents our first attempt at healing defects in both surface and bulk, after SC growth. As an example, we studied the impact of controlled annealing and post-growth treatment of pure $MAPbBr_3$ crystals with perovskite precursor MACl vapours. This process was accompanied with a partial liquefaction of the crystal surface, leading to the creation of a $MAPbBr_3 \bullet x$ MACl layer, later recrystalising in $MAPb(Br_{1-x}Cl_x)_3$ mixed halide perovskite. Even though a fraction of the surface was lost by this, penetration depths of the Cl^- anions were estimated for distinct regions of the crystal. The penetration of Cl was observed to be within the first hundred micrometres for the bare SC and within a dozen micrometres for the SC with Cr electrodes. The study evidenced that Cr interferes with the incorporation of Cl and that the vapour treatment deteriorates the electrodes. A healing mechanism was also demonstrated when high Cl content in the crystals was systematically associated with close to stoichiometry Pb/X ratios. This meant that, close to the surface, point defects such as V_{Br} might have been repaired by Cl incorporation, leading to Cl_{Br} substitutions, but maybe also to the formation of other point defects such as Cl_i. The optoelectronic performances of healed devices were then tested under X-rays but given the low number of samples tested, no conclusive answers were obtained. Despite the sample statistics, the MACl treatment seems to improve the key figures of merit such resistivity, sensitivity and dark current density.

All three studies bring into the light the different afflictions that this family of materials has. While they show how susceptible is $MAPbBr_3$ towards its surroundings and an external stimulus, they also bring several clues on what to further investigate to boost the performance under X-rays of $MAPbBr_3$. The ion migration and long biasing protocols complicate the evaluation of the semiconductors, while comparing perovskites of different chemical composition or with the same one, but from different synthesis methods. Sample-to-sample

variability poses a problem when drawing conclusions for the different studies, that is why sufficient statistical support is primordial to extract trends for a given condition. While this work confirms the generally favourable charge transport properties of $MAPbBr_3$ and $MAPb(Br_{1-x}Cl_x)_3$ perovskites, it emphasises the necessity for additional efforts to achieve the high performance levels demonstrated by state-of-the-art materials like CdTe and CZT. The dark current density was slightly reduced by the Cl incorporation, but its level remains significantly higher by several orders of magnitude for the medical imaging application. In all studies, improved stoichiometry seems to be systematically correlated to improved performances. Yet those given through the different analyses were relative and not absolute values, which means that further equilibration of Pb/Br and MA/Br ratios might still be required. A solution to test would be to experiment with longer healing treatments, while adapting at the same time experimental conditions such as pressure and temperature, to avoid strong physical modifications of the surface, such as sublimations or liquefactions. It would then be interesting to see if post-growth incorporation of volatile constituents, coming from the sublimation of perovskite precursors such as MACl, MABr, MAI, FABr or inorganic CsBr, can diffuse to the core of the crystal to effectively improve the overall stoichiometry. As mentioned at the end of Chapter 5, one could take advantage of the parasitic ion migration within the crystal. The relaxation of newly-introduced defects by such healing treatments may occur in a very substantial volume via this systematic ion migration, which would be exacerbated under biasing. Biasing cycles could be performed in a manner that facilitates the relaxation of defects, thereby resulting in a composition closer to stoichiometry throughout the entire crystal volume. This, in turn, would enhance the long-term stability of the device. Finally, by reducing the density of vacancies, it could also limit ion migration and accumulation of ions at the electrodes, thus homogenising the internal electric field and consequently improving the charge transport in the perovskite structure.[11,12] In a broader context, these future studies would contribute to a better understanding of the specific defects present in the structure and which ones need to be eliminated to enhance the high-energy radiation response of the semiconductor. The presented work also emphasises the advantages of device preparation and potential encapsulation in inert gas atmospheres or crystal growth under controlled humidity in atmospheric conditions. These measures would be particularly beneficial due to the surface reactivity of hybrid perovskites.

References

(1) Euvrard, J.; Yan, Y.; Mitzi, D. B. Electrical Doping in Halide Perovskites. *Nat Rev Mater* **2021**, *6* (6), 531–549. https://doi.org/10.1038/s41578-021-00286-z.

(2) Cahen, D.; Kronik, L.; Hodes, G. Are Defects in Lead-Halide Perovskites Healed, Tolerated, or Both? *ACS Energy Lett.* **2021**, 4108–4114. https://doi.org/10.1021/acsenergylett.1c02027.

(3) Guzelturk, B.; Winkler, T.; Van de Goor, T. W. J.; Smith, M. D.; Bourelle, S. A.; Feldmann, S.; Trigo, M.; Teitelbaum, S. W.; Steinrück, H.-G.; de la Pena, G. A.; Alonso-Mori, R.; Zhu, D.; Sato, T.; Karunadasa, H. I.; Toney, M. F.; Deschler, F.; Lindenberg, A. M. Visualization of Dynamic Polaronic Strain Fields in Hybrid Lead Halide Perovskites. *Nat. Mater.* **2021**, *20* (5), 618–623. https://doi.org/10.1038/s41563-020-00865-5.

(4) Musiienko, A.; Moravec, P.; Grill, R.; Praus, P.; Vasylchenko, I.; Pekarek, J.; Tisdale, J.; Ridzonova, K.; Belas, E.; Landová, L.; Hu, B.; Lukosi, E.; Ahmadi, M. Deep Levels, Charge Transport and Mixed Conductivity in Organometallic Halide Perovskites. *Energy Environ. Sci.* **2019**, *12* (4), 1413–1425. https://doi.org/10.1039/C9EE00311H.

(5) Mannodi-Kanakkithodi, A.; Park, J.-S.; Martinson, A. B. F.; Chan, M. K. Y. Defect Energetics in Pseudo-Cubic Mixed Halide Lead Perovskites from First-Principles. *J. Phys. Chem. C* **2020**, *124* (31), 16729–16738. https://doi.org/10.1021/acs.jpcc.0c02486.

(6) Shi, T.; Yin, W.-J.; Hong, F.; Zhu, K.; Yan, Y. Unipolar Self-Doping Behavior in Perovskite $CH_3NH_3PbBr_3$. *Appl. Phys. Lett.* **2015**, *106* (10), 103902. https://doi.org/10.1063/1.4914544.

(7) Manser, J. S.; Saidaminov, M. I.; Christians, J. A.; Bakr, O. M.; Kamat, P. V. Making and Breaking of Lead Halide Perovskites. *Acc. Chem. Res.* **2016**, *49* (2), 330–338. https://doi.org/10.1021/acs.accounts.5b00455.

(8) Kirmani, A. R.; Mansour, A. E.; Yang, C.; Munir, R.; El-Zohry, A. M.; Mohammed, O. F.; Amassian, A. Facile and Noninvasive Passivation, Doping and Chemical Tuning of Macroscopic Hybrid Perovskite Crystals. *PLoS ONE* **2020**, *15* (3), e0230540. https://doi.org/10.1371/journal.pone.0230540.

(9) Zuo, S.; Niu, W.; Chu, S.; An, P.; Huang, H.; Zheng, L.; Zhao, L.; Zhang, J. Water-Regulated Lead Halide Perovskites Precursor Solution: Perovskite Structure Making and Breaking. *J. Phys. Chem. Lett.* **2023**, 4876–4885. https://doi.org/10.1021/acs.jpclett.3c00683.

(10) Wang, C.; Ecker, B. R.; Wei, H.; Huang, J.; Gao, Y. Environmental Surface Stability of the $MAPbBr_3$ Single Crystal. *J. Phys. Chem. C* **2018**, *122* (6), 3513–3522. https://doi.org/10.1021/acs.jpcc.7b12740.

(11) García-Batlle, M.; Deumel, S.; Huerdler, J. E.; Tedde, S. F.; Guerrero, A.; Almora, O.; Garcia-Belmonte, G. Mobile Ion-Driven Modulation of Electronic Conductivity Explains Long-Timescale Electrical Response in Lead Iodide Perovskite Thick Pellets. *ACS Appl. Mater.*

Interfaces **2021**, *13* (30), 35617–35624. https://doi.org/10.1021/acsami.1c06046.

(12) García-Batlle, M.; Baussens, O.; Amari, S.; Zaccaro, J.; Gros-Daillon, E.; Verilhac, J.; Guerrero, A.; Garcia-Belmonte, G. Moving Ions Vary Electronic Conductivity in Lead Bromide Perovskite Single Crystals through Dynamic Doping. *Adv. Electron. Mater.* **2020**, *6* (10), 2000485. https://doi.org/10.1002/aelm.202000485.

Appendix – Chapter 2

Table of contents

Appendix – Chapter 2

Appendix – Chapter 2
Materials and methods

1 Calibration of the crystal growth setup

The calibration of the crystal growth setup was performed in order to know the actual temperature in the vials as a function of the system setpoint. The solution volume in each vial was fixed to 3.5 mL to ensure that the solution meniscus was aligned with the plate upper level, to be slightly colder than the rest of the solution and avoid spontaneous nucleation. The calibration consisted in two different studies.

The first study evaluated the vertical temperature gradient in 3.5 mL of DMF contained in a vial, representing 7 mm of solution height. A thermocouple was immersed in the liquid: 0 and 7 mm define the bottom of the flask and the liquid meniscus, respectively. Two different positionings can be identified in the plate as shown in **Figure A 2-1-1**: lateral and central positions. Two temperature gradients are then obtained, one for each positioning, as seen in **Figure A 2-1-2**. Given that the solution is naturally convected, the gap between the setpoint and actual temperatures rises with increasing temperature, and from the flask bottom to its top.

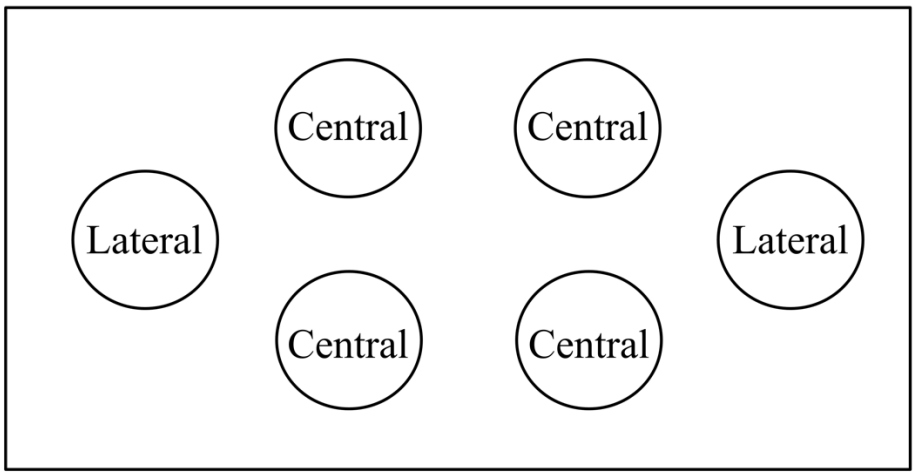

Figure A 2-1-1. Crystal growth Al plate top view schematic distinguishing the two types of positioning existing on the setup.

The second study establishes the correlation between the setpoint temperature and that at the flask bottom, for the different slots. A linear fit was performed for the flask bottom temperature as a function of the setpoint temperature for both positions, as depicted in

Figure A 2-1-3. Average setpoints were then extracted from both positions. Key growth steps (growth solution initial temperature (56 °C), $T_{level\ 1}$ (58.8 °C), $T_{level\ 2}$ (62.6 °C) and final temperature (81.5 °C)) were then plotted according to theses averages values, as made explicit by **Figure A 2-1-4**. Thus, the correction that must be taken into account to have the right temperature for crystal growth is described by **Equation (A 2-1)**:

$$T_{setpoint} = 0.9421\ T_{flask\ bottom} + 0.9424 \qquad \text{(A 2-1)}$$

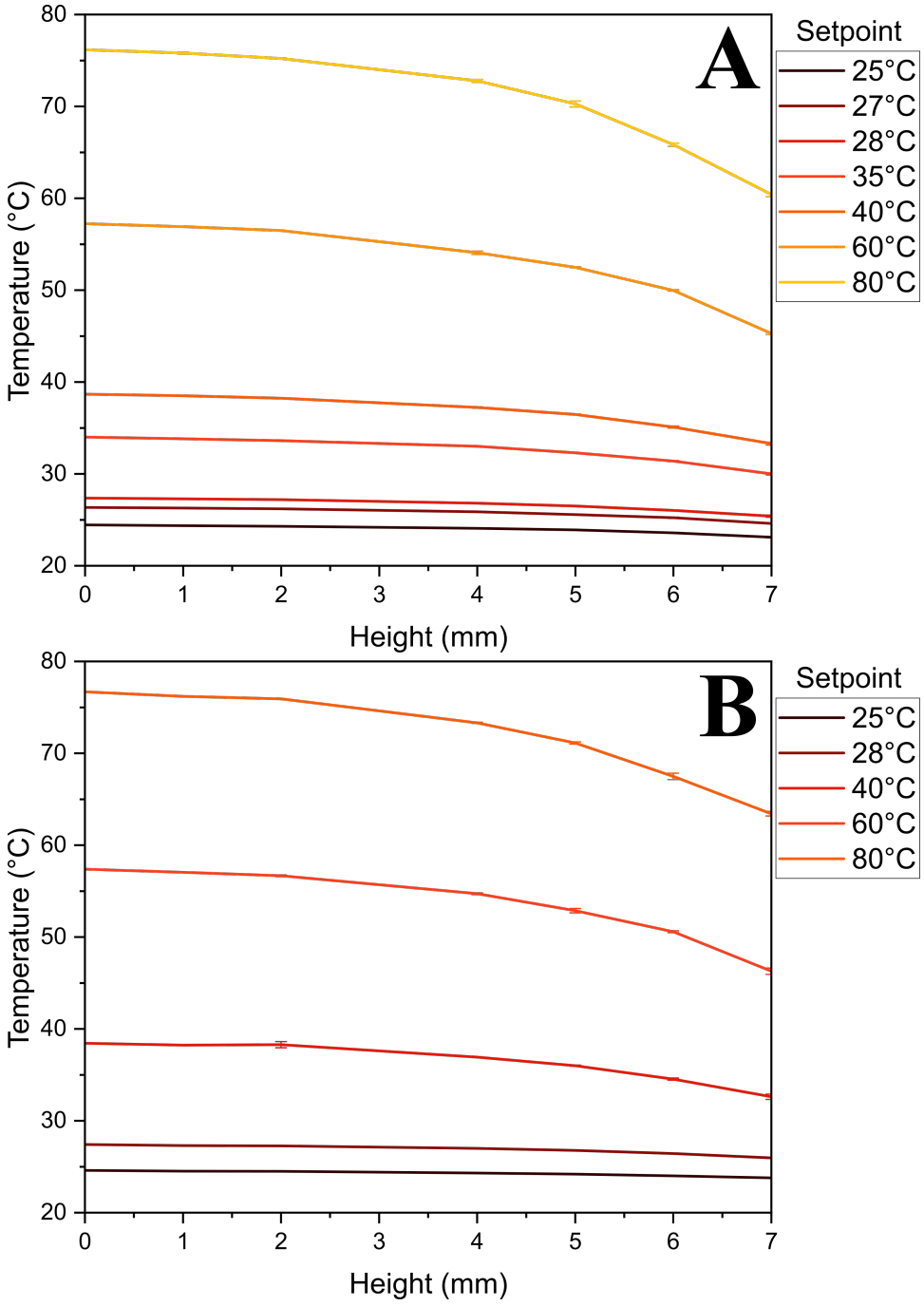

Figure A 2-1-2. Temperature gradient inside 3.5 mL of DMF for different setpoint temperatures for both the **(A)** lateral and **(B)** central positions.

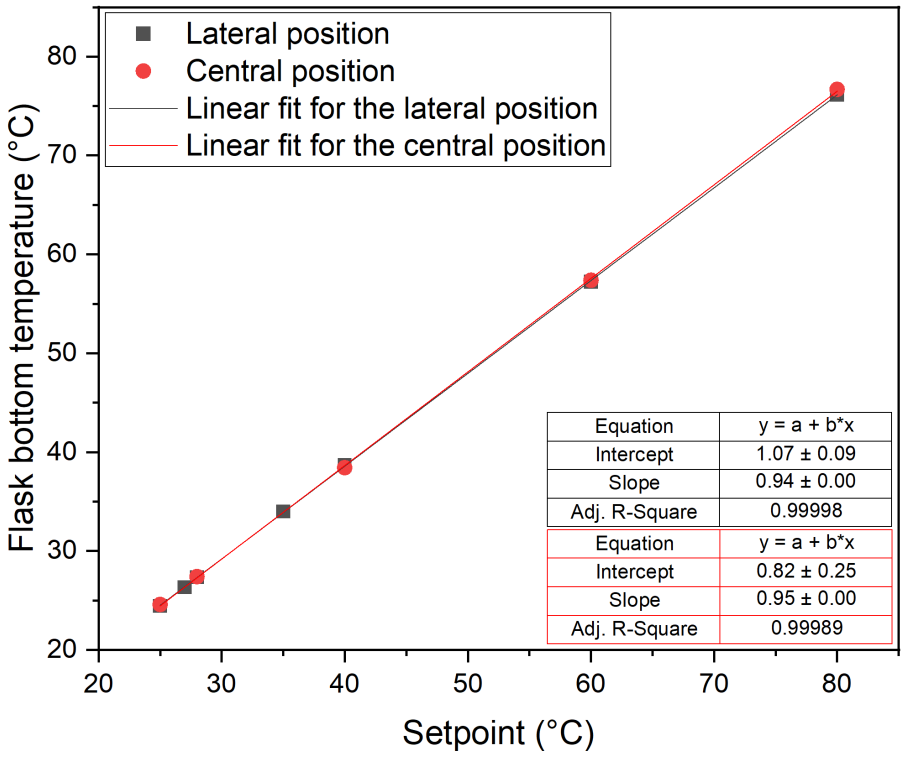

Figure A 2-1-3. Resulting correlation between the flask bottom and setpoint temperatures for both lateral and central positions.

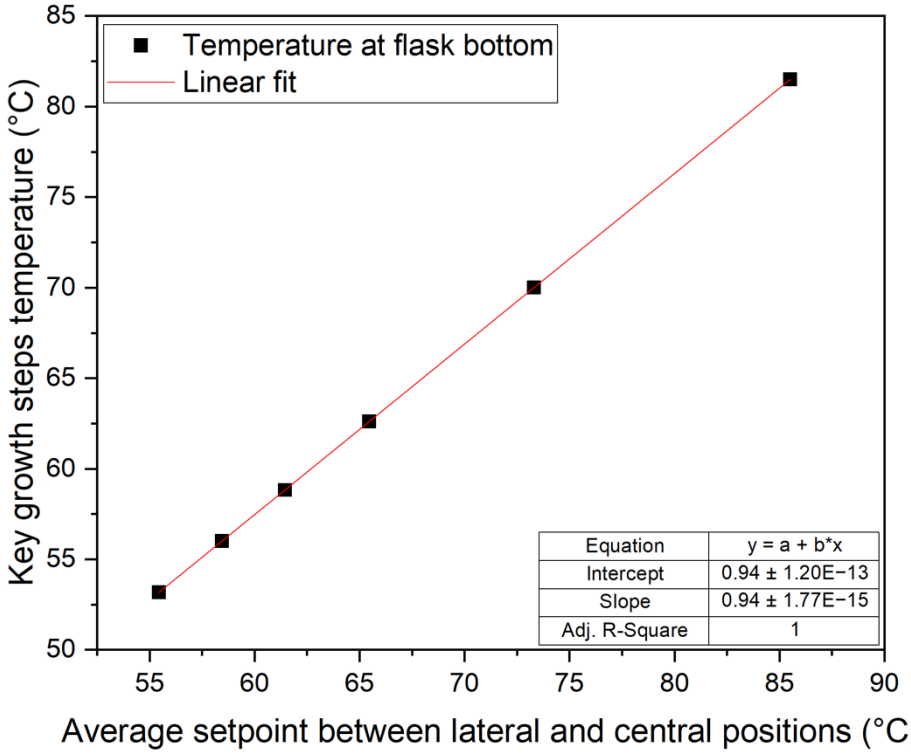

Figure A 2-1-4. Key growth steps temperature (regrowth protocol, beginning and end temperatures) as a function of the average setpoint temperature between lateral and central positions.

Appendix – Chapter 3

Table of contents

Appendix – Chapter 3

Appendix – Chapter 3

Mixed halide compositions: Anion engineering in $MAPb(Br_{1-x}Cl_x)_3$ solid solution

1 Solubility of $MAPb(Br_{0.85}Cl_{0.15})_3$

In the case of $MAPb(Br_{0.85}Cl_{0.15})_3$, the solubility as a function of the temperature in DMF was determined. $MAPb(Br_{0.85}Cl_{0.15})_3$ residual crystals from the associated growths were ground and added to 7 mL of DMF until the solution reaches total saturation at 70 °C. After an hour, a little volume was then collected and weighted, then the solvent was evaporated to determine the amount of soluble perovskite and the mass solvent needed. Even though the volume of the collected solution sampling is known, its volume was corrected by using the evaporated solvent mass and a DMF density value of 0.9445 g mL^{-1} (at 25°C).[1] This yields a solubility expressed in grams of $MAPbBr_3$ per millilitre of solvent. Subsequently, the solubility was determined the same way at 65, 60, 50, 40, and 30 °C. The DMF density was considered constant within the temperature range. The volume extraction took place one hour after reaching the targeted temperature, measured with a thermocouple. The solution was stirred within a borosilicate glass vial. The temperature dependence of the solubility limit of $MAPbBr_3$ and mixed halide compositions in DMF can be fitted with a Van't Hoff type equation (**Equation (A 3-1)**):[2]

$$s = A\, e^{\frac{B}{T+273.15}} \qquad \text{(A 3-1)}$$

Where s is the solubility (g mL^{-1}), A and B are terms linked to the entropy and enthalpy of dissolution, respectively, and T is the temperature (°C).

Table A 3-1-1 summarises the parameters extracted via the Van't Hoff fit of the solubility curves for both materials. As for $MAPbBr_3$, $MAPb(Br_{0.85}Cl_{0.15})_3$ has retrograde solubility in DMF but lower in comparison. Even though the term associated to the enthalpy of reaction is slightly greater for $MAPb(Br_{0.85}Cl_{0.15})_3$ than $MAPbBr_3$, the pre-exponential term linked to the entropy variation has been lowered of one order of magnitude. The presence of Cl lowers the entropy of mixing, meaning that the entropy of the crystallised phase is bigger for the chloride compound. The experimental data and associated Van't Hoff fit are plotted in **Figure A 3-1-1**.

Appendix – Chapter 3

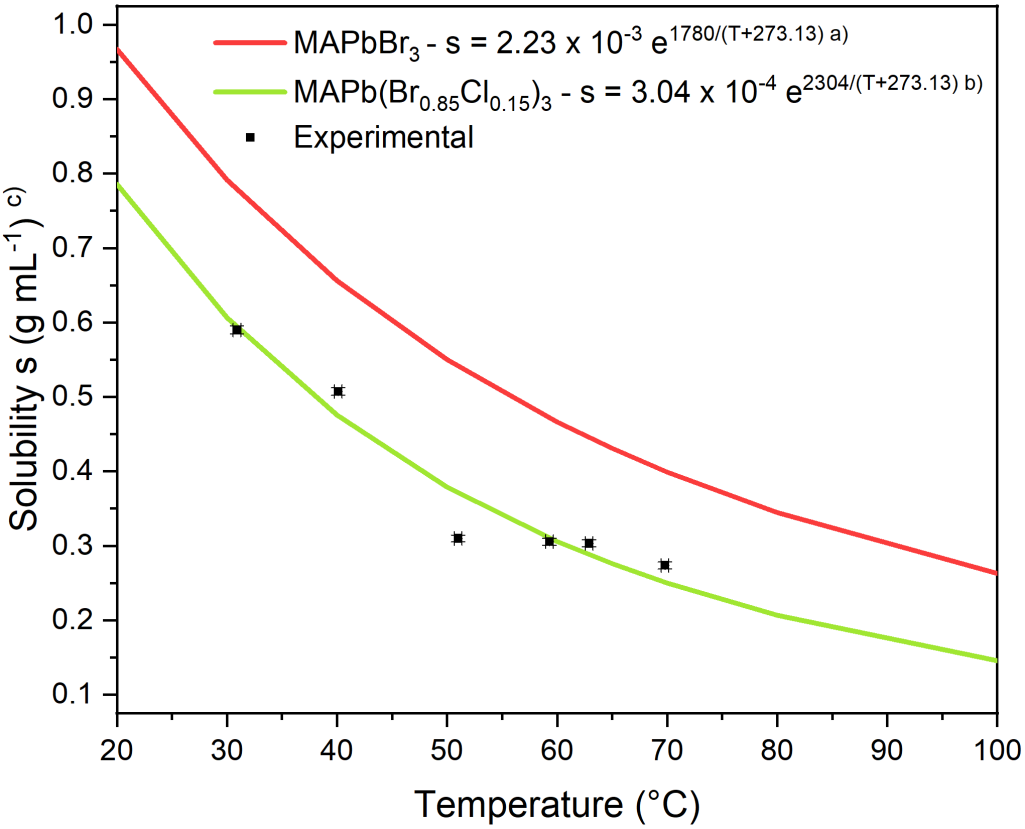

Figure A 3-1-1. Retrograde solubility of $MAPbBr_3$ and $MAPb(Br_{0.85}Cl_{0.15})_3$ ($\%Cl_{sol}$ = 10 %) in DMF. [a] $MAPbBr_3$ Van't Hoff fitting is extracted from previous work.[2] [b] $MAPb(Br_{0.85}Cl_{0.15})_3$ Van't Hoff fitting was computed on experimental points taking into consideration a constant DMF density value of 0.9445 g mL^{-1} (at 25°C)[1] in the considered temperature range. [c] Grams of perovskite per millilitre of solvent at 25 °C.

Table A 3-1-1. Solubility as a function of the temperature Van't Hoff fit parameters for $MAPbBr_3$ and $MAPb(Br_{0.85}Cl_{0.15})_3$.

Parameter	*A*	*B*
$MAPbBr_3$	2.23×10^{-3} g mL^{-1}	1780 K
$MAPb(Br_{0.85}Cl_{0.15})_3$	3.04×10^{-4} g mL^{-1}	2304 K

2 FESEM-EDX

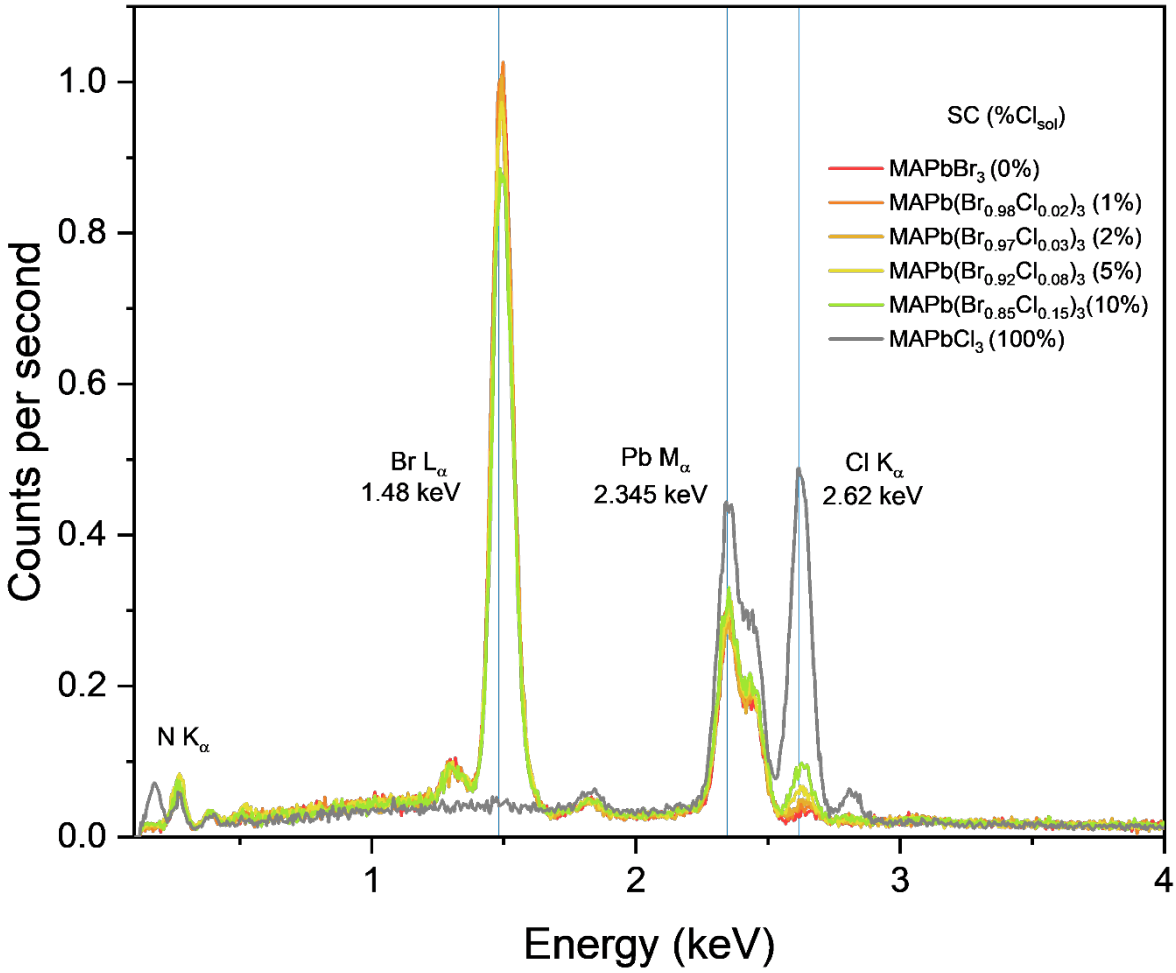

Figure A 3-2-1. Overall EDX spectra overlaid. The spectra were normalised using $MAPbBr_3$ Br L_α emission line to highlight progressive and preferential substitution of Br^- with Cl^-anions.

3 XRD and Le Bail refinement

Table A 3-3-1. Reliability factors for points with Bragg contributions: conventional Rietveld and Bragg R-factors for all compositions patterns after Le Bail analysis for a single series of SCs. [a)]

Material[b)]	Profile factor R_p	Weighted profile factor R_{wp}	Expected weighted profile factor R_{exp}	χ^2	Bragg factor R_B	Crystallographic factor R_F	Deviance Y	Global user-weighted χ^2 (Bragg contribution)
$MAPbBr_3$	21.9	25.3	8.65	8.55	1.16	1.08	0.469×10^5	8.55
$MAPb(Br_{0.98}Cl_{0.02})_3$	14.1	16.1	8.04	4.03	0.967	1.53	0.204×10^5	4.03
$MAPb(Br_{0.97}Cl_{0.03})_3$	13.7	16.5	6.65	6.13	1.70	1.41	0.268×10^5	9.63
$MAPb(Br_{0.92}Cl_{0.08})_3$	12.2	15.5	7.03	4.84	0.787	0.605	0.248×10^5	7.43
$MAPb(Br_{0.85}Cl_{0.15})_3$	16.1	20.1	9.45	4.53	0.660	0.709	0.243×10^5	4.53
$MAPbCl_3$	14.4	18.2	8.39	4.71	0.520	0.384	0.264×10^5	5.88

[a)] All agreement indices shown in this table are defined in detail in reference.[3]
[b)] The x values given in the above chemical formulae is given by $\%Cl_{cryst}$, determined using Vegard's law (VL) and the XRD data.

4 ICP-MS

Table A 3-4-1. Pb and Br concentrations determined via ICP-MS in a H_2O/HNO_3 mixture and associated Pb/X ratio for two $MAPbBr_3$ SC samples. [a)]

Sample	^{207}Pb [µg/kg]	^{79}Br [µg/kg]	Resulting Pb/Br ratio via ICP-MS [%]
$MAPbBr_3$ #1	103.41 ± 1	120.45 ± 0.8	33.11 ± 0.78
$MAPbBr_3$ #2	138.06 ± 0.7	162.98 ± 0.4	32.67 ± 0.37

[a)] The Pb and Br concentrations presented here are given per kg of $MAPbBr_3$ SC. Only the most common isotope was considered for quantification.
According to bulk composition, Pb-X stoichiometry is already close to 33.3 % for $MAPbBr_3$.

5 J-V sweeps

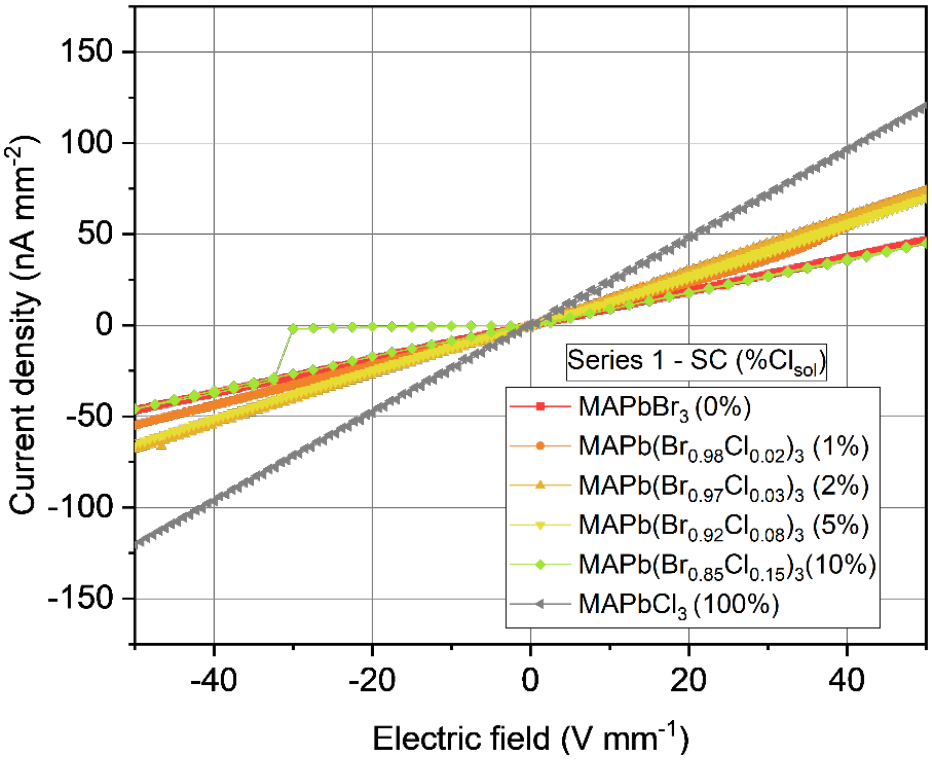

Figure A 3-5-1. J-V sweeps performed for series 1 of $MAPb(Br_{1-x}Cl_x)_3$ SC devices forward from 0 to -50 V mm^{-1}, then from -50 to +50 V mm^{-1}, and back to 0 V mm^{-1}.

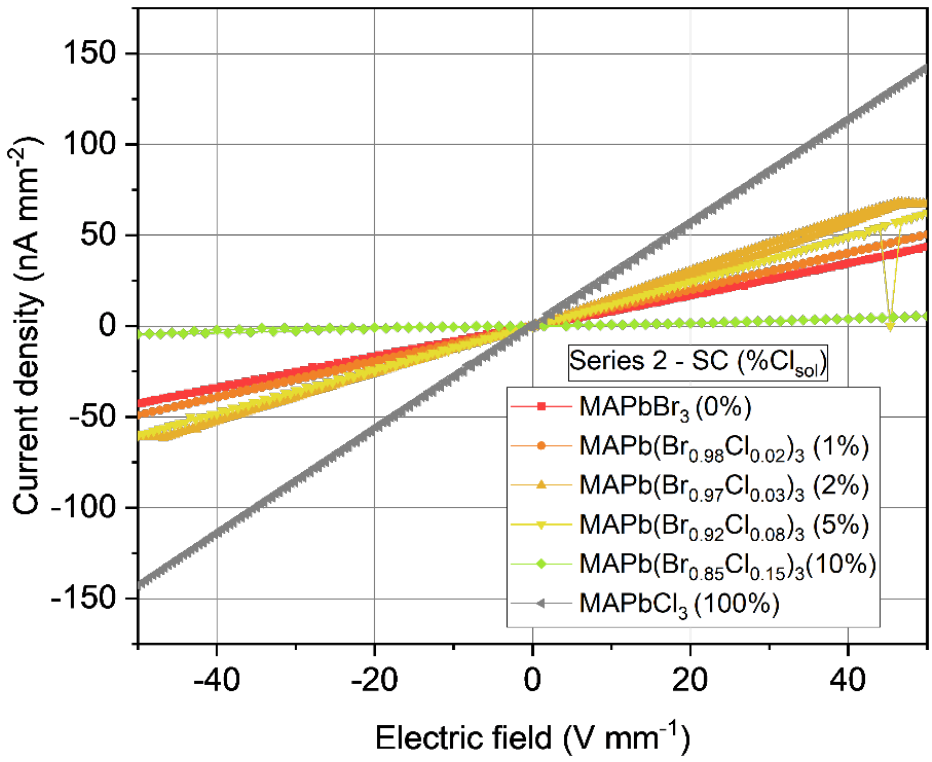

Figure A 3-5-2. J-V sweeps performed for series 2 of $MAPb(Br_{1-x}Cl_x)_3$ SC devices forward from 0 to -50 V mm^{-1}, then from -50 to +50 V mm^{-1}, and back to 0 V mm^{-1}.

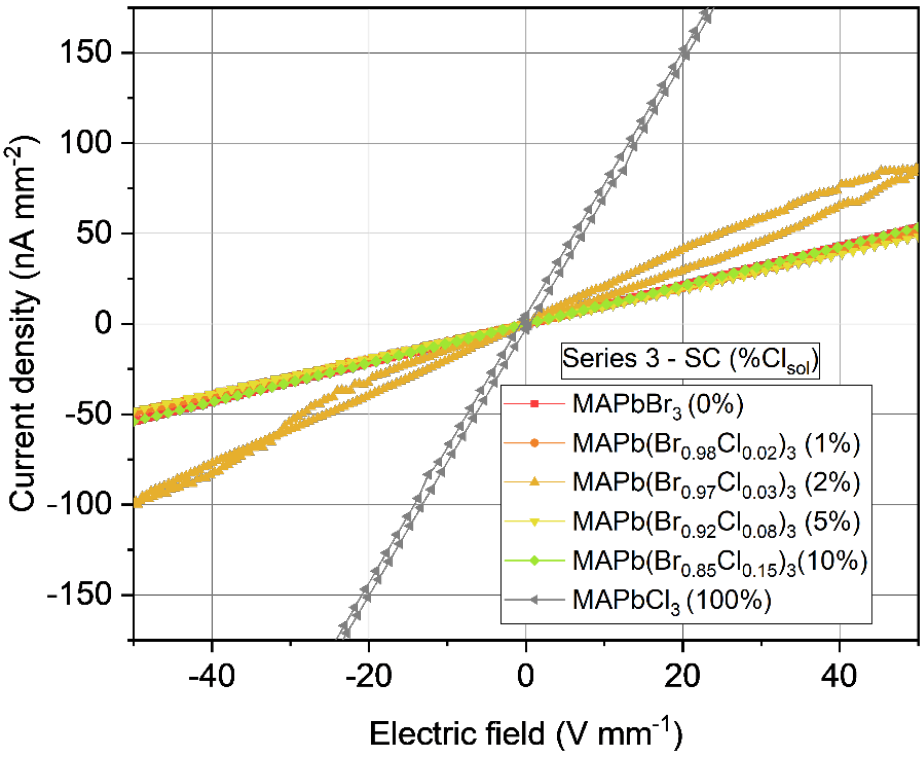

Figure A 3-5-3. J-V sweeps performed for series 3 of $MAPb(Br_{1-x}Cl_x)_3$ SC devices forward from 0 to -50 V mm^{-1}, then from -50 to +50 V mm^{-1}, and back to 0 V mm^{-1}.

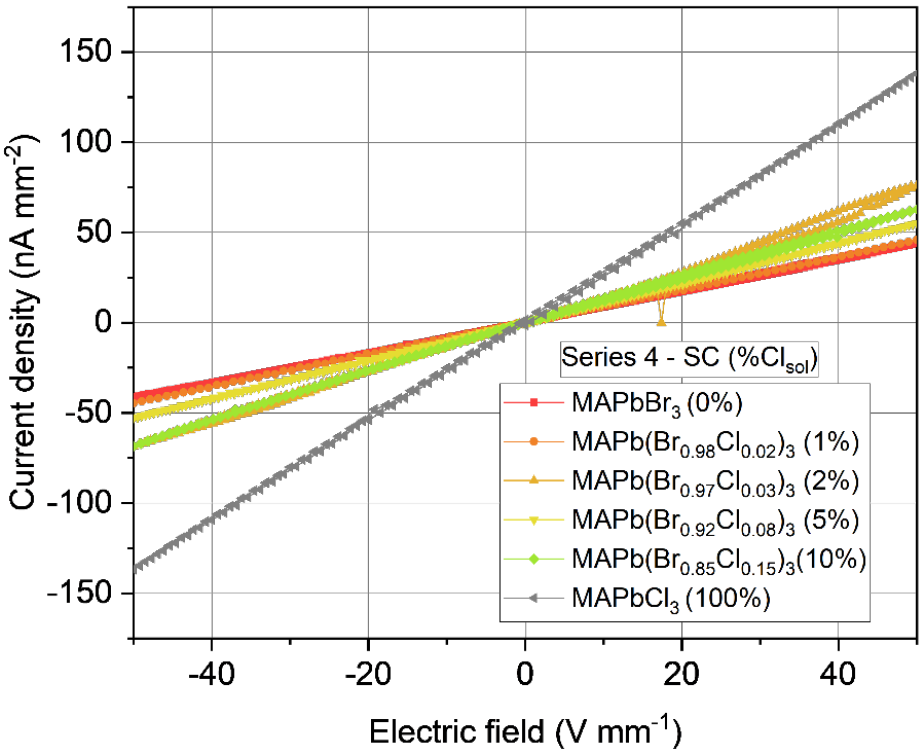

Figure A 3- 5-4. J-V sweeps performed for series 4 of $MAPb(Br_{1-x}Cl_x)_3$ SC devices forward from 0 to -50 V mm^{-1}, then from -50 to +50 V mm^{-1}, and back to 0 V mm^{-1}.

6 Sensitivity measurements

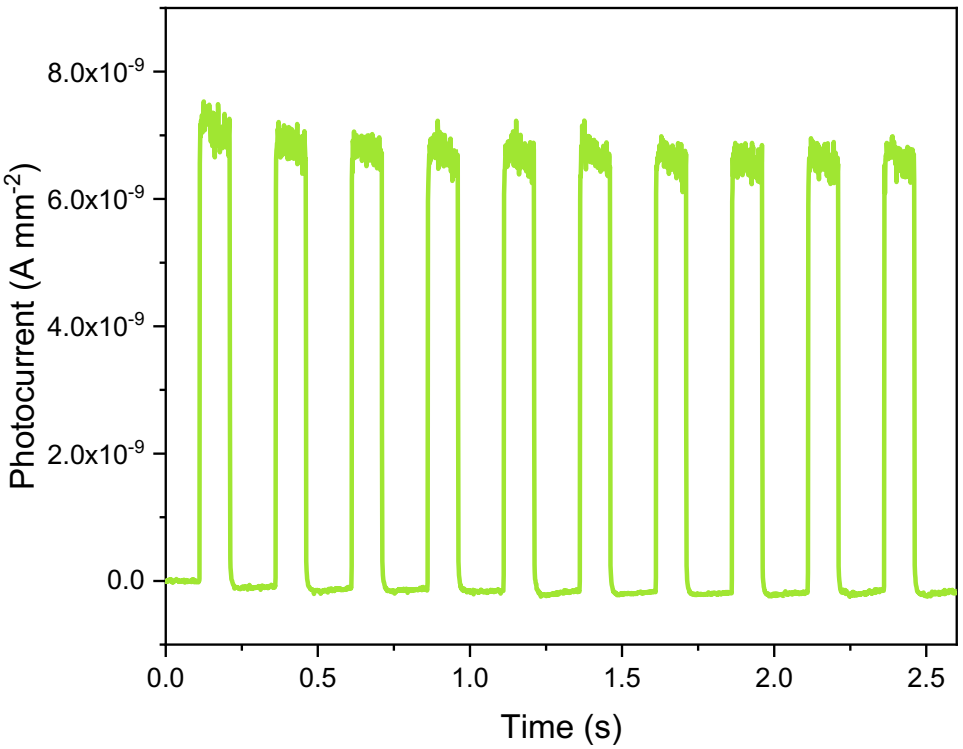

Figure A 3-6-1. Photocurrent generated under pulsed X-ray irradiation during 100 ms at 4 Hz on $MAPb(Br_{0.85}Cl_{0.15})_3$ SC device for sensitivity measurements.

Table A 3- 6-1. $MAPb(Br_{1-x}Cl_x)_3$ SC devices $\mu\tau$ product values for electrons and holes extracted from two-charge carriers Hecht fitting

Material [a]	Series 1		Series 2		Series 3		Series 4	
	$\mu_e\tau_e$ [$cm^2\ V^{-1}$]	$\mu_h\tau_h$ [$cm^2\ V^{-1}$]	$\mu_e\tau_e$ [$cm^2\ V^{-1}$]	$\mu_h\tau_h$ [$cm^2\ V^{-1}$]	$\mu_e\tau_e$ [$cm^2\ V^{-1}$]	$\mu_h\tau_h$ [$cm^2\ V^{-1}$]	$\mu_e\tau_e$ [$cm^2\ V^{-1}$]	$\mu_h\tau_h$ [$cm^2\ V^{-1}$]
$MAPbBr_3$	9×10^{-9}	1×10^{-4}	9×10^{-7}	4×10^{-5}	9×10^{-7}	1×10^{-4}	1×10^{-6}	2×10^{-4}
$MAPb(Br_{0.98}Cl_{0.02})_3$	5×10^{-5}	6×10^{-5}	9×10^{-7}	5×10^{-5}	9×10^{-8}	4×10^{-5}	6×10^{-7}	3×10^{-5}
$MAPb(Br_{0.97}Cl_{0.03})_3$	1×10^{-4}	6×10^{-5}	6×10^{-9}	2×10^{-4}	2×10^{-5}	1×10^{-4}	3×10^{-6}	1.5×10^{-4}
$MAPb(Br_{0.92}Cl_{0.08})_3$	8×10^{-6}	7×10^{-5}	8×10^{-5}	7×10^{-4}	5×10^{-5}	3×10^{-5}	1×10^{-7}	6×10^{-5}
$MAPb(Br_{0.85}Cl_{0.15})_3$	9×10^{-7}	3×10^{-5}	-	-	1×10^{-4}	5×10^{-5}	2.5×10^{-4}	8×10^{-4}
$MAPbCl_3$	9×10^{-7}	4×10^{-5}	-	-	-	-	9×10^{-8}	2×10^{-5}

[a] The x values given in the above chemical formulae is given by $\%Cl_{cryst}$, determined using Vegard's law (VL) and the XRD data.

References

(1) Green, D. W.; Perry, R. H. *Perry's Chemical Engineers' Handbook, Eighth Edition*; McGraw-Hill Education, 2008.

(2) Amari, S.; Verilhac, J.-M.; Gros D'Aillon, E.; Ibanez, A.; Zaccaro, J. Optimization of the Growth Conditions for High Quality $CH_3NH_3PbBr_3$ Hybrid Perovskite Single Crystals. *Crystal Growth & Design* **2020**, *20* (3), 1665–1672. https://doi.org/10.1021/acs.cgd.9b01429.

(3) Rodríguez-Carvajal, J. Introduction to the Program FullProf. **2003**, 24.

Appendix – Chapter 4

Table of contents

Appendix – Chapter 4

Appendix – Chapter 4

Influence of crystal growth environment and testing atmosphere

1 GDMS

Table A 4-1-1. Complete GDMS analytical results on $MAPbBr_3$ SCs grown from both ambient (AC) and inert (IC) conditions. Two samples per conditions were used. (1st part)

Element	AC SC #1 [ppm wt.]	AC SC #2 [ppm wt.]	IC SC #1 [ppm wt.]	IC SC #2 [ppm wt.]
Li	< 0.01	< 0.01	< 0.01	< 0.01
Be	< 0.01	< 0.01	< 0.01	< 0.01
B	< 0.01	0.03	< 0.01	< 0.01
C	Matrix	Matrix	Matrix	Matrix
N	Matrix	Matrix	Matrix	Matrix
O	-	-	-	-
F	< 0.5	< 0.5	< 0.5	< 0.5
Na	0.43	0.37	< 0.1	0.52
Mg	< 0.05	< 0.05	< 0.05	< 0.05
Al	0.43	0.43	0.09	0.09
Si	0.10	0.16	0.11	0.11
P	0.19	1.0	0.08	0.74
S	< 0.05	0.06	< 0.05	0.10
Cl	52	27	10	3.5
K	0.13	1.7	< 0.1	2.7
Ca	< 0.5	< 0.5	< 0.5	< 0.5
Sc	< 0.005	< 0.005	< 0.005	< 0.005
Ti	< 0.01	< 0.01	< 0.01	< 0.01

Appendix – Chapter 4

Table A 4-1-2. Complete GDMS analytical results on $MAPbBr_3$ SCs grown from both ambient (AC) and inert (IC) conditions. Two samples per conditions were used. (2^{nd} part)

Element	AC SC #1 [ppm wt.]	AC SC #2 [ppm wt.]	IC SC #1 [ppm wt.]	IC SC #2 [ppm wt.]
V	< 0.01	< 0.01	< 0.01	< 0.01
Cr	< 0.3	< 0.3	< 0.3	< 0.3
Mn	< 0.05	< 0.05	< 0.05	< 0.05
Fe	< 0.1	< 0.1	< 0.1	< 0.1
Co	< 0.01	< 0.01	< 0.01	< 0.01
Ni	< 0.05	< 0.05	< 0.05	< 0.05
Cu	< 0.05	< 0.05	< 0.05	< 0.05
Zn	< 0.1	< 0.1	< 0.1	< 0.1
Ga	< 0.5	< 0.5	< 0.5	< 0.5
Ge	< 0.5	< 0.5	< 0.5	< 0.5
As	< 0.5	< 0.5	< 0.5	< 0.5
Se	< 5	< 5	< 5	< 5
Br	Matrix	Matrix	Matrix	Matrix
Rb	< 0.5	< 0.5	< 0.5	< 0.5
Sr	< 0.05	< 0.05	< 0.05	< 0.05
Y	< 0.005	< 0.005	< 0.005	< 0.005
Zr	< 0.05	< 0.05	< 0.05	< 0.05
Nb	< 5	< 5	< 5	< 5
Mo	< 5	< 5	< 5	< 5
Ru	< 0.1	< 0.1	< 0.1	< 0.1
Pd	< 0.1	< 0.1	< 0.1	< 0.1
Ag	< 0.5	< 0.5	< 0.5	< 0.5
Cd	< 0.5	< 0.5	< 0.5	< 0.5
In	< 0.5	< 0.5	< 0.5	< 0.5
Sn	< 0.5	< 0.5	< 0.5	< 0.5
Sb	< 0.5	< 0.5	< 0.5	< 0.5
Te	< 0.5	< 0.5	< 0.5	< 0.5
I	< 0.5	< 0.5	< 0.5	< 0.5

Table A 4-1-3. Complete GDMS analytical results on $MAPbBr_3$ SCs grown from both ambient (AC) and inert (IC) conditions. Two samples per conditions were used. (3^{rd} part)

Element	AC SC #1 [ppm wt.]	AC SC #2 [ppm wt.]	IC SC #1 [ppm wt.]	IC SC #2 [ppm wt.]
Cs	< 0.5	< 0.5	< 0.5	< 0.5
Ba	< 0.5	< 0.5	< 0.5	< 0.5
La	< 0.05	< 0.05	< 0.05	< 0.05
Ce	< 0.05	< 0.05	< 0.05	< 0.05
Pr	< 0.05	< 0.05	< 0.05	< 0.05
Nd	< 0.05	< 0.05	< 0.05	< 0.05
Sm	< 0.05	< 0.05	< 0.05	< 0.05
Eu	< 0.05	< 0.05	< 0.05	< 0.05
Gd	< 0.05	< 0.05	< 0.05	< 0.05
Tb	< 0.05	< 0.05	< 0.05	< 0.05
Dy	< 0.05	< 0.05	< 0.05	< 0.05
Ho	< 0.05	< 0.05	< 0.05	< 0.05
Er	< 0.05	< 0.05	< 0.05	< 0.05
Tm	< 0.05	< 0.05	< 0.05	< 0.05
Yb	< 0.05	< 0.05	< 0.05	< 0.05
Lu	< 0.05	< 0.05	< 0.05	< 0.05
Hf	< 0.5	< 0.5	< 0.5	< 0.5
Ta	Binder	Binder	Binder	Binder
W	< 1	< 1	< 1	< 1
Re	< 0.1	< 0.1	< 0.1	< 0.1
Os	< 0.05	< 0.05	< 0.05	< 0.05
Ir	< 0.05	< 0.05	< 0.05	< 0.05
Pt	< 5	< 5	< 5	< 5
Au	Interference	Interference	Interference	Interference
Hg	< 0.5	< 0.5	< 0.5	< 0.5
Tl	< 0.5	< 0.5	< 0.5	< 0.5
Pb	Matrix	Matrix	Matrix	Matrix
Bi	< 5	< 5	< 5	< 5

Table A 4-1-4. Complete GDMS analytical results on $MAPbBr_3$ SCs grown from both ambient (AC) and inert (IC) conditions. Two samples per conditions were used. (4^{th} part)

Element	AC SC #1 [ppm wt.]	AC SC #2 [ppm wt.]	IC SC #1 [ppm wt.]	IC SC #2 [ppm wt.]
Th	< 0.05	< 0.05	< 0.05	< 0.05
U	< 0.05	< 0.05	< 0.05	< 0.05

2 ATR-FTIR

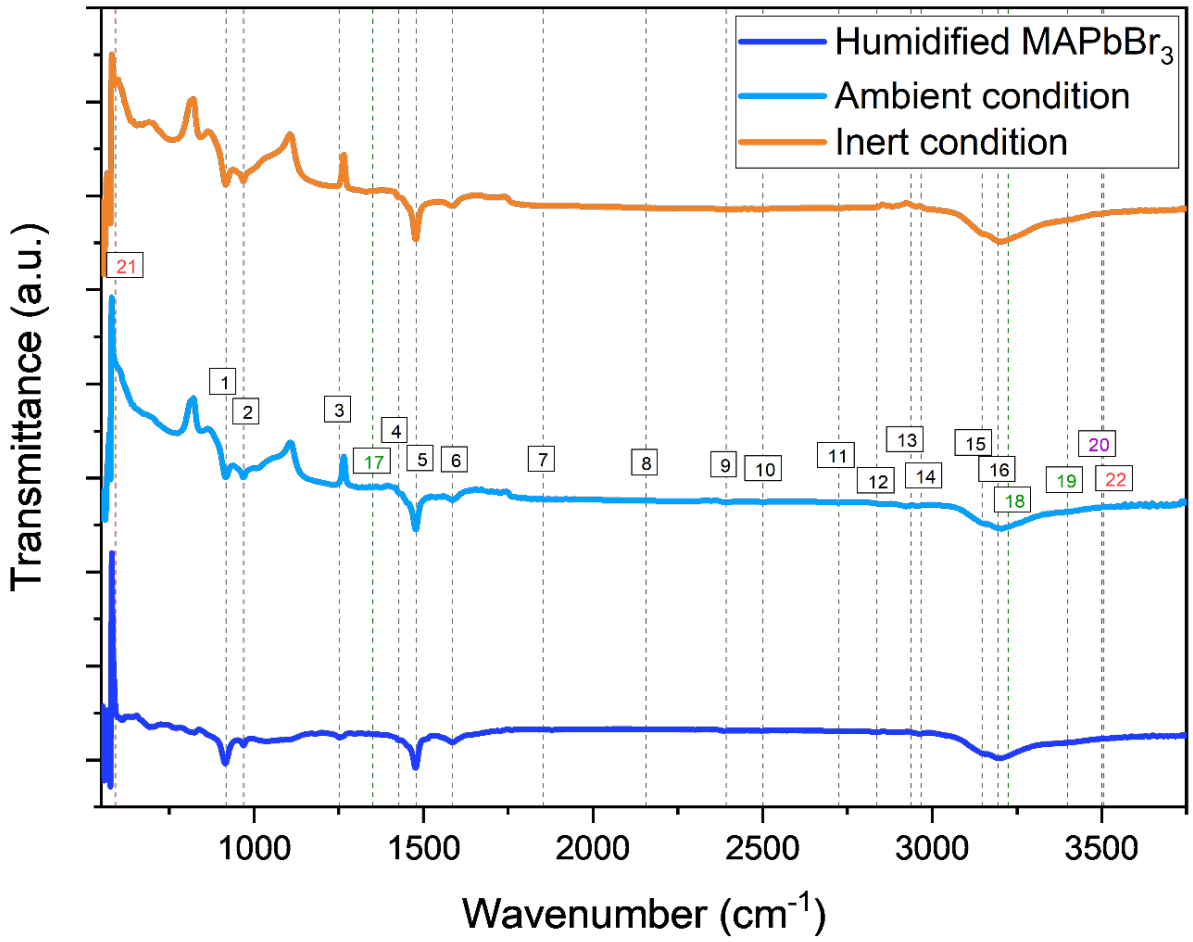

Figure A 4-2-1. ATR-FTIR transmittance data for evaluation of vibrational modes related to water presence in ground SCs grown from both growth conditions and humidified $MAPbBr_3$. Spectrum goes from 550 to 3750 cm^{-1}. For index description refer to **Table A 4-2-1** and **Table A 4-2-2**.

Table A 4-2-1. Complete assignment of the different peaks measured in ATR-FTIR based on the literature. Below are the wavenumbers of vibrational modes, corresponding to those identified in various studies for similar materials or potentially present chemical species. (1st part)

Index	Wavenumber [cm^{-1}]	Peak assignment	Material studied
1	917	CH_3-NH_3^+ rock υ_{12}	$MAPbBr_3$ SC/PC [a) 1]
2	969	C-N stretch υ_5	$MAPbBr_3$ SC/PC [1]
3	1252	CH_3-NH_3^+ rock υ_{11}	$MAPbBr_3$ SC/PC [1]
4	1427	Asym. CH_3 bend, υ_{10}	$MAPbBr_3$ SC/PC [1]
5	1477	Sym. NH_3^+ bend υ_3	$MAPbBr_3$ SC/PC [1]
6	1585	Asym. NH_3^+ bend υ_9	$MAPbBr_3$ SC/PC [1]
7	1852	$\upsilon_5 + \upsilon_{12}$	$MAPbBr_3$ SC/PC [1]
8	2156	$\upsilon_{11} + \upsilon_{12}$	$MAPbBr_3$ SC/PC [1]
9	2392	$\upsilon_5 + \upsilon_{10}$	$MAPbBr_3$ SC/PC [1]
10	2501	$2 \times \upsilon_{11}$	$MAPbBr_3$ SC/PC [1]
11	2724	$\upsilon_3 + \upsilon_{11}$	$MAPbBr_3$ SC/PC [1]
12	2836	$\upsilon_9 + \upsilon_{11}$	$MAPbBr_3$ SC/PC [1]
13	2937	Sym. CH_3 stretch υ_2	$MAPbBr_3$ SC/PC [1]
14	2966	Asym. CH_3 stretch υ_8	$MAPbBr_3$ SC/PC [1]
15	3148	Sym. NH_3 stretch υ_1	$MAPbBr_3$ SC/PC [1]
16	3194	Asym. NH_3 stretch υ_7	$MAPbBr_3$ SC/PC [1]

[a)] PC = polycrystal (thin film).

Table A 4-2-2. Complete assignment of the different peaks measured in ATR-FTIR based on the literature. Below are the wavenumbers of vibrational modes, corresponding to those identified in various studies for similar materials or potentially present chemical species. (2nd part)

Index	Wavenumber [cm^{-1}]	Peak assignment	Material studied
17	1350	C-OH in-plane bend	$MAPb(I_{1-x}Br_x)_3$ PC [a) 2]
18	3225	Intercalated H_2O	$MAPb(I_{1-x}Br_x)_3$ PC [2]
19	3400	υ(OH) modes of C-OH	$MAPb(I_{1-x}Br_x)_3$ PC [2]
20	~ 3500	O-H signature	$MAPbI_3$ PC [a) 3]
21	592	δ(OH)	PbOHBr [b) 4]
22	3505	υ(OH)	PbOHBr [4]

a) PC = polycrystal (thin film).
b) PbOHBr is synthesised in an aqueous solution containing KBr and lead (II) acetate.

3 XPS

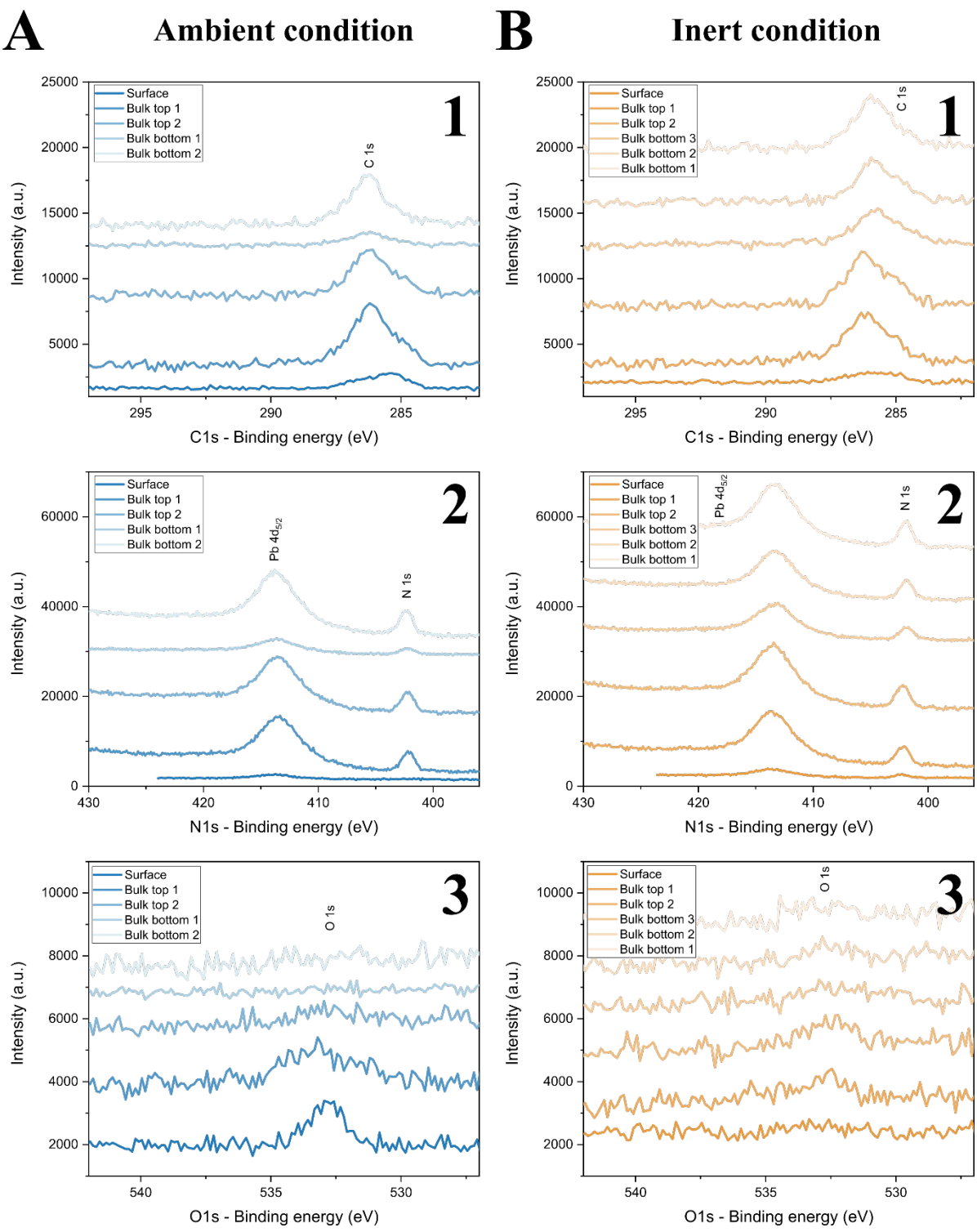

Figure A 4-3-1. XPS spectra of light organic elements for both **(A)** ambient and **(B)** inert crystal growth conditions and for both SC surface and bulk analysis: **(1)** C 1s, **(2)** N 1s and **(3)** O 1s.

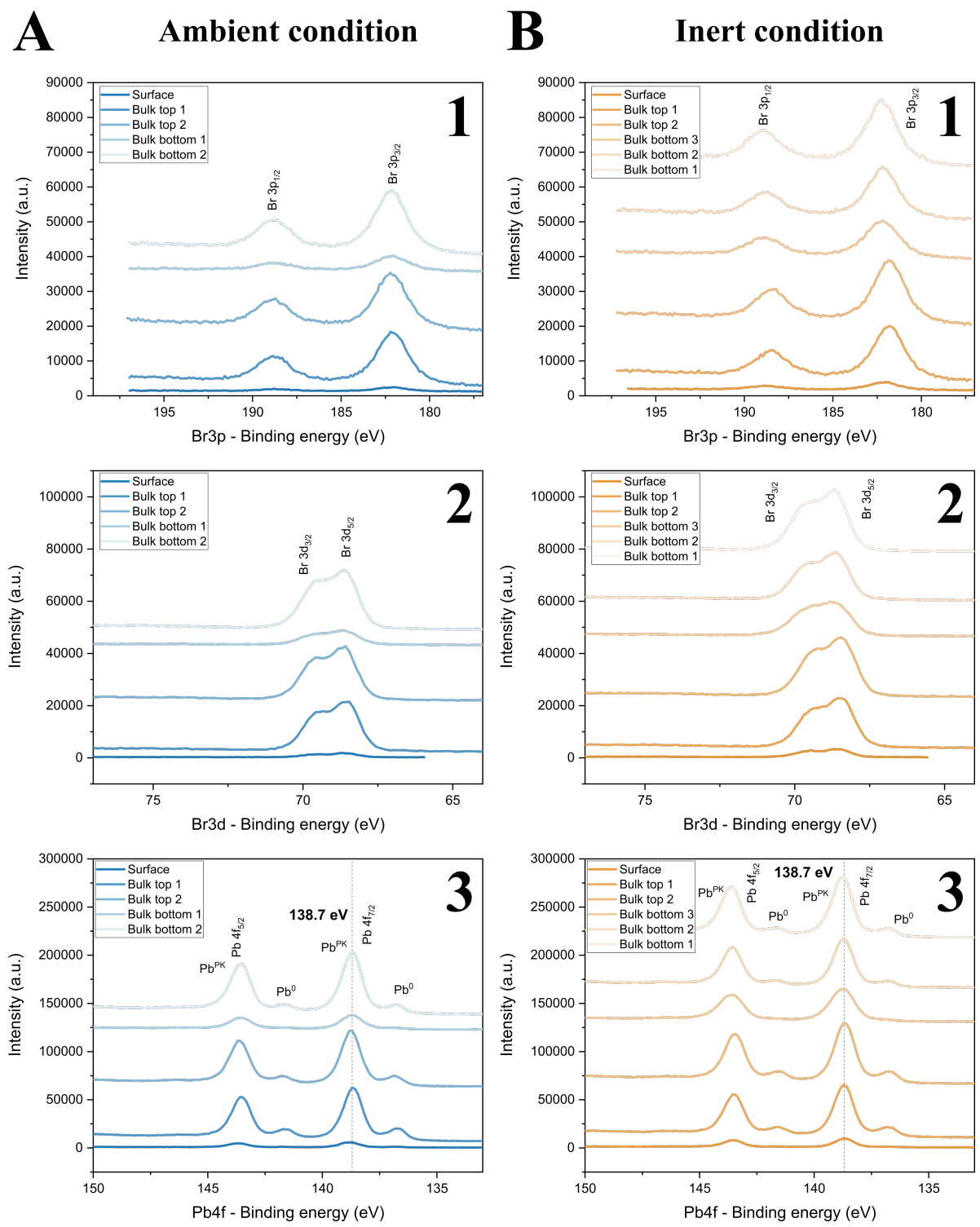

Figure A 4-3-2. XPS spectra of heavy inorganic elements for both **(A)** ambient and **(B)** inert crystal growth conditions and for both SC surface and bulk analysis: **(1)** Br 3p, **(2)** Br 3d and **(3)** Pb 4f.

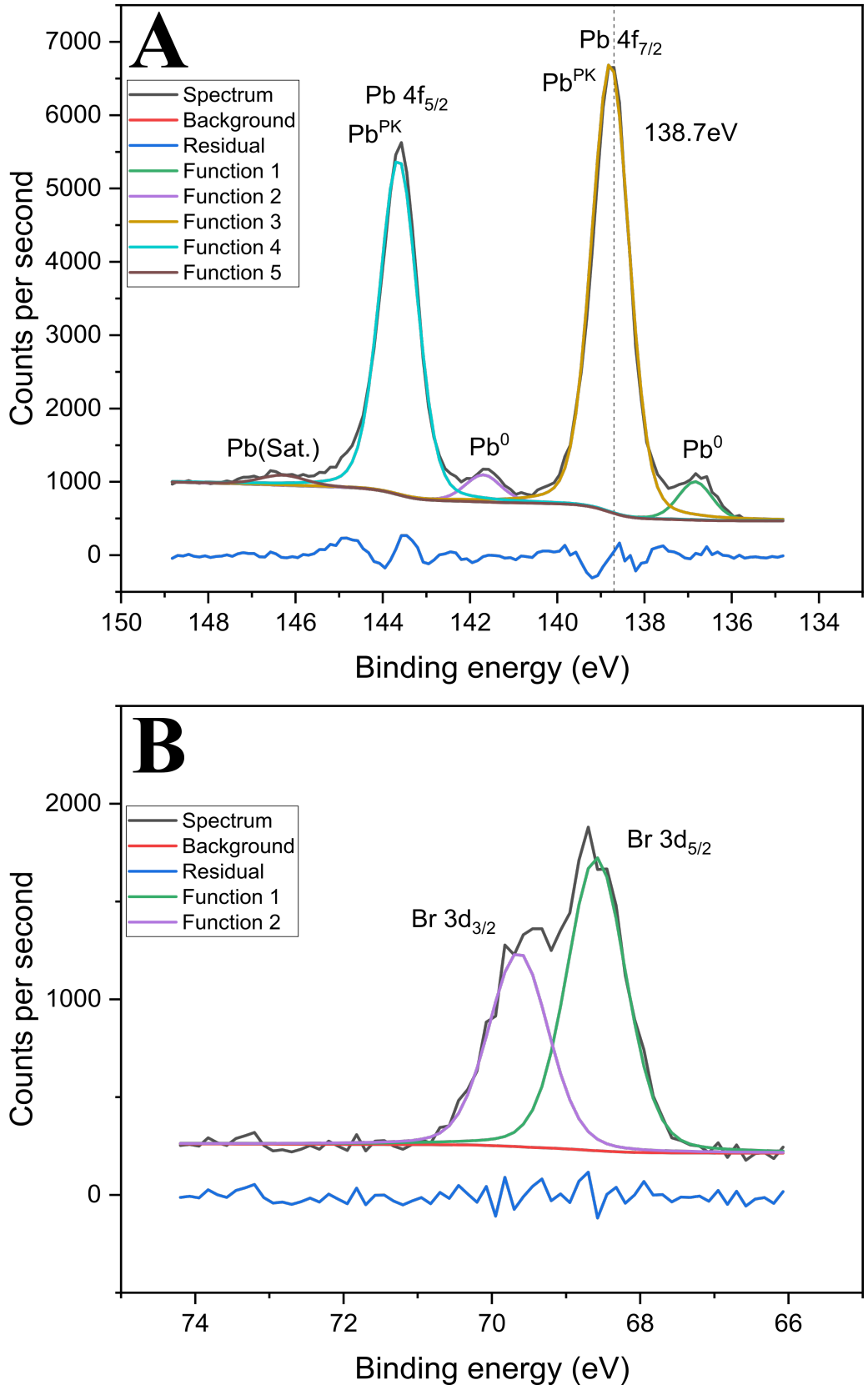

Figure A 4-3-3. XPS deconvolution examples for quantitative measurements of **(A)** Pb and **(B)** Br on $MAPbBr_3$ SCs. For Pb, $4f_{7/2}$ and associated $4f_{5/2}$ orbitals were deconvoluted for quantification of different Pb-species present on the surface: perovskite lead Pb^{PK}, metallic lead Pb^0, and unknown Pb satellite. For Br, $3d_{5/2}$ and associated $3d_{3/2}$ orbitals were deconvoluted for quantification.

4 TGA-MS

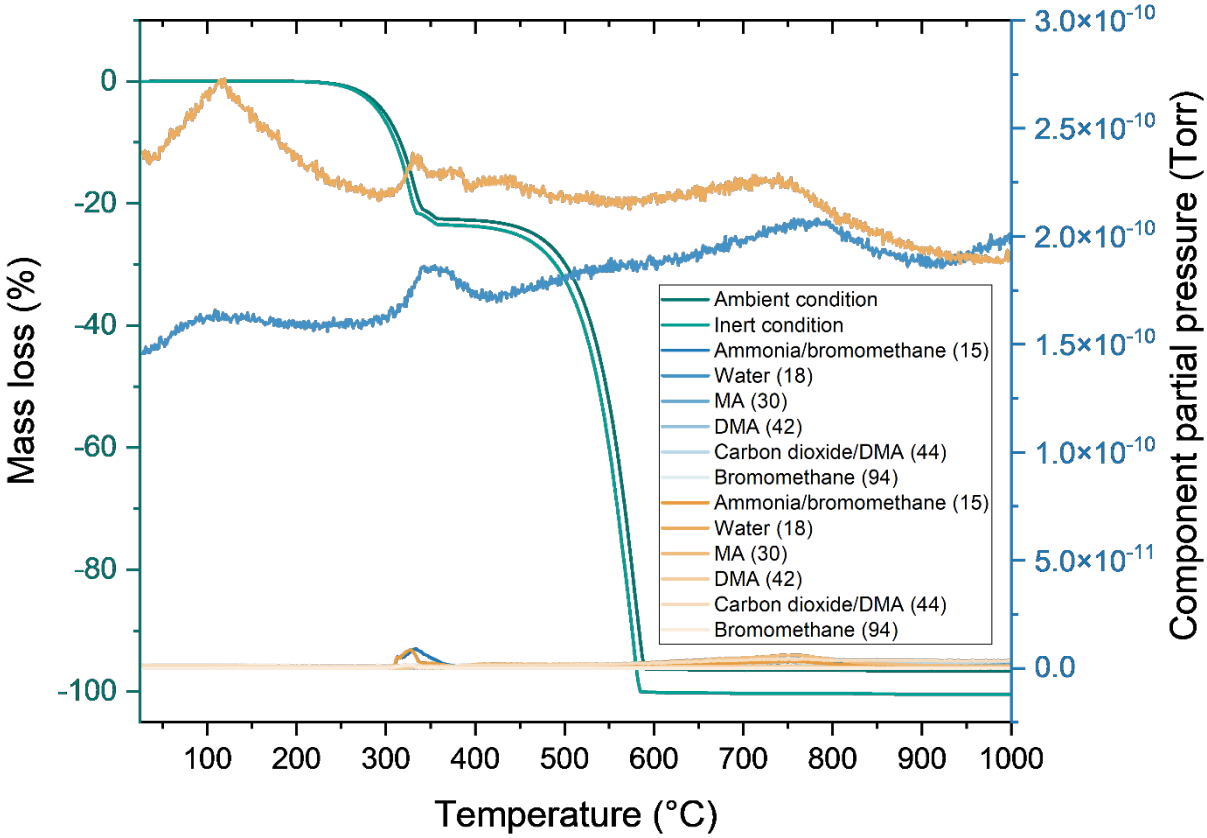

Figure A 4-4-1. Complete TGA-MS data showing principal mass losses and associated degradation products. Given the relative higher partial pressure for water, the rest of degradation compounds are barely visible. The plot highlights the water contents related to the experiments and not to $MAPbBr_3$ SCs.

5 Sensitivity and J-t measurements

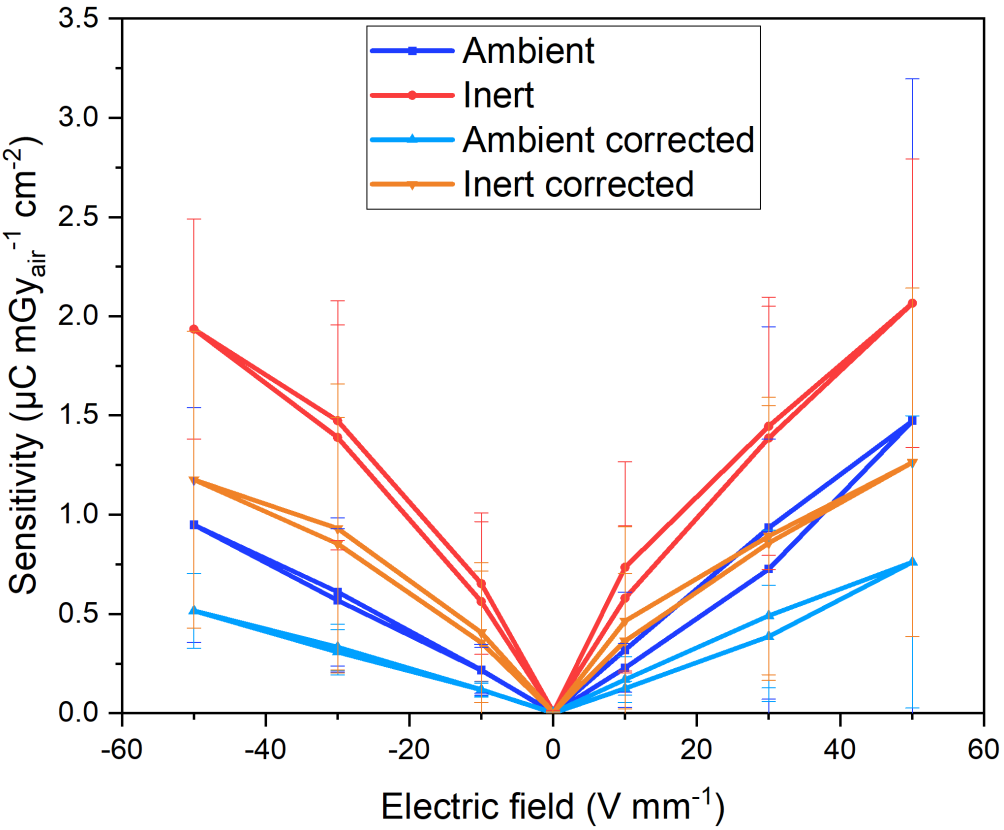

Figure A 4-5-1. Both uncorrected and corrected sensitivities as a function of the resulting electric field for both set of crystals in inert conditions. The plots above consider the 4 SC devices that were analysed in Ar atmosphere: 2 AC and 2 IC SC devices.

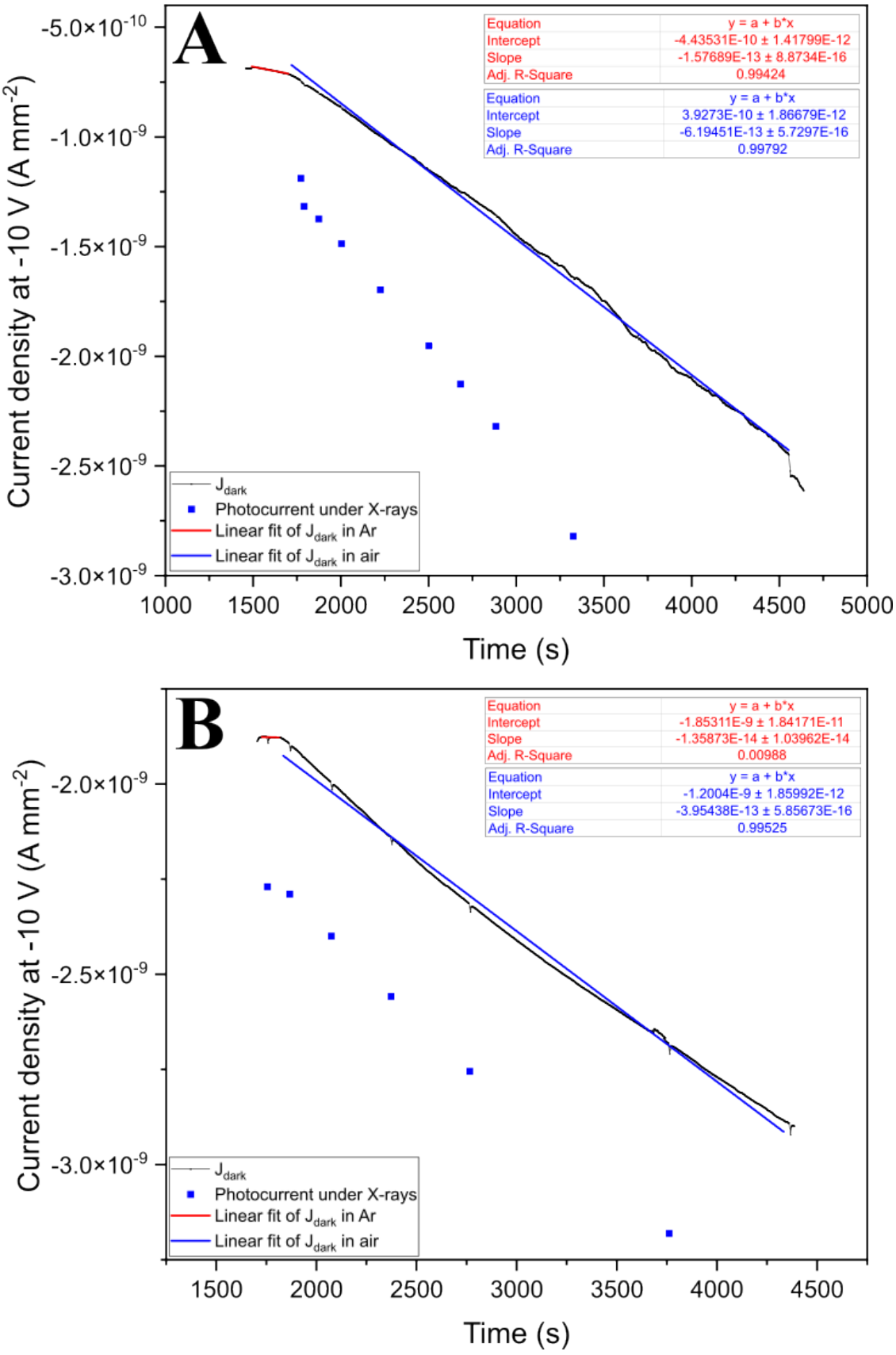

Figure A 4-5-2. AC SCs Ar-to-air transition J-t measurements. (A) AC SC **(1)** and **(B) (2)** J-t data, both at -10 V, with associated photocurrent under X-rays for sensitivity measurements (blue squares). Two linear fits are performed corresponding to the segments where the SC device is in Ar (red) and air (blue) atmospheres.

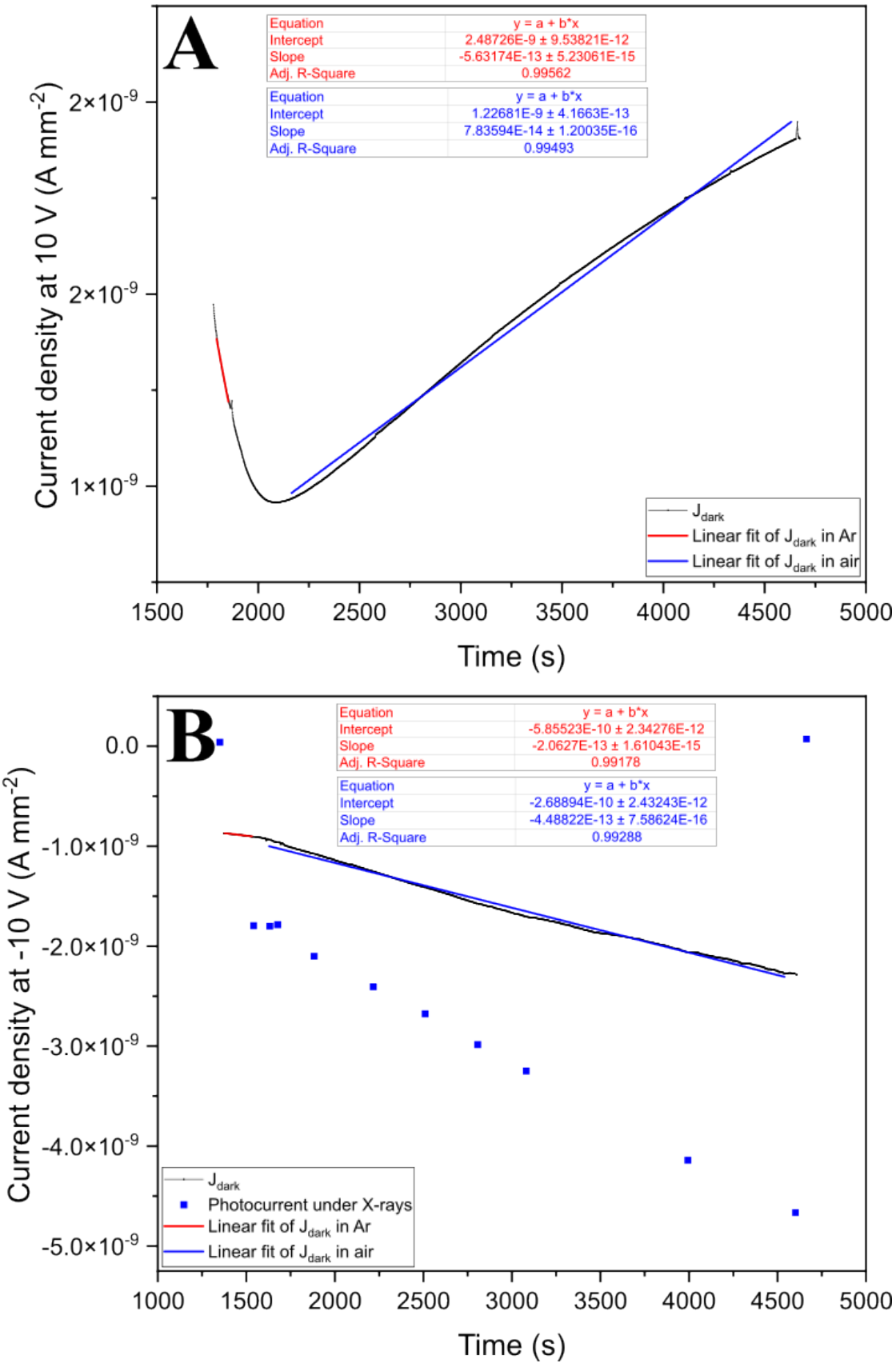

Figure A 4-5-3. IC SCs Ar-to-air transition J-t measurements. (A) IC SC **(1)** and **(B) (2)** J-t data at +10 V and -10 V, respectively, with associated photocurrent under X-rays for sensitivity measurements (blue squares). Two linear fits are performed corresponding to the segments where the SC device is in Ar (red) and air (blue) atmospheres.

References

(1) Glaser, T.; Müller, C.; Sendner, M.; Krekeler, C.; Semonin, O. E.; Hull, T. D.; Yaffe, O.; Owen, J. S.; Kowalsky, W.; Pucci, A.; Lovrinčić, R. Infrared Spectroscopic Study of Vibrational Modes in Methylammonium Lead Halide Perovskites. *J. Phys. Chem. Lett.* **2015**, *6* (15), 2913–2918. https://doi.org/10.1021/acs.jpclett.5b01309.

(2) Gan, Z.; Yu, Z.; Meng, M.; Xia, W.; Zhang, X. Hydration of Mixed Halide Perovskites Investigated by Fourier Transform Infrared Spectroscopy. *APL Materials* **2019**, *7* (3), 031107. https://doi.org/10.1063/1.5087914.

(3) Müller, C.; Glaser, T.; Plogmeyer, M.; Sendner, M.; Döring, S.; Bakulin, A. A.; Brzuska, C.; Scheer, R.; Pshenichnikov, M. S.; Kowalsky, W.; Pucci, A.; Lovrinčić, R. Water Infiltration in Methylammonium Lead Iodide Perovskite: Fast and Inconspicuous. *Chem. Mater.* **2015**, *27* (22), 7835–7841. https://doi.org/10.1021/acs.chemmater.5b03883.

(4) Ramamurthy, P.; Secco, E. A.; Badri, M. Studies on Metal Hydroxy Compounds. X. Thermal Analyses, Decomposition Kinetics, and Infrared Spectra of Lead Halide (Cl, Br, I) Derivatives. *Can. J. Chem.* **1970**, *48* (16), 2617–2622. https://doi.org/10.1139/v70-438.

Appendix – Chapter 5

Table of contents

Appendix – Chapter 5

Appendix – Chapter 5

Post-treatments: thermal annealing and chemical healing

1 Resistivity

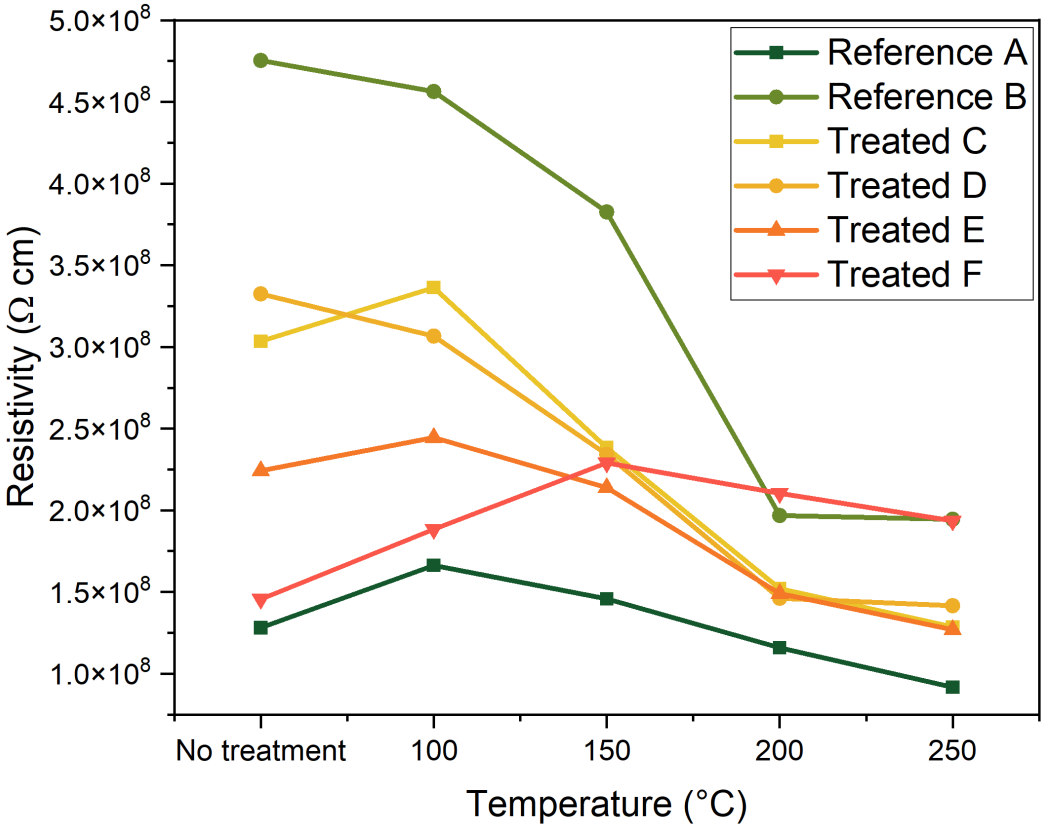

Figure A 5-1-1. Resistivity evolution as a function of the annealing temperature for both reference and treated samples.

2 S-V data

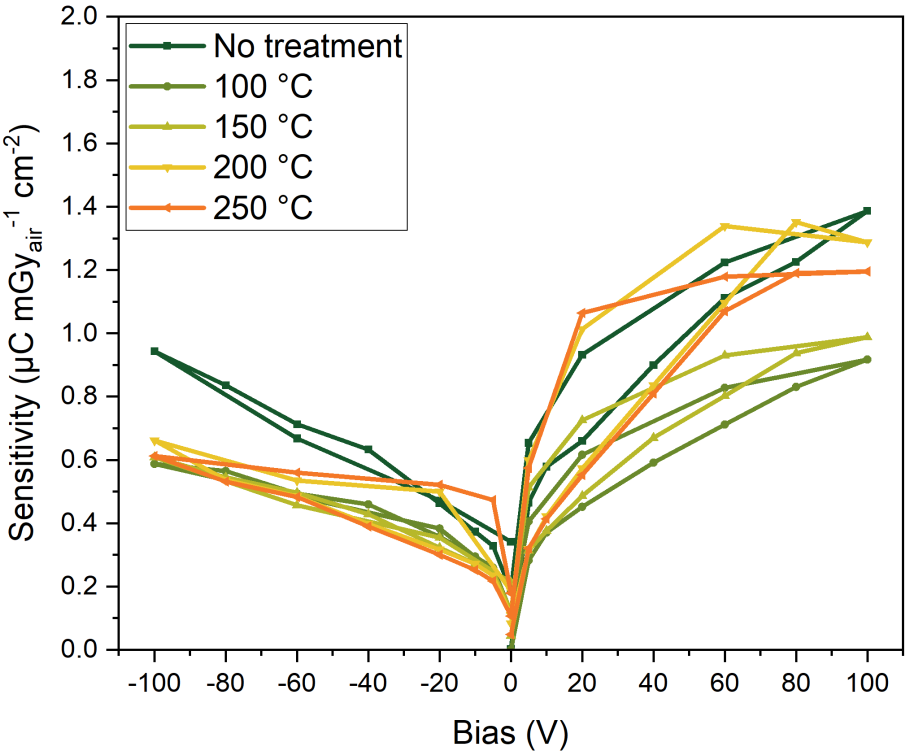

Figure A 5-2-1. Reference sample **(A)** S-V data evolution as a function of the annealing temperature. Reference samples were not annealed: legend used as comparative tool.

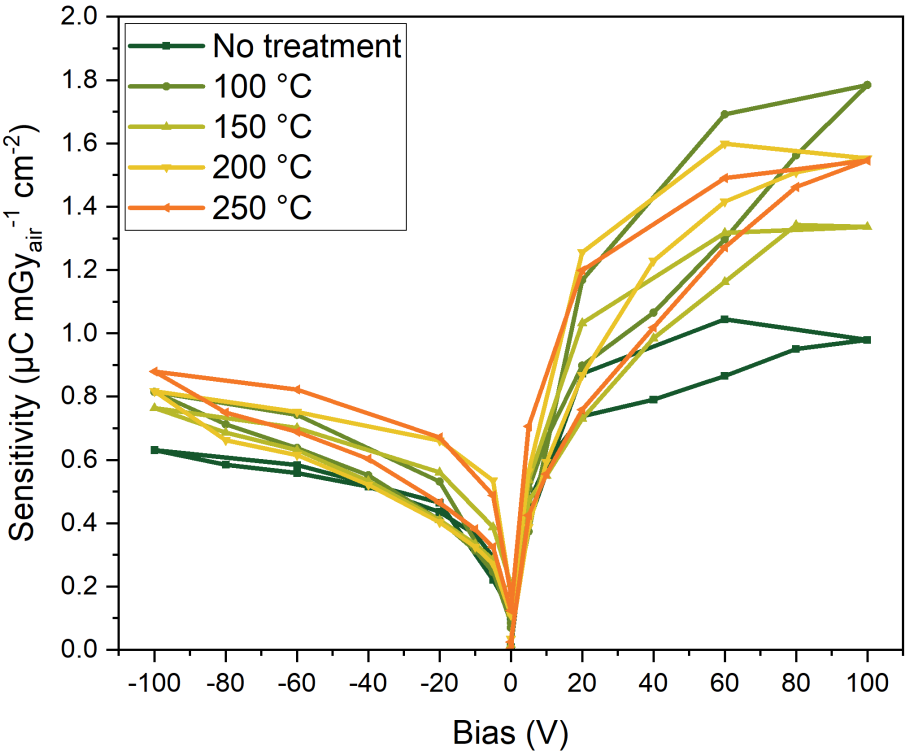

Figure A 5-2-2. Reference sample **(B)** S-V data evolution as a function of the annealing temperature. Reference samples were not annealed: legend used as comparative tool.

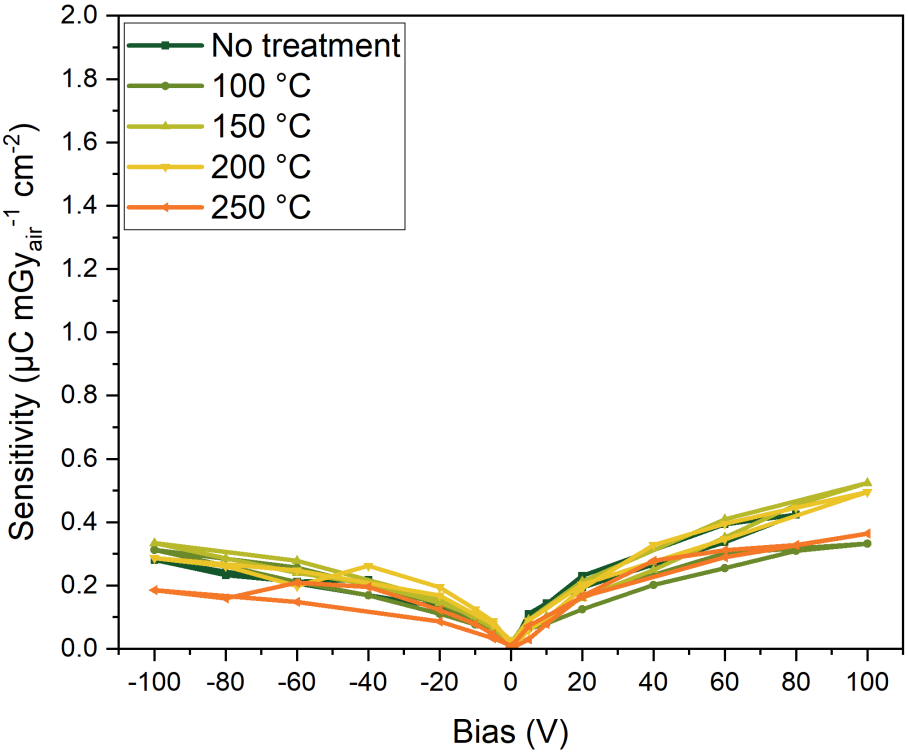

Figure A 5-2-3. Annealed sample **(C)** S-V data evolution as a function of the annealing temperature.

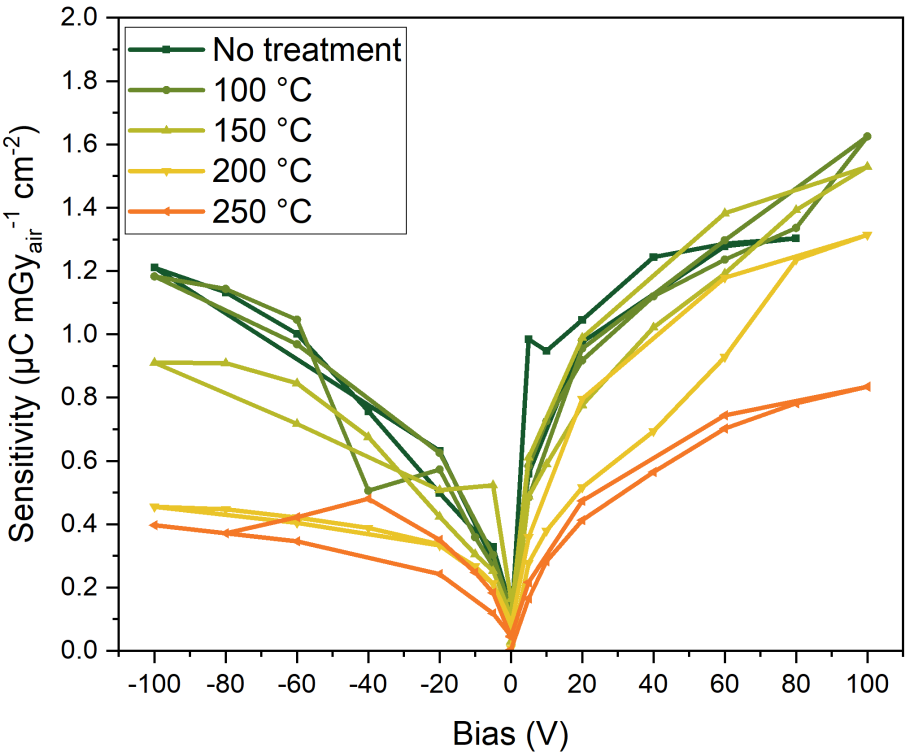

Figure A 5-2-4. Annealed sample **(D)** S-V data evolution as a function of the annealing temperature.

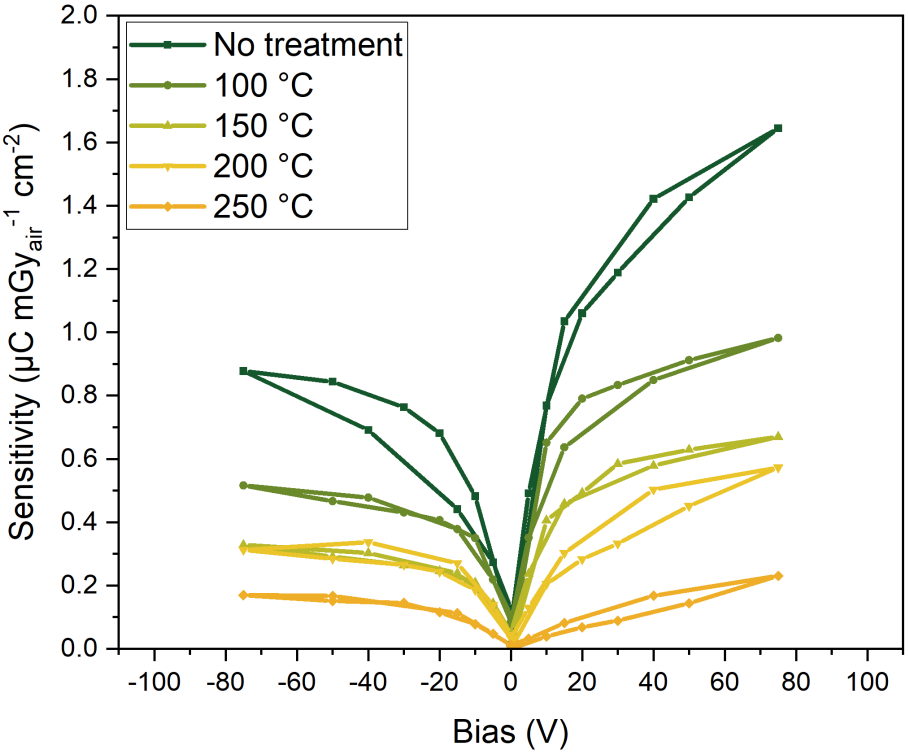

Figure A 5-2-5. Annealed sample **(E)** S-V data evolution as a function of the annealing temperature.

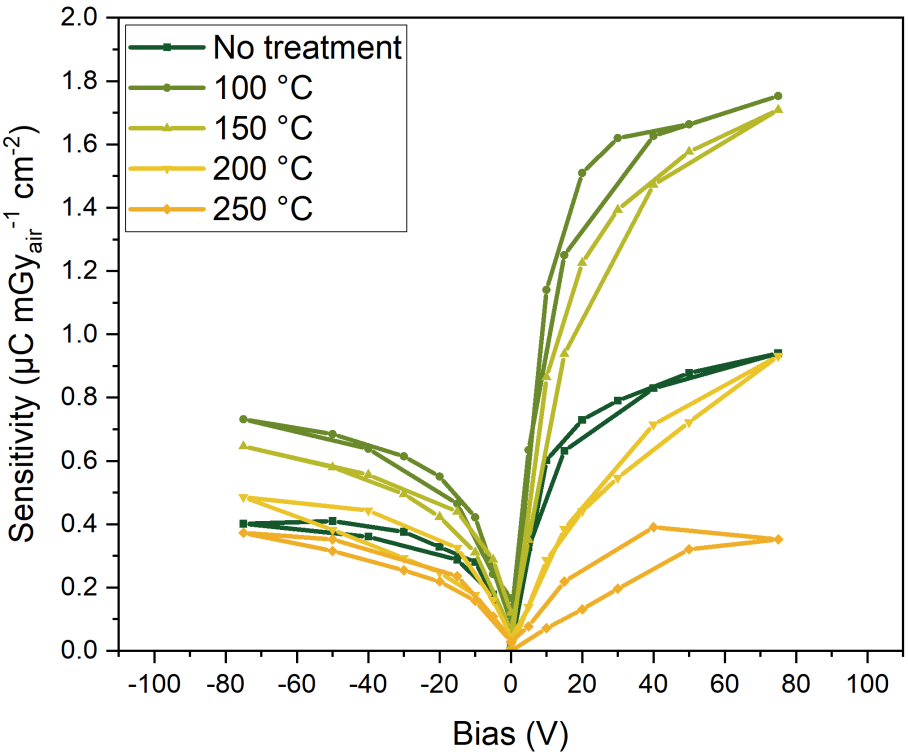

Figure A 5-2-6. Annealed sample **(F)** S-V data evolution as a function of the annealing temperature.

3 EDX

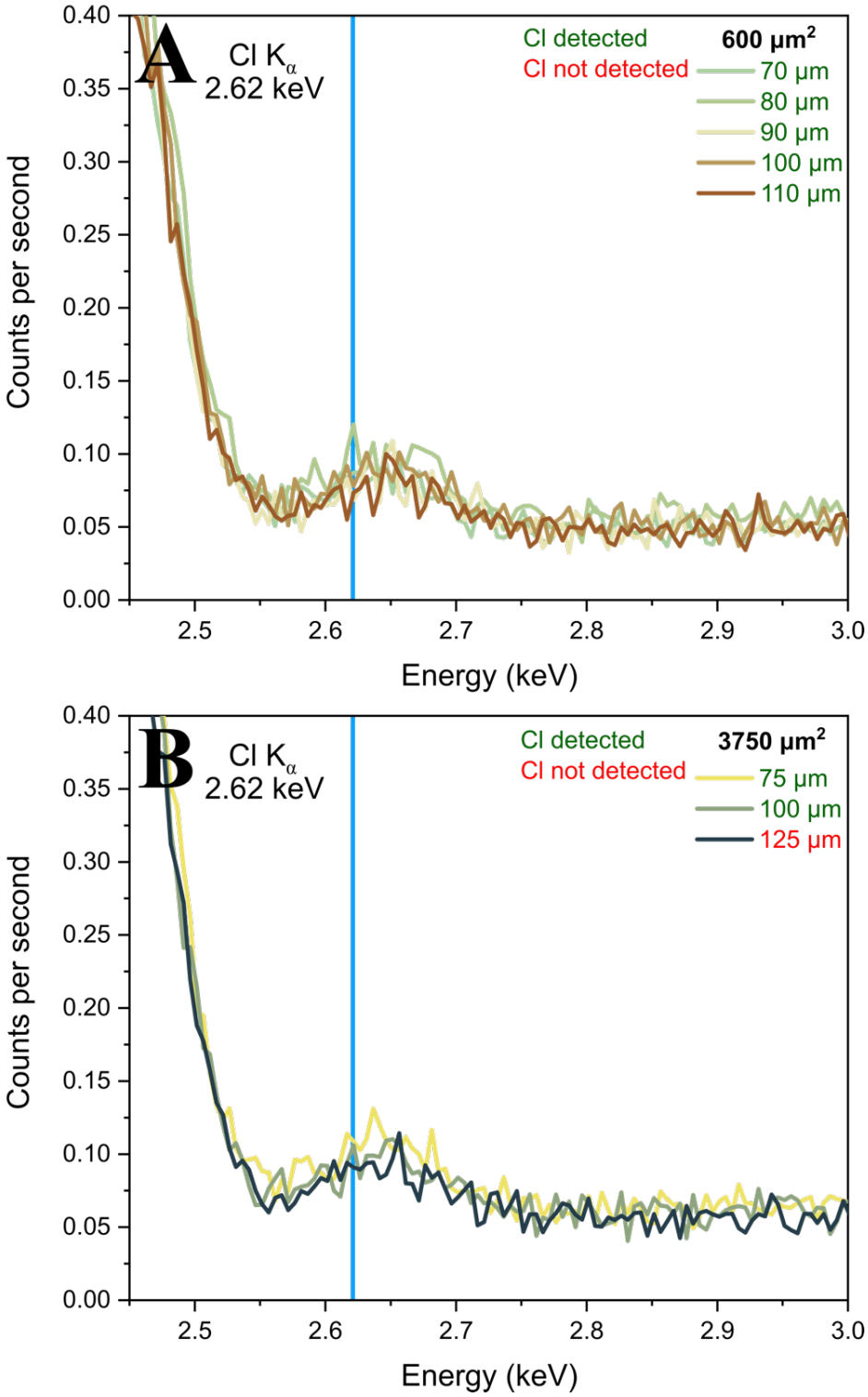

Figure A 5-3-1. Bottom region EDX spectra additional measurement windows for bare SC. (A) 600 µm^2 (60 µm × 10 µm) and **(B)** 3750 µm^2 (150 µm × 25 µm). The spectra are centred in the Cl K$_\alpha$ emission peak. In the legend, the header in black indicates the surface of the segment used for the measurements. Depth values come in two colours: green for when a Cl content was measured, and red for when it was not.

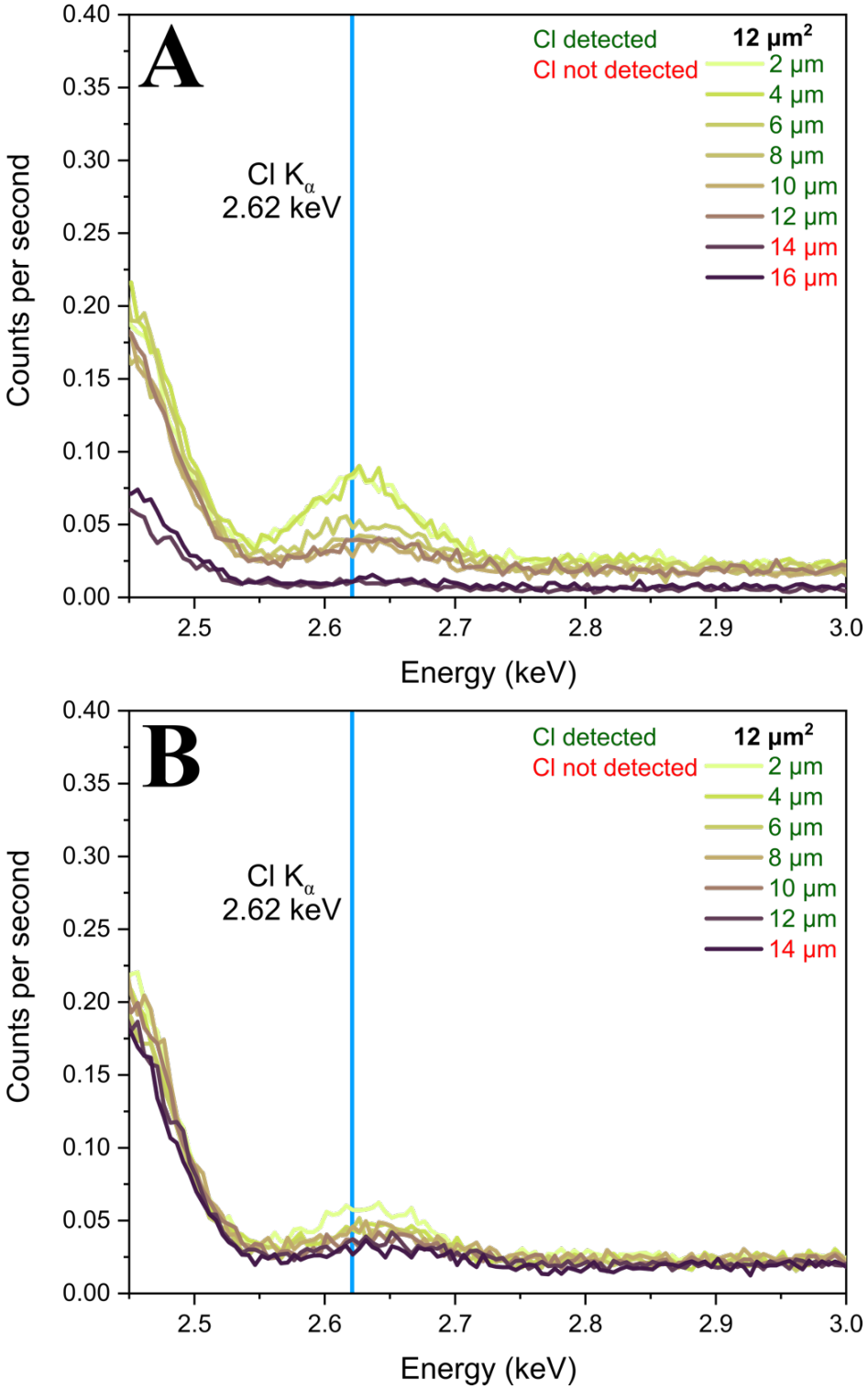

Figure A 5-3-2. Top region EDX spectra. Spectra for **(A)** bare SC and **(B)** SC with Cr electrodes. The spectra are centred in the Cl K_α emission peak. In the legend, the header in black indicates the surface of the segment used for the measurements. Depth values come in two colours: green for when a Cl content was measured, and red for when it was not.

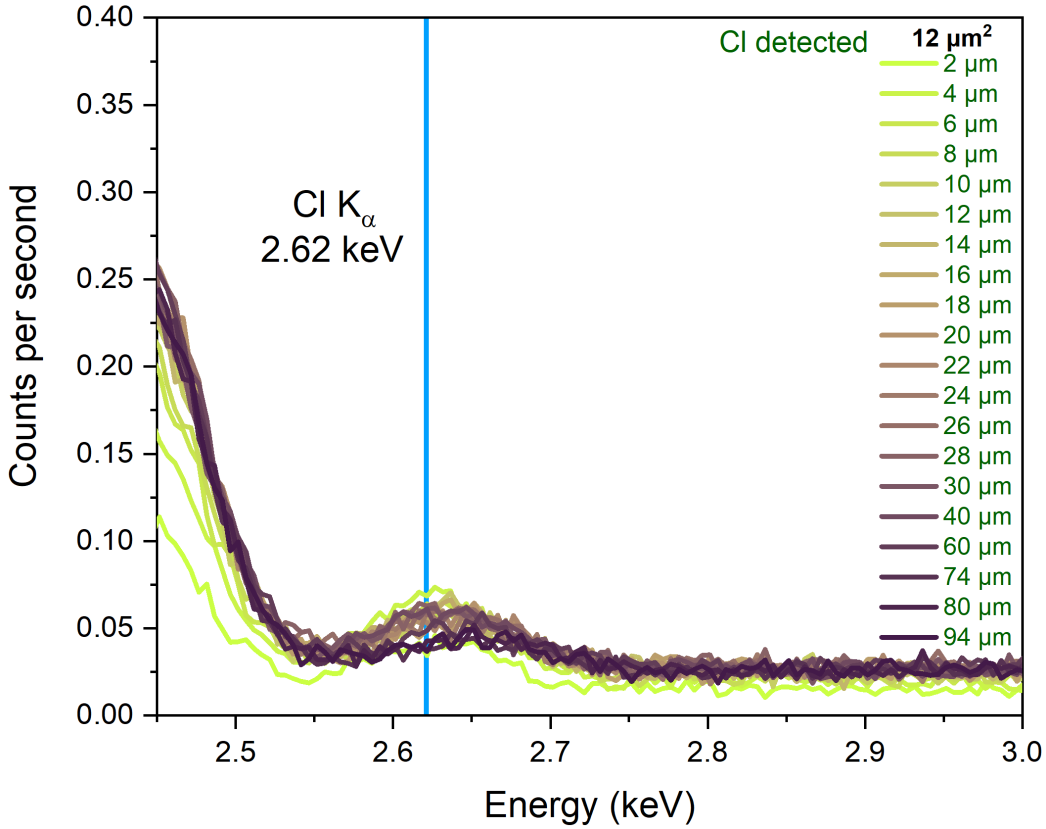

Figure A 5-3-3. EDX spectra for bare SC in the lateral region. The spectra are centred in the Cl K_α emission peak. In the legend, the header in black indicates the surface of the segment used for the measurements. Depth values come in two colours: green for when a Cl content was measured, and red for when it was not.

Abstract

Hybrid lead halide perovskites have been studied during the last decade for the detection of X-rays. In this work, $MAPbBr_3$ has been chosen as sensing material for X-ray detection for medical imaging. $MAPbBr_3$ shows good X-ray absorption, sufficient charge transport properties, and simple solution growth. $MAPbBr_3$ single crystals growth has been optimised. The optoelectronic evaluation exhibited good sensitivity but large dark current. Three approaches to improve the performance of $MAPbBr_3$ are exposed. Firstly, chlorine was added, leading to the improvement of charge carrier transport. Secondly, the importance of the growth atmosphere and the beneficial doping that atmospheric water can have on the surface are highlighted. Lastly, post-treatments healing point defects are introduced. The thesis emphasises the potential of $MAPbBr_3$ in medical X-ray imaging devices.

Résumé

Les pérovskites hybrides halogénées de plomb ont été étudiées au cours de la dernière décennie pour la détection des rayons X. Dans ce travail, $MAPbBr_3$ a été choisi comme matériau pour la détection des rayons X pour l'imagerie médicale. $MAPbBr_3$ présente une bonne absorption des rayons X, des propriétés de transport de charge suffisantes et une croissance en solution simple. La croissance de monocristaux de $MAPbBr_3$ a été optimisée. L'évaluation optoélectronique a montré une bonne sensibilité, mais un courant d'obscurité élevé. Trois approches pour améliorer les performances de $MAPbBr_3$ sont exposés. D'abord, du chlore est ajouté, améliorant le transport des porteurs de charge. Puis, l'importance de l'atmosphère de croissance et du dopage bénéfique que l'eau atmosphérique peut avoir à la surface sont mise en évidence. Enfin, des post-traitements visant à réparer les défauts ponctuels sont introduits. La thèse met l'accent sur le potentiel de $MAPbBr_3$ dans les imageurs médicaux de rayons X.